Real-Time Non-Destructive Inspection and Image Analysis of Carbon Fibre Orientation Using Polarisation Vision

Abdullah F Alzayed

A thesis submitted in partial fulfilment of the requirements for the degree of Doctor of Philosophy

The University of Sheffield
Advanced Manufacturing Research Centre (AMRC)

Submission Date

February 2025

ACKNOWLEDGEMENTS

I am deeply grateful to my parents and siblings for their unwavering love and support throughout my academic journey. I would also like to express my sincere thanks to my wife and children for their constant support, love, and understanding during the challenging times we faced over these years.

I extend my sincere gratitude to the Government of the Kingdom of Saudi Arabia and Prince Sattam bin Abdulaziz University for their generous funding of my PhD studies. This support has been instrumental in my academic development.

I would like to express my sincere gratitude to my supervisors, Patrick Fairclough and Kevin Kerrigan. Professor Patrick is a highly insightful academic who consistently challenged me with thought-provoking questions about my research. These questions often addressed aspects I had not previously considered, significantly enhancing my critical thinking and problem-solving abilities. I deeply appreciate his invaluable guidance in the field of composite materials and his unwavering support throughout the challenging periods of my doctoral studies. Kevin is a distinguished researcher and a leader in the field of composite machining. He provided me with a profound understanding of the key principles and techniques involved in machining composite materials. Furthermore, he supported me in my doctoral journey by closely monitoring my experimental progress and providing invaluable feedback to refine my experimental skills.

A big thank you to all the university staff who supported me in my experimental work, including Jack Leach, Paul Mattinson, Richard Kay, Luke Jones, and Samuel Gibson. I also would like to thank my group research for the knowledge and skills I gained through the group meetings and the useful critical thinking. I would like to express my gratitude to Vaughan Dickinson (Huntsman Corporation) for his help and support in supplying the resin and hardener used in the experimental works. Also, I would like to thank Thomas Bunn and Anthony Williams (OEM Automatic) for their help and technical support with the Polarisation camera. Thank you to Keith

Godber (Chemical Release Company Ltd) for his help and for supplying the release agent used in the experimental work.

To my friends here in Sheffield, thank you so much for all your help and support. I felt we were one family, and celebrating all the events here together and going through difficulties as one person made me feel like I did not leave home.

ABSTRACT

Fibre orientation critically affects the mechanical performance of carbon fibre-reinforced composites. Aligning fibres with the loading direction improves strength and stiffness, while slight misalignments reduce performance. This thesis employs a novel optical technique, primarily a polarisation camera, to study fibre orientation and enhance the efficiency and precision of the Tailored Fibre Placement (TFP) technique.

Carbon fibres reflect polarised light when illuminated by an unpolarised source, allowing the Angle of Linear Polarisation (AoLP) to indicate fibre orientation. XPL software was used to process and display the raw saturation, Degree of Linear Polarisation (DoLP), and fibre orientation images (in RGB and HSV formats) as real-time video. In HSV, the hue channel encodes AoLP, and saturation encodes DoLP. The raw saturation image helps identify over- and underexposed areas, while the grayscale DoLP image shows the polarisation level from 0% to 100%.

During tensile testing, images were captured and analysed using an online inspection rig equipped with a polarisation camera, enabling real-time monitoring of fibre orientation in the HSV colour space. An offline rig was employed to assess the influence of lighting and to accurately evaluate fibre orientation both with and without epoxy. Fibre behaviour under strain was analysed by fitting a Gaussian curve to the AoLP histogram and applying colour thresholding to the hue channel.

This study used a polarisation camera to examine fibre orientation around reinforced holes in Tailored Fibre Placement (TFP) samples during tensile testing. Symmetric and unbalanced loop reinforcements were compared to assess the effect on fibre orientation. The influence of resin-rich areas was also evaluated by varying the machined hole diameter within a constant reinforced area.

The fibre orientation of dry carbon fibre samples with different architectures was initially examined under tension using a polarisation camera. Silicon rubber was then infused to assess orientation at an intermediate stage prior to epoxy resin use. Finally, fibre orientation around machined holes of varying diameters was investigated in woven and unidirectional samples during tensile testing.

The findings suggest that slight changes in the placement of supporting stitching in non-crimp fabric, (the position of the machined hole relative to the thread holding

the carbon fibre), influence the strength of the composites. Furthermore, the results demonstrate that the stitching position of the reinforced hole in the TFP-reinforced hole sample and the loop-back path of the stitching have a notable impact on the sample's mechanical properties.

DECLARATION

I am the author and I confirm that the thesis is my work. This work has not been submitted for other university or to receive another degree.

POSTERS

1. “Optical Inspection of Carbon Fibre’s Orientation Using Polarisation camera”, Composite at Sheffield, University of Sheffield Internal Conference, March 2024.

Table of content

Acknowledgements ii
Abstract iv
Declaration vi
Posters vi
1 Introduction 1
1.1 Aims and objectives 3
1.2 Novelty statement 4
1.3 Thesis outline 5
2 LITERATURE REVIEW 8
2.1 Introduction 8
2.2 Composite materials 8
2.2.1 Matrix 9
2.2.2 Fibre reinforcement 11
2.2.3 Glass fibres 13
2.2.4 Carbon fibres 13
2.3 Fabrics and preforms 15
2.3.1 Weaving 16
2.3.2 Braiding 18
2.3.3 Knitting 20
2.3.4 Non-crimp fabric (NCF) 20
2.3.5 Stitching and Tailored Fibre Placement 21
2.4 Composites Manufacturing methods 21
2.4.1 Wet lay-up 22
2.4.2 Prepreg lay-up 23
2.4.3 Filament winding 23
2.4.4 Liquid moulding 24
2.4.5 Automated fibre placement (AFP) 24
2.5 Fibre orientation 26
2.6 Composite samples containing holes 28
2.6.1 Open-hole tensile testing 29
2.6.2 TFP reinforced hole samples 33
2.7 Composite inspection 35
2.7.1 Non-destructive testing (NDT) and characterisation 36
2.7.1.1 Digital image correlation (DIC) 36
2.7.1.2 Shearography 38
2.7.1.3 3D laser scanning 41
2.7.1.4 Terahertz (THz) imaging 42
2.7.1.5 Polarisation methods 44
2.7.1.6 Summary 48
3 Methodology 50

3.1 Materials 51
3.1.1 Carbon Fibre 51
3.1.2 Glass Fibre 52
3.1.3 Epoxy Resin 52
3.1.4 Silicone Rubber Resin 53
3.2 Manufacturing Composites Panel 53
3.2.1 Vacuum Assisted Resin Transfer Moulding (VARTM) 54
3.2.2 Resin Transfer Moulding (RTM) 55
3.2.3 Composite Panel Curing Cycle 57
3.2.4 Manufacturing TFP preform 58
3.3 Tensile test samples 62
3.3.1 Machining the samples 62
3.3.2 Manufacturing tabs for tensile test samples 65
3.3.3 Preparing the tensile sample's surface 66
3.3.4 Examples of incompletely Impregnated UD-NCF Panels 66
3.1 Characterisation of carbon fibre reinforced polymer (CFRP) 68
3.2 Polarisation camera 70
3.2.1 Introduction 70
3.2.2 Principle 71
3.2.3 Camera's specification 73
3.2.4 Colour map calibration 76
3.3 Experimental set-up 79
3.3.1 The setup using a LED ring lighting source. 79
3.3.2 The modified experimental setup 81
3.4 Examples of offline inspection for samples with a different structure using the polarisation camera. 84
3.4.1 Dry woven carbon fibres 84
3.4.2 Dry Unidirectional (UD) carbon fibre 85
3.4.3 Dry unidirectional non-crimp fibre (UD-NCF) 86
3.4.4 Dry ± 45° non crimp fabric (NCF) 87
3.5 Image processing and analysis 89
3.5.1 Colour thresholding process 90
3.5.2 Gaussian curve fitting 94
3.6 Methodology summary 96
3.7 Aims and objectives of the conducted experiments 97
4 Polarisation analysis of fibre orientation of Dry carbon fibre and impregnated silicone rubber resin during tensile testing 99
4.1 Introduction 99
4.2 Dry sample preparation 100
4.3 Dry carbon fibre 101
4.3.1 Unidirectional carbon fibre (UD) 101
4.3.2 UD non-crimp carbon fibre (UD-NCF) 110

4.3.3 Twill 2x2 carbon fibre 117
4.3.4 Tailored fibre placement (TFP) preform 124
4.3.5 Comparison between different dry carbon fibre architectures .. 139
4.3.6 Discussion 140
4.3.7 Conclusion 143
4.4 Applying silicone rubber resin on carbon fibre 144
4.4.1 Introduction 144
4.4.2 Sample preparation 144
4.4.3 Twill 2x2 carbon fibre 146
4.4.4 Tailored fibre placement preform 152
4.4.5 Discussion 164
4.4.6 Comparison between the dry and silicone-impregnated samples 166
4.4.7 Conclusion 169
5 Polarisation analysis of fibre orientation behaviour around machined holes of carbon fibre composite samples during Open-Hole Tensile Testing 171
5.1 Introduction 171
5.2 Sample preparation 172
5.3 UD-NCF carbon fibre 172
5.4 Twill 2x2 carbon fibre 206
5.5 Conclusion 233
6 Polarisation analysis of fibre orientation of Tailored fibre placement samples with local reinforced hole during tensile testing 236
6.1 Introduction 236
6.2 Sample preparation 236
6.3 Variability 237
6.4 VARTM UD-TFP reinforced hole with four layers 238
6.5 UD-TFP reinforced hole with two layers 265
6.6 Discussion 282
6.7 Conclusion 283
7 Conclusion and Future work 285
7.1 Conclusion 285
7.2 Future work 288
8 Reference 289

List of figures

Figure 1.1 - Illustration of tailored fibre placement (TFP) principle, [reprinted with permission [4]]. 2
Figure 1.2 - illustrates an example of the loop-back path used in manufacturing TFP-reinforced hole preform. The red dashed lines indicate the fibre tow path, which forms curvatures around the reinforced hole. 2
Figure 2.1 - Formation of the composite materials using reinforcement and matrix. 9
Figure 2.2 - Illustration of composite material formation based on the reinforcement and matrix classification. 9
Figure 2.3 - Polymer matrix classification. 11
Figure 2.4 - The difference between lamina and laminate lay-up using unidirectional plies, where (a) shows the fibres in the plies have the same orientation, while (b) shows the plies stacking with different fibre orientations. 12
Figure 2.5 - Illustration of the plain weave pattern, using TexGen..... 17
Figure 2.6 - Illustration of the Twill 2x2 weave pattern, using TexGen 17
Figure 2.7 - Illustration of the four-harness satin weave pattern, Using TexGen.. 18
Figure 2.8 - Braiding machine: (a) schematic of circular braiding process; (b) photograph of circular braiding machine; (c) tracks of spools in opposite directions [reprinted with permission [25]]..... 19
Figure 2.9 - Shows an example of (a) diamond braid (1/1) and (b) regular braid (2/2), [reprinted with permission [26]]..... 20
Figure 2.10 - Principle of tailored fibre placement (a), and typical applications (b and c), [reprinted with permission [35]] 22
Figure 2.11 - Schematic illustrates the resin transfer moulding (RTM). 25
Figure 2.12 - Illustration of the Vacuum assisted resin transfer moulding (VARTM). 25
Figure 2.13 - Illustration of AFP machine with TP head. (A) incoming tape; (B) previously laid layer; (C) compaction roller; (D) heat source; (E) hot gas; (F) nip-point. (Reprinted with permission from [37], IEEE J. Int Info 2020 © IEEE). 26
Figure 2.14 - A CFRP sample with unidirectional fibre orientation under loading represents the influence of the change in the fibre orientations corresponding to the loading direction on the mechanical properties of the material, Reprinted from [50], with permission from Elsevier. 28
Figure 2.15 - Schematic illustrating the tensile failure mode crossing the centre of the hole, where (F) represent the force load direction. 30
Figure 2.16 - Explanation of damage propagation path for different hole sizes machined in specimens, Reprinted from [52], with permission from Elsevier. 31
Figure 2.17 - Schematic presentation of the hole's shapes for open-hole tensile testing, where (a) present the baseline sample without a hole, (b) the circular shape,

(c) square shape, (d) elliptical shape with major axis along the loading direction, and (e) elliptical shape with major axis transverse the loading direction, Reprinted from [65], with permission from Springer Nature. 32
Figure 2.18 - Schematic illustrating the different paths used to create TFP reinforced hole sample, Tailored-hole-1 (b) and Tailored-hole-2 (c), Reprinted from [72], with permission from Elsevier. 34
Figure 2.19 - Snapshots illustrating the tailored fibre placement (TFP) process and the stitching parameters, fixing the fibres to the base material using the zigzag stitch pattern, Reprinted from [50], with permission from Elsevier. 35
Figure 2.20 - Schematic illustrates the typical 2D-DIC inspection method. 37
Figure 2.21 - A Schematic diagram illustrating (a) the photographic shearography; (b) the digital shearography. ([98], reprinted from Optics and Lasers in Engineering, 24, Y.Y.Hung, Shearography for Non-destructive Evaluation of Composite Structures, 161-182, 2000,with permission from Elsevier) 39
Figure 2.22 - HP-C-V3D Apodius Vision System. (a) Absolute Arm; (b) HP-C-V3D Apodius Vision Sensor. 42
Figure 2.23 - Schematic diagram of the THz TDS system in reflection mode, where M1, M2, ..., M8 representing the used mirrors [reprinted with permission from [119]]. 44
Figure 2.24 - Illustration of Brewster's law for the polarizing angle [Redraw from [108]]. 45
Figure 3.1 - Illustration of the VARTM set-up. 55
Figure 3.2 - RTM steel mould, where (a) shows the resin inlet and outlet ports, and (b) shows the direction of the resin flow to infuse the carbon fibre. 56
Figure 3.3 - RTM steel mould inside the hydraulic press. 57
Figure 3.4 - The Thermo Scientific Heraeus (UT 6200) programmable oven (Senna) used for the curing process of panels with epoxy resin and silicone rubber resin. 58
Figure 3.5 - Unidirectional TFP reinforced hole preforms consisting of two and four layers for tensile testing, manufactured by Carbon Three-Sixty. 59
Figure 3.6 - Schematic illustrating the process of manufacturing UD preforms using TFP technique. 60
Figure 3.7 - An example of the gap between the fibres caused by the stitching process during manufacturing a TFP preform, captured using the Alicona. 60
Figure 3.8 - Schematic illustration of the fibre placement and loop-back path used to manufacture the reinforced hole TFP preform. 61
Figure 3.9 - Schematic for baseline and open-hole tensile sample. 64
Figure 3.10 - Machining the UD-TFP reinforced hole samples with different hole diameters into the local reinforcement using the CNC machine (Axiom, AR-8 Pro) and (OSG, DIA-BNC-4) tool. 64

Figure 3.11 - An example of four layers UD-TFP reinforced hole samples with three different hole diameters (12 mm, 10 mm, and 8 mm) were machined into the 12 mm local reinforcement. 65
Figure 3.12 - Example of raw saturation images for Twill 2x2 sample with one layer imaged using the polarisation camera before, (a), and after, (b), sanding process. The yellow area at the bottom of Figure (a) is an overexposed area..... 67
Figure 3.13 - Example of not fully impregnated UD-NCF panels manufactured using the VARTM technique, where (a) shows the UD-NCF panel with 22 layers and (b) UD-NCF panel with 18 layers. 68
Figure 3.14 - Example of not fully impregnated UD-NCF panel with 16 layers manufactured using the RTM technique..... 69
Figure 3.15 - Schematic of the polarisation array used on Sony polarisation camera. 71
Figure 3.16 - The polarisation inspection camera, Sony XCG-CP510 polarised camera. 73
Figure 3.17 - TFP preform captured using the polarisation camera to show the overexposed and underexposed areas in the image (yellow and red, respectively) when choosing the raw (display invalid pixels) option in the XPL software. 74
Figure 3.18 - TFP preform captured using the polarisation camera shows the 4 section images representing different polarisation directions at the same time when choosing the raw (4 split) option in the XPL software. 75
Figure 3.19 - TFP preform captured using the polarisation camera, showing the DoLP image when choosing the (DoLP) option in the XPL software. 77
Figure 3.20 - TFP preform captured using the polarisation camera, showing the fibres' orientation when choosing the (normal surface) option in the XPL software. 77
Figure 3.21 - Carbon fibre tow was captured using the polarisation camera to reference the colours in the HSV colour map to the corresponding fibres' angle after fixing the camera's position. 78
Figure 3.22 - Carbon fibre tow was captured using the polarisation camera to reference the colours in the RGB colour map to the corresponding fibres' angle after fixing the camera's position. 79
Figure 3.23 - The initial inspection set-up using LED ring lighting source. 80
Figure 3.24 - TFP preforms with different fibres' orientations, (Hole reinforcement, Spiral and Unidirectional fibres' orientation), were used to examine the effect of the lighting source on the polarisation camera. 80
Figure 3.25 - TFP preforms with different fibres' orientations [Hole reinforcement (a), Spiral (b), and Unidirectional fibres' orientation (c)] were captured using the polarisation camera to test the influence of the LED ring illumination source on the preforms' structure..... 82

Figure 3.26 - The illumination source (LED strip) was applied to the final inspection set-up to illuminate the sample from four directions to ensure uniform illumination. 82
Figure 3.27 - The modified inspection rig set-up. 83
Figure 3.28 -The unidirectional carbon fibre preform (UD-TFP), shown in Figure 3.25-c, was captured by the polarisation camera using the LED strip as an illumination source..... 83
Figure 3.29 - Dry Twill 2x2 carbon fibre images were captured using the polarisation camera, where (a) shows the raw saturation image, (b) the DoLP image, (c) the raw 4 split image, (d) the fibres' orientation image in HSV colour map and (e) the fibres' orientation image in RGB colour map..... 84
Figure 3.30 - Dry unidirectional (UD) carbon fibre images were captured using the polarisation camera, where (a) shows the raw saturation image, (b) the DoLP image, (c) the raw 4 split image, (d) the fibres' orientation image in HSV colour map and (e) the fibres' orientation image in RGB colour map. 85
Figure 3.31 - The selected regions in the UD carbon fibre, Figure 3.30, show the fibres' orientation in the HSV colour map corresponding to the waviness in the carbon fibres, where the fibres in yellow represent orientations between 20° and 30° while fibres in pink show orientations between 150° and 160° (-30 and -20°). 86
Figure 3.32 - Dry UD-NCF images were captured using the polarisation camera, where (a) shows the raw saturation image, (b) the DoLP image, (c) the raw 4 split image, (d) the fibres' orientation image in HSV colour map and (e) the fibres' orientation image in RGB colour map..... 87
Figure 3.33 - Dry ± 45° NCF carbon fibre images were captured using the polarisation camera, where (a) shows the raw saturation image, (b) the DoLP image, (c) the raw 4 split image, (d) the fibres' orientation image in HSV colour map and (e) the fibres' orientation 88
Figure 3.34 - Defects detecting, such as missing fibre's tow and fibre's misalignment, on the ± 45° NCF carbon fibre by inspecting the carbon fibres' orientation using the polarisation camera. 88
Figure 3.35 - Flow chart illustrate the process of presenting the selected fibre orientation using ImageJ software from the HSV image that captured by the polarisation camera. 91
Figure 3.36 - Example of ImageJ software applied to a Twill 2×2 carbon fibre image captured using the polarisation camera to isolate fibres within a defined orientation range: (a) threshold values selected across the three channels to identify the fibre orientation..... 92
Figure 3.37 - Fibres' orientation image of dry Twill 2x2 carbon fibre was used as an example to show the separation of the fibres' orientation using the ImageJ program, where the fibres in the selected range are presented in white. 93

Figure 3.38 - Flow chart illustrate the process of calculating the mean of the AoLP with increasing strain using MATLAB software..... 95
Figure 4.1 - The online (during tensile testing) fibre orientation inspection setup using the polarisation camera..... 101
Figure 4.2 - Dry UD sample imaged using the polarisation camera, where (a) the raw saturation image, (b) the DoLP image, and (c) the fibres' orientation image. 102
Figure 4.3 - A sequence of fibres' orientation images of dry UD sample captured during tensile testing using the polarisation camera. The strain corresponding to each image is presented above the figure..... 104
Figure 4.4 - The selected region of the fibres' orientation image in the dry UD sample was used to investigate and compare the fibres' angles at 0 % and 0.94 % strain. 105
Figure 4.5 - The selected region of the fibre orientation images in the dry UD sample, where (a) shows the fibre orientation images at different strains and (b) represents the corresponding histogram of the AoLP information (hue channel) in (a)..... 105
Figure 4.6 – MATLAB fitting of Gaussian curve to the histogram of AoLP data for dry UD sample at 0 % and 0.94 % strain..... 106
Figure 4.7 - Separating the fibres' orientation of the selected region image in the dry UD sample at 0 % and 0.94 % strain by separating the colours using a colour threshold..... 107
Figure 4.8 - The mean of the AoLP behaviour for one-layer dry UD sample with increasing strain (for the six selected images in Figure 4.3)..... 109
Figure 4.9 - The mean of the AoLP behaviour for the same sample used in Figure 4.8. The data in red are presenting the fibre orientation for the selected fibre orientation images (Figure 4.3), while data in blue are presenting the fibre orientation for all the captured images in the same sample. 109
Figure 4.10 - The force and position curve for one layer of dry UD carbon fibre sample..... 110
Figure 4.11 - Dry UD-NCF sample captured using the polarisation camera, where (a) the raw saturation image, (b) the DoLP image, and (c) the fibres' orientation, AoLP, image..... 111
Figure 4.12 - A sequence of fibres' orientation images of dry UD-NCF sample captured during tensile testing using the polarisation camera. The strain corresponding to each image is presented above the figure. 112
Figure 4.13 - The selected region of the fibres' orientation image in the dry UD-NCF sample was used to investigate and compare the fibres' angles at 0 % and 1.11 % strain. 113
Figure 4.14 - The selected region of the fibre orientation images in the dry UD-NCF sample, where (a) shows the fibre orientation images at different strains and (b)

represents the corresponding histogram of the AoLP information (hue channel) in (a). 113
Figure 4.15 - MATLAB fitting of Gaussian curve to the histogram of AoLP data for dry UD-NCF at 0 % and 1.11 % strain. 114
Figure 4.16 - Separating the fibres' orientation of the selected region image in the dry UD-NCF sample at 0 % and 1.11 % strain by separating the colours using a colour threshold. 115
Figure 4.17 - The mean of the AoLP behaviour for one-layer dry UD-NCF sample with increasing strain (for the six selected images in Figure 4-12). 116
Figure 4.18 - The mean of the AoLP behaviour for the same sample used in Figure 4-17. The data in red are presenting the fibre orientation for the selected fibre orientation images (Figure 4-12), while data in blue are presenting the fibre orientation for all the captured images in the same sample. 117
Figure 4.19 - The force and position curve for dry, one layer, UD-NCF carbon fibre sample. 117
Figure 4.20 - Dry Twill 2x2 sample captured using the polarisation camera, where (a) the raw saturation image, (b) the DoP image, and (c) the fibres' orientation image. 118
Figure 4.21 - A sequence of fibres' orientation images of dry Twill 2x2 sample captured during tensile testing using the polarisation camera. The strain corresponding to each image is presented above the figure. 119
Figure 4.22 - The selected region of the fibres' orientation image in the dry Twill 2x2 sample to investigate the orientation of the fibres with strain increased. 120
Figure 4.23 - The histogram of the selected region of the dry Twill 2x2 sample with different strains (0 % and 1.78 %), where (a) shows the histogram presenting the AoLP data from the range 0° to 180° and (b) shows the histogram for the same sample after peak shifting process. 121
Figure 4.24 - MATLAB fitting of Gaussian curve to the histogram of AoLP data (after shifting process) for dry Twill 2x2 at 0 % and 1.78 % strain. 121
Figure 4.25 - Separating the fibre's orientation of the selected region image in the dry Twill 2x2 sample at 0 % and 1.78 % strain using a colour threshold. 122
Figure 4.26 - The mean of the AoLP behaviour for one-layer dry Twill 2x2 sample with increasing strain (for the six selected images in Figure 4-21) for the two peaks. 124
Figure 4.27 - The force and position curve for the dry Twill 2x2 sample. 124
Figure 4.28 - The fibres loop-back path of two layers, UD-reinforced hole TFP preform. Image (a) is the raw saturation image and image (b) is the DoLP image captured using the polarisation camera. 125

Figure 4.29 – UD-TFP reinforced hole preform with two layers, captured using the polarisation camera, where (a) the raw saturation image, (b) the DoLP image, and (c) the fibres' orientation image. 126
Figure 4.30 – The fibres' orientation images of TFP reinforced hole preform with two layers were captured using the polarisation camera during the tensile test. The strain corresponding to each image is presented above the figure. 127
Figure 4.31 – The selected region of the fibres' orientation image for the TFP reinforced hole preform with two layers to investigate the AoLP before starting the test at (0 %) strain and (5.06 %) strain. 128
Figure 4.32 – The histogram of the selected region of the dry TFP reinforced hole with two layers sample presenting the AoLP data at different strains (0 % and 5.06 %). 128
Figure 4.33 - MATLAB fitting of Gaussian curve to the histogram of AoLP data for dry TFP reinforced hole with two layers at 0 % and 5.06 % strain..... 129
Figure 4.34 - Separating the fibre's orientation of the selected region image in the dry TFP reinforced hole preform with two layers at 0 % and 5.06 % strain using a colour threshold. 130
Figure 4.35 - The mean of the AoLP behaviour for two-layers of dry TFP reinforced hole preform with increasing strain (for the six selected images in Figure 4-30). 131
Figure 4.36 - The force and position curve for unidirectional TFP reinforced hole preform consists of two layers. 132
Figure 4.37 - UD-TFP reinforced hole preform with four layers captured using the polarisation camera, where (a) the raw saturation image, (b) the DoLP image, and (c) the fibres' orientation image. 133
Figure 4.38 - The fibres' orientation images of TFP-reinforced hole preform consists of four layers were captured using the polarisation camera during the tensile test. The strain corresponding to each image is presented above the figure. 134
Figure 4.39 - The selected region of the fibres' orientation for TFP reinforced hole preform with four layers to investigate the fibres' angles before starting the test (0 %) strain and at maximum force load (4.67 %) strain. 135
Figure 4.40 - The histogram of the selected region of the dry TFP reinforced hole with four layers sample at different strains (0 % and 4.67 %)..... 135
Figure 4.41 - MATLAB fitting of Gaussian curve to the histogram of AoLP data for dry TFP reinforced hole with four layers at 0 % and 4.67 % strain. 136
Figure 4.42 - Separating the fibre's orientation of the selected region image in the dry TFP reinforced hole preform with four layers at 0 % and 4.67 % strain using a colour threshold. 137
Figure 4.43 - The mean of the AoLP behaviour for four-layers of dry TFP reinforced hole preform with increasing strain (for the six selected images in Figure 4-38). 138

Figure 4.44 - The force and position curve for unidirectional TFP reinforced hole preform consists of four layers. 139
Figure 4.45 - Average maximum force load (N) for different dry carbon fibre architectures; the error bar is the standard deviation for three samples. 141
Figure 4.46 - An example of a cured Twill 2x2 sample with one layer that is impregnated with silicone rubber resin, where (a) shows the smooth surface of the carbon, while (b) shows the surface to which the resin was applied. 145
Figure 4.47 - A Twill 2x2 sample, (sample-1), consisting of one layer impregnated with silicone rubber was captured using the polarisation camera, where (a) the raw saturation image, (b) the DoLP image, and (c) the fibres' orientation image. 146
Figure 4.48 - Fibre orientation images of the Twill 2x2 sample, (sample-1), impregnated with silicone rubber resin, consisting of one layer were captured during the tensile test. The stress and strain corresponding to each image during the test are presented above the figure..... 147
Figure 4.49 - The selected region of the fibres' orientation image in the Twill 2x2 sample, with one layer, impregnated with silicone rubber resin to investigate the fibre orientation before starting the test (0 %) strain and with increasing strain to (1.68 %)..... 148
Figure 4.50 - The histogram of the selected region of the one-layer Twill 2x2 sample impregnated with silicone rubber resin at different strains (0 % and 1.68 %), where (a) shows the histogram presenting the AoLP data (before the shifting process) from the range 0° to 180° and (b) shows the histogram for the same sample after peak shifting process. 148
Figure 4.51 - MATLAB fitting of Gaussian curve to the histogram of AoLP data after the shifting process for the Twill 2x2 sample impregnated with silicone rubber resin at 0 % and 1.68 % strain. 149
Figure 4.52 - Separating the fibre orientation of the selected region image in the Twill 2x2 sample, (sample-1), impregnated with silicone rubber resin at 0 % and 1.68 % strain using a colour threshold. 150
Figure 4.53 - The mean of the AoLP behaviour for one-layer Twill 2x2 sample, (sample-1), impregnated with silicone rubber resin, with increasing strain (for the six selected images in Figure 4-48) for the two peaks. 151
Figure 4.54 - The stress and strain curves for three samples of Twill 2x2 carbon fibre impregnated with silicone rubber resin. 152
Figure 4.55 - The TFP-reinforced hole sample images were captured using the polarisation camera, where (a) shows the raw saturation, (b) the DoLP, and (c) the fibres' orientation image. The top row represents the TFP sample with two layers, and the bottom row shows row shows the TFP sample with four layers. 153
Figure 4.56 - Fibres' orientation images of TFP-reinforced hole sample with two layers were captured during the tensile test using the polarisation camera. The

stress and strain corresponding to each image during the test are presented above the figure. 154
Figure 4.57 - The selected region of interest around the reinforced hole of the UD-TFP sample consists of two layers, where (a) shows the fibres' orientation image at different strains and (b) represents the corresponding histogram of the AoLP information..... 155
Figure 4.58 - MATLAB fitting of Gaussian curve to the histogram data of two layers UD-TFP reinforced hole sample at different strains..... 156
Figure 4.59 - Separating the fibre orientation of the selected region image in the UD-TFP reinforced hole sample with two layers at 0 % and 2.68 % strain using a colour threshold..... 156
Figure 4.60 - The mean of the AoLP behaviour for two-layers of dry TFP reinforced hole preform with increasing strain (for the six selected images in Figure 4-56). 158
Figure 4.61 - The stress and strain curve for unidirectional-TFP reinforced hole sample consists of two layers..... 158
Figure 4.62 - Fibres' orientation images of UD-TFP reinforced hole sample with four layers were captured during the tensile test using the polarisation camera. The stress and strain corresponding to each image during the test are presented above the figure. 159
Figure 4.63 - The selected region of interest around the reinforced hole of the UD-TFP sample consists of four layers, where (a) shows the fibres' orientation image at different strains and (b) represents the corresponding histogram of the AoLP data. 160
Figure 4.64 - MATLAB fitting of Gaussian curve to the histogram data of four layers UD-TFP reinforced hole sample at 0 % and 1.92% strain. 161
Figure 4.65 - Separating the fibre orientation of the selected region image in the UD-TFP reinforced hole sample with four layers at 0 % and 1.92 % strain using a colour threshold..... 162
Figure 4.66 - The mean of the AoLP behaviour for four-layers of UD-TFP reinforced hole sample with increasing strain (for the six selected images in Figure 4-62). 163
Figure 4.67 - The stress and strain curve for UD-TFP reinforced hole sample with four layers impregnated with silicone rubber resin. 164
Figure 5.1 - Raw image example of UD-NCF samples consists of two layers with 12 mm hole diameter captured using the polarisation camera. The white streak around the hole results from the machining process 173
Figure 5.2 - The UD-NCF sample, (sample-3), with a 12 mm hole diameter was imaged using a polarisation camera, where images (a-c) are the raw saturation, DoLP and fibre orientation images, respectively. 174

Figure 5.3 - A selected region of interest of UD-NCF sample with 12 mm machined hole around the machined hole to investigate the fibre orientation around the machined hole. 174
Figure 5.4 - The histogram of the AoLP data (a) for the UD-NCF sample with two layers at the selected area around the 12 mm machined hole, (b) shows the MATLAB fitting of Gaussian curve to AoLP data for the fibres with orientations between 60° and 120°. 175
Figure 5.5 - Fibres' orientation images of UD-NCF sample, (sample-3), with two layers and 12 mm machined hole were captured during the tensile test using the polarisation camera. The stress and strain corresponding to each image during the test are presented above the figure. 176
Figure 5.6 - The selected region of interest around the 12 mm machined hole of the UD-NCF sample consists of two layers, where (a) shows the fibres' orientation image at different strains and (b) represents the corresponding histogram of the AoLP data 177
Figure 5.7 - MATLAB fitting of Gaussian curve to the histogram data of two layers UD-NCF sample with 12 mm machined hole at 0 % and 2.12 % strain. 178
Figure 5.8 - Separating the fibre orientation of the selected region image in the two layers UD-NCF sample, (sample-3), with a 12 mm machined hole at 0 % and 2.12% strain using a colour threshold 179
Figure 5.9 - Schematic diagram showing how the weft material affects the fibres when the strain increases. 180
Figure 5.10 - Schematic diagram illustrating the tip points after tensile testing in the carbon fibre sample due to machining the hole [redraw from[52]]. 180
Figure 5.11 - DoLP images for three samples of UD-NCF with a 12 mm hole were captured using the polarisation camera, showing the difference in the warp and weft materials after the machining process. 182
Figure 5.12 - The DoLP images for three UD-NCF samples, shown in Figure 5-11, after failure. 183
Figure 5.13 - The mean of the AoLP changes behaviour for UD-NCF sample, (sample-3), containing a 12 mm machined hole with increasing strain (for the eight selected images in Figure 5-5). 184
Figure 5.14 - The mean of the AoLP behaviour for the UD-NCF sample, (sample-3), with a 12 mm machined hole. The data in red are presenting the fibre orientation for the selected fibre orientation images (Figure 5-5), while data in blue are presenting the fibre orientation for all captured images. 185
Figure 5.15 - The stress and strain curve for three samples of UD-NCF carbon fibre with a 12 mm hole diameter and consisting of two layers. 186

Figure 5.16 - The stress and strain curve for the UD-NCF sample with a 12 mm machined hole (sample-3) and the fibre orientation images representing the dips with increasing the stress are presented. 187
Figure 5.17 - The raw image of the two layers UD-NCF sample with a 10 mm hole diameter captured using the polarisation camera. 188
Figure 5.18 - A two layers UD-NCF sample, (sample-2), with 10 mm hole diameter imaged using the polarisation camera, where images (a-c) are the raw saturation, DoLP and fibre orientation images, respectively. 188
Figure 5.19 - Fibre orientation images of two layers UD-NCF sample, (sample-2), with a 10 mm hole captured during the tensile test using the polarisation camera. The stress and strain corresponding to each image during the test are presented above the figure..... 189
Figure 5.20 - The selected region of interest around the 10 mm machined hole of the UD-NCF sample consists of two layers, where (a) shows the fibres' orientation image at different strains and (b) represents the corresponding histogram of the AoLP data..... 190
Figure 5.21 - MATLAB fitting of Gaussian curve to the histogram data of two layers UD-NCF sample with 10 mm machined hole at 0 % and 1.86 % strain..... 191
Figure 5.22 - Separating the fibre orientation of the selected region image in the two layers UD-NCF sample, (sample-2), with a 10 mm machined hole at 0 % and 1.86 % strain using a colour threshold. 192
Figure 5.23 - DoLP images for three samples of UD-NCF with a 10 mm hole were captured using the polarisation camera, showing the difference in the warp and weft materials after the machining process. 193
Figure 5.24 - The mean of the AoLP changes behaviour for UD-NCF sample, (sample-2), with a 10 mm machined hole with increasing strain (for the seven selected images in Figure 5-19). 195
Figure 5.25 - The stress and strain curve for three samples of UD-NCF carbon fibre with a 10 mm machined hole and consisting of two layers. 196
Figure 5.26 - The stress and strain curve for the UD-NCF sample with a 10 mm machined hole (sample-2) and the fibre orientation images representing the dips with increasing the stress are presented. 196
Figure 5.27 - An example of the raw image of a UD-NCF sample with an 8 mm hole diameter and consisting of two layers was imaged using the polarisation camera. 197
Figure 5.28 - The two layers UD-NCF sample, (sample-1), with an 8 mm hole diameter was captured using the polarisation camera, where images (a-c) are the raw saturation, DoLP and fibre orientation images, respectively. 197
Figure 5.29 - Fibre orientation images of the two layers UD-NCF sample, (sample-1), with an 8 mm hole representing the orientation of the fibres before and during

the tensile test. The stress and strain corresponding to each image during the test are presented above the figure..... 198
Figure 5.30 - The selected region of interest around the 8 mm machined hole of the UD-NCF sample consists of two layers, where (a) shows the fibres' orientation image at different strains and (b) represents the corresponding histogram of the AoLP data..... 199
Figure 5.31 - MATLAB fitting of Gaussian to the histogram data of two layers UD-NCF sample with an 8 mm machined hole at 0 % and 2.70 % strain. 200
Figure 5.32 - Separating the fibre orientation of the selected region image in the two layers UD-NCF sample, (sample-1), with an 8 mm machined hole at 0 % and 2.70 % strain using a colour threshold. 201
Figure 5.33 - The mean of the AoLP changes behaviour for UD-NCF sample, (sample-1), with an 8 mm machined hole with increasing strain (for the eight selected images in Figure 5-29). 203
Figure 5.34 - The stress and strain curve for three samples of UD-NCF carbon fibre with an 8 mm machined hole and consisting of two layers. 203
Figure 5.35 - The average modulus (GPa) is shown as a bar chart for UD-NCF samples, baseline (no hole), and different hole diameters (12,10 and 8) mm, with the error bar as the standard deviation for three samples. 205
Figure 5.36 - Twill 2x2 sample, (sample-3), consisting of one layer, with a 12 mm hole diameter captured using the polarisation camera, where images (a-c) are the raw saturation, DoLP and the fibre orientation, respectively. 206
Figure 5.37 - A selected region of interest around the machined hole, presenting the fibre orientation in the image (c). 207
Figure 5.38 - The histogram of the AoLP data (a: before the shifting process and b: after the shifting process) and the MATLAB fitting of Gaussian curve results after the shifting process (c) for the Twill 2x2 sample with one layer at the selected area around the 12 mm machined hole. 208
Figure 5.39 - The raw saturation and fibres’ orientation images of Twill 2x2 sample, (sample-3), with a 12 mm hole diameter were captured using the polarisation camera before and during the tensile test. The yellow colour in the raw saturation images shows the lighting effect on the sample surface with increasing strain. The stress and strain corresponding to each image during the test are presented above the figure. 209
Figure 5.40 - The selected region of interest around the 12 mm machined hole of the Twill 2x2 sample consists of one layer, where (a) shows the fibres' orientation image at different strains and (b) represents the corresponding histogram of the AoLP data..... 210

Figure 5.41 - MATLAB fitting of Gaussian curve to the histogram of AoLP data after the shifting process for the Twill 2x2 sample with 12 mm machined hole at 0 % and 1.46 % strain. 211
Figure 5.42 - Separating the fibre orientation of the selected region image in the Twill 2x2 sample, (sample-3), with a 12 mm machined hole at 0 % and 1.46 % strain using a colour threshold. 211
Figure 5.43 - A schematic diagram shows the effect of weft fibres on the fibre orientation when strain increases, (sample-3). 212
Figure 5.44 - The fibres' orientation and the corresponding DoLP images for three samples of Twill 2x2 with a 12 mm hole were imaged using the polarisation camera, showing the difference in weft and warp material after machining the hole..... 214
Figure 5.45 - The mean of the AoLP behaviour for a one-layer of Twill 2x2 sample, (sample-3), containing a 12 mm machined hole with increasing strain (for the six selected images in Figure 5.39) for the two peaks. 216
Figure 5.46 - The stress and strain curve for three Twill 2x2 samples, consist of one-layer, with a 12 mm machined hole. 216
Figure 5.47 - Raw image of one-layer Twill 2x2 sample, (sample-2), with 10 mm machined hole captured using the polarisation camera. 217
Figure 5.48 - The one-layer Twill 2x2 sample, (sample-2), with a 10 mm machined hole was captured using the polarisation camera. Images (a-c) present the raw saturation, DoLP, and fibre orientation images..... 217
Figure 5.49 - The raw saturation and fibres' orientation images of the one-layer Twill 2x2 sample, (sample-2), with a 10 mm machined hole were captured using the polarisation camera before and during the tensile test. The stress and strain corresponding to each image during the test are presented above the figure.... 218
Figure 5.50 - The selected region of interest around the 10 mm machined hole of the Twill 2x2 sample consists of one layer, where (a) shows the fibres' orientation image at different strains and (b) represents the corresponding histogram of the AoLP data..... 219
Figure 5.51 - MATLAB fitting of Gaussian curve to the histogram of AoLP data after the shifting process for the Twill 2x2 sample with 10 mm machined hole at 0 % and 0.93 % strain. 220
Figure 5.52 - Separating the fibre orientation of the selected region image in the Twill 2x2 sample, (sample-2), with a 10 mm machined hole, consisting of one layer of fabric, at 0 % and 0.93 % strain using a colour threshold..... 221
Figure 5.53 - The DoLP and the corresponding fibres' orientation images for three samples of Twill 2x2 with a 10 mm hole were captured using the polarisation camera, showing the difference in the weft and warp material at the edge of the machined hole. 222

Figure 5.54 - The mean of the AoLP behaviour for a one-layer of Twill 2x2 sample, (sample-2), containing a 10 mm machined hole with increasing strain (for the six selected images in Figure 5-49) for the two peaks. 223
Figure 5.55 - The stress and strain curve for three Twill 2x2 samples, consist of one-layer, with a 10 mm machined hole. 224
Figure 5.56 - Raw image of one-layer Twill 2x2 sample with 8 mm machined hole captured using the polarisation camera. 224
Figure 5.57 - The one-layer Twill 2x2 sample, (sample-2), with an 8 mm machined hole was captured using the polarisation camera. Images (a-c) present the raw saturation, DoLP, and fibre orientation images. 225
Figure 5.58 - The raw saturation and fibres' orientation images of the one-layer Twill 2x2 sample, (sample-2), with an 8 mm machined hole were captured using the polarisation camera before and during the tensile test. The stress and strain corresponding to each image during the test are presented above the figure. ... 226
Figure 5.59 - The selected region of interest around the 8 mm machined hole of the Twill 2x2 sample consists of one layer, where (a) shows the fibres' orientation image at different strains and (b) represents the corresponding histogram of the AoLP data. 227
Figure 5.60 - MATLAB fitting of Gaussian curve to the histogram of AoLP data after the shifting process for the Twill 2x2 sample with 8 mm machined hole at 0 % and 0.97 % strain. 228
Figure 5.61 - Separating the fibre orientation of the selected region image in the Twill 2x2 sample, (sample-2), with a 12 mm machined hole at 0 % and 1.46 % strain using a colour threshold. 228
Figure 5.62 - The fibres' orientation and the corresponding DoLP images for three samples of Twill 2x2 with an 8 mm hole were imaged using the polarisation camera, showing the difference in weft and warp material after machining the hole. 230
Figure 5.63 - The mean of the AoLP behaviour for a one-layer of Twill 2x2 sample, (sample-2), containing an 8 mm machined hole with increasing strain (for the six selected images in Figure 5-58) for the two peaks. 231
Figure 5.64 - The stress and strain curve for three Twill 2x2 samples, consist of one-layer, with an 8 mm machined hole. 232
Figure 5.65 - The average modulus (GPa) is shown as a bar chart for Twill 2x2 samples, baseline and with different hole diameters (12,10 and 8) mm, with an error bar as the standard deviation for three samples. 233
Figure 6.1 - Examples of manufacturing uncertainty of UD-TFP reinforced hole samples with four layers, (a) shows that sample's width less than what expected, (b) shows the loop-back path, and (c) shows the loop-back position regarding the reinforced hole. 237

Figure 6.2 - Three UD-TFP reinforced hole preforms showing an example of stitch placement around the local reinforced hole. a) shows a lack of stitches in the loop-back, b) shows stitches applying tension on the fibre, c) shows an overlapping between the stitches..... 238
Figure 6.3 - UD-TFP reinforced hole (12 mm local reinforced hole and 12 mm machined hole) sample, (sample-1), with four layers was imaged using the polarisation camera, where (a) the raw saturation image, (b) the DoLP image and (c) the fibres' orientation image. 239
Figure 6.4 - The fibres' orientation images of a four-layer UD-TFP reinforced hole sample, (sample-1) with a 12 mm machined hole were captured during tensile testing using the polarisation camera. The corresponding stress and strain for each image are presented above the figure. 240
Figure 6.5 - The selected region of interest around the reinforced hole of the UD-TFP sample with a 12 mm machined hole, where (a) shows the fibres' orientation image at different strains and (b) represents the corresponding histogram of the AoLP information (hue channel) in (a). 241
Figure 6.6 - MATLAB fitting of Gaussian curve to the histogram data of four layers UD-TFP reinforced hole sample with 12 mm machined hole before starting the tensile test and at maximum load force. 242
Figure 6.7 - The fibres with orientations between ± 5° from the mean of the AoLP in the Gaussian distribution (89.72°) of a four-layer UD-TFP reinforced hole sample, (sample-1), with a 12 mm machined hole are presented in white. Image (a) represents the fibres with orientations between 84.72° and 94.72° for the fibres' orientation image at 0 % strain, while image (b) at strain equals 1.34 %. Image (c) shows the subtracting results of image (b) from image (a). 243
Figure 6.8 - Example of three samples UD-TFP reinforced hole, (before starting the test), with four layers and 12 mm machined hole subjected to tensile test, showing the difference between the samples regarding the loop-back position and fibres orientations, samples' width and the resin at the samples' edge, and stitch position. (a) represents the raw image and (b) the corresponding fibres' orientation image for three samples captured using the polarisation camera. 244
Figure 6.9 - The mean of the AoLP behaviour for sample-1 during the tensile test for the UD-TFP reinforced hole sample with four layers and a 12 mm machined hole. 245
Figure 6.10 - The mean of the AoLP behaviour during the tensile test (of the selected images) for three UD-TFP reinforced hole samples with four layers and a 12 mm machined hole. 246
Figure 6.11 - The mean of the AoLP behaviour during tensile testing (of all images captured during tensile testing) for three UD-TFP reinforced hole samples with four layers and a 12 mm machined hole and the selected images (6-values). 247

Figure 6.12 - The stress and strain curve for three UD-TFP reinforced hole samples with four layers and a 12 mm machined hole. 248
Figure 6.13 - UD-TFP reinforced hole sample, (sample-3), with four layers and a 10 mm machined hole into the 12 mm reinforced hole was imaged using the polarisation camera, where (a) the raw saturation image, (b) the DoLP image and (c) the fibres' orientation image. 248
Figure 6.14 - The fibres' orientation images of a four-layer UD-TFP reinforced hole sample, (sample-3), with a 10 mm hole machined into a 12 mm reinforced hole were captured during tensile testing using the polarisation camera. The corresponding stress and strain for each image are presented above the figure. 249
Figure 6.15 - The selected region of interest around the reinforced hole of the four layers of UD-TFP reinforced hole sample with a 10 mm hole machined into the 12 mm reinforced hole. (a) represent the fibres' orientation images at different strains, and (b) shows the corresponding histogram of the AoLP information in (a). 251
Figure 6.16 - MATLAB fitting of Gaussian curve to the histogram data of four layers UD-TFP reinforced hole sample, with 10 mm hole machined into the 12 mm reinforced hole, before starting the tensile test (0 % strain) and at maximum force load (1.56 % strain). 251
Figure 6.17 - The separation of fibres' orientations of four layers UD-TFP reinforced hole sample, (sample-3), with 10 mm machined hole into 12 mm reinforced hole, using the hue channel information. The fibres with orientations between 85.51° and 95.51° are presented in white, and the other fibres' orientations are in black, where (a) at 0 % strain, (b) at 1.56 % strain, and (c) is the result of subtracting image (b) from (a). 253
Figure 6.18 - The mean of the AoLP behaviour during the tensile test (selected images) for the UD-TFP reinforced hole sample, (sample-3), with four layers and a 10 mm machined hole. 254
Figure 6.19 - The stress and strain curve for three UD-TFP reinforced hole samples with four layers and a 10 mm hole machined into the 12 mm reinforced hole. ... 255
Figure 6.20 - UD-TFP reinforced hole sample, (sample-1), with four layers and an 8 mm machined hole into the 12 mm reinforced hole was imaged using the polarisation camera, where (a) the raw saturation image, (b) the DoLP image and (c) the fibres' orientation image. 256
Figure 6.21 - The fibres' orientation images of a four-layer UD-TFP reinforced hole sample, (sample-1), with an 8 mm hole machined into a 12 mm reinforced hole were captured during tensile testing using the polarisation camera. The corresponding stress and strain for each image are presented above the figure. 257
Figure 6.22 - The selected region of interest around the reinforced hole of the four layers of UD-TFP reinforced hole sample with an 8 mm hole machined into the 12

mm reinforced hole. (a) represent the fibres' orientation images at different strains, and (b) shows the corresponding histogram of the AoLP information in (a). 258
Figure 6.23 - MATLAB fitting of Gaussian curve to the histogram data of four layers UD-TFP reinforced hole sample, with an 8 mm hole machined into the 12 mm reinforced hole, before starting the tensile test (0 % strain) and at maximum force load (1.60 % strain). 259
Figure 6.24 - The separation of fibres' orientations of four layers UD-TFP reinforced hole sample, (sample-1), with 8 mm machined hole into 12 mm reinforced hole, using the hue channel information. The fibres with orientations between 85.64° and 95.64° are presented in white, and the other fibres' orientations are in black, where (a) at 0 % strain, (b) at 1.60 % strain, and (c) is the result of subtracting image (b) from (a). 260
Figure 6.25 - The mean of the AoLP behaviour during the tensile test (selected images) for the UD-TFP reinforced hole sample, (sample-1), with four layers and an 8 mm machined hole. 261
Figure 6.26 - The stress and strain curve for three UD-TFP reinforced hole samples with four layers and an 8 mm hole machined into the 12 mm reinforced hole. ... 262
Figure 6.27 - The average of elastic modulus (GPa) is shown as a bar chart for the UD-TFP reinforced hole samples with four layers, baseline and with different machined hole diameters (12,10 and 8) mm, with an error bar as the standard deviation for three samples. 265
Figure 6.28 - The selected region of interest around the reinforced hole of the two layers of UD-TFP reinforced hole sample, (sample-1), with a 12 mm hole machined into the 12 mm reinforced hole. (a) represent the fibres' orientation images at different strains, and (b) shows the corresponding histogram of the AoLP information in (a). 266
Figure 6.29 - MATLAB fitting of Gaussian curve to the histogram data of two layers UD-TFP reinforced hole sample, with a 12 mm hole machined into the 12 mm reinforced hole, before starting the tensile test (0 % strain) and at maximum force load (0.98 % strain). 267
Figure 6.30 - The separation of fibres' orientations of two layers UD-TFP reinforced hole sample, (sample-1), with 12 mm machined hole into 12 mm reinforced hole, using the hue channel information. The fibres with orientations between 84.24° and 94.24° are presented in white, and the other fibres' orientations are in black, where (a) at 0 % strain, (b) at 0.98 % strain, and (c) is the result of subtracting image (b) from (a). 267
Figure 6.31 - The mean of the AoLP behaviour during the tensile test (selected images) for the UD-TFP reinforced hole sample, (sample-1), with two layers and a 12 mm machined hole. 269

Figure 6.32 - The mean of the AoLP behaviour during tensile testing (of all images captured during tensile testing) for three UD-TFP reinforced hole samples with two layers and a 12 mm machined hole..... 270
Figure 6.33 - The stress and strain curve for three UD-TFP reinforced hole samples with two layers and a 12 mm hole machined into the 12 mm reinforced hole. ... 271
Figure 6.34 - The selected region of interest around the reinforced hole of the two layers of UD-TFP reinforced hole sample, (sample-3), with a 10 mm hole machined into the 12 mm reinforced hole. (a) represent the fibres' orientation images at different strains, and (b) shows the corresponding histogram of the AoLP information in (a). 271
Figure 6.35 - MATLAB fitting of Gaussian curve to the histogram data of two layers UD-TFP reinforced hole sample, with a 10 mm hole machined into the 12 mm reinforced hole, before starting the tensile test (0 % strain) and at maximum force load (1.12 % strain). 272
Figure 6.36 - The separation of fibres' orientations of two layers UD-TFP reinforced hole sample, (sample-3), with 10 mm machined hole into 12 mm reinforced hole, using the hue channel information. The fibres with orientations between 85.31° and 95.31° are presented in white, and the other fibres' orientations are in black, where (a) at 0 % strain, (b) at 1.12% strain, and (c) is the result of subtracting image (b) from (a)..... 273
Figure 6.37 - The mean of the AoLP behaviour during the tensile test (selected images) for the UD-TFP reinforced hole sample, (sample-3), with two layers and a 10 mm machined hole. 275
Figure 6.38 - The stress and strain curve for three UD-TFP reinforced hole samples with two layers and a 10 mm hole machined into the 12 mm reinforced hole. ... 275
Figure 6.39 - The selected region of interest around the reinforced hole of the two layers of UD-TFP reinforced hole sample, (sample-2), with an 8 mm hole machined into the 12 mm reinforced hole. (a) represent the fibres' orientation images at different strains, and (b) shows the corresponding histogram of the AoLP information in (a). 276
Figure 6.40 - MATLAB fitting of Gaussian curve to the histogram data of two layers UD-TFP reinforced hole sample, with an 8 mm hole machined into the 12 mm reinforced hole, before starting the tensile test (0 % strain) and at maximum force load (1.16 % strain). 277
Figure 6.41 - The separation of fibres' orientations of two layers UD-TFP reinforced hole sample, (sample-2), with 8 mm machined hole into 12 mm reinforced hole, using the hue channel information. The fibres with orientations between 82.77° and 92.77° are presented in white, and the other fibres' orientations are in black, where (a) at 0 % strain, (b) at 1.16% strain, and (c) is the result of subtracting image (b) from (a)..... 277

Figure 6.42 - The mean of the AoLP behaviour during the tensile test (selected images) for the UD-TFP reinforced hole sample, (sample-2), with two layers and an 8 mm machined hole. 280
Figure 6.43 - The stress and strain curve for three UD-TFP reinforced hole samples with two layers and an 8 mm hole machined into the 12 mm reinforced hole. ... 280
Figure 6.44 - The average of elastic modulus (GPa) is shown as a bar chart for the UD-TFP reinforced hole samples with two layers and different machined hole diameters (12,10 and 8) mm, with an error bar as the standard deviation for three samples. 281

List of tables

Table 3.1 - Carbon fibre properties..... 51
Table 3.2 - T700S carbon fibre properties..... 52
Table 3.3 - Mechanical properties of cured silicone Rubber..... 53
Table 3.4 - DIA-BNC with 4 mm diameter specifications..... 62
Table 3.5 - DIA-BNC with 4 mm recommended conditions 63
Table 3.6 - Sanding process for tensile samples..... 66
Table 3.7 - The fibre volume fraction for the tested materials..... 70
Table 4.1 - The mean of the AoLP and standard deviation results in the corresponding strain after applying the Gaussian curve fitting to the fibres' orientation images of dry UD sample that were captured during tensile testing, (Figure 4.3)..... 108
Table 4.2 - The mean of the AoLP and standard deviation results in the corresponding strain after applying the Gaussian curve fitting to the fibres' orientation images of dry UD-NCF sample that were captured during tensile testing, (Figure 4-12)..... 115
Table 4.3 - The mean of the AoLP and standard deviation results in the corresponding strain after applying the Gaussian curve fitting to the fibres' orientation images of dry Twill 2x2 sample that were captured during tensile testing, (Figure 4-21)..... 123
Table 4.4 - The mean of the AoLP and standard deviation results in the corresponding strain after applying the Gaussian curve fitting to the fibres' orientation images of dry TFP reinforced hole sample with two layers that were captured during tensile testing, (Figure 4-30)..... 131
Table 4.5 - The mean of the AoLP and standard deviation results in the corresponding strain after applying the Gaussian curve fitting to the fibres' orientation images of dry TFP reinforced hole sample with four layers that were captured during tensile testing, (Figure 4-38)..... 138
Table 4.6 - The average, standard deviation, and coefficient of variation of the maximum force load for dry samples..... 141
Table 4.7 - The mean of the AoLP and standard deviation results in the corresponding strain after applying the Gaussian curve fitting to the fibres' orientation images of the Twill 2x2 sample, (sample-1), impregnated with silicone rubber resin that were captured during tensile testing, (Figure 4-48). 150
Table 4.8 - The mechanical properties of the Twill 2x2 carbon fibre samples impregnated with silicone rubber resin. 152
Table 4.9 - The mean of the AoLP and standard deviation results in the corresponding strain after applying the Gaussian curve fitting to the fibres'

orientation images of UD-TFP reinforced hole sample with two layers that were captured during tensile testing, (Figure 4-56)..... 157
Table 4.10 - The mean of the AoLP and standard deviation results in the corresponding strain after applying the Gaussian curve fitting to the fibres' orientation images of UD-TFP reinforced hole sample with four layers that were captured during tensile testing, (Figure 4-62)..... 163
Table 5.1 - The mechanical properties of three UD-NCF samples with 12 mm hole diameter. 181
Table 5.2 - The mean of the AoLP and standard deviation results in the corresponding strain after applying the Gaussian curve fitting to the fibres' orientation images of two layers UD-NCF sample, (sample-3), with a 12 mm machined hole that were captured during tensile testing, (Figure 5-5). 184
Table 5.3 - The mechanical properties of three UD-NCF samples consist of two layers and contain a 10 mm hole diameter..... 192
Table 5.4 - The mean of the AoLP and standard deviation results in the corresponding strain after applying the Gaussian curve fitting to the fibres' orientation images of two layers UD-NCF sample, (sample-2), with a 10 mm machined hole that were captured during tensile testing, (Figure 5-19). 194
Table 5.5 - The mechanical properties of three UD-NCF samples consist of two layers and contain an 8 mm hole diameter..... 201
Table 5.6 - The mean of the AoLP and standard deviation results in the corresponding strain after applying the Gaussian curve fitting to the fibres' orientation images of two layers UD-NCF sample, (sample-1), with a 8 mm machined hole that were captured during tensile testing, (Figure 5-29). 202
Table 5.7 - The average, standard deviation, and coefficient of variation correspond to the elastic modulus for the baseline and three different hole diameters of UD-NCF samples consisting of two layers. 205
Table 5.8 - The tensile test information for three Twill 2x2 samples, consist of one layer, with a 12 mm machined hole. 214
Table 5.9 - The mean of the AoLP and standard deviation result in the corresponding strain after applying the Gaussian curve fitting to the fibres' orientation images of the one-layer Twill 2x2 sample, (sample-3), with a 12 mm machined hole captured during tensile testing (Figure 5-39). 215
Table 5.10 - The tensile test information for three Twill 2x2 samples, consist of one layer, with a 10 mm machined hole. 221
Table 5.11 - The mean of the AoLP and standard deviation result in the corresponding strain after applying the Gaussian curve fitting to the fibres' orientation images of the one-layer Twill 2x2 sample, (sample-2), with a 10 mm machined hole captured during tensile testing (Figure 5-49)..... 223

Table 5.12 - The tensile test information for three Twill 2x2 samples, consist of one layer, with an 8 mm machined hole. 229
Table 5.13 - The mean of the AoLP and standard deviation result in the corresponding strain after applying the Gaussian curve fitting to the fibres' orientation images of the one-layer Twill 2x2 sample, (sample-2), with an 8 mm machined hole captured during tensile testing (Figure 5-58). 231
Table 5.14-The average, standard deviation and coefficient of variation corresponding to the elastic modulus for the baseline and three different hole diameters of Twill 2x2 samples. 233
Table 6.1 - The tensile test information for three UD-TFP reinforced hole samples with four layers and a 12 mm machined hole. 244
Table 6.2 - The mean of the AoLP and standard deviation results to the corresponding strain after applying the Gaussian curve fitting to the fibres' orientation images that were captured during the tensile test (Figure 6-4), (sample-1). 245
Table 6.3 - Tensile test information for three UD-TFP reinforced hole samples with four layers and a 10 mm machined hole into the 12 mm local reinforcement hole. 253
Table 6.4 - The mean of the AoLP and standard deviation results to the corresponding strain after applying the Gaussian curve fitting to the fibres' orientation images with that were captured during the tensile test (Figure 6-14), (sample-3). 254
Table 6.5 - Tensile test information for three UD-TFP reinforced hole samples with four layers and an 8 mm machined hole into the 12 mm local reinforcement. 260
Table 6.6 - The mean of the AoLP and standard deviation results to the corresponding strain after applying the Gaussian curve fitting to the fibres' orientation images that were captured during the tensile test (Figure 6-21), (sample-1). 261
Table 6.7 - The average, standard deviation and coefficient of variation correspond to the elastic modulus for the baseline and three different hole diameters of the UD-TFP reinforced hole with four layers. 264
Table 6.8 - Tensile test information for three UD-TFP reinforced hole samples with two layers and a 12 mm machined hole into the 12 mm local reinforcement. 268
Table 6.9 - The mean and standard deviation results of the AoLP with increasing strain after applying the Gaussian curve fitting to the fibres' orientation images that were captured during the tensile test for the UD-TFP reinforced hole sample, (sample-1), with two layers and a 12 mm machined hole. 268
Table 6.10 - Tensile test information for three UD-TFP reinforced hole samples with two layers and a 10 mm machined hole into the 12 mm local reinforcement. 273

Table 6.11 - The mean and standard deviation results of the AoLP with increasing strain after applying the Gaussian curve fitting to the fibres' orientation images that were captured during the tensile test for the UD-TFP reinforced hole sample, (sample-3), with two layers and a 10 mm machined hole..... 274
Table 6.12 - Tensile test information for three UD-TFP reinforced hole samples with two layers and an 8 mm machined hole into the 12 mm local reinforcement. 278
Table 6.13 - The mean and standard deviation results of the AoLP with increasing strain after applying the Gaussian curve fitting to the fibres' orientation images captured during the tensile test for the UD-TFP reinforced hole sample, (sample-2), with two layers and an 8 mm machined hole..... 279
Table 6.14 - The average, standard deviation and coefficient of variation correspond to the elastic modulus for the baseline and three different hole diameters of the UD-TFP reinforced hole with two layers. 281

Nomenclature

Symbols

σ_N	Ultimate strength laminate with hole
σ_o	Ultimate strength laminate without hole
θ°	Fibre orientation
ρ_c	Density of composite
ρ_m	Density of matrix
A_r	Mass of one sheet of reinforcement
D	Hole diameter
h	Sample thickness
F	Force
H	Hue channel
K	Stress concentration factor
N_p	Number of sheets
V_f	Fibre content
V_m	Volume of matrix
W	Sample width
W_m	Weight of matrix

Acronyms

AoLP	Angle of linear polarisation
ASC	Average stress criteria
CFRP	Carbon fibre reinforced polymer
CAD	Computer aided design
CNC	Computer numerical control
DIC	Digital image correlation
DoLP	Degree of linear polarisation
DT	Destructive testing
FEA	Finite element analysis
FVF	Fibre volume fraction
HSV	Hue, Saturation, and Value colour space
NCF	Non-crimp fabric
NDE	Non-destructive examination
NDI	Non-destructive inspection
NDT	Non-destructive testing
PAN	Polyacrylonitrile
PEEK	Polyether ether ketone
PSC	Point stress criteria
RGB	Red, Green, and Blue colour space
ROI	Region of interest
RTM	Resin transfer moulding
TFP	Tailored fibre placement
UD	Unidirectional
VARTM	Vacuum assisted resin transfer moulding
VI	Visual inspection
VT	Visual testing

1 INTRODUCTION

Composite materials exhibit high strength-to-weight ratios, a critical advantage in applications demanding lightweight yet strong structures. Composite materials are commonly used in various applications, including aerospace, automotive, wind energy, and sports. Composite materials are fabricated by combining two or more materials, resulting in unique and often superior mechanical properties compared to those exhibited by the individual material [1]–[3].

Many applications of carbon fibre-reinforced polymers (CFRP) require joining the parts either using adhesives or mechanical fixings. Joining composite parts using the mechanical fixings can be achieved using bolts, screws, rivets and pins. These offer the advantage of simplified assembly and disassembly. However, this approach necessitates the introduction of holes into the CFRP components, typically achieved through drilling. These introduced holes create damage and delamination, leading to stress concentration and discontinuity of the carbon fibres, potentially compromising the overall mechanical properties of the joined components [1], [2], [4], [5].

The Tailored Fibre Placement (TFP) manufacturing process offers a solution for manufacturing samples with the required hole diameters without drilling the fibres in the composite parts, which reduces the possibility of delamination caused by the machining process. TFP facilitates the placement of reinforcing fibres in any desired orientation. Figure 1.1 illustrates the principle of the Tailored Fibre Placement (TFP) process, in which a needle is employed to stitch and fix a yarn roving onto the base material. Moreover, various approaches exist for creating localised reinforcement around holes within the TFP preform [4]–[6]. One such approach is the loop-back path, in which the fibre tow is stitched onto the base material until it reaches the edge of the pre-defined reinforced hole. Then, the tow is reversed in direction, forming a curvature as illustrated in Figure 1.2. However, the angular variation between the fibre orientation and the applied load significantly influences the overall strength of the composite material. Even minor deviations in fibre orientation from the optimal loading direction can result in substantial strength reductions, reaching up to 20% of the maximum strength [4], [7]–[9]. Therefore, the accurate

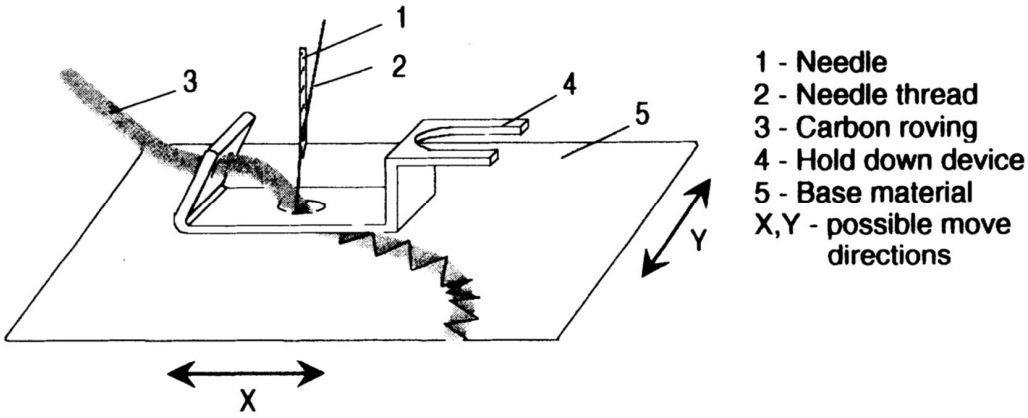


Figure 1.1 - Illustration of tailored fibre placement (TFP) principle, [reprinted with permission [4]].

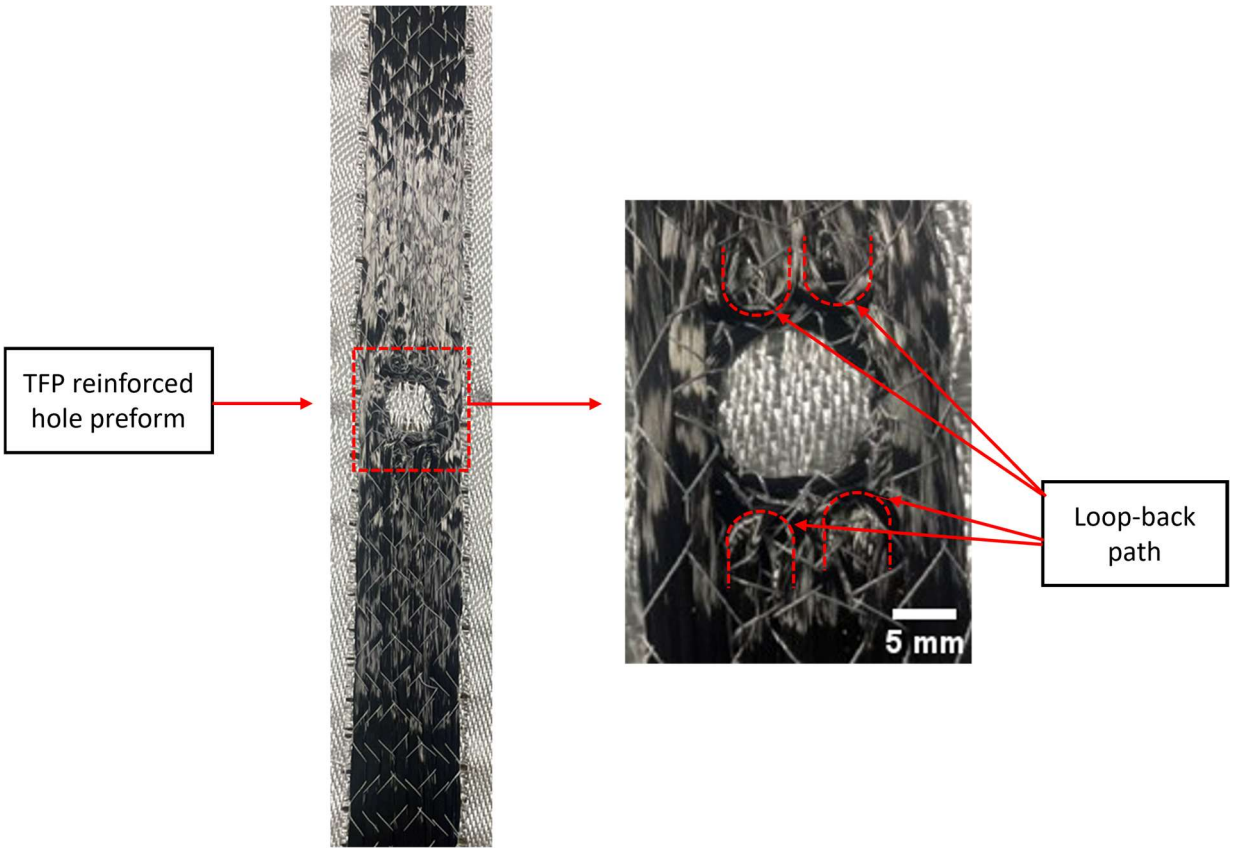


Figure 1.2 - illustrates an example of the loop-back path used in manufacturing TFP-reinforced hole preform. The red dashed lines indicate the fibre tow path, which forms curvatures around the reinforced hole.

determination of fibre orientation is crucial for achieving optimal fibre placement and, consequently, improved performance in TFP carbon fibre reinforced polymer

(CFRP) composites. Therefore, this study aims to investigate the behaviour of fibre orientation within CFRP samples by employing a new camera specifically designed for composite materials to enhance the manufacturing process. The polarisation camera is an optical, non-contact, and non-destructive inspection method capable of visualising carbon fibre orientations in both the dry and consolidated stages of composite fabrication. Various studies have employed polarisation cameras to investigate fibre orientation in different fibre architectures, including both dry and consolidated carbon fibre samples [10]–[13]. The present work uniquely examines, for the first time, the behaviour of fibre orientation around machined holes during tensile testing in real-time using the polarisation camera.

1.1 Aims and objectives

This thesis aims to inspect and analyse the fibre orientation behaviour of the UD-TFP samples containing local hole reinforcement during tensile testing to understand its effect on the mechanical properties. The inspection is conducted using an optical, non-contact, and non-destructive inspection technique, primarily the polarisation camera. Moreover, this study will contribute to the development and enhancement of the TFP manufacturing process by monitoring fibre orientation using a polarisation camera during fibre placement, thereby ensuring accuracy. The focus is on the orientational behaviour of carbon fibres located around the machined hole samples and the loop-back fibre placement path.

In order to achieve the intended outcome, the following objectives have been established:

- Conducting a literature review of the fibre orientation of carbon fibre composite samples to understand the fundamental effect of the fibre orientations on the mechanical properties. Also, a literature review on the open-hole tensile testing of CFRP samples is undertaken to understand the failure mechanism and stress distribution around the machined hole. Finally, a literature review of optical, non-destructive, and non-contact inspection techniques is applied to CFRP samples to understand the capabilities and limitations of the utilised inspection techniques in detecting defects.
- Understanding the tailored fibre placement (TFP) process and the fibre placement paths used to create a reinforced hole (local reinforcement) when manufacturing open-hole tensile testing preforms. The polarisation camera is employed to assess the fibre orientations of the manufactured

preforms, enabling the evaluation of fibre placement accuracy and supporting the enhancement of the manufacturing process.

- Outline the research methodology used to manufacture and machine the CFRP samples and prepare them for tensile testing. Build an offline and online inspection rig (before and during tensile testing, respectively) to ensure the lighting source does not affect the inspection process. The influence of lighting is examined during tensile testing to determine the optimal conditions for monitoring fibre orientation during the fibre placement stage of the TFP process. Also, the fibre orientation results obtained by the polarisation camera are validated by applying colour to angle reference and offline testing of different carbon fibre architectures.
- Studying the orientational behaviour of carbon fibres within a carbon fibre composite material around the machined hole during tensile testing using the polarisation camera. Different fibre architectures with different hole diameter sizes are employed to understand the effects of these parameters on the fibre orientation behaviour.

1.2 Novelty statement

The novelty of this thesis consists of using the polarisation camera to understand the effect of the fibre orientation behaviour during tensile testing on the mechanical properties of the unidirectional tailored fibre placement (UD-TFP) with reinforced hole to improve the manufacturing process. Furthermore, the effect of the resin-rich area around the machined hole on the loop-back path of carbon fibre orientation, as well as the stitching threads' position with respect to the machined hole edges, is discussed.

The polarisation camera is an optical, non-contact, and non-destructive inspection technique which has the ability to determine the carbon fibre orientation information, where the carbon fibres polarise light on reflection when illuminated by an unpolarised source.

Fibre orientation of the dry carbon fibre with different architectures is inspected on the offline stage (i.e., no tension applied) using the polarisation camera to validate

the accuracy of the angle representations obtained by the polarisation camera. Second, understanding the lighting effect on the carbon fibre in the dry and composite cases is ensured to avoid any loss in the data will occur due to the reflections from overexposed areas. Third, the fibre orientation behaviour of dry carbon fibre with different architectures is inspected during tensile testing to gain a better understanding of the fundamentals of fibre orientation response with increasing strain. Fourth, to understand the fibre orientation behaviour in composite materials, silicone rubber resin is used to impregnate the samples and act as soft resin (i.e., the samples are in the stage between a dry and infused with epoxy resin) and the polarisation camera is used to inspect the fibre orientation during the tensile test. Fifth, machined holes with different diameters are applied to the non-crimp fabric (NCF) and woven carbon fibre to study the fibre orientation behaviours around the machined holes during tensile testing using the polarisation camera. Also, the effect of the position of the machined hole with respect to the warp material on the fibre orientation and the mechanical properties of the tested samples is analysed. Finally, holes with three different diameters are machined into the local reinforced hole of the tailored fibre placement (TFP) samples to inspect the behaviour of fibre orientations around the local reinforced hole during the tensile test using the polarisation camera. The holes with smaller diameters than the local reinforced hole are machined to inspect the fibre orientation behaviour near the resin-rich area. Also, the effect of the fibre orientation on the loop-back path and stitching position near the local reinforced hole on the mechanical properties is investigated.

1.3 Thesis outline

This thesis is organised into seven chapters, which explore:

- Introduction (chapter 1): This chapter defines the research's primary aim and objectives and states the novelty statement of the proposed work.
- Literature review (chapter 2): This chapter reviews composite materials, including the manufacturing process and non-destructive inspection techniques. It also discusses the effect of fibre orientations, machined holes, and reinforced holes on mechanical properties. Moreover, the polarisation method is discussed as an inspection method for carbon fibre composite materials, primarily to determine the fibre orientation.

- Methodology (chapter 3): This chapter presents the materials and processes used to manufacture the CFRP samples, including carbon fibre, glass fibre, epoxy resin, silicon rubber resin, the Vacuum Assisted Resin Transfer Moulding (VARTM) method, and the Resin Transfer Moulding (RTM) method. It also presents the concept of fibre orientation inspection using polarisation, illustrated by images captured by the polarisation camera. The methodology for manufacturing the UD-TFP reinforced-hole preform is presented, along with the inspection of fibre orientation across different preforms. This approach enables the evaluation of online inspection during the TFP process by employing a polarisation camera to ensure accurate fibre placement. Moreover, the process of preparing the tensile test sample's surface for online inspection (during tensile testing) to overcome the lighting effect during the inspection using the polarisation camera is explained.
- Polarisation analysis of fibre orientation of dry carbon fibre and impregnated silicone rubber resin during tensile testing (chapter 4): In this chapter, dry carbon fibre samples with different architectures are subjected to tensile testing, and the fibre orientation is inspected using a polarisation camera to understand how it responds during the tensile testing in the composite samples. Also, this chapter studies the fibre orientation behaviour of the carbon fibre when the samples are impregnated with silicone rubber resin as an intermediate stage between dry samples and samples infused with epoxy resin. Online inspection carried out during tensile testing using a polarisation camera is employed to identify the factors influencing inspection efficiency, such as lighting conditions. The insights gained from this stage are taken into account in order to establish a reliable inspection setup for fibre monitoring during the TFP manufacturing process.
- Polarisation analysis of fibre orientation behaviour around machined holes of carbon fibre composite samples during open-hole tensile testing (chapter 5): This chapter presents the fibre orientation behaviour of non-crimp fabric and woven carbon fibre with three machined hole diameters inspected using the polarisation camera during tensile testing. It also presents the possible effect of the machined hole position corresponding to the weft material on the mechanical properties. The size of the machined hole and the resulting tip point on the machined hole edges are discussed. The analysis of fibre

orientation behaviour around machined holes provides valuable insights for improving the manufacturing of reinforced-hole TFP preforms.

- Polarisation analysis of fibre orientation of tailored fibre placement samples with local reinforced hole during tensile testing (chapter 6): In this chapter, the fibre orientation behaviour of the tailored fibre placement (TFP) samples with locally reinforced holes is inspected during tensile testing using the polarisation camera. Three machined holes with different diameters are machined into the local reinforced hole to investigate the effect of the resin-rich area around the machined hole. Additionally, the impact of fibre orientation on the fibre's loop-back path when creating the local reinforced hole is inspected during the tensile test using the polarisation camera. The analysis evaluates the accuracy of fibre placement around the reinforced hole and examines the influence of loop-back path variations on the mechanical properties. Thus, monitoring fibre orientations during the manufacturing process enhances the reliability and efficiency of TFP reinforced hole preforms.
- Conclusion and future work (chapter 7): The conclusions of the results obtained from the experimental work and suggested future work are presented in this chapter.

2 LITERATURE REVIEW

2.1 Introduction

This chapter introduces the fundamental concepts of composite materials, with a particular emphasis on carbon fibre. The manufacturing processes employed in the fabrication of composite samples will be outlined. Furthermore, the critical influence of carbon fibre orientation on the resulting mechanical properties of the composite will be discussed. Finally, this chapter will explore the implementation of optical non-destructive inspection techniques on composite materials and their advantages and limitations. Optical non-destructive inspection techniques used for assessing the fibre orientation within carbon fibre composites will also be discussed.

2.2 Composite materials

Composite materials are two or more materials that are combined, resulting in a material with improved properties compared to the separate materials. This is commonly termed a synergistic combination. The composite materials consist of at least two components, which are the reinforcement and matrix, as shown in Figure 2.1. Composite materials have existed in nature for a long time. One example of a natural composite is wood, which consists of cellulose fibres as the reinforcement and lignin as the matrix. There are many advantages of using composite materials, primarily in engineering fields, such as their high strength, stiffness, and low weight. The reinforcement phase provides the strength and stiffness properties because, in most cases, the matrix is not as strong and stiff as the reinforcement. Composite materials were commercialised because of their properties and the ability to be designed and manufactured for many applications, such as aerospace parts, automotive parts and sporting goods [1], [14], [15].

Composite materials can be classified using various criteria, including the type of reinforcement and the matrix material. The matrix can be metallic, ceramic, or polymeric. Reinforcement can take the form of fibres and/or particles. Fibres can be further divided into continuous (long) or short fibres. Continuous fibres are commonly carbon, glass, aramid, or natural sources. Figure 2.2 summarises the different classification methods for composite materials[14].

The focus of this thesis will be on the carbon fibre as reinforcement and polymer (epoxy) as matrix.

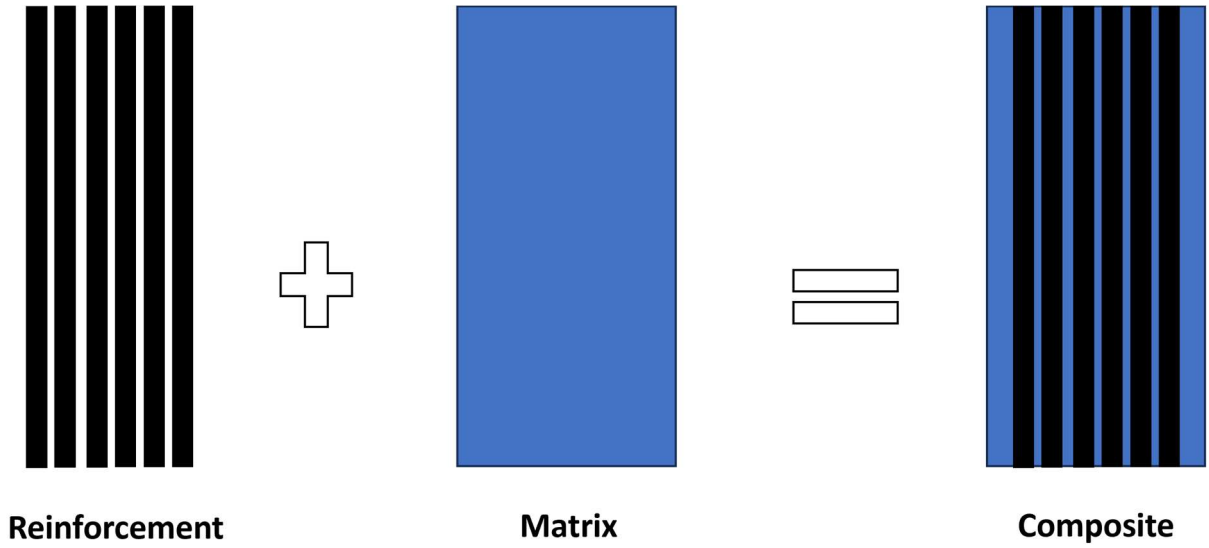


Figure 2.1 - Formation of the composite materials using reinforcement and matrix.

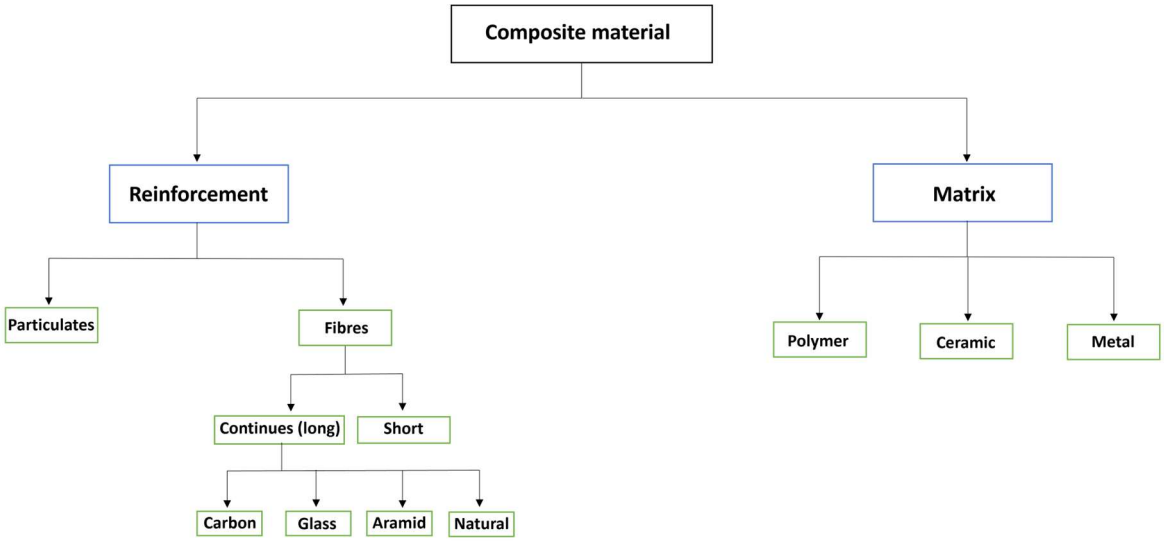


Figure 2.2 - Illustration of composite material formation based on the reinforcement and matrix classification.

2.2.1 Matrix

The matrix within a composite material serves several critical functions. It acts as a binding agent, maintaining the alignment of the reinforcing fibres and protecting the fibres from abrasion and corrosion. While the reinforcement provides the primary

strength and stiffness, the matrix is essential for enhancing the composite's overall toughness, improving its ability to withstand damage and impact loads. There are different types of matrices, such as polymer matrices, metal matrices, and ceramic matrices. Polymer matrices can be classified into two categories: thermosets and thermoplastics [1], [15]–[17].

Thermosets are a class of polymers characterized by their cross-linked structure, rendering them infusible upon heating. This three-dimensional network arises from chemical reactions that form the bonds from the short chains. Owing to their short chain lengths, thermosets possess low viscosity in their uncured state. Epoxy resins, alongside polyesters and vinylesters, are commonly encountered thermosetting materials. While polyesters and vinylesters offer lower production costs, epoxy resin is more prevalent in applications because it has less shrinkage during the curing process than polyesters and vinylesters. Furthermore, fibre-reinforced epoxy composites exhibit enhanced fatigue resistance compared to those reinforced with polyester resins [1], [14]–[17].

Thermoplastics are a class of polymers that can be repeatedly melted and solidified. Their high viscosity in the molten state poses a challenge for effective fibre impregnation, potentially resulting in poor-quality composite materials. For this reason, high temperatures and pressures are required during the infusion process. Common examples of thermoplastic resins encompass polyethylene, polystyrene, and polyether ether ketone (PEEK).[1], [14]–[17].

The present research will utilize a polymer matrix with epoxy resin as the primary focus. A classification of polymer matrices, along with illustrative examples of different resin types, is presented in Figure 2.3.

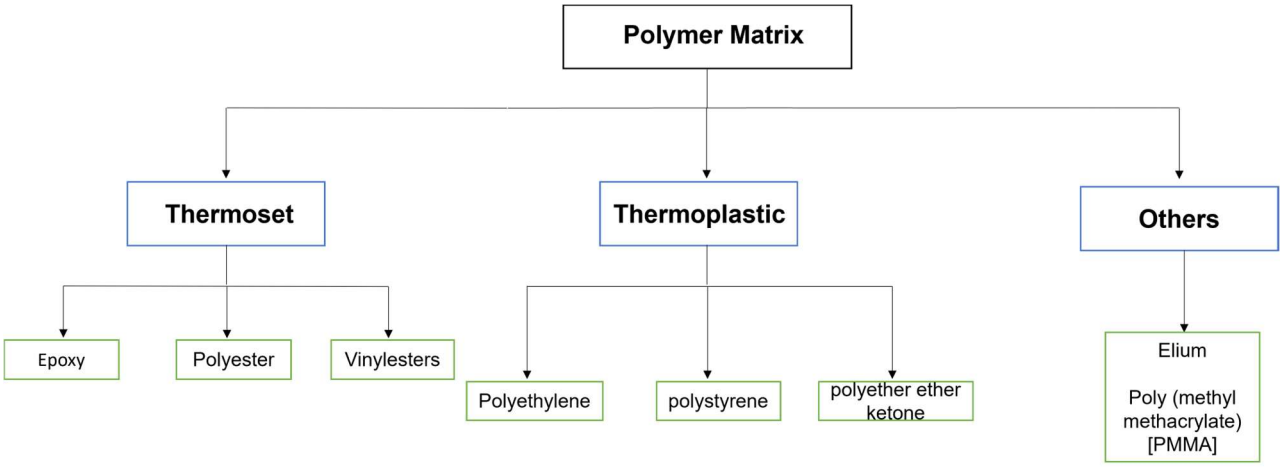


Figure 2.3 - Polymer matrix classification.

2.2.2 Fibre reinforcement

Fibre and particulate reinforcements are two commonly employed types to form the reinforcement. Particulate composites ideally exhibit near-uniform distribution throughout the matrix. The particles may possess regular or irregular geometries. Compared to continuous fibre composites, particulate composites generally exhibit lower strength and stiffness. Moreover, the high viscosities inherent in particulate systems present processing challenges and limit the achievable particulate concentrations within the matrix. Fibres are available in a diverse range of materials, lengths, and diameters. The cross-sectional geometry of the fibre significantly influences its strength; consequently, decreasing the cross-sectional area can enhance fibre strength. Based on diameter, fibres can be classified as follows: nanofibers (diameter ≤ 100 nm), microfibres (diameter between 0.1 and 1 μm), and the more common carbon and glass fibres (diameter between 1 and 10 μm). Fibres with diameters exceeding 10 μm are often termed 'rough fibres'."[1].

Continuous fibres are characterised by a significant length-to-diameter ratio and are typically aligned in a specific direction to optimise material properties. Common fabric types incorporating continuous fibre reinforcement include unidirectional, woven, 3D, and braided fabrics. Unidirectional fabrics can be produced as single-direction structures (aligned in a single direction, e.g., 0° or 90°) or as multi-directional structures (aligned in both 0° and 90° directions). Woven fabrics exhibit

diverse structural arrangements, encompassing plain, twill, satin, basket, and leno weaves [1], [14], [16].

The lay-up of fibre reinforcement involves stacking individual plies on top of one another. When all plies within a stack exhibit the same fibre orientation, the resulting structure is termed a lamina. Conversely, laminates are formed when plies are stacked with varying fibre orientations. Figure 2.4 provides a schematic representation of both lamina (a) and laminate (b) configurations. In the lamina (a), all fibre plies are aligned in a single direction (0°). In contrast, the laminate (b) showcases plies with diverse orientations (90°, 45°, and 0°); these specific orientations are employed solely for illustrative purposes [1].

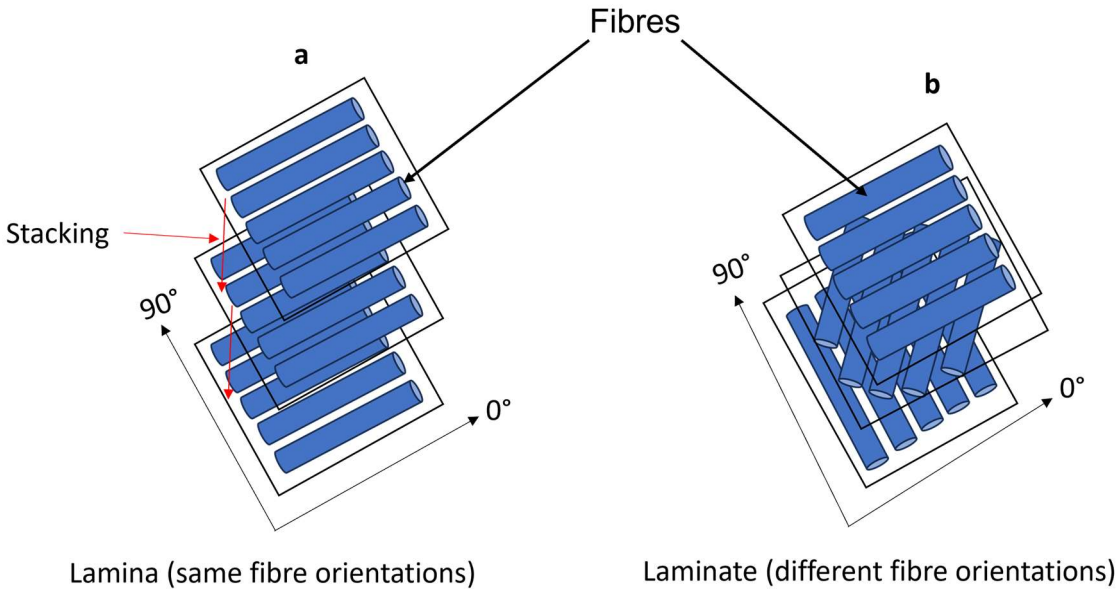


Figure 2.4 - The difference between lamina and laminate lay-up using unidirectional plies, where (a) shows the fibres in the plies have the same orientation, while (b) shows the plies stacking with different fibre orientations.

This research investigates the use of fibre-reinforced composites, with a particular focus on carbon fibre as the primary reinforcement material. Other common fibre types include glass fibre, aramid fibre, and natural fibres. While this study will primarily employ carbon fibre, glass fibre will serve as the base material for fabricating carbon fibre preforms through the Tailored Fibre Placement (TFP) technique.

2.2.3 Glass fibres

Glass fibres are manufactured by melting the raw material within a furnace and extruding it through multiple platinum bushings. Owing to their advantageous properties, glass fibres find extensive application in a wide range of composite materials. A key economic benefit of glass fibre is its significantly lower cost than carbon fibre. Various types of glass have been utilised in composite materials, with E-glass being the most prevalent. The designation 'E' signifies its excellent electrical properties, in addition to its desirable strength and stiffness. The typical diameter of E-glass fibres lies within the range of 8 µm to 15 µm [1], [16].

The selection of glass fibre type is determined by the desired properties. For instance, C-glass may be favoured over E-glass due to its superior corrosion resistance. Conversely, E-glass exhibits greater strength compared to C-glass. S-glass, the third type, possesses enhanced temperature resistance and higher strength than E-glass, although at a higher cost [16].

The isotropic nature of glass fibre results in its axial and transverse Young's modulus being equal. While glass fibre exhibits favourable properties such as high tensile strength and impact resistance, these properties are lower than those of carbon fibre [1], [16].

2.2.4 Carbon fibres

Due to their exceptional properties, carbon and graphite fibres are widely utilised in high-performance composite materials. These fibres exhibit a favourable combination of high tensile and compressive strength, excellent corrosion resistance, and high modulus, making them highly desirable for advanced applications [1].

While the terms 'graphite' and 'carbon fibres' are often used interchangeably, they have distinct differences. One key difference lies in their heat treatment processes. Furthermore, graphite fibres exhibit a substantially higher carbon content, exceeding 99%, whereas carbon fibres typically possess a lower carbon content, ranging between 93% and 95% [1].

Carbon fibres typically have a diameter of 8 µm. Three primary starting materials are used for carbon fibre production: polyacrylonitrile (PAN) fibres, mesophase pitch, and pyrolytic deposition. PAN fibres are generally considered preferable for producing carbon fibres with a high modulus. The widespread use of PAN for carbon fibre production stems from its higher carbon yield. For instance, the carbon yield from PAN is nearly double that of rayon fibres, although rayon fibres are less expensive than PAN [1], [16].

The production of carbon fibres from polyacrylonitrile (PAN) involves a multi-stage process. Firstly, the copolymer PAN undergoes either wet or dry spinning, followed by stretching to form the initial fibre structure. Subsequently, a stabilisation step is crucial to enhance structural stability and prevent degradation during the subsequent carbonisation phase. This involves controlled heating to convert the polymer structure, preparing it for the high-temperature environment.
Carbonisation, conducted under a nitrogen atmosphere at temperatures between 980°C and 1595°C, transforms the stabilised PAN into a carbon-rich material. This process results in the formation of “turbostatic graphite”, characterised by a preferred alignment of hexagonal carbon ribbons parallel to the fibre direction.
Graphitisation, the final high-temperature treatment (1980°C to 3040°C), further enhances the carbon structure, increasing its crystallinity. The degree of graphitisation significantly influences the fibre's modulus, with higher temperatures yielding higher modulus fibres.
Finally, surface treatment and sizing are applied to remove weak surface layers and improve the fibre's handling and compatibility within the composite matrix. Sizing agents provide protection and enhance the cohesion of individual filaments within the fibre bundle [1].

The second route employed for carbon fibre production involves mesophase pitch. Carbon and graphite fibres manufactured using the pitch process are derived from heating coal tar pitch for up to 40 hours at 425°C. This heating process of coal tar pitch yields a well-known liquid termed 'mesophase'. Mesophase is a liquid characterised by high viscosity and a significant degree of molecular order. Fibres produced from pitch can be categorised as isotropic pitch fibres and mesophase pitch fibres. Mesophase pitch fibres exhibit distinct characteristics compared to

isotropic pitch fibres. In terms of cost, mesophase pitch fibres are generally more expensive than isotropic pitch fibres. However, the use of mesophase pitch fibres results in fibres with a higher modulus [1], [16].

The third method employed for carbon fibre production is pyrolytic deposition. However, the fibres produced through this method find limited commercial application due to difficulties in accurately controlling fibre diameter.

2.3 Fabrics and preforms

The term 'preform' designates the arrangement of fibrous materials, such as fibres, yarns, or fabrics, prior to the introduction of a matrix. Carbon and glass fibres, known for their high modulus, are commonly employed to construct these preforms. Subsequent to performing, the structure of the composite is achieved through a curing process [18], [19].

From the perspective of manufacturing composite preforms, some examples of the common methods are weaving, knitting, and braiding. A key advantage of textile preforms lies in their ability to precisely control fibre displacement. Furthermore, textile preforms significantly enhance the mechanical performance of composite materials, notably in terms of damage tolerance and impact resistance [18]–[20].

Composite preforms can be categorised into one-dimensional (1-D), two-dimensional (2-D), or three-dimensional (3-D) forms. 1-D preforms, such as fibre tows and spun yarns, exhibit an unbalanced architecture suitable for applications requiring symmetry in the axial direction relative to the fibre orientation. 2-D weaving is the most prevalent method for manufacturing preforms. The 2-D weaving process involves interlacing two orthogonal sets of threads: the weft and the warp. 3D fabrics can be produced using the 2D weaving technique by incorporating a specific method to introduce a through-thickness direction (z-direction). In this approach, warp and weft yarns are interlaced with binder warp yarns to create interlaced 3D fabrics [18], [21], [22].

2.3.1 Weaving

The fabrics employed within the composites industry can be classified into woven and non-crimp fabrics. Typically, fabrics resulting from 2D weaving exhibit a fibre orientation structure usually (0°, 90°). Woven fabrics are manufactured using two sets of yarns, known as warp and weft, which are perpendicular to each other and interlaced using a loom. The initial step involves separating the warp yarns and subsequently inserting the weft yarns between them. Ordinarily, the warp and weft are composed of the same material type. However, in instances where specific properties are required, hybrid weaves are utilised, wherein the material employed for the warp differs from that of the weft. Combining carbon fibres with glass fibre or carbon with aramid exemplifies hybrid weaves that give advantages in achieving desired properties. One such example is toughness, which can be attained by incorporating aramid with carbon. Moreover, combining glass with carbon fibres contributes to a reduction in production costs. A variety of weave types exist, including the fundamental weave types: plain, twill, and satin [1], [14].

Plain weave, characterised by its straightforward over-and-under interlacing of weft and warp yarns, represents the most basic weaving structure. This dense interlacement contributes to superior shear resistance within the fabric plane. However, the high degree of fibre interlacing inherent in plain weave can impede drapability [1], [16], [18], [23]. Figure 2.5 provides a visual representation of the plain weave pattern.

Twill weave fabric is characterised by a distinctive diagonal pattern resulting from a specific weaving technique. Weft yarns interlace with warp yarns in a staggered manner, passing over and under two or more warp yarns successively. This creates the characteristic diagonal lines visible on the fabric's surface. Compared to plain weave, twill weave exhibits superior drapability and wettability. Furthermore, it generally has lower crimp, the waviness of the fibres, which significantly influences mechanical properties, and fewer interlacing points between fibres [1], [16], [18], [23]. A visual representation of a 2x2 twill weave pattern is provided in Figure 2.6.

.

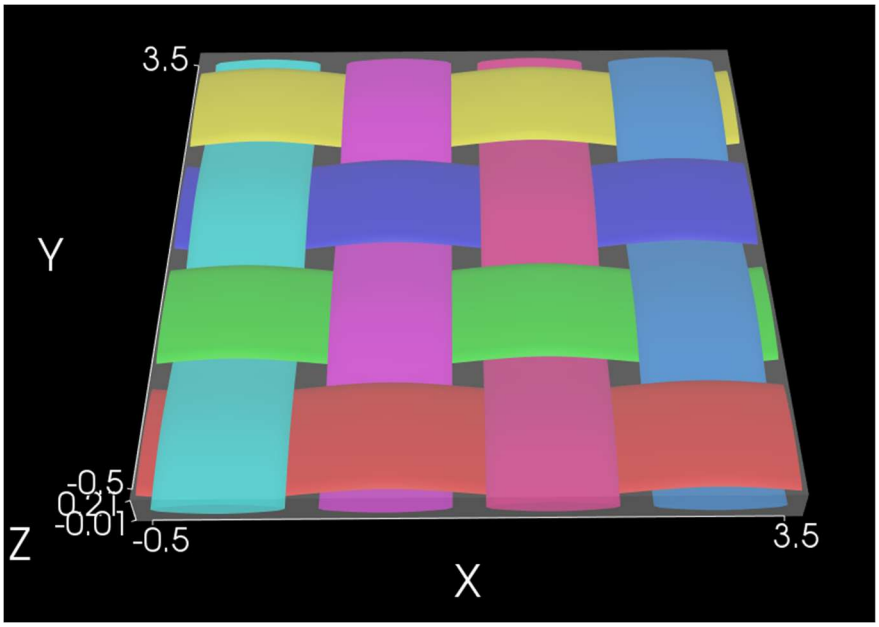


Figure 2.5 - Illustration of the plain weave pattern, using TexGen.

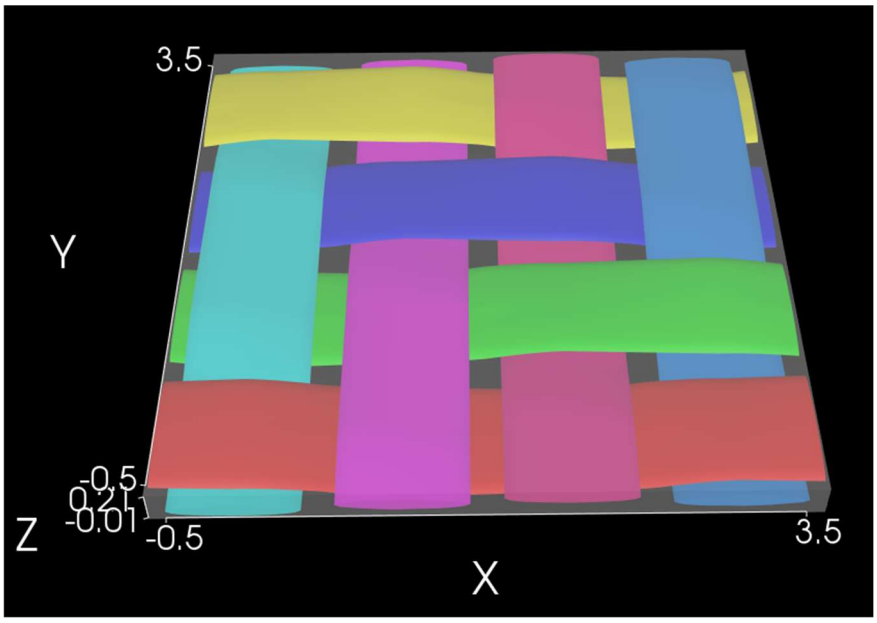


Figure 2.6 - Illustration of the Twill 2x2 weave pattern, using TexGen

The satin weave exhibits fewer interlacing fibres, resulting in lower in-plane shear resistance compared to plain weave. However, satin weave demonstrates superior drapability and lower crimp than both plain and twill weaves. In a four-harness satin weave, weft yarns pass over three warp yarns before interlacing with a single warp yarn. Similarly, in five- and eight-harness satin weaves, weft yarns pass over four

and seven warp yarns, respectively, followed by interlacing with a single warp yarn [1], [16]–[18], [23]. Figure 2.7 illustrates the pattern of a four-harness satin weave.

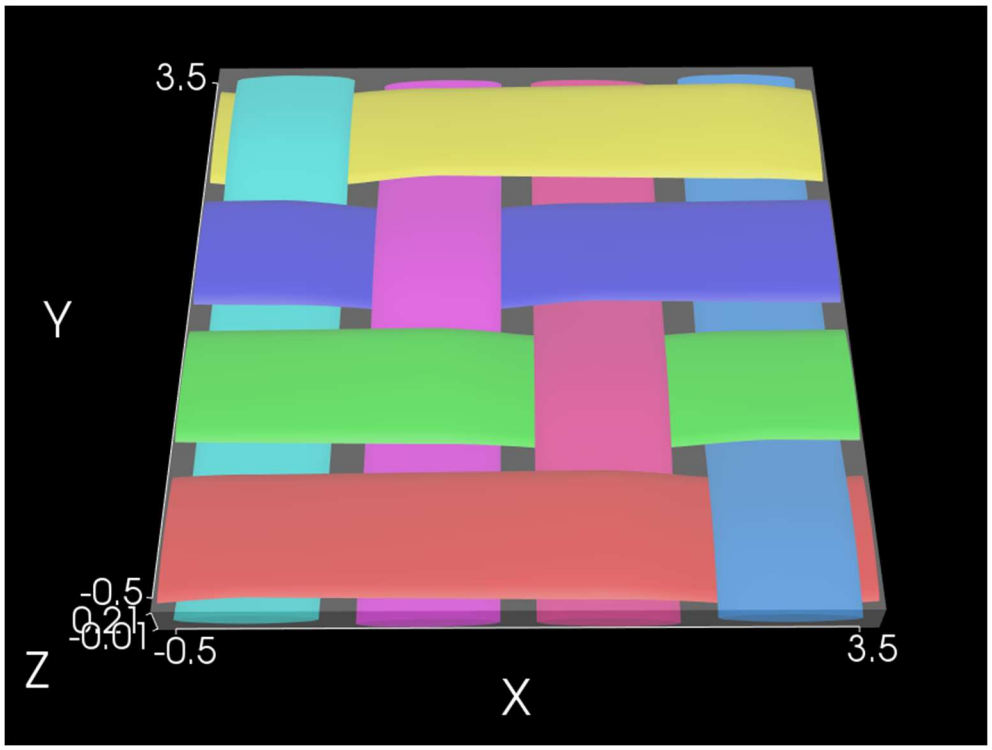


Figure 2.7 - Illustration of the four-harness satin weave pattern, Using TexGen.

2.3.2 Braiding

The braiding process, with origins in textile manufacturing in the early 19th century, has evolved into a significant technique for producing composite material preforms. This method offers a key advantage: enhanced through-thickness strength. Central to the braiding process is a mandrel, around which dry fibres are precisely arranged (Figure 2.8). These fibres interlace in helical and longitudinal orientations, resulting in the formation of single or multiple braided preform layers. Braided preforms exhibit numerous benefits, including improved damage tolerance and greater design flexibility. Furthermore, the automated nature of the braiding manufacturing process contributes to its cost-effectiveness [1], [14], [18], [24].

The braiding machine controls numerous process parameters, including the rate at which mandrels are fed through the machine's centre and the carriers' rotational

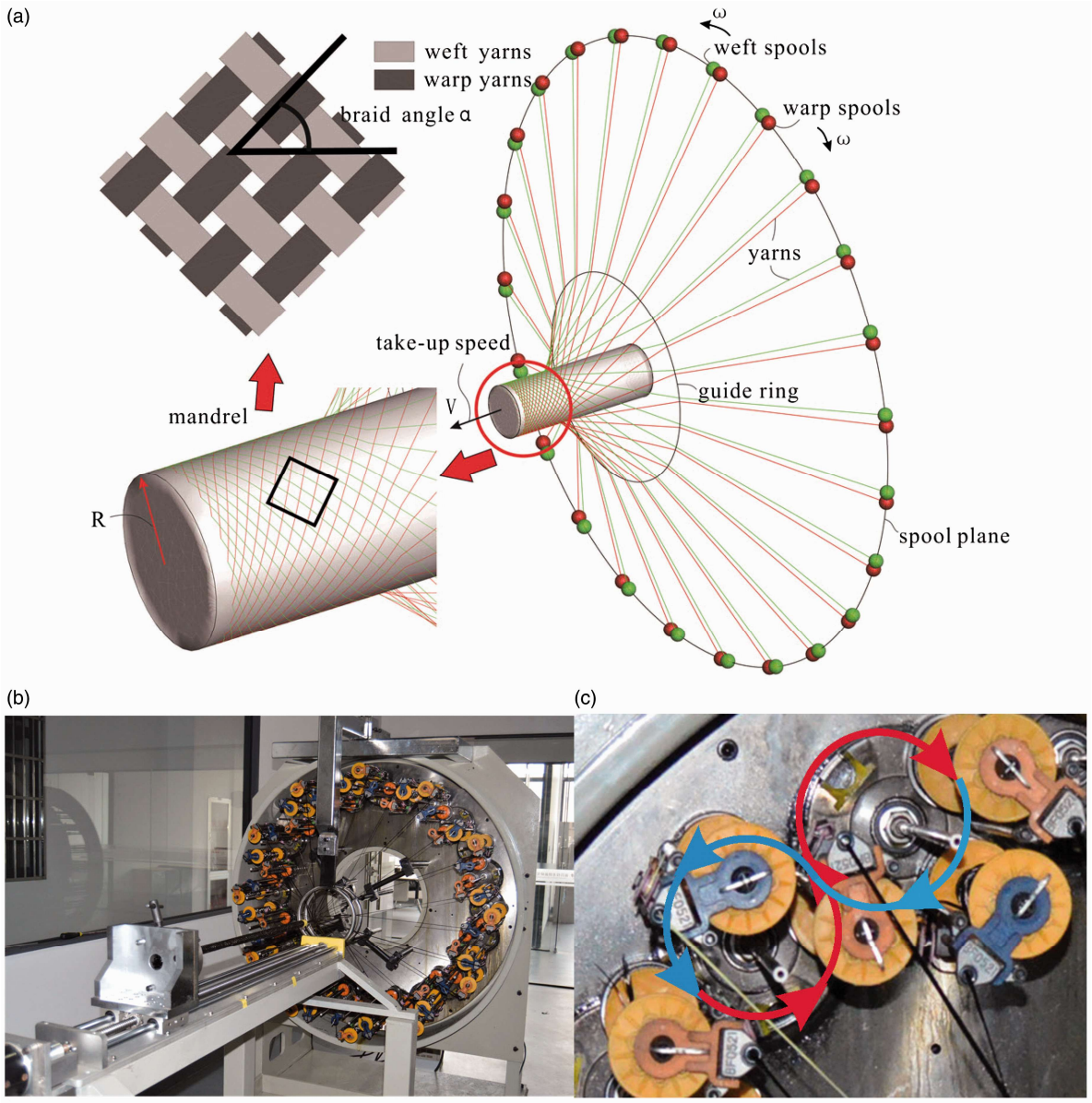


Figure 2.8 - Braiding machine: (a) schematic of circular braiding process; (b) photograph of circular braiding machine; (c) tracks of spools in opposite directions [reprinted with permission [25]**].**

speed. The braid angle is also influenced by multiple factors, such as the mandrel feed rate, carrier rotation speed, and mandrel size. One of the drawbacks of the braiding process is the difficulty in achieving a low braid angle. Widely utilised braid architectures include Hercules, regular, and diamond braids, with an example illustrated in Figure 2.9. The distinction between these three types is based on the yarn's pattern [1], [24], [26].

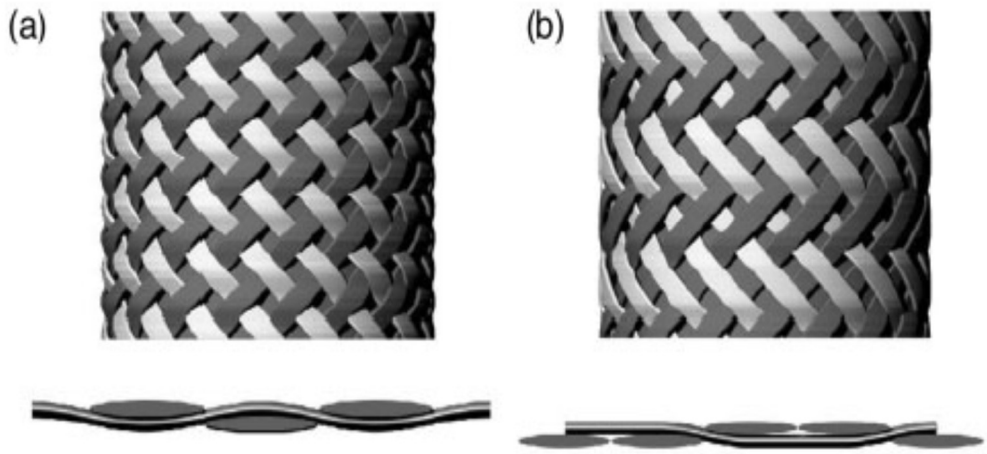


Figure 2.9 - Shows an example of (a) diamond braid (1/1) and (b) regular braid (2/2), [reprinted with permission [26]**].**

2.3.3 Knitting

Knitting is a technique employed to create fabrics by interlinking numerous loops of yarn using knitting needles. Courses and wales are terms used to describe rows and columns, respectively, within the knit structure. A single knitting needle produces a wale of loops, while a set of knitting needles is utilised to form a course of loops. The knitting technique can be categorised into weft and warp knitting. This technique offers several advantages, including flexibility, energy absorption, the ability to form both simple and complex shapes, impact resistance, and low cost. Many types of machines are used for weft and warp knitting, including flat bed and circular machines for weft knitting and Tricot and Raschel machines for warp knitting. For weft knitting, the flat bed machines consist of two needle beds with linear needle arrangement, while the circular machines can be either single bed or double bed with circular needle arrangement. In the case of warp knitting, the needle bed of Tricot machines is straight and has a place on the width of the machine, while the Raschel machines might have one or two [1], [18], [27]–[29].

2.3.4 Non-crimp fabric (NCF)

Non-crimp fabrics (NCF) are characterised by their straight fibres, precisely aligned in parallel and interconnected via stitching. The utilisation of NCF is gaining importance due to its inherent advantage of minimising composite property degradation associated with high yarn crimp. This material finds widespread application in diverse sectors, including marine and aerospace, primarily attributed

to its superior mechanical properties. Beyond its mechanical performance, NCF offers several key benefits, such as reduced production costs, enhanced drapability and impregnability, unlimited shelf life, and significant labour time savings [16], [18], [30]–[34].

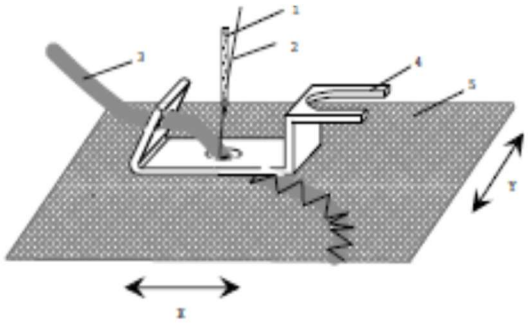
2.3.5 Stitching and Tailored Fibre Placement

Stitching is a technique employed to enhance damage resistance by providing reinforcement through the thickness of the structure. Through-thickness stitching improves delamination resistance and reduces the size of delamination within the structure. Numerous parameters significantly influence the stitching process, including the spacing between stitch rows, stitch length, stitching material, and the weight of the stitching yarn [1], [18], [35], [36].

Tailored Fibre Placement (TFP) is a manufacturing technique that utilises principles derived from embroidery to create textile structures. In the TFP process, fibre tows are precisely positioned along predefined paths using dedicated software. This method offers several advantages during manufacturing, including the versatility to employ a wide range of fibre types and the ability to orient fibres at any angle between 0° and 360°, facilitating the production of intricate shapes. Figure 2.10 illustrates the fundamental principles of the TFP process and presents examples of manufactured preforms [35], [37]–[39].

2.4 Composites Manufacturing methods

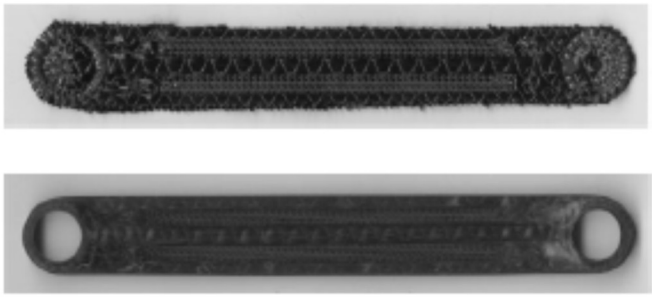
Various methods exist for manufacturing carbon fibre reinforced polymer (CFRP) panels to achieve high-quality outcomes, including wet lay-up, prepreg hand lay-up, resin transfer moulding (RTM), vacuum-assisted resin transfer moulding (VARTM), automated fibre placement (AFP), filament winding, automated tape laying (ATL), and resin injection moulding. This section will outline some of these manufacturing processes. However, the experimental work within this thesis will exclusively employ RTM and VARTM manufacturing methods.



(a)

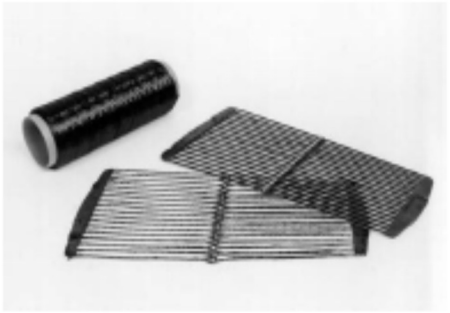
1- Needle
2- Needle thread
3- Carbon roving
4- Hold down device
5- Base material
X, Y- possible move directions

Principle of tailored fibre placement



(b)

Tension-Compression-Strut, Preform and Component



(c)

Machine part for a loom, Preform and Component

Figure 2.10 - Principle of tailored fibre placement (a), and typical applications (b and c), [reprinted with permission [35]**] .**

2.4.1 Wet lay-up

The wet lay-up technique is a fundamental manufacturing method extensively employed in commercial industries. In this process, liquid resin is manually applied to dry reinforcing fabric using a brush or spray. This method offers the advantage of cost-effective production of large-scale components due to the relatively simple tooling requirements. However, a significant drawback of the wet lay-up process is its reliance on the operator's skill to ensure complete and even resin impregnation

of the fabric, which is crucial for achieving optimal mechanical properties in the final composite part [1], [15], [16].

Wet lay-up involves a sequential process. Firstly, dry reinforcing fabrics are placed within a mould prepared with a release agent and gel coat to facilitate subsequent panel removal. Liquid resin is then applied to the fabric, either manually with a brush or through spraying. Then, the lay-up is compacted using tools such as squeegees or rollers to ensure complete resin impregnation and a dense structure. Finally, multiple layers are stacked to achieve the desired laminate thickness [1], [14]–[16].

2.4.2 Prepreg lay-up

Pre-impregnated plies (prepreg lay-up) are widely used in the aerospace industry. The prepreg lay-up process enables the manufacture of complex structures with a high fibre volume fraction, delivering superior mechanical properties. However, this method necessitates a larger workforce, is more labour-intensive compared to alternative processes, and requires refrigeration for material storage [1], [14], [16].

Prepreg materials consist of fibres embedded within a partially cured resin matrix, facilitating direct integration into composite manufacturing processes. These materials can be utilised in both unidirectional and multidirectional configurations, providing flexibility in achieving desired reinforcement patterns [40].

2.4.3 Filament winding

Filament winding is an automated technique where resin-impregnated fibres are precisely positioned onto a rotating mould (mandrel) at predetermined angles. This method allows for the creation of thick-walled structures by repeating the winding process. It is capable of producing a wide range of shapes such as cylinders, shafts, and spheres, making it particularly well-suited for the manufacture of pressure vessels. However, the production of components with concave surfaces presents a significant challenge for this technique [1], [14]–[17].

2.4.4 Liquid moulding

Liquid moulding involves various fabrication processes that can fabricate accurate parts with complex shapes. One of the advantages of liquid moulding is the capability of making parts that are often made individually into one moulded part. Resin transfer moulding (RTM) is commonly used in the liquid moulding process, to produce three-dimensional structures. One of the advantages of using RTM is the ability to produce structural parts cost-effectively with low-cost tools [1], [14], [17], [41].

Conventional Resin Transfer Moulding (RTM) is a closed mould process employing two mould halves that clamp around the reinforcing fabric. Following the placement of the fabric within the closed mould, the resin is infused under pressure from a pump. Once the mould is filled with low-viscosity resin, the curing process commences. Subsequently, the mould is opened to extract the finished composite part [1], [14], [17]. Figure 2.11 presents a schematic representation of the RTM mould (closed mould) used for infusing preforms under high pressure.

Vacuum-assisted resin transfer moulding (VARTM) differs from resin transfer moulding (RTM) in terms of the pressure applied during resin infusion. In the VARTM process, the dry fabric is positioned between the mould and a vacuum bag. This arrangement facilitates the removal of trapped air and enhances resin flow into the fabric by accelerating resin penetration [1], [14], [16], [42]. Figure 2.12 shows a schematic illustration of the VARTM setup.

2.4.5 Automated fibre placement (AFP)

Automated Fibre Placement (AFP), as illustrated in Figure 2.13, is a system employed to manufacture high-volume CFRP components with consistent quality, thereby overcoming the limitations of low productivity [17], [43], [44]. The AFP process is considered a hybrid technique, as it leverages the advantages of filament winding and Automated Tape Laying (ATL) methods, while mitigating their respective limitations. This process enables the fabrication of a wide range of structures, including both flat and cylindrical geometries [44], [45]. Owing to its

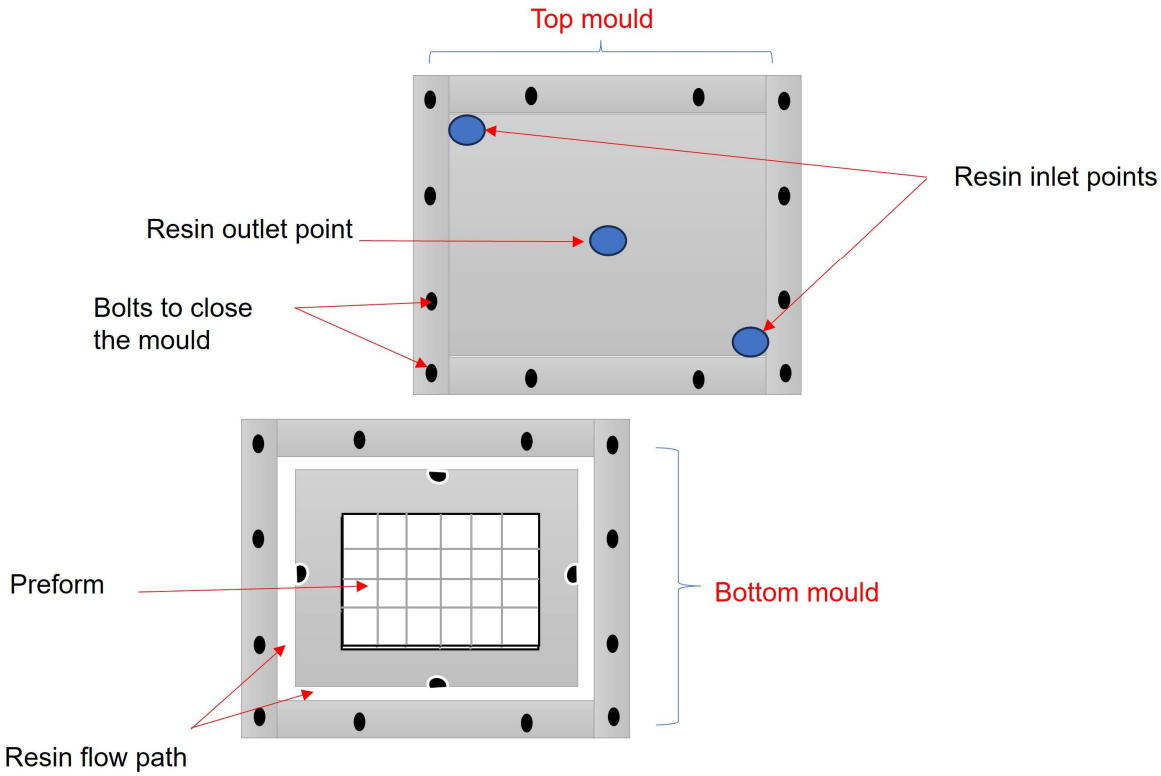


Figure 2.11 - Schematic illustrates the resin transfer moulding (RTM).

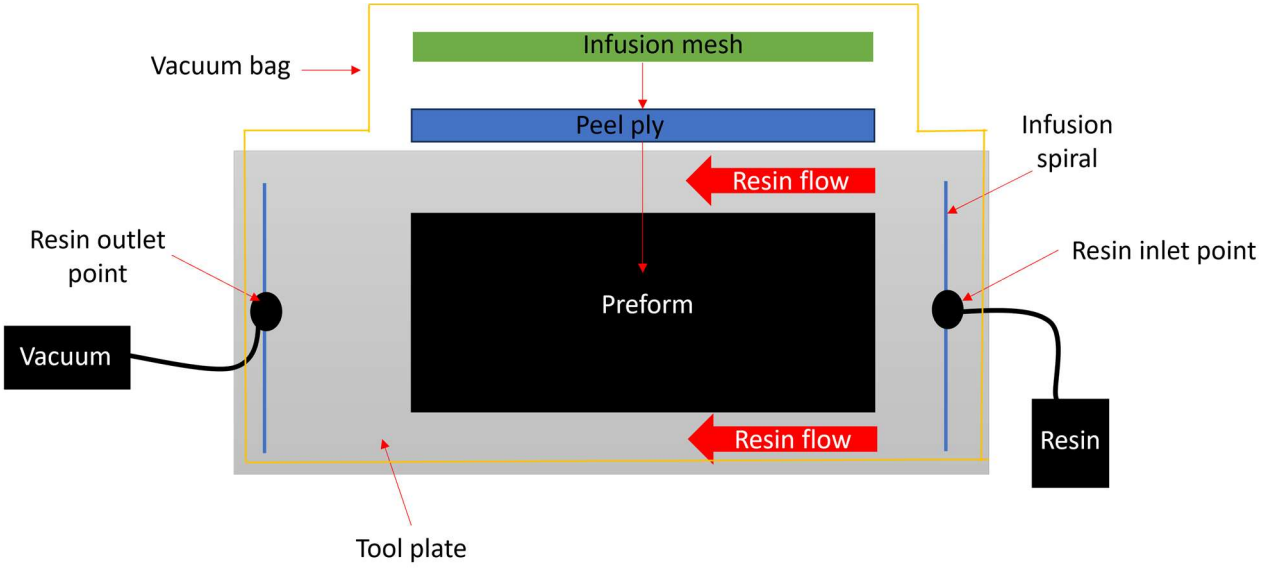


Figure 2.12 - Illustration of the Vacuum assisted resin transfer moulding (VARTM).

numerous advantages, including precision, quality assurance, time efficiency, and cost-effectiveness, the AFP system has become an integral part of the aerospace industry [17], [43]–[45].

The AFP system comprises a robotic arm, computer-controlled, and a placement head for depositing prepreg tows onto a mould to create the lay-up. The AFP process employs the placement head to deposit multiple prepreg tows onto the mould at precise angles and high speed, enabling the cutting and re-feeding of the tow within the manufacturing constraints [17], [44]–[46].

Although the AFP system offers numerous advantages in composite manufacturing, the AFP process involves several critical parameters, including feed rate, lay-up speed, and curing conditions. These parameters significantly influence the quality and structural integrity of the final product [43]–[45], [47]. Incorrect parameter selection can lead to various defects, such as improper tow end placement, gaps between tows, twisted tows, and overlapping tows [43]–[45].

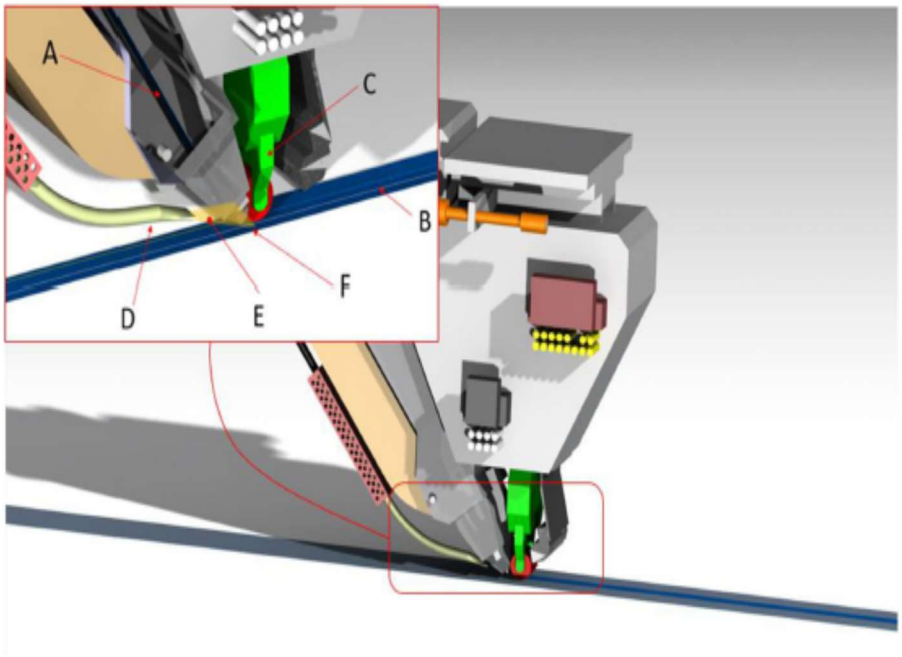


Figure 2.13 - Illustration of AFP machine with TP head. (A) incoming tape; (B) previously laid layer; (C) compaction roller; (D) heat source; (E) hot gas; (F) nip-point. (Reprinted with permission from [37], IEEE J. Int Info 2020 © IEEE).

2.5 Fibre orientation

The alignment of fibres within specimens significantly influences their mechanical performance. Extensive research has examined the factors impacting the mechanical properties of carbon fibre-reinforced polymers (CFRPs). Rahmani *et al*.

[7] investigated various parameters, including fibre orientation, building on the work of Keleemulla and Siddeswarappa [48], to assess the mechanical behaviour of CFRP samples reinforced with epoxy resin. Their findings highlighted fibre orientation as the most critical factor influencing mechanical properties. Tensile test results demonstrated that superior tensile strength and modulus were achieved when the fibre orientations within the laminates were [0°, 35°, 0° and 0°, -35°, 0°, +35°, 0°]. The influence of fibre orientation on the mechanical properties of continuous carbon fibre thermoplastic composites fabricated via fused filament fabrication has been investigated by Parmiggiani *et al*. [8]. Their study, encompassing both unidirectional and mixed fibre orientations, revealed a significant correlation between fibre alignment and mechanical performance. Specifically, samples with 0° fibre orientation (aligned with the loading direction) demonstrated superior tensile strength and stiffness. These findings highlight the critical role of fibre orientation in optimizing the mechanical properties of composite materials within the context of additive manufacturing. Knibbs and Morris [9] demonstrated that minor deviations in fibre alignment within composite materials can have a substantial impact on their mechanical performance. Their research explored the theoretical link between fibre orientation and the elastic response of a uniaxial composite. Importantly, their findings highlighted the sensitivity of the longitudinal Young's modulus to fibre misalignment, with an 11° deviation resulting in a significant 20 % reduction in this crucial mechanical property.

The mechanical behaviour of unidirectional carbon fibre composites is strongly dependent on the orientation of the fibres, Mohamed and Abdelbary [49] employed both theoretical and experimental approaches to examine the effect of fibre orientation on tensile strength across a range of angles (0°, 30°, 45°, 60°, and 90°). Their findings revealed a significant variation in tensile strength with fibre orientation, with fibres aligned parallel to the loading direction (0°) exhibiting the highest strength and those perpendicular to the loading direction (90°) displaying the lowest. These results underscore the critical role of fibre orientation in determining the overall mechanical performance of unidirectional carbon fibre composites. This relationship is further illustrated in Figure 2.14.

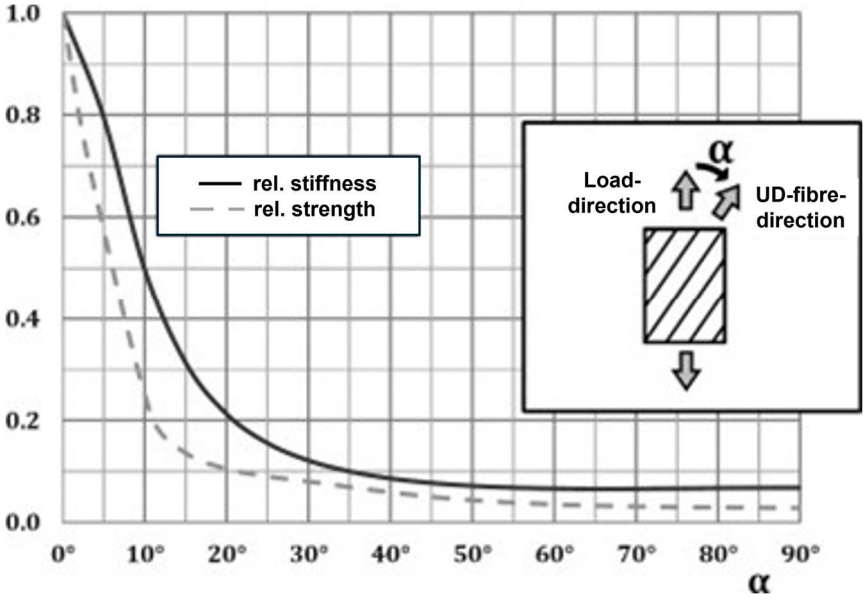


Figure 2.14 - A CFRP sample with unidirectional fibre orientation under loading represents the influence of the change in the fibre orientations corresponding to the loading direction on the mechanical properties of the material, Reprinted from [50]**, with permission from Elsevier.**

2.6 Composite samples containing holes

The composite samples containing holes (or notches) introduce a stress concentration related to the discontinuity in the sample's geometry, which in turn influences the material's properties. Compared to the samples that did not contain holes, the strength of the samples with holes might be reduced because of the material's brittleness and the introduced stress concentration around the machined hole. Furthermore, the strength of the composite sample containing a hole depends on the size of the created hole, where the strength reduction for samples with a large hole greater than for samples with a smaller hole. However, due to the difference in the failure modes, the effect on strength reduction would be expected to differ between tensile and compressive loading [51].

The hole's creation process creates a fibre-bridging zone near the tip of the hole, and the damage types appear as fibre pullout, matrix microcracking, and fibre-matrix interfacial failure. However, different factors influence the type of damage, including the type of fibre, the type of used resin, and the choice of sequence laminate stacking [51].

The stress concentration factor of the composite sample at the edge of a circular hole is used to estimate the strength reduction, as illustrated in the following equation:

$$\frac{\sigma_N}{\sigma_0} = \frac{1}{K}$$

Equation 2-1

where σ_N corresponds to the ultimate strength of the laminate containing a hole, σ_0 represents the ultimate strength of the laminate without a hole, and K is the stress concentration factor. Two of the strength models that are commonly accepted and include the effects of the hole's size are the point stress criteria (PSC) and the average stress criteria (ASC). In the PSC, the failure of laminate in the tension process is assumed when the stress at a distance from the edge of the hole equals the laminate (without hole) strength. For the ASC, the failure of the laminate in tension is predicted to occur when the stress that is averaged across a specific area surrounding the hole's edge equals the strength of the laminate without a hole [51].

2.6.1 Open-hole tensile testing

Carbon fibre reinforced polymer composites are commonly used in industry and aerospace applications because of their excellent mechanical properties. However, the machining hole creates a local stress around the hole edge, which affects the mechanical properties by reducing the material's strength due to damage initiated near the machined hole [52]–[58].

The standard test method for open-hole tensile testing (D5766/D5766M-11), [59], is usually used to prepare the tested samples. The standard explained the effect associated with the ratio of the sample's width (W) to hole diameter (D) and the ratio of hole diameter (D) to the sample's thickness (h). The recommended open-hole sample's geometry maintains the ratio between the sample's width and the hole diameter (W/D) to be equal to 6, and the ratio of the hole diameter to the sample thickness (D/h) is in the range between (1.5 and 3). Furthermore, the recommended sample's length is between (200 mm and 300 mm), and for shorter samples, it is between (150 mm and 200 mm). The standard recommends following the mentioned ratios unless the purpose of the experiment is to investigate the influence of these ratios.

The standard emphasises that the failure mode that is acceptable for open-hole tensile testing is when passing through the hole (crossing the centre of the hole), as illustrated in Figure 2.15.

Guo *et al*. [52] studied the effect of the machined hole size on the tensile properties of 3D woven composite plates. Three different hole sizes were tested to investigate the impact of the hole size on the tensile strength. The stress concentration around the machined holes was reported using digital image correlation (DIC), a non-destructive inspection technique. The results show, as expected, that the tensile strength decreases when the hole size for a fixed sample's width is increased. Furthermore, the authors state that machining the holes led to the creation of “tip points” of the carbon fibre, which in turn created a stress concentration region at the edge of the machined hole. The damage initiates from the stress concentration region. The damage shape depends on the machined hole size, as illustrated in Figure 2.16.

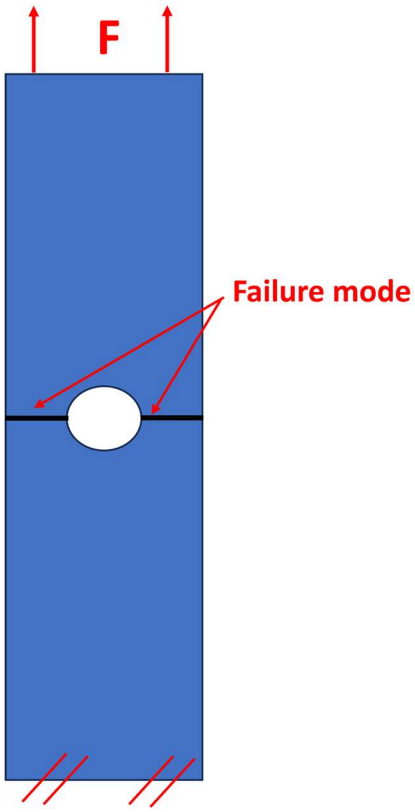


Figure 2.15 - Schematic illustrating the tensile failure mode crossing the centre of the hole, where (F) represent the force load direction.

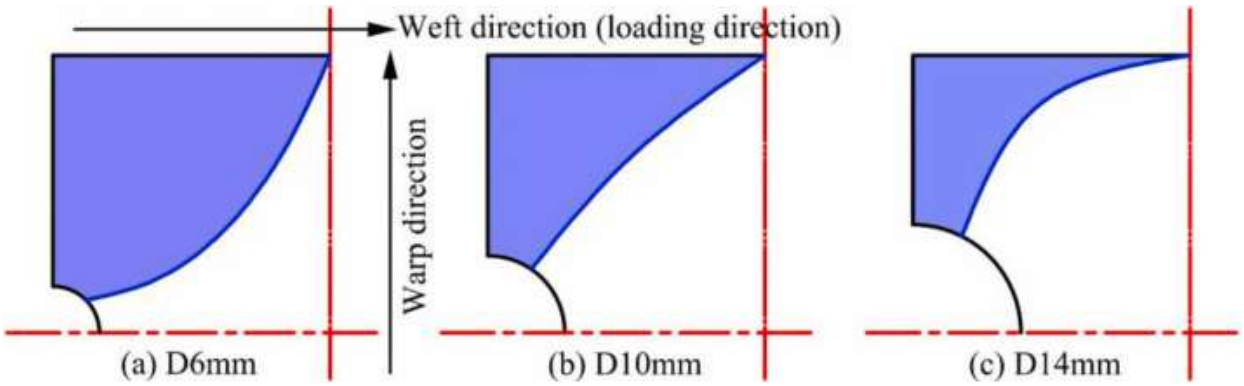


Figure 2.16 - Explanation of damage propagation path for different hole sizes machined in specimens, Reprinted from [52]**, with permission from Elsevier.**

Strungar *et al*. [60] investigated the strength of the open-hole samples for different patterns of 3D interlaced woven preforms that were subjected to tensile and compression tests. The process of machining the hole introduces minor defects around the edge of the machined hole. Moreover, the authors mentioned the significant effect of hole size on the ultimate strength. The results show the stress distribution around the edge of the machined hole using the DIC, with increasing strain. Liu *et al*. [61] investigated the effect of low temperatures on the tensile behaviour of CFRP samples with different machined hole sizes. The results show the impact of the hole size on the material's strength, where with an increase in the size of the machined hole, the strength decreased. However, the low-temperature results show improvement in the machined hole strength over room temperature data. Shaari and Jumahat [62] investigated the effect of the hole size on the tensile properties of hybrid composite laminates (Kevlar-glass fibre). The results show that increasing the hole size results in a greater reduction in the material strength. Zixing *et al*. [63] provide a mathematical model to obtain the stress in composite laminate around the hole's edge. The authors suggested that optimising the shape of the hole can be based on the stress distribution information. Mohammadi *et al*. [64] subjected a unidirectional composite glass fibre to open-hole tensile testing to study the damage behaviour using Acoustic emission (AE) and Finite element analysis (FEA), where the damage modes studied were fibre breakage, debonding, and matrix cracking. Gupta *et al*. [65] studied the influence of the hole's shapes on the mechanical response and damage behaviour during open-hole tensile testing and used finite element simulations on carbon fibre-aluminium laminates with three

laminate configurations. The shapes investigated were circle, square, ellipse with a major axis along the loading direction, and ellipse with a major axis transverse the loading direction, as illustrated in Figure 2.17. The results show that the circular hole's shape obtained the maximum net notch strength in the first two laminate configurations compared with the other hole's shapes, while the elliptical hole's shape shows the maximum net notch strength and least notch sensitivity in the third laminate configuration. Moreover, the elliptical hole's shape with the major axis in the transverse direction to the load direction shows in all three laminate configurations a minimum net notch strength due to strain concentration caused by the curvature in the transverse direction.

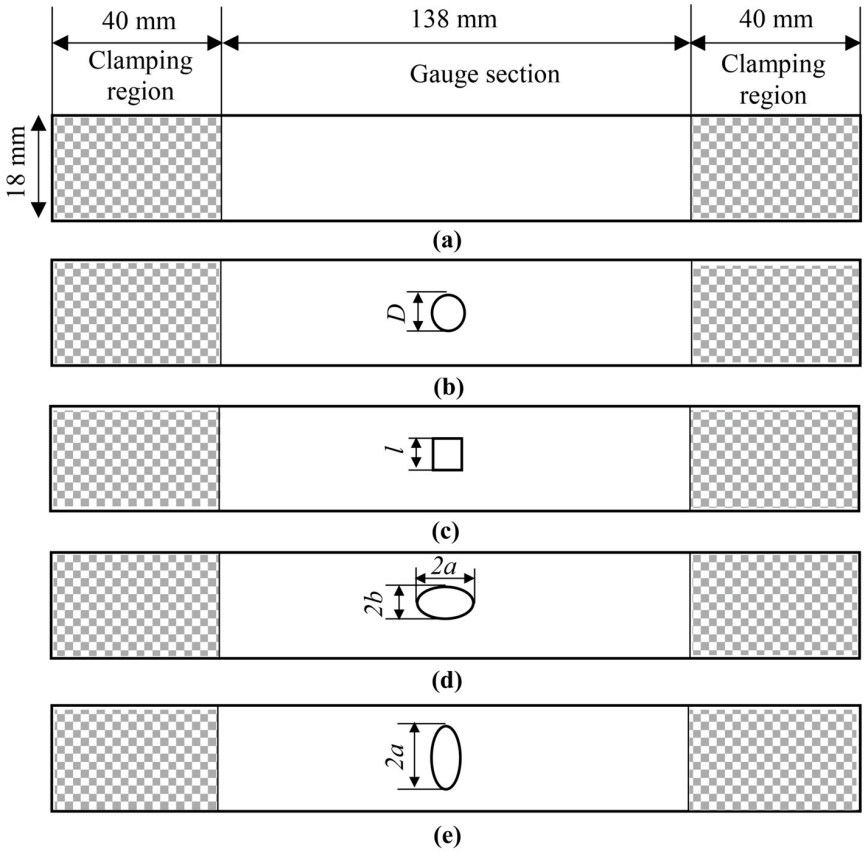


Figure 2.17 - Schematic presentation of the hole's shapes for open-hole tensile testing, where (a) present the baseline sample without a hole, (b) the circular shape, (c) square shape, (d) elliptical shape with major axis along the loading direction, and (e) elliptical shape with major axis transverse the loading direction, Reprinted from [65]**, with permission from Springer Nature.**

2.6.2 TFP reinforced hole samples

The Tailored Fibre Placement technology (TFP), developed at the Institute of Polymer Research Dresden, allows fibres to be placed in the desired position and angle to manufacture the preforms layer by layer. The TFP process uses the common embroidery technique, in which the design of the direction and angle for the fibres is applied using CAD technology. One of the advantages of the TFP manufacturing technique is the ability to place the fibres at different angles, creating complex shapes in the range of 0° to 360° during lay-up [6], [38], [66]–[68].

Gliesche *et al* [38] used the tailored fibre placement (TFP) technique to manufacture an open-hole sample by creating a local reinforcement instead of removing and breaking fibres during the machining process. The results show that the local reinforcement created by the TFP process helped in reducing the stress concentration around the hole. Furthermore, the tensile strength of the local reinforced open-hole sample, with lay-up of [(-45/90/+45/0)2]sym, was improved due to the improvement of stress distribution around the reinforced hole. Uhlig *et al*. [67] compared the strength of the TFP samples with NCF and braided samples with different lay-up configurations. The authors reported that TFP and NCF samples have “similar” tensile strength and show “similar” damage behaviour. Orlov *et al*. [69] investigated the physical and mechanical properties of samples manufactured using TFP, studying the effect of the density of the carbon fibre and stitching on the material strength. The authors reported that using aramid fibres as stitching material helps slow the crack propagation and reduce the jumps in crack propagation during three-point bending tests. Bittrich *et al*. [70] investigated the effect of stitching parameters, such as the stitching distance and width, on the infusion properties using RTM infusion. The authors reported that the permeability and fibre volume content is influenced by the stitching width and distance. Mattheij *et al*. [71] represented the mechanical properties of samples manufactured using the TFP process and showed possible applications and the advantages of using the TFP process. Furthermore, the authors present the local hole reinforcement samples for open-hole and bearing tests, which increase the strength by 45 % and 68 %, respectively. El-dessouky *et al*. [72] studied the effect of the fibres' orientation on the tensile strength of the TFP-circular reinforced hole samples manufactured using commingled carbon-nylon fibre by comparing different fibres' trajectories to create

the reinforced hole, as illustrated in Figure 2.18, and applying the open-hole test. The first design (Figure 2.18-b), which used a loop-back approach to make the local reinforcement, showed lower stiffness than the machined hole sample caused by the chosen tow's path. Furthermore, the loop-back design created a resin-rich area near the reinforced hole. However, the results show that the second design, (Figure 2.18-c), used to create the TFP-reinforced hole provides a higher tensile modulus than the machined hole sample.

Kim *et al*. [73] presented the defects introduced by the tow's deformation during the TFP process, including the gaps between the tows, the tow's overlaps, fibre misalignment, and the thickness variation. Furthermore, the tow wrinkle defect is caused by the high tension applied during the stitching process. Also, Uhlig *et al*. [50] studied the effect of the TFP process on the stiffness and stress behaviour of CFRP. Figure 2.19 illustrates the TFP process parameters and the induced defects, including fibre waviness and gaps between the roving, caused by the stitching process. The stitching process required moving the roving, as illustrated in the images (1-7), while fixing the fibres to the base material, causing the fibre's waviness. Schiebel *et al*. [74] investigated the deformation on the curved path of the roving caused by the TFP processing using an analytical model and FEA simulation, where the cross-section geometry of the roving is influenced by the stitching process.

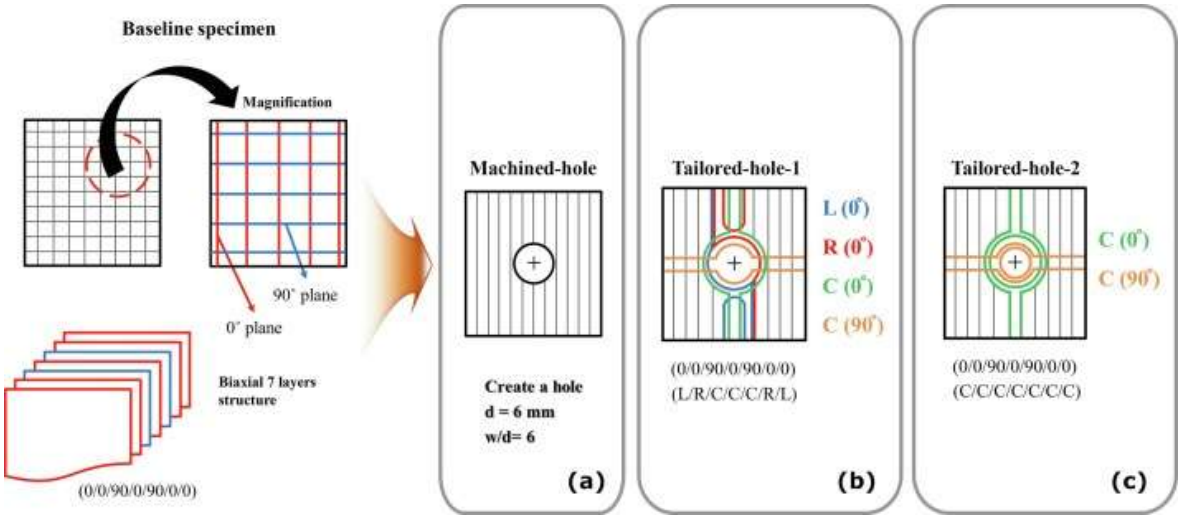


Figure 2.18 - Schematic illustrating the different paths used to create TFP reinforced hole sample, Tailored-hole-1 (b) and Tailored-hole-2 (c), Reprinted from [72]**, with permission from Elsevier.**

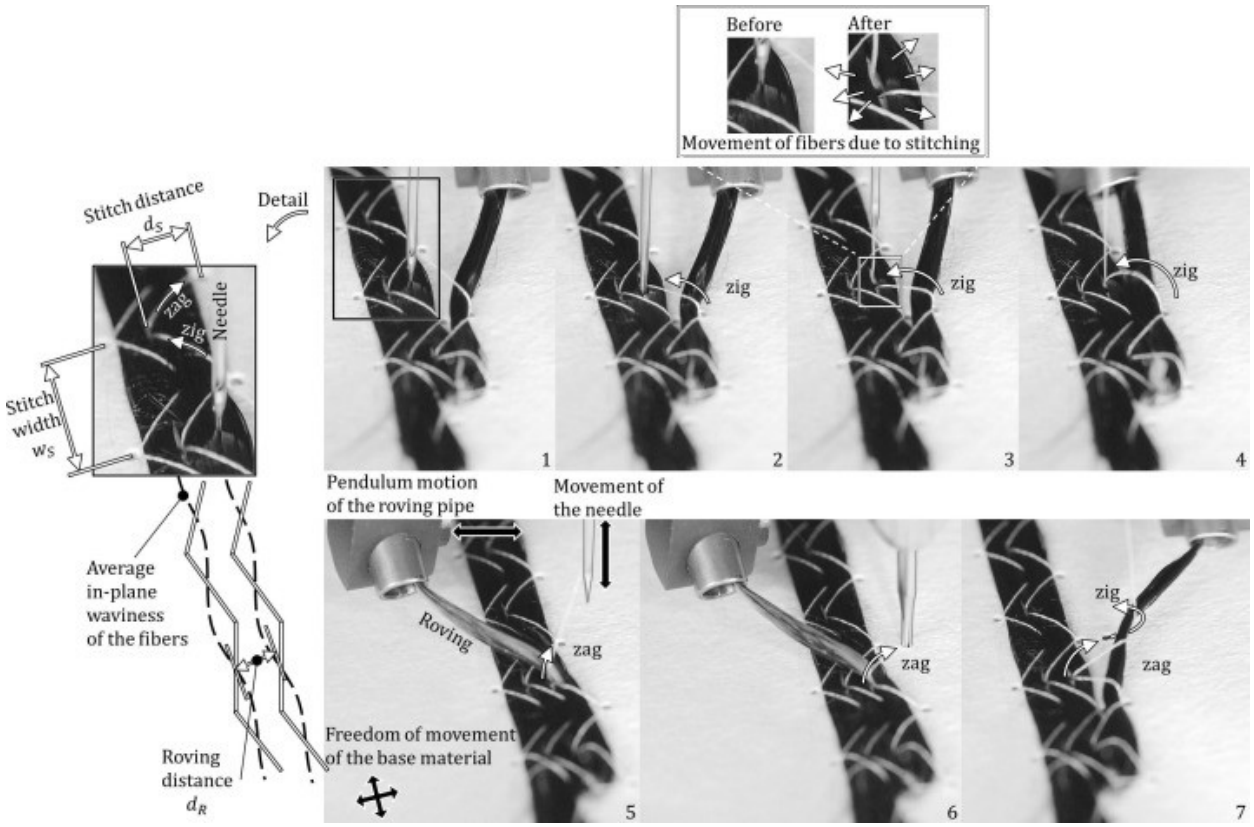


Figure 2.19 - Snapshots illustrating the tailored fibre placement (TFP) process and the stitching parameters, fixing the fibres to the base material using the zigzag stitch pattern, Reprinted from [50]**, with permission from Elsevier.**

2.7 Composite inspection

Many types of damage can appear in composites during their lives, whether during manufacturing, fabrication, or in-service. Manufacturing complex composite parts causes, in some cases, damage to the composite's structure, which needs to be inspected. The choice of inspection method depends on the type of damage because each technique has advantages and the potential to detect different defects in composites. Some examples of damage that may appear in the composite material are cracks, broken or distorted fibres, and delamination, which will reduce the composite's structural integrity. For this reason, an inspection process is required for composite structures. Inspecting the composite parts can be a destructive test (DT) or non-destructive test [10], [75]–[78]. This work will consider the NDT to inspect the fibres' orientation.

2.7.1 Non-destructive testing (NDT) and characterisation

Non-destructive testing (NDT) techniques evaluate defects on an object's surface or internal defects, without damaging the object. Vaara and Leinonen [79], list the different terminologies for NDT, including NDE (non-destructive examination) and NDI (non-destructive inspection), and there is also non-destructive evaluation (NDE) [75], [79]–[81].

Many NDT techniques are used to inspect and evaluate composite materials, and each one has advantages over the others in inspecting some specific types of defects. Therefore, the technique used to reveal the defect depends on the inspection technique's capability and the type of defect. For this reason, understanding the many types of NDT methods by knowing their ability and limitations is important to evaluate the right choice because, in some cases, the combination of more than one NDT technique may be required to determine the defect [75], [78], [80].

Many NDT inspection methods are used for composite materials, including visual testing (VT), also known as visual inspection (VI), ultrasonic and optical testing, shearography testing, and infrared thermography testing. The NDT inspection methods can be classified into two categories: contact and non-contact methods. The contact method requires physical contact with the tested object, such as ultrasonic testing, while non-contact methods, which does not need any contact with the tested object, has the advantage of saving time and speeding up the data collection process. The principle of the visual (or optical) testing is to inspect and evaluate the surface of the tested object, which is considered to be an rapid, inexpensive, and effective inspection method [75], [78]–[83]. To serve the purpose of this work, optical non-destructive non-contact inspection methods will be considered.

2.7.1.1 Digital image correlation (DIC)

Digital image correlation (DIC) is an optical and non-contact full-field inspection technique that is used to measure the in-plain displacements and strain in the tested samples. The principle of the DIC technique is to apply speckles to the surface of the tested object to track the movement of the speckle's pattern using video

cameras. Then, images will be captured and analysed to provide information about deformation and strain [84]–[86].

One of the advantages of using the DIC system is the ability to study the crack propagation and sample deformation in the tested material and detect the damage development. Also, DIC is considered cost-effective compared with other optical inspection techniques, such as laser shearography and speckle interferometry. Furthermore, the DIC imaging system does not require extensive surface preparation, such as a polishing process but does require painting the surface to be inspected. One requirement for operating the DIC technique is the calibration process, which sometimes requires the use of a certified calibration plate [84]–[89]. Figure 2.20 represents a schematic illustrating the experimental setup for the 2D-DIC inspection method.

Uhlig *et al*. [67] used the two-dimensional digital image correlation (2D-DIC) to evaluate the damage during open-hole tensile testing for non-crimp fabric (NCF), tailored fibre placement (TFP), and braided preforms with different lay-ups.

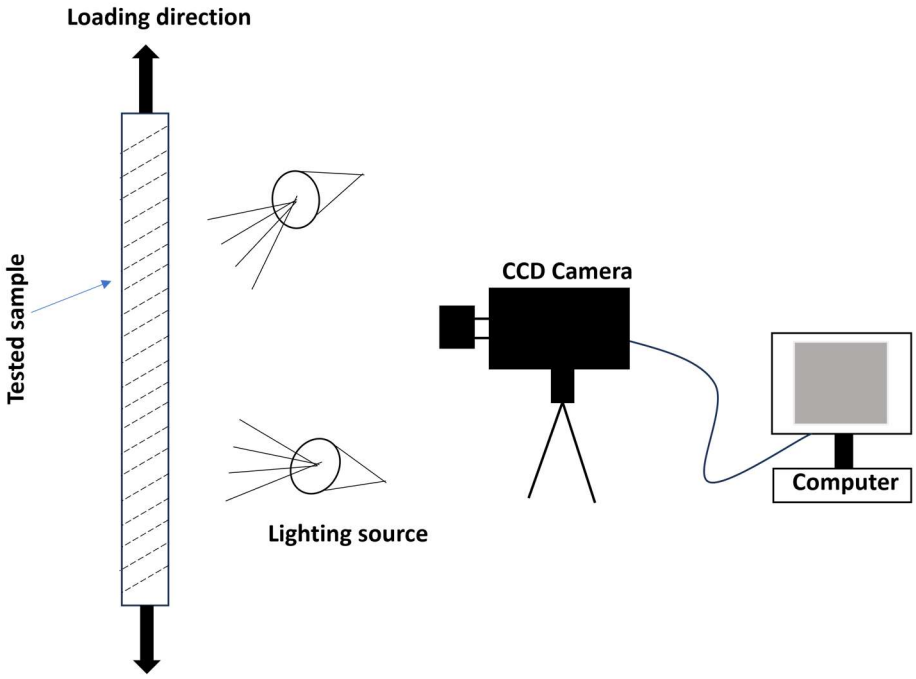


Figure 2.20 - Schematic illustrates the typical 2D-DIC inspection method.

Zhang *et al*. [90] applied the DIC technique to 3D-printed woven composite samples containing a 6 mm hole size that underwent tensile and shear testing to understand the failure mechanisms. The study investigated two types of holes: drilled and tailor-woven holes. The authors used FEM and Hashin failure criteria for damage initiation prediction of both hole types. They reported that the strength of the woven laminates increased considerably using the tailor-woven printing technique and prevented the cracks from propagating. Humberto *et al*. [68] employed DIC to study the strain and the behavioural failure of TFP reinforced-hole samples using different fibre paths to create the hole. The authors reported that strength increased for the samples with fibres aligned with the principal direction of stress. Strungar *et al*. [60] utilized the DIC to inspect the effect of the hole within open-hole tensile testing samples during the test on the 3D woven preforms with different interlacing types. The data shows the effect of increasing the load on the stress concentration, which appears on the hole's edges for the different interlacing types. Also, Guo *et al*. [52] employed DIC on 3D woven composite samples with three different hole diameters to inspect the effect of the hole size on the material strength and to determine the stress concentration area with increasing strain. The authors reported that as the hole size increased, the mode of failure changed from fibre pull-out to fibre breakage. Elyoussef *et al*. [91] applied DIC to woven carbon fibre samples containing a hole to investigate the effect of the temperature on the material's mechanical properties during tensile testing. The authors reported that increasing the temperature decreased the sensitivity of the notch. Venkatachalam *et al*. [92] studied the damage evolution of CFRP samples undergoing fatigue testing by applying the DIC inspection technique.

2.7.1.2 Shearography

The shearography is considered a coherent, non-destructive, and non-contact optical inspection method. The reason this method is called shearography, or speckle shearing interferometry, is due to the fact that the method uses an image-shearing camera to produce a pair of sheared images in the film plane. The shearography technique basically uses coherent laser light in order to illuminate the tested object and then uses the image-shearing camera, where the speckle pattern is produced from the interference that occurs between the two sheared images and

by combining the two speckle patterns (deformed and non-deformed) images. The outcome of the shearography inspection technique is a fringe pattern that describes the strain distribution and the displacement on the surface after deformation. The defects that occur in the tested object will cause strain concentrations, which leads to anomalies in the fringe pattern, and from there, the defects will be determined [93]–[97]. Figure 2.21 shows a schematic diagram illustrating the shearography inspection technique.

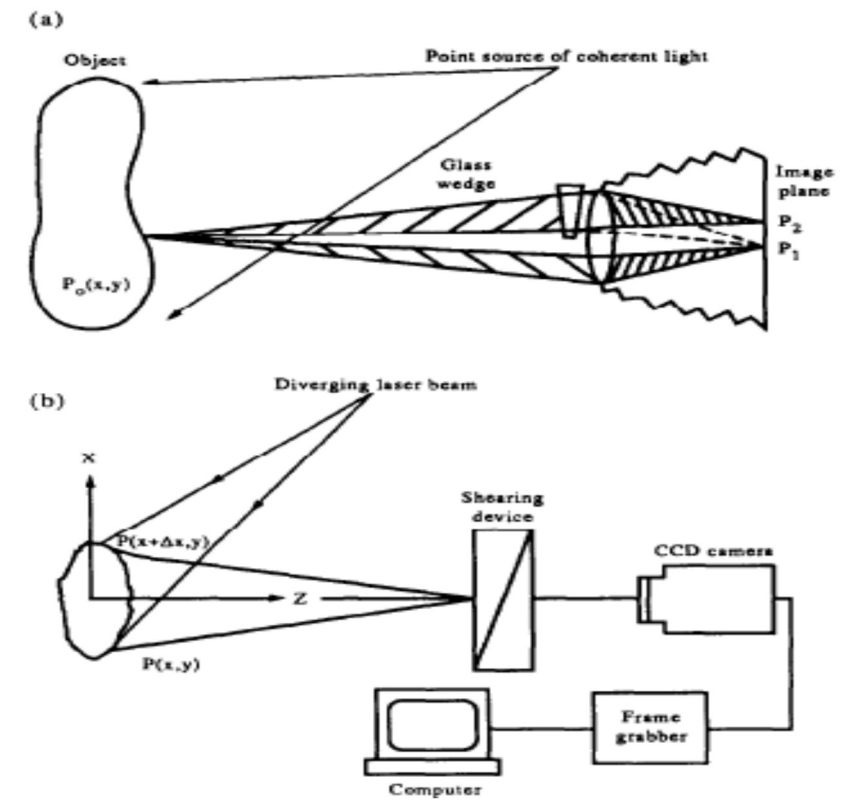


Figure 2.21 - A Schematic diagram illustrating (a) the photographic shearography; (b) the digital shearography. ([98], reprinted from Optics and Lasers in Engineering, 24, Y.Y.Hung, Shearography for Non-destructive Evaluation of Composite Structures, 161-182, 2000,with permission from Elsevier)

The shearography inspection technique has many features, including a non-destructive technique, non-contact, and full field of inspection. It is useful for strain measurement. Furthermore, the shearography technique has proven its capability of inspection, and for that, it has been endorsed by the rubber industry for inspecting tyres and also for inspecting composites by the aerospace industry. In addition, one of the features of the shearography technique is the ability to withstand and resist

the disturbance and vibrations caused by the surrounding environment better than other interferometric inspection techniques [93]–[97], [99].

From the recording aspect, there are three types of recording in shearography which are photographic, thermoplastic and digital. Digital shearography overcomes the limitations faced by conventional shearography, which are based on photographic and thermoplastic recording methods, by measuring the phase change in an automated way. The sheared Michelson interferometer is commonly used as an optical shearing device in the digital shearography to measure the derivatives of the surface displacements directly. The double-refractive Wollaston prism is another optical shearing device used in shearography [93], [95], [100].

Burkov *et al*. [101] applied digital shearography to four samples with different thicknesses, stacking sequences, and impacted energies to reveal the defects in the tested samples and successfully detect delamination and debonding in these samples. Moreover, De Angelis *et al*. [102] show that digital shearography can accurately determine the size of defects by not less than 90%. Georges *et al*. [103] showed that with vibration excitation, shearography was able to detect air gaps in hybrid sandwich structure samples. Also, Xu *et al*. [104] showed the ability of the digital shearography, after modifying the experimental setup, to be applied to smooth surfaces and it was capable of detecting defects that occur on specular or quasi-specular reflections. Moreover, due to the fact that the shearing direction plays an important role in selecting the direction of sensitivity for the digital shearography, the directional-shaped defects might not be detectable when using only one shearing direction [105]. For this reason, Xie *et al*. [105] discovered a new setup method to record the fringe pattern using digital shearography in two orthogonal directions simultaneously, and this system was capable of detecting directionally shaped defects. In addition, Blain *et al*. [106] used shearography to inspect many types of artificial defects applied to composite structures, including flat-bottom holes, Teflon inserts and pull-outs. Shearography was able to detect defects in the case of the flat-bottom hole, and Teflon insert showing depth resolution. In the case of pull-out, it was challenging to determine the contrast using the shearography. Ye *et al*. [107] developed the shearography inspection technique to be an automated inspection technique with full-field inspection, which could

inspect the external surface of a cylindrical structure with a thermal insulation layer. Comparing the developed system with the traditional shearography inspection technique, the automated system provided better inspection efficiency and was easier to operate [107].

Hung [93] compared shearography and holography techniques as optical inspection techniques and showed shearography is superior in detecting cracks in pressure vessels over holography, because of rigid body motion. Hung also compared digital shearography and C-scan ultrasonic techniques in detecting delamination and edge pullout of laminated graphite panels, and showed that digital shearography was faster than the C-scan and, unlike ultrasonics, digital shearography does not need fluid coupling to inspect the object's surface [99].

2.7.1.3 3D laser scanning

A laser is a device that emits coherent light. The word laser is an abbreviated form of light amplification stimulated emission radiation [108]. Lasers are used in numerous applications, including communication, medical surgery, cutting and in holograms [108]. Frommknecht and Effenberger [109] show that a laser line sensor system, as an optical method, can obtain 3D surface information and detect many types of defects, including delamination and cracks. Girolamo *et al*. [110] applied a laser scanning system on composite structures, honeycomb, to estimate the Barely Visible Impact Damage (BVID) and flaws that occur in the structure. Moreover, Bondyra *et al*. [111] used a 3D laser scanner as an inspection tool in order to measure deformation in composite structures. Shadmehri *et al*. [112] used a laser vision inspection system, which consists of two systems, (1) a laser projection system and (2) a vision system, to be applied to the AFP manufacturing process in order to detect different types of defects, such as the location of ply, angle of tows and the gap size.

One of the commercial systems is available to inspect the fibre orientations of composite parts is the 3D Apodius Vision Systems from Hexagon, as shown in Figure 2.22 [113]. The system has an advanced vision system and software that can calculate and measure fibre orientation in three dimensions to be compared with simulation data or the original design. The HP-C-V3D Apodius Vision sensor,

Figure 2.22-b, is used to map the surface and show the geometries for composite components using a 3.5 mW laser at 650 nm. Besides the ability to check for fibre orientation in composite parts, this system can be integrated with composite lay-up machines [114].

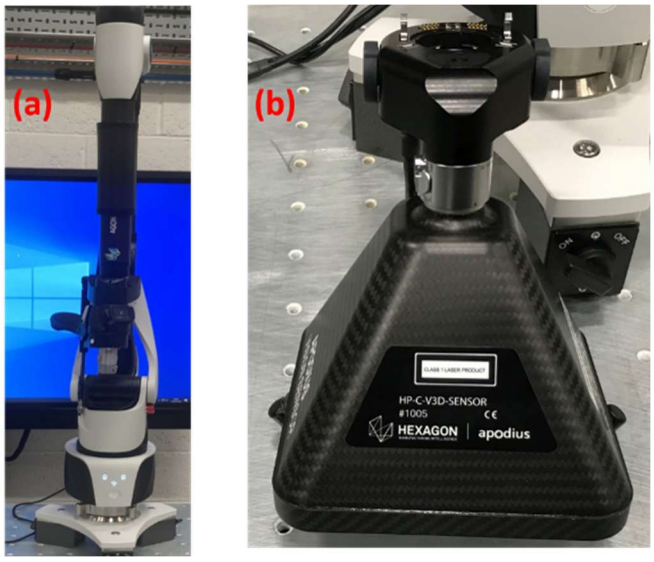


Figure 2.22 - HP-C-V3D Apodius Vision System. (a) Absolute Arm; (b) HP-C-V3D Apodius Vision Sensor.

2.7.1.4 Terahertz (THz) imaging

The terahertz (THz) region of the electromagnetic spectrum lies between microwave and infrared frequencies, typically defined as extending from 0.1 to 10 THz, corresponding to wavelengths of 30 μm to 3 mm. For many years, the development of THz imaging as a non-destructive testing (NDT) technique was restricted by the absence of efficient sources and detectors, a limitation often referred to as the "terahertz gap". However, advances in photonics and electronics, particularly in the fabrication of ultra-fast components, have enabled the technique to evolve into a valuable tool for NDT applications [115]–[118].

The growing use of composite materials in aerospace, automotive, marine and wind energy sectors has further underscored the need for advanced inspection techniques capable of ensuring both quality and structural performance. In this regard, THz imaging has been investigated as a non-contact and non-destructive approach to composite inspection [118], [119]. Abbott and Zhang [116] have also highlighted the ambiguity of terminology in this field, recommending that the

expression “terahertz radiation” be avoided in favour of “T-rays” to prevent confusion with the unit of frequency. Where the term is employed, it should be understood as shorthand for “radiation centred within the terahertz gap”.

A key property of THz radiation is its ability to penetrate non-transparent media such as plastics, cardboard and textiles. This advantage, combined with the shorter wavelength of THz radiation compared to microwaves, provides superior spatial resolution and makes the technique particularly useful for imaging applications. Nevertheless, the inspection of conductive materials such as metals and carbon fibre composites present challenges due to their strong reflectivity in the THz range. The degree of reflection depends on the polarisation of the radiation relative to the fibre orientation, with parallel polarisation producing stronger reflections than perpendicular polarisation [120]–[122].

THz inspection can be performed using either continuous-wave (CW) systems or pulsed systems, most commonly realised through terahertz time-domain spectroscopy (THz-TDS). CW systems provide information on intensity only, relying on fixed-frequency sources and single detectors. Although limited in terms of temporal and depth resolution, they offer advantages of simplicity, lower cost, reduced optical complexity and rapid image acquisition, as they do not require time-delay scanning. In contrast, pulsed THz systems provide both intensity and phase information, allowing the extraction of additional physical properties of the sample. These systems typically use femtosecond laser pulses to generate ultrafast photocurrents in semiconductors [118], [121], [123]. A laboratory-built THz-TDS systems, such as the one developed at the Maxwell Centre (Cavendish Laboratory, University of Cambridge), can be operated in both transmission and emission modes depending on the optical arrangement [124]. Figure 2.23 presents a schematic representation of the THz-TDS system configured in reflection mode.

THz imaging has shown significant potential in the evaluation of composites. Stoik et al. [125] demonstrated the applicability of THz-TDS in reflection mode, detecting hidden voids and surface defects in aerospace-grade glass fibre composites, while additionally using the reflection configuration to measure refractive indices and absorption coefficients. Beyond defect detection, THz imaging has been investigated as a tool for quality control. Rutz et al. [126] demonstrated the ability of

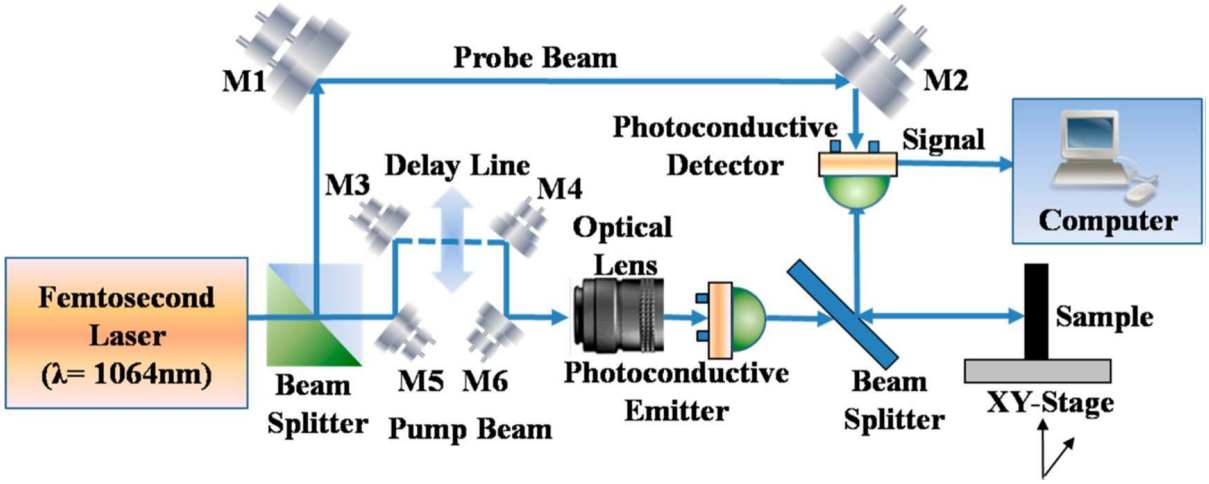


Figure 2.23 - Schematic diagram of the THz TDS system in reflection mode, where M1, M2, ..., M8 representing the used mirrors [reprinted with permission from [119]**].**

THz-TDS to detect inhomogeneities, mechanical damage and fibre structures in polymeric products, as well as to measure the dimensions of injection-moulded parts with complex geometries. A further advantage of THz-TDS is the capacity to manipulate spatial resolution, as this parameter is inversely proportional to the THz beam spot size, which decreases with increasing frequency [127]. This capability allows the imaging system to be tailored to specific inspection requirements, thereby enhancing its versatility as a non-destructive evaluation method.

2.7.1.5 Polarisation methods

Light is electromagnetic waves that consist of both an electric field and a magnetic field. These fields oscillate at a right angle to each other and to the direction of propagation. Unpolarised light are waves vibrating in different directions. Numerous techniques and methods are used to produce polarised light from incident unpolarised light. Surface scattering can convert unpolarised into polarised light, and this is particularly present in oriented fibre materials. Other methods used to obtain polarised light from incident unpolarised light are, double refraction, scattering, dichroism and transmission of light through polarising films. The simplest method of obtaining polarised light from unpolarised incident light is the reflection method. In this method, when the incident beam of light has a certain angle on the shiny surface of the glass, one can notice that the reflected light is plane-polarised. The term plane-polarised is used in the reflection method when all the reflected light

is vibrating and continues not to change in a parallel way corresponding to the plane [108].

Considering an incident of unpolarised light with an angle (θ) on glass, for example, one can realise that part of the light will be reflected, and part will be refracted. From there, Brewster's law, shown in Figure 2.24, states that to have a polarising angle, the angle between the reflected and refracted rays is 90°. In the case of ordinary glass with partially plane-polarised reflected rays, the incident angle that achieves the polarising angle is about 57°. Furthermore, Brewster's law shows the relation between polarisation and the material's refractive index, where the refractive index has an effective role in defining the incident angle for maximum polarisation. When incident unpolarised light strikes the surface at the polarising angle, all the light that is vibrating parallel to the plane of the incident will be refracted, while only 85% of perpendicularly vibrating light will be refracted, and the rest will be reflected [108].

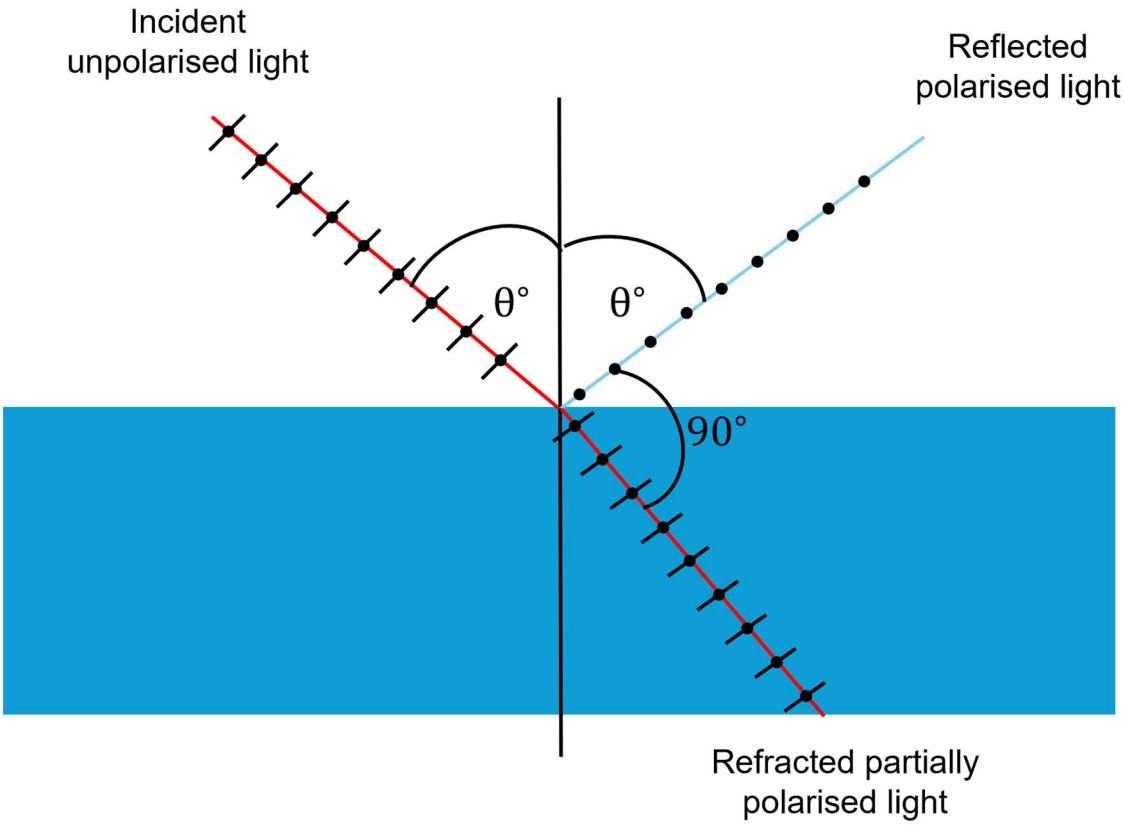


Figure 2.24 - Illustration of Brewster's law for the polarizing angle [Redraw from [108]**].**

Another method of polarisation uses more than one plate. In this method, when unpolarised light with a polarisation angle is incident on more than one plate, all parallel vibrations to the plane of incidence will be refracted, while some of the perpendicular vibrations corresponding to each surface will be reflected. In this case, the transmitted beam is partially plane-polarised because it loses many perpendicular vibrations through each surface. However, all reflected beams in the same plane are plane-polarised [108].

Carbon fibre has the property of converting unpolarised light to polarised light showing the fibre's direction. This method can be useful in the industry, including quality inspection and manufacturing of carbon fibre samples or preforms. It is very important to know the direction of carbon fibres to manage the mechanical strength and the ability to tolerate the load (see Section 2.5). Therefore, it is important to measure the fibre directions to ensure accuracy when manufacturing composite materials for aircraft and automobile constructions requiring high safety [128].

Many companies have started to introduce different types of polarisation cameras that have the potential to measure the fibre's orientation in carbon fibre material. One example of polarisation cameras that can be used for quality assurance of carbon fibre reinforced polymer production and analysing the carbon fibre bundles direction is POLKA from the Fraunhofer Institute for Integrated Circuits IIS [129]. Another example is Phoenix, which has been used to inspect both dry and finished carbon fibres [130]. The Baumer CX series polarisation camera is another example of a polarisation camera that has been used to identify defects in glass, CFRP, and reflective surfaces [131]. The final example is the Sony camera (XCG-CP510) [132].

POLKA, which stands for "POLarization KAmera", can record the waves of light that have different polarisation angles by, (pixel-based filters), filters that are based on pixels and concentrated on different orientations (0°, 45°, 90° and 135°). This polarisation camera has been used in industry applications as a non-destructive testing method for CFRP in order to determine the fibres' orientation [133].

Schöberl *et al*. [10] use a polarisation camera (POLKA02) in order to measure the orientation of carbon fibre. Knowing the degree of polarisation helps to locate the fibre's position and measure the reflected light's polarisation to give the orientation of the fibres. The ratio of polarised to unpolarised light can be determined from the degree of linear polarisation, where a high degree of linear polarisation results from light directly reflected from the fibres. The angle of the direction of the fibres is represented by the angle of maximum polarisation, where no measurement can be made for the angle when the degree of linear polarisation is zero, and that is because measuring the angle is useful only with the presence of a certain degree of polarisation. The authors presented the limitation of the measurement to the uppermost layer. However, they took advantage of the small gaps that exist in the upper layer to see the layer below and analyse the orientation of these fibres. The authors also show the capability of the POLKA camera by inspecting CFRP parts from an aircraft and the clear result of the orientation of the fibre by visualising the defect [10].

Atkinson *et al*. [134] used the IMX250MZR sensor from Sony to measure the fibres' orientation of dry and cured carbon fibres. Different types of illumination, including dark field, bright field, dome, ambient and point illumination, were tested on various types of carbon fibre materials. The results show that different factors influence the precision of the measured angles, including the material type, illumination source, and the chosen lens. The right combination will reduce the errors in the measured angles. Furthermore, the authors used the mean of the angle of linear polarisation (AoLP) and degree of linear polarisation (DoLP) information and corresponding standard deviation, by applying the Gaussian curve fitting, of dry and cured carbon fibre to test the accuracy of the angle's measurement method.

Damghani *et al*. [11] used the Sony (XCG-CP510) polarisation camera to determine the location and size of damage that appears in the carbon fibre laminates subjected to impact experiments. The authors found that the ability to detect damage using the polarisation camera is increased by increasing the impact energy. However, the polarisation images could not locate the damage when using glass fibre material because it does not have a crystalline structure like carbon fibre.

Chiominto *et al*. [13] used a polarisation camera to measure the carbon fibre tow's orientation. Analysing the angle of linear polarisation (AoLP) information helps to find the average winding angle using the Gaussian curve fitting approach to the AoLP data. The authors used an inspection set-up regarding the camera and lighting position to capture the cylindrical surface of the component.

Furthermore, the polarisation shows its efficiency in helping to obtain carbon fibre orientation when it is used as an accompanying method with the non-destructive testing technique, terahertz (THz). Dong *et al*. [115] used the terahertz non-destructive testing (THz) to obtain intra- and inter-laminar damage in cross-play stack patterns of hybrid fibre-reinforced composite laminate samples that consist of unidirectional plies of glass/epoxy and carbon/epoxy, $[0_2^G \ / \ 90_3^C]s$, and found that even though the THz waves have limited penetration of the carbon fibres, due to the conductivity of the fibres, THz polarisation is able to identify the features that appear around the interface of hybrid fibre-reinforced composite laminate with the existence of the intra- and inter-laminar damage. By taking advantage of the directional sensitivity of THz polarisation, the intra- and inter-laminar damage are successfully differentiated. Also, the authors take advantage of the polarisation method in the THz inspection technique to detect subsurface damage, such as matrix cracking, fibre distortion, and delamination in woven carbon fibre-reinforced composites [135]. Moreover, Kharkovsky *et al*. [136] used the polarisation in a microwave NDT technique to have an inspection system with a "dual-polarised microwave near-field waveguide probe" to detect many types of defects, including dis-bonds, damage, cracks and fibre misalignment in CFRP structures.

2.7.1.6 Summary

This chapter has outlined the fundamental principles of composite materials, with particular emphasis on carbon fibre and its associated manufacturing processes. Emphasis was placed on the significance of fibre orientation in influencing the mechanical performance of composite structures. In addition, the chapter has reviewed the application of optical non-destructive inspection techniques for composite materials, highlighting their benefits as well as their limitations. Specific attention has been given to optical methods employed for assessing fibre orientation

within carbon fibre composites. Therefore, the polarisation camera was chosen as an optical, non-destructive inspection method to monitor fibre orientation during tensile testing, thereby assessing its applicability for real-time monitoring of fibre orientation throughout the manufacturing of TFP preforms.

3 METHODOLOGY

This chapter focuses on carbon fibre-reinforced polymer (CFRP) samples, including material selection, composite panel fabrication, sample preparation for tensile testing, and machining of the holes for open-hole tensile test specimens. Additionally, it explains the characterisation applied to the CFRP samples and the specific mechanical testing methodology employed.

This chapter will focus heavily on optical non-contact inspection via the polarisation camera. The polarisation camera was used to examine the behaviour of fibre orientation under increasing strain during tensile testing.

The methods introduced in this chapter will be employed in the experimental chapters, including vacuum-assisted resin transfer moulding (VARTM), computer numerical control (CNC) machining, tensile testing, programmable oven curing, image processing and analysis, and polarisation-based optical inspection technique. The VARTM infusion technique will be utilised to fabricate the tensile specimens presented in Chapters 5 and 6, thereby ensuring a consistent manufacturing process for all samples containing holes. The CNC machine will be applied to produce machined holes in specimens intended for open-hole tensile testing, which will be used in Chapters 5 and 6.

To maintain uniform curing conditions across all manufactured specimens, a programmable oven will be used for all the samples that used in the experimental studies. Fibre orientation during tensile testing will be monitored using a polarisation camera, while tensile loading will be applied at a constant speed rate for all samples, with strain progressively increased in Chapters 4, 5, and 6. During testing, all specimens will be imaged under similar illumination conditions using the same inspection rig. The hue–saturation–value (HSV) images obtained, in the experimental chapters, will include a scale bar representing fibre orientations in the range of 0°–180°.

Furthermore, colour thresholding and Gaussian curve fitting will be applied to the experimental data to evaluate the evolution of fibre orientation with increasing strain.

3.1 Materials

This section will detail the specific carbon and glass fibre types, as well as the matrix resin, employed in fabricating the experimental samples. Carbon fibres with varying architectural configurations will be utilized to examine and analyse fibre orientation using the polarisation camera. The glass fibre will be used as the base material in the manufacturing process for tailored fibre placement (TFP) preforms.

3.1.1 Carbon Fibre

A range of carbon fibre composites with diverse architectural configurations, including unidirectional (UD), unidirectional non-crimp fabric (UD-NCF), twill 2x2, and unidirectional tailored fibre placement (UD-TFP) preforms, were selected for offline and online (under tension) inspection using polarisation camera technology. The primary objective of this study was to investigate the fibre orientation of these materials with increasing strain during tensile testing.

The dry UD carbon fibre was made of T300 fibres with an areal weight of 250 g/m² and a nominal thickness of 0.22 mm. The dry UD-NCF was produced using T700 fibres with an areal weight of 294 ± 5% g/m² and a nominal thickness of 0.28 mm. Dry Twill 2x2 was constructed from Grafil 34-700 fibres with an areal weight of 650 g/m² and a nominal thickness of 0.9 mm. The fibre orientation in the Twill 2x2 fabric was 0° and 90°, with a 2x2 weave pattern. The properties of the UD, UD-NCF, and Twill 2x2 fibres were summarised in Table 3.1. Additionally, the TFP preforms were produced using T700S carbon fibres, the fibre properties of which are detailed in Table 3.2.

Table 3.1 - Carbon fibre properties

Fibre Properties	T300	T700	Grafil 34-700
Tensile Strength (MPa)	3530	4900	4830
Tensile Modulus (GPa)	230	230	234
Density (g/cm^3)	1.76	1.8	1.8
Filament Diameter (μm)	7	7	7
Tex (g/1000 m)	198	800	800
Tow	3K	12K	12K

Table 3.2 - T700S carbon fibre properties

Fibre Properties	T700S
Tensile Strength (MPa)	4900
Tensile Modulus (GPa)	230
Density (g/cm³)	1.8
Filament Diameter (μm)	7
Tex (g/1000 m)	800
Tow	12K

3.1.2 Glass Fibre

A satin weave glass fibre fabric (8 End Satin) with an areal weight of 297 g/m² and a thickness of 0.23 mm was chosen as the base material for manufacturing the TFP preforms. In the TFP process, carbon fibres are positioned on the base material and secured using a stitching thread. A detailed description of the TFP preform manufacturing process is provided in **3.2.4**.

The polyester continuous filament (Serafil Comphil-180), specially developed for composite material applications, employs the Tailored Fibre Placement (TFP) method to fix the roving to the backing material. This polyester thread exhibits a linear density (Tex) of 16 g/1000m and a 19% elongation at break, as determined by DIN EN ISO 2062 standards.

3.1.3 Epoxy Resin

An epoxy resin and hardener system, Araldite (LY 1564) resin and Aradur (2954) hardener (supplied by Huntsman, UK), was selected for the infusion process due to its suitability for Vacuum-Assisted Resin Transfer Moulding (VARTM) and compatibility with the TFP preforms. This selection was influenced by the system's low viscosity and extended pot life.

At 25°C, Araldite (LY 1564) exhibits a viscosity range of 1200-1400 mPa.s, while Aradur (2954) has a viscosity range of 70-120 mPa.s. The pot life at 23°C is 480-600 minutes, reaching 140-160 minutes at higher temperatures (40°C). The recommended mixing ratio for this system is 100:35 by weight and 100:42 by volume [137].

3.1.4 Silicone Rubber Resin

To investigate the orientation behaviour of carbon fibres under increasing strain, tensile tests were conducted on both dry and composite samples. A polarisation camera was employed to capture the fibre orientation during the testing process. To bridge the gap between dry fibres and epoxy-infused composites, silicone rubber resin was used to impregnate the samples, see chapter (4) **Section 4.4**. This softer matrix, compared to epoxy, allowed for greater fibre flexibility, facilitating the observation of orientation changes under tensile loading.

Addition Cure Silicone Rubber AS40 and AS40 Catalyst were selected as the soft resin system. The silicone rubber resin exhibited a viscosity range of 40,000 to 78,000 mPa·s at 20°C, while the hardener viscosity was between 200 and 300 mPa·s under the same conditions. A 100:10 weight ratio was employed for the mixing process. The mechanical properties of the cured silicone rubber are presented in Table 3.3 [138]. Regarding the curing time, the following conditions can be applied:

- 24 hours at 20 °C.
- 2 hours at 60 °C.
- 1 hour at 70 °C.
- 30 minutes at 80 °C.

Table 3.3 - Mechanical properties of cured silicone Rubber

Density at 25 °C (g/ml)	**1.05-1.09**
Linear shrinkage (%)	0.1
Tensile strength (MPa)	> 3.5
Tear strength (KN/m)	> 13
Elongation at break (%)	> 250

3.2 Manufacturing Composites Panel

Vacuum-Assisted Resin Transfer Moulding (VARTM) was the primary resin infusion method employed to manufacture the UD, UD-NCF, Twill 2x2 and TFP samples for tensile test to investigate the behaviour of the fibres' orientation. Due to the inherent limitations of UD-NCF architecture in achieving full impregnation with VARTM,

particularly for thicker panels, alternative approaches were explored. One proposed solution involved applying an infusion mesh above and below the UD-NCF material during the VARTM infusion process. However, applying the infusion mesh on both sides compromises the smooth surface finish. For fibre orientation inspection the polarisation camera must have one smooth surface.

As another proposed solution, Resin Transfer Moulding (RTM) was considered as an alternative technique to produce UD-NCF samples with controlled thickness. However, the resulting panels were also incompletely impregnated; see **3.3.4**.

3.2.1 Vacuum Assisted Resin Transfer Moulding (VARTM)

CFRP samples were fabricated using the Vacuum Assisted Resin Transfer Moulding (VARTM) technique for tensile testing, samples were used for open-hole tensile testing (see **Chapter-5**) and for reinforced-hole UD-TFP samples (**Chapter-6**). A schematic representation of the VARTM setup is provided in Figure 3.1. The primary components of the VARTM process include a glass panel, peel ply, infusion mesh, silicone connectors, infusion spiral tube, and a vacuum bag.

The fabrication process involved the following steps:

1. Fibre placement: Carbon fibre layers were carefully placed on a glass panel to ensure a smooth surface after curing, facilitating the fibres' orientation inspection using the polarisation camera.
2. Peel ply: A peel ply was applied over the fibre layers to aid in resin infusion and was later removed post-curing.
3. Infusion mesh: An infusion mesh was positioned atop the peel ply to enhance resin distribution throughout the carbon fibre layers.
4. Connector: Silicone connectors and an infusion spiral tube were installed at designated inlet and outlet points.
5. Vacuum bagging: A vacuum bag was sealed over the entire layup to create a vacuum environment during the resin infusion process.

Following a summary of the primary materials employed in the VARTM technique, a detailed step-by-step explanation of the CFRP panel manufacturing process will be presented.

Initially, the glass panel is carefully cleaned using acetone and polymer remover (Ambersil) to ensure a clean surface for the fibre orientation inspection using the

polarisation camera. A release agent (Fastcote, Marbocote Release Technology) is then applied to facilitate the post-curing removal of the composite panel.

After preparing the glass panel, the carbon fibre layup, peel ply, and infusion mesh are sequentially placed on the glass panel, as illustrated in Figure 3.1. Silicone connectors and the infusion spiral tube are also positioned on the glass panel to serve as inlet and outlet points for the infused resin. The entire layup is then covered within a vacuum bag using vacuum bagging sealant tape.

Prior to the infusion process, the epoxy resin system (as mentioned in **Section 3.1.3**) is thoroughly degassed to eliminate trapped air. The mixed resin and hardener are then infused through the inlet point at a pressure of 0.95 bar and room temperature.

Upon completion of the infusion process, the panel is cured in a programmable oven. A comprehensive description of the curing process using the programmable oven will be provided in **Section 3.2.3**.

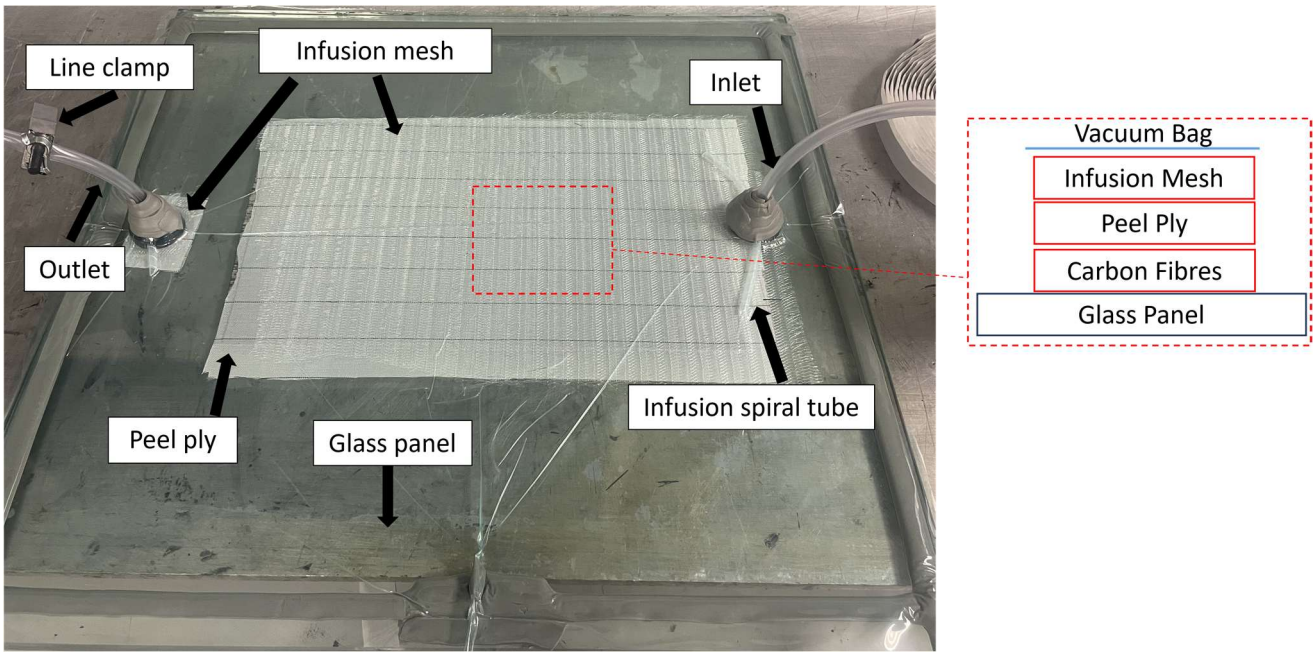


Figure 3.1 - Illustration of the VARTM set-up.

3.2.2 Resin Transfer Moulding (RTM)

Due to incomplete impregnation of the UD-NCF panels using the VARTM infusion technique, the RTM method was employed to assess their impregnation potential.

A series of tests were conducted to determine the maximum number of layers achievable with complete resin penetration.

The UD-NCF layup was positioned within a steel mould, and resin was introduced via two inlet ports on the mould's sides, as illustrated in Figure 3.2-a. This configuration facilitated resin flow through the layup from four directions, enabling both parallel and perpendicular impregnation relative to the fibre orientation, as illustrated in Figure 3.2-b. Before applying the UD-NCF layup to the mould, the steel mould underwent a thorough cleaning and preparation process similar to that of the glass panel used in the VARTM method.

A sealed steel mould was employed to ensure uniform thickness during the hydraulic pressing process (Figure 3.3). The epoxy resin system, with a total mixture of 405g, was used for the infusion process. A Hypaject pump was used to infuse the resin at various pressure stages. The infusion started at 2 bars for 5 minutes, then increased to 3 bars for 10 minutes, and finally to 4 bars for another 10 minutes. After the infusion process was completed, the steel mould was placed in a programmable oven for curing. The curing process using the programmable oven will be described in more detail in next section, **Section 3.2.3**.

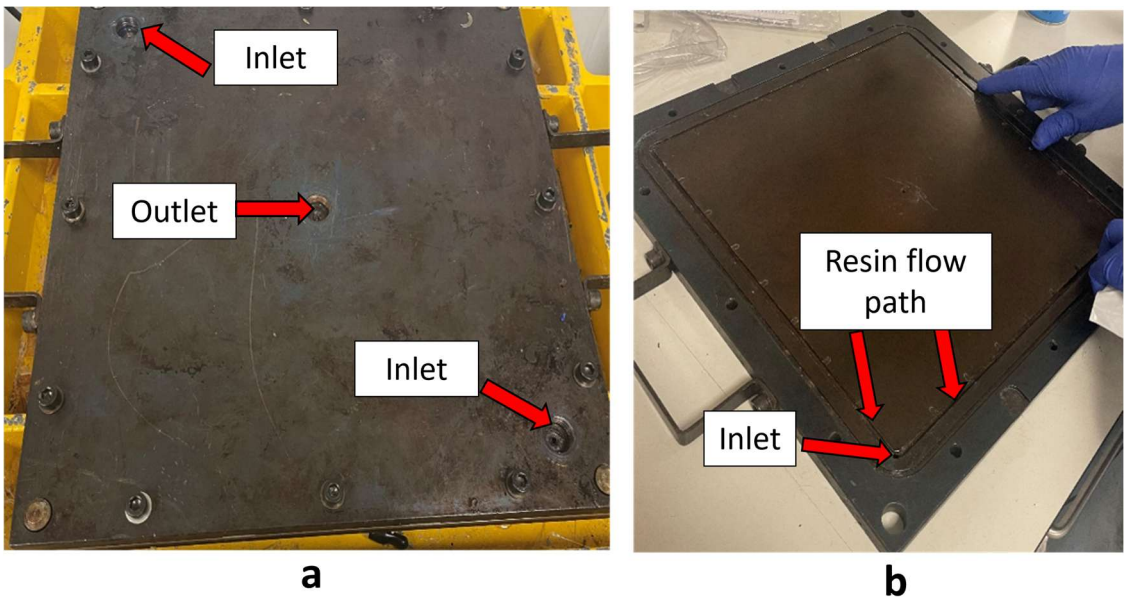


Figure 3.2 - RTM steel mould, where (a) shows the resin inlet and outlet ports, and (b) shows the direction of the resin flow to infuse the carbon fibre.

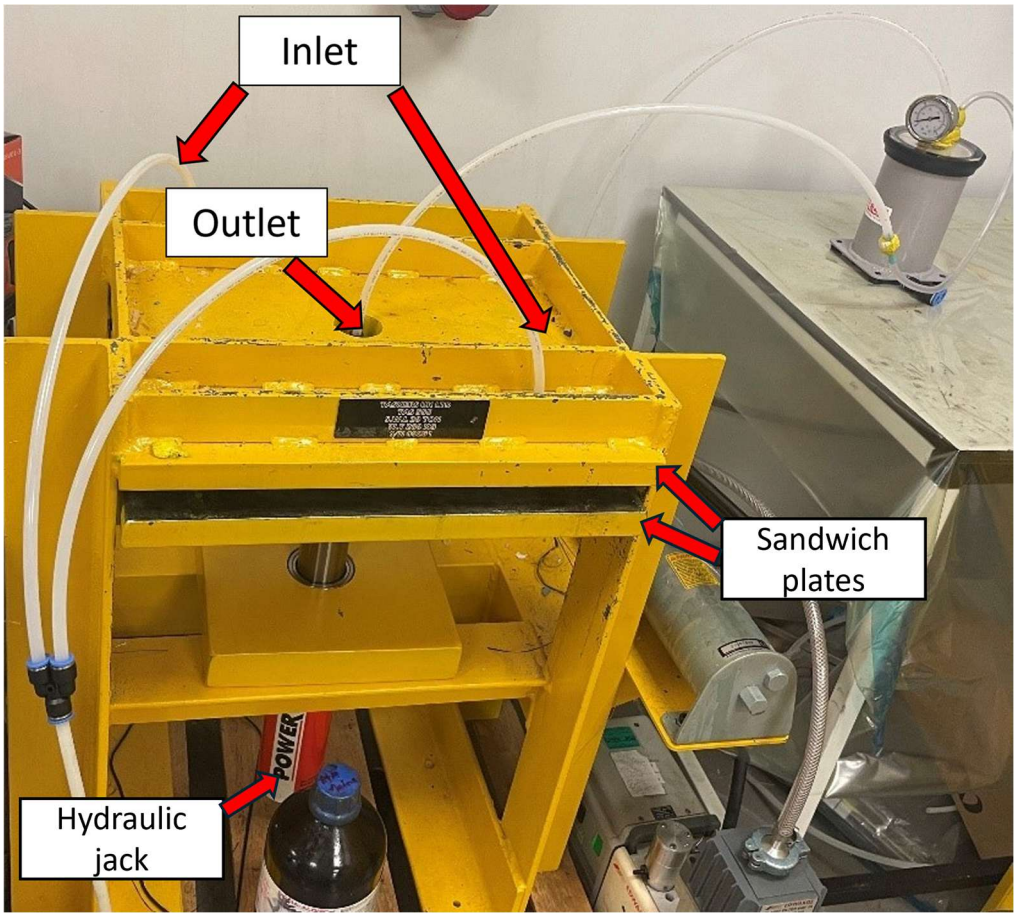


Figure 3.3 - RTM steel mould inside the hydraulic press.

3.2.3 Composite Panel Curing Cycle

Following the infusion process, the manufactured panels were subjected to a controlled curing cycle within a programmable oven. The specific curing cycle varied depending on the resin system employed: epoxy or silicone rubber.

All the epoxy resin panels underwent the following segment curing cycle:

1- Segment-1 (heating segment): The temperature was increased at a rate of 2°C/min until it reached 80°C.
2- Segment-2 (dwell segment): The temperature was maintained at 80°C for a duration of two hours.
3- Segment-3 (cooling segment): After two hours, the temperature was decreased at a rate of 3°C/min until it reached room temperature.
4- Segment-4: The cycle ends upon reaching room temperature.

The silicone rubber resin panels followed a similar curing cycle to the epoxy resin, with the exception of the dwell segment. The final temperature for the silicone rubber resin was 60°C, lower than the 80°C used for the epoxy resin. Figure 3.4 provides a visual representation of the curing cycle segments in the control screen as implemented in the programmable oven.



Figure 3.4 - The Thermo Scientific Heraeus (UT 6200) programmable oven (Senna) used for the curing process of panels with epoxy resin and silicone rubber resin.

3.2.4 Manufacturing TFP preform

The tailored fibre placement (TFP) preforms were sourced from the Advanced Manufacturing Research Centre (AMRC) and Carbon Three-Sixty. AMRC-manufactured TFP preforms (Figure 3.7 and Figure 3.24) were utilised to assess the polarisation camera's capabilities and demonstrate the inspection results, see **Section 3.3.1**. Reinforced hole tensile test preforms, consisting of two and four layers, were supplied by Carbon Three-Sixty (Figure 3.5), these preforms were used in **Chapter-4** (**Section 4.3.4** and **4.4.4**) and in **Chapter-6**..

In this process, fibre tows are oriented on the base material in the desired directions, according to CAD models. Continuous stitching secures the tows to the base, as illustrated schematically in Figure 3.6, for a one-layer unidirectional carbon fibre (UD-TFP) preform. Fibre tows are continuously laid on the glass fibre and fixed with

polyester thread until the desired length is achieved. The TFP machine then reverses to position the next tow adjacent to the previous one. However, the stitching process introduces small gaps between the carbon fibre tows, as illustrated in Figure 3.7. These gaps can result in resin-rich areas within the final composite which affects the mechanical properties of the tested samples. The machine continues this process until the desired width of the TFP preform is achieved. Following fabrication, the TFP preforms were infused with an epoxy resin system by VARTM to produce tensile test specimens.

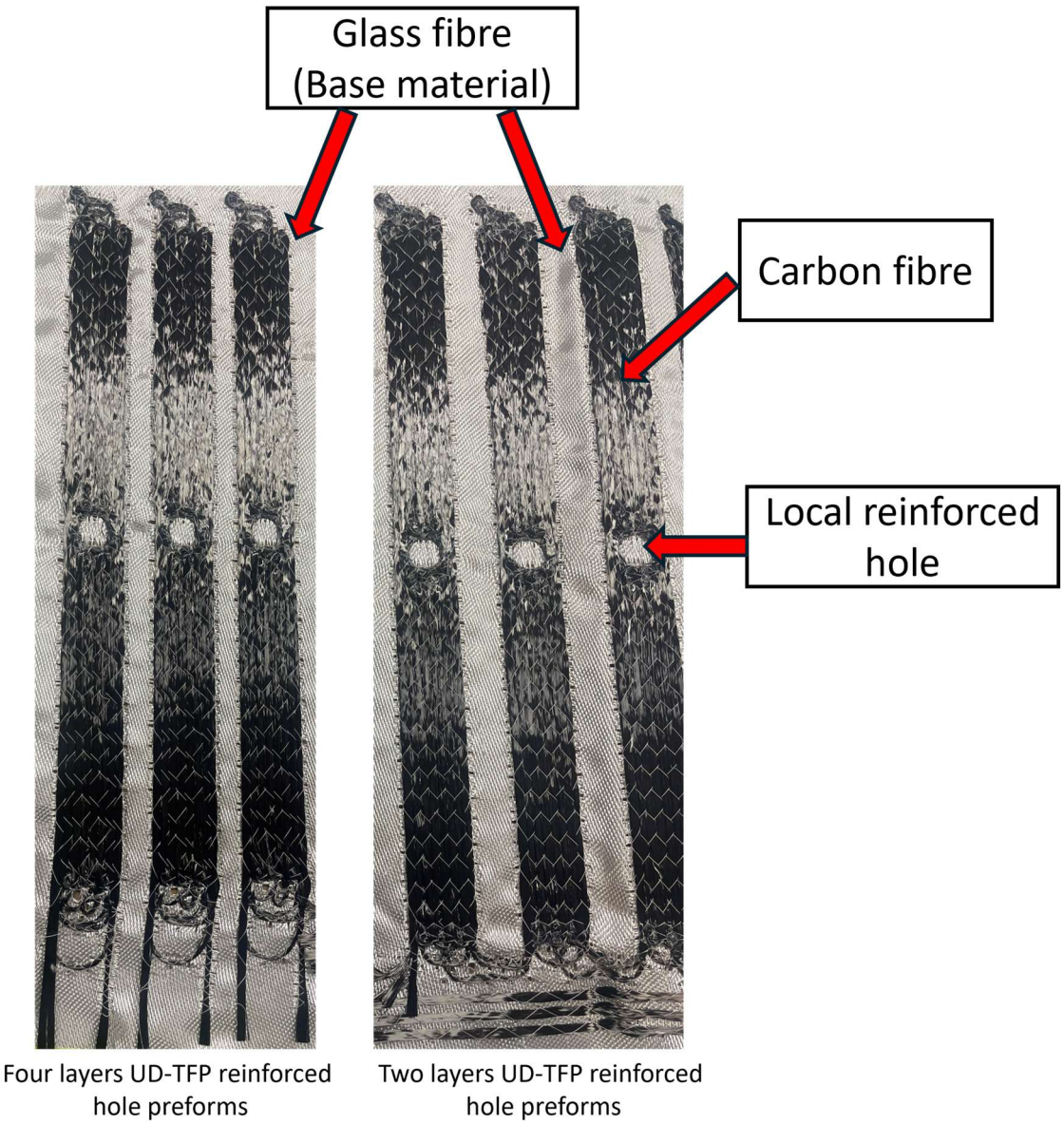


Figure 3.5 - Unidirectional TFP reinforced hole preforms consisting of two and four layers for tensile testing, manufactured by Carbon Three-Sixty.

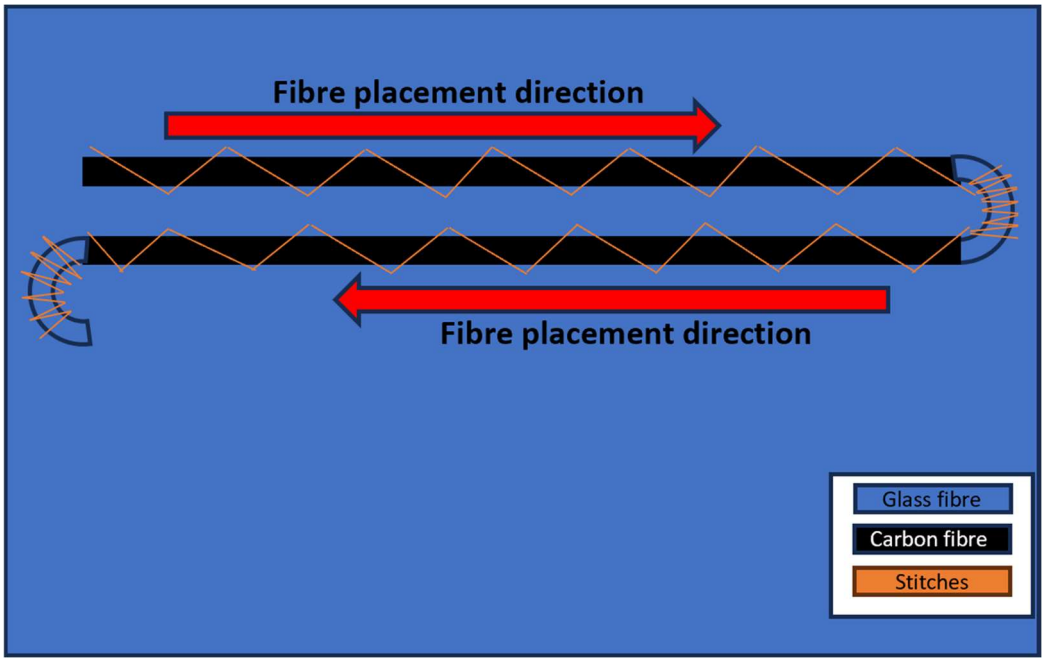


Figure 3.6 - Schematic illustrating the process of manufacturing UD preforms using TFP technique.

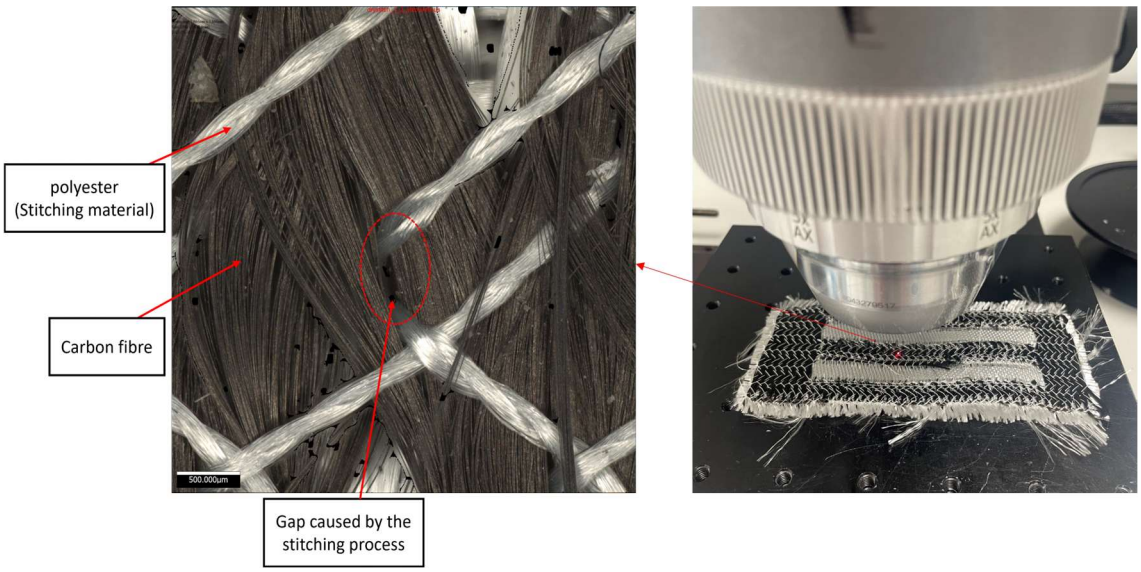


Figure 3.7 - An example of the gap between the fibres caused by the stitching process during manufacturing a TFP preform, captured using the Alicona.

One significant advantage of the TFP process is its ability to create open-hole tensile specimens without compromising fibre integrity through traditional drilling methods. This technique involves encircling the intended hole location with fibre tows to create reinforcement in the area to form a preform with the required hole diameter. However, the fabrication of reinforced-hole TFP preforms necessitates careful consideration of several factors. A crucial parameter is the number of layers required

to achieve symmetry around the reinforced hole, which is influenced by the fibre placement path. In this study, two- and four-layer TFP preforms were investigated to examine fibre orientation behaviour around the reinforced hole during tensile testing.

Figure 3.8 illustrates the selected fibre path configuration for producing unidirectionally reinforced hole TFP preforms with two and four layers. A carbon fibre tow was employed to reinforce a 12 mm diameter hole by stitching it onto the glass fibre (base material). A 250 mm length of tow was first placed and Fixed onto the glass fibre, then reversed to position an adjacent tow, as illustrated in Figure 3.6. This sequence was repeated until the tow reached the reinforced hole, where it was reversed to form a loop-back path near the hole (Figure 3.8- in red). The process was continued until the required number of reinforcement layers was obtained. The final reinforced hole preform has dimension of 250 mm length and 25 mm width. However, Figure 3.8 also shows the loop-back path of the carbon fibre tow as it approaches the reinforced hole, resulting in a resin-rich area.

Tensile tests will be conducted on TFP reinforced hole samples with three distinct hole diameters: 12 mm, 10 mm, and 8 mm, (See chapter-6). The initial TFP preform will incorporate a 12 mm diameter reinforced hole, as depicted in Figure 3.8. After curing, CNC machining will be employed to drill the desired hole diameter.

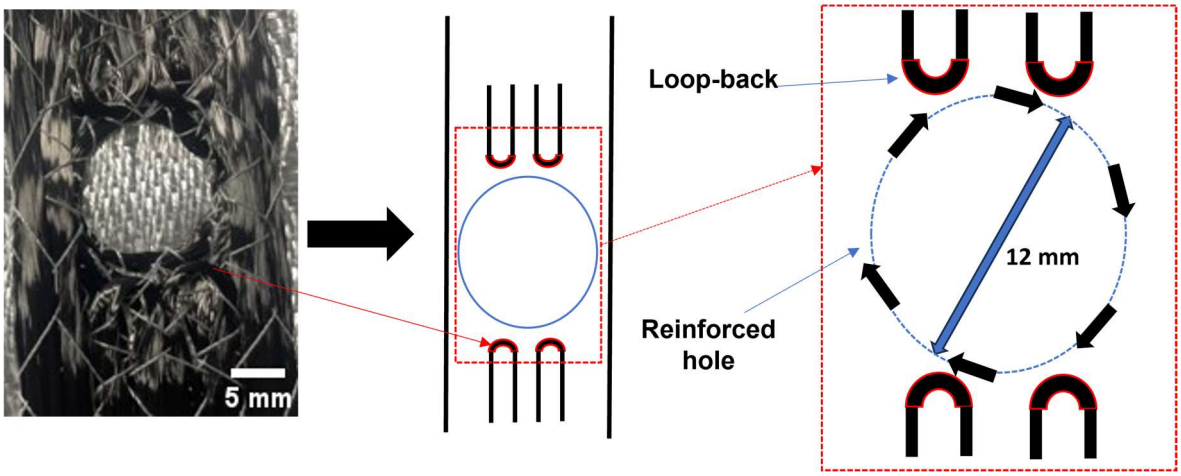


Figure 3.8 - Schematic illustration of the fibre placement and loop-back path used to manufacture the reinforced hole TFP preform.

The 12 mm machined hole aligns with the reinforced hole diameter, completely removing the resin in this region. While this may have a minimal impact on the reinforced fibres due to the machining process, the 10 mm and 8 mm machined holes result in varying sizes of resin-rich areas surrounding the reinforced hole. The 10 mm hole will create a relatively smaller resin-rich zone, whereas the 8 mm hole yields a larger one.

The influence of these varying hole diameters and resin-rich zones on fibre orientation during tensile testing is investigated using a polarisation camera.

3.3 Tensile test samples

The tensile tests were conducted on various fibre architectures to examine the carbon fibre orientations with increasing strain in both dry and composite forms. Additionally, open-hole tensile tests were performed with varying hole sizes to investigate the fibre orientation behaviour surrounding the machined hole during testing and assess its impact on mechanical properties.

3.3.1 Machining the samples

Tensile samples were machined from the composite panel using a computer numerical control (CNC) machine, (Axiom, AR-8 Pro). A diamond-coated router (OSG, DIA-BNC-4) with a 4 mm milling diameter was employed for this task. The specifications and recommended operating conditions for the DIA-BNC tool are detailed in Table 3.4 and Table 3.5.

Table 3.4 - DIA-BNC with 4 mm diameter specifications

Length of cut (mm)	Overall length (mm)	Shank diameter (mm)	Number of flutes (mm)	Helix
12	62	4	6	Right

Table 3.5 - DIA-BNC with 4 mm recommended conditions

Work material	**CFRP**
Milling speed (m/min)	100 ~ 180
RPM (min^{-1})	8000 ~ 14300
Feed rate (mm/rev)	0.05 ~ 0.06

Tensile specimens were prepared with dimensions of 250 mm in length and 25 mm in width. To investigate the effect of open holes on tensile behaviour, three-hole diameters (12 mm, 10 mm, and 8 mm) were drilled, (samples were used in the experimental chapters (**Chapter-5 and Chapter-6**). A baseline specimen without a hole was also prepared for comparison.

A (DIA-BNC) milling machine with a 4 mm diameter end mill was employed to drill and mill the holes to the desired diameters, where it started with a 4 mm hole and kept milling around the hole to reach the 12, 10, or 8 mm diameters. All holes were machined using the same cutting process and tool. Hole diameters were measured using a Kennedy hole gauge tool from Cromwell. Figure 3.9 illustrates a schematic representation of the baseline and open-hole tensile specimens.

The same machine and cutting process were applied to the UD-TFP reinforced hole samples, as illustrated in Figure 3.10. However, these samples possess a 12 mm local reinforcement. Machining a hole with a diameter smaller than this reinforcement results in a resin-rich area surrounding the reinforcement fibres. This occurs because the infusion process fills the entire 12 mm reinforced area with resin. Consequently, drilling a hole smaller than 12 mm leaves excess resin around the reinforcement.

Figure 3.11 presents the three different hole diameters machined on the UD-TFP samples with 12 mm local reinforcement. The 12 mm hole demonstrates no resin-rich area, as the entire resin in the 12 mm local reinforcement area is removed. In contrast, the 10 mm hole exhibits a clear resin-rich zone due to the diameter of the machined hole with respect to the diameter of the local reinforcement. A more resin-rich area is observed in the 8 mm hole compared to the 10 mm diameter hole.

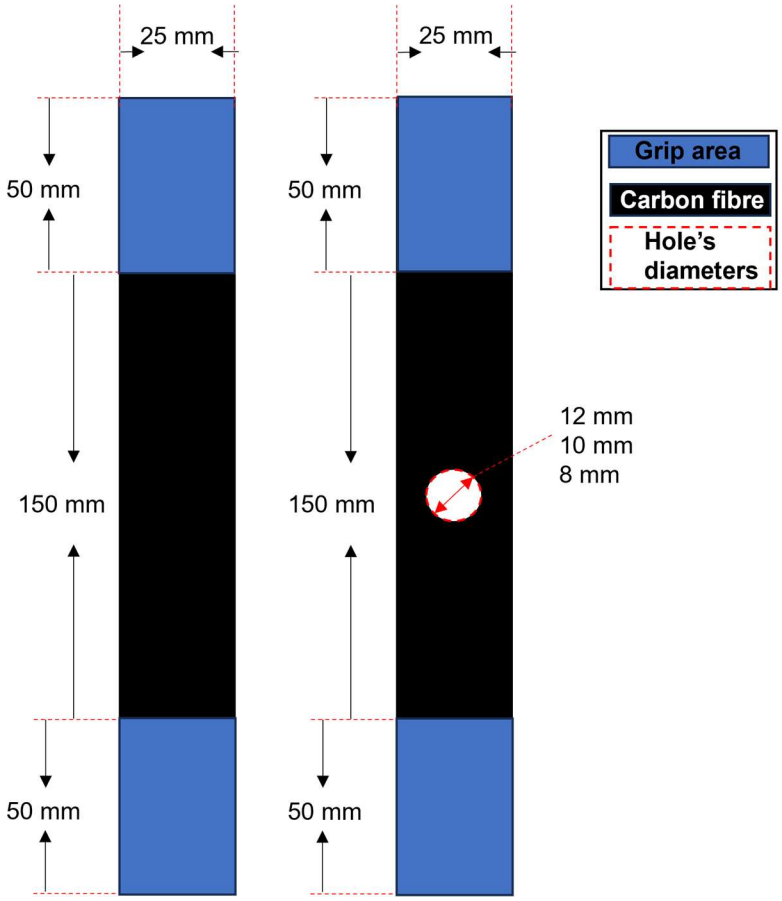


Figure 3.9 - Schematic for baseline and open-hole tensile sample.

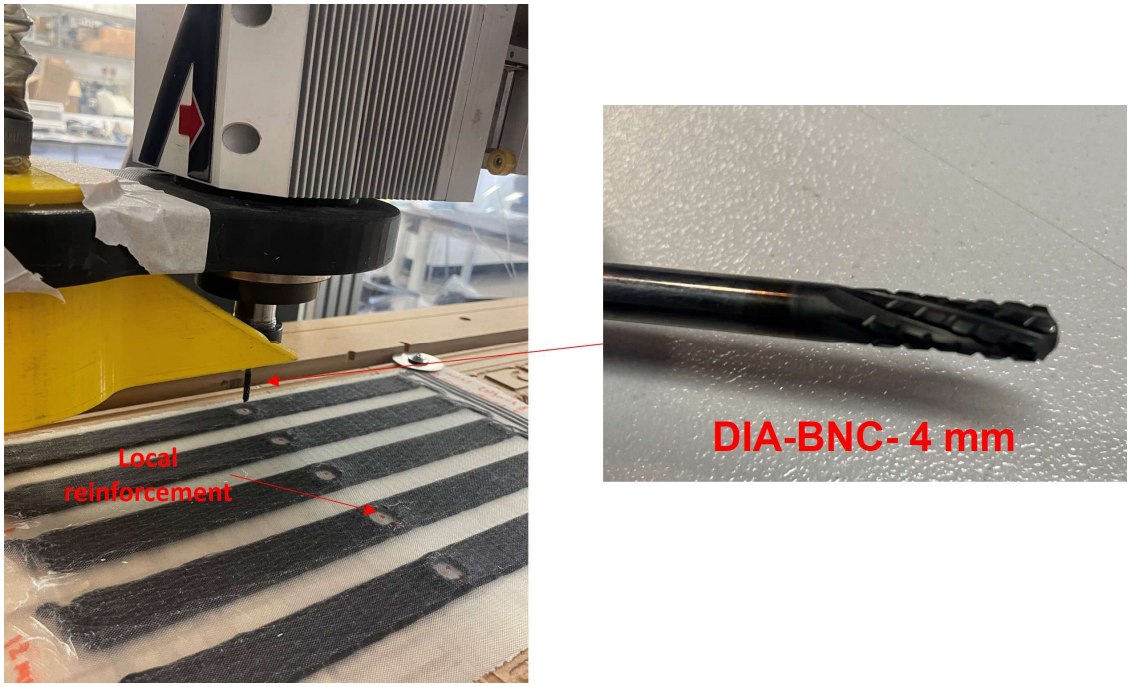


Figure 3.10 - Machining the UD-TFP reinforced hole samples with different hole diameters into the local reinforcement using the CNC machine (Axiom, AR-8 Pro) and (OSG, DIA-BNC-4) tool.

The strain of the specimens presented in the experimental chapters was determined from the test displacement recorded by the testing machine. The primary objective was to investigate the change in the fibre orientation within the samples under increasing strain. Due to the variation in the thickness of the TFP specimens, the thickness was measured at multiple locations across each sample, including positions adjacent to the reinforced hole on both sides. These measurements were employed to calculate the stress, which was then used to plot the stress–strain curves. This methodology was consistently applied to all specimen types, (the UD-NCF, Twill 2×2, and UD-TFP reinforced-hole samples), thereby ensuring that equivalent conditions were maintained across all experimental comparisons.

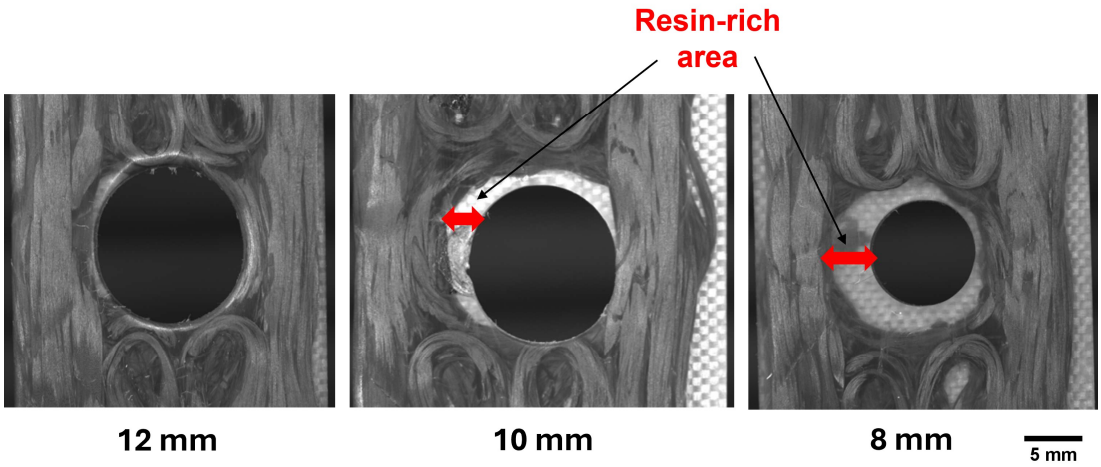


Figure 3.11 - An example of four layers UD-TFP reinforced hole samples with three different hole diameters (12 mm, 10 mm, and 8 mm) were machined into the 12 mm local reinforcement.

3.3.2 Manufacturing tabs for tensile test samples

The VTC401 epoxy prepreg, a 245 gsm 2x2 twill weave T300 3K carbon fibre material, was employed to fabricate end tabs for the tensile test specimens. The prepreg exhibited a fibre volume fraction of 48.84% and a cured ply thickness of 0.28 mm, as determined by the standard method B of BS EN ISO 14127 [139]).

Eight layers of the prepreg, each measuring 250 mm x 250 mm, were applied and cured in a programmable oven for one hour at 100°C. Following the curing process, the resulting panel was sectioned into 50 mm x 25 mm, which were attached to both ends of the tensile test samples as end tabs. The choice of this material was due to

their strong and compatible interface with the specimen, ensuring effective load transfer. Also, this material was available and practical for use in our laboratory, making it a suitable choice for the preparation of tensile test samples.

3.3.3 Preparing the tensile sample's surface

The polarisation camera will be employed for both offline and online inspection of tensile test samples. During tensile testing, certain samples may exhibit overexposed regions (even when applying the Auto-exposure option in the XPL software) due to the influence of the illumination source on the sample's surface, resulting in information loss. To overcome this issue and ensure optimal image quality, especially during online inspection, a smooth surface finish is essential.

To achieve the required smooth surface, samples were subjected to a sanding process using sandpaper of varying grain sizes, as detailed in Table 3.6. Figure 3.12 presents a comparison of a Twill 2x2 composite sample captured using the polarisation camera before and after the sanding process, illustrating the significant impact of surface preparation on image quality and the reduction of illumination-induced effects. The methodology was employed for the specimens subjected to tensile testing (open hole tensile testing samples, **Chapter-5**, and reinforced hole UD-TFP samples, **Chapter-6**).

Table 3.6 - Sanding process for tensile samples

Grain size (grit)	Sanding time (min)
60	2
240	2
400	2
1000	2
2500	2

3.3.4 Examples of incompletely Impregnated UD-NCF Panels

This section presents examples of UD-NCF panels that exhibited incomplete resin impregnation when manufactured using VARTM and RTM infusion techniques. Achieving the 4 mm thickness proved challenging due to the compact fibre

arrangement and the large number of layers applied, which hindered resin flow through the fibres.

Figure 3.13-a illustrates a 22-layer UD-NCF panel manufactured via the VARTM technique. A 12 mm hole was machined using a CNC machine to reveal incomplete resin impregnation areas of within the panel. Figure 3.13-b shows a similar 18-layers

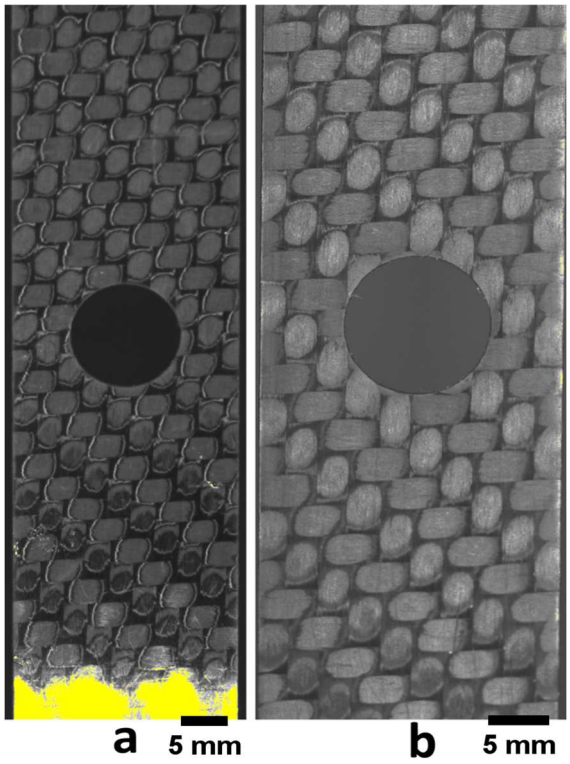


Figure 3.12 - Example of raw saturation images for Twill 2x2 sample with one layer imaged using the polarisation camera before, (a), and after, (b), sanding process. The yellow area at the bottom of Figure (a) is an overexposed area.

UD-NCF panel, also manufactured using VARTM, where full impregnation was not achieved despite reducing the number of layers.
Figure 3.14 depicts a 16-layer UD-NCF panel fabricated using the RTM technique. This panel exhibits a larger area of incomplete impregnation in its central region.

To address the issue of incomplete resin impregnation in manufactured panels, a potential solution involves applying two infusion meshes positioned above and below the UD-NCF layers during the VARTM infusion process. However, the polarisation camera necessitates a smooth, finished surface for inspecting the

carbon fibre orientation. Consequently, panel thicknesses were reduced in the experimental chapters to ensure the full resin impregnation of the UD-NCF samples to study the fibres' orientation behaviour during the tensile testing.

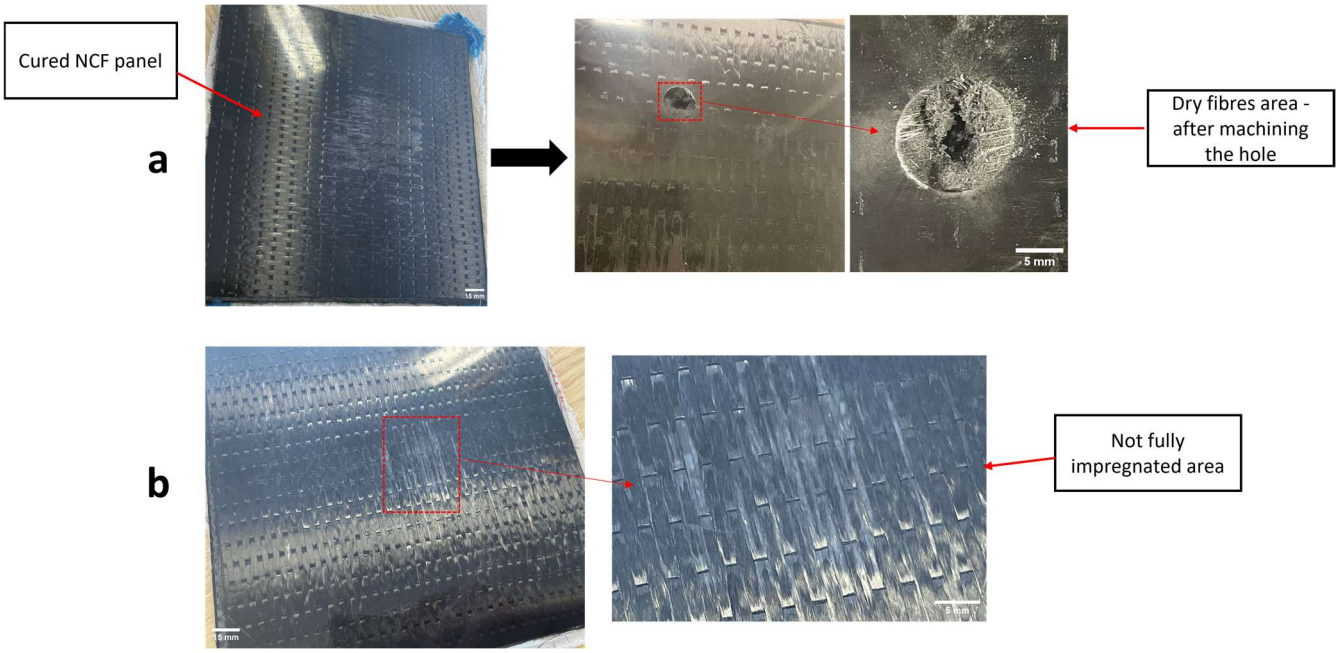


Figure 3.13 - Example of not fully impregnated UD-NCF panels manufactured using the VARTM technique, where (a) shows the UD-NCF panel with 22 layers and (b) UD-NCF panel with 18 layers.

3.1 Characterisation of carbon fibre reinforced polymer (CFRP)

To determine the fibre volume fraction (FVF) of a carbon fibre-reinforced polymer (CFRP) panel, which is a critical parameter influencing the mechanical properties, density measurements were conducted. Eight random sections were cut from the manufactured panel and subjected to density measurement using the Micrometrics AccuPyc II 1340 machine. Similarly, the density of the epoxy resin matrix was measured using the same procedure to use the details in the FVF calculation.

The following equations represent how to calculate the FVF with the use of the density information of the matrix and composite, based on the standards test method (D3171):

$$W_m = 100 - \left(\frac{A_r \; X \; N_p \; X \; 0.1}{\rho_c \; X \; h}\right)$$

Equation 3-1

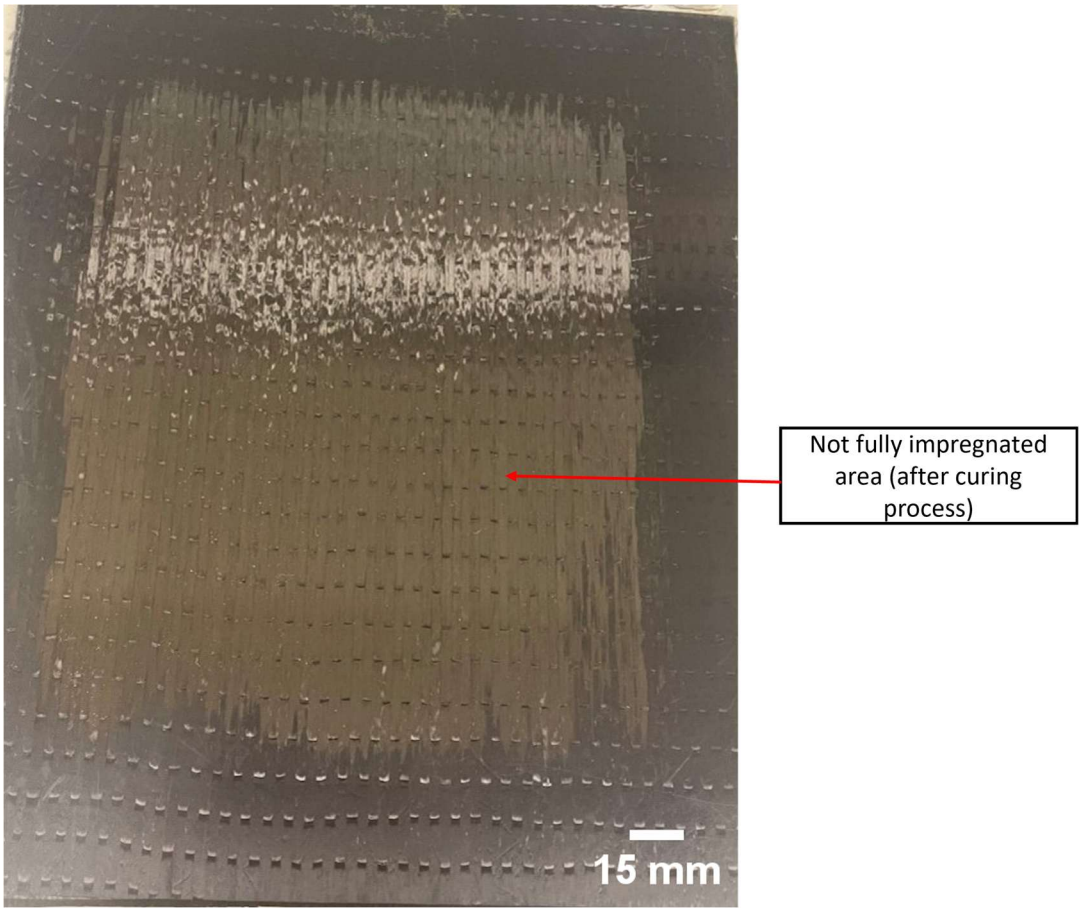


Figure 3.14 - Example of not fully impregnated UD-NCF panel with 16 layers manufactured using the RTM technique.

where W_m is the calculated matrix's weight, A_r is the mass of one sheet of the reinforcement, N_p is representing the number of sheets that used in the test samples, ρ_c is the density of the composite, and h is representing the sample's thickness. After that, the volume of the matrix will be calculated as follows:

$$V_m = W_m \, X \, \frac{\rho_c}{\rho_m}$$

Equation 3-2

where V_m is the volume of the matrix, and ρ_m is the density of the matrix. After calculating the volume of the matrix, the fibre content, V_f, can be calculated using the following equation:

$$V_f = 100 - V_m$$

Equation 3-3

The average of the fibre volume fraction (FVF) for the manufactured samples, UD-NCF, Twill 2x2, and UD-TFP with two and four layers, is presented in Table 3.7. Additionally, the optical microscopy was used to image samples after the tensile testing to visualise the damage and the impact of machining the hole to the fibre's orientation.

Table 3.7 - The fibre volume fraction for the tested materials

Material	Fibre volume fraction (%)
UD-NCF	33.06
Twill 2x2	32.83
UD-TFP	32.04

3.2 Polarisation camera

3.2.1 Introduction

Sony has introduced a novel polarised sensor integrated into their camera technology. The CMOS sensor (IMX250, 5.1 MP) serves as the foundation, with a polarisation array strategically placed between the on-chip microlens and pixel array. As illustrated in Figure 3.15, the polarisation array is divided into four directional sections (0°, 45°, 90°, and 135°), assigning a unique direction to each pixel. This configuration enables the capture of a single image with four different polarisation channels.

A 2x2 pixel block, as illustrated in Figure 3.15, aligns these directional sections: 90° and 45° occupy the top left and right positions, respectively, while 135° and 0° are positioned at the bottom left and right. This pixel block serves as the fundamental unit for calculating light intensity within each pixel. A significant advantage of this technology is the real-time calculation of both the degree and angle of linear polarisation.

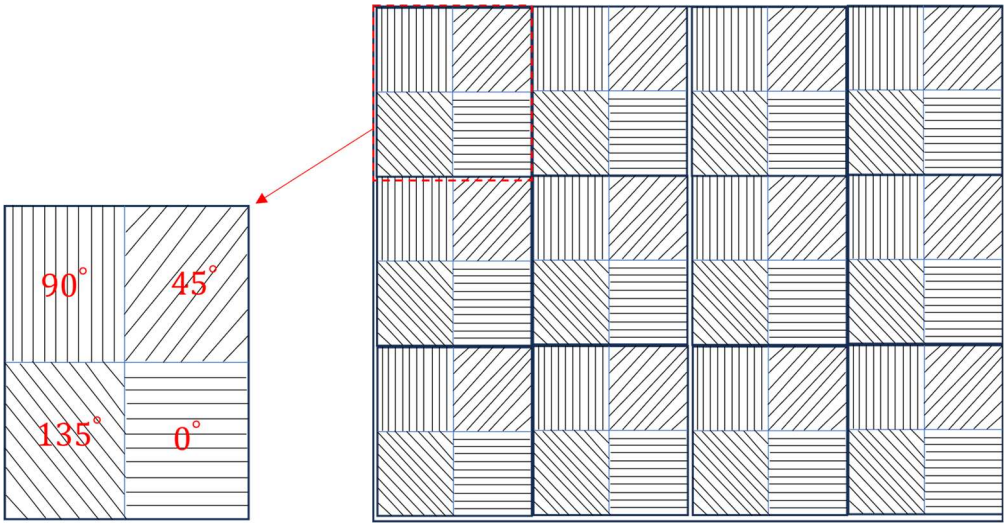


Figure 3.15 - Schematic of the polarisation array used on Sony polarisation camera.

The degree of linear polarisation (DoLP) is representing the ratio of the intensity of polarised to unpolarised part of the light where the total intensity will present for the polarised light whilst the intensity will be zero for the unpolarised light. The use of DoLP image will give the ability to distinguish the areas with higher and lower polarisation. For the angle of linear polarisation (AoLP), the information about the surface normal for the object can be extracted from the direction of polarisation. The HSV colour mapping is used to show the polarisation information where the hue channel is used for the direction of polarisation while the saturation channel used for the degree of linear polarisation.

3.2.2 Principle

The polarisation camera captured images containing information on the Degree of Linear Polarisation (DoLP) and the Angle of Linear Polarisation (AoLP), derived from Stokes parameters. The Stokes polarisation parameters, Stokes vector, describes the polarisation state of light. The four parameter representations are as follows: the first parameter represents the total intensity of the light, S_0. The second parameter describes the liner polarisation states, S_1, which show the difference between vertical and horizontal polarisation. The third parameter describes the polarisation state at 45°, S_2, which shows the difference between the polarisation at + 45° and the polarisation at - 45°. The fourth parameter describes the circular part, S_3, which results from the difference between the right circular polarisation and the left circular polarisation [108], [140]–[142].

The equations that used to calculate the DoP and AoP are as following:

$$\begin{pmatrix} S_0 \\ S_1 \\ S_2 \\ S_3 \end{pmatrix} = \begin{pmatrix} I_0 + I_{90} \\ I_0 - I_{90} \\ I_{45} - I_{-45} \\ I_R - I_L \end{pmatrix}$$

Equation 3-4

where (I_0) in Equation 3-4 represent the vertical polarisation for light intensity, (I_{90}) is the horizontal polarisation, (I_{45}) is the polarisation at 45°, (I_{-45}) is the polarisation at -45°, (I_R) represents the right circular polarisation, and (I_L) is for the left circular polarisation. For fully polarised light, the square of the total intensity, ${S_0}^2$, is equal to the sum of the squares of the Stokes parameters: ${S_0}^2 = {S_1}^2 + {S_2}^2 + {S_3}^2$. Conversely, for fully unpolarised light, the Stokes parameters S_1, S_2, and S_3 are zero. The degree of polarisation, DoP, used to represent the partial polarisation which can be defined mathematically as follows:

$$DOP = \frac{\sqrt{{S_1}^2 + {S_2}^2 + {S_3}^2}}{S_0}$$

Equation 3-5

When the circular polarisation (S_3) is equal to zero, the degree of linear polarisation, DOLP, will be defined mathematically as following:

$$DOLP = \frac{\sqrt{{S_1}^2 + {S_2}^2}}{S_0}$$

Equation 3-6

The Angle of Linear Polarisation (AoLP) is calculated using the inverse tangent function. The result provides insight into the direction of polarisation, which, in turn, indicates the orientation of the carbon fibre. The AoLP is defined by the following equation[108], [143] :

$$AoLP = \arctan\frac{S_2}{S_1}$$

Equation 3-7

3.2.3 Camera's specification

A Sony XCG-CP510 polarised camera (Figure 3.16) was employed for optical, non-destructive inspection offline and during the tensile tests for CFRP samples. The 5.1 MP camera, supplied by OEM Automatic, utilizes a global shutter IMX250MZR CMOS sensor with monochrome quad-polarised filters to capture polarised light in four directions. The camera offers a 2448 x 2048 pixel resolution and a frame rate of 23 fps. It supports GigE Vision 1.2/2.0 and Power over Ethernet (PoE). Image processing can be performed using various programming languages such as Python and MATLAB [134], [144], or through Sony's XPL software.



Figure 3.16 - The polarisation inspection camera, Sony XCG-CP510 polarised camera.

In the experimental work, the XPL-SDKW software was employed to process received images and present the results in a video format. The XPL software's user interface offers various sections for controlling image display, polarisation parameters, and reflection settings. This section explains the key settings within the control screen, including image (1) and image (2) settings, colour map selection, and reflection control options.

The image (1) setting provides a range of options for visualizing the image data and can be summarised as follows:

Raw: Displays the original, unprocessed black-and-white image.

Raw (display invalid pixels): Highlights the overexposed and underexposed areas in the image and represents them in yellow and red, respectively. This option will be employed to present the experimental images captured during tensile testing throughout all experimental chapters.

Raw (4 split): Divides the image into four quadrants, each displaying a polarisation image at a different angle (0°, 45°, 90°, and 135°).

Polarisation angle: Allows the display of a full image at one of the polarisation angles (0°, 45°, 90°, or 135°).

Average: This function calculates and displays an average image from the four polarisation images, resulting in a fully depolarised image.

Virtual polariser: This enables the option to adjust the polarisation angle from 0° to 180° using a slider and displays the calculated image.

A tailored fibre placement (TFP) preform was utilized to exemplify selected options in image (1) setting. When the raw (display invalid pixels) option was selected, overexposed and underexposed regions were observed, as illustrated in Figure 3.17. These areas are highlighted in yellow and red, respectively. The overexposed regions occur in the glass fibre materials, which is the preform's base material. However, the underexposed regions are located on the base table supporting the sample.

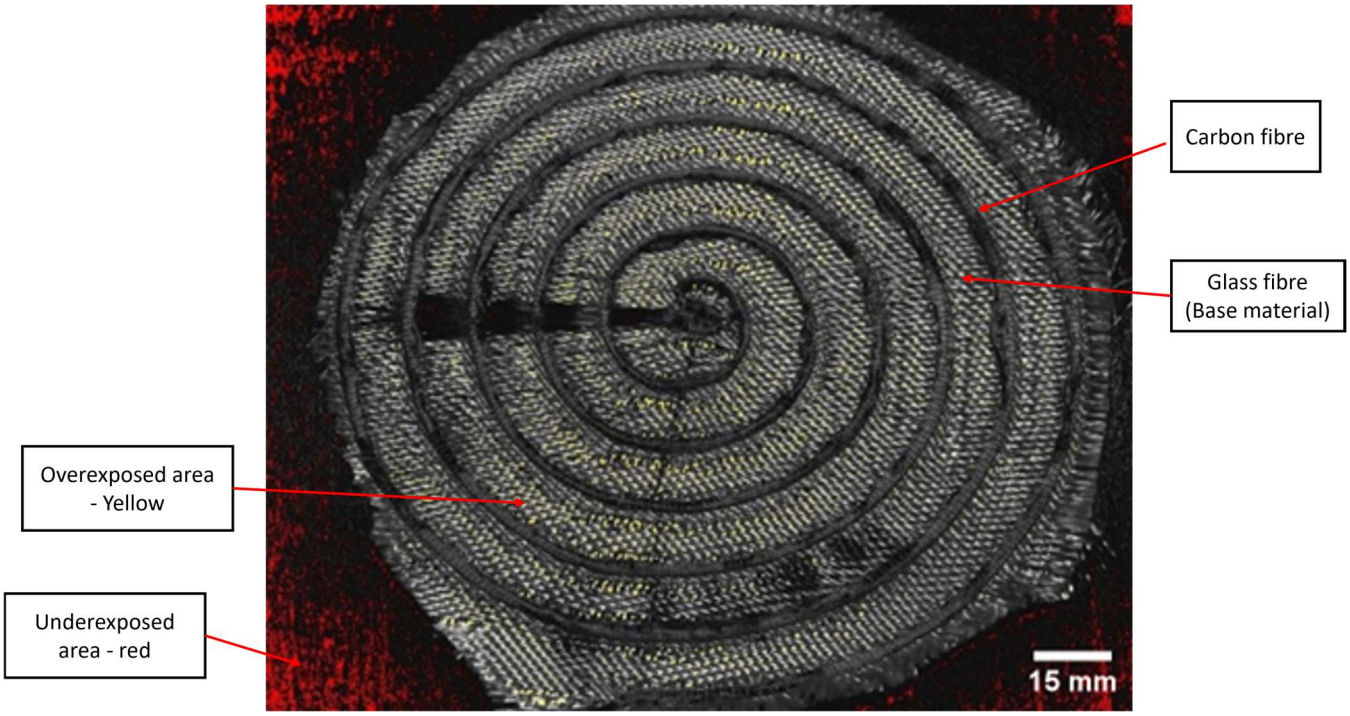


Figure 3.17 - TFP preform captured using the polarisation camera to show the overexposed and underexposed areas in the image (yellow and red, respectively) when choosing the raw (display invalid pixels) option in the XPL software.

Figure 3.18 illustrates the image's polarisation orientations splitting resulting from the raw (4 split) option in image (1) settings. This setting enables simultaneous visualization of the four polarisation directions. The top-left quadrant represents the 90° polarisation direction, while the top-right quadrant displays the 45° direction. The bottom-left quadrant corresponds to the 135° direction, and the bottom-right quadrant shows the 0° direction.

For the Image (2) setting, the Degree of Linear Polarisation (DoLP) option quantifies the polarisation of incident light for each pixel, ranging from unpolarised (0%) to fully polarised (100%). The Surface Normal option visualises the direction (angle) of polarisation, which can be represented using two different colour maps: RGB and

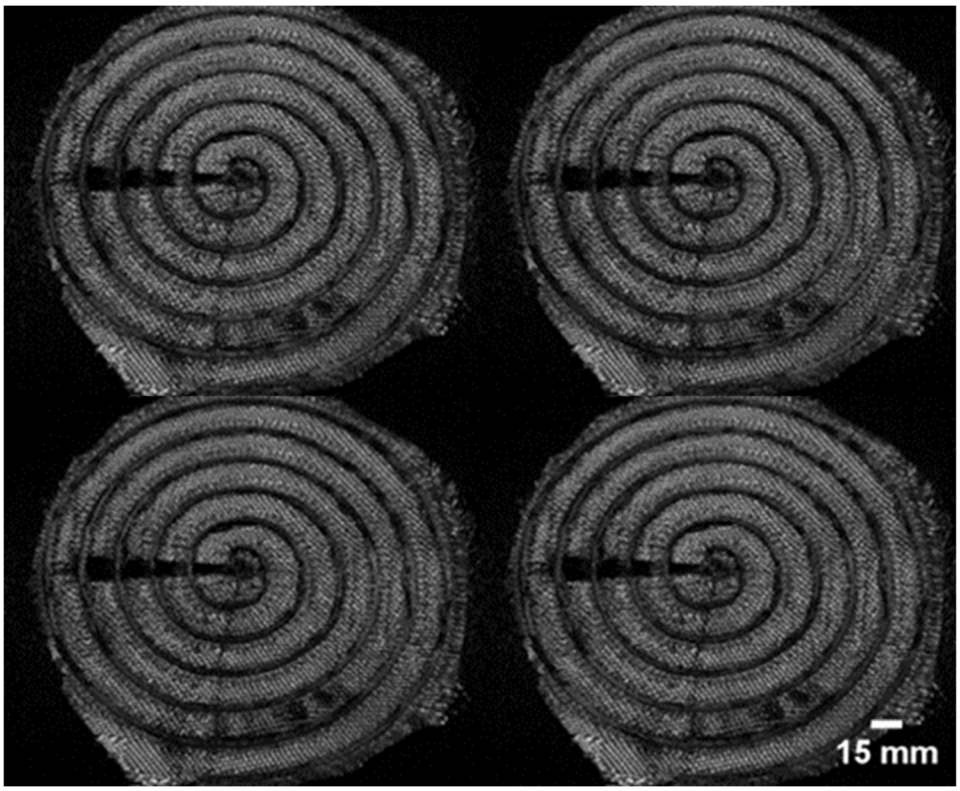


Figure 3.18 - TFP preform captured using the polarisation camera shows the 4 section images representing different polarisation directions at the same time when choosing the raw (4 split) option in the XPL software.

HSV. The surface normal imaging option, represented using the HSV colour map, will be employed to illustrate fibre orientation throughout the experimental investigations presented in **Chapters 4, 5, and 6**. When selecting the Reflection option in the Image (2) setting, users can choose from multiple techniques to

manipulate reflection components, such as enhancement, cancellation, or extraction.

To illustrate the DoLP image output, the same TFP preform was used (Figure 3.19). In this image, carbon fibre is depicted in grey and the glass fibre and polyester stitching thread in black. The stitching thread is used to fix the carbon fibre to the glass fibre base material.
The Surface Normal image option, which represents the Angle of Linear Polarisation (AoLP) information, visualizes the orientation of the carbon fibres. Figure 3.20 displays the TFP preform using two different colour maps (RGB and HSV) to represent the fibre orientations.

It is important to note that not all XPL software options in the image (1 and 2) settings were used during both the offline and online inspection stages. The offline inspection, conducted on samples without applied force (dry or resin-infused), primarily focused on the options; raw saturation, degree of linear polarisation (DoLP), and normal surface images. The raw saturation image helps identify overexposed and underexposed regions within the sample. The DoLP image visually represents the polarisation state of carbon fibres on a greyscale. The normal surface image provides information about the fibres' orientation.
During the online inspection, samples were captured under tensile loading, with a focus on the XPL software's raw saturation and normal surface image options.

3.2.4 Colour map calibration

RGB and HSV colour maps are commonly employed in image processing to represent image data. The RGB colour space utilizes a combination of red, green, and blue primary colours to define a wide spectrum of hues. By varying the intensity of each primary colour, different colours can be generated.

The HSV colour space represents colours using three components: hue, saturation, and value. Hue specifies the colour's position on the colour wheel, measured in degrees from 0° to 360°. Saturation indicates the colour's purity or intensity,

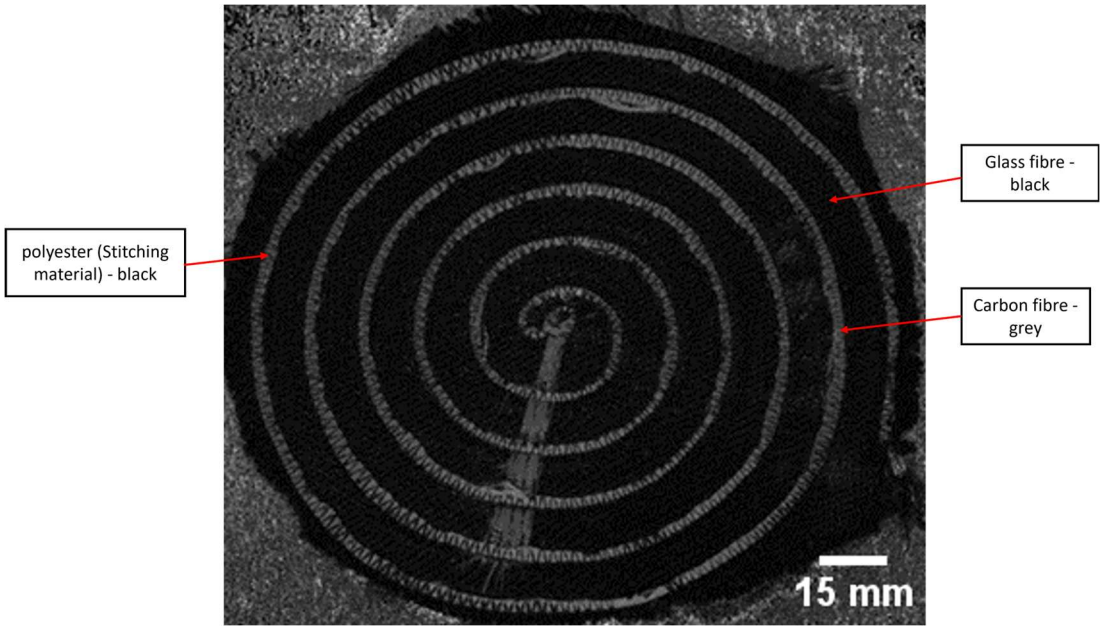


Figure 3.19 - TFP preform captured using the polarisation camera, showing the DoLP image when choosing the (DoLP) option in the XPL software.

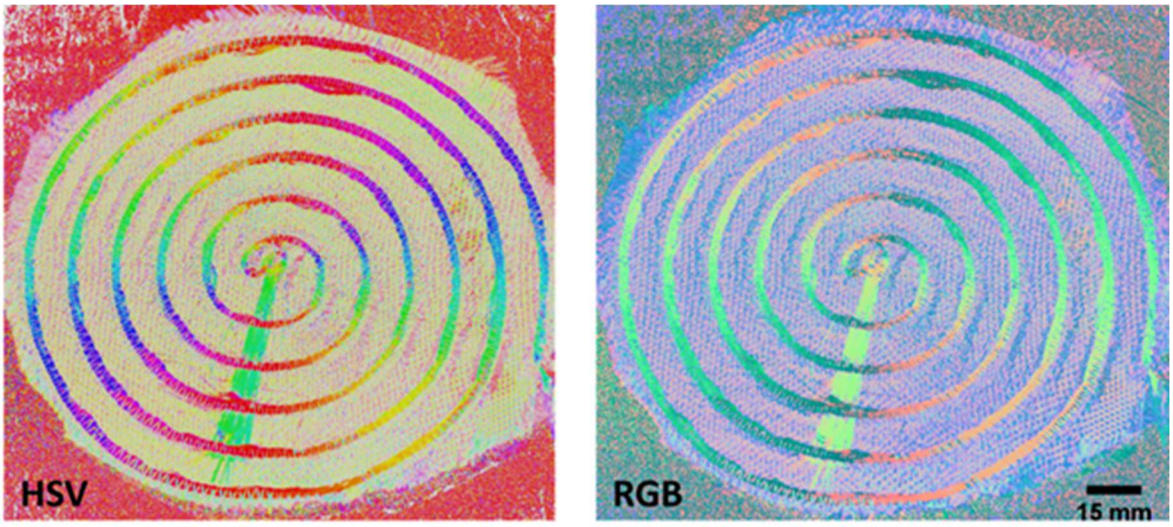


Figure 3.20 - TFP preform captured using the polarisation camera, showing the fibres' orientation when choosing the (normal surface) option in the XPL software.

representing the deviation from a grayscale colour. Value, also known as brightness, determines the luminance or darkness of a colour. In this thesis, all images captured during the experimental investigations (**Chapters 4, 5, and 6**) are presented using the HSV colour map, which was employed to visualise and monitor fibre orientation.

To establish a consistent colour reference for fibre orientation, a polarisation camera was fixed in a specific position. This ensured that both offline and online inspections would utilize the same colour-angle mapping for all samples. To calibrate the colour-angle relationship, a carbon fibre tow was rotated from 0° to 180°, capturing the resulting colour values using the polarisation camera. Figure 3.21 and Figure 3.22 illustrate the calibration results in HSV and RGB colour maps, respectively.

For the experimental results, the HSV colour map was selected to represent fibre angles. This choice was motivated by the HSV colour map's ability to differentiate between various angles compared to the RGB colour map. In the HSV image, the hue channel encodes the fibre orientation based on the Angle of Linear Polarisation (AoLP) information, while the saturation channel represents the Degree of Linear Polarisation (DoLP) information. The value channel, which encodes brightness, was not utilized in this analysis.

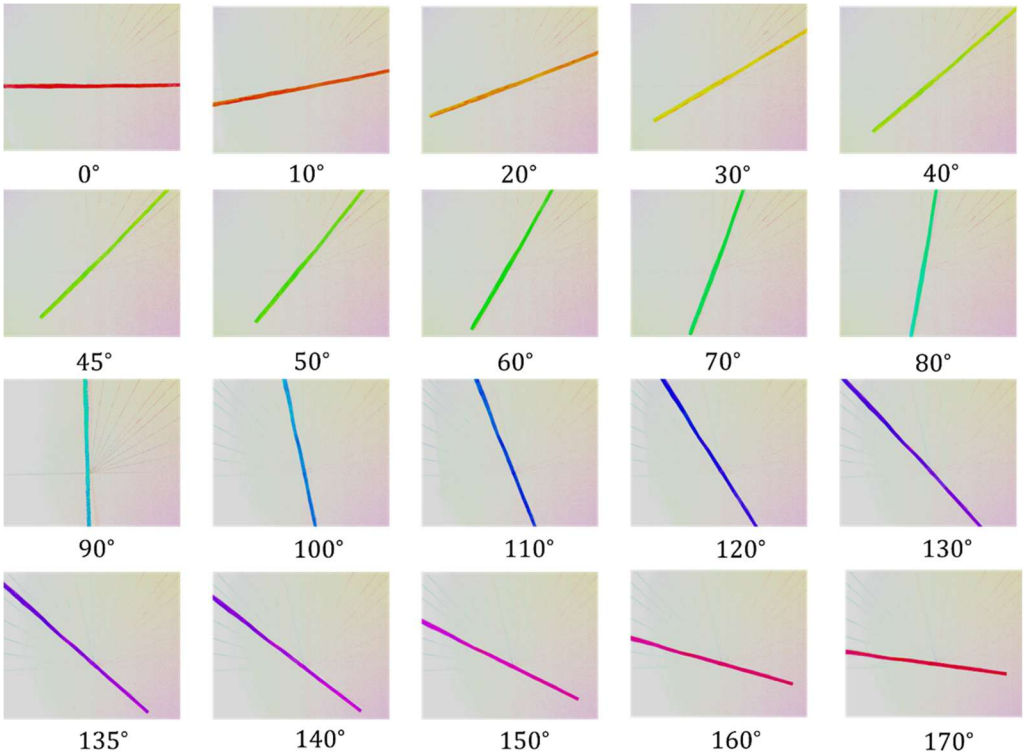


Figure 3.21 - Carbon fibre tow was captured using the polarisation camera to reference the colours in the HSV colour map to the corresponding fibres' angle after fixing the camera's position.

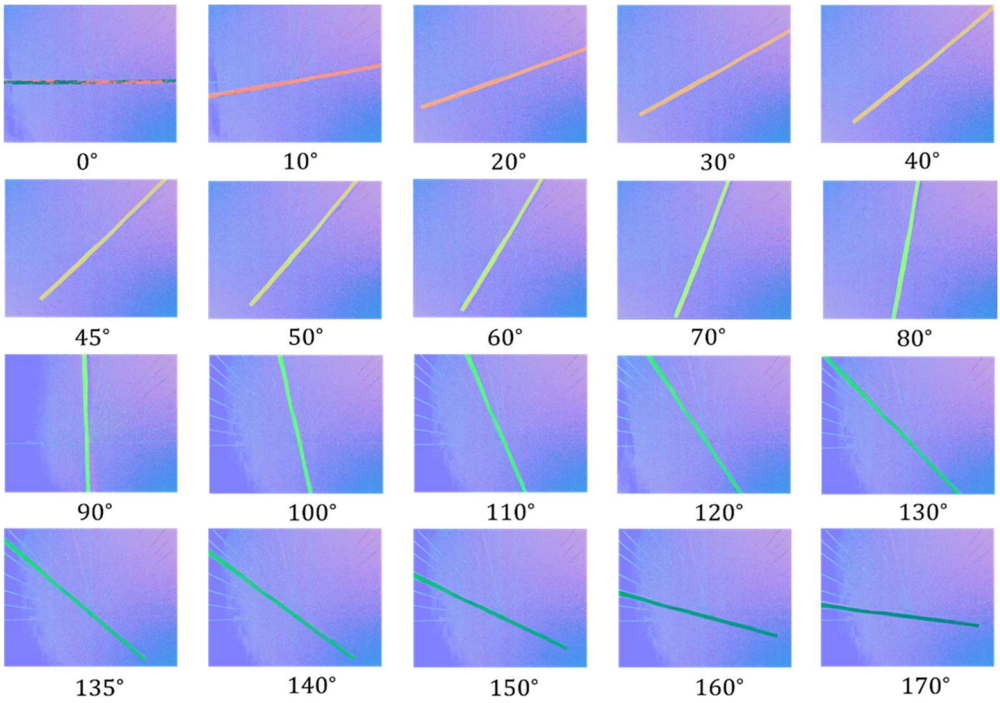


Figure 3.22 - Carbon fibre tow was captured using the polarisation camera to reference the colours in the RGB colour map to the corresponding fibres' angle after fixing the camera's position.

3.3 Experimental set-up

3.3.1 The setup using a LED ring lighting source.

An inspection frame was constructed and secured to an optical table using extrusion components. This setup minimized the impact of external disturbances, such as vibrations or movement, on the experimental results. Also, a blackout curtain was employed to prevent the samples from external light sources for further control of the testing environment.

The polarisation camera was positioned on one side of the inspection rig and angled to capture the sample plate effectively. At the same time, the illumination source, an LED ring, was mounted on the opposite side of the rig, as illustrated in Figure 3.23. To validate the experimental setup and assess the influence of illumination on the polarisation camera, TFP preforms with various fibre orientations were utilized, Figure 3.24, these included reinforcement hole, spiral, and unidirectional fibre orientations, as the polarisation camera imaging was employed to capture the TFP preforms. The image results revealed that the unidirectional carbon fibres were

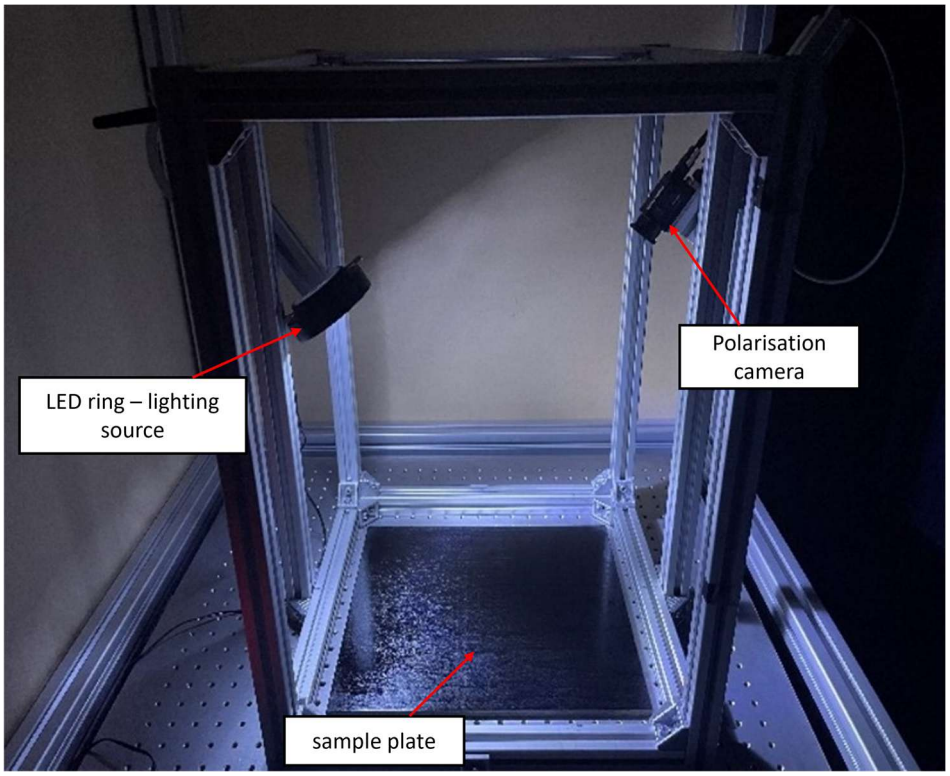


Figure 3.23 - The initial inspection set-up using LED ring lighting source.

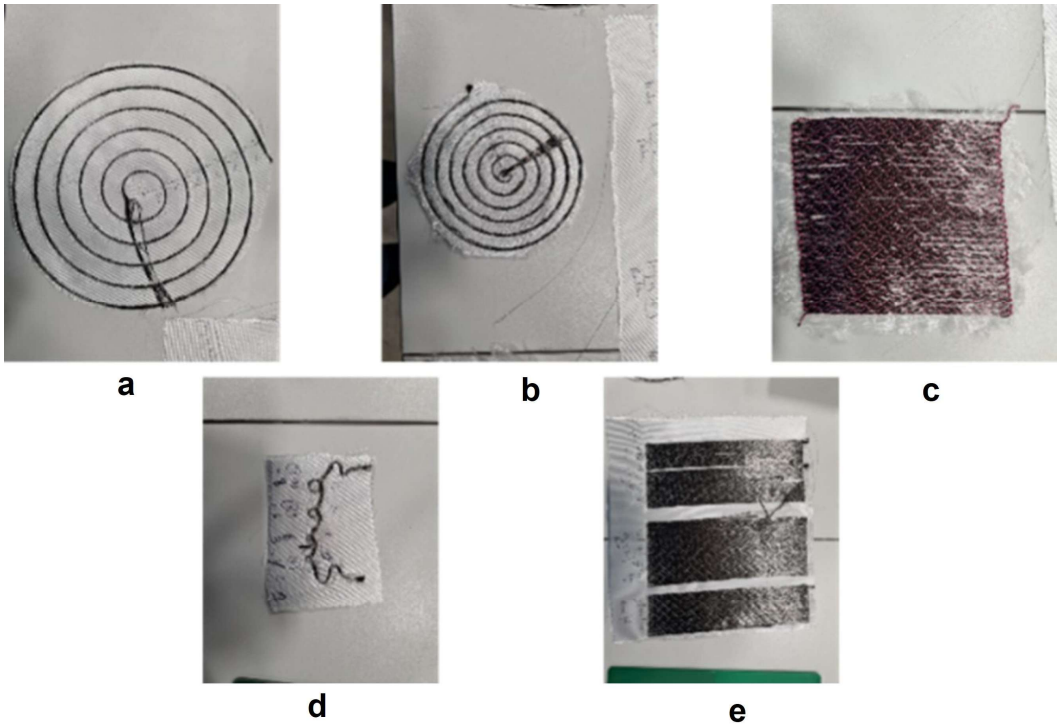


Figure 3.24 - TFP preforms with different fibres' orientations, (Spiral (a and b), Unidirectional fibres' orientation (c and e) and Hole reinforcement (d)), were used to examine the effect of the lighting source on the polarisation camera.

influenced by the lighting source. Figure 3.25 presents comparative imaging results for different TFP preforms (hole reinforcement (a), spiral (b), and unidirectional fibres (c)) under the same lighting conditions. Image (c) highlights the impact of the illumination source on the unidirectional carbon fibres, where the red box indicates the specular area caused by the illumination source. Therefore, the selection of an illumination source must consider the fibre's structural properties to reduce the lighting effects.

3.3.2 The modified experimental setup

The inspection rig underwent modifications to optimise the polarisation camera's position and the illumination source. The camera was reoriented to a vertical position relative to the sample plane, with an adjustable distance between the camera and the sample. Additionally, the LED ring illumination source was replaced with an LED strip. The LED strip consists of 70 LEDs per meter and has a width of 8 mm, providing a consistent 14.28 mm spacing between individual LEDs. To ensure uniform illumination, the LED strip was fixed to the aluminium extrusion in four directions (square), as depicted in Figure 3.26. The final inspection setup, illustrated in Figure 3.27, offers the advantage of precise control over both camera and lighting distances from the sample under inspection. This experimental inspection setup will be employed for offline inspection (see **Section 3.4**) in order to assess the fibre orientation of the carbon-fibre samples.

Figure 3.28 illustrates the result of capturing the same unidirectional carbon fibre preform using the polarisation camera after modifying the inspection setup. The LED strip illumination source setup overcomes the lighting effects on the unidirectional carbon fibre preform caused by the ring illumination source. Various sample structures were examined using the proposed setup, and no effects from the illumination source were detected.

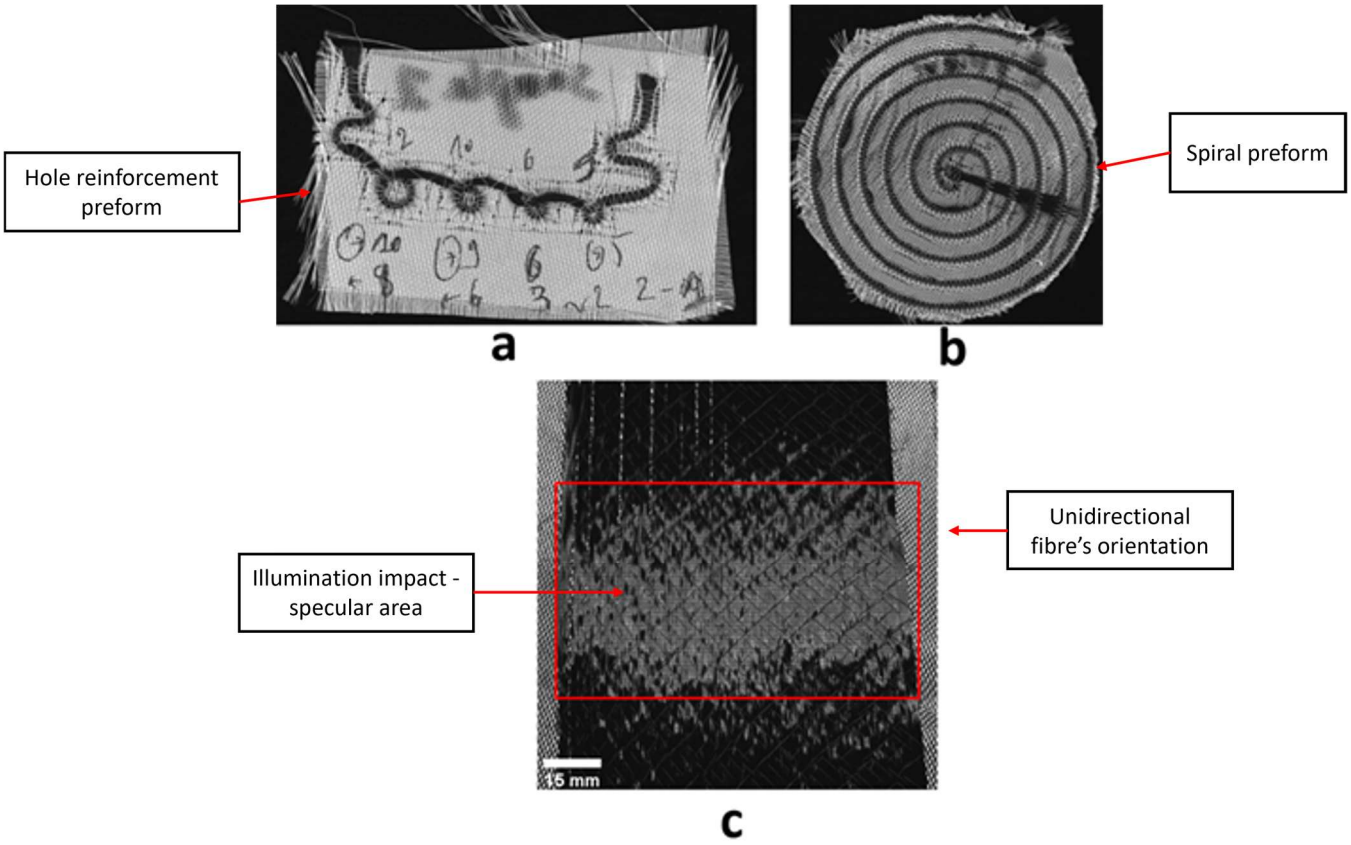


Figure 3.25 - TFP preforms with different fibres' orientations [Hole reinforcement (a), Spiral (b), and Unidirectional fibres' orientation (c)] were captured using the polarisation camera to test the influence of the LED ring illumination source on the preforms' structure.

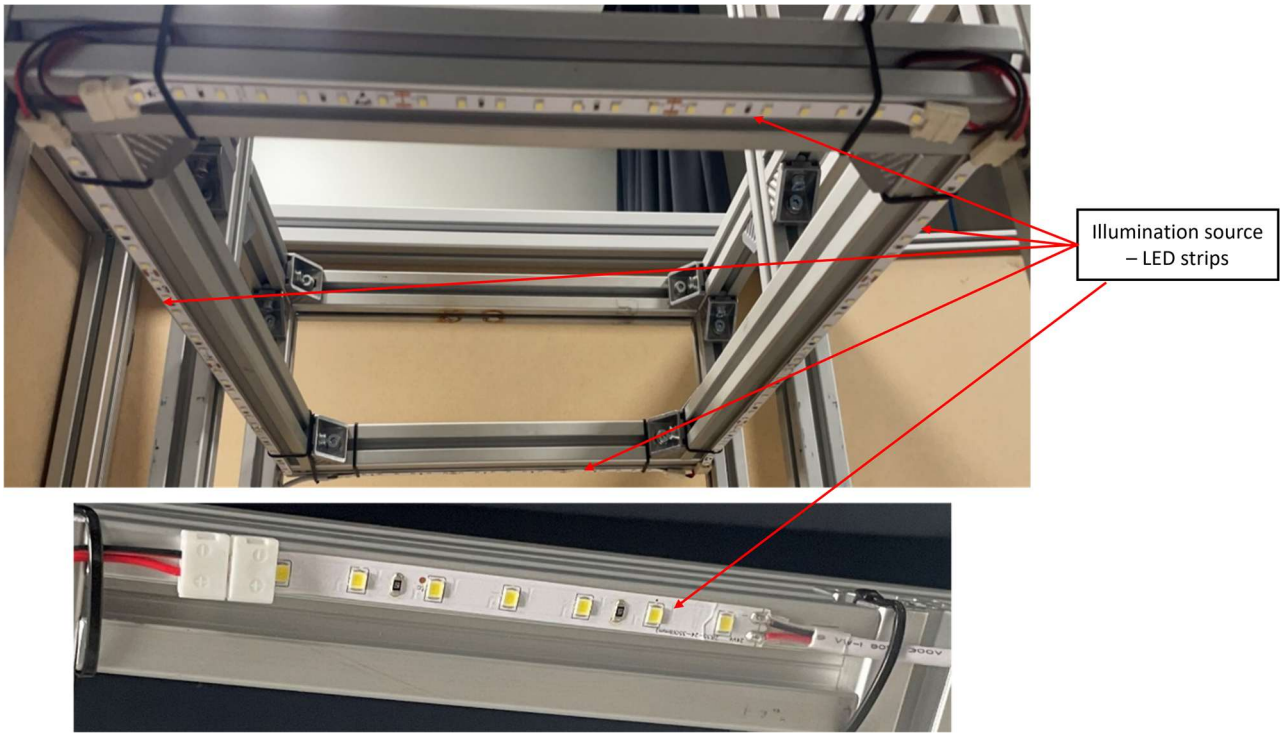


Figure 3.26 - The illumination source (LED strip) was applied to the final inspection set-up to illuminate the sample from four directions to ensure uniform illumination.

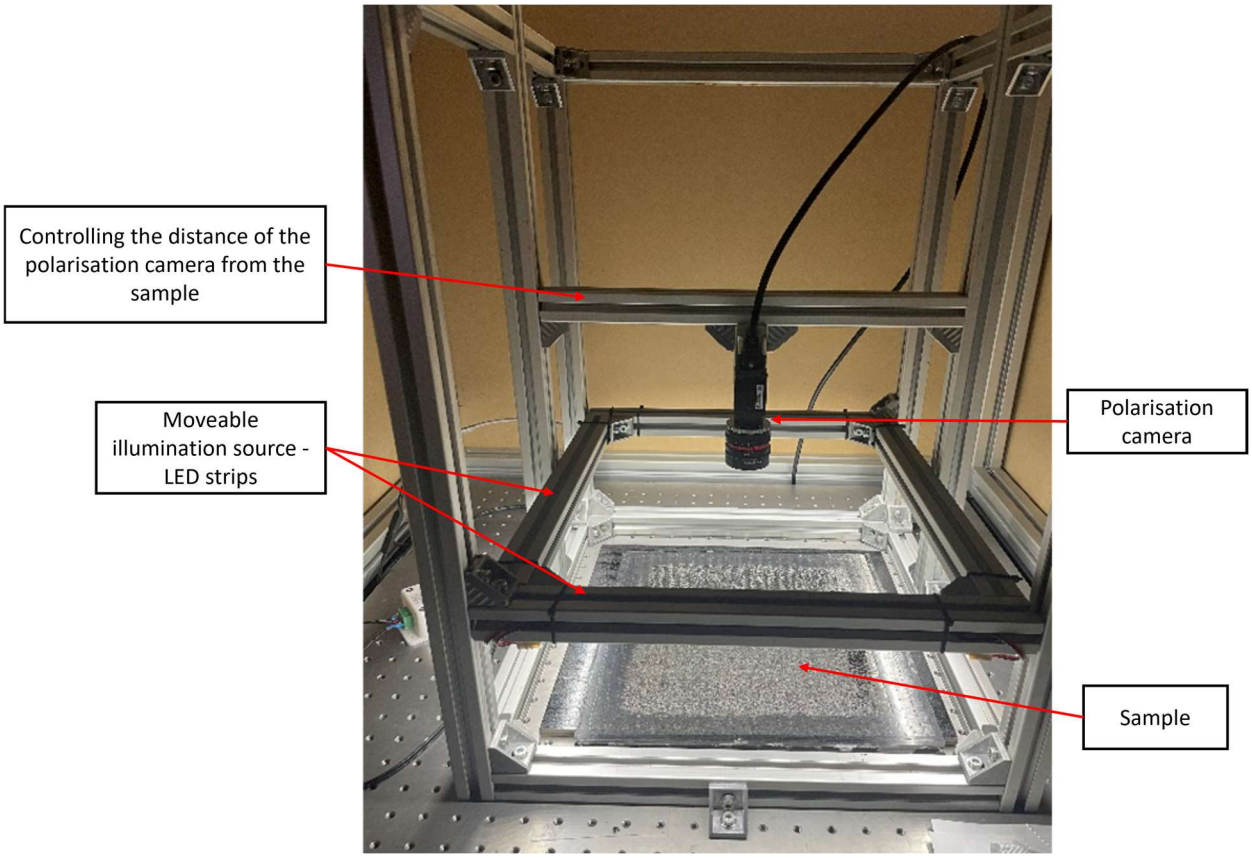


Figure 3.27 - The modified inspection rig set-up.

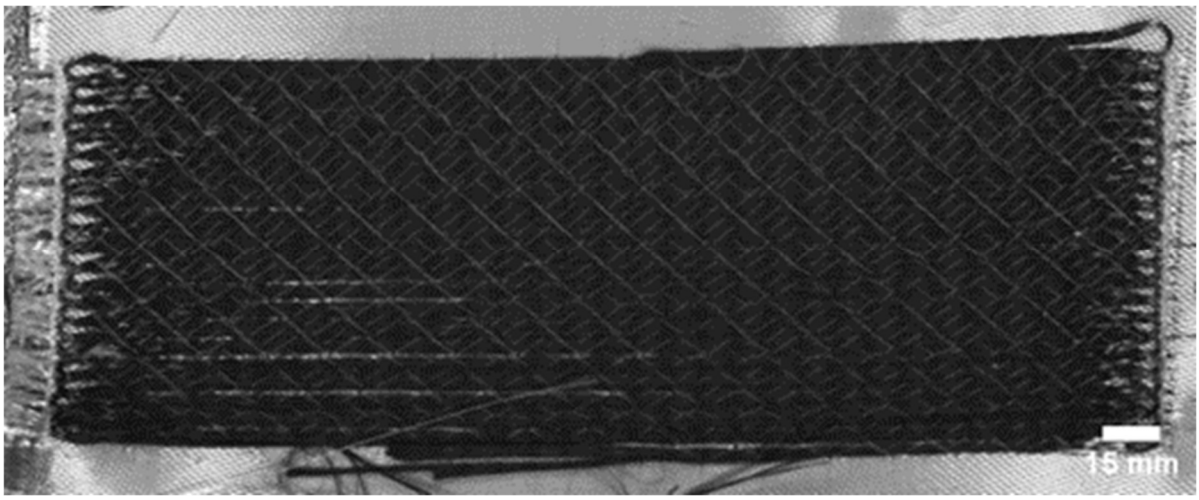


Figure 3.28 -The unidirectional carbon fibre preform (UD-TFP), shown in Figure 3.25-c, was captured by the polarisation camera using the LED strip as an illumination source.

3.4 Examples of offline inspection for samples with a different structure using the polarisation camera.

3.4.1 Dry woven carbon fibres

The dry Twill 2x2 carbon fibre (one layer) was imaged using the polarisation camera to visualize the fibre orientation in the offline stage. Figure 3.29 presents the captured images, where (a) shows the raw saturation image, revealing overexposed and underexposed regions, if found. Image (b) shows the Degree of Linear Polarisation (DoLP) image, highlighting the degree of polarisation of reflected light from the carbon fibres in grayscale. Image (c) shows the raw four-split image, representing the fibres in four polarisation directions (0°, 45°, 90°, 135°). Images (d) and (e) show the fibre orientations represented in HSV and RGB colour maps, respectively. The HSV colour map distinguishes fibres with a 0° angle in red and those with a 90° angle in cyan. The varying shades of cyan and red in the HSV colour map are caused by the weaving pattern, which induces curvatures, into the plane of the fabric, in the fibres.

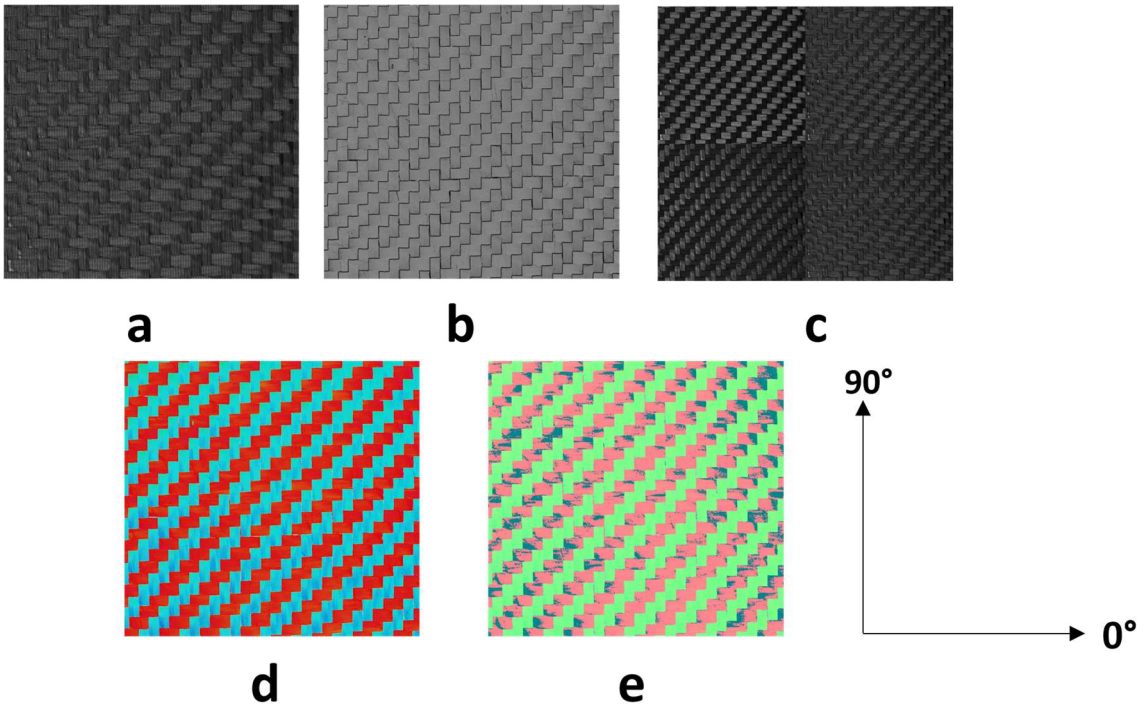


Figure 3.29 - Dry Twill 2x2 carbon fibre images were captured using the polarisation camera, where (a) shows the raw saturation image, (b) the DoLP image, (c) the raw 4 split image, (d) the fibres' orientation image in HSV colour map and (e) the fibres' orientation image in RGB colour map.

3.4.2 Dry Unidirectional (UD) carbon fibre

The polarisation camera was employed to capture the dry UD carbon fibres (one layer) and the fibre orientation. Figure 3.30 shows a series of images similar to those obtained for the Twill 2x2 carbon fibre (Figure 4.28). Image (d) displays the fibres' orientation mapped onto an HSV colour scale, where red represents a 0° fibre orientation and cyan represents a 90° fibre orientation. However, the presence of colours other than red indicates variations in fibre orientation.

To further investigate variations in fibre orientation, selected regions of the UD carbon fibre, as highlighted in Figure 3.31, were processed to inspect the fibre orientation. By referring to the fibre angle reference in Figure 3.21, it can be inferred that the yellow-coloured fibres in the HSV map exhibit orientations between 20° and 30°, while the pink-coloured fibres indicate orientations between 150° and 160°. These variations in orientation, as captured by the polarisation camera, provide evidence of fibre waviness within the UD carbon fibre.

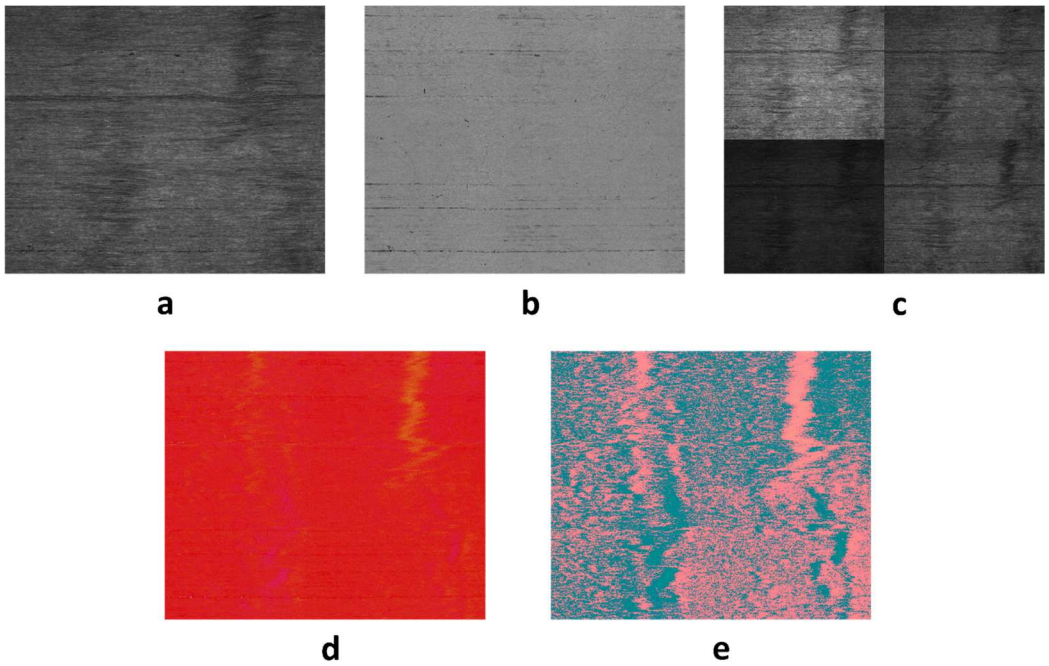


Figure 3.30 - Dry unidirectional (UD) carbon fibre images were captured using the polarisation camera, where (a) shows the raw saturation image, (b) the DoLP image, (c) the raw 4 split image, (d) the fibres' orientation image in HSV colour map and (e) the fibres' orientation image in RGB colour map.

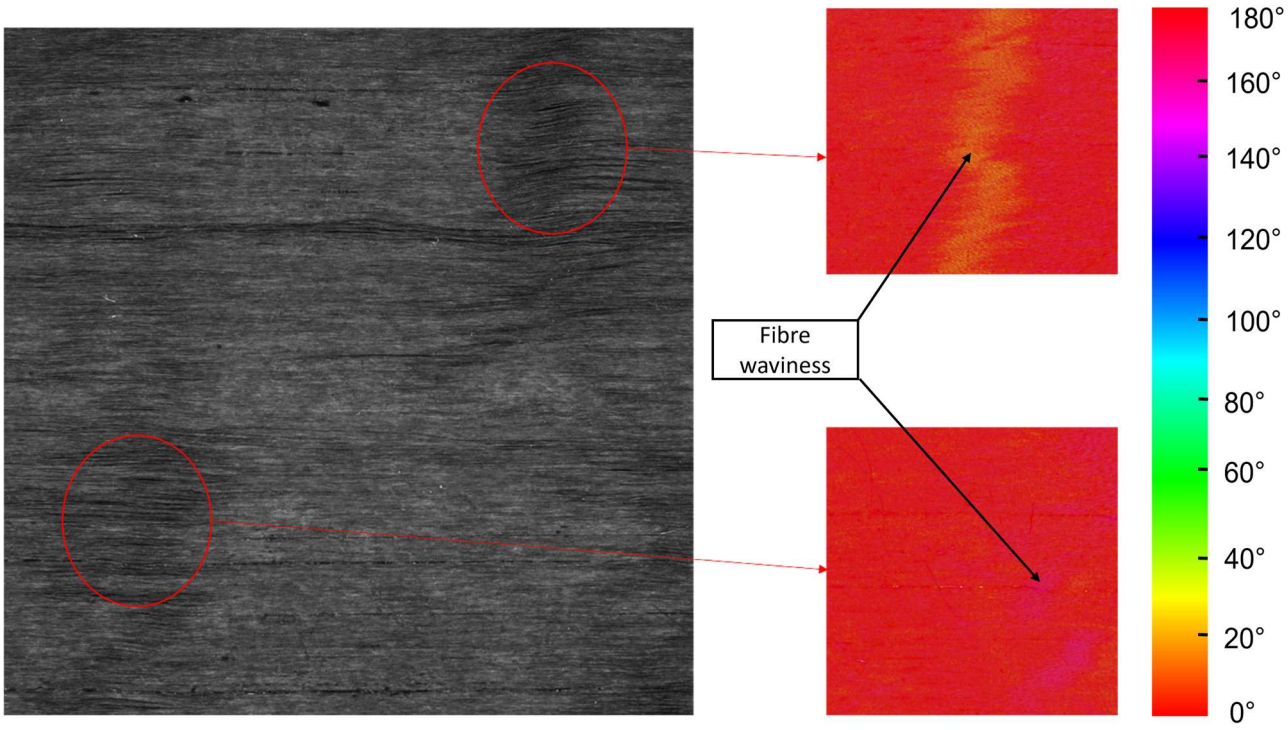


Figure 3.31 - The selected regions in the UD carbon fibre, Figure 3.30, show the fibres' orientation in the HSV colour map corresponding to the waviness in the carbon fibres, where the fibres in yellow represent orientations between 20° and 30° while fibres in pink show orientations between 150° and 160° (-30 and -20°).

3.4.3 Dry unidirectional non-crimp fibre (UD-NCF)

The dry UD-NCF material (one layer), composed of 12K carbon fibres aligned in the warp direction and fixed by a thermoplastic material in the weft direction, was captured using the polarisation camera. Figure 3.32 (a-e) illustrates the raw saturation image, degree of linear polarisation (DoLP) image, raw 4-split image, and fibre orientation images in both HSV and RGB colour maps, respectively.

The DoLP image (b) visually differentiates the carbon fibres, depicted in grayscale, from the thermoplastic material, shown in black. The fibre orientation image in the HSV colour map (d) highlights the orientations of the fibres, where the fibres in red represent the orientation of 0°. The thermoplastic material, traversing both above and below the carbon fibres in the weft direction, induces curvature in the fibres, consequently leading to the observed variations in fibre orientation.

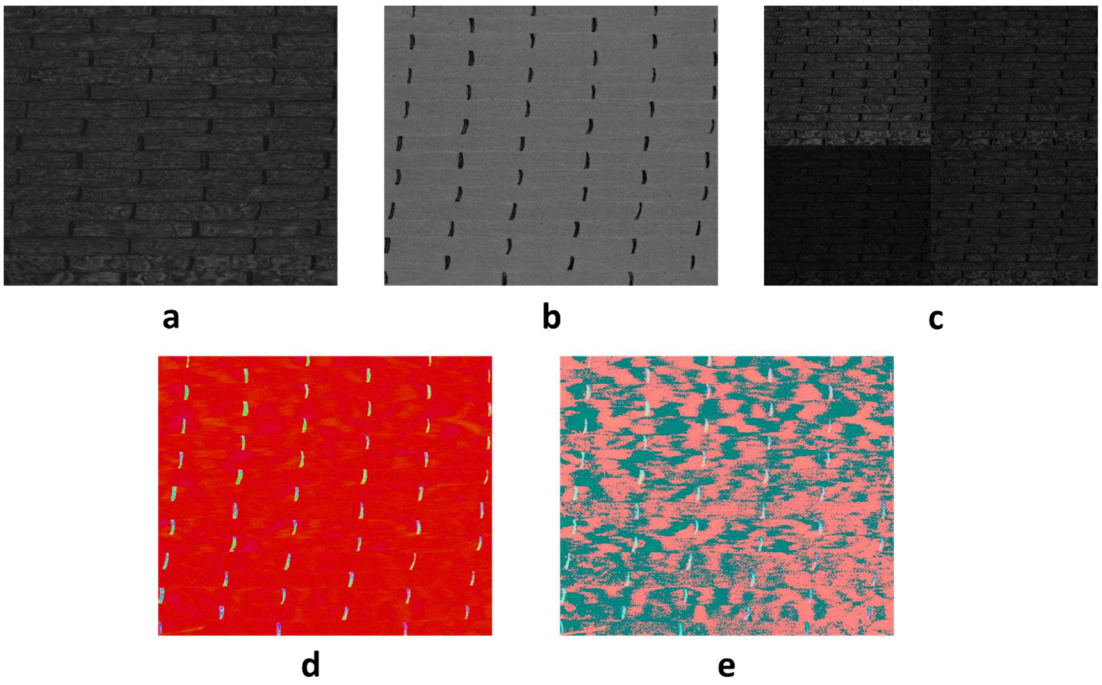


Figure 3.32 - Dry UD-NCF images were captured using the polarisation camera, where (a) shows the raw saturation image, (b) the DoLP image, (c) the raw 4 split image, (d) the fibres' orientation image in HSV colour map and (e) the fibres' orientation image in RGB colour map.

3.4.4 Dry ± 45° non crimp fabric (NCF)

The dry ± 45° non-crimp fabric (NCF) carbon fibre, which comprises two layers with opposite fibre orientations, was captured using the polarisation camera. The raw saturation image, degree of linear polarisation (DoLP) image, raw four-split image, and fibre orientation in both HSV and RGB colour map images were captured (Figure 3.33 a-e). The raw saturation image (a) highlights overexposed areas on the stitch material in yellow. The DoLP image (b) differentiates between carbon fibres (grey) and stitch material (black). The fibre orientation image in the HSV colour map (d) reveals fibres oriented at + 45°. However, as previously discussed, the green colour gradient is attributed to the stitch pattern, which induces curvatures in the carbon fibres.

Figure 3.34 illustrates selected regions of the ± 45° NCF carbon fibre fabric, exhibiting defects identified through the fibre orientation image, such as missing fibre tows and fibre misalignment. The HSV colour map fibre orientation image in

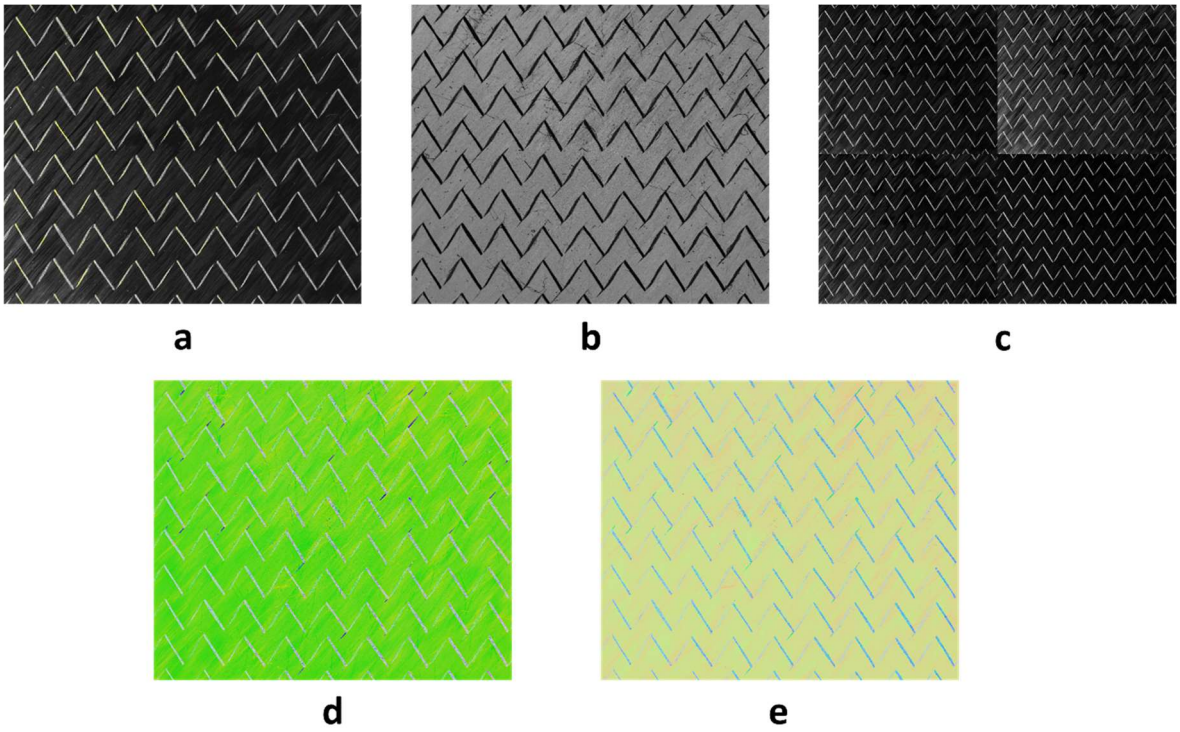


Figure 3.33 - Dry ± 45° NCF carbon fibre images were captured using the polarisation camera, where (a) shows the raw saturation image, (b) the DoLP image, (c) the raw 4 split image, (d) the fibres' orientation image in HSV colour map and (e) the fibres' orientation

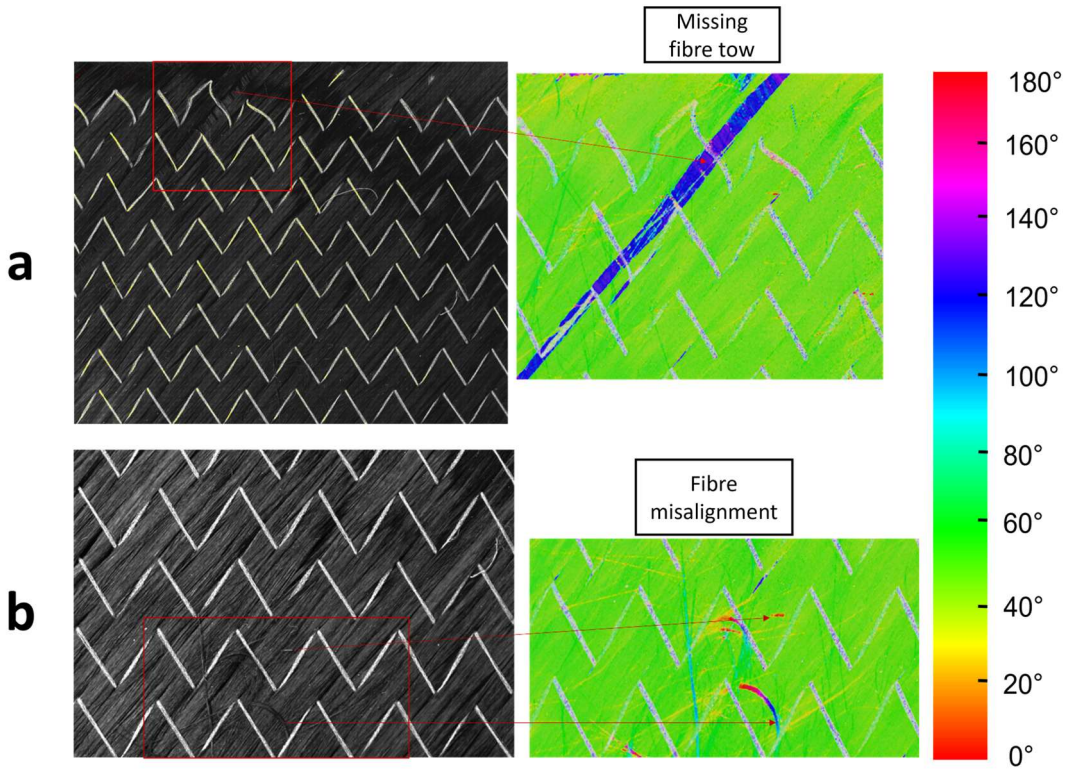


Figure 3.34 - Defects detecting, such as missing fibre's tow and fibre's misalignment, on the ± 45° NCF carbon fibre by inspecting the carbon fibres' orientation using the polarisation camera.

Figure 3.34-a presents a + 45° missing fibre tow, where the red arrow points to a -45° oriented fibre tow (blue) located in the second layer. In Figure 3.34-b, the fibre orientation image detects fibres deviating from the +45° orientation, exhibiting angles of 0°, 10°, 110°, and 140°.

To conclude the offline inspection section, the presented examples of offline inspection using a polarisation camera demonstrate the camera's capability to assess the fibre orientation within various fibre architectures. Moreover, the captured fibre orientation images highlight the potential to detect specific defects, such as missing fibre tows and fibre misalignment, by analysing the orientations of the carbon fibres.

3.5 Image processing and analysis

Images captured using the polarisation camera, displayed in the HSV colour map, were employed to analyse the fibre orientation behaviour of carbon fibre specimens during tensile testing. To evaluate the influence of increasing strain on fibre orientation, and to detect subtle orientation changes, image processing techniques were applied to the acquired images at various strain levels.

MATLAB software was utilised to process the fibre orientation data. The Curve Fitting Toolbox was specifically employed to generate histograms of fibre orientation and to fit the resulting distributions to a Gaussian function [145], thereby enabling the determination of the mean Angle of Linear Polarisation (AoLP).

In addition, ImageJ software was used to investigate incremental changes in fibre orientation under increasing strain. This analysis was conducted through examination of the hue channel, which provided direct information to the fibre orientation. ImageJ is a free, open-source software developed at the National Institutes of Health for image processing and analysis. It is widely used in many scientific fields because it is easy to use, works on different operating systems, and can be extended with a large number of plugins and macros. Researchers use it in a broad range of tasks, from basic adjustments and measurements to more advanced functions such as segmentation, deconvolution, and three-dimensional rendering [146]–[149]. For example, Chen et al. [146] showed how ImageJ can be

used to accurately quantify collagen fibres in histological images. Schindelin et al. [147] described its role as an open and flexible platform supported by a large scientific community. Abràmoff et al. [148] highlighted its accessibility and adaptability, and Collins [149] emphasised its value for microscopy through specialised bundles designed for laboratory use. Together, these studies show that ImageJ has become a reliable and versatile tool for both routine and advanced image analysis in research.

3.5.1 Colour thresholding process

In the experimental chapters (4,5 and 6), the orientation of carbon fibres during tensile testing was investigated to understand their behavioural response to increasing strain. For this purpose, fibre orientation images were captured before and at the maximum load force, allowing for a comparative analysis.

Given that the hue channel in the HSV colour map image encodes information about the Angle of Linear Polarisation (AoLP), which directly correlates with fibre orientation, this channel was the primary focus of the analysis. For the first time, fibre orientation was evaluated through images obtained using a polarisation camera, providing a novel means of characterising orientation behaviour under mechanical loading. The captured images were represented within the HSV colour space, enabling visualisation and quantification of fibre alignment. Imaging analysis in ImageJ facilitated the extraction of orientation data at different fibre orientation angles. This methodology allowed the investigation of small variations in fibre orientation as tensile strain increased, offering new insights into the deformation response of carbon fibre samples. To isolate specific fibre orientations, the hue values corresponding to these orientations were identified within the region of interest (ROI) image. For this reason, ImageJ software was used.

Using ImageJ software, a colour threshold was applied to the HSV images, enabling the selection of a specific hue range. This masked the image, highlighting only the fibres within the chosen orientation range. Figure 3.35 presents the flow chart of the procedure employed to illustrate fibre orientation at various angles. In the first step, the specific fibre orientation angles to be extracted from the image are identified.

Next, a binary mask is applied, whereby the selected fibre orientations are displayed in white, while all other orientations are represented in black.

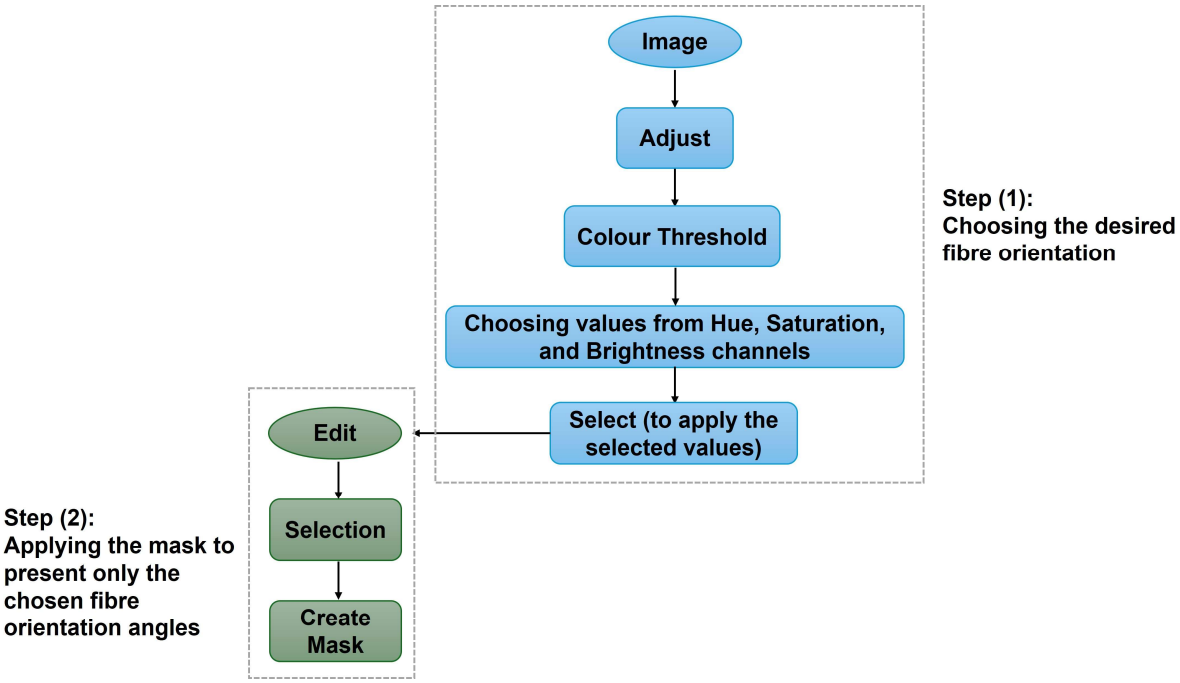


Figure 3.35 - Flow chart illustrate the process of presenting the selected fibre orientation using ImageJ software from the HSV image that captured by the polarisation camera.

Figure 3.36 provides an illustrative example of the application of ImageJ software, using a Twill 2×2 carbon fibre specimen. The hue channel scale extends from 0 to 255, corresponding to fibre orientations between 0° and 180°. In step (1), fibres oriented between 82° and 93° were selected as an example, corresponding to hue values of 116–132, as shown in Figure 3.36-a. In Figure 3.36-b, the fibres within this orientation range are highlighted in yellow, (after choosing “select”). Next, in step (2), a binary mask was generated (Figure 3.36-c), in which the selected fibre orientations are represented in white.

In ImageJ software, the hue channel is represented on a scale ranging from 0 to 255. However, in order to interpret fibre orientations in angular terms, these values must be converted into degrees within the range of 0° to 180°. To achieve this, a mathematical relationship was required to map each hue value to its corresponding orientation angle. The following equation was therefore employed to determine the fibre orientation:

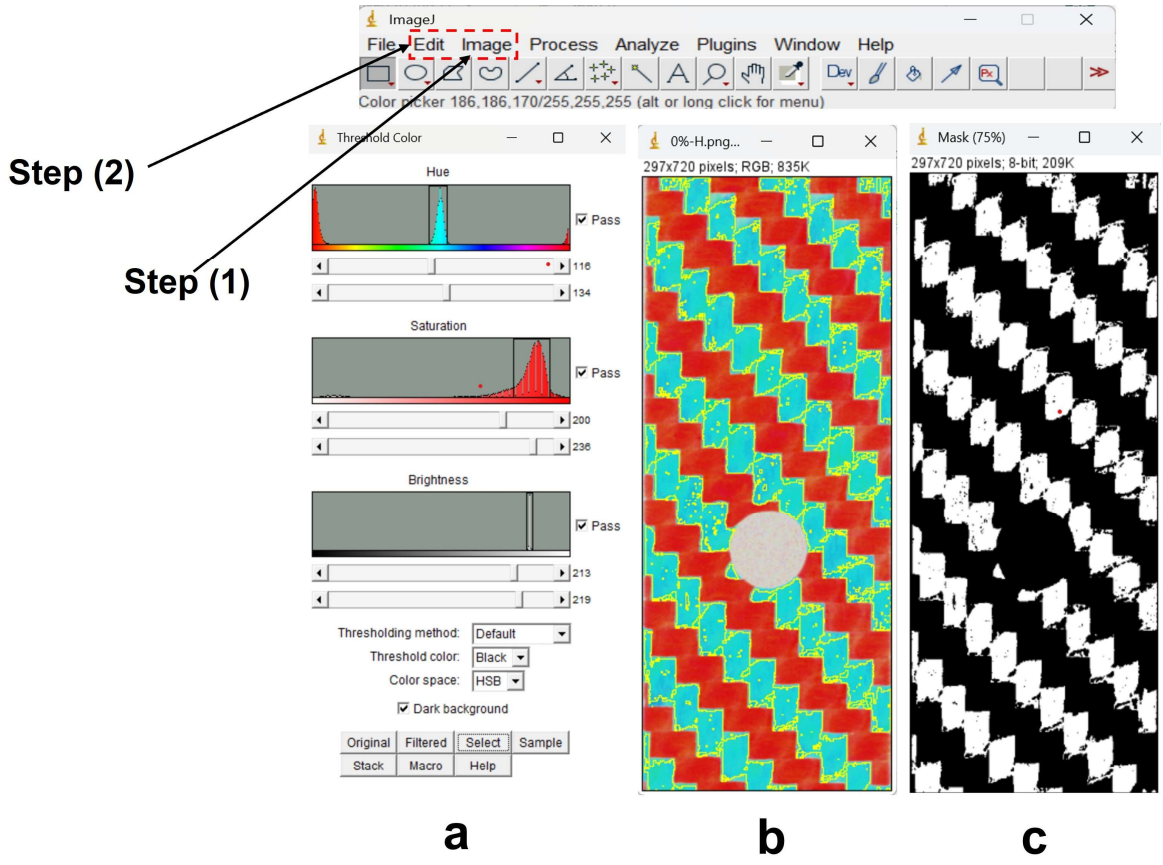


Figure 3.36 - Example of ImageJ software applied to a Twill 2×2 carbon fibre image captured using the polarisation camera to isolate fibres within a defined orientation range: (a) threshold values selected across the three channels to identify the fibre orientation.

$$\theta° = \frac{H}{255} \times 180$$

Equation 3-8

where H is the hue channel's value and $\theta°$ is the fibre orientation. To verify the validity of the mathematical relationship, two boundary conditions were considered. When the Hue value is equal to zero, the fibre orientation must correspond to 0°. Also, when the Hue value is 255, the fibre orientation is expected to be 180°. Substitution of these values into Equation (3.8) confirms that the relation satisfies both conditions.

Figure 3.37 illustrates the application of this colour thresholding technique to a dry Twill 2x2 carbon fibre sample. Fibres oriented at 0° are depicted in red, while those at 90° are shown in cyan. By applying the mask based on the calculated orientation

ranges, fibres within specific orientation ranges are highlighted in white, with the remaining fibres appearing black. This method was employed in the experimental chapters (**Chapters 4, 5, and 6**), following the presentation of fibre orientation images obtained during tensile testing.

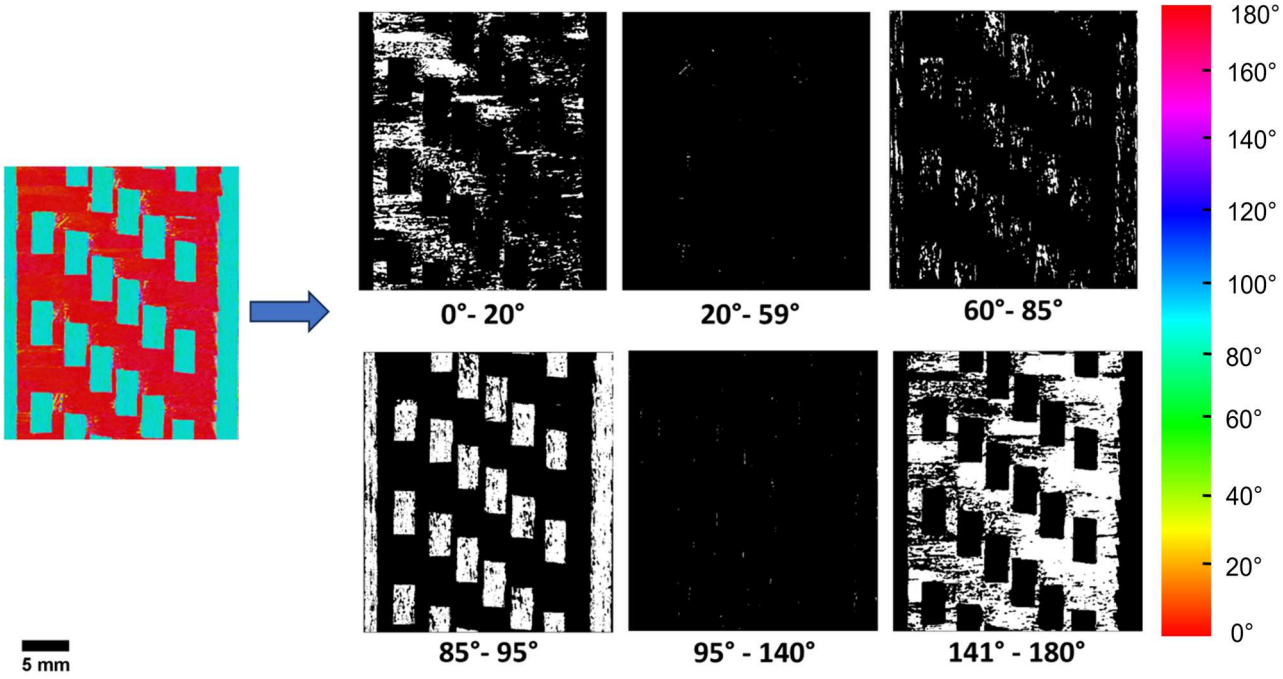


Figure 3.37 - Fibres' orientation image of dry Twill 2x2 carbon fibre was used as an example to show the separation of the fibres' orientation using the ImageJ program, where the fibres in the selected range are presented in white.

Upon analysis, it was observed that while some fibres exhibited orientations between 60° and 85°, the majority were concentrated within the following ranges: 0° to 20°, 85° to 95°, and 141° to 180°. Fibres oriented between 0° and 20° corresponded to hue channel values between 0 and 28, covering 14.38 % of the total image area. Those between 20° and 59° (hue values 29-84) accounted for a negligible 0.05 % of the total area. The 60° to 85° range (hue values 85-120) covered 4.48 % of the total area, while the 85° to 95° range (hue values 121-135) covered a significant 30.68 %. Finally, fibres oriented between 95° and 140° (hue values 136-199) and 141° to 180° (hue values 200-255) comprised 0.09% and 38.60% of the total area, respectively.

The fibre orientation separation process will be employed in the experimental chapters to compare fibre orientation images captured before tensile testing (at 0% strain) and at maximum load force. This analysis will enable the monitoring of fibre orientation behaviour during the tensile testing process.

3.5.2 Gaussian curve fitting

Data processing was conducted using MATLAB software. Specifically, the hue channel of the fibres' orientation image, represented in an HSV colour map and containing the Angle of Linear Polarisation (AoLP) information, was extracted, and a histogram of this data was generated. A Gaussian curve was fitted to the histogram data using the MATLAB curve fitter toolbox, yielding the mean AoLP value and its standard deviation. The fitting procedure was employed in **Chapters 4, 5, and 6** to evaluate the mean Angle of Linear Polarisation (AoLP) within the defined region of interest across all investigated samples.

In the experimental chapter, a selection of fibres' orientation images captured during the tensile test using the polarisation camera were presented. This selection will contain images captured before the test initiation, at the maximum force load, and at selected points both before and after reaching the maximum force load. The Gaussian curve fitting procedure was applied to each of these selected images. The resulting mean AoLP values will then be correlated with their corresponding strain values to explain the evolving fibre orientation behaviour with increasing strain.

Furthermore, the analysis will involve the separation of fibres based on their orientation. Specifically, fibres exhibiting orientations within ± 5° of the mean AoLP were isolated and compared between the initial state (before the test) and the state at maximum load force.

The methodology adopted for analysing fibre orientation using MATLAB is summarised as follows. The HSV images, previously selected and captured with the polarisation camera during tensile testing, were first uploaded into MATLAB. A region of interest (ROI) was then defined, and the images were cropped accordingly. From the cropped images, the hue channel which encodes fibre orientation

information was extracted. After that, the histogram data of AoLP were generated and analysed using the Curve Fitting Toolbox. A Gaussian function was fitted to the histogram data, thereby enabling determination of the mean Angle of Linear Polarisation (AoLP). Figure Figure 3.38 presents a flow chart that outlines the procedure employed to calculate the mean value of the Angle of Linear Polarisation (AoLP). This process was implemented in MATLAB, where the AoLP values were extracted from the Hue channel of HSV images captured during tensile testing with the polarisation camera.

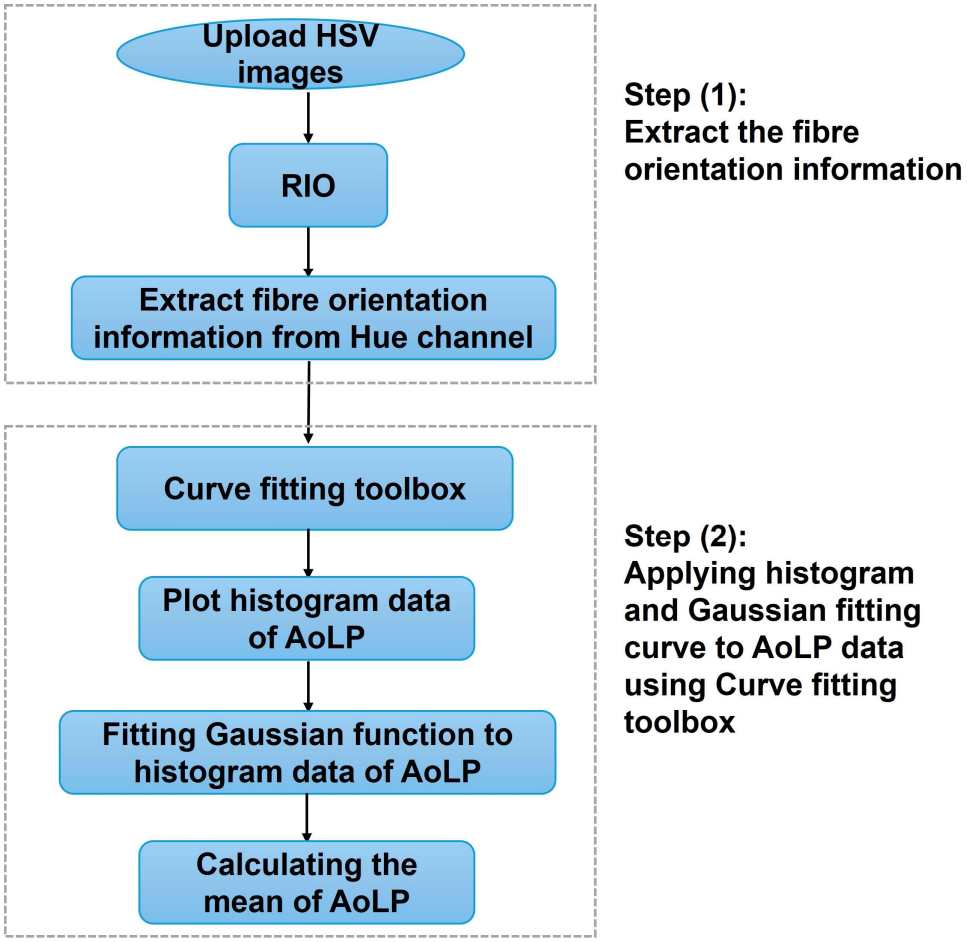


Figure 3.38 - Flow chart illustrate the process of calculating the mean of the AoLP with increasing strain using MATLAB software.

As previously discussed, Gaussian fitting was employed to calculate the mean value of the Angle of Linear Polarisation (AoLP). However, this method did not consistently perform well, particularly for the Tailored Fibre Placement (TFP) specimens. Alternative fitting functions, including Lorentzian fitting, were explored, but these did not result in any notable improvement. Therefore, Gaussian fitting was adopted for

all specimens in order to facilitate direct comparison across datasets with reporting the standard deviation associated with the peak widths for each fit as strain increased. This approach is consistent with methodologies employed by other researchers, such as Atkinson et al.[12], who also applied Gaussian fitting to determine the mean AoLP for different fibre architectures.

3.6 Methodology summary

This research utilises a polarisation camera to investigate the orientation behaviour of carbon fibre materials with various architectures to enhance the manufacturing process of TFP preforms through the on-line monitoring of fibre orientations. The camera captures images of the materials in both dry and resin-infused states. Degree of Linear Polarisation (DoLP) images quantify the percentage of polarised light reflected by the carbon fibres, while fibres' orientation images illustrate their alignment, extracted from Angle of Linear Polarisation (AoLP) data.

The experimental chapters primarily focus on analysing fibres' orientation images, visualised using an HSV colour map, to study their behaviour during tensile testing. A region of interest within these images is selected to study the fibres' orientation before testing (0% strain) and at the strain corresponding to maximum load. This analysis aims to observe changes in fibre orientation with increasing strain. Therefore, histograms of AoLP data are plotted, and Gaussian curve fitting is employed to determine the mean AoLP.

In Chapter 4, the orientation response of dry unidirectional (UD), UD-non-crimp fabric (UD-NCF), Twill 2x2, and unidirectional reinforced hole (UD-TFP) preforms, consisting of two and four layers is investigated during tensile loading. The polarisation camera captures images of each sample every second throughout the test to understand the behaviour of the carbon fibre's orientation. Afterwards, the experiment is repeated using silicon rubber to study the influence of a softer resin compared to epoxy on fibre orientation behaviour.

Chapter 5 examines the evolution of fibre orientation around machined holes during tensile testing. Open-hole tensile tests are conducted on UD-NCF and Twill 2x2

carbon fibre samples infused with epoxy resin featuring varying hole diameters (12 mm, 10 mm, and 8 mm). The polarisation camera captures images around the machined hole area every second during the test, enabling the investigation of fibre orientation changes near the hole edges with increasing strain.

Chapter 6 investigates the fibre orientation behaviour around reinforced holes in UD-TFP with two and four layers. Machined holes with three different diameters (12 mm, 10 mm, and 8 mm) are introduced into the local hole reinforcement. The 12 mm hole removes the entire resin-rich area within the local reinforcement and, in some cases, may affect the local carbon fibre reinforcement during the machining process. However, the 10 mm and 8 mm holes are smaller than the local reinforcement, resulting in resin-rich areas surrounding it.

The findings presented in these experimental chapters contribute to a deeper understanding of fibre orientation behaviour during tensile testing across different fibre architectures. This knowledge provides valuable insights that may be utilised to refine and enhance the manufacturing processes of Tailored Fibre Placement (TFP) preforms. The results highlight the potential of integrating on-line monitoring through polarisation imaging, thereby enabling improved control and optimisation of fibre placement during the production of TFP preforms.

3.7 Aims and objectives of the conducted experiments

The experiments conducted aimed to investigate the behaviour of fibre orientation in carbon fibre samples during tensile testing and to evaluate its influence on mechanical properties using a polarisation camera. The findings are intended to be used to improve the Tailored Fibre Placement (TFP) preforms by enabling the monitoring of fibre orientation during the manufacturing process. The polarisation camera proved effective in capturing fibre orientation behaviour at the edges of machined holes and demonstrated the effect on the mechanical performance of the tested specimens. Also, it revealed how the position of the machined hole in woven samples, together with the weaving pattern surrounding the hole, influenced the mechanical properties. Furthermore, monitoring the fibre orientation behaviour using the polarisation camera demonstrated the influence of the loop-back path

used in the manufacture of reinforced-hole UD-TFP preforms. This manufacturing approach led to the formation of localised resin-rich regions, which in turn affected the overall mechanical performance of the composite.

4 POLARISATION ANALYSIS OF FIBRE ORIENTATION OF DRY CARBON FIBRE AND IMPREGNATED SILICONE RUBBER RESIN DURING TENSILE TESTING

4.1 Introduction

The motivation for conducting tensile testing on dry (non-infused) carbon fibre specimens is to examine the behaviour of fibre orientation under mechanical loading. In resin-infused composites, only minimal movement in fibre orientation are anticipated during tensile testing; therefore, testing the dry specimens enables a clearer assessment of the fibre reorientation behaviour, which underpins the motivation for this experimental approach. Furthermore, monitoring fibre orientation in dry carbon-fibre samples with varying architectures is expected to provide valuable insights into the distinct behaviours of fibre orientation under tensile loading. This understanding is anticipated to contribute to the improvement of the Tailored Fibre Placement (TFP) preform manufacturing process, particularly by enabling greater precision in fibre steering and enhancing the consistency of reinforcement in critical regions.

The polarisation camera was used to inspect the orientation of carbon fibre using the angle of linear polarisation (AoLP) information. The thin carbon fibre polarises light as it is reflected. This polarisation is aligned with the fibre direction. For more details on the presentation of carbon fibre orientation using the polarisation camera, see Methodology **Section 3.2**.

Tensile tests were conducted on a variety of dry carbon fibre architectures, including unidirectional (UD), unidirectional non-crimp fabric (UD-NCF), Twill 2x2, and tailored fibre placement (TFP) preform. Inspection was carried out during the test using the polarisation camera to investigate the fibre's orientation behaviour from the AoLP information.

The chapter is divided into two sections. In the first section, dry carbon fibre specimens will undergo tensile testing. In the second section, the specimens were impregnated with a silicone rubber resin. During the test, the HSV images obtained

from the polarisation camera, which encodes the AoLP and degree of linear polarisation information (DoLP), were used to present the fibre's orientation.

4.2 Dry sample preparation

Three specimens were prepared for each dry tensile test of the selected carbon fibre architectures: UD, UD-NCF, and Twill 2x2. Due to limitations in sample availability, only one TFP-reinforced hole preform was tested for each of the four and two layers. Dry samples were cut to 250 mm in length and 25 mm in width. Tensile testing was conducted using a Tinius Olsen 5 KN load cell at a testing speed of 2.00 mm/min. The experimental setup for fibre orientation inspection during the tensile test is shown in Figure 4.1, for more details about the experimental setup (see **Section 3.3**). All experiments were conducted in a controlled dark environment, with illumination provided exclusively by the LED lighting rig. This approach ensured that no external light sources influenced the polarisation measurements, thereby reducing potential sources of error and improving the reliability of the results. The LED strip was selected as the illumination source for both the offline and online inspection rigs due to its ability to provide uniform lighting across the sample, with a coverage angle of approximately 120°. This configuration minimises the non-uniformity commonly associated with alternative light sources, such as LED ring illumination source, thereby mitigating lighting effects and ensuring consistent image acquisition. The LED strip proved to be a particularly effective lighting source for carbon-fibre samples of varying architectural configurations. Since fibres with differing architectures exhibit varying responses to illumination, the use of an LED strip lighting source was found to provide a reliable means of achieving uniform illumination while overcoming issues of overexposure. For online inspection, it is therefore recommended that a moveable lighting rig be employed (as illustrated in Figure 4.1), allowing the lighting source to be adjusted appropriately to accommodate the requirements of different fibre architectures.

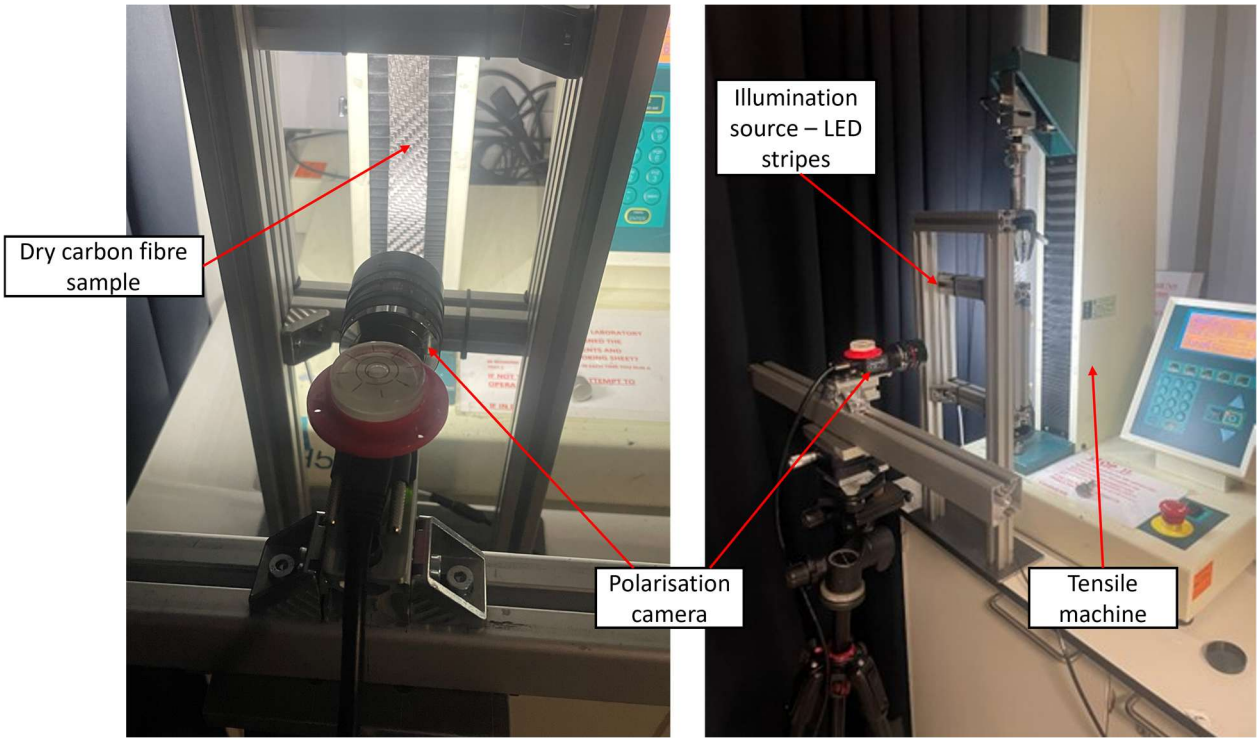


Figure 4.1 - The online (during tensile testing) fibre orientation inspection setup using the polarisation camera.

4.3 Dry carbon fibre

The tensile test was conducted on UD, UD-NCF, Twill 2x2, and TFP dry specimens to monitor the fibre orientation behaviour when strain increases using the polarisation camera. The raw saturation and HSV images were captured every second during the tensile test, where the raw saturation image presented the over and under-exposed areas in the specimens. The fibre orientation information was extracted from the hue channel in the HSV image obtained from the polarisation camera, where the hue channel contains the AoLP information while the saturation channel contains the DoLP information.

4.3.1 Unidirectional carbon fibre (UD)

A UD sample image was captured before conducting the test (offline inspection) using the polarisation camera. The raw saturation, degree of linear polarisation (DoLP) and fibres' orientation images (a-c), respectively, were obtained, as seen in Figure 4.2. The grey scale in the DoLP image shows the position of the carbon fibres from the reflected polarised information. The other materials are in black in the raw

and DoLP images but multicoloured, mainly red and grey in the HSV image. Image-c in Figure 4.2 represents the fibre's orientation from the HSV image information. The hue channel in the HSV image encodes the AoLP information, which matches the direction of the carbon fibre, while the saturation channel contains the DoLP information. The value channel is not used in this process. The fibres at 90° are presented in cyan in image-c, which are in the tension direction. However, different fibres' orientations appeared at the sample's edge (green, blue, yellow,…) caused by the cutting process.

The tensile machine background creates the colours behind the sample in Image-c, which are presented in black in the DoLP and raw saturation images (image-b and a). After the offline inspection stage, the sample was prepared for the tensile test, and the online fibre orientation inspection process was performed using the polarisation camera.

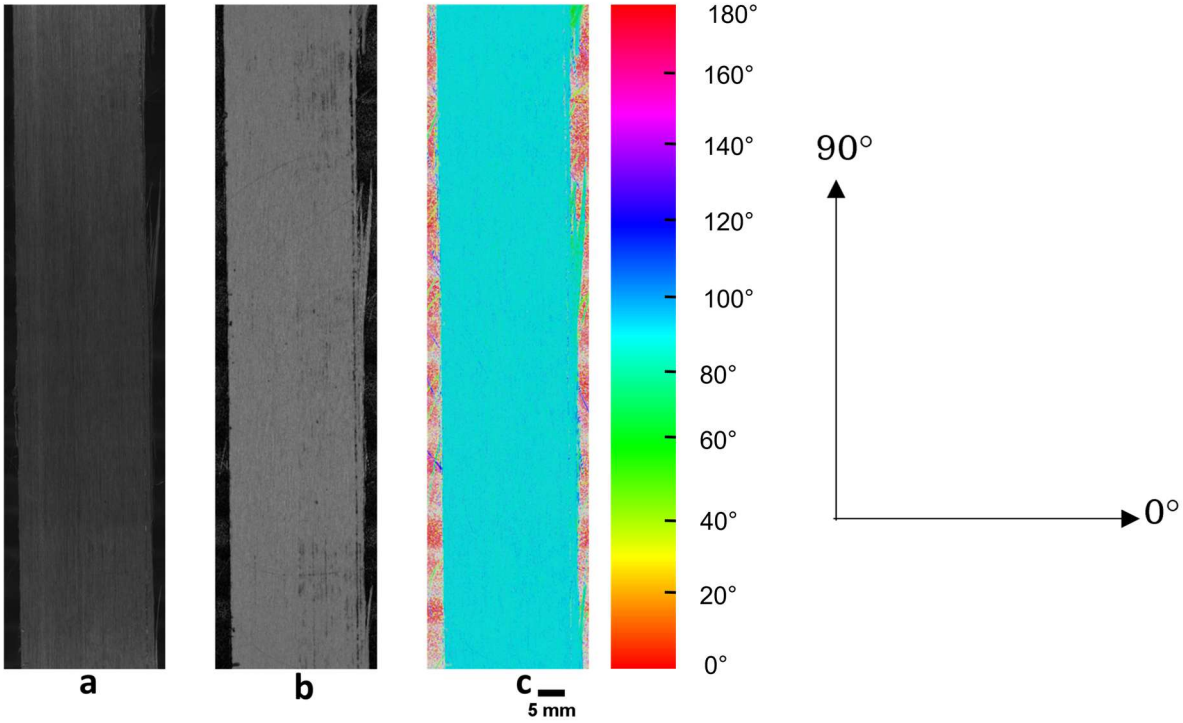


Figure 4.2 - Dry UD sample imaged using the polarisation camera, where (a) the raw saturation image, (b) the DoLP image, and (c) the fibres' orientation image.

Images were captured every second from when the test started. Each image is correlated with the tensile test results to follow the fibre's orientation behaviour during the test.

Because of the substantial number of images captured by the polarisation camera during tensile tests, a selection of images was chosen to illustrate the fibres' orientation behaviour through the test. The selection method includes images before the test initiation, one second after the test starts, and at maximum force load. Also, selected images after the beginning of the test and before reaching the maximum force load was presented to show the fibres' orientation behaviour with strain increases. The loading rate applied during the test was maintained at 2.00 mm/min, further information regarding the specimen dimensions, the testing apparatus, and the overall experimental configuration is provided in **Section 4.2**.

Figure 4.3 showed a sequence of fibre orientation images corresponding to the tensile test of the UD dry sample, which can be used as an example of the fibre orientation image selection during the tensile test. Image (a) was captured before the test began and used as a reference. Image (b) was captured after one second from starting the test, image (c) after 40 seconds, image (d) after 60 seconds, image (e) at the maximum load when the strain reached 0.94%, and image (f) was taken 8 seconds after reaching the maximum force load.

To better understand fibres' orientation behaviour during the test, a region of interest in the fibres' orientation image before starting the test and at maximum load force was compared. The selected region of the sample before starting the test (0 % strain) and at maximum load force (0.94 %) is shown in Figure 4.4. To provide more information about the fibres' orientation in the selected area, a histogram of the AoLP (hue) channel, Figure 4.5-b, was presented to understand the distribution of the fibres' orientation. The histogram data shows that the orientation of the fibres is between 85° and 95°.

Figure 4.6 shows the Gaussian curve fitting applied to the histogram data, Figure 4.5, for the fibre orientations between 60° and 120°. The standard MATLAB curve fitting algorithm was used to apply the fitting curve. The mean and standard deviation of the AoLP were obtained for both fibre orientation images, before starting

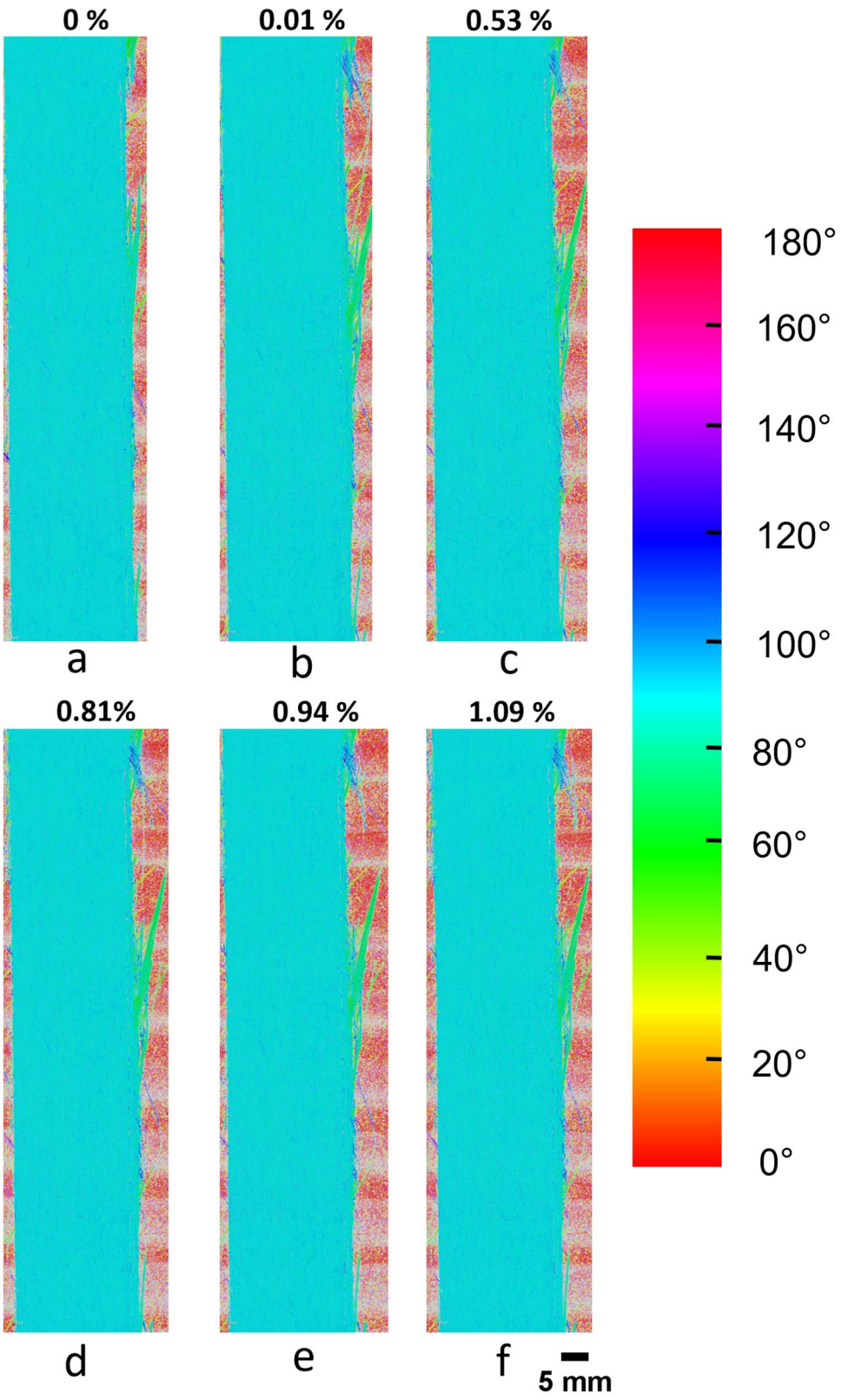


Figure 4.3 - A sequence of fibres' orientation images of dry UD sample captured during tensile testing using the polarisation camera. The strain corresponding to each image is presented above the figure.

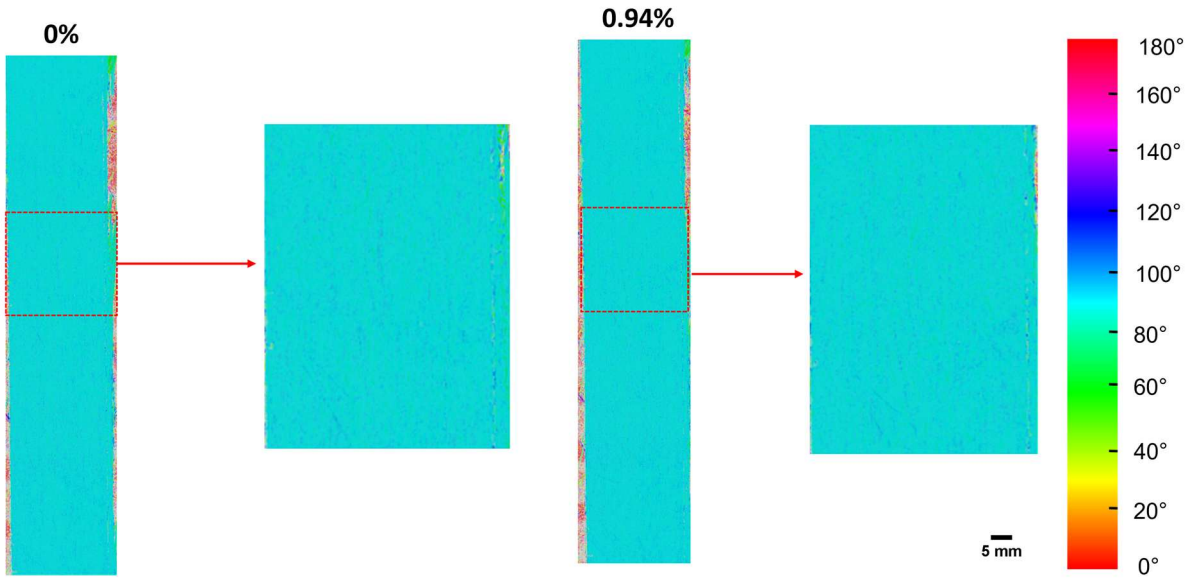


Figure 4.4 - The selected region of the fibres' orientation image in the dry UD sample was used to investigate and compare the fibres' angles at 0 % and 0.94 % strain.

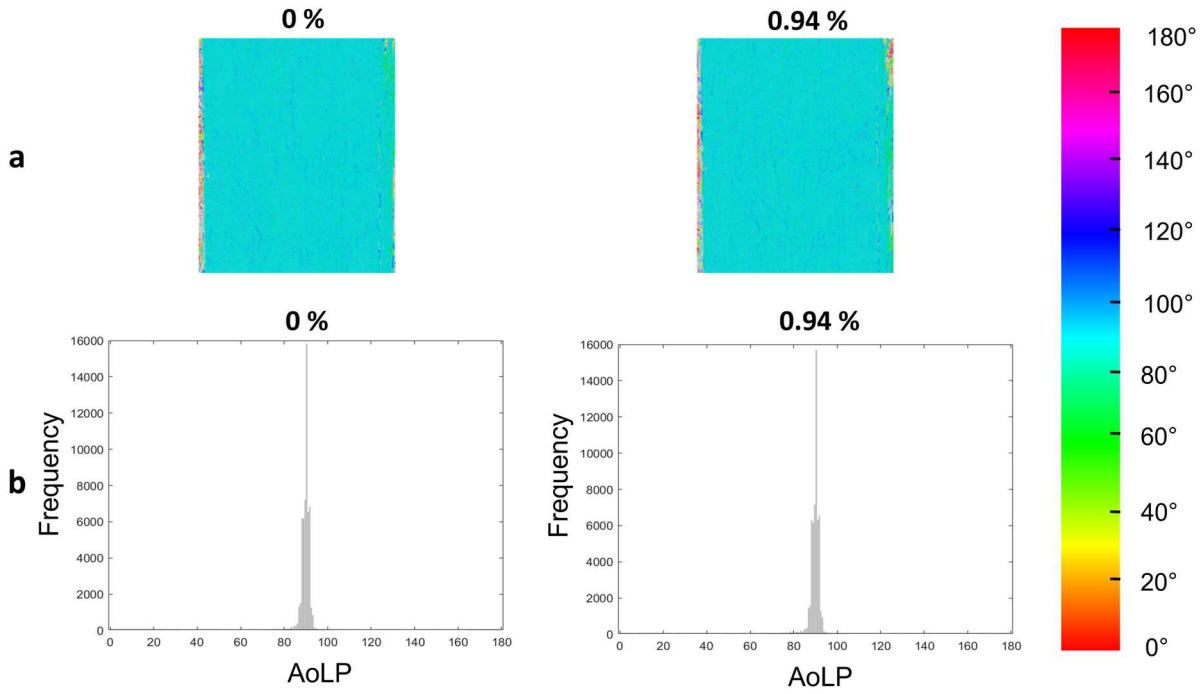


Figure 4.5 - The selected region of the fibre orientation images in the dry UD sample, where (a) shows the fibre orientation images at different strains and (b) represents the corresponding histogram of the AoLP information (hue channel) in (a).

the test (0 % strain) and the strain equal to 0.94 %. The mean of the AoLP was 90.18° ± 0.27 with a standard deviation of 1.87° ± 0.39 at 0 % strain. With increasing the strain to 0.94 %, the mean of the AoLP decreased slightly to 90.16° ± 0.28 with a standard deviation of 1.9° ± 0.40.

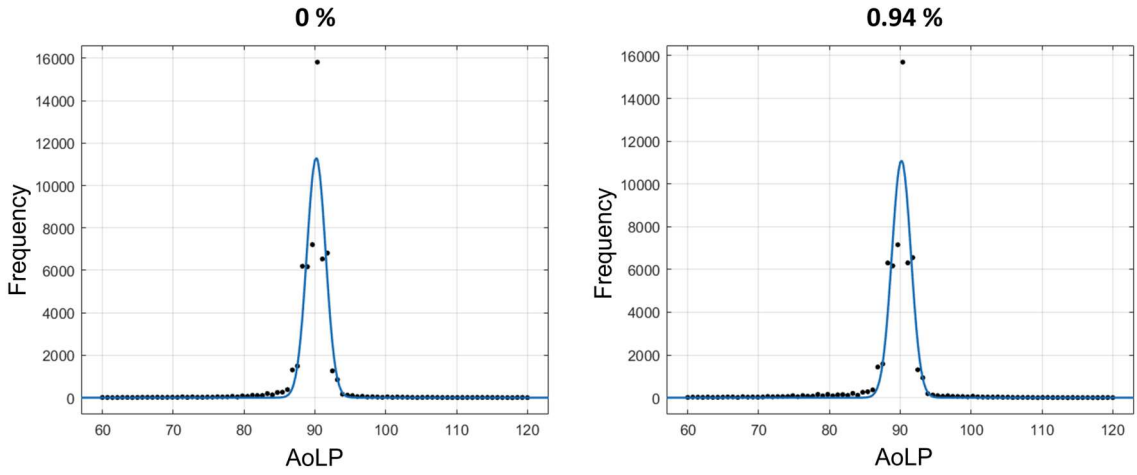


Figure 4.6 – MATLAB fitting of Gaussian curve to the histogram of AoLP data for dry UD sample at 0 % and 0.94 % strain.

Figure 4.7 shows the results of separating the fibres' angles by separating the colours in the HSV image using a colour threshold. The hue channel in the colour threshold is scaled from 0 - 255, corresponding to the fibres' orientation from 0° - 180°. The fibres that have orientations between 60° and 85°are presented in Figure 4.7 in white, corresponding to the hue channel in the range of 85 – 120. The fibres with orientations between 85° and 95° (which represent the ± 5° from the mean of the AoLP) are presented in hue channel scale from 121 – 135, and between 95° and 140° are presented from 136 -199. Furthermore, the figure shows that most fibres have orientations between 85° and 95°, with 95.46 % of the total area of the 0 % strain image, while the fibres that have orientations between 60° and 85° represented 0.88 % of the total area. With increased strain, the fibres' orientation image with 0.94 % strain shows that the fibres with orientations between 85° and 95° represent 96.21 % of the total area, while the fibres with orientations between 60° and 85° represented 0.36 % of the total area. As expected from the UD carbon fibre samples, the fibre's orientation will not significantly change during the tensile test because the fibres are along the tension direction.

The fibre orientation separation process provides a more detailed characterisation of fibre orientation behaviour with increasing strain than can be obtained through Gaussian fitting, where the Gaussian fitting is a global fitting that focuses on all data rather than small changes in the fibre orientations. Figure 4.7 illustrated the changes in the fibres with orientations between (60°- 85° and 95° - 140°) with increasing strain to have orientations between 85° and 95°, as indicated by the red circles.

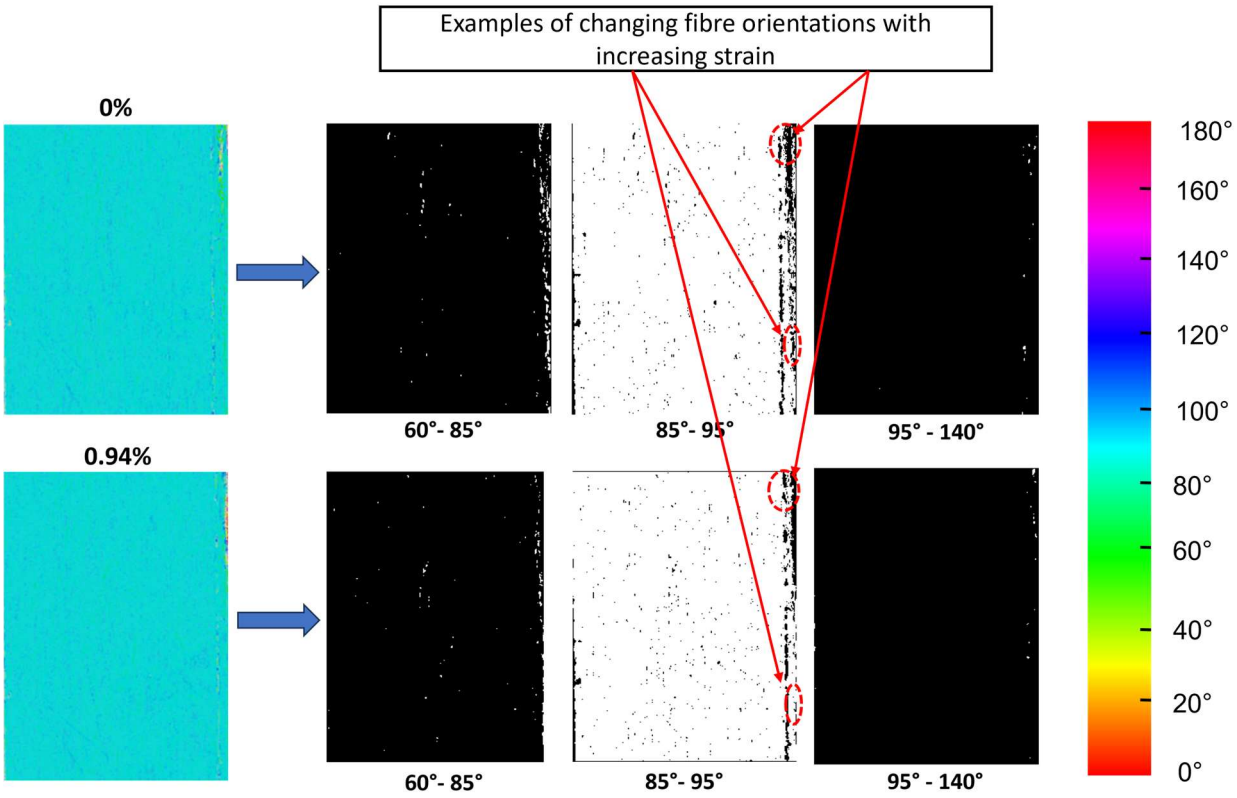


Figure 4.7 - Separating the fibres' orientation of the selected region image in the dry UD sample at 0 % and 0.94 % strain by separating the colours using a colour threshold.

Table 4.1 represents the mean of the AoLP and the standard deviation values, which is generated by MATLAB, for each image with a different strain, as shown in Figure 4.3. The standard deviation generated by MATLAB represents the width of the peak. The results of the AoLP of the dry UD sample show that there are no significant changes in the fibre orientation with an increase in the strain. Figure 4.8 visually presents the fibre orientation behaviour during tensile testing, Figure 4.3, of the dry UD sample. Only a 0.02° change in the fibre orientation since the strain increased from 0 % to 0.94 %.

Figure 4.9 shows the fibre orientation behaviour from the AoLP information, with increasing strain during tensile testing for all captured images using the polarisation camera. The data points in red show the fibre orientation behaviour for the six selected images with different strains (Figure 4.3). The fitting was applied using the standard MATLAB algorithm and fitting application, where the fitting was applied for each image individually. The data points in blue represent the fibre orientation behaviour for all captured images during tensile testing for the same sample using Python.

Table 4.1 - The mean of the AoLP and standard deviation results in the corresponding strain after applying the Gaussian curve fitting to the fibres' orientation images of dry UD sample that were captured during tensile testing, (Figure 4.3).

The mean of AoLP (degree)	Standard deviation (the width of the peak)	Strain (%)
90.18 ± 0.27	1.87 ± 0.39	0
90.17 ± 0.27	1.88 ± 0.39	0.01
90.16 ± 0.28	1.91 ± 0.40	0.53
90.16 ± 0.28	1.89 ± 0.39	0.81
90.16 ± 0.28	1.90 ± 0.40	0.94
90.15 ± 0.29	1.93 ± 0.41	1.09

The force and position curve for the dry UD sample are shown in Figure 4.10, where the increased linear line represents the elastic behaviour up to the maximum load force, equal to the corresponding strain of 0.94 % in the case of the sample shown in Figure 4.3. After that, the curve shows a decrease in the force caused by the damage initiation in the fibres. The presented curve depicts the relationship between force and position, rather than stress and strain, due to the variations in the cross-sectional area.

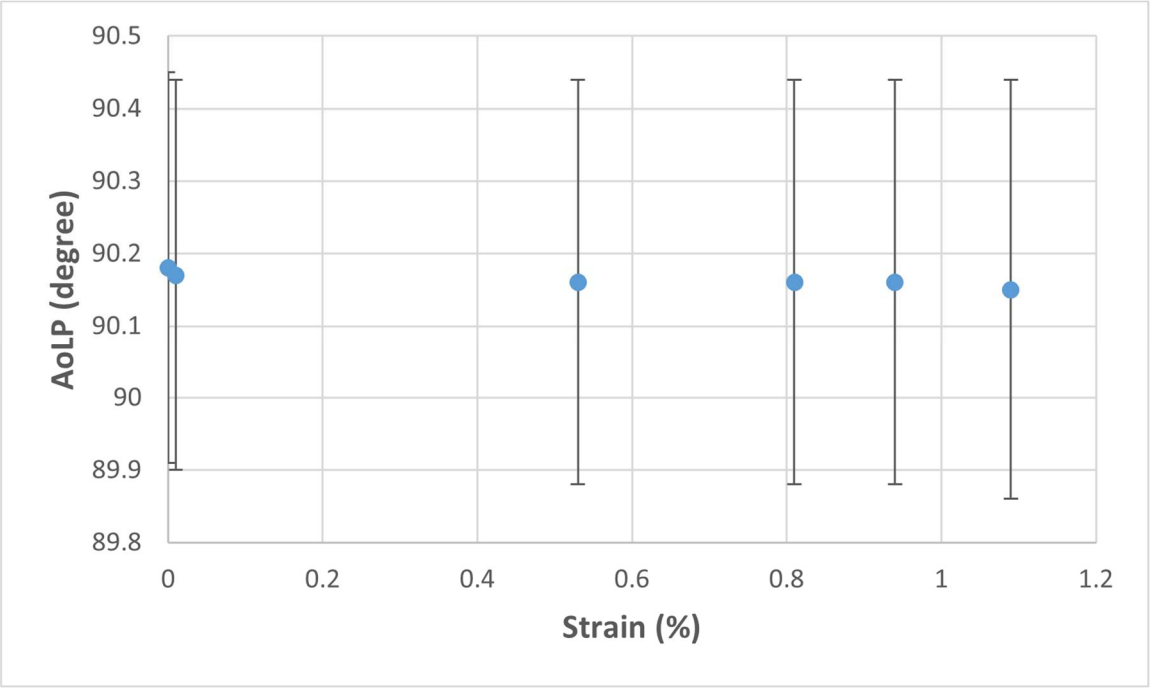


Figure 4.8 - The mean of the AoLP behaviour for one-layer dry UD sample with increasing strain (for the six selected images in Figure 4.3).

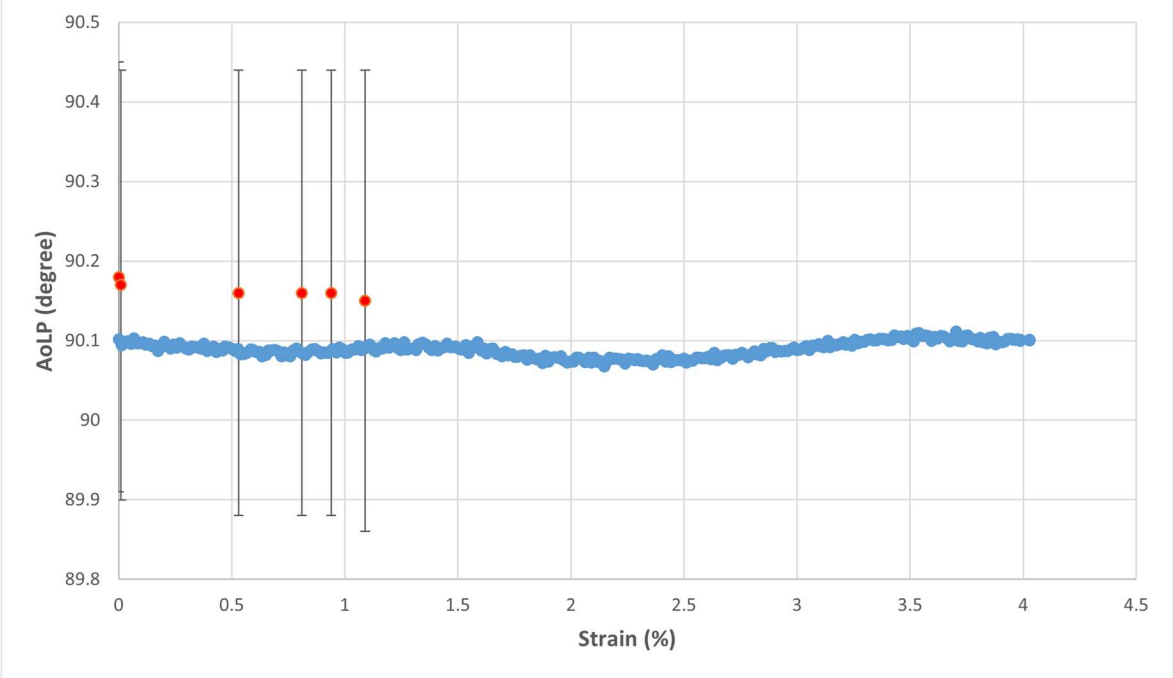


Figure 4.9 - The mean of the AoLP behaviour for the same sample used in Figure 4.8. The data in red are presenting the fibre orientation for the selected fibre orientation images (Figure 4.3), while data in blue are presenting the fibre orientation for all the captured images in the same sample.

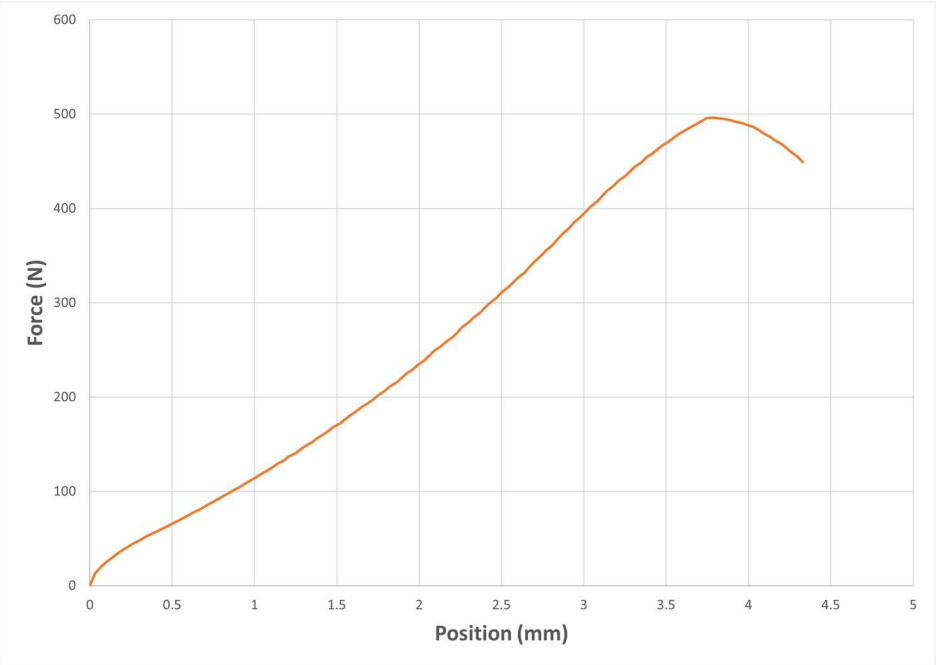


Figure 4.10 - The force and position curve for one layer of dry UD carbon fibre sample.

4.3.2 UD non-crimp carbon fibre (UD-NCF)

The same investigation process used for the UD sample was applied to the UD-NCF carbon fibre using the polarisation camera. Before conducting the tensile test, the sample was inspected offline using the polarisation camera to capture the raw saturation, DoLP, and fibres' orientation images, as shown in Figure 4.11. The DoLP image, (b), represents the carbon fibre in grey, while the thermoplastic material, that holds the fibres from the weft direction, is presented in black. Image (c) presents the fibres' orientation from the AoLP information.

A sequence of selected fibre orientation images presenting the UD-NCF sample during the tensile test is shown in Figure 4.12. Image (a) represents the fibre's orientation before starting the test at 0 % strain, while image (e) was taken at maximum load force corresponding to 1.11 % strain. The fibres' orientations were influenced by increasing strain, where the fibres near the weft 0° direction are changing orientation in each image in Figure 4.12. The influence of the strain on the fibres' orientation behaviour was investigated by comparing the fibres' orientation images before starting the test and at maximum force load.

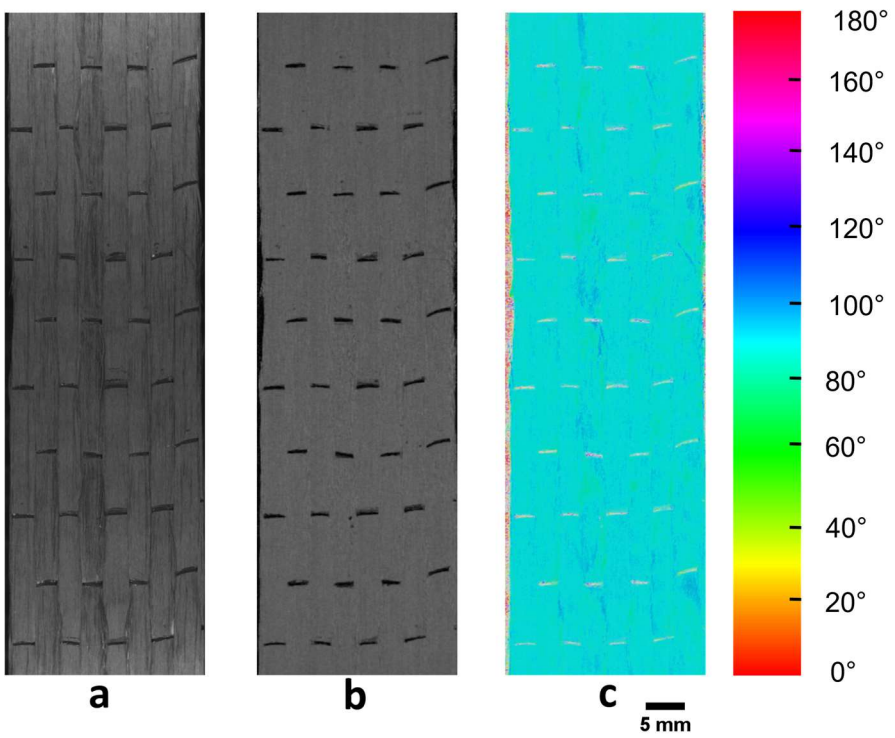


Figure 4.11 - Dry UD-NCF sample captured using the polarisation camera, where (a) the raw saturation image, (b) the DoLP image, and (c) the fibres' orientation, AoLP, image.

Figure 4.13 shows the selected region in the fibres' orientation image before starting the test at 0 % strain and 1.11 % strain, corresponding to the maximum force load, to investigate the orientation of the fibres with increasing strain.

The histogram of the AoLP data (hue channel), Figure 4.14, corresponds to the selected area to show the fibre orientation distribution, where (a) represents the selected area at different strains (0 % and 1.11 %) while (b) shows the corresponding histogram to the AoLP data. The histogram shows that the distribution of the fibre's orientation is between 85° and 95°.

The Gaussian curve fitting was applied to the AoLP data to find the mean of the AoLP before starting the test (at 0 % strain) and at maximum load force (equal to 1.11 % strain). The curve was fitted to the fibres with orientations between 60° and 120°, Figure 4.15. The mean and standard deviation of the AoLP for the fibre orientation image with 0 % strain is 89.51° ± 0.25 and 2.02° ± 0.35, and the fibre orientation image with 1.11 % strain obtained 89.51° ± 0.24 mean of AoLP with a standard deviation of 1.83° ± 0.33.

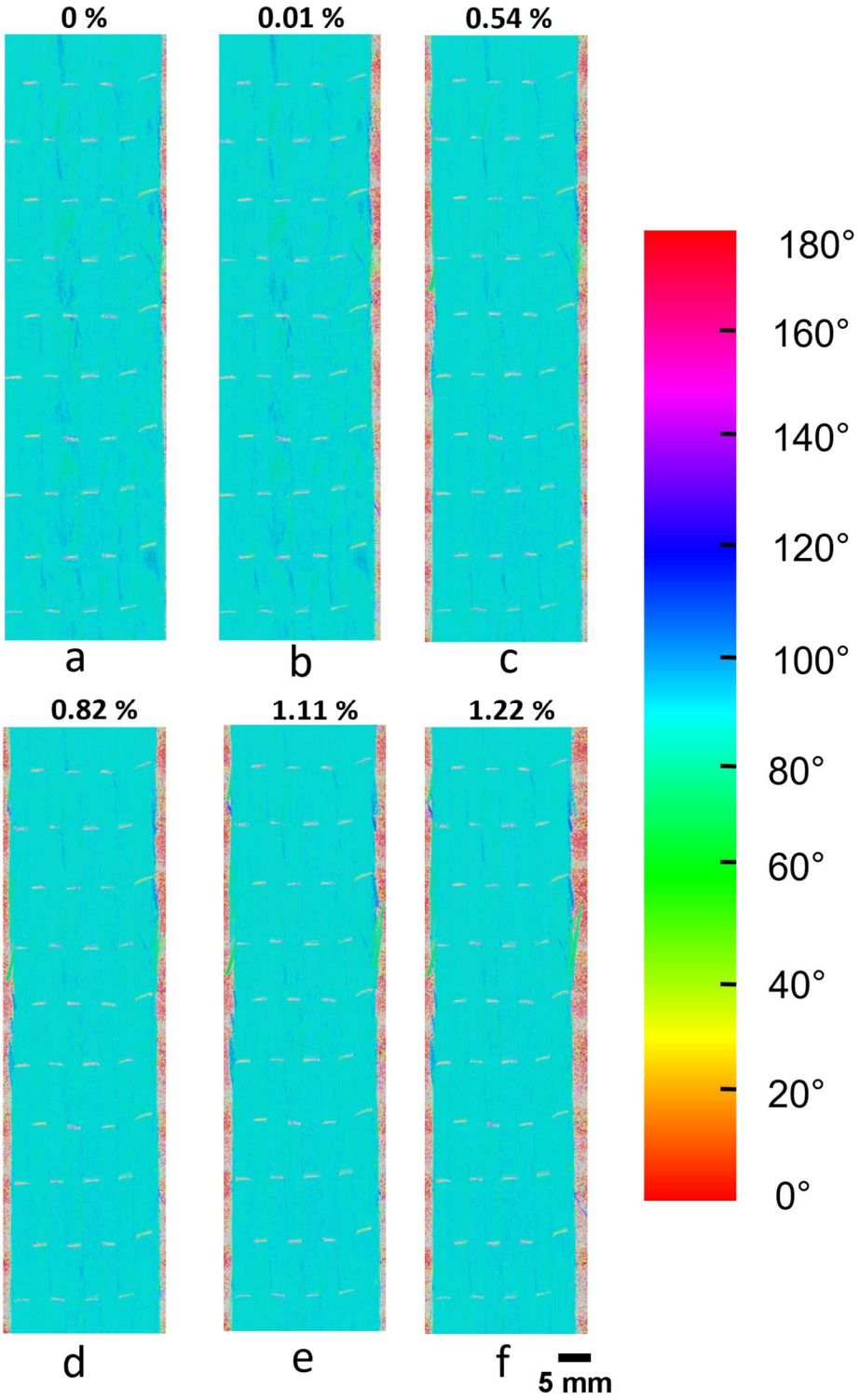


Figure 4.12 - A sequence of fibres' orientation images of dry UD-NCF sample captured during tensile testing using the polarisation camera. The strain corresponding to each image is presented above the figure.

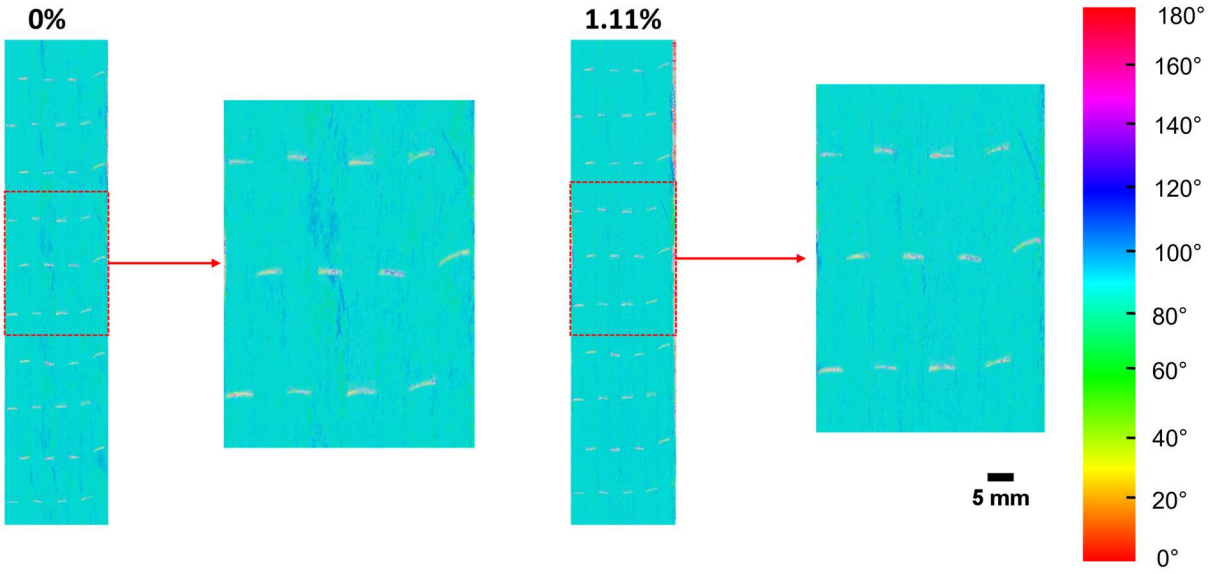


Figure 4.13 - The selected region of the fibres' orientation image in the dry UD-NCF sample was used to investigate and compare the fibres' angles at 0 % and 1.11 % strain.

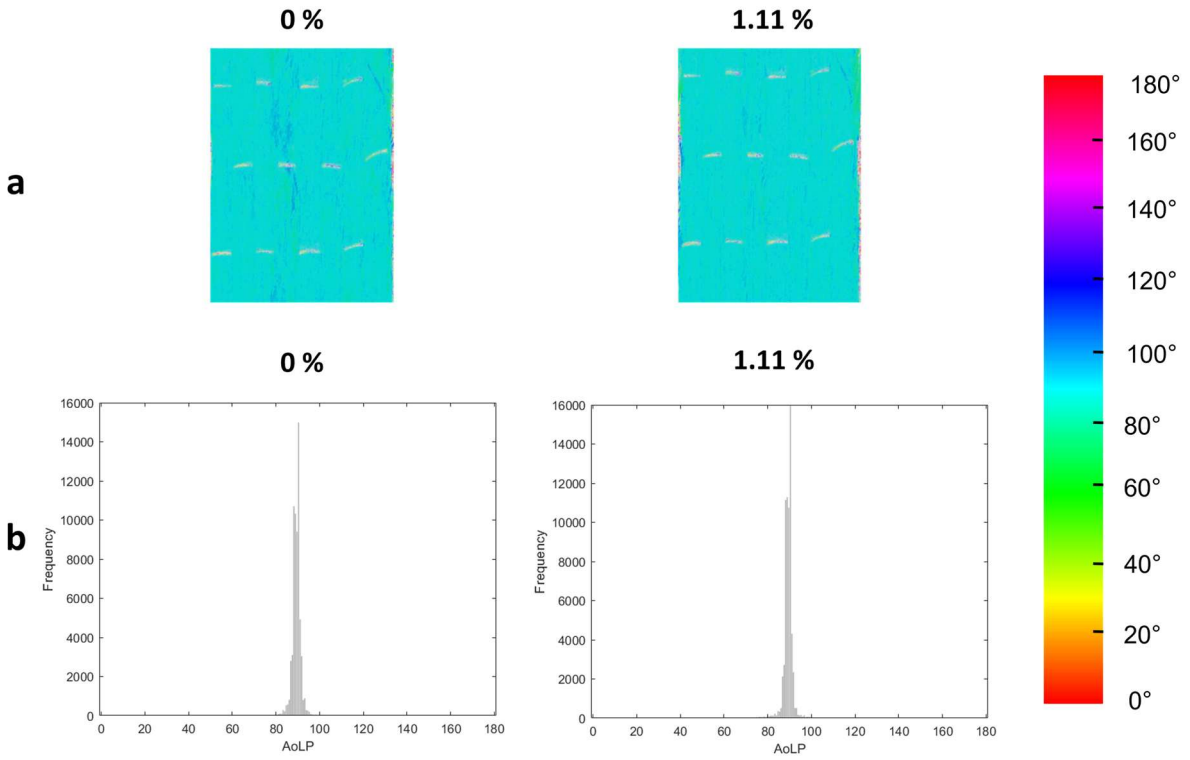


Figure 4.14 - The selected region of the fibre orientation images in the dry UD-NCF sample, where (a) shows the fibre orientation images at different strains and (b) represents the corresponding histogram of the AoLP information (hue channel) in (a).

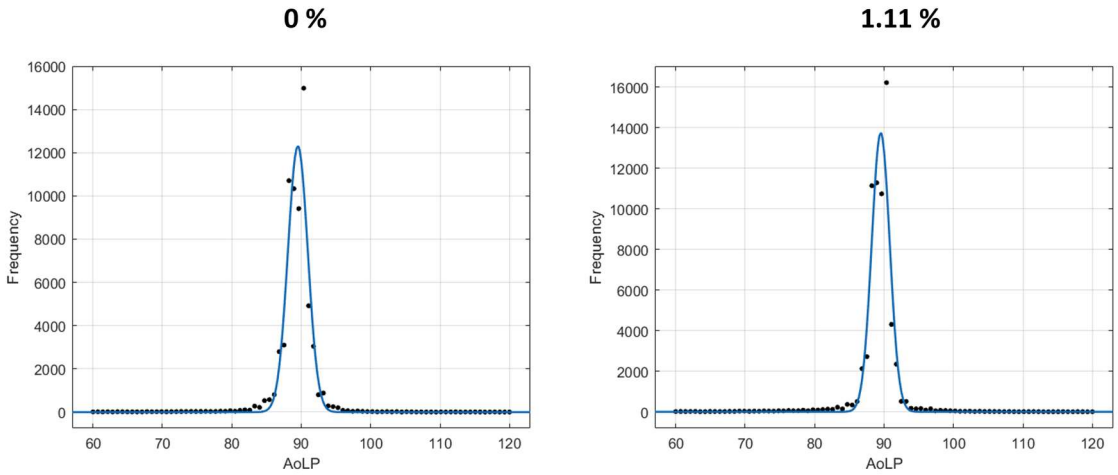


Figure 4.15 - MATLAB fitting of Gaussian curve to the histogram of AoLP data for dry UD-NCF at 0 % and 1.11 % strain.

Figure 4.16 shows the results of separating the orientation of fibres at 0 % strain and 1.11 % strain, where most of the fibre orientations are between 85° and 95°. Additionally, the separated images indicate that with increased strain, some fibres tend to change orientation to 85° and 95°. The percentage of the fibres that have an orientation between 85° and 95° is 93.29 % of the total area of the fibre orientation image with 0 % strain, while it is 93.82 % of the total area of the fibre orientation image with 1.11 % strain. The fibres with orientations between 60° and 85° represent 1.53 % of the total area in the image with 0 % strain, while it represents 0.71 % of the total area in the 1.11 % strain image.

The fibre orientation separation process provides more detail about small changes in the fibre orientations with increasing strain. The figure shows the fibre orientation changes when strain increased (in red circles), from 0 % and reached 1.11 %, where the fibres with orientations between (60° - 85° and 95° - 140°) changed to have orientations between 85° - 95°.

Table 4.2 represents the mean of the AoLP and the standard deviation values for each image with strain-increasing images in Figure 4.12. The results of the AoLP of the dry UD-NCF sample show no significant changes in the fibre orientation with an increase in the strain. Figure 4.17 provides a visual representation of the fibre orientation behaviour during tensile testing, Figure 4.12, of the dry UD-NCF sample. The fibre orientation changed slightly when the strain reached 0.54 % strain (from

89.51° ± 0.25 to 89.47° ± 0.24). After that, the fibre orientation changed to the same orientation at 0 % strain when the strain reached 1.11 %.

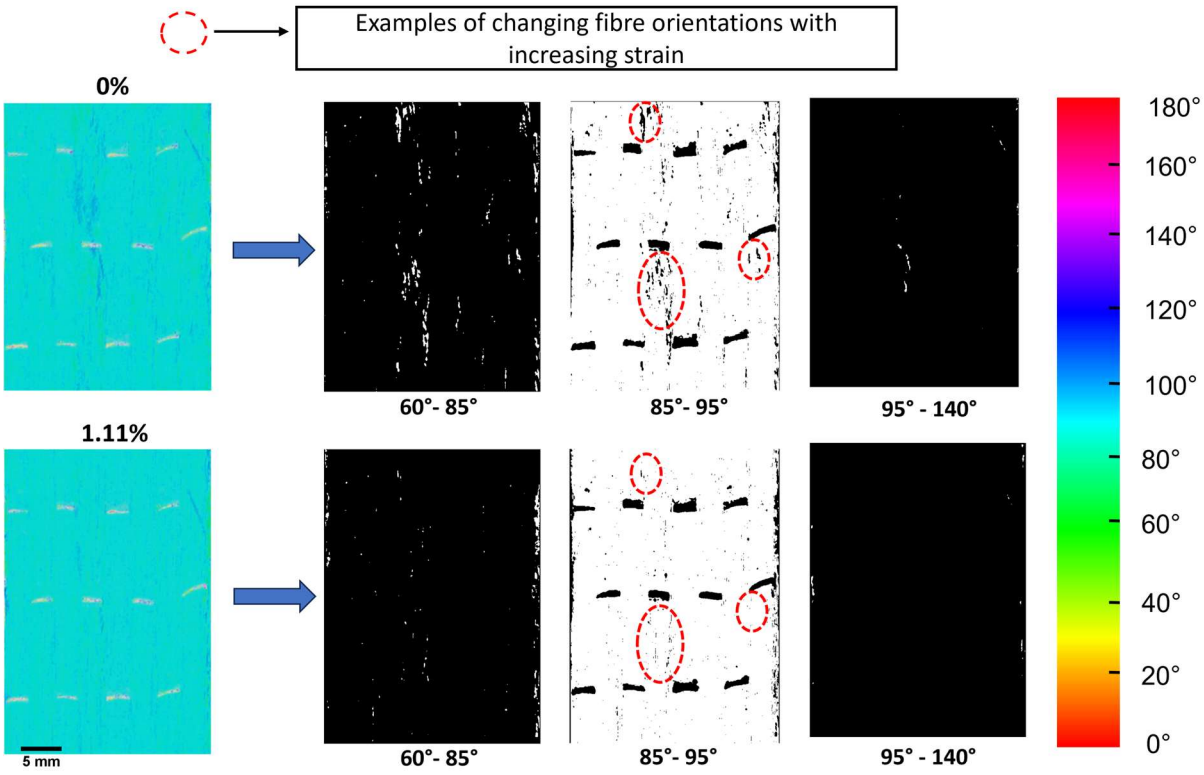


Figure 4.16 - Separating the fibres' orientation of the selected region image in the dry UD-NCF sample at 0 % and 1.11 % strain by separating the colours using a colour threshold.

Table 4.2 - The mean of the AoLP and standard deviation results in the corresponding strain after applying the Gaussian curve fitting to the fibres' orientation images of dry UD-NCF sample that were captured during tensile testing, (Figure 4.12).

The mean of AoLP (degree)	Standard deviation (the width of the peak)	Strain (%)
89.51 ± 0.25	2.02 ± 0.35	0
89.51 ± 0.27	2.08 ± 0.38	0.01
89.47 ± 0.24	1.87 ± 0.34	0.54
89.50 ± 0.23	1.85 ± 0.33	0.82
89.51 ± 0.23	1.83 ± 0.33	1.11
89.59 ± 0.24	1.81 ± 0.34	1.22

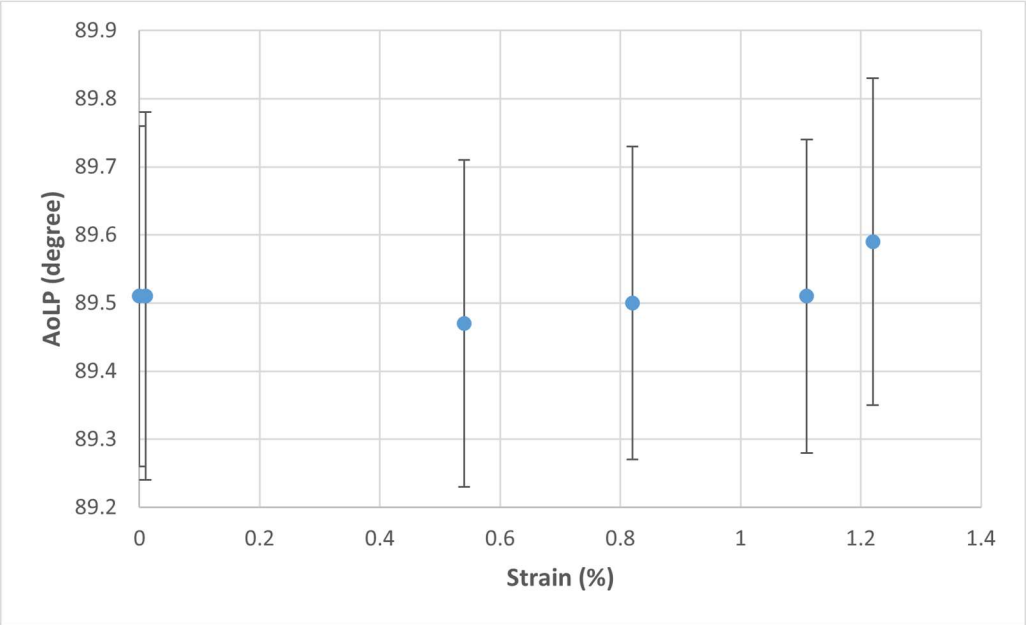


Figure 4.17 - The mean of the AoLP behaviour for one-layer dry UD-NCF sample with increasing strain (for the six selected images in Figure 4.12).

Figure 4.18 shows the fibre orientation behaviour from the AoLP data (blue data points), with increasing strain during tensile testing for all captured images using the polarisation camera. The data points in red show the fibre orientation behaviour for the six selected images with different strains (Figure 4.12). The standard MATLAB fitting curve application was utilised to obtain the mean of AoLP values in red, while Python was used to obtain the data for all images during the tensile test presented in blue.

The force and position curve of the UD-NCF sample is shown in Figure 4.19. The curve represents a linear response corresponding to the elastic behaviour up to the maximum load force point, equal to 1.11 % strain; then the line will decrease because of the damage initiation in the fibres. The presented curve shows the relationship between force and position, rather than stress and strain, due to the variations in the cross-sectional area.

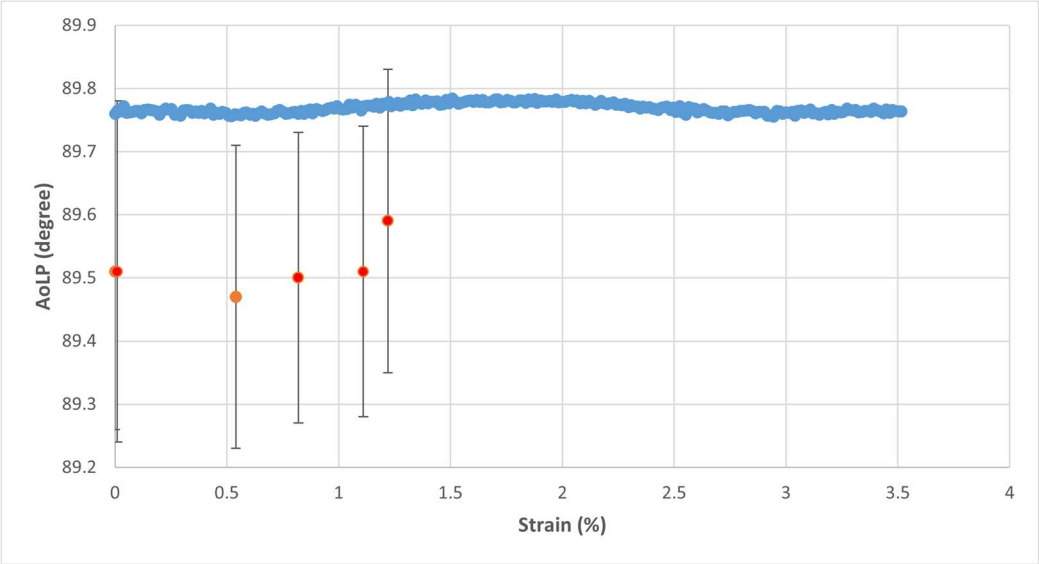


Figure 4.18 - The mean of the AoLP behaviour for the same sample used in Figure 4.17. The data in red are presenting the fibre orientation for the selected fibre orientation images (Figure 4.12), while data in blue are presenting the fibre orientation for all the captured images in the same sample.

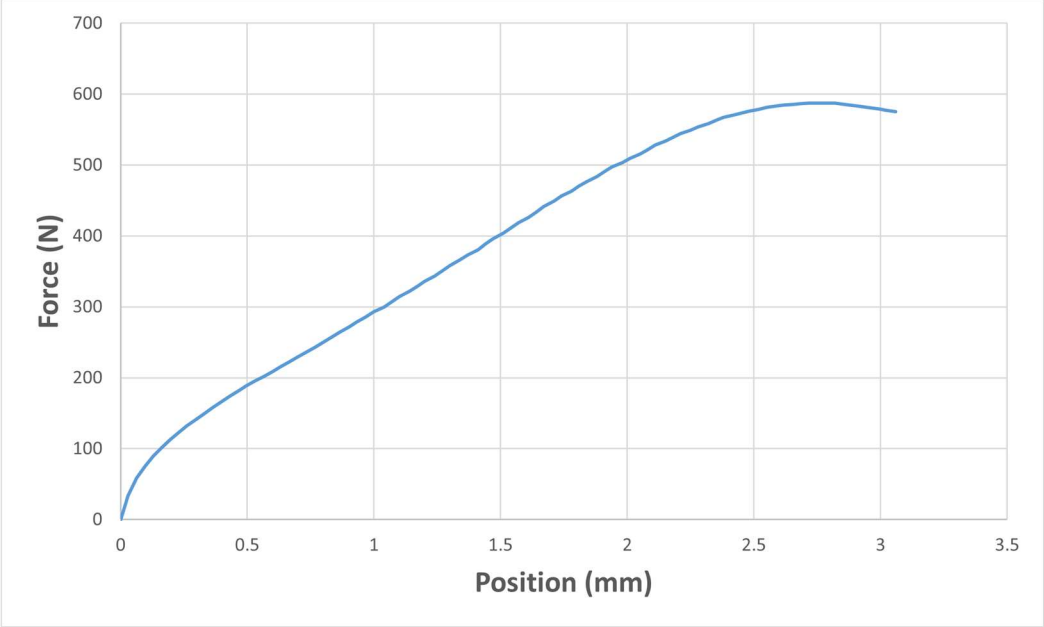


Figure 4.19 - The force and position curve for dry, one layer, UD-NCF carbon fibre sample.

4.3.3 Twill 2x2 carbon fibre

Again, using the polarisation camera, the same fibres' orientation investigation process was applied to the Twill 2x2 carbon fibre sample. The polarisation camera was used to capture the dry sample before starting the test, as shown in Figure 4.20, where (a) shows the raw saturation, (b) DoP and (c) fibres' orientation images.

Image-c shows the fibres' orientation of the Twill 2x2 sample, where fibres have 0° and 180° orientation, weft direction, are presented in red while fibres in 90° orientation are presented in cyan.

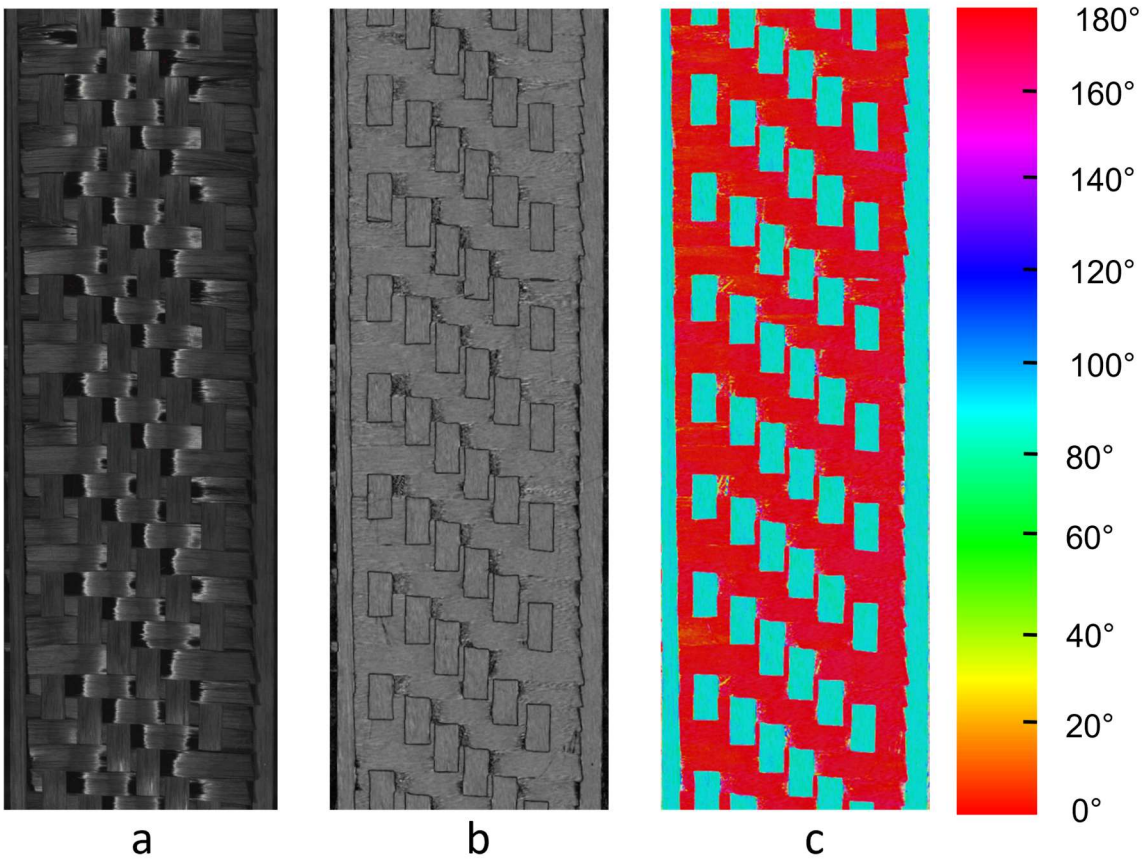


Figure 4.20 - Dry Twill 2x2 sample captured using the polarisation camera, where (a) the raw saturation image, (b) the DoP image, and (c) the fibres' orientation image.

The fibres' orientation images for the Twill 2x2 sample captured during the tensile test are presented in Figure 4.21. Image (a) shows the sample's fibre orientation before starting the test at 0 % strain, while image (e) shows the fibre orientation when the sample reached the maximum load force corresponding to 1.78 % strain. Images (a and e) indicate that increasing strain influences the fibres' orientation, especially at the fibres' edges.

For further investigation of the fibres' orientation, a selected region in the fibres' orientation image before starting the test (0 %) and at maximum force load (1.78 %) (Figure 4.22) were compared.

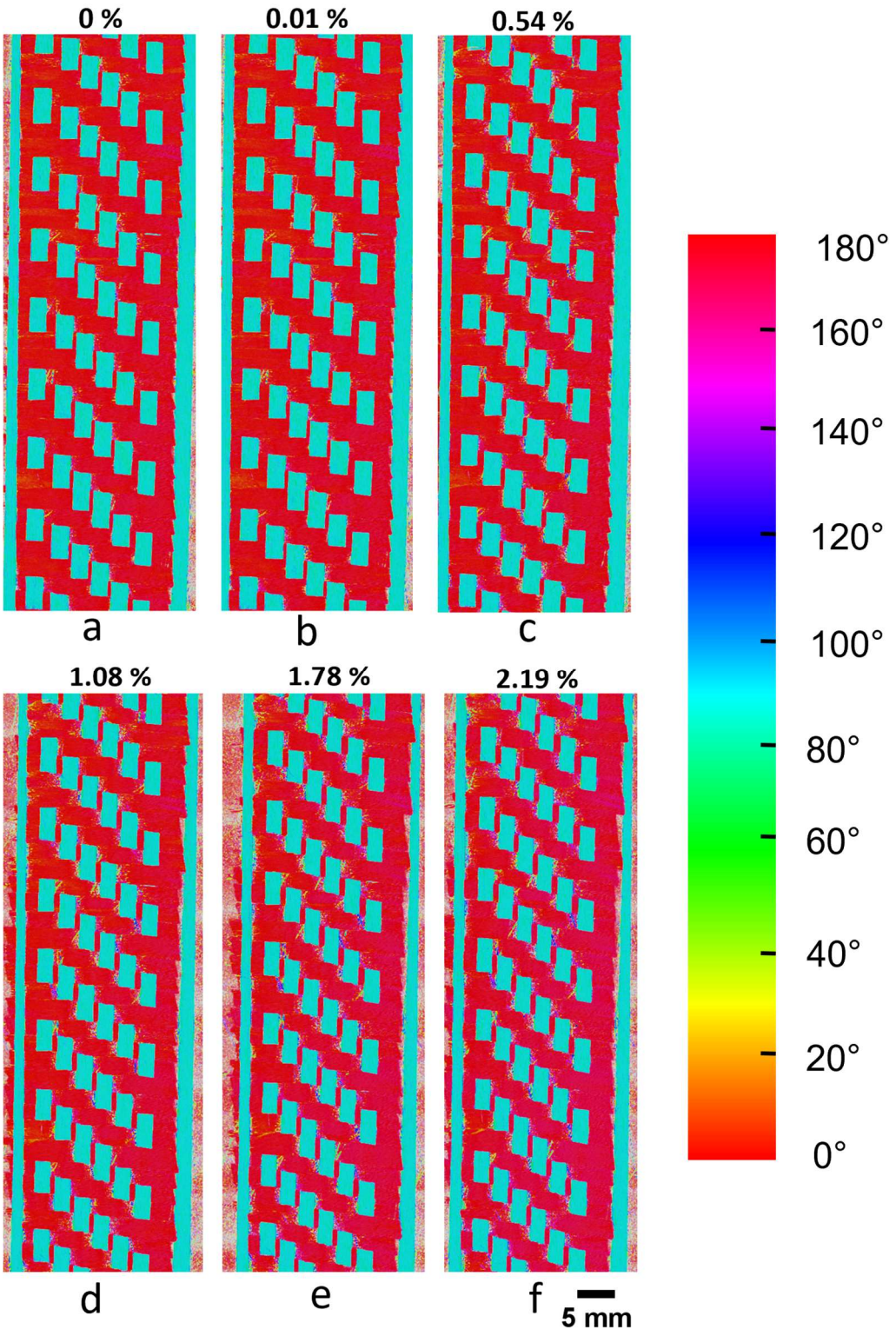


Figure 4.21 - A sequence of fibres' orientation images of dry Twill 2x2 sample captured during tensile testing using the polarisation camera. The strain corresponding to each image is presented above the figure.

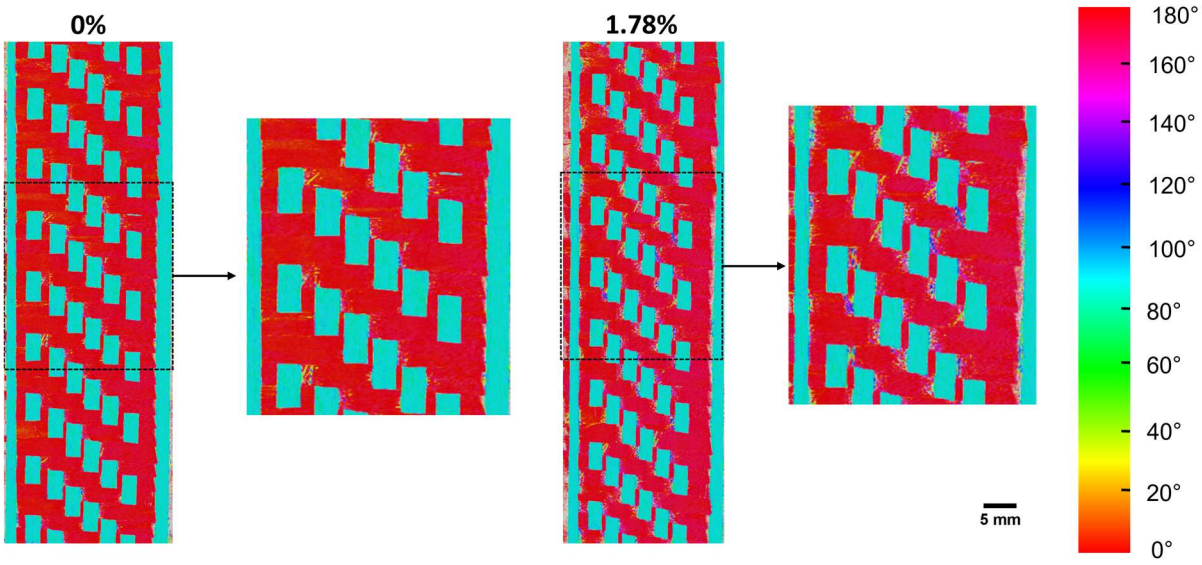


Figure 4.22 - The selected region of the fibres' orientation image in the dry Twill 2x2 sample to investigate the orientation of the fibres with strain increased.

Figure 4.23 shows the histogram of the AoLP data at different strains. In (a), the histogram for the AoLP before starting the tensile test (at 0 % strain) and when the sample reached maximum load force (equal to 1.78 %) is shown with fibres orientation distributed from 0° to 180°. Since the 0° and 180° presented the same fibre orientation (both represented in red in the fibre orientation image), the AoLP data (in the X-axis) were shifted to create the second peak. The range of the data in the X-axis from the range 160° to 180° were shifted to be presented in the range from (-20° to 0°). Figure 4.23-b shows the histogram after the shifting process.

The Gaussian curve fitting was applied to the AoLP data of the Twill 2x2 sample to find the mean of the AoLP before starting the test (at 0 % strain) and at maximum load force (equal to 1.78 % strain). Two peaks were fitted representing the fibres in the weft (first peak from -20° to 20°) and the fibres in the warp direction (second peak from 80° to 100°), Figure 4.24. The analysis of fibre orientation images for the first peak revealed a mean of the AoLP of (-2.39° ± 0.33) with a standard deviation of 4.55° ± 0.46 at 0 % strain and (-5.02° ± 0.41) with a standard deviation of 5.14° ± 0.59 when strain increased to 1.78 %. For the second peak, the value of the mean of the AoLP at 0 % strain was 88.08° ± 0.32 with a standard deviation of 3.31° ± 0.45 and 88.49° ± 0.29 with a standard deviation of 2.91° ± 0.59 at 1.78 % strain.

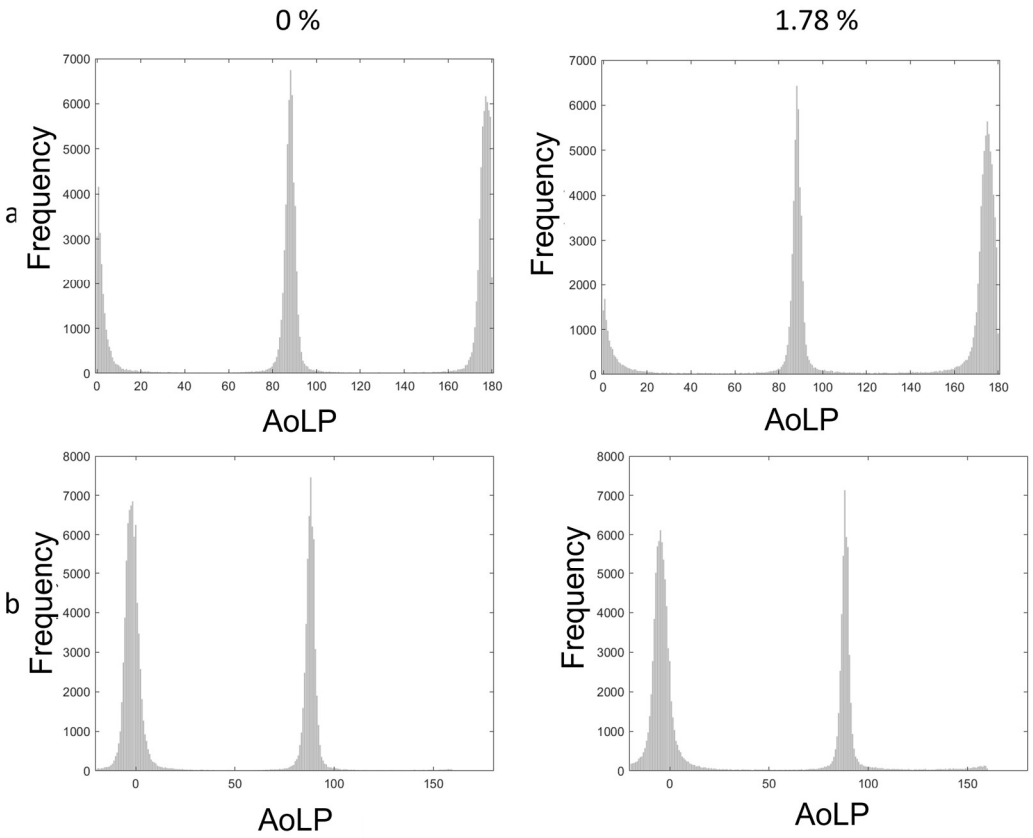


Figure 4.23 - The histogram of the selected region of the dry Twill 2x2 sample with different strains (0 % and 1.78 %), where (a) shows the histogram presenting the AoLP data from the range 0° to 180° and (b) shows the histogram for the same sample after peak shifting process.

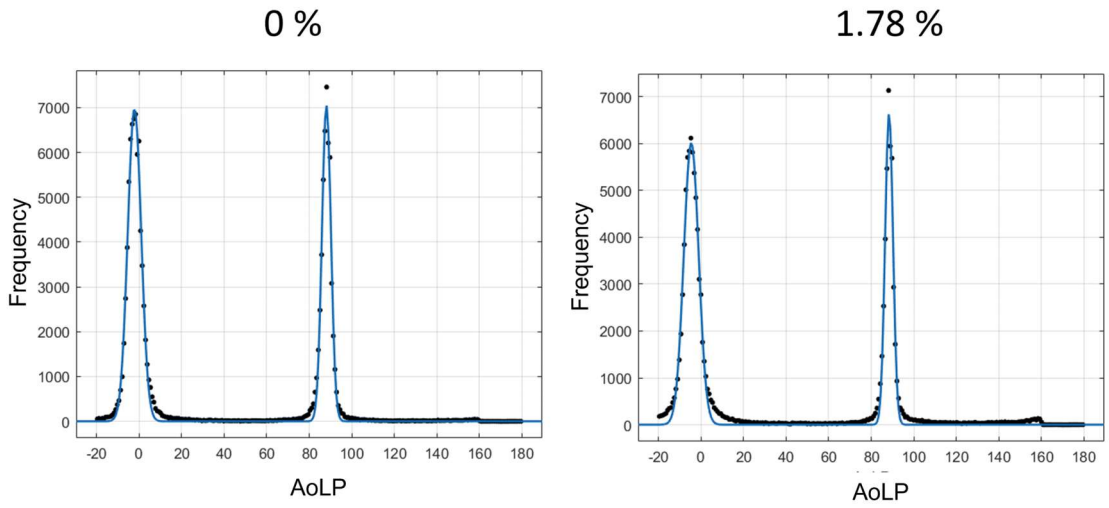


Figure 4.24 - MATLAB fitting of Gaussian curve to the histogram of AoLP data (after shifting process) for dry Twill 2x2 at 0 % and 1.78 % strain.

The results of separating the orientation of the carbon fibres in the selected region image at 0 % and 1.78 % strain are shown in Figure 4.25. The result shows that

most of the fibres have orientations between 80° - 100° (warp in the tension direction) and (0° - 20°), (160° - 180°) in the weft direction. However, fibres in the weft direction (perpendicular to the tension direction) are represented by the polarisation camera as 0° and 180° orientations (shown in red). So, it is worth mentioning that the fibres at 0° and 180° in the image after separation, i.e. images for 0° - 20° and 160° - 180° representing the same direction but in two orientations from the polarisation angle perspective.

In the image with 0 % strain, the fibres with orientations between 80° and 100° represent 35.02 % of the total area, fibres with orientations between 0° and 20° represent 14.38 %, and fibres with orientations between 160° and 180° represent 38.58 % of the total area in the fibres' orientation image with 0 % strain. In the 1.78 % strain image, the fibres with orientations between 80° and 100° represent 30.24 % of the total area, fibres with orientations between 0° and 20° represent 6.05 %, and fibres with orientations between 160° and 180° represent 45.05 % of the total area in the fibres' orientation image with 1.78 % strain.

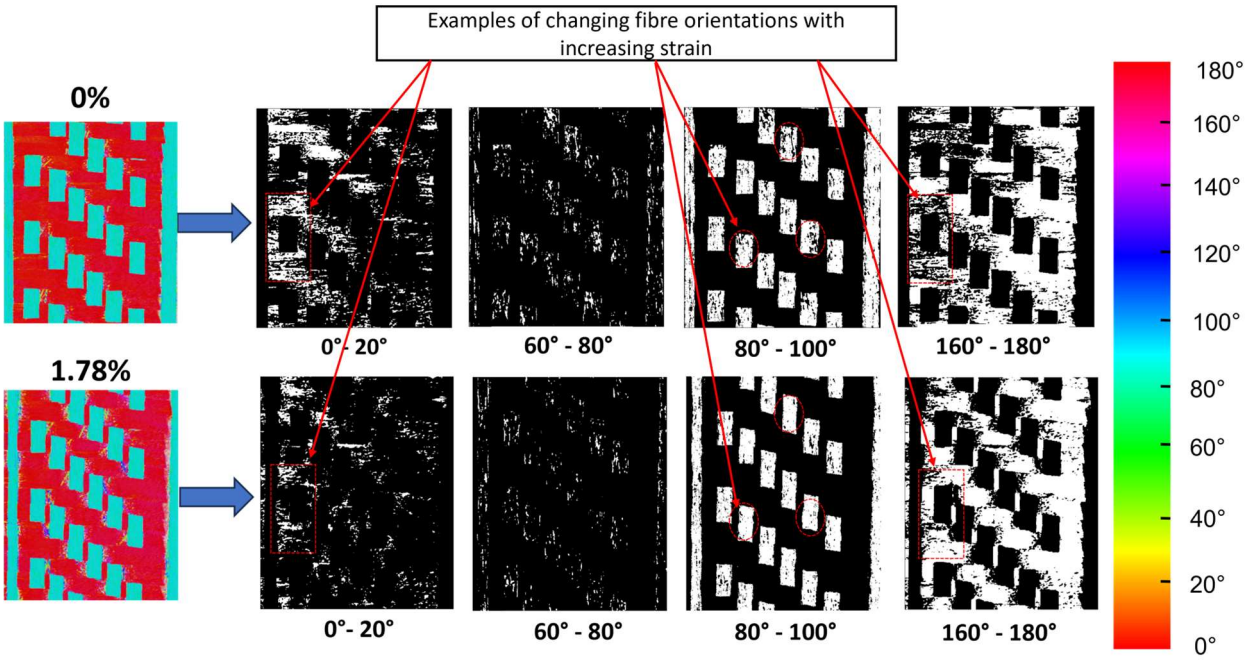


Figure 4.25 - Separating the fibre's orientation of the selected region image in the dry Twill 2x2 sample at 0 % and 1.78 % strain using a colour threshold.

The fibre orientation separation process provides further insight into the change of fibre orientation with increasing strain. Figure 4.25 (red circles) illustrates

representative changes in fibre orientation within fibres aligned with the tension direction. Specifically, fibres initially oriented between 60° and 80° shifted to orientations between 80° and 100° with increasing strain. The red rectangles in the figure highlight alterations in fibre orientation for fibres that are perpendicular to the tensile direction. With increasing strain, fibres oriented between 0° and 20° changed to have orientations between 160° and 180°.

Table 4.3 represents the mean of the AoLP and the standard deviation for the fibre orientation images during the tensile testing, Figure 4.21, for both fitting peaks. The results of the mean of the AoLP of the dry Twill 2x2 sample show the change behaviour in the fibre orientation with an increase in the strain. Figure 4-26 provides a visual representation of the fibre orientation behaviour with increasing strain for fibres in the warp and weft directions of the dry Twill 2x2 sample. The mean of the AoLP of the fibres in the weft direction (Peak-1) changes from (-2.39° ± 0.33) at 0 % strain to (-5.02° ± 0.41) when strain reached 1.78 %, while the AoLP of the fibres in the warp direction (peak-2) changes from (88.08° ± 0.32) at 0 % strain to (88.49° ± 0.29) at 1.78 %. The figure illustrates the change in fibre orientation with increasing strain. The perpendicular to the tensile direction (Peak-1), fibres change orientation towards -8°, while fibres aligned with the tensile direction (Peak-2) exhibit minimal change in orientation because they are already aligned with the applied force.

Table 4.3 - The mean of the AoLP and standard deviation results in the corresponding strain after applying the Gaussian curve fitting to the fibres' orientation images of dry Twill 2x2 sample that were captured during tensile testing, (Figure 4.21).

The mean of AoLP (degree) – Peak (1)	Standard deviation (the width of the peak)	Strain (%)	The mean of AoLP (degree) – Peak (2)	Standard deviation (the width of the peak)
-2.39 ± 0.33	4.55 ± 0.46	0	88.08 ± 0.32	3.31 ± 0.45
-2.40 ± 0.32	4.54 ± 0.46	0.01	88.09 ± 0.32	3.34 ± 0.45
-2.71 ± 0.38	4.81 ± 0.52	0.54	88.39 ± 0.28	2.97 ± 0.52
-3.14 ± 0.39	4.98 ± 0.56	1.08	88.45 ± 0.27	2.87 ± 0.56
-5.02 ± 0.41	5.14 ± 0.59	1.78	88.49 ± 0.29	2.91 ± 0.59
-7.63 ± 0.46	4.62 ± 0.65	2.19	88.56 ± 0.16	1.62 ± 0.56

Figure 4.27 presents the force and position curve of the dry Twill 2x2 sample. The curve shows a linear response up to the maximum load point, which is equal to 1.78 % strain. Then, the damage initiation caused the force to decrease at a high load. Due to the variations in the cross-sectional area, the curve represents the relationship between force and position rather than stress and strain.

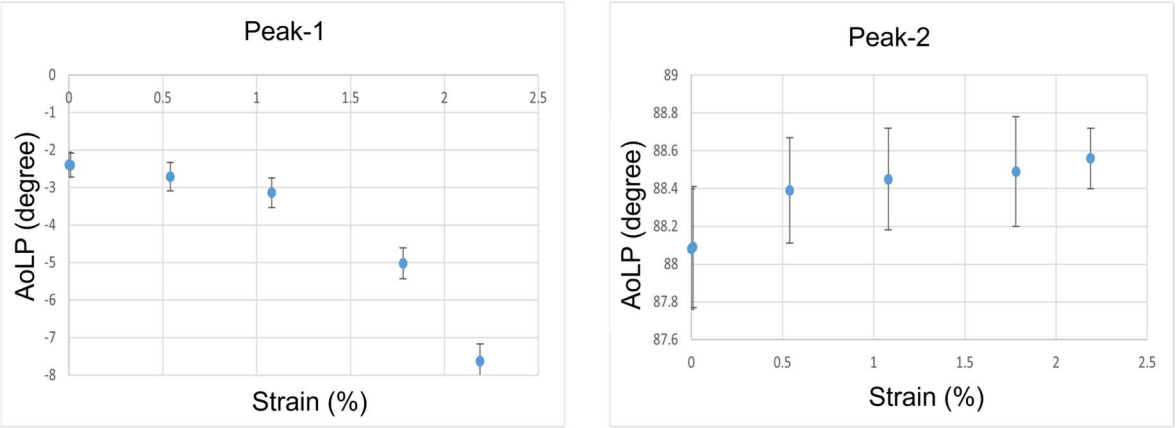


Figure 4.26 - The mean of the AoLP behaviour for one-layer dry Twill 2x2 sample with increasing strain (for the six selected images in Figure 4.21) for the two peaks.

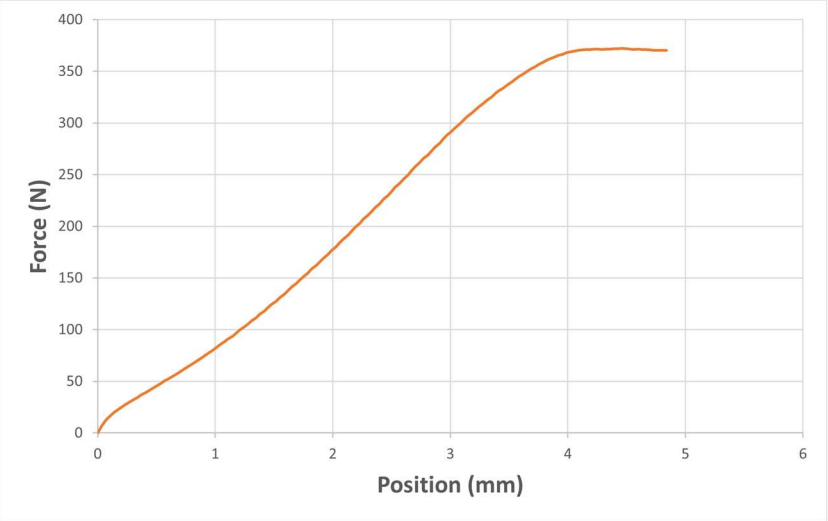


Figure 4.27 - The force and position curve for the dry Twill 2x2 sample.

4.3.4 Tailored fibre placement (TFP) preform

The UD-TFP preform reinforced hole with two and four layers underwent the same investigation process. However, the region of interest was around the reinforced hole and the loop-back fibres path to investigate the fibres' orientation behaviour during the tensile test. For more details about manufacturing the TFP reinforced

hole preforms using the loop-back fibre path approach, see the Methodology chapter 3.2.4.

Figure 4.28 shows the fibre's loop-back path near the reinforced hole for the two layers preform, before starting the test, where image (a) is the raw saturation showing the overexposed area (yellow) on the glass fibre (base material). Image (b) is the DoLP showing the carbon fibre in greyscale and the glass fibre and stitching thread in black. The red rectangles in image (a) show the path of the loop-back fibre, while the red circles in image (b) show how the loop-back fibre path caused the creation of an area that has no carbon fibre. The area that has no carbon fibre will create a resin-rich area when the preform is infused with resin.

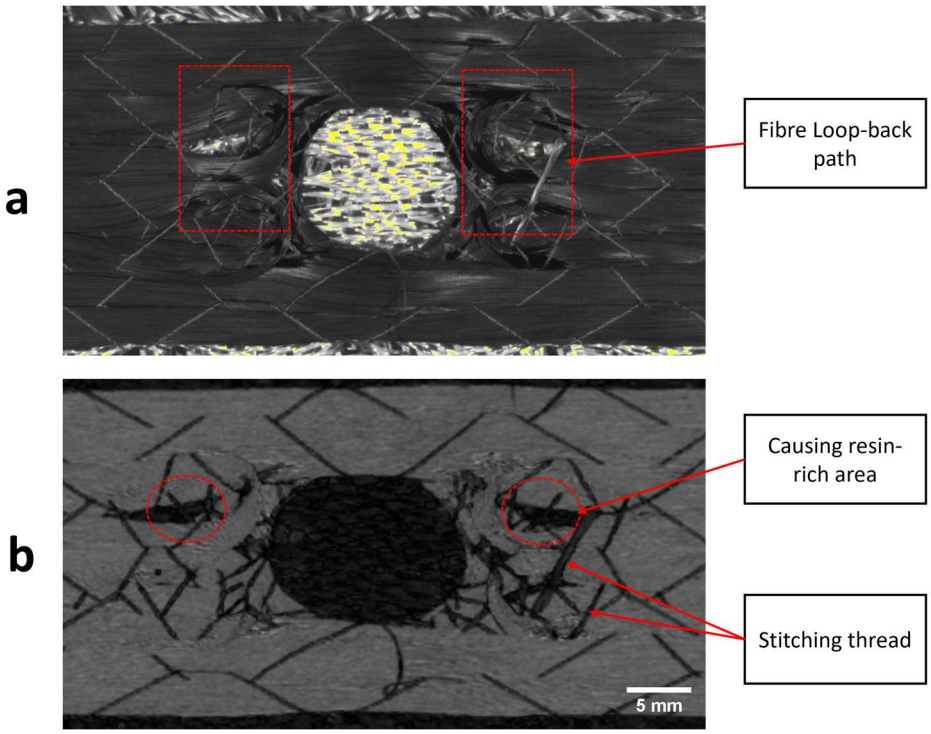


Figure 4.28 - The fibres loop-back path of two layers, UD-reinforced hole TFP preform. Image (a) is the raw saturation image and image (b) is the DoLP image captured using the polarisation camera.

Before starting the tensile test, the sample was inspected using the polarisation camera, and the raw saturation, DoLP, and fibres' orientation images were captured, as shown in Figure 4.29. The DoLP image (b) shows the carbon fibre in grey, while the glass fibre and the stitching thread are in black. Image (c) represents the carbon fibre orientation from the AoLP information that encodes from the hue channel in the HSV image.

Figure 4.30 shows the fibres' orientation images during the tensile test of TFP reinforced hole preform with two layers. Image (a) was captured before starting the test with an equal strain of 0 %, while image (f) was captured at 5.06 % strain. The fibre orientation images show how the fibre's loop-back path and fibres around the reinforced hole orientation were influenced by increasing strain.

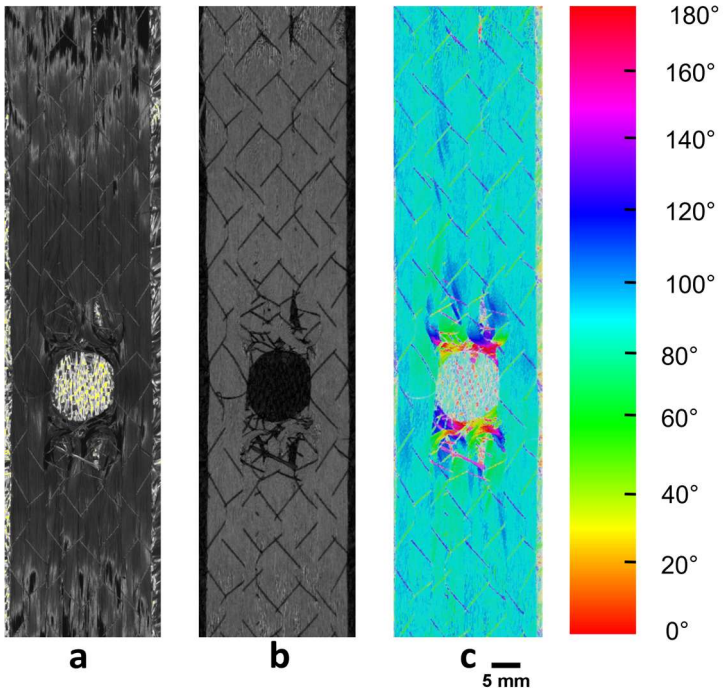


Figure 4.29 – UD-TFP reinforced hole preform with two layers, captured using the polarisation camera, where (a) the raw saturation image, (b) the DoLP image, and (c) the fibres' orientation image.

A selected region around the reinforced hole and the fibre's loop-back, Figure 4.31, was investigated to better understand the fibres' orientation behaviour with increasing strain, (0 % and 5.06 %). Figure 4.32 presents the AoLP information for the selected region images and shows the fibres' orientation distribution. The histogram shows that the fibres have orientations from 0° to 180°, which is because of the path used to create the reinforced hole. However, most of the fibres' orientations are distributed between 60° and 120°. For that, the Gaussian curve fitting was applied to the AoLP data between 60° and 120° to calculate the mean of the AoLP. The Gaussian curve fitting was applied to the AoLP data of the dry TFP reinforced hole sample consisting of two layers to find the mean of the AoLP before starting the test (at 0 % strain) and at strain equal to 5.06 %. Figure 4.33 shows the results of fitting on the fibre orientation images, where the mean of the AoLP at 0 %

strain was 89.39° ± 0.60 with a standard deviation of 7.33° ± 0.86. With increasing strain, the mean of the AoLP changes to 89.80° ± 0.28 with a standard deviation of 3.63° ± 0.41 at 5.06 % strain.

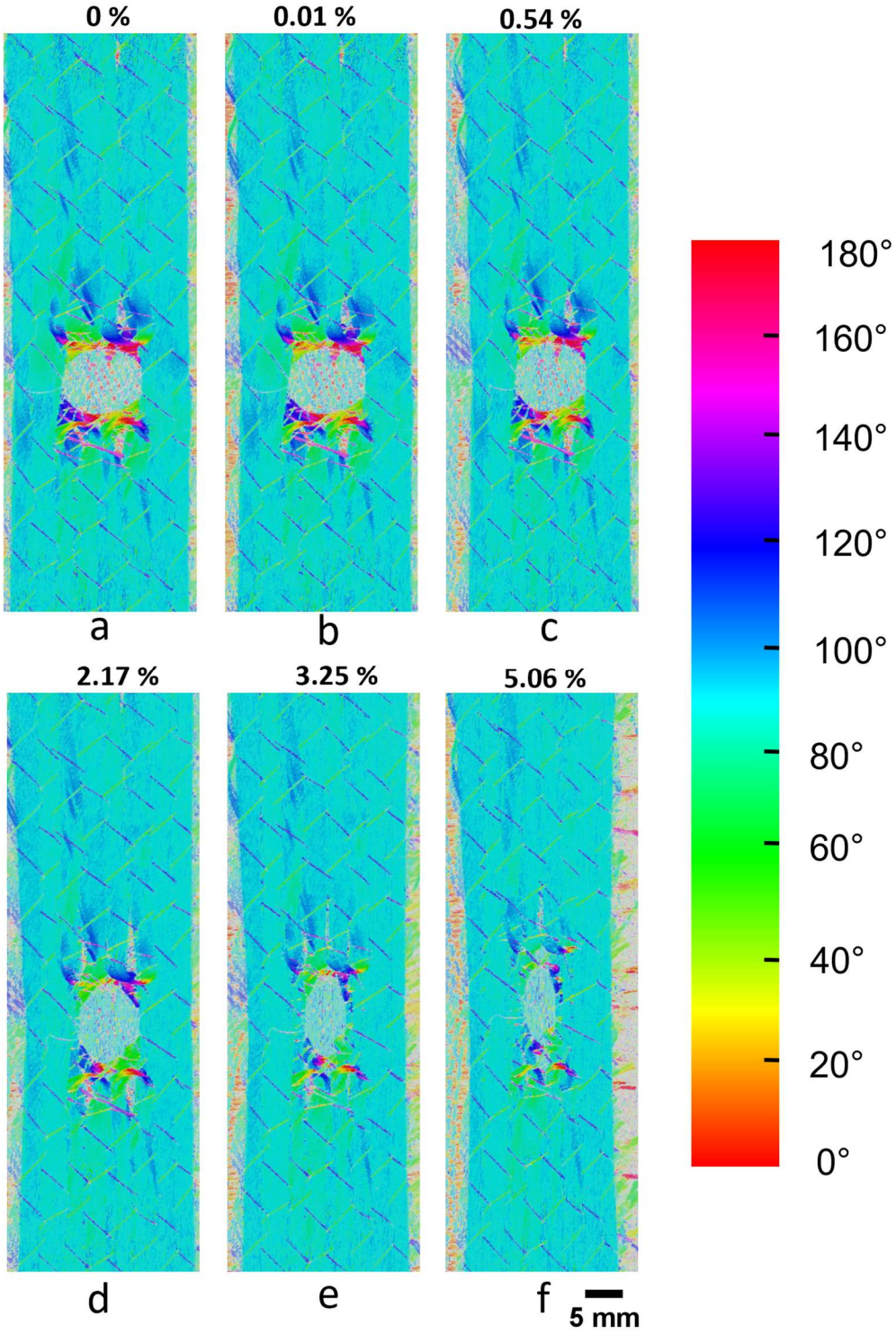


Figure 4.30 – The fibres' orientation images of TFP reinforced hole preform with two layers were captured using the polarisation camera during the tensile test. The strain corresponding to each image is presented above the figure.

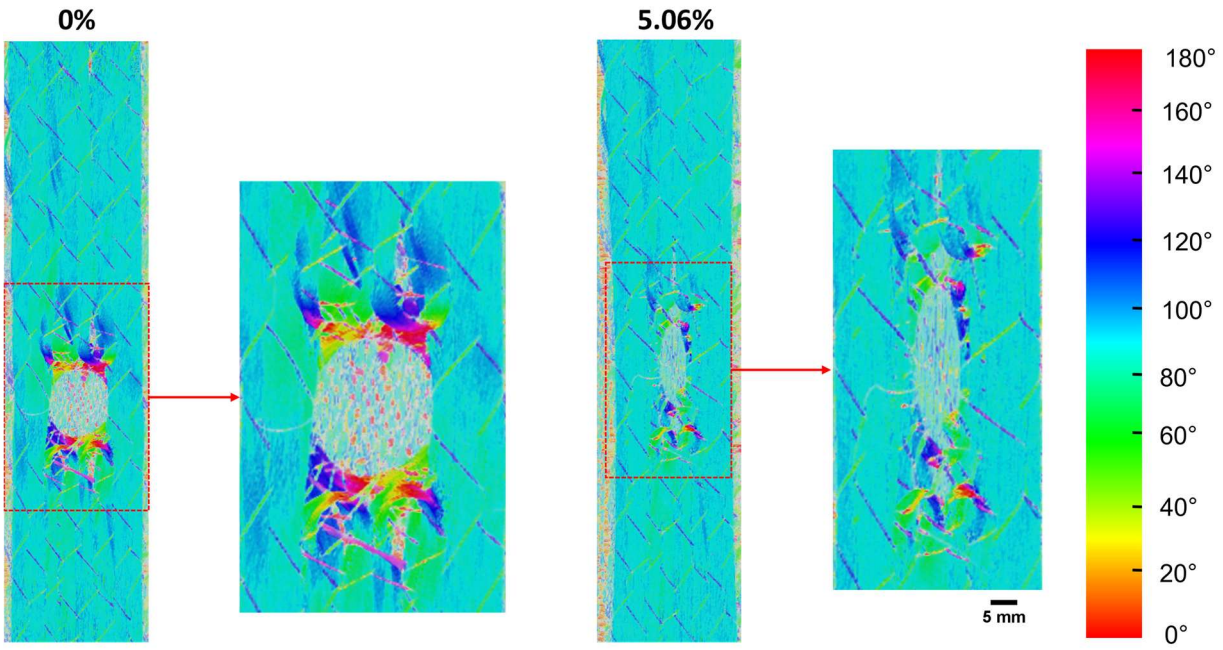


Figure 4.31 – The selected region of the fibres' orientation image for the TFP reinforced hole preform with two layers to investigate the AoLP before starting the test at (0 %) strain and (5.06 %) strain.

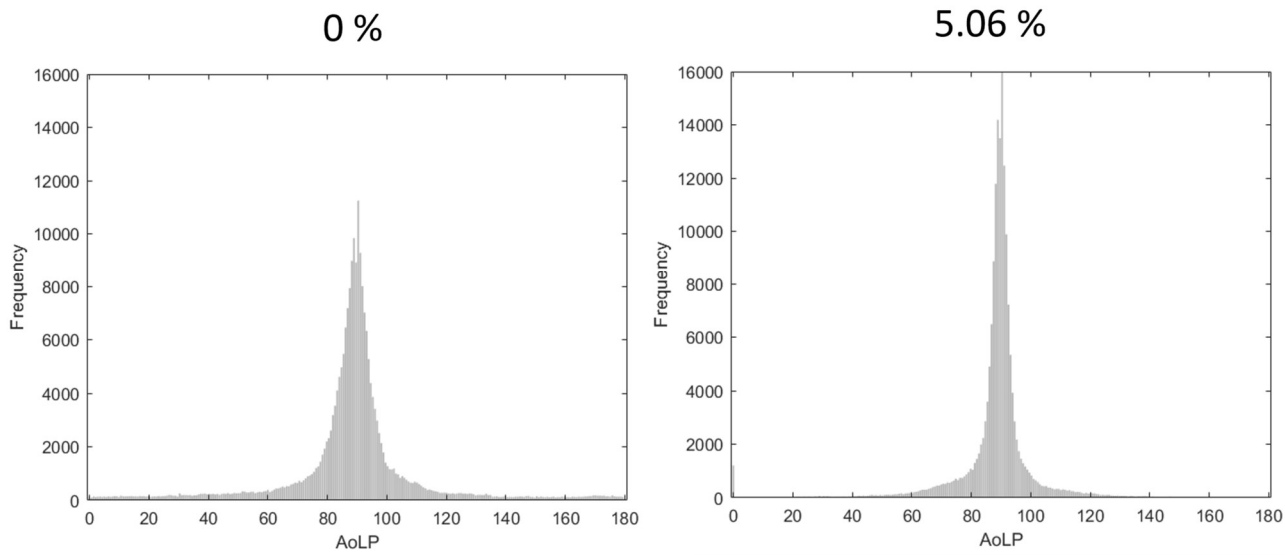


Figure 4.32 – The histogram of the selected region of the dry TFP reinforced hole with two layers sample presenting the AoLP data at different strains (0 % and 5.06 %).

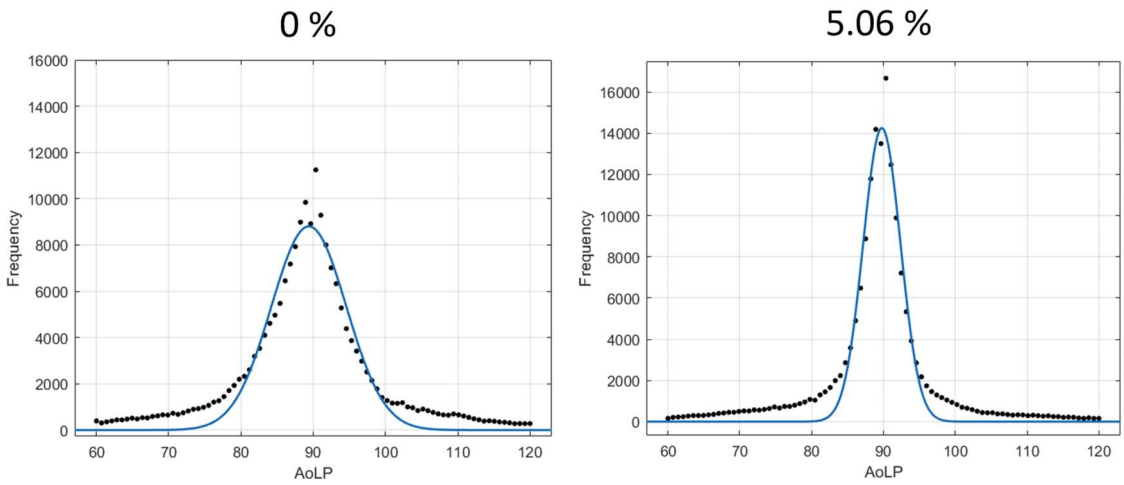


Figure 4.33 - MATLAB fitting of Gaussian curve to the histogram of AoLP data for dry TFP reinforced hole with two layers at 0 % and 5.06 % strain.

The fibre orientation was separated using the colour threshold for the selected area images with different strains to understand the fibre orientation behaviour with increased strain. The results of separating the orientation of the fibres in the selected region image, at 0 % and 5.06 % strain, are shown in Figure 4.34. The result shows that most of the fibres have orientations between 80° and 100°, presented in white.

The fibres with orientations between 80° and 100° represent 55.84 % of the image's total area with 0 % strain, fibres having orientations between 60° and 80° represent 6.61 % of the total area, and the fibres with 100°- 120° orientations represent 4.07 % of the total area. For the image with 5.06 % strain, fibres with orientations between 80° and 100° represent 66.84 % of the image's total area, the fibres that have orientations between 60° and 80° represent 3.34 % of the total area, and the fibres with orientations between 100° and 120° represent 1.85 % of the total area.

Table 4.4 represents the mean of the AoLP and the standard deviation for the fibre orientation images during the tensile testing, Figure 4.30, after applying the fitting curves. The results of the mean of the AoLP of the dry TFP reinforced hole preform with two layers show the change behaviour in the fibre orientation with an increase in the strain. Figure 4.35 visually represents the fibre orientation behaviour with increasing strain in the TFP reinforced hole sample consisting of two layers. The

mean of the AoLP of the fibres at 0 % strain changes from (89.39° ± 0.60) to (89.80° ± 0.28) with increasing strain to 5.06 %.

The fibre orientation separation process shows small changes in fibre orientation with increasing strain. For illustrative purposes, fibres initially oriented between 0° and 20°, 20° and 40°, and 40° and 60° were selected. As depicted by the red circles, these fibres, located at the reinforced hole, exhibit a reorientation with increasing strain, reaching 5.06%.

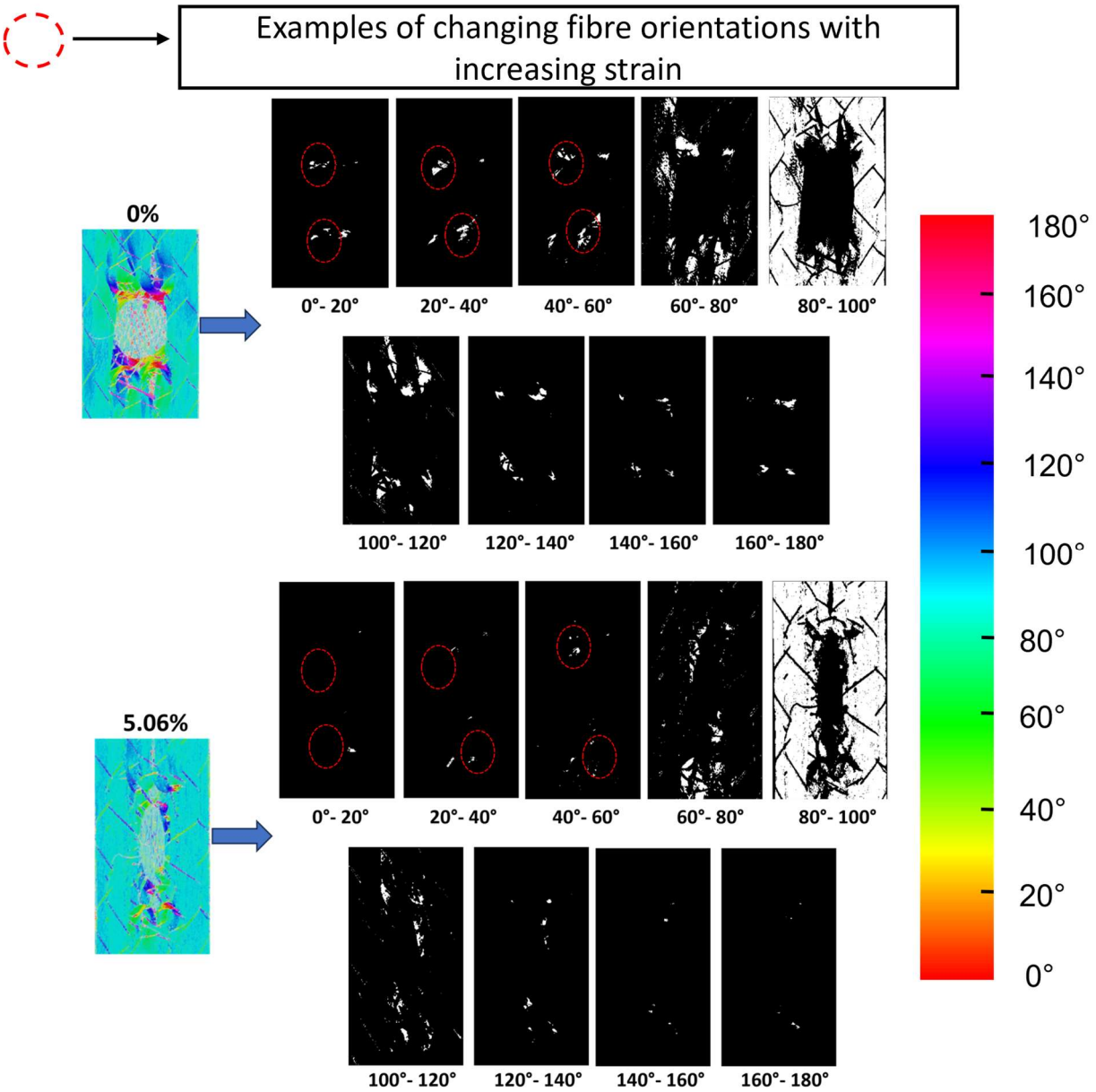


Figure 4.34 - Separating the fibre's orientation of the selected region image in the dry TFP reinforced hole preform with two layers at 0 % and 5.06 % strain using a colour threshold.

Table 4.4 - The mean of the AoLP and standard deviation results in the corresponding strain after applying the Gaussian curve fitting to the fibres' orientation images of dry TFP reinforced hole sample with two layers that were captured during tensile testing, (Figure 4.30)

The mean of AoLP (degree)	Standard deviation (the width of the peak)	Strain (%)
89.39 ± 0.60	7.33 ± 0.86	0
89.57 ± 0.35	4.12 ± 0.49	0.01
89.56 ± 0.33	3.91 ± 0.47	0.54
89.67 ± 0.26	3.59 ± 0.37	2.17
89.65 ± 0.24	3.15 ± 0.35	3.25
89.80 ± 0.28	3.63 ± 0.41	5.06

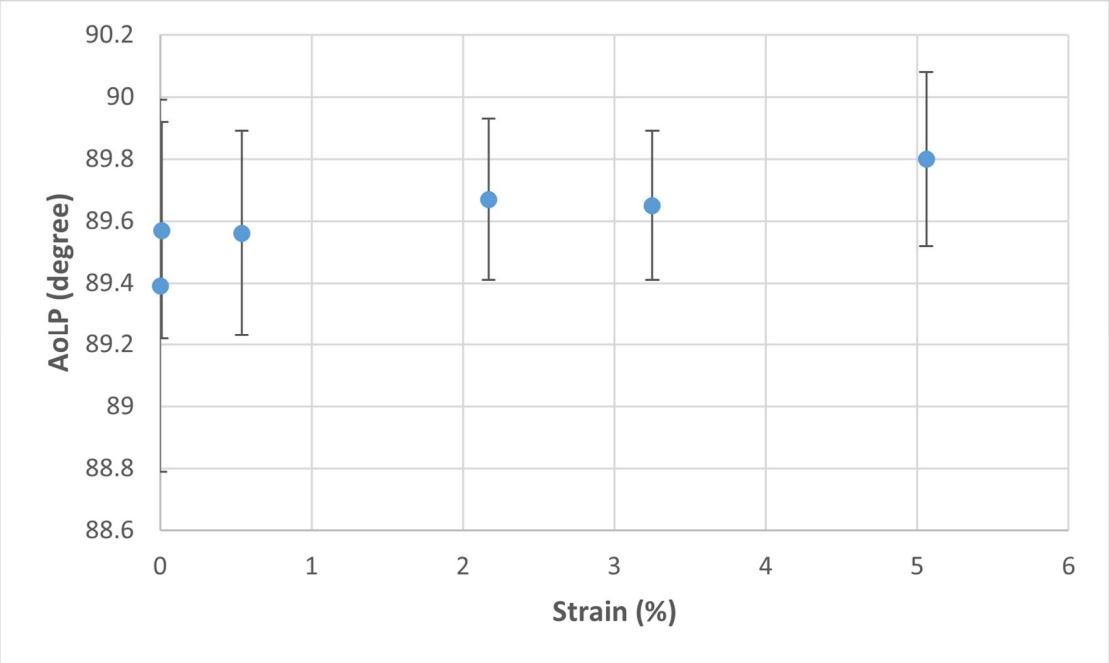


Figure 4.35 - The mean of the AoLP behaviour for two-layers of dry TFP reinforced hole preform with increasing strain (for the six selected images in Figure 4.30).

The force and position curve of the unidirectional TFP preform is shown Figure 4.36. This shows an increase in the force until a dip as the hole deforms and the fibres close up. The dips are caused by the breakage in the stitches that hold the fibres. The fibre orientation images at the dips are presented in Figure 4.36, which shows the reinforced hole deformation.

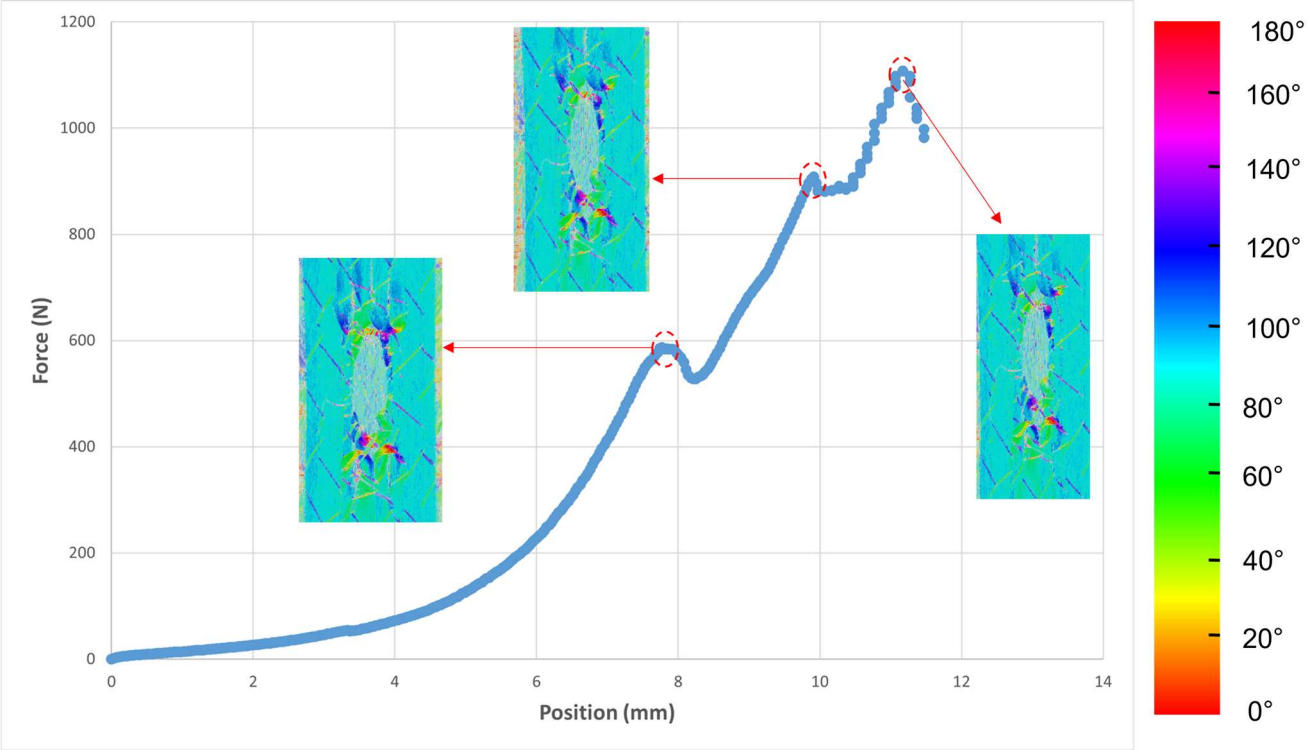


Figure 4.36 - The force and position curve for unidirectional TFP reinforced hole preform consists of two layers.

The same process was repeated for the TFP reinforced hole preform, which consists of four layers. The raw saturation, DoLP, and fibres' orientation images captured using the polarisation camera before conducting the tensile test are shown in Figure 4.37. The DoLP image (b) shows that, unlike the TFP performed with two layers, the polarisation camera detected no resin-rich area in the loop-back fibre's path. That might be because increasing the number of layers made the repetition process of creating the loop-back path not identical, which made the polarisation camera detect the carbon fibres in that area.

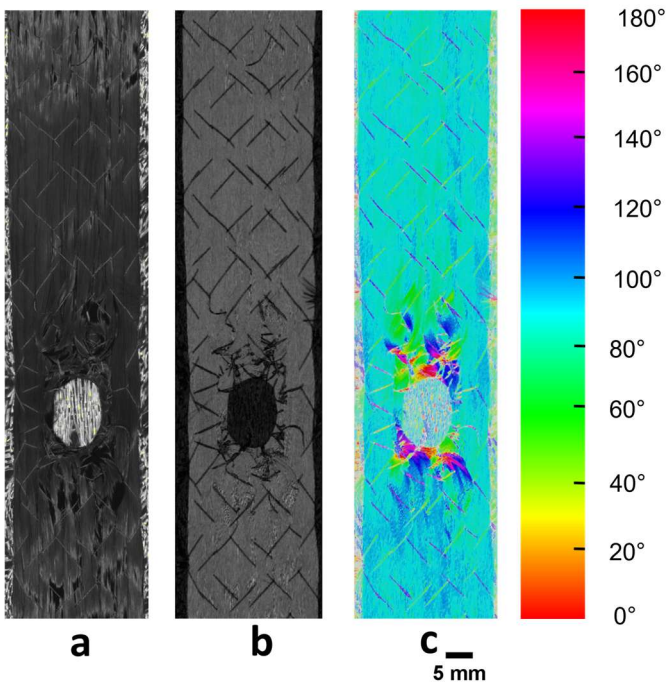


Figure 4.37 - UD-TFP reinforced hole preform with four layers captured using the polarisation camera, where (a) the raw saturation image, (b) the DoLP image, and (c) the fibres' orientation image.

Figure 4.38 presents the fibres' orientation images captured during the tensile test. Image (a) shows the orientation of the fibres before starting the tensile test at a strain equal to 0 %. Image (f) shows the fibres' orientation image at a strain equal to 4.67 %. The figure shows how increasing the strain influences the fibre orientation behaviour around the reinforced hole and the loop-back path.

A region of interest around the reinforced hole and the loop-back fibre path of the fibres' orientation image at 0 % and 4.67 % strain was selected to investigate the fibre's orientation behaviour with increasing strain, Figure 4.39. Figure 4.40 presents the AoLP data for the selected region images and shows the fibres' orientation distribution. The histogram shows that the fibre orientations range from 0° to 180°, with most of the fibres having orientations between 60° and 120°.

The Gaussian curve fitting was applied to the AoLP data of the dry TFP reinforced hole sample consisting of four layers to find the mean of the AoLP before starting the test (at 0 % strain) and at strain equal to 4.67 %. The fitting was applied to the data between 60° and 120°.

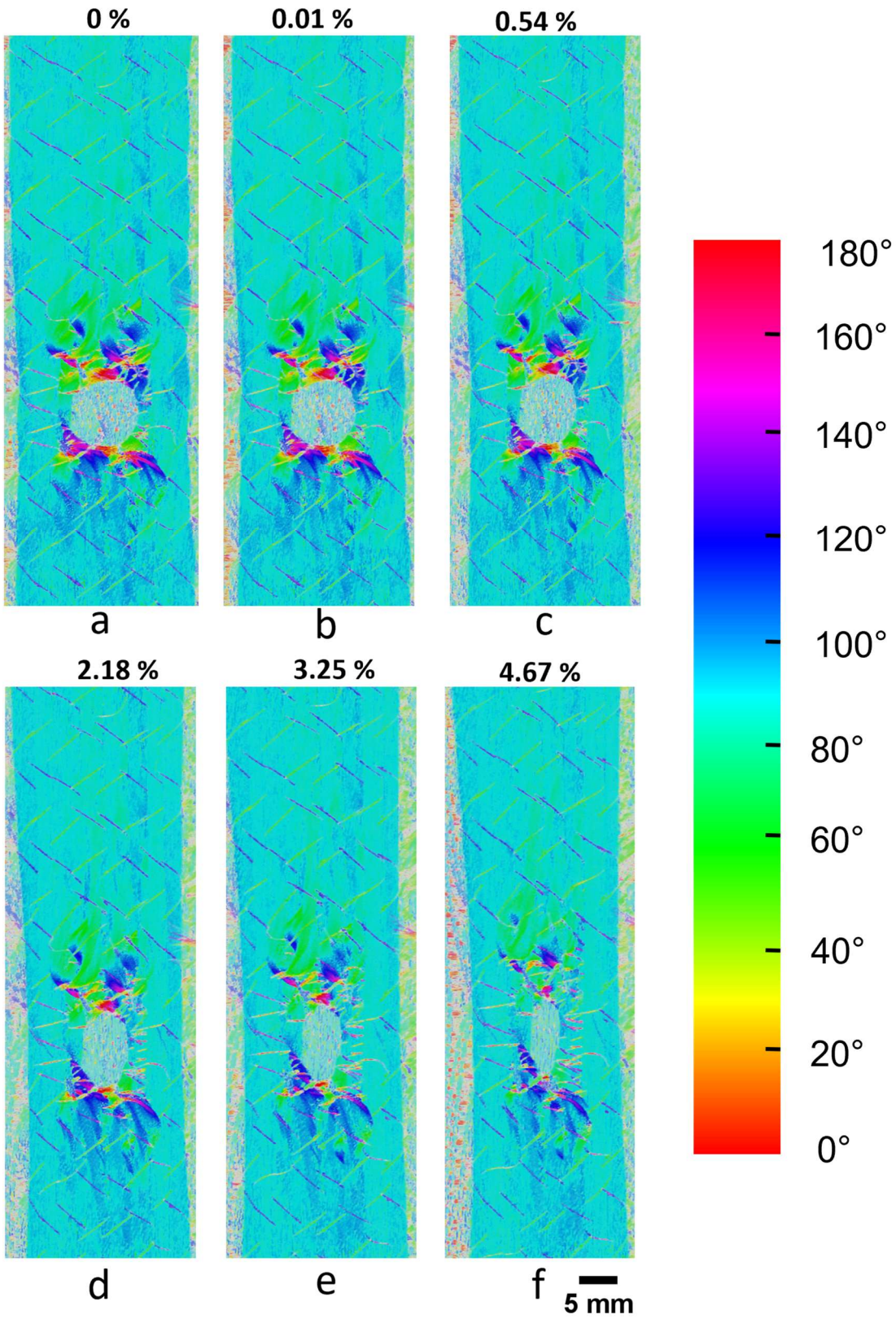


Figure 4.38 - The fibres' orientation images of TFP-reinforced hole preform consists of four layers were captured using the polarisation camera during the tensile test. The strain corresponding to each image is presented above the figure.

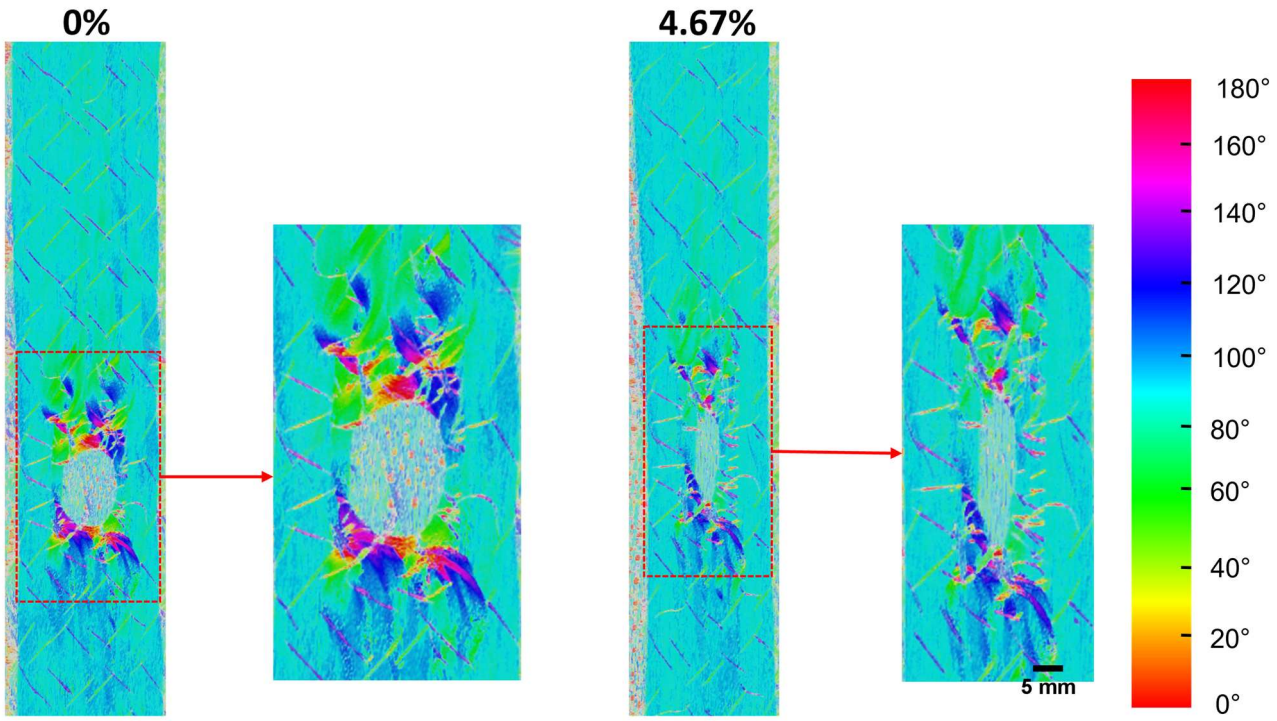


Figure 4.39 - The selected region of the fibres' orientation for TFP reinforced hole preform with four layers to investigate the fibres' angles before starting the test (0 %) strain and at maximum force load (4.67 %) strain.

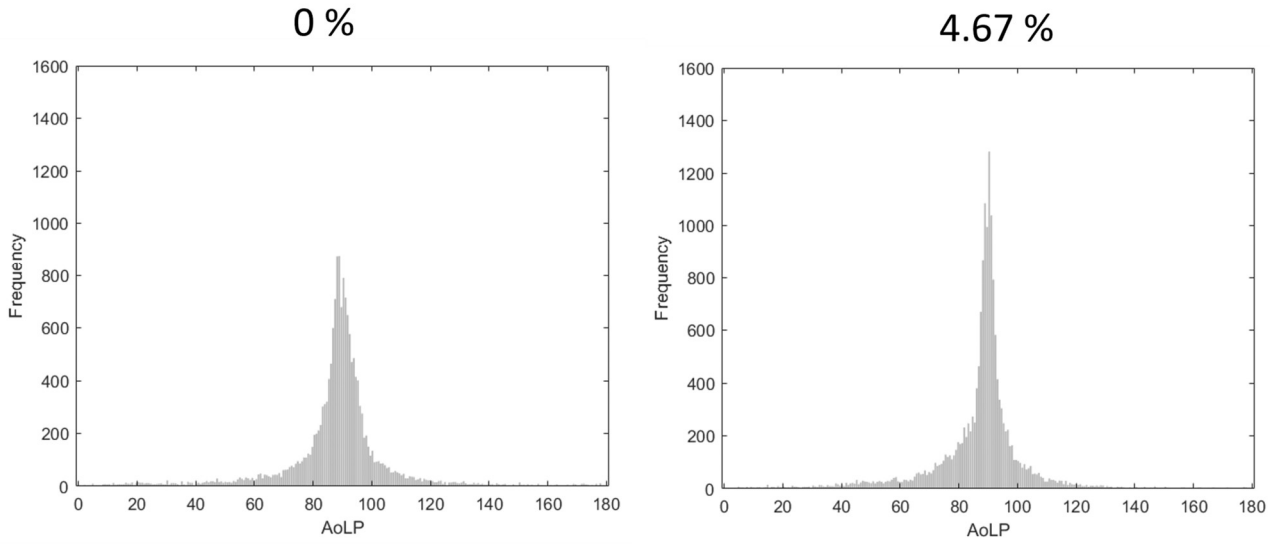


Figure 4.40 - The histogram of the selected region of the dry TFP reinforced hole with four layers sample at different strains (0 % and 4.67 %).

Figure 4.41 shows the results of fitting on the fibre orientation images, where the mean of the AoLP at 0 % strain was 89.69° ± 0.65 with a standard deviation of 7.10° ± 0.92. With increasing strain, the mean of the AoLP changes to 89.88° ± 0.53 with a standard deviation of 4.08° ± 0.75 at 4.67 % strain.

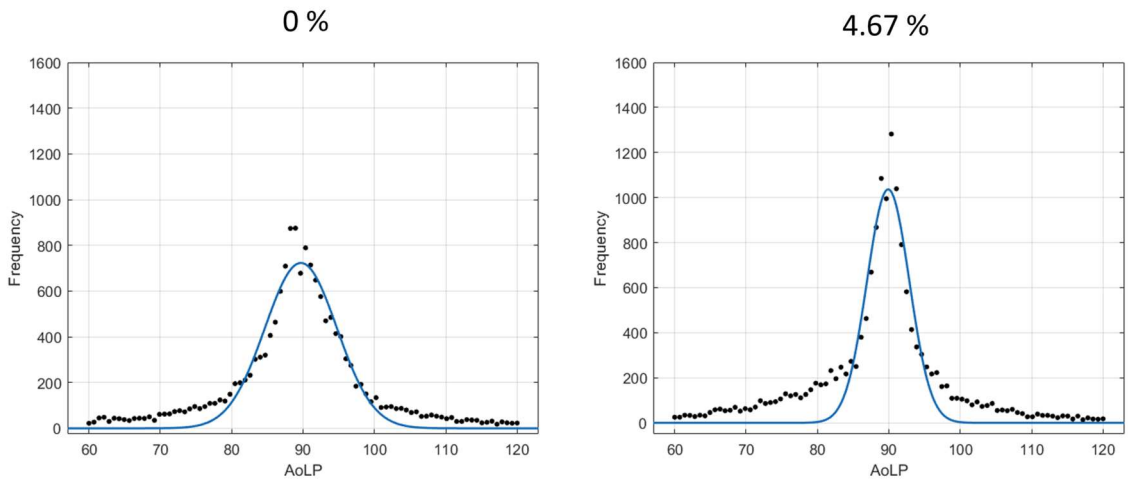


Figure 4.41 - MATLAB fitting of Gaussian curve to the histogram of AoLP data for dry TFP reinforced hole with four layers at 0 % and 4.67 % strain.

For more details about the fibre orientation behaviour with increasing strain, the fibre orientations were separated using the colour threshold for the selected area images in different strains. Figure 4.42 presents the results of separating the orientation of the fibres in the selected region images at 0 % and 4.67 % strain. The result, presented in white, shows that most of the fibre orientations of the TFP reinforced hole preform consisting of four layers are between 80° and 100°.

In the fibre orientation image at 0 % strain, the fibres with orientations between 80° and 100° represent 49.73 % of the image's total area, fibres with orientations between 60° and 80° represent 9.22 % of the total area, and the fibres with 100°-120° orientations represent 1.44 % of the total area. When strain increased (fibre orientation image at 4.67 % strain), the fibres with orientations between 80° and 100° represent 59.83 % of the image's total area, the fibres that have orientations between 60° and 80° represent 6.14 % of the total area, and the fibres with orientations between 100° and 120° represent 1.00 % of the total area.

Again, for illustrative purposes, the fibres with orientations between 0° and 20°, 20° and 40°, and 40° and 60° show small changes in the fibre orientations with increasing strain.

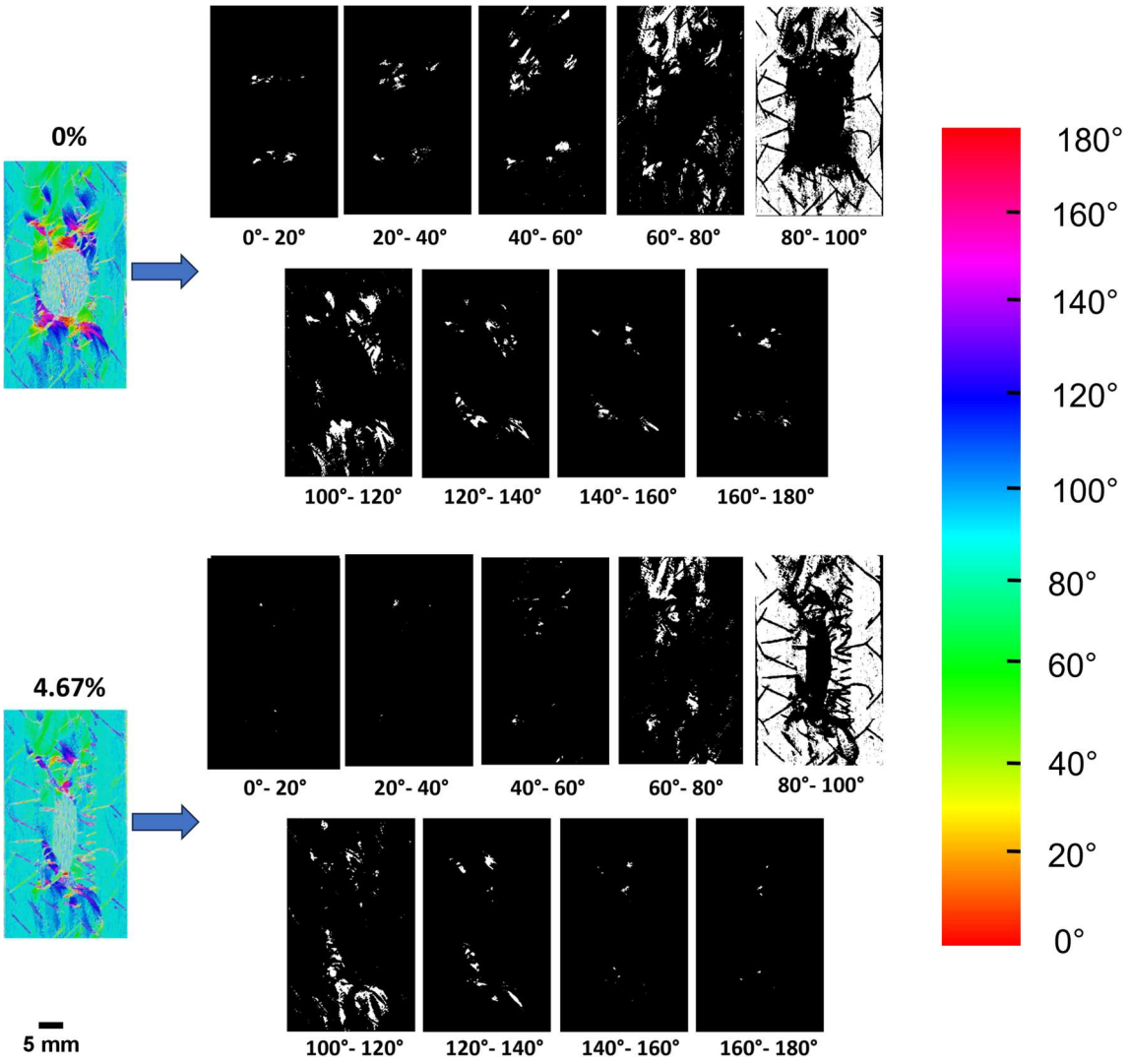


Figure 4.42 - Separating the fibre's orientation of the selected region image in the dry TFP reinforced hole preform with four layers at 0 % and 4.67 % strain using a colour threshold.

Table 4.5 represents the mean of the AoLP and the standard deviation for the fibre orientation images during the tensile testing, Figure 4.38, after applying the fitting curves. The results of the mean of the AoLP of the dry TFP reinforced hole with four layers show the change behaviour in the fibre orientation with an increase in the strain. The fibre orientation behaviour with increasing strain in the TFP reinforced hole sample consisting of four layers is presented in Figure 4.43. The mean of the

AoLP of the fibres at 0 % strain changes from (89.69° ± 0.65) to (89.88° ± 0.53) with increasing strain to 4.67 %.

Table 4.5 - The mean of the AoLP and standard deviation results in the corresponding strain after applying the Gaussian curve fitting to the fibres' orientation images of dry TFP reinforced hole sample with four layers that were captured during tensile testing, (Figure 4.38)

The mean of AoLP (degree)	Standard deviation (the width of the peak)	Strain (%)
89.69 ± 0.65	7.10 ± 0.92	0
89.68 ± 0.66	7.00 ± 0.93	0.01
89.79 ± 0.65	6.32 ± 0.92	0.54
89.98 ± 0.63	4.96 ± 0.89	2.18
89.90 ± 0.54	4.20 ± 0.77	3.25
89.88 ± 0.75	4.08 ± 0.75	4.67

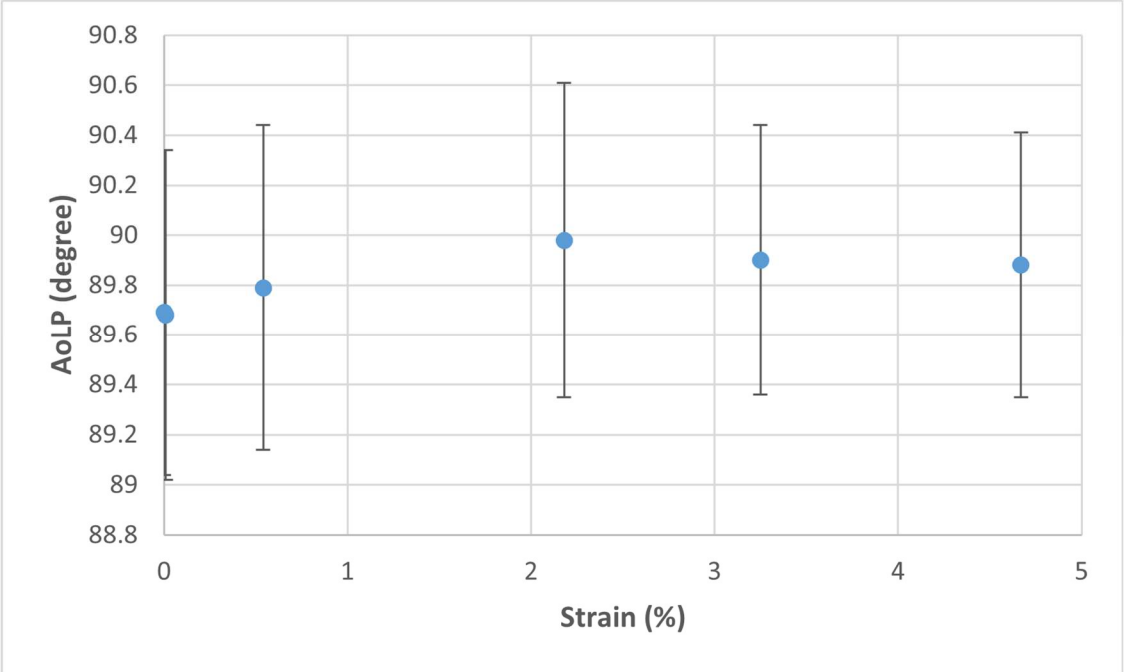


Figure 4.43 - The mean of the AoLP behaviour for four-layers of dry TFP reinforced hole preform with increasing strain (for the six selected images in Figure 4.38).

The force and position curve of the unidirectional TFP preform consists of four layers, as shown in Figure 4.44. The graph illustrates a rising force followed by a decline as the hole in the fabric deforms and the fibres compress. The dips in the force occur when the stitches holding the fibres together break. Moreover, the fibre orientation images at the dips are presented in the figure, showing the deformation in the reinforced hole.

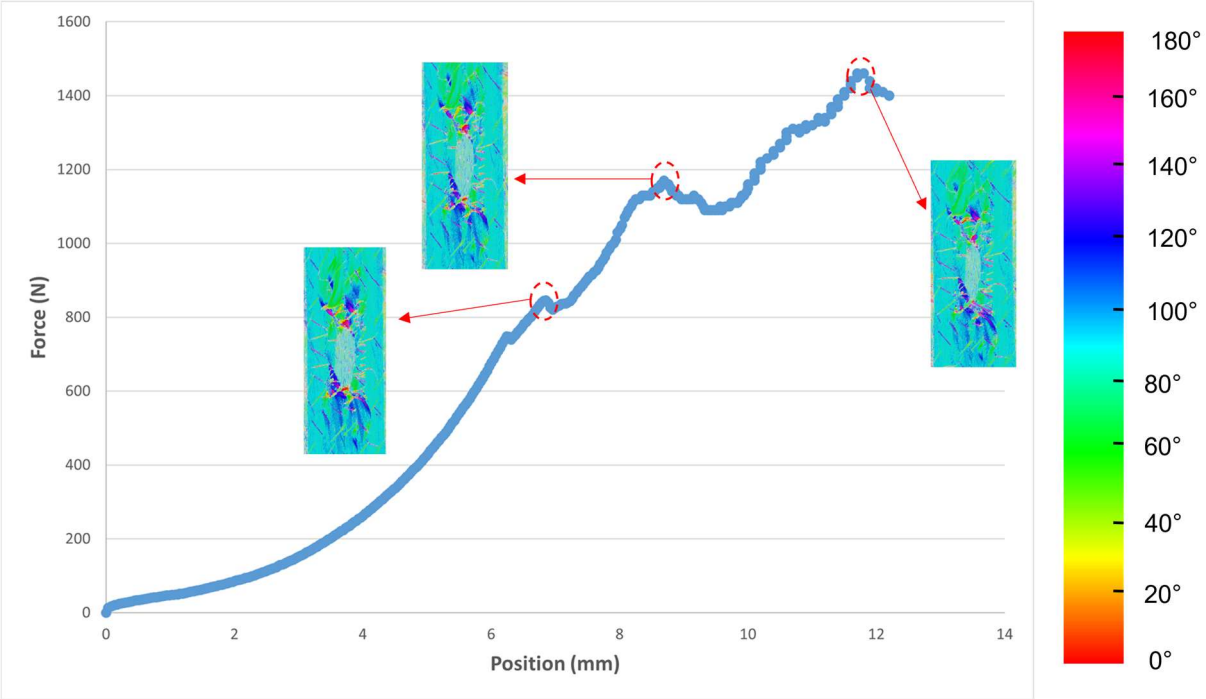


Figure 4.44 - The force and position curve for unidirectional TFP reinforced hole preform consists of four layers.

4.3.5 Comparison between different dry carbon fibre architectures

The average maximum force load (N) for dry carbon fibre samples with different architectures (unidirectional [UD], UD-non-crimp fabric [NCF], Twill 2x2) is shown in Figure 4.45. The results reveal clear differences in the tensile response of the three dry carbon fibre architectures. The UD specimens exhibited a relatively high maximum force, averaging around (450 N). This can be attributed to the continuous alignment of fibres along the loading direction, which means the load was carried mainly by the high-strength carbon filaments. The small error bars indicate good repeatability, suggesting that UD dry fibres have a relatively consistent load-bearing capacity under tensile loading. The UD-NCF samples displayed a slightly higher mean maximum force (467 N) compared with UD specimens. However, the error

bars for UD-NCF samples are much larger than UD samples. This result suggests that the performance of UD-NCF sample is less predictable than UD sample. This variation can be caused by local variations in fibre waviness, which induced by the stitching threads. Another reason linked to this variation is small misalignment in the fibres or losing some fibres during handling the fabric. In contrast, the twill 2×2 weave architecture exhibited the lowest maximum force among the three samples, at approximately (310 N), with moderate variability. This reduced performance arises from the inherent crimp and woven structure, which leads to local fibre misalignment. The interlacing pattern reduces the proportion of fibres aligned with the tensile axis at any given point, lowering the effective load transfer capacity compared with straight fibre architectures. Table 4.6 provides additional information about the average, standard deviation, and coefficient of variation of the maximum force load for these dry samples

Overall, the results highlight the influence of fibre architecture on tensile behaviour. Straight and aligned fibres (UD and UD-NCF) provide higher maximum load capacity than woven architectures. However, the comparison between UD and UD-NCF also indicates that small differences in fibre placement and stabilisation can significantly affect variability, even when fibres are nominally aligned. The twill weave shows clear disadvantages in terms of maximum tensile force in its dry state [150]–[155].

Some dry samples were damaged during the cutting process, with some fibres becoming loose or moving before the tensile test began. To investigate the fibres' orientation behaviour in a stage between the dry state and the application of epoxy resin, silicon rubber resin will be applied in the next section.

4.3.6 Discussion

The analysis of fibre orientation during tensile testing revealed the fibre orientation behaviours across the UD, UD-NCF, Twill 2×2, and TFP architectures, which can be directly attributed to their structural characteristics and associated mechanical responses. For the UD specimens, fibre orientation remained essentially

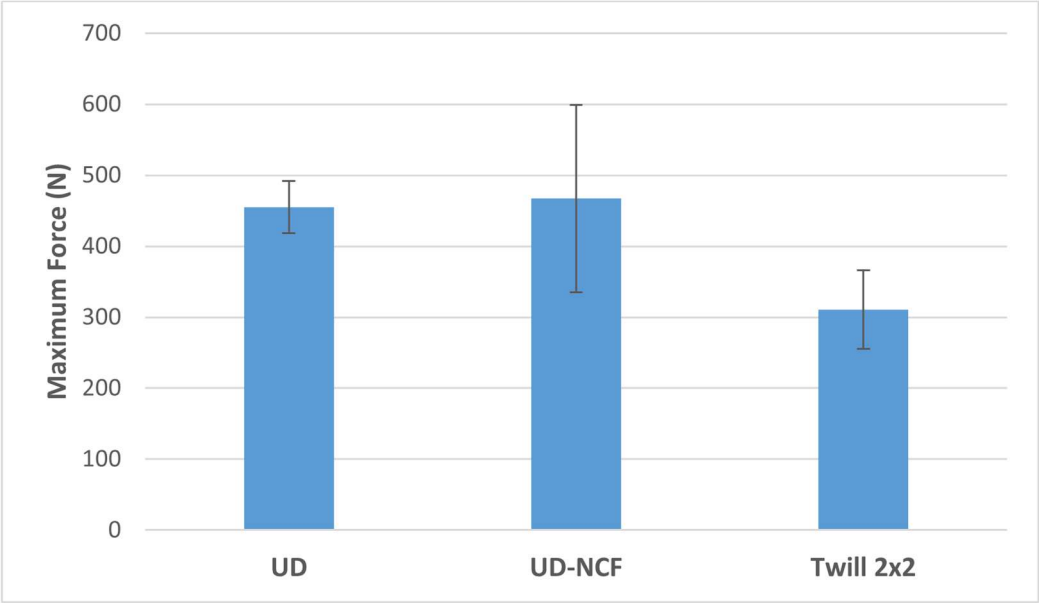


Figure 4.45 - Average maximum force load (N) for different dry carbon fibre architectures; the error bar is the standard deviation for three samples.

Table 4.6 - The average, standard deviation, and coefficient of variation of the maximum force load for dry samples.

	Maximum force load (N)		
Fibre's architecture	**Average**	**Standard deviation**	**Coefficient of variation (%)**
UD	455.27	36.86	8.09
UD-NCF	467.32	131.92	28.22
Twill 2x2	310.38	55.42	17.85

unchanged, with over 95% of fibres aligned within ±5° of the loading axis throughout the test. The mean Angle of Linear Polarisation (AoLP) shifted by less than 0.02° as strain increased to the maximum applied load, confirming that the fibres were highly stable under tension and fully aligned with the loading direction. Moreover, the fibre orientation process indicates that fibres initially aligned within the ranges of approximately 60°–85° and 95°–140° progressively reorient with increasing strain towards the range of 85°–95°. In dry fibre preforms, this behaviour reflects the movement of the fibre tows and their tendency to rotate in order to align with the applied loading direction. Such realignment highlights the rearrangement of the textile architecture under tension, which can contribute to a more uniform fibre distribution along the loading axis. Although this process does not yet involve resin–fibre interactions, the results provide valuable insight into how the fibre orientation

behave with increasing strain and how may influence the eventual mechanical performance once the preform is consolidated into a composite. This outcome highlights the efficiency of UD configurations in sustaining alignment during tensile loading.

The UD-NCF specimens, although unidirectional, exhibited slightly greater variability in orientation due to the influence of the weft yarns binding the tow bundles. The mean AoLP remained essentially unchanged at ~89.5° across the test, but the separation analysis indicated minor re-alignment of fibres as the strain increased. Some of fibres initially oriented between approximately 60°–85° and 95°–140° progressively shifted towards an orientation within the 85°–95° range as the applied strain increased. Approximately 93 % of fibres were within ±5° of the tensile direction at the start of the test, rising to ~94 % at maximum load. While these changes were subtle, they reflect the influence of the non-crimp architecture, where the presence of transverse binding yarns imposes variation in the fibre orientation.

In contrast, the Twill 2×2 specimens displayed more obvious changes in fibre orientation under tensile loading, particularly in the weft direction. The Gaussian analysis showed that fibres in the warp direction, which were aligned with the load, remained relatively stable, shifting by less than 0.5° as strain increased to 1.78 %. However, fibres in the weft direction shifted more significantly, from around –2.4° at zero strain to –5.0° at maximum strain, accompanied by increased peak broadening, indicating more substantial re-orientation. The separation analysis confirmed that the percentage of fibres oriented between 0–20° decreased from ~14 % to ~6 %, while those at 160–180° increased from ~39 % to ~45 %, suggesting a reorientation of fibres in the weft direction under load. The results explain the fibre orientation behaviour of samples with woven architectures during tensile testing and how it will reflect on the mechanical properties.

For the TFP preforms, across both preforms, the AoLP-based analysis indicates a common trend towards alignment with the loading axis as strain increases, but the rate and locality of this re-orientation differ in ways that are consistent with their loop-back path construction. In the two-layer preform, the loop-back path produced a detectable gap with no carbon fibres (visible on the saturation / DoLP images), which

would become resin-rich after infusion. This local discontinuity and the associated stitch architecture appear to make the region around the reinforced hole more compliant, allowing fibres initially away from the load direction (e.g., 60°–80° and 100°–120°) to reorient to have orientations between the range (80° and 100°) as strain rises to 5.06 %. The percentage of the fibres with orientations between 80°–100° grows from 55.84 % to 66.84 %, while 60°–80° and 100°–120° decreased from 6.61 % to 3.34 % and 4.07 % to 1.85 %, respectively. Gaussian fitting supports this trend: although the mean angle of linear polarisation (AoLP) remained close to 90° (89.39° ± 0.60 and 89.80° ± 0.28), the distribution peak narrowed substantially (standard deviation reduced from 7.33° ± 0.86 to 3.63° ± 0.41). This evidence a progressive concentration of fibre orientations towards the load-aligned direction as strain increased. Also, this fibre orientation distribution is explaining the local (closing-up) of the loop-back with increasing strain.

The four-layer preform exhibits the same tendency of progressive movement of fibre orientations into the 80°–100° range under loading. However, the initial state and the magnitude of narrowing differ, likely because the repeated loop-back operations reduce the chances of leaving a clear resin-rich area and distribute the stitching threads over thickness. Before loading, the percentage of the fibres with orientations between (80° and 100°) was lower (49.73 %) than in the two-layer case, and the 60°–80° and 100°–120° are higher (9.22 % and 1.44 %). This is showing that different fibre orientation directions are present at the reinforced hole edge. With strain increased to 4.67 %, the percentage of fibres with orientations between (80° and 100°) increases by about ten percentage points (to 59.83 %), while 60°–80° and 100°–120° decrease to 6.14 % and 1.00 %. The fitted means again remain close to 90° (89.69° ± 0.65 and 89.88° ± 0.53), but the peak narrowing is less than in the two-layer case (standard deviation 7.10° ± 0.92 to 4.08° ± 0.75). The analysis of fibre orientation indicate that the four-layer architecture still reoriented with the load direction under tension but affecting the reinforced hole edge.

4.3.7 Conclusion

To conclude the tensile test of the dry carbon fibre section, different carbon fibre architectures (UD, UD-NCF, Twill 2x2, and TFP) were used to investigate the fibre's orientation behaviour using the polarisation camera. Dry fibre preforms were chosen

so that the changes in the fibre orientation would be large, and thus, the data would show significant variation in the images. The fibres' angular behaviour was compared before starting the tensile test (0 % strain) and increasing the strain. As expected, the UD and UD-NCF carbon fibres along the tension direction do not show significant changes in the fibres' orientation during the tensile test. However, the Twill 2x2 shows the fibres' orientation, with the increase in strain, resulting in a discussion of the Twill pattern.

Furthermore, the reinforced hole TFP preforms with two and four layers, showing the orientation of the fibres around the reinforced hole and at the fibres' loop-back path with increased strain. Fibres moved to have an orientation between 85° and 95° with increasing strain. The tensile data showed significant changes as the stitching broke, and the carbon fibre was able to align to the stress.

The next section focuses on applying a clear soft silicon rubber resin, as a step towards a conventional resin, on the Twill 2x2 carbon fibre and the TFP-reinforced hole preforms. The UD preforms will be excluded from this analysis as the changes are slight.

4.4 Applying silicone rubber resin on carbon fibre

4.4.1 Introduction

Samples were impregnated with silicone rubber resin to test the fibres' orientation behaviour in the stage between the dry fibre samples and samples infused with epoxy resin. From the conclusion of the dry fibre section, the focus will be on the Twill 2x2, and the TFP reinforced hole carbon fibre to investigate the orientation of the carbon fibre during the tensile test.

4.4.2 Sample preparation

The mixture was prepared by weight, where 100 g silicon rubber resin, Addition Cure Silicone Rubber AS40, was mixed with 10 g hardener, AS40 Catalyst, using an electric stirrer at 500 rpm speed for 5 minutes. After the resin and hardener were correctly mixed, the mixture was degassed to remove the trapped air. After applying

the resin, the samples were cured in the oven. See Methodology **Section 3.1.4** for more details.

Figure 4.46 shows an example of a Twill 2x2 sample consisting of one-ply with dimensions 250 mm length and 25 mm width. Image (a) shows the sample's smooth surface, which was placed on the glass panel, while image (b) shows the sample surface on which the resin was applied.

Overexposed areas caused by the sample's surface roughness leads to a loss of information. The auto-exposure function in the polarisation camera software can be used in the offline inspection (with no tension applied). However, the auto-exposure function in the online inspection (during the tensile test) is ineffective because the reflection state changes with the sample's geometries. An example of the lighting effect during tensile testing of an open-hole Twill 2x2 sample will be explained in detail in the next chapter.



Figure 4.46 - An example of a cured Twill 2x2 sample with one layer that is impregnated with silicone rubber resin, where (a) shows the smooth surface of the carbon, while (b) shows the surface to which the resin was applied.

4.4.3 Twill 2x2 carbon fibre

The Twill 2x2 sample, (sample-1), impregnated with silicone rubber resin and was offline inspected using the polarisation camera to capture the raw saturation, DoLP, and fibres' angles images, Figure 4.47 (a-c) respectively. The raw saturation image (a) represents the overexposed areas in yellow caused by bright reflections from the resin. The overexposed areas in image (a) are shown in black in the DoLP image (b); extracting the information from these areas is not possible. Image (c) represents the orientation of the carbon fibre from the hue channel in the HSV image, as described earlier (see **Section 3.5**).

The fibres along the tension direction are presented in cyan, while those perpendicular to the tension direction are presented in red. As explained before, the difference in the colours presenting fibres in the same direction (i.e., fibres in the warp or weft direction) are caused by the weaving pattern.

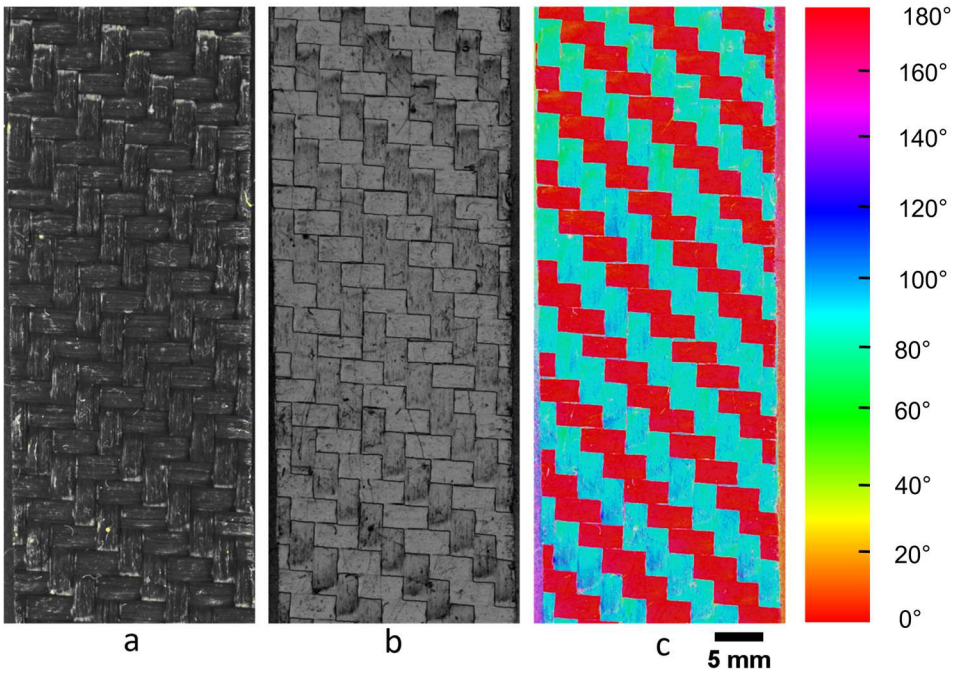


Figure 4.47 - A Twill 2x2 sample, (sample-1), consisting of one layer impregnated with silicone rubber was captured using the polarisation camera, where (a) the raw saturation image, (b) the DoLP image, and (c) the fibres' orientation image.

Figure 4.48, (sample-1), shows the fibres' orientation images captured during the tensile test. Image (a) was captured before starting the tensile test at 0 % strain, while image (e) was captured at maximum load force with 1.68 % strain.

Figure 4.49 shows the selected region of interest of the fibre orientation images at 0 % and 1.68 % strain. The histogram of the AoLP data at different strains is presented in Figure 4.50. The figure, (a), shows the histogram for the AoLP data at 0 % and 1.68 % strains, which presented the fibre orientation distribution from 0° to 180°, while (b) shows the AoLP data after the shifting process [from (160° - 180) to (- 20° - 0°)]. It is clear from the histogram that there is a slight misalignment of the camera about the vertical.

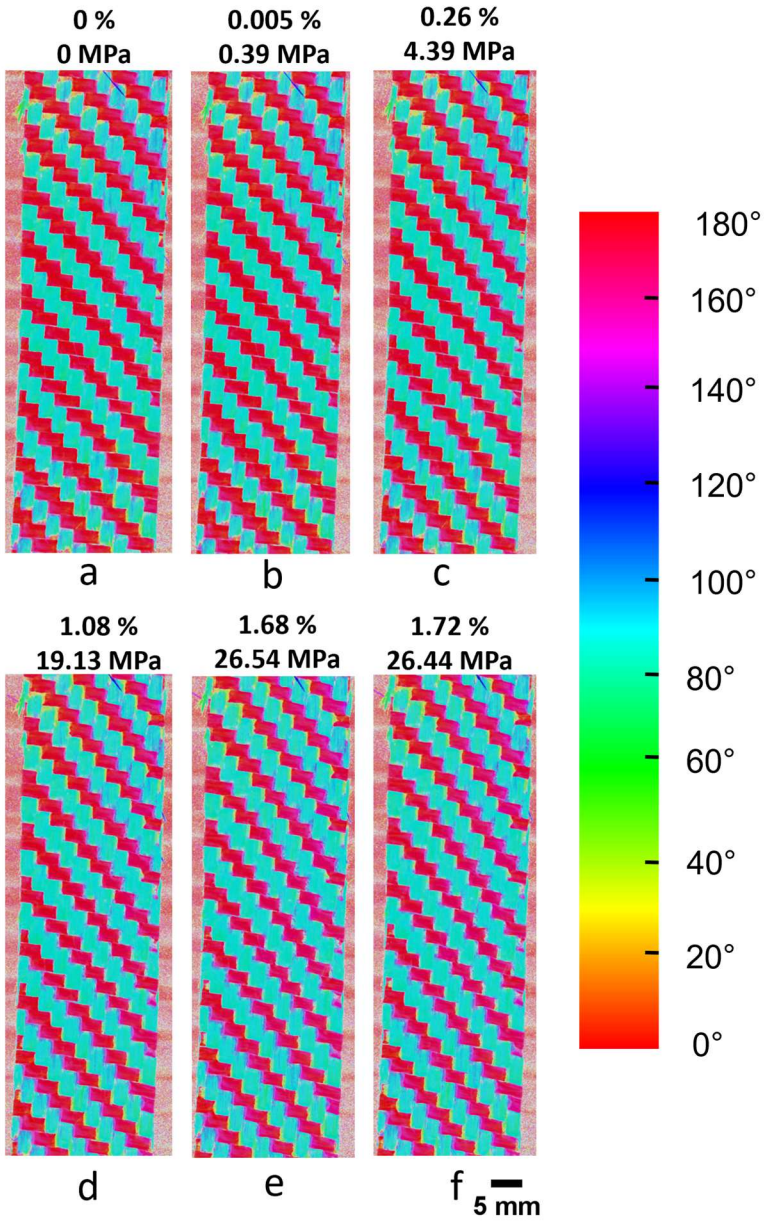


Figure 4.48 - Fibre orientation images of the Twill 2x2 sample, (sample-1), impregnated with silicone rubber resin, consisting of one layer were captured during the tensile test. The stress and strain corresponding to each image during the test are presented above the figure.

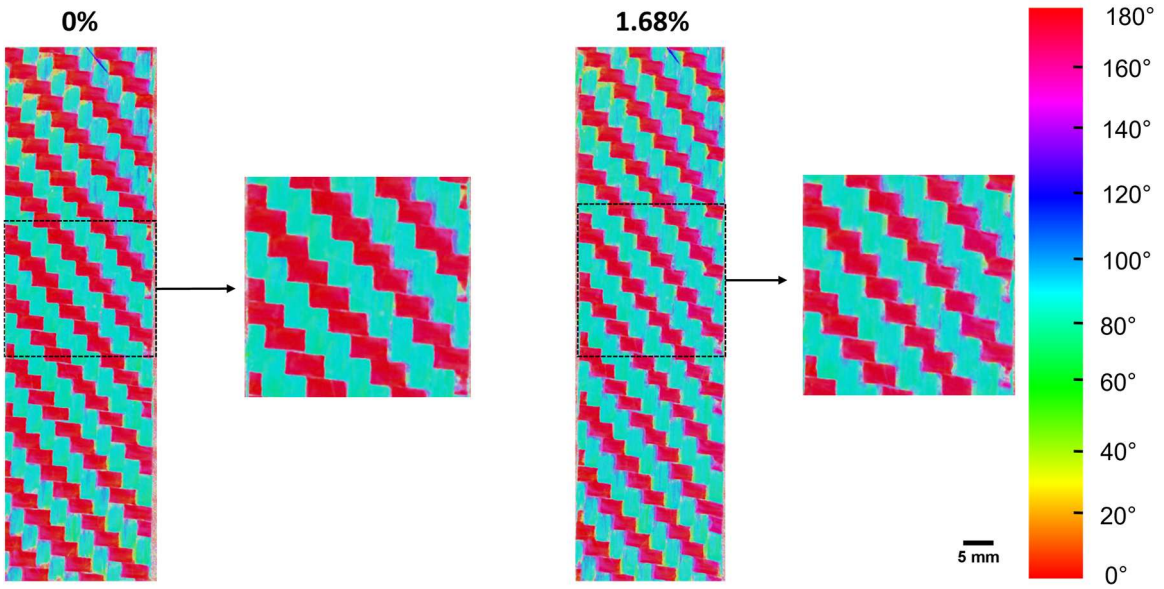


Figure 4.49 - The selected region of the fibres' orientation image in the Twill 2x2 sample, with one layer, impregnated with silicone rubber resin to investigate the fibre orientation before starting the test (0 %) strain and with increasing strain to (1.68 %).

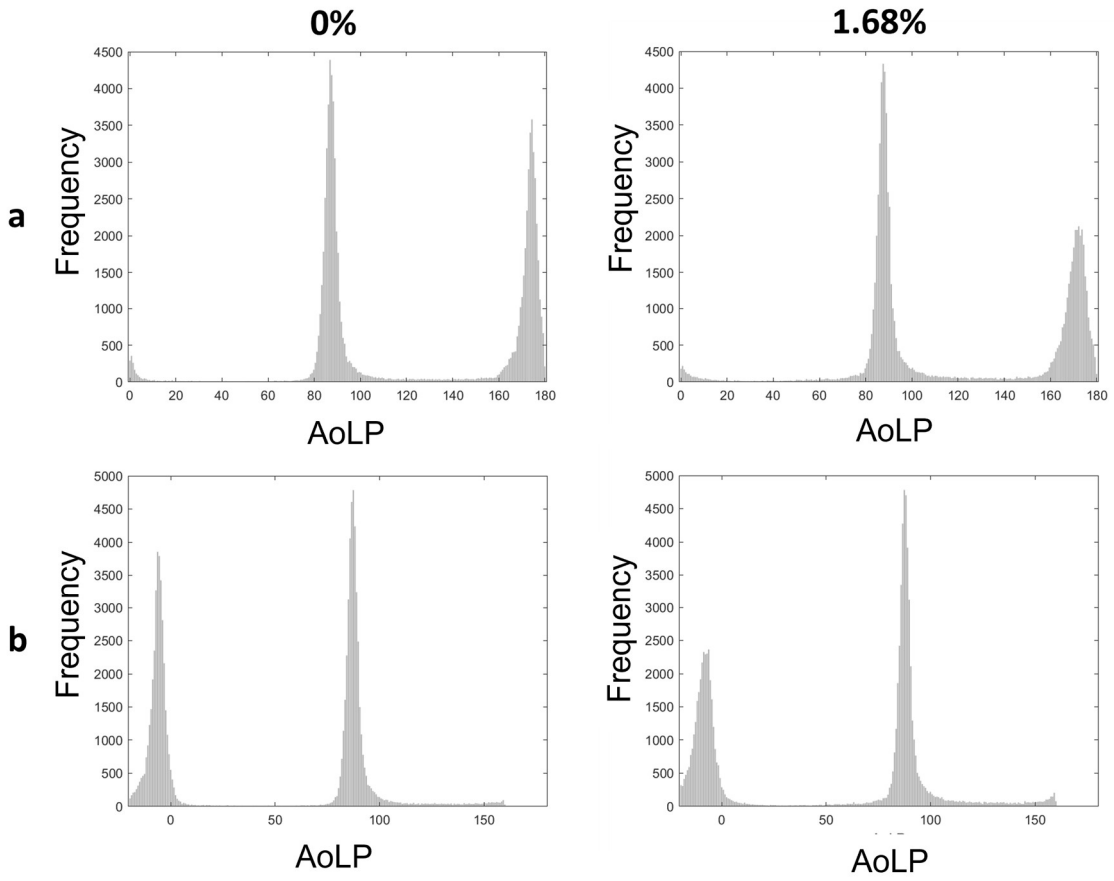


Figure 4.50 - The histogram of the selected region of the one-layer Twill 2x2 sample impregnated with silicone rubber resin at different strains (0 % and 1.68 %), where (a) shows the histogram presenting the AoLP data (before the shifting process) from the range 0° to 180° and (b) shows the histogram for the same sample after peak shifting process.

Figure 4.51 shows the Gaussian curve fitting applied to the AoLP data of the Twill 2x2 sample impregnated with silicone rubber resin to find the mean of the AoLP at 0 % and 1.78 % strain. Two peaks were fitted representing the fibres in the weft and warp directions (first peak from -20° to 20°) and (second peak from 80° to 100°). The analysis of fibre orientation images for the first peak shows that the mean of the AoLP at 0 % strain was (-5.88° ± 0.18) with a standard deviation of 4.05° ± 0.27 and (-8.39° ± 0.34) with a standard deviation of 6.02° ± 0.49 at 1.68 % strain. The value of the mean of the AoLP at 0 % strain for the second peak was 87.08° ± 0.14 with a standard deviation of 3.55° ± 0.19 and 87.64° ± 0.13 with a standard deviation of 3.52° ± 0.19 at 1.68 % strain.

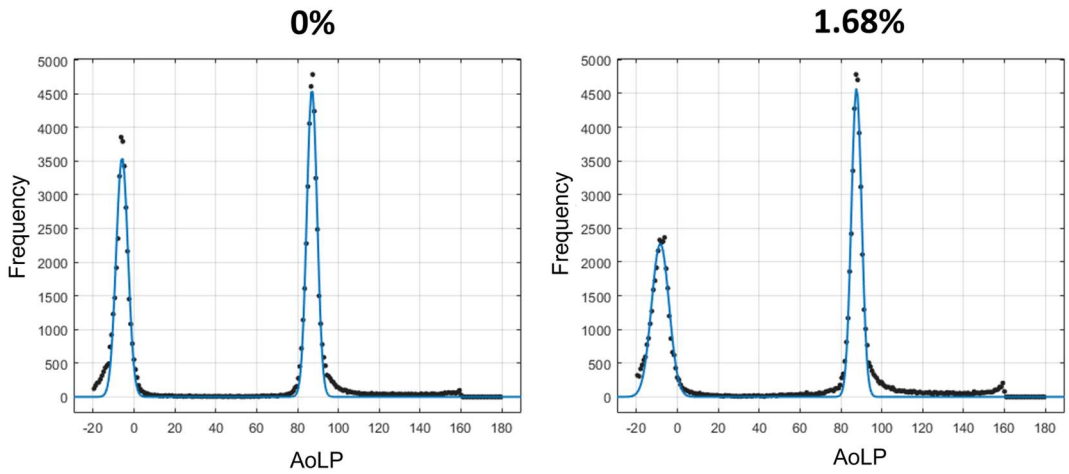


Figure 4.51 - MATLAB fitting of Gaussian curve to the histogram of AoLP data after the shifting process for the Twill 2x2 sample impregnated with silicone rubber resin at 0 % and 1.68 % strain.

Figure 4.52 shows the results of separating the orientation of the carbon fibres in the selected region image at 0 % and 1.68 % strains. The result shows that most of the fibres have orientations between 80° and 100° in the warp direction and (0° and 20°), (160° and 180°) in the weft direction.

The fibres with orientations between 80° and 100° in the fibre orientation image with 0 % strain represent 47.19 % of the image's total area, fibres with orientations between 0° and 20° represent 1.72 % of the total area, and fibres with orientations between 160° and 180° represent 41.68 % of the total area. In the fibre orientation image with 1.68 % strain, the fibres with orientations between 80° and 100° represent 48.53 % of the image's total area, fibres with orientations between 0° and

20° represent 1.10 %, and fibres with orientations between 160° and 180° represent 37.06 % of the total area.

The red circles in the figure illustrate examples of slight changes in fibre orientation for fibres aligned with the tensile direction, observed with increasing strain up to 1.68%. Also, the red squares represent changes in fibre orientation for fibres perpendicular to the tensile direction.

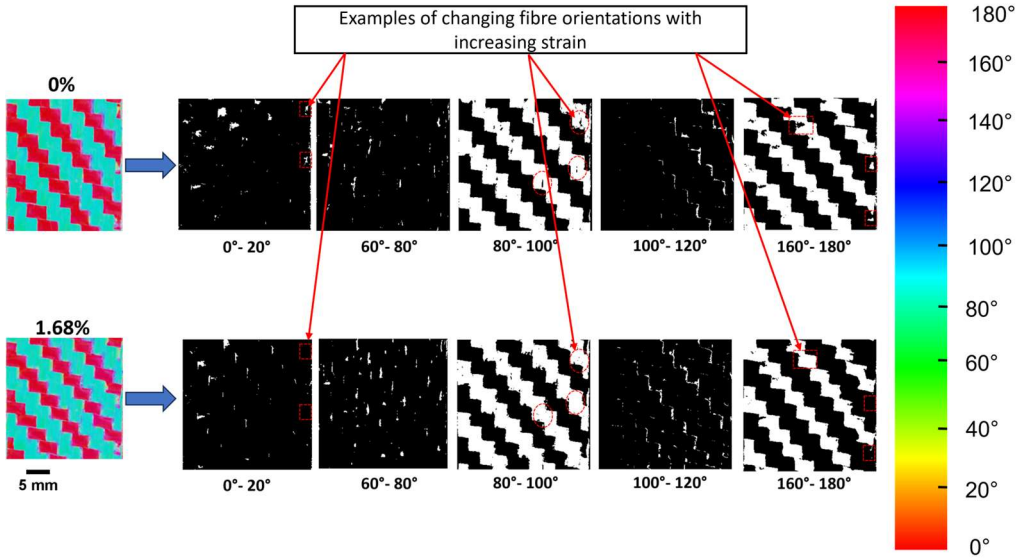


Figure 4.52 - Separating the fibre orientation of the selected region image in the Twill 2x2 sample, (sample-1), impregnated with silicone rubber resin at 0 % and 1.68 % strain using a colour threshold.

Table 4.7 - The mean of the AoLP and standard deviation results in the corresponding strain after applying the Gaussian curve fitting to the fibres' orientation images of the Twill 2x2 sample, (sample-1), impregnated with silicone rubber resin that were captured during tensile testing, (Figure 4.48).

The mean of AoLP (degree) – Peak (1)	Standard deviation (the width of the peak)	Strain (%)	The mean of AoLP (degree) – Peak (2)	Standard deviation (the width of the peak)
-5.88 ± 0.18	4.05 ± 0.27	0	87.08 ± 0.14	3.55 ± 0.19
-6.51 ± 0.40	4.26 ± 0.57	0.005	87.34 ± 0.23	3.10 ± 0.31
-7.12 ± 0.44	4.51 ± 0.61	0.26	87.50 ± 0.23	3.25 ± 0.33
-7.83 ± 0.50	4.97 ± 0.71	1.08	87.60 ± 0.22	3.18 ± 0.31
-8.39 ± 0.34	6.02 ± 0.49	1.68	87.64 ± 0.13	3.52 ± 0.19
-9.46 ± 0.68	6.10 ± 0.96	1.72	87.81 ± 0.22	3.21 ± 0.32

Table 4.7 represents the mean of the AoLP and the standard deviation for the fibre orientation images during the tensile testing, Figure 4.48, for both fitting peaks. The results of the mean of the AoLP of the Twill 2x2 sample impregnated with silicone rubber resin show the change behaviour in the fibre orientation with an increase in the strain. Figure 4.53 visually demonstrates the movement of the fibre orientation behaviour with increasing strain for fibres in the warp and weft directions of the Twill 2x2 sample. The mean of the AoLP of the fibres in the weft direction (Peak-1) changes from (-5.88° ± 0.18) at 0 % strain to (-8.39° ± 0.34) when strain reached 1.68 %, while the AoLP of the fibres in the warp direction (peak-2) changes from (87.08° ± 0.14) at 0 % strain to (87.64° ± 0.13) at 1.68 %. The figure demonstrates a change in the orientation of fibres initially perpendicular to the tensile direction (Peak-1) towards -9° with increasing strain. Conversely, fibres aligned with the tensile direction (Peak-2) exhibit minimal change in orientation due to their pre-existing alignment with the applied force.

The stress and strain curves for the three samples of Twill 2x2 impregnated with silicone rubber resin are shown in Figure 4.54. The curves show a linear increase in stress with strain up to the ultimate tensile strength point. Also, the curves demonstrate variation in the strain breakpoints for the three samples.

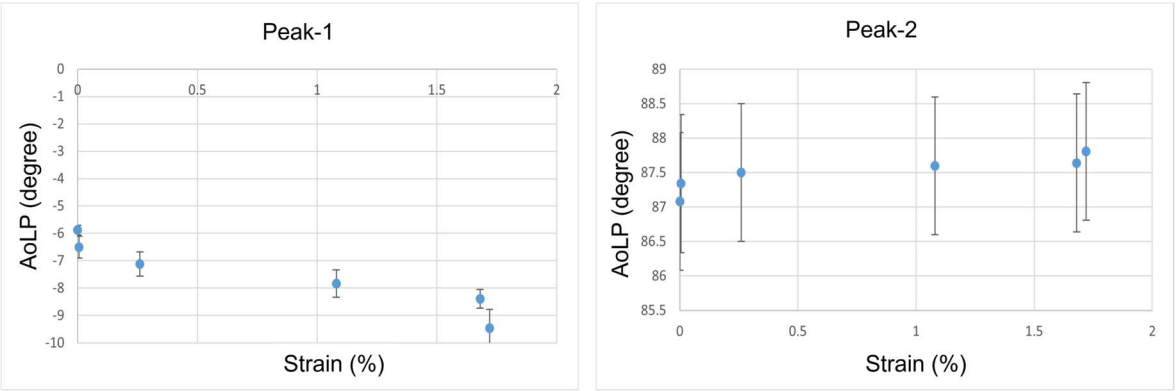


Figure 4.53 - The mean of the AoLP behaviour for one-layer Twill 2x2 sample, (sample-1), impregnated with silicone rubber resin, with increasing strain (for the six selected images in Figure 4.48) for the two peaks.

Table 4.8 summarizes the maximum force load, tensile strength, failure strain, and tensile modulus for Twill 2x2 samples impregnated with silicone rubber resin. The

fibre orientation behaviour for each sample is one reason for the variation in the results.

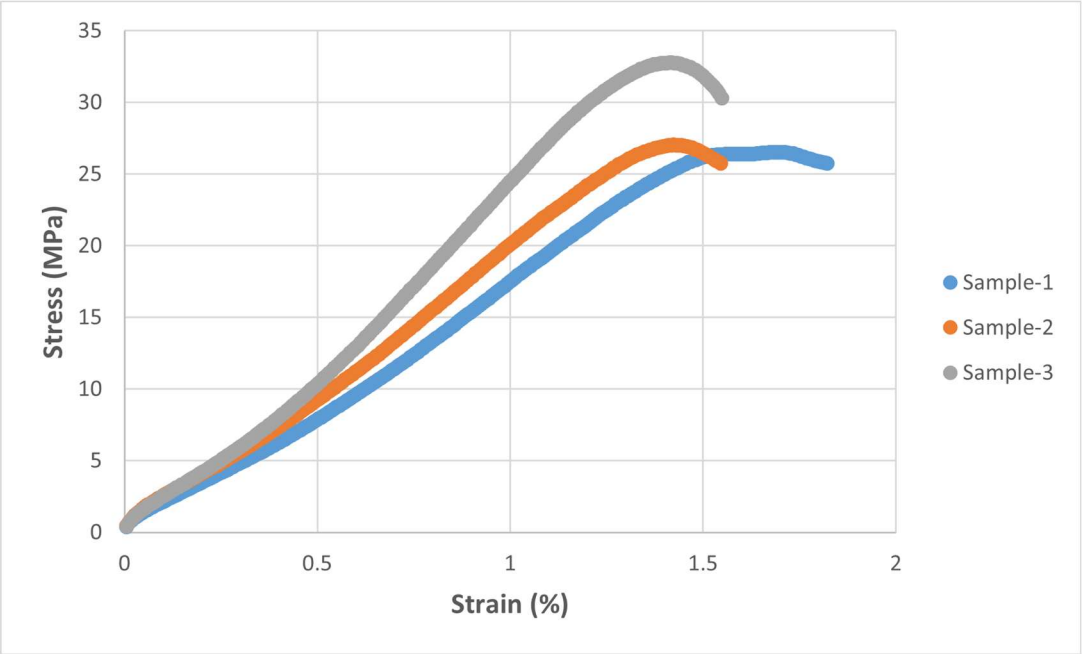


Figure 4.54 - The stress and strain curves for three samples of Twill 2x2 carbon fibre impregnated with silicone rubber resin.

Table 4.8 - The mechanical properties of the Twill 2x2 carbon fibre samples impregnated with silicone rubber resin.

Sample's Number	Maximum force (N)	Ultimate tensile strength (MPa)	Strain (%)	E-modulus (GPa)
Sample-1	464.5	26.54	1.68	1.57
Sample-2	473.33	27.04	1.42	1.89
Sample-3	573.66	32.78	1.41	2.30
Average	503.83	28.62	1.51	1.92
Standard Deviation	60.63	3.46	0.15	0.36

4.4.4 Tailored fibre placement preform

The TFP-reinforced hole samples with two and four layers were prepared to investigate the orientation of the carbon fibre before and during the tensile test after applying the silicon rubber resin. The focus was on the fibres around the reinforced hole to monitor the fibres' orientation behaviour with increased strain. The polarisation camera captured the raw saturation, DoLP, and the fibres' orientation

image at the offline inspection stage, Figure 4.55 (a-c), respectively. The raw saturation image (a) shows an overexposed area, presented in yellow, on the glass fibre and some parts of the silicone rubber resin. However, since the overexposed areas are not on the carbon fibre, the fibre's orientation information can still be extracted. On the other hand, the DoLP image (b) shows a difference in the DoLP level caused by the silicone rubber resin.

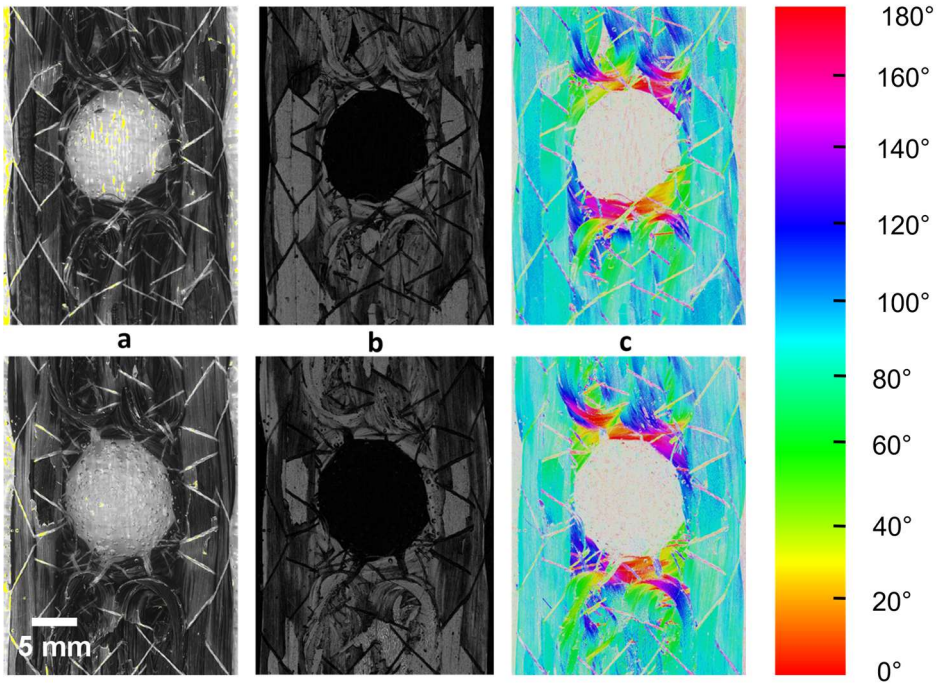


Figure 4.55 - The TFP-reinforced hole sample images were captured using the polarisation camera, where (a) shows the raw saturation, (b) the DoLP, and (c) the fibres' orientation image. The top row represents the TFP sample with two layers, and the bottom row shows row shows the TFP sample with four layers.

A sequence of fibres' orientation images captured during the tensile test for the TFP-reinforced hole sample with two layers using the polarisation camera is shown in Figure 4.56. Image (a) presents the fibres' orientation before starting the tensile test at 0 % strain, while image (f) shows the fibres' orientation at strain equals to 2.68 %. The fibres' orientation images show no effect on the orientation of the fibres around the reinforced hole with increasing strain. For that reason, the same investigation process (histogram of the hue channel and separating the fibres' angles) were applied to better understand the fibres' orientation around the reinforced hole of the TFP sample.

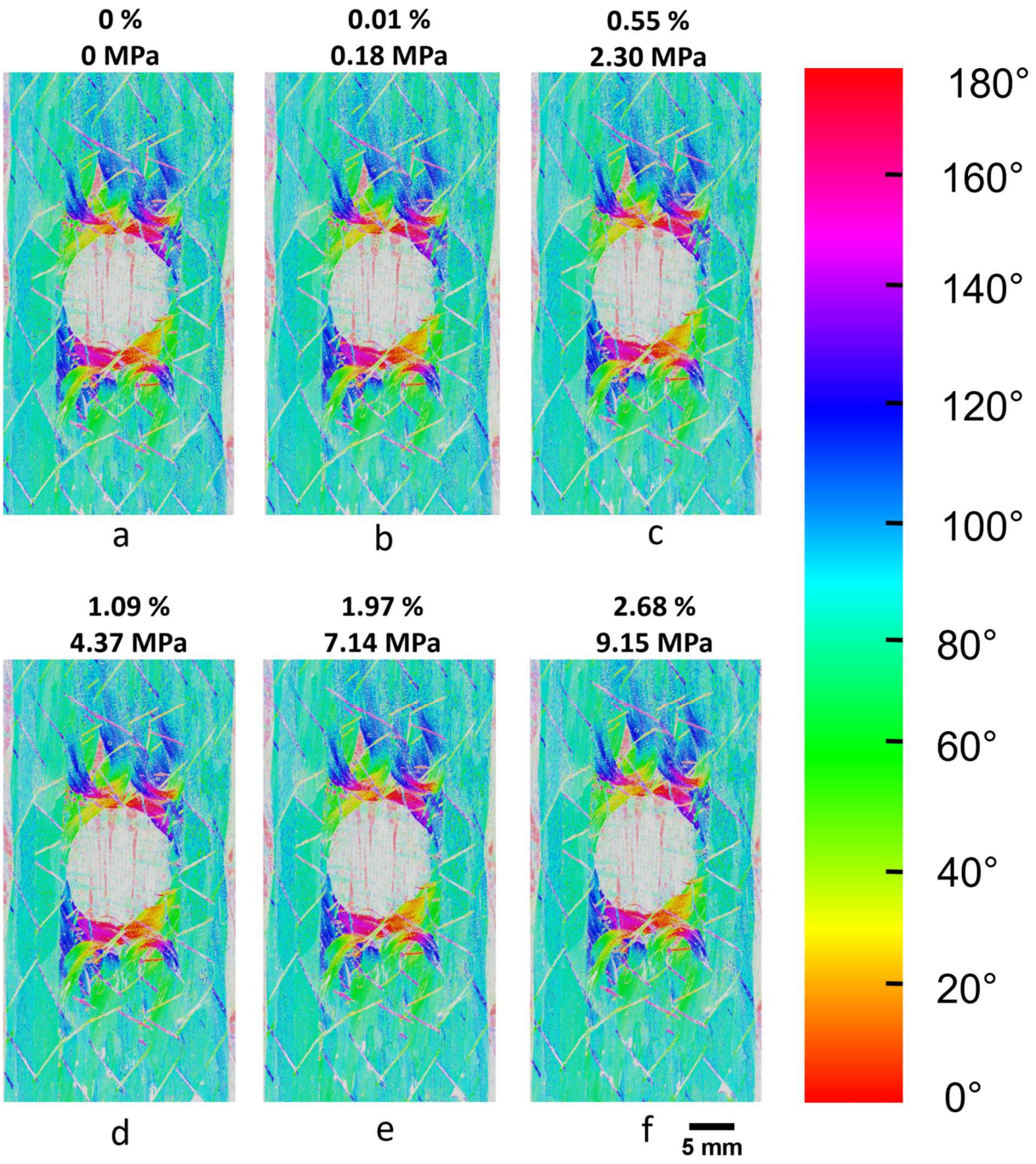


Figure 4.56 - Fibres' orientation images of TFP-reinforced hole sample with two layers were captured during the tensile test using the polarisation camera. The stress and strain corresponding to each image during the test are presented above the figure.

Figure 4.57 shows the selected region of interest around the reinforced hole (a) for the fibre orientation images at different strains, while (b) represents the histogram for the AoLP data, which is extracted from the hue channel. The histogram shows that the fibre has orientations distributed from 0° to 180°, and that is caused by the fibre path used to create the reinforced hole and the loop-back fibre path. However, the focus was on the fibre orientation that is distributed between 60° and 120° to investigate the fibre orientation change during tensile testing around the reinforced hole.

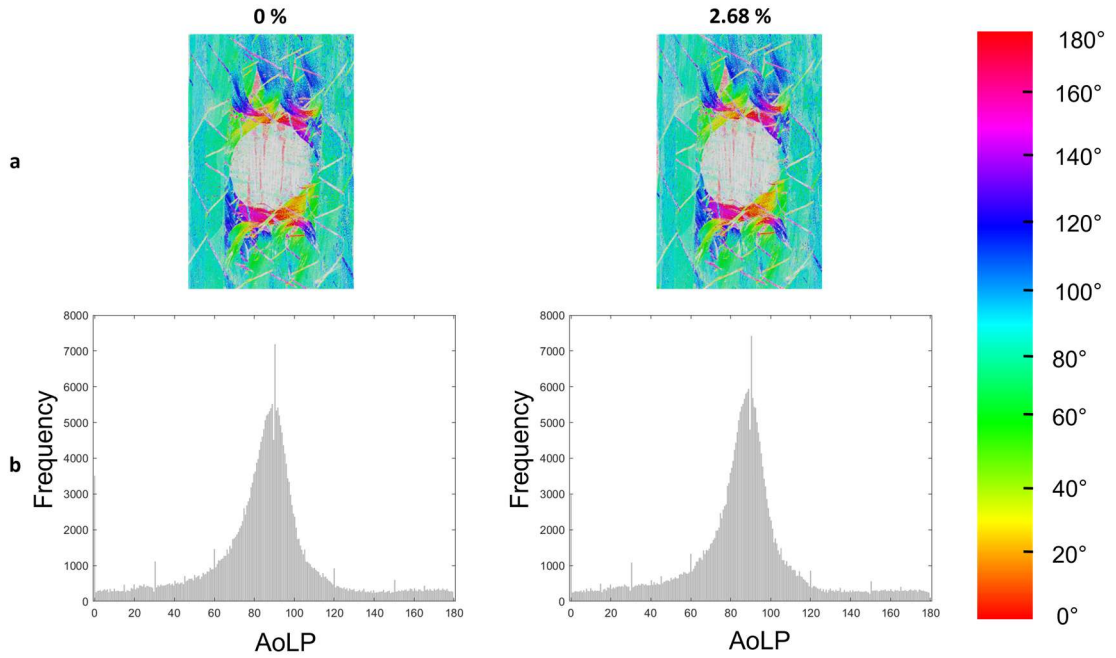


Figure 4.57 - The selected region of interest around the reinforced hole of the UD-TFP sample consists of two layers, where (a) shows the fibres' orientation image at different strains and (b) represents the corresponding histogram of the AoLP information.

Figure 4.58 shows the results of fitting on the fibre orientation images of the UD-TFP reinforced hole sample with two layers. The mean of the AoLP at 0 % strain was 87.68° ± 1.18 with a standard deviation of 16.20° ± 1.69. With increasing strain, the mean of the AoLP changes to 87.83° ± 1.12 with a standard deviation of 15.08° ± 1.59 at 2.68 % strain.

The colour threshold was applied to the fibre orientation images in the selected region of interest at different strains to better understand how the fibre orientation

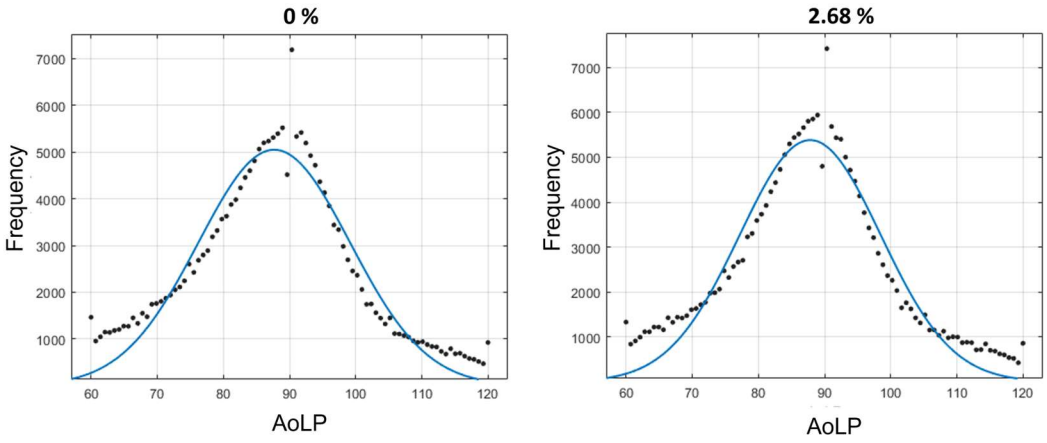


Figure 4.58 - MATLAB fitting of Gaussian curve to the histogram data of two layers UD-TFP reinforced hole sample at different strains.

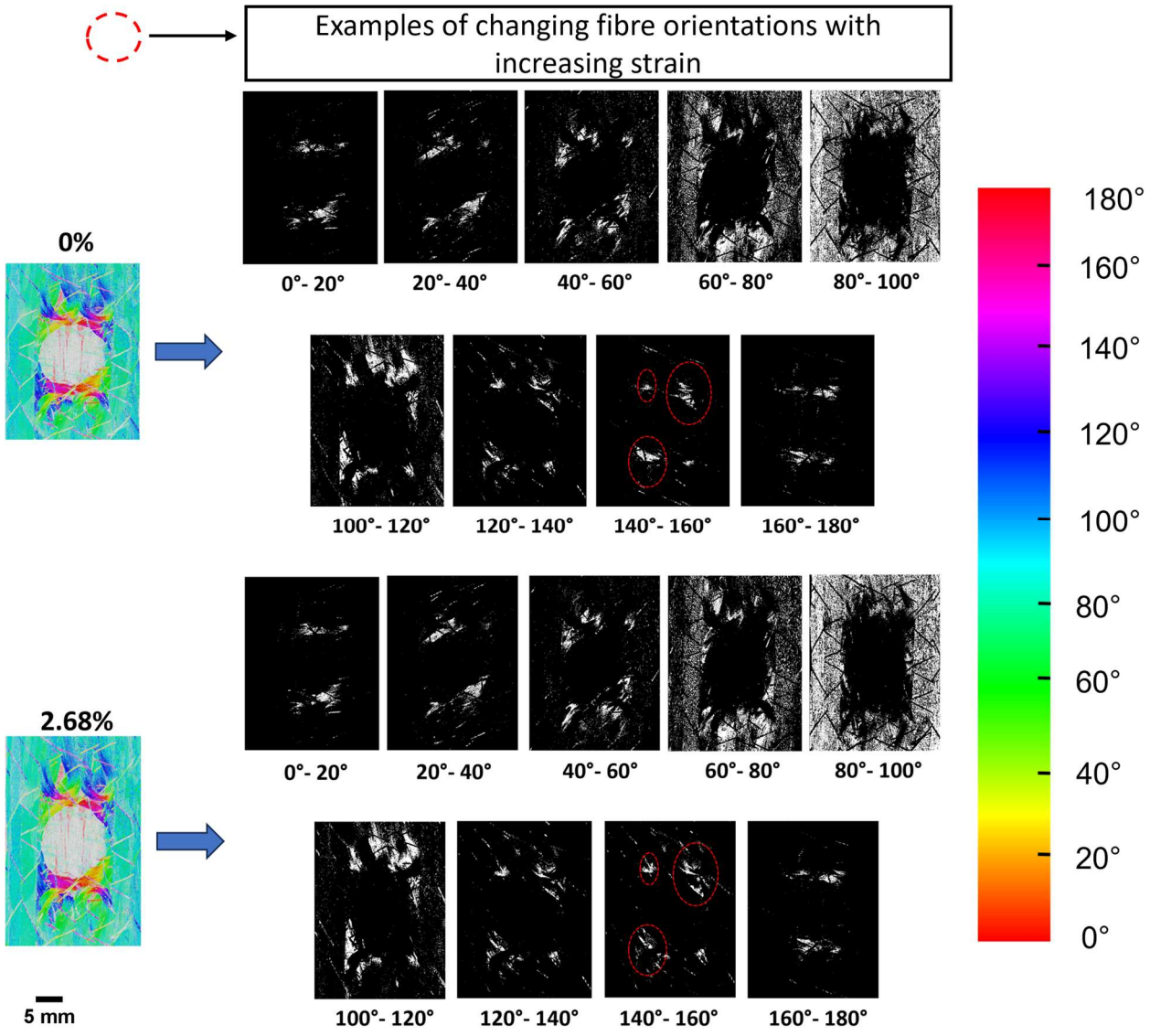


Figure 4.59 - Separating the fibre orientation of the selected region image in the UD-TFP reinforced hole sample with two layers at 0 % and 2.68 % strain using a colour threshold.

changes with increasing strain. Figure 4.59 shows the results of the fibre orientation separation at 0 % and 2.68 % strain. The figure shows that most fibres have orientations between 80° and 100°. Small changes in the fibre orientation were observed around the reinforced hole with increased strain at orientations between 140° and 160°, as illustrated in red circles.

The separation of the fibre's orientation shows that in the image with 0 % strain, the fibres with orientations between 80° and 100° represent 32.33 % of the image's total area, fibres with orientations between 60° and 80° represent 16.14 % of the total area, and fibres with orientations between 100° and 120° represent 7.67 % of the total area. With increasing the strain and reaching 2.68 %, the fibres with orientations between 80° and 100° represent 33.48 % of the total image's area, the fibres having orientations between 60° and 80° represented 15.09 % of the total area, and fibres with having orientations between 100° and 120° shows 7.59 % of the total area.

Table 4.9 - The mean of the AoLP and standard deviation results in the corresponding strain after applying the Gaussian curve fitting to the fibres' orientation images of UD-TFP reinforced hole sample with two layers that were captured during tensile testing, (Figure 4.56)

The mean of AoLP (degree)	Standard deviation (the width of the peak)	Strain (%)
87.68 ± 1.18	16.2 ± 1.69	0
88.03 ± 1.83	13.99 ± 2.61	0.01
87.97 ± 1.72	13.26 ± 2.43	0.55
87.86 ± 1.71	13.27 ± 2.42	1.09
87.90 ± 1.69	13.03 ± 2.40	1.97
87.83 ± 1.59	15.8 ± 1.59	2.68

Table 4.9 shows the mean of the AoLP and standard deviation for the selected fibre orientation images of the UD-TFP reinforced hole sample during tensile testing, Figure 4.56. The results show how the strain influences the fibre orientation

behaviour. Figure 4.60 visually represents the behaviour of fibre orientation changes with increasing strain.

Figure 4.61 shows the stress and strain curve of the UD-TFP reinforced hole sample with two layers, with a linear increase in the stress up to the ultimate strength point. After reaching the ultimate strength point, the damage initiation in the fibres causes the decrease.

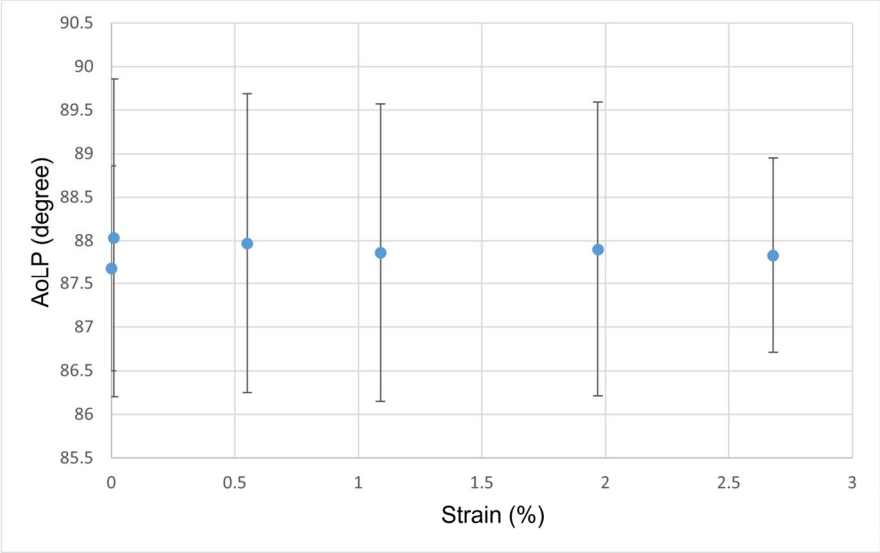


Figure 4.60 - The mean of the AoLP behaviour for two-layers of dry TFP reinforced hole preform with increasing strain (for the six selected images in Figure 4.56).

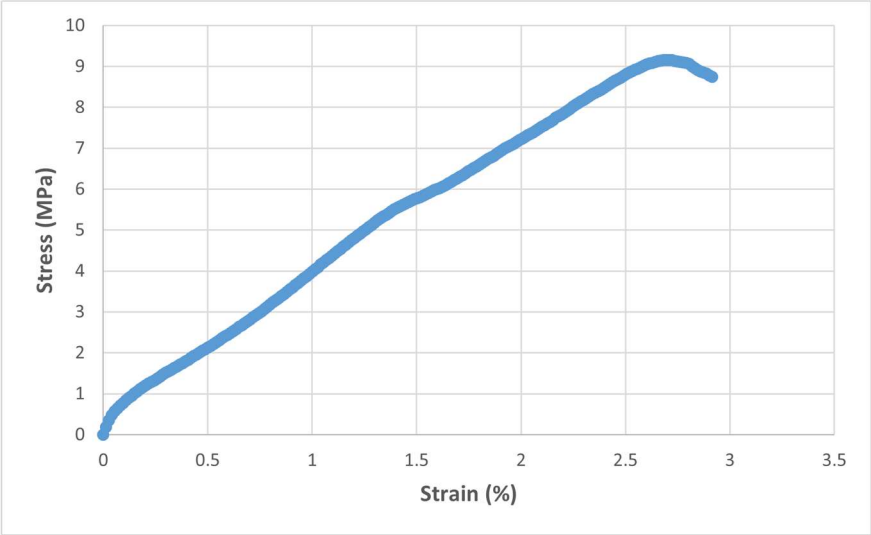


Figure 4.61 - The stress and strain curve for unidirectional-TFP reinforced hole sample consists of two layers.

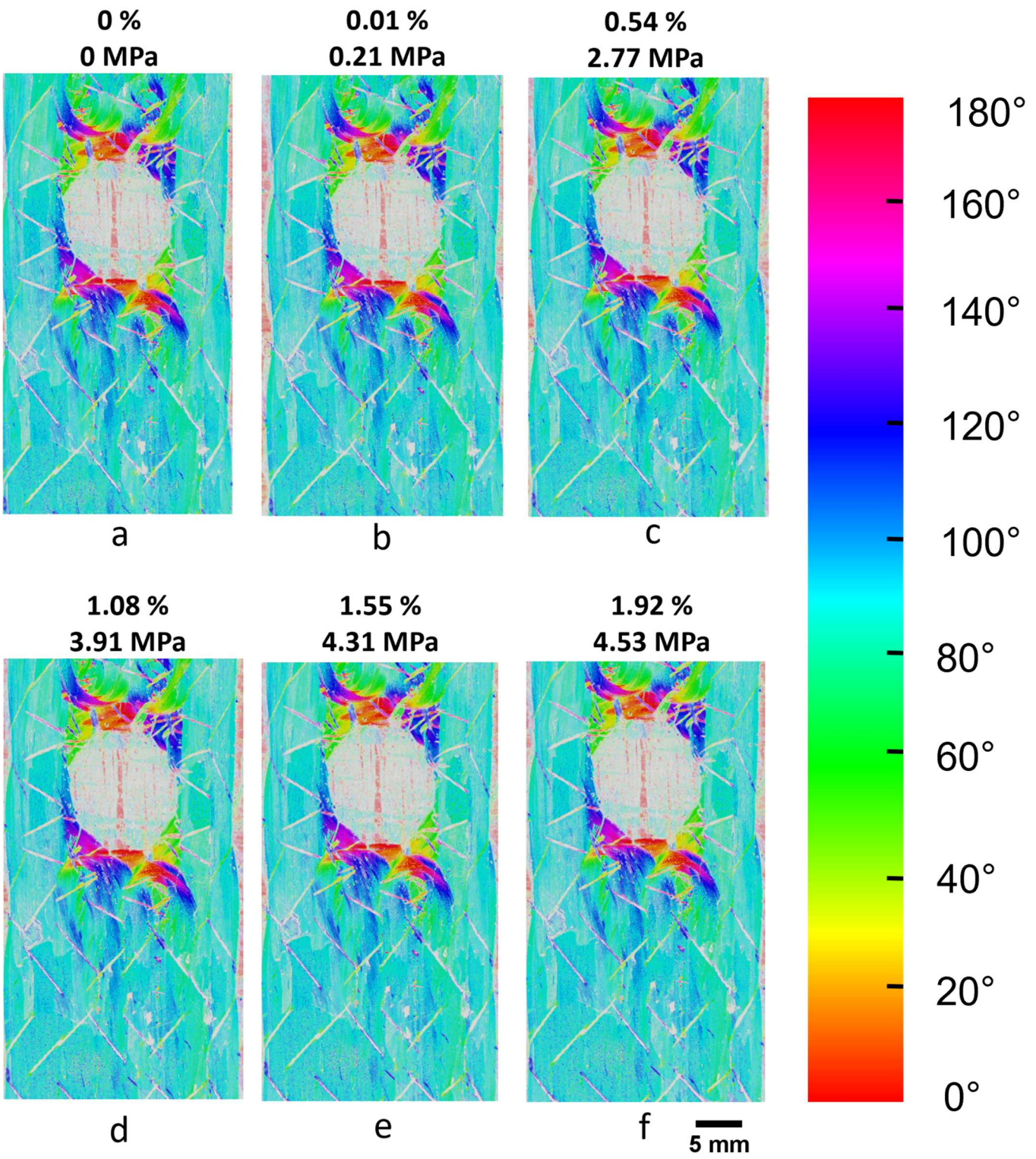


Figure 4.62 - Fibres' orientation images of UD-TFP reinforced hole sample with four layers were captured during the tensile test using the polarisation camera. The stress and strain corresponding to each image during the test are presented above the figure.

The same inspection process was applied to the TFP-reinforced hole sample with four layers. The fibre orientation images during the tensile test are shown in Figure 4.62, where image (a) shows the fibres' orientation before starting the tensile test at 0 % strain. Image (f) represents the fibres' orientation at strain equals to 1.92 %.

Figure 4.63 shows the selected region of interest around the reinforced hole (a) for the fibre orientation images at 0 % and 1.92 % strain, while (b) represents the histogram for the corresponding AoLP data extracted from the hue channel in the fibre orientation image. The histogram shows that the fibre has orientations from 0° to 180°. The Gaussian curve fitting was applied to the fibres with orientations between 60° and 120°.

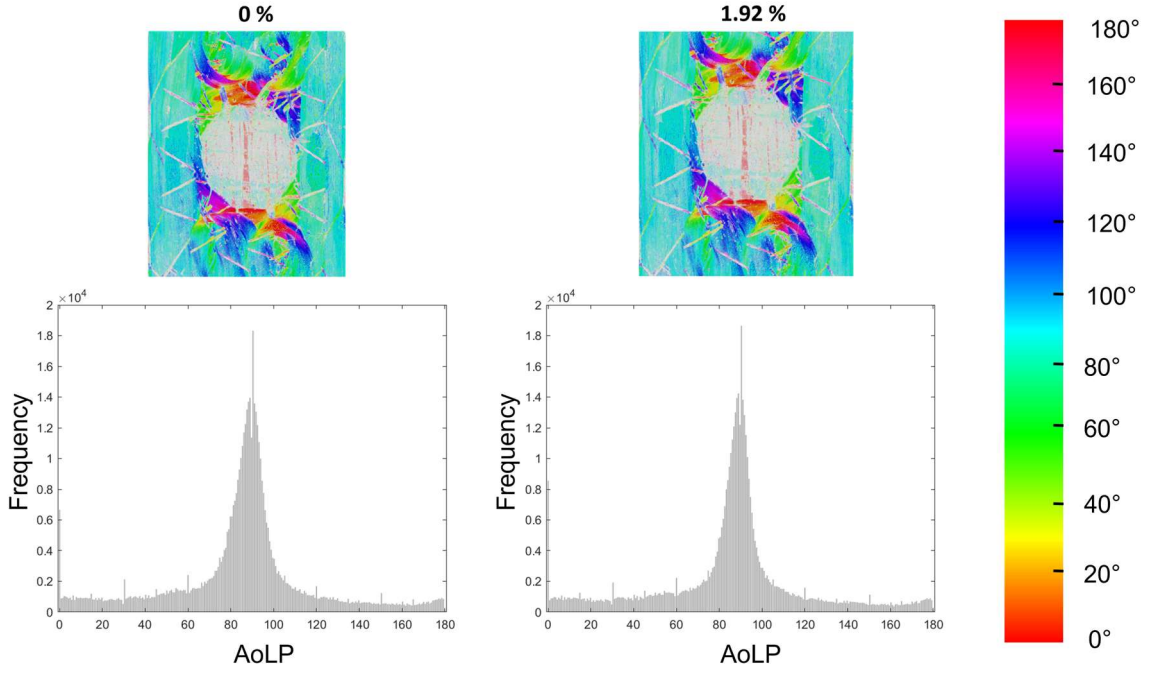


Figure 4.63 - The selected region of interest around the reinforced hole of the UD-TFP sample consists of four layers, where (a) shows the fibres' orientation image at different strains and (b) represents the corresponding histogram of the AoLP data.

Figure 4.64 shows the results of AoLP data after applying the Gaussian fitting curve on the fibre orientation images of the UD-TFP reinforced hole sample with four layers. The mean of the AoLP at 0 % strain was 88.70° ± 1.02 with a standard deviation of 10.80° ± 1.45. With increasing strain to 1.92 %, the mean of the AoLP changes to 88.93° ± 0.90 with a standard deviation of 8.84° ± 1.27.

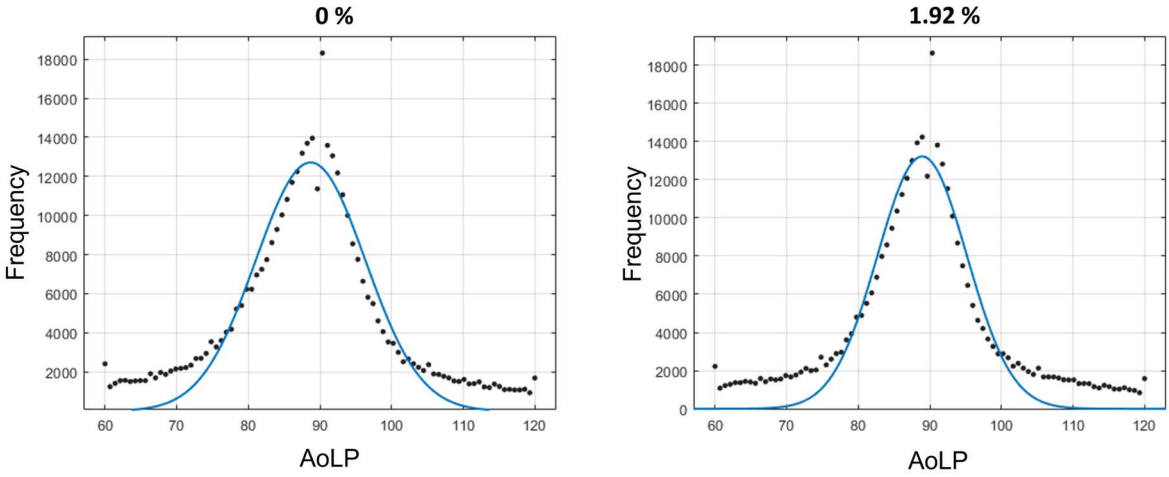


Figure 4.64 - MATLAB fitting of Gaussian curve to the histogram data of four layers UD-TFP reinforced hole sample at 0 % and 1.92% strain.

To have more information about the fibre orientation behaviour with increasing the strain, the threshold was applied to the fibre orientation images in the selected region of interest at 0 % and 1.92 % strain. Figure 4.65 represents the results of separating the fibre orientations, showing that a higher percentage of fibres are aligned in the orientations between 80° and 100°.

In the fibre orientation image at 0 % strain, the fibres with orientations between 80° and 100° represent 38.32 % of the image's total area, fibres with orientations between 60° and 80° represent 10.00 % of the total area, and the fibres with 100°-120° orientations represent 6.35 % of the total area. When strain increased to 1.92 %, the fibres with orientations between 80° and 100° represent 39.08 % of the image's total area, the fibres that have orientations between 60° and 80° represent 7.41 % of the total area, and the fibres with orientations between 100° and 120° represent 6.17 % of the total area.

The red circles illustrated the changes in the fibre orientations around the reinforced hole with increased strain, with the fibres with orientations between 60° and 80° changing to orientations between 80° and 100°.

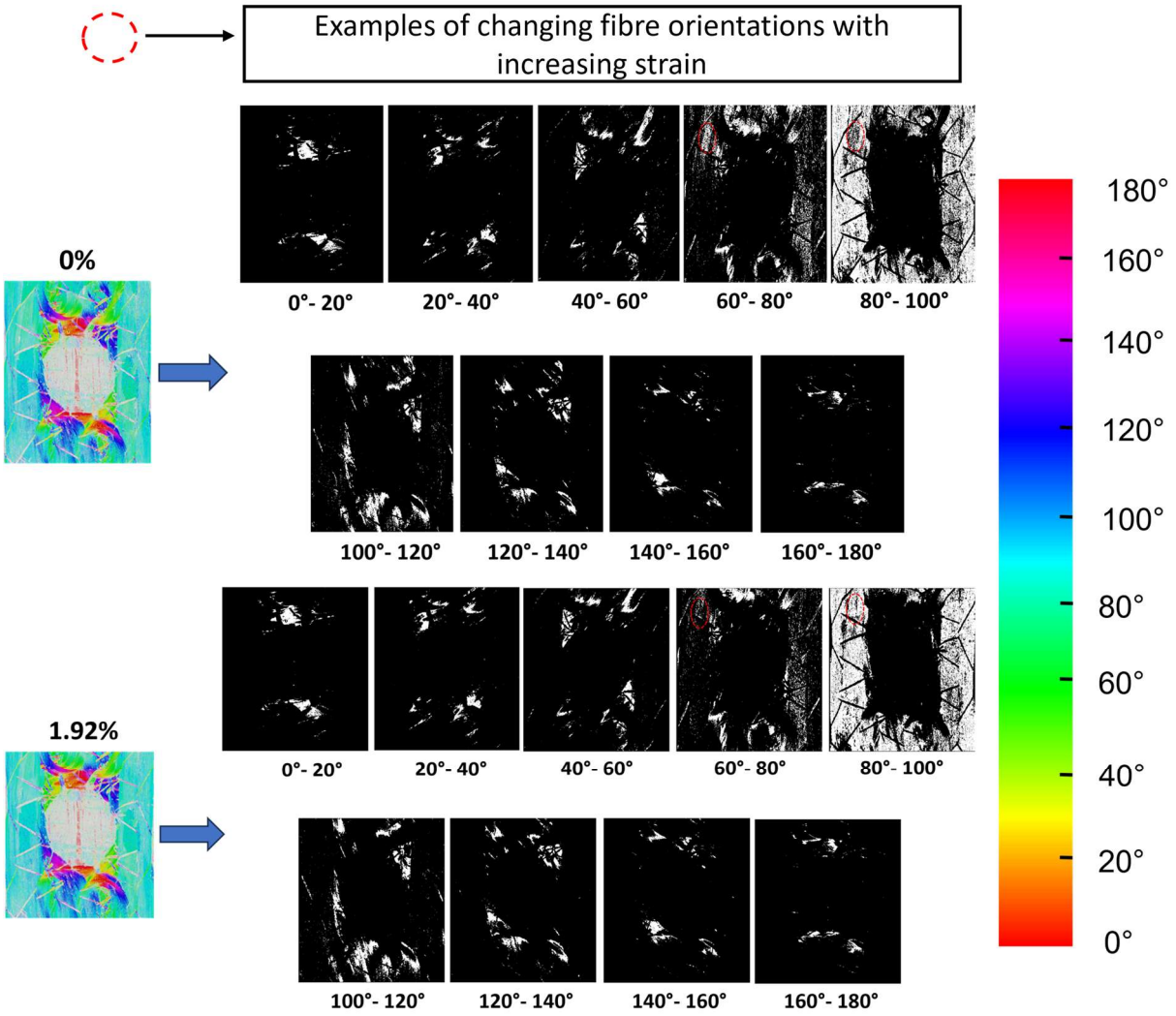


Figure 4.65 - Separating the fibre orientation of the selected region image in the UD-TFP reinforced hole sample with four layers at 0 % and 1.92 % strain using a colour threshold.

Table 4.10 represents the mean of the AoLP and the standard deviation for the fibre orientation images during the tensile testing, Figure 4.62, after applying the Gaussian fitting curve. The results of the mean of the AoLP of the UD-TFP reinforced hole with four layers show the change behaviour in the fibre orientation with an increase in the strain. The visual representation of the fibre orientation behaviour around the reinforced hole with an increase in strain is shown in Figure 4.66. The mean of the AoLP of the fibres at 0 % strain changes from (88.70° ± 1.02) to (88.93° ± 0.90) with increasing strain to 1.92 %.

Table 4.10 - The mean of the AoLP and standard deviation results in the corresponding strain after applying the Gaussian curve fitting to the fibres' orientation images of UD-TFP reinforced hole sample with four layers that were captured during tensile testing, (Figure 4.62)

The mean of AoLP (degree)	Standard deviation (the width of the peak)	Strain (%)
88.70 ± 1.02	10.80 ± 1.45	0
89.08 ± 1.33	9.55 ± 1.39	0.01
89.08 ± 1.20	8.64 ± 1.70	0.54
89.19 ± 1.17	8.48 ± 1.65	1.08
89.25 ± 1.14	8.27 ± 1.62	1.55
88.93 ± 0.90	8.84 ± 1.27	1.92

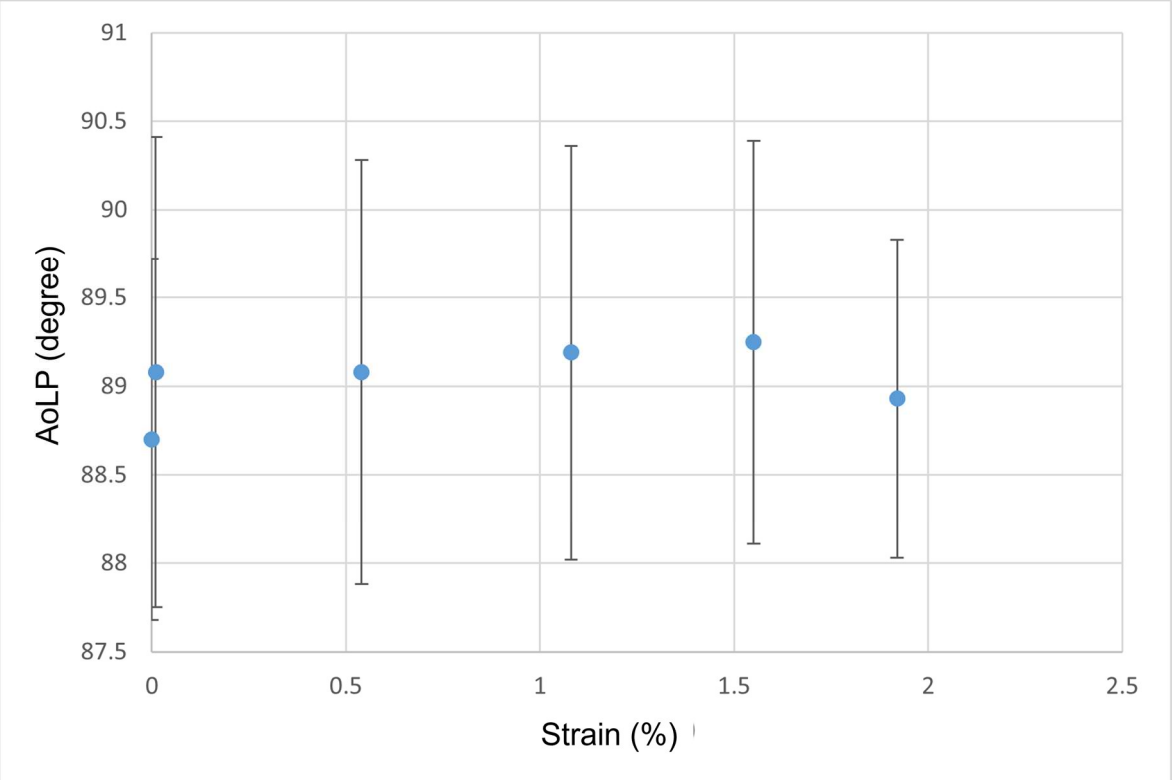


Figure 4.66 - The mean of the AoLP behaviour for four-layers of UD-TFP reinforced hole sample with increasing strain (for the six selected images in Figure 4.62).

The stress and strain curve of the UD-TFP reinforced hole sample with four layers is presented in Figure 4.67, which shows a response for different stages where it starts with the linear response from 2 MPa up to 3.8 MPa, then the curve shows the effect of the deformation in the stitching threads.

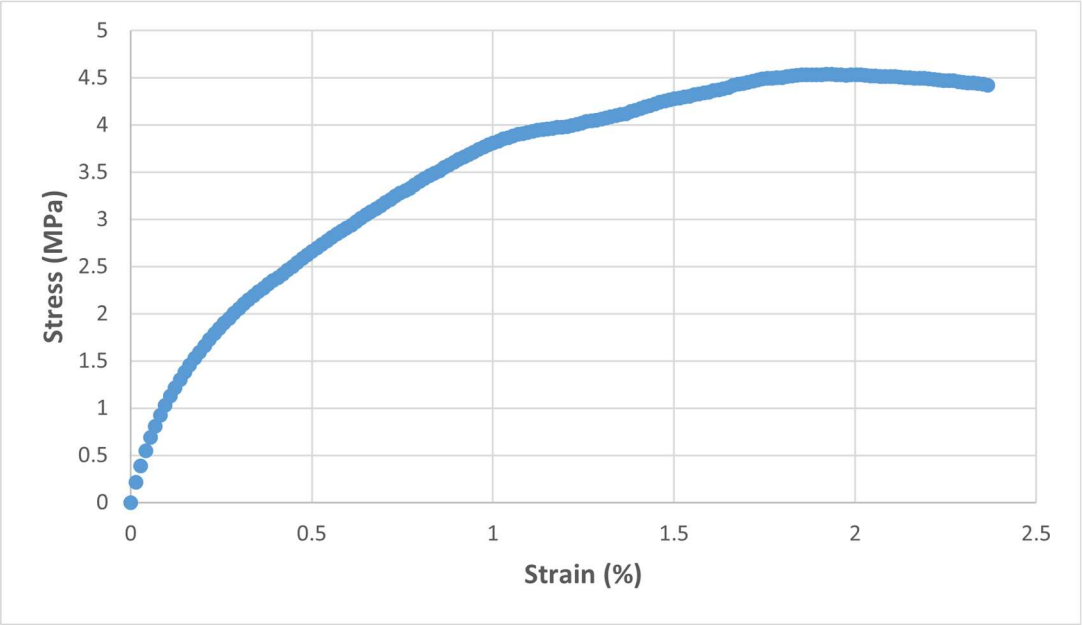


Figure 4.67 - The stress and strain curve for UD-TFP reinforced hole sample with four layers impregnated with silicone rubber resin.

4.4.5 Discussion

The fibre orientation behaviour of the Twill 2×2 samples impregnated with silicone rubber resin exhibited trends broadly similar to those observed in the dry samples, but with additional effects attributable to resin impregnation. The AoLP distributions prior to loading were characterised by two distinct peaks corresponding to the warp (aligned with the tensile direction) and the weft (perpendicular), and Gaussian fitting confirmed this orientation structure. As strain increased to 1.68 %, the warp fibres remained relatively stable, with the mean AoLP shifting only from 87.08° to 87.64°, accompanied by almost unchanged standard deviations. This consistency reflects the inherent alignment of warp fibres with the tensile axis, which restricts re-orientation during loading. In contrast, the weft fibres displayed more cleard changes, with the mean AoLP shifting from (–5.88° to –8.39°) and the peak width broadening, indicating progressive reorientation and greater variability in alignment with increasing strain. This redistribution was corroborated by the fibre orientation

colour separation analysis, which revealed a small increase in warp-aligned fibres (80°–100° rising from 47.19 % to 48.53 %) with increasing strain, alongside a reduction in the percentage of fibres within the perpendicular ranges (0°–20° decreasing from 1.72 % to 1.10 %, and 160°–180° decreasing from 41.68 % to 37.06 %). These shifts suggest that the weft system was more sensitive to tensile loading and rotated slightly towards the warp-dominated alignment, while the warp system sustained the majority of the load with minimal changes in fibre orientation.

Compared with the dry condition, the silicone rubber resin introduced surface reflections that were visible in the saturation and DoLP images, thereby reducing the ability to extract orientation information from certain regions. Nonetheless, the overall distributions remained consistent with the expected warp–weft separation, and the fibre orientation behaviour was still detectable under load. The broader peaks in the Gaussian fitting and the increased standard deviation in the weft direction with increasing strain suggest that the resin layer not only affected the optical measurement but also influenced the mechanical interaction between the fibres. Overall, the results demonstrate that silicone rubber impregnation acts as an intermediate state between dry textiles and fully cured epoxy laminates, as it preserves the architectural signature of woven Twill 2×2 fabrics in relation to fibre reorientation under increasing strain, thereby offering valuable insight into how fibre orientation evolves when transitioning from dry to resin-impregnated conditions.

The fibre orientation analysis of the UD-TFP reinforced hole specimens with two and four layers, impregnated with silicone rubber resin, reveals meaningful differences in their deformation responses during tensile loading. Inspection using the polarisation camera enabled the tracking of fibre reorientation through the analysis of the Angle of Linear Polarisation (AoLP) and the corresponding hue histogram.

For the two-layer UD-TFP sample, the mean AoLP value at 0 % strain was approximately 87.68° ± 1.18, with a standard deviation of 16.20° ± 1.69, indicating a relatively broad distribution of fibre orientations around the loading direction. With increasing strain to 2.68 %, the mean AoLP changed marginally to 87.83° ± 1.59, while the standard deviation decreased slightly to 15.80° ± 1.59, suggesting limited fibre rotation and minor re-orientation within the stitched region surrounding the

reinforced hole. The area-based analysis confirms this observation, showing that the percentage of fibres oriented between 80° and 100° increased slightly from 32.33 % to 33.48 %, implying that most fibres retained their initial alignment despite the increasing strain.

In contrast, the four-layer UD-TFP sample exhibited a narrower orientation distribution from the outset, with an initial mean AoLP of 88.70° ± 1.02 and a standard deviation of 10.80° ± 1.45, reflecting improved stability and reduced fibre waviness due to the higher layer count and the greater alignment provided by the stitching. Upon increasing the strain to 1.92 %, the mean AoLP shifted slightly to 88.93° ± 0.90, while the standard deviation decreased to 8.84° ± 1.27, signifying enhanced fibre alignment with the loading direction and a smaller angular spread compared with the two layers configuration. The threshold analysis further indicated that the percentage of fibres oriented between 80° and 100° increased from 38.32 % to 39.08 %, while fibres initially within 60°–80° gradually re-oriented towards the loading direction.

Comparatively, the four-layer sample exhibited greater orientation stability and lower variability, attributed to the increased number of stitched layers, which restricted fibre slippage and limited local bending near the reinforced hole. In contrast, the two layers specimen displayed slightly greater variation in fibre distribution and a wider AoLP spread. However, both systems showed a small degree of reorientation of the main fibre bundles under increasing strain, in the loading direction. These findings suggest that increasing the number of TFP layers enhances the angular stability of fibres during tensile deformation and reduces fibre waviness around critical zones such as reinforced holes.

4.4.6 Comparison between the dry and silicone-impregnated samples

The comparison between the dry and silicone-impregnated Twill 2×2 samples reveal clear differences in the behaviour of fibre orientation with increasing strain, particularly for the weft, (Peak 1), fibres. At zero strain, both conditions exhibit two distinct orientation peaks corresponding to the warp (~88°) and weft (~0°/180°) fibres. However, the impregnated sample begins with a slightly larger initial

misalignment in the weft direction (–5.88°) than the dry sample (–2.39°), likely caused by the resin application process.
When strain starts to increase (0 % to 0.01 % strain), the dry sample shows practically no change in weft orientation (–2.39° to –2.40°) and a negligible change in the warp direction (88.08° to 88.09°). In contrast, the impregnated specimen already exhibits a clear rotation in the weft direction from (–5.88° to –6.51°), accompanied by a small shift in the warp direction from (87.08° to 87.34°). These small changes in fibre orientation indicate that the fibres begin to respond at the earliest stage of loading, depending on the condition of the sample (i.e., whether there are pre-existing defects in fibre orientation introduced during the sample preparation process).

With strain increased to approximately 0.26 %, the impregnated sample continues to exhibit changes in fibre orientation in the weft direction to (–7.12°), giving a total shift of about (1.24°) from the initial state. In contrast, the dry sample at a strain of 0.54 % shows a change in weft orientation only to (–2.71°), a difference of just (0.32°). Therefore, the impregnated sample demonstrates approximately four times greater change in fibre orientation (during the early stage of strain increase) in the weft fibres compared with the dry fabric. The warp fibres, however, remain largely stable in both cases, with the fibre orientations changing from (87.08° to 87.50°), (0.42° change), in the impregnated sample and from (88.08° to 88.39°), (0.31° change), in the dry sample.

As the strain increases to around 1 % and 1.1 %, the divergence becomes more pronounced. The weft orientation in the impregnated fabric reaches (–7.83°) at 1.08 % strain (a change of 1.95° from starting the test), whereas the dry fabric at the same strain changes the fibre orientations to –3.14° (a change of 0.75° in fibre orientation). This indicates that the change in fibre orientation is approximately 2.6 times greater in the impregnated case.

Near maximum loading (1.68% and 1.78% strain), the impregnated sample’s weft fibres rotate further to (–8.39°), while the dry sample at 1.78% strain reaches (–5.02°). The total changes in fibre orientation at maximum load relative to the initial state are (2.63°) for the dry sample and (2.51°) for the silicone-impregnated sample.

Further samples are required to enable a comprehensive statistical analysis of the influence of fibre orientation with increasing strain for both dry and silicone-impregnated specimens. Even minor deviations in fibre alignment from the loading axis can markedly affect the material's mechanical properties (for detailed discussion of the influence of fibre orientation on mechanical performance, refer to **Section 2.5** of the Literature Review chapter). Despite variations in the strain corresponding to the maximum load, the results suggest that the fibre-orientation behaviour of the Twill 2×2 sample impregnated with silicone rubber resin follows a similar trend to that observed in the dry sample as strain increases. These findings provide valuable insights that will inform future investigations involving epoxy-infused specimens.

For the UD-TFP samples, the comparison between the dry and silicone rubber impregnated specimens demonstrates how resin impregnation influences fibre orientation behaviour under tensile loading. The analysis of the Angle of Linear Polarisation (AoLP) and its standard deviation provides valuable insight into the distribution and evolution of fibre orientation with increasing strain.

In the case of the two-layer UD-TFP preform, the dry sample exhibited a mean AoLP of 89.39° ± 0.60° and a standard deviation of 7.33° ± 0.86° at 0 % strain, indicating a high degree of fibre alignment along the loading direction. With increasing strain to 0.28 %, the standard deviation progressively decreased to 3.63° ± 0.41°, reflecting a gradual straightening of the fibres. This reduction suggests that the applied stress promoted fibre alignment and minimised local misorientation around the reinforced hole. In contrast, the silicone-impregnated two-layer sample exhibited a wider distribution of fibre orientations, with an initial mean AoLP of 87.68° ± 1.18 and a standard deviation of 16.20° ± 1.69. Despite a relatively stable mean AoLP throughout the test (remaining close to 88°), the high standard deviation (ranging between 13° and 16°) indicates that the fibre orientation was influenced by the impregnation process, which in turn affected the reorientation behaviour with increasing strain.

The four-layer UD-TFP samples exhibited enhanced orientation stability in both dry and impregnated conditions due to the increased number of stitched layers, which

provided greater confinement near the reinforced hole. For the dry four-layer sample, the mean AoLP at 0 % strain was 89.69° ± 0.65, with a standard deviation of 7.10° ± 0.92, which steadily decreased to 4.08° ± 0.75 at 4.67 % strain. This behaviour confirms that additional stitched layers reduce the fibre orientation distribution and maintain the structural integrity of the loop-back path during loading more effectively than in the two-layer case. In the silicone-impregnated four-layer sample, the mean AoLP changed slightly from 88.70° ± 1.02 to 88.93° ± 0.90, while the standard deviation decreased from 10.80° ± 1.45 to 8.84° ± 1.27 as the strain increased from 0 % to 1.92 %. Although fibre alignment improved marginally, the overall angular dispersion remained higher than that of the dry specimen. Nevertheless, the presence of four layers provided sufficient confinement to limit fibre slippage compared with the two-layer impregnated sample.

4.4.7 Conclusion

To conclude the fibres' orientation inspection during the tensile test for carbon fibre samples impregnated with a silicone rubber resin, the polarisation camera was employed to inspect the fibres' angles in the Twill 2x2 and UD-TFP reinforced hole samples from the angle of linear polarisation (AoLP) information. The hue channel in the HSV image encodes the AoLP information, which matches the fibres' directions, while the saturation channel contains the degree of linear polarisation (DoLP) information. Thus, the histogram of the hue channel was used to represent the fibres' orientation distribution for a selected region in the fibres' orientation image (before starting the tensile test and with increasing strain). Also, the Gaussian curve fitting was applied to measure the mean of the AoLP at different strains.

To better understand the fibres' orientation behaviour, the fibres' angles were separated in the selected region's image using the colour threshold to investigate the influence of increasing strain on the behaviour of changing the fibres' orientations, where the fibres' orientation was divided into ranges based on the hue channel information to compare the orientations of the fibres at different strains.
However, the UD-TFP reinforced hole samples show that the silicone rubber resin influenced the inspection using the polarisation camera. The DoLP image shows

that some fibres were represented in different DoLP levels caused by silicone rubber resin which affects the extraction of fibre orientation information.

The results demonstrate a significant change in the mean of (AoLP) of fibres perpendicular to the tension direction in the Twill 2x2 samples, both dry and silicone rubber resin-impregnated, with increasing strain. The mean AoLP of the dry Twill 2x2 sample shifted from -2.39° ± 0.33 to -7.63° ± 0.46 with increasing strain. Similarly, the silicone rubber resin-impregnated Twill 2x2 sample exhibited a change in the mean of AoLP from -5.88° ± 0.18 to -9.46° ± 0.68. However, fibres aligned with the tension direction in both the Twill 2x2 and UD-TFP samples showed slight changes in AoLP because the fibres are already aligned in the applied force direction. The fibres tend to rotate toward the tension direction.

Moreover, the results show that the Gaussian fitting is not sensitive to the small changes in the fibre orientations with increasing strain as it represents the whole area. On the other hand, the individual separated into the angle range was capable of better detecting the small changes in the fibre orientations at different strains. However, this process requires advanced analysis, potentially coupled with machine learning, to improve the detection of fibre orientation changes with increasing strain.

The analysis of fibre orientation presented in this chapter, both in the dry state and following impregnation with silicone rubber resin, provides meaningful insights into fibre orientation behaviour during tensile testing. These findings will form the basis for the following investigation of the behaviour of fibre orientation in open-hole tensile samples, particularly in the regions adjacent to machined holes, as discussed in the next chapter.

5 POLARISATION ANALYSIS OF FIBRE ORIENTATION BEHAVIOUR AROUND MACHINED HOLES OF CARBON FIBRE COMPOSITE SAMPLES DURING OPEN-HOLE TENSILE TESTING

5.1 Introduction

Open-hole tensile tests were applied to UD-NCF and Twill 2x2 carbon fibre to investigate the tensile response when using different hole diameters with a fixed sample width. Three-hole diameters, 12mm, 10mm, and 8mm, were used to examine the effect of the fibres' orientation, weave pattern, and hole position relative to the weave during the tensile test using the polarisation camera.

The D5766 standard specifies a recommended ratio between the open-hole tensile test's sample width, thickness, and hole diameter. However, the recommended ratio between sample width and hole diameter, as specified in D5766, could not be followed as the tensile load was above the capabilities of the available instrumentation. More details about the effect of the hole's diameter ratio with the sample's thickness and width are mentioned in **Section 2.6.1**.

Several studies have deviated from the standard while investigating the influence of hole diameter on the behaviour of composite laminates subjected to open-hole tensile testing. Guo *et al*. [52] employed the open-hole tensile test with three-hole diameters and a constant sample width of 36 mm. Their findings revealed a transition in the damaged zone shape from convex to concave with increasing hole diameter. Furthermore, when the hole diameter increases, the damage mechanism changes from fibre pull-out to fibre breakage. Liu *et al*. [61] investigated the combined effects of hole diameter and width ratio on the strength of laminates at low and room temperature. They employed a tensile test with three different hole diameters and a fixed sample width of 25 mm. Shaari and Jumahat [62] employed an open-hole tensile test to investigate the influence of hole diameter on the strength of hybrid composite laminates. They used samples with a fixed width of 36 mm and five different hole diameters. Their findings demonstrated a decrease in sample strength retention with increasing hole diameter.

The present study in this chapter focuses on investigating the evolution of fibre-orientation behaviour around machined holes under increasing strain for different hole diameters. Two types of carbon-fibre architectures, Twill 2×2 and unidirectional non-crimp fabric (UD-NCF), were examined to evaluate how the weaving pattern near the machined hole influences the fibre geometry along the hole edge. This geometrical variation, in turn, affects the fibre-orientation response with progressive straining and impacts the overall mechanical performance of the tested specimens. The analysis of the angle of linear polarisation (AoLP) and degree of linear polarisation (DoLP) images provides insights into the distribution and alignment of fibres surrounding the machined holes, enabling a more comprehensive understanding of their contribution to the mechanical response. The outcomes of this investigation are expected to advance understanding of fibre-orientation behaviour around machined holes and to inform the optimisation of manufacturing strategies for Tailored Fibre Placement (TFP) reinforced-hole samples.

5.2 Sample preparation

The panel was manufactured by VARTM and cured in the programmable oven. Three-hole diameters were chosen: 12mm,10mm, and 8mm. For each hole diameter, three test specimens were prepared. All specimens have a uniform width of 25 mm and a length of 250 mm. A CNC machine was used to create the open-hole geometries within the test specimens. Additionally, all tensile specimens were bonded with tabs measuring 50 mm in length and 25 mm in width. For full details of sample preparation, see Methodology **Section 3.2** and **Section 3.3**.

5.3 UD-NCF carbon fibre

UD-NCF samples with two layers were prepared for tensile testing. These samples were further categorised based on the presence and diameter of a central hole machined using a CNC machine. The sample set with a 12 mm diameter hole (Figure 5.1), (sample-3), was the first set inspected using the polarisation camera during tensile testing. Figure 5.1 shows the raw image of the UD-NCF sample with a 12mm hole, where the carbon fibres are aligned in one direction (warp) while the

thermoplastic holds the fibres from the weft direction. The thermoplastic holds the carbon fibres in a weaving pattern, which creates curvature in the fibres. The white streak around the hole results from the machining process.

Prior to tensile testing, the sample was placed on black matte paper and imaged using the polarisation camera to establish a reference image. The captured images included raw saturation, degree of linear polarisation (DoLP), and angle of linear polarisation (AoLP)image, as presented in Figure 5.2 (a-c), respectively. The DoLP image (Figure 5.2-b) presents the carbon fibre on a greyscale, while the matte paper around the hole and thermoplastic material (weft direction) are in black. The image in Figure 5.2-c represents the fibre orientation using the HSV colour map, where the hue channel encodes the AoLP, and the saturation channel encodes the DoLP. The value channel is not used to encode information in these images.

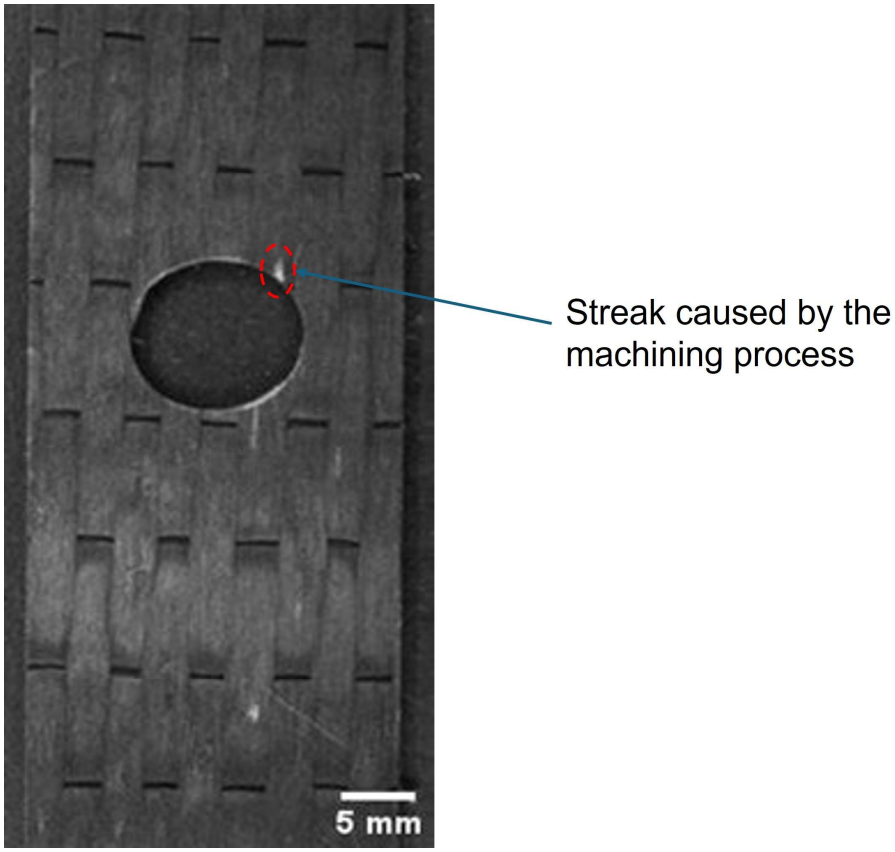


Figure 5.1 - Raw image example of UD-NCF samples consists of two layers with 12 mm hole diameter captured using the polarisation camera. The white streak around the hole results from the machining process

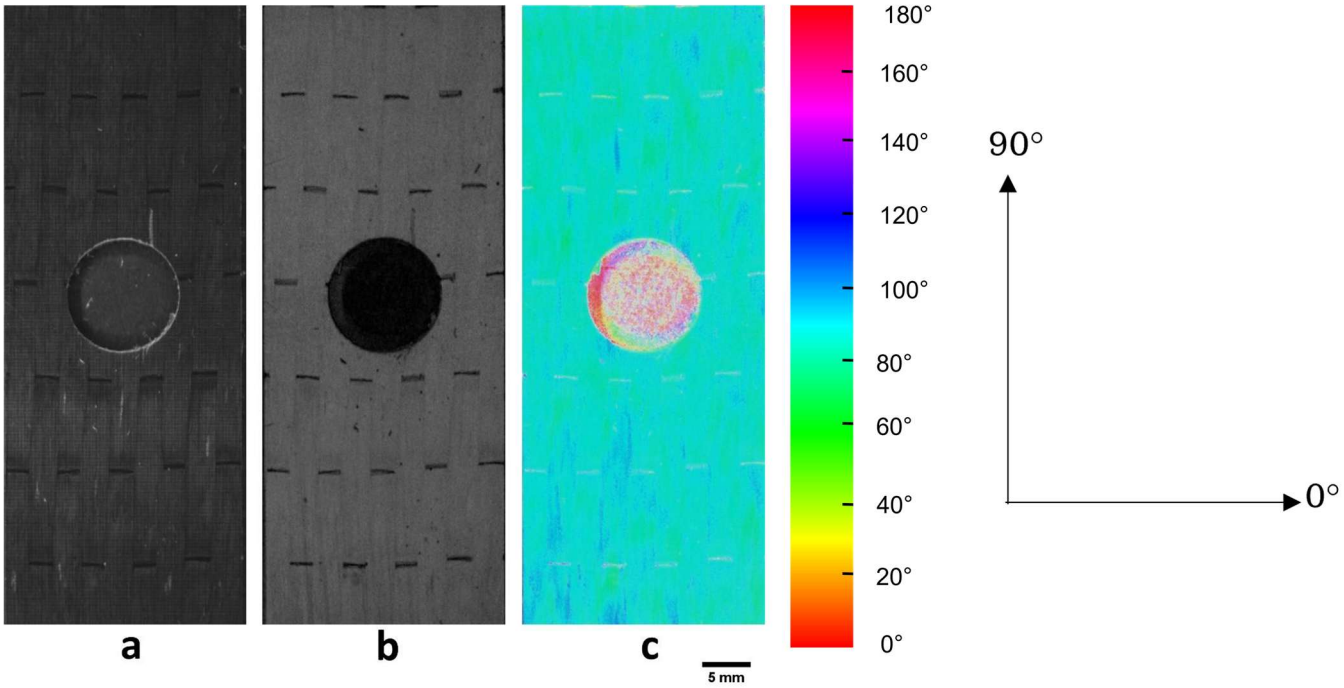


Figure 5.2 - The UD-NCF sample, (sample-3), with a 12 mm hole diameter was imaged using a polarisation camera, where images (a-c) are the raw saturation, DoLP and fibre orientation images, respectively.

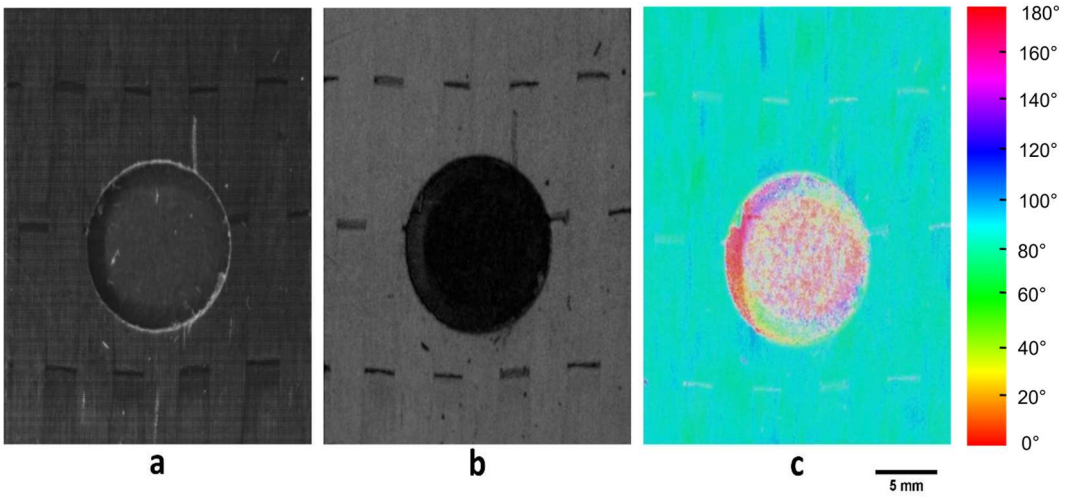


Figure 5.3 - A selected region of interest of UD-NCF sample with 12 mm machined hole around the machined hole to investigate the fibre orientation around the machined hole.

A region of interest was selected (Figure 5.3) to investigate the fibre orientations around the machined hole (before starting the tensile test). The figure shows three fibre orientations that appeared with different colours (green, cyan, and blue) corresponding to fibres with orientations between 80° and 100°. However, to better

understand the fibre orientation distribution, a histogram of the AoLP data, which is extracted from the fibre orientation image (Figure 5.3-c), was presented.

Figure 5.4-a presents the histogram of the AoLP data for the fibre orientations between 0° and 180°. The histogram shows that the fibre orientation is distributed between 80° and 100°. The fibre orientation distributed from 0°-20° and 160°-180° corresponds to the colours inside the hole (from the background black matte paper and the stitching).

The Gaussian fitting curve was applied to the fibre with orientations between 60° and 120°, Figure 5.4-b, to calculate the mean of the AoLP. The mean of the AoLP of the UD-NCF sample with a 12 mm hole diameter is 87.46° ± 0.08 with a standard deviation of 2.64° ± 0.12.

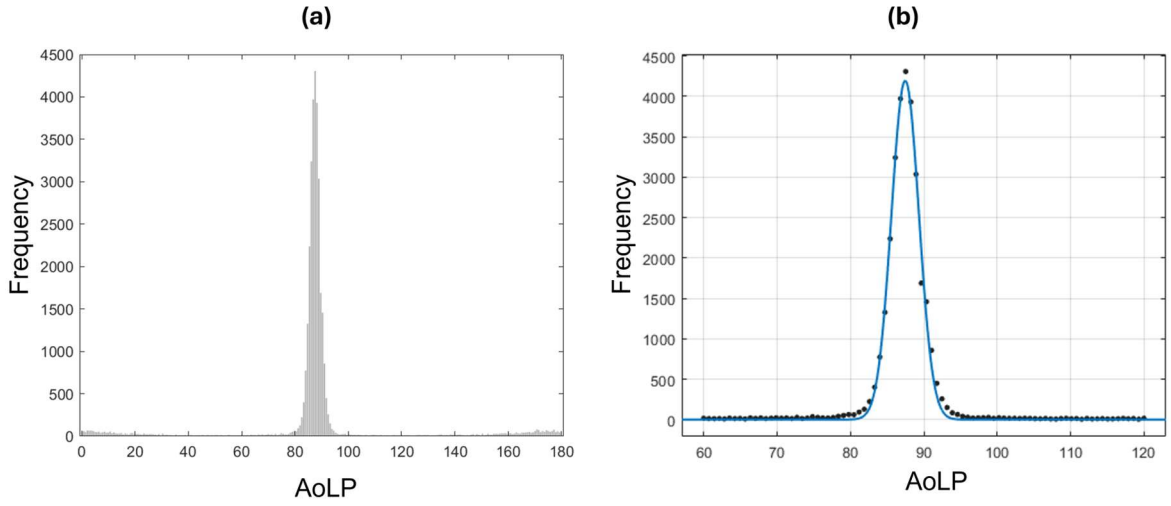


Figure 5.4 - The histogram of the AoLP data (a) for the UD-NCF sample with two layers at the selected area around the 12 mm machined hole, (b) shows the MATLAB fitting of Gaussian curve to AoLP data for the fibres with orientations between 60° and 120°.

A sequence of fibres' orientation images captured during the tensile test for the UD-NCF sample, (sample-3), with a 12 mm machined hole using the polarisation camera is shown in Figure 5.5. Image (a) presents the fibres' orientation before starting the tensile test at 0 % strain. Image (b) shows the sample one second after starting the test at a strain equal to 0.01 %. Images (c) through (f) were captured at 40-second intervals throughout the test, while images (g) and (h) were captured after the sample reached maximum load and total failure, respectively. With an

increase in the strain, the fibres start splitting apart until the sample reaches failure, images (e-h). Moreover, increasing the strain affects the fibre orientation, especially near the vertical edges of the machined hole.

To investigate the fibre orientations with increasing strain, Figure 5.6-a shows the selected area of the fibre orientation image around the 12 mm machined hole before starting the test at a strain equal to 0 % and when the strain reaches 2.12 %. Figure 5.6-b presents the histogram of the AoLP data encoded from the fibre orientation images (hue channel).

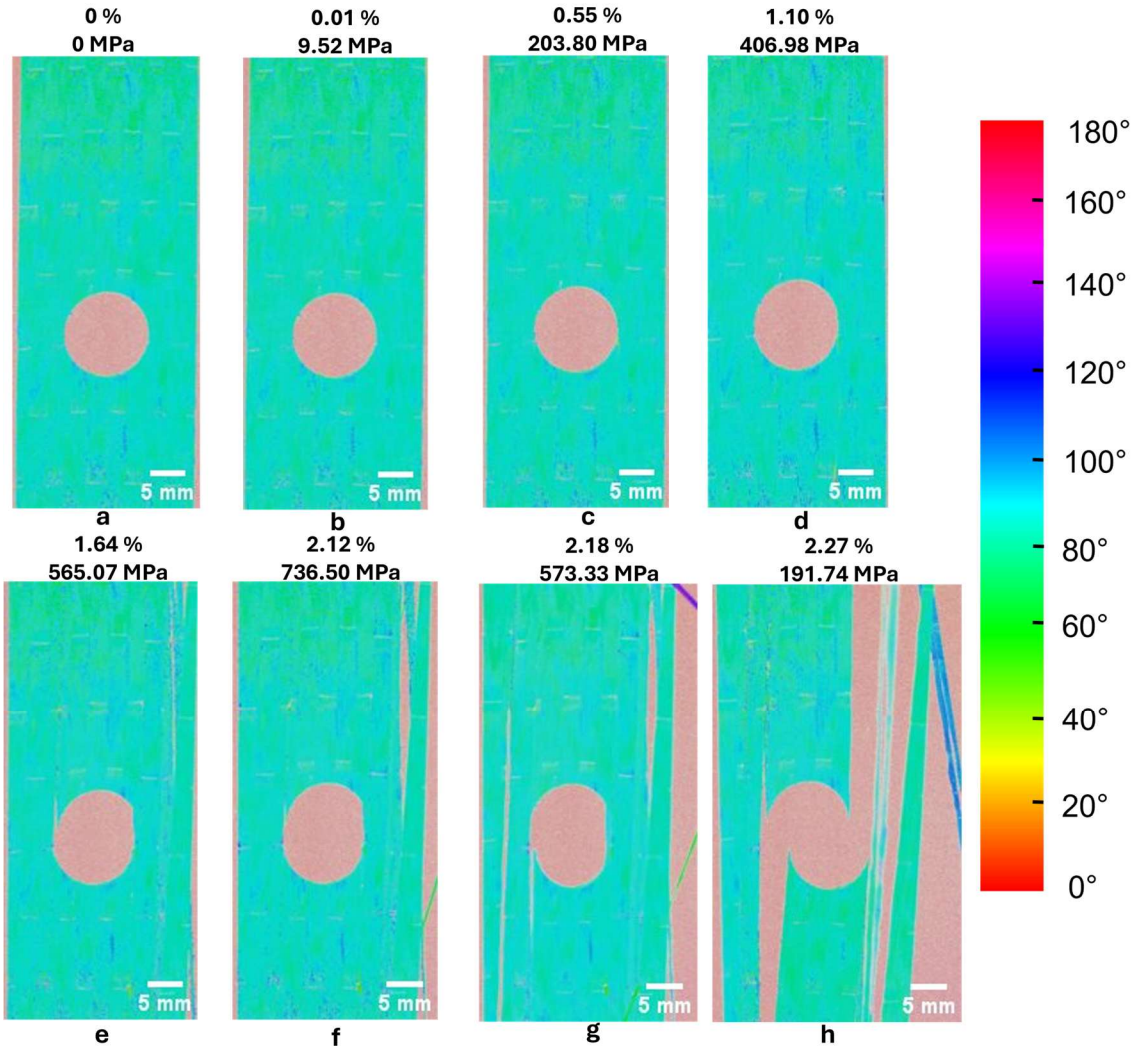


Figure 5.5 - Fibres' orientation images of UD-NCF sample, (sample-3), with two layers and 12 mm machined hole were captured during the tensile test using the polarisation camera. The stress and strain corresponding to each image during the test are presented above the figure.

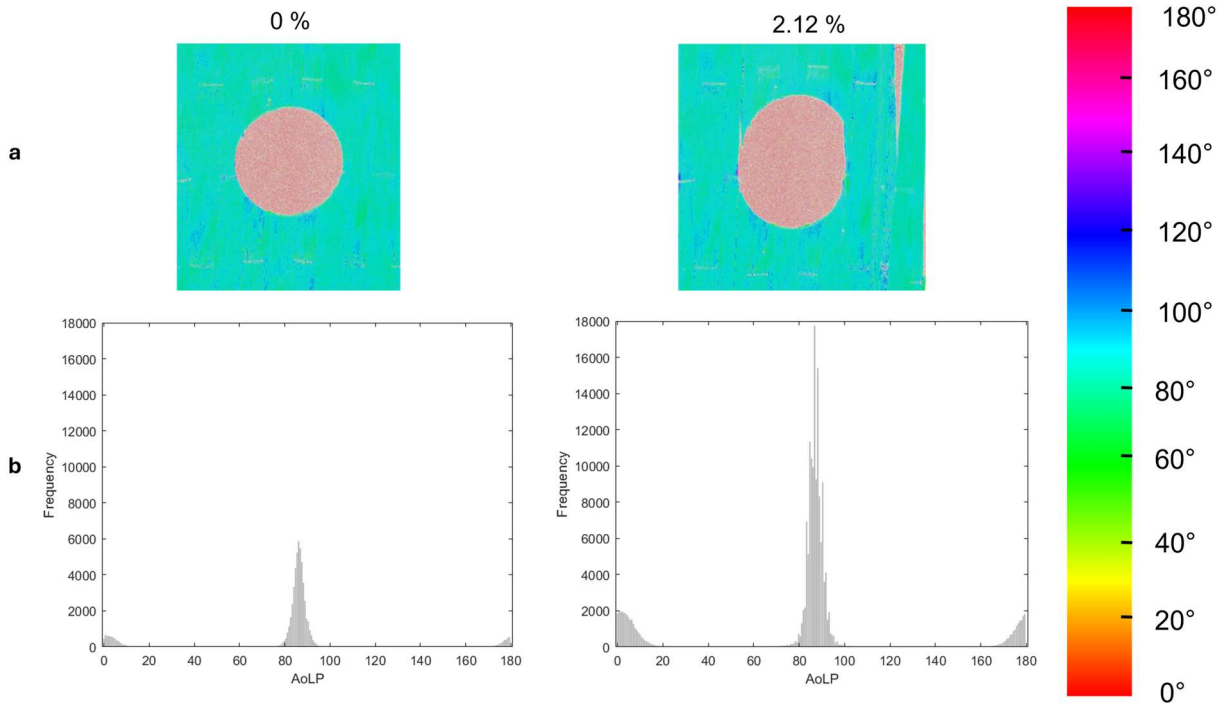


Figure 5.6 - The selected region of interest around the 12 mm machined hole of the UD-NCF sample consists of two layers, where (a) shows the fibres' orientation image at different strains and (b) represents the corresponding histogram of the AoLP data.

The histogram at 2.12 % strain shows clearly how the fibre orientation is influenced by increased strain. Figure 5.7 presents the results of fitting the Gaussian curve on the AoLP data to compare the mean of the AoLP at 0 % and 2.12 % strain. The mean of the AoLP at 0 % is 87.46° ± 0.08 with a standard deviation of 2.64° ± 0.12, while the mean of the AoLP when strain reaches 2.12 % is 87.04° ± 0.46 with a standard deviation of 3.89° ± 0.66.

To further investigate the fibre orientation response with increasing strain, the fibre orientations of the selected region of interest around the machined hole at 0 % and 2.12 % strain were separated using a threshold. Figure 5.8 shows the fibre orientation separation results, with most of the fibres having orientations between 85° and 90°.

The fibres with orientations between 85° and 90° in the fibre orientation image with 0 % strain present 67.27 % of the image's total area, while fibres having orientations between 80° and 85° present 10.01 % of the total area. When strain increased to

2.12 %, the fibres with orientations between 85° and 90° presented 52.71 % of the image's total area, while 17.27 % of the total area for the fibres with orientations between 80° and 85°.

The fibre orientation separation process provides a more detailed characterisation of fibre orientation behaviour with increasing strain than can be obtained through Gaussian fitting, where the Gaussian fitting is a global fitting that focuses on all data rather than small changes in the fibre orientations. Figure 5.8 illustrates the changes in the fibres with orientations between (80°- 85°, 85° - 90° and 90° - 95°) with increasing strain, as indicated by the red circles. The fibres with orientations between (80° - 85°) and (90° - 95°) around the machined hole change to have orientations between 85° and 90° to align with the tension direction. Moreover, the fibres at the edge of the machined hole with orientations between 80° and 85° change to have orientations between 90° and 95°, while the fibres with orientations between 90° and 95° change orientations to 80° and 85° with increasing strain.

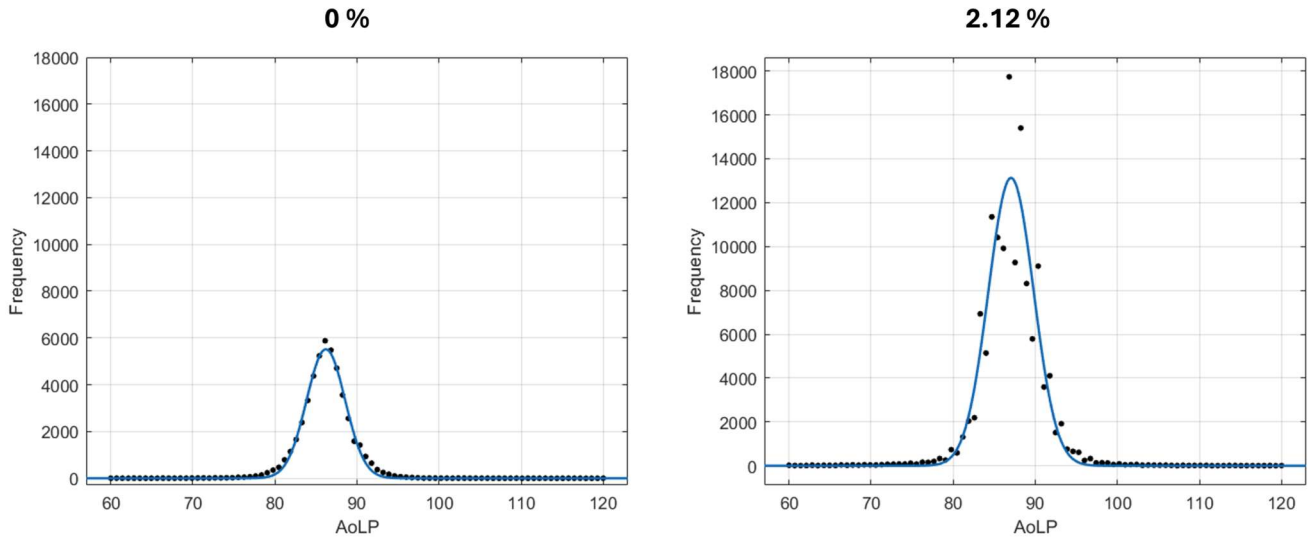


Figure 5.7 - MATLAB fitting of Gaussian curve to the histogram data of two layers UD-NCF sample with 12 mm machined hole at 0 % and 2.12 % strain.

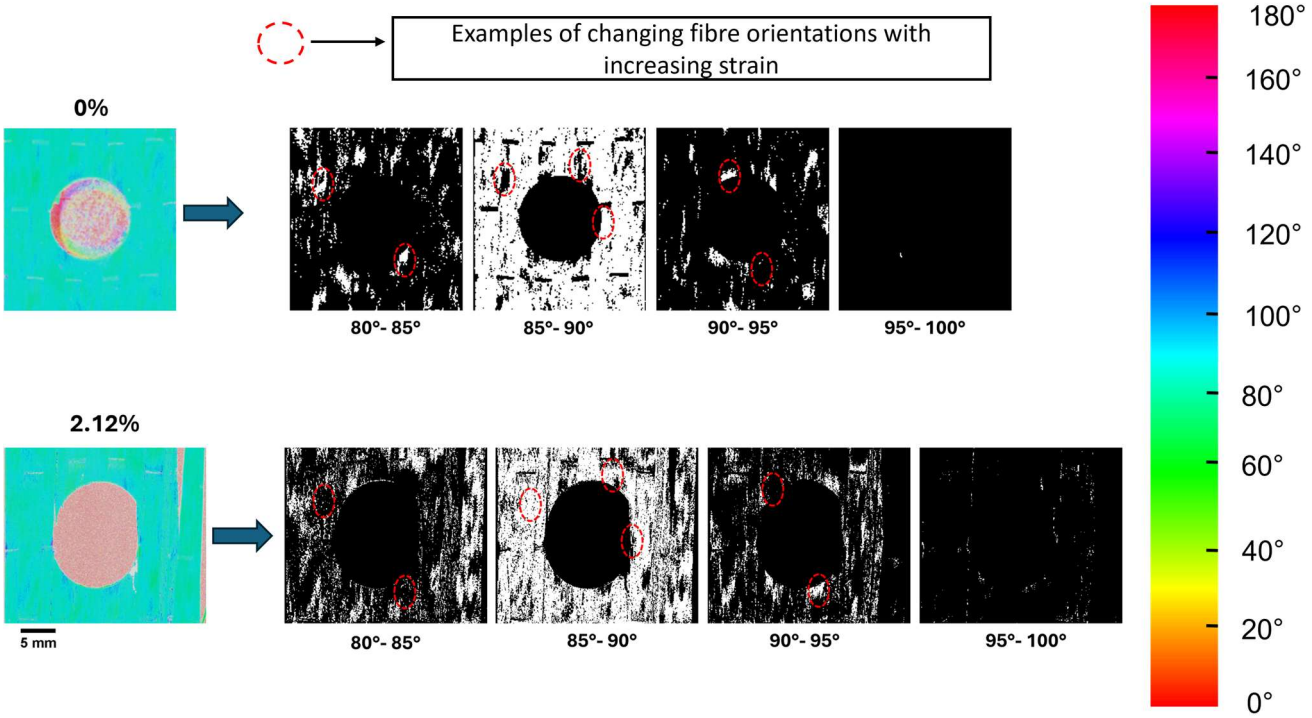


Figure 5.8 - Separating the fibre orientation of the selected region image in the two layers UD-NCF sample, (sample-3), with a 12 mm machined hole at 0 % and 2.12% strain using a colour threshold.

Figure 5.9 shows a schematic diagram illustrating how weft material affects the fibres by increasing strain. The load in the open-hole sample is taken primarily by the uncut fibres. The cut fibres are constrained at the interface with the uncut fibres, and the shear forces are largest here. As a result, machining the hole creates tip points in the carbon fibre at the edge of the machined hole, which generates a region of stress concentration.

Figure 5.10 shows the UD-NCF sample with a 12 mm hole after failure and a schematic diagram illustrating the tip points in the machined sample. The diameter of the machined hole affects the geometry of fibres in the tension direction, which in turn affects the mechanical properties. Also, the centre of the hole's position will influence the final fibre's geometry.

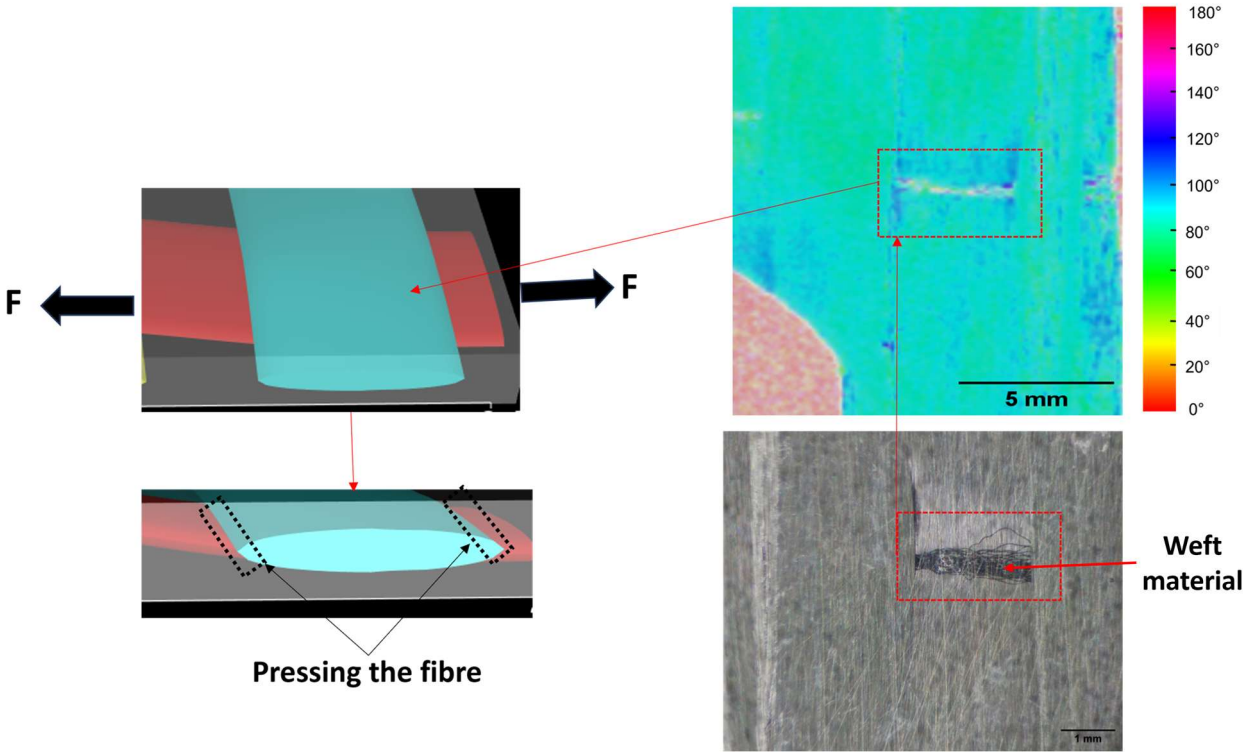


Figure 5.9 - Schematic diagram showing how the weft material affects the fibres when the strain increases.

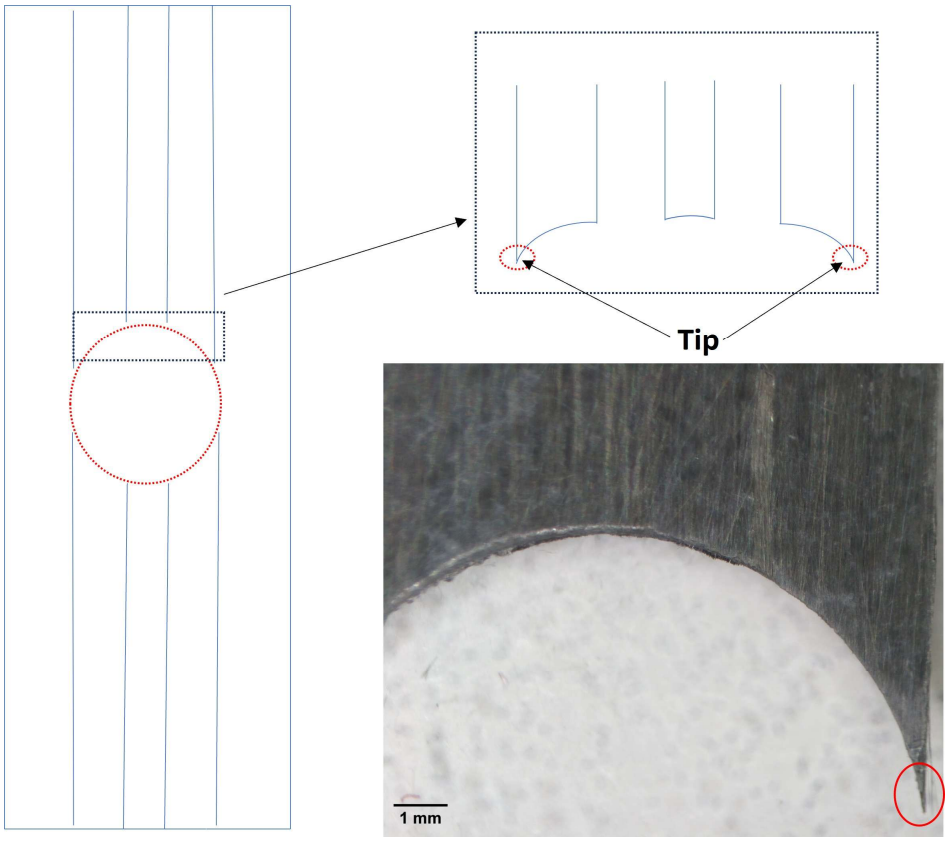


Figure 5.10 - Schematic diagram illustrating the tip points after tensile testing in the carbon fibre sample due to machining the hole [redraw from[52]**].**

A summary of maximum force load, tensile strength, failure strain and tensile modulus for the two layers UD-NCF tested samples with a 12 mm hole is presented in Table 5.1. The result shows a variation between the three samples. Even though the samples were prepared from the same panel, the warp and weft materials were removed from the sample because the machined holes were slightly different for each sample (hole position relative to the weave), which may affect the mechanical properties of these samples. The DoLP image for (samples 1, 2 and 3), Figure 5.11, was presented as an example to show the difference after machining the hole. The carbon fibre is presented in greyscale while the thermoplastic stitching thread is in black (above the fibres). The red rectangles, labelled (a), show the distance difference between the weft material and the machined hole in the three samples, where the weft material in sample (1) is near the machined hole, compared to sample (3), which leads to creating curvatures in the fibres (Figure 5.9). Also, the red boxes, labelled (b), show the weft material at the right edge of the machined hole, where the weft material in sample (1) is under the carbon fibre, (as weaving pattern), while it is over the fibres in sample (3) which leads to affect the fibre's orientation near the hole.

Table 5.1 - The mechanical properties of three UD-NCF samples with 12 mm hole diameter.

Sample Number	Maximum force (N)	Ultimate tensile strength (MPa)	Strain at break (%)	E-modulus (GPa)
Sample-1	8900	647.27	1.62	39.75
Sample-2	10000	740.74	2.02	36.67
Sample-3	11600	736.50	2.12	34.61
Average	10166.67	708.10	1.92	37.01
Standard Deviation	1357.69	52.78	0.26	2.59

The maximum force and ultimate tensile strength (UTS) values presented in Table 5.1 highlight the differences in performance among the tested samples. The results

indicate that sample (3) exhibited superior mechanical performance compared with the other specimens, suggesting that the presence and configuration of the weft material significantly influence the mechanical properties. A similar trend was observed for the UD-NCF specimen containing a 10 mm machined hole, further supporting this hypothesis. This observation aligns with the findings obtained from the Degree of Linear Polarisation (DoLP) image analysis conducted before and after testing (Figure 5.11 and Figure 5.12).

Further investigation, as outlined in the Future Work section, is required to validate this hypothesis and confirm the observed correlation. Upon validation, the DoLP imaging technique could be utilised as a predictive tool to identify optimal locations for machining holes, thereby enhancing the mechanical performance of the open-hole tested samples.

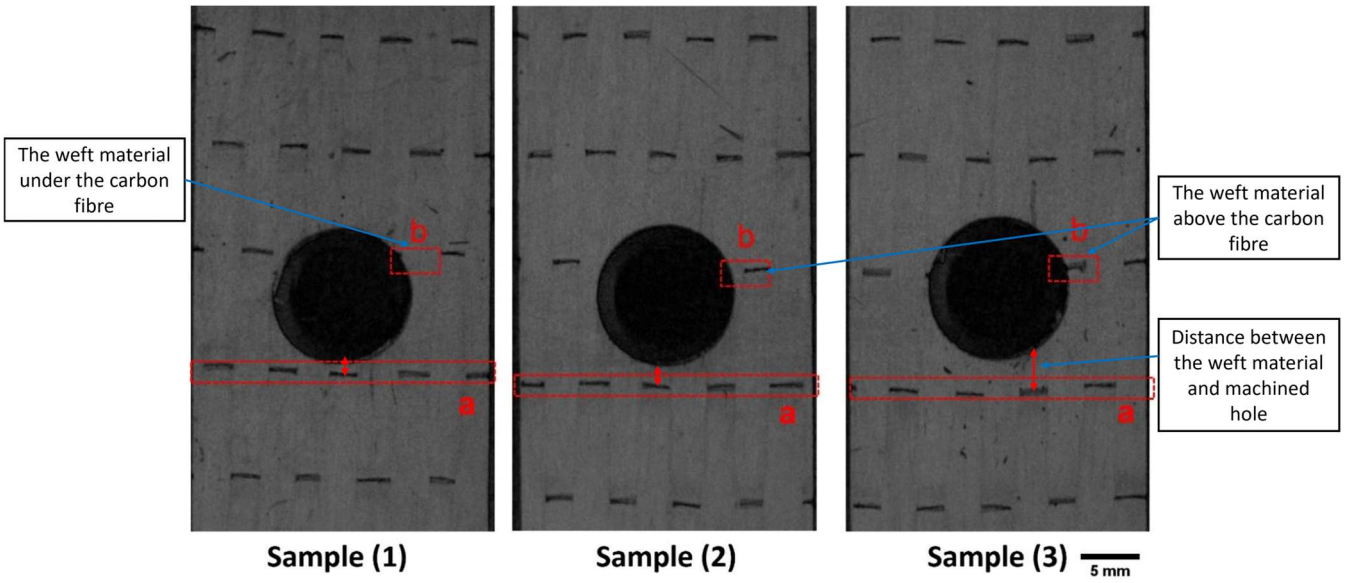


Figure 5.11 - DoLP images for three samples of UD-NCF with a 12 mm hole were captured using the polarisation camera, showing the difference in the warp and weft materials after the machining process.

Figure 5.12 shows the DoLP images captured using the polarisation camera of three UD-NCF samples, shown in Figure 5.11, with a 12 mm machined hole after being subjected to tensile testing. The figure presents how the fibres split near the machined hole before the total failure. Moreover, samples (2 and 3) show similar failures at the machined hole edge with similar tip points at higher loads. The failure mode in sample (3) initiated at the edges of the machined hole, caused by stress

concentration points resulting from local fibre discontinuities. As the strain increased, fibre splitting occurred due to the breakage of the weft material, which appeared as dips in the stress–strain curve, as shown in Figure 5.15. The progression of fibre splitting can be observed in Figure 5.16 as the strain increased. Sample (2) exhibited the same failure mode as sample (3), but with more pronounced fibre splitting with increasing strain, as illustrated in Figure 5.15. However, the different behaviour of fibre splitting in sample (1) is attributed to variations in the position of the weft material near the machined hole, which caused fibre curvature at the hole edge compared with the other samples.

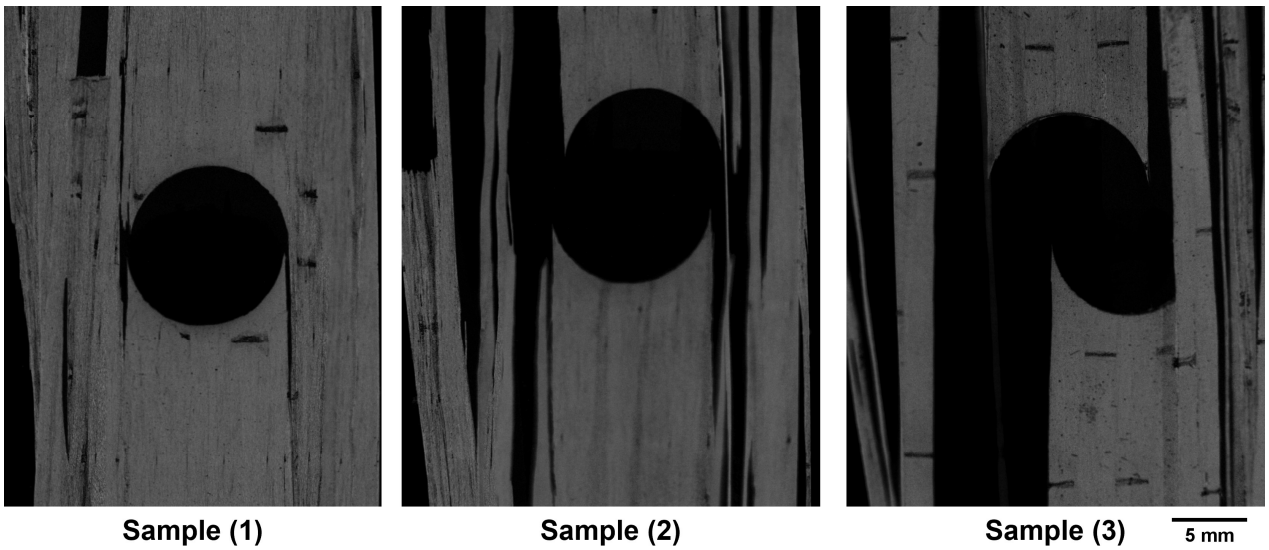


Figure 5.12 - The DoLP images for three UD-NCF samples, shown in Figure 5.11, after failure.

Table 5.2 represents the mean of the AoLP and the standard deviation for the fibre orientation images during the tensile testing, Figure 5.5, after applying the Gaussian fitting curve, the mean of the AoLP of the UD-NCF sample with a 12 mm machined hole shows the change in fibre orientation with an increase in strain. Figure 5.13 represents a visual representation of the fibre orientation behaviour around the reinforced hole with an increase in strain. The mean of the AoLP of the fibres at 0 % strain changes from (87.46° ± 0.08) to (87.04° ± 0.47) with increasing strain to 2.12 %.

Table 5.2 - The mean of the AoLP and standard deviation results in the corresponding strain after applying the Gaussian curve fitting to the fibres' orientation images of two layers UD-NCF sample, (sample-3), with a 12 mm machined hole that were captured during tensile testing, (Figure 5.5).

The mean of AoLP (degree)	Standard deviation (the width of the peak)	Strain (%)
87.46 ± 0.08	2.64 ± 0.12	0
86.48 ± 0.45	3.77 ± 0.64	0.01
86.85 ± 0.44	3.67 ± 0.62	0.55
87.70 ± 0.41	3.30 ± 0.58	1.10
87.64 ± 0.44	3.52 ± 0.62	1.64
87.04 ± 0.46	3.89 ± 0.66	2.12
87.52 ± 0.47	3.82 ± 0.65	2.18
86.71 ± 0.51	4.18 ± 0.73	2.27

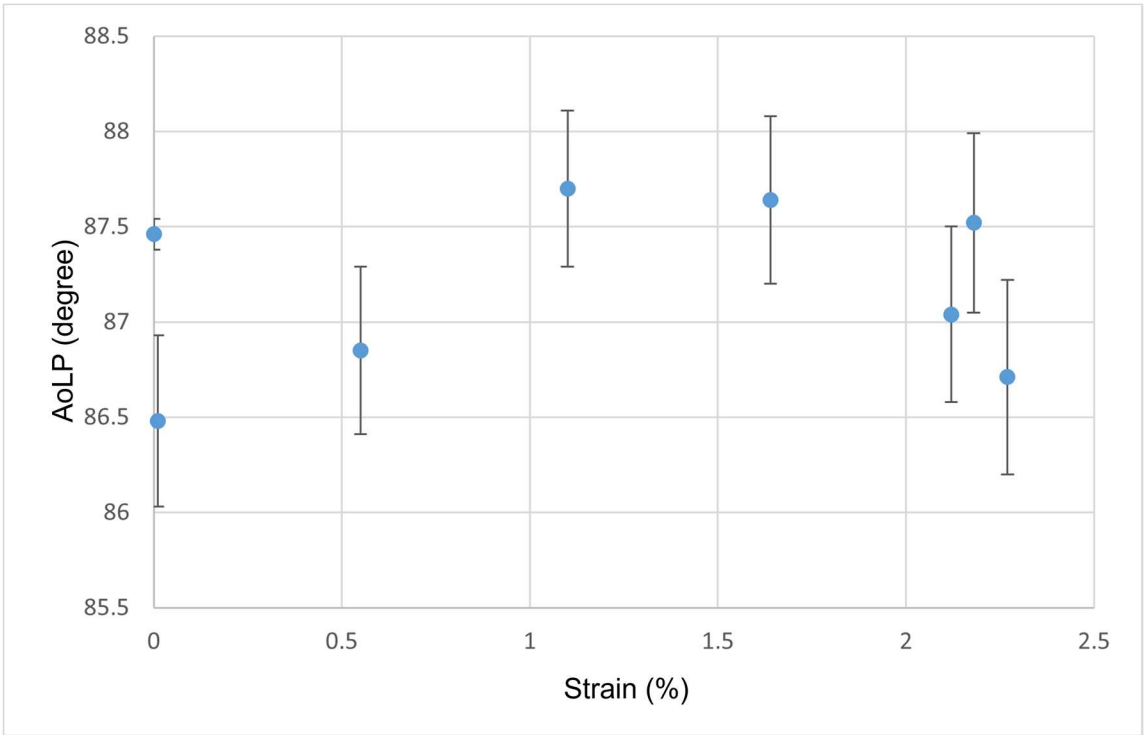


Figure 5.13 - The mean of the AoLP changes behaviour for UD-NCF sample, (sample-3), containing a 12 mm machined hole with increasing strain (for the eight selected images in Figure 5.5).

Figure 5.14 represents the behaviour changes in the fibre orientation by the AoLP data during tensile testing, Figure 5.5, for all the fibre orientation images captured using the polarisation camera. The data points representing the fibre orientation with increasing strain, shown in red, are obtained using the standard MATLAB algorithm and fitting application, where the fitting was applied for each image individually. The data points in blue represent the fibre orientation behaviour for all captured images during tensile testing for the same sample using Python.

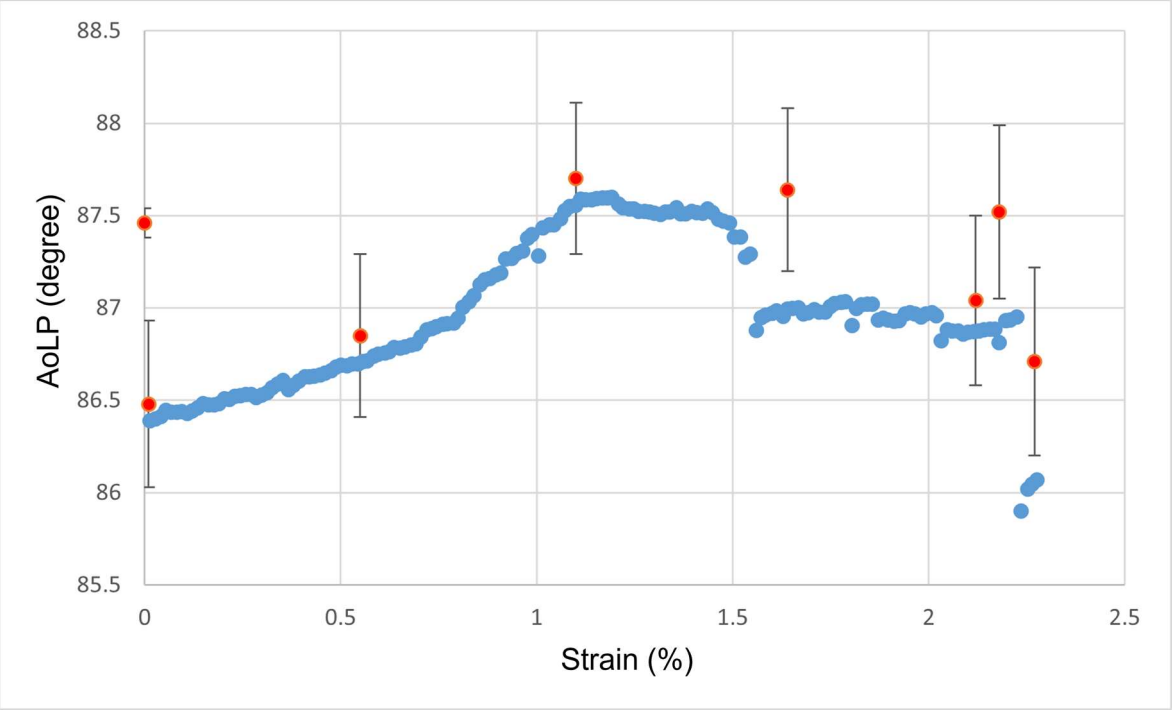


Figure 5.14 - The mean of the AoLP behaviour for the UD-NCF sample, (sample-3), with a 12 mm machined hole. The data in red are presenting the fibre orientation for the selected fibre orientation images (Figure 5.5), while data in blue are presenting the fibre orientation for all captured images.

Figure 5.15 presents the stress-strain curves for three UD-NCF carbon fibre samples consisting of two layers with a 12 mm diameter hole. The curves illustrate the distinct stages of material behaviour observed during the tensile test. The initial stage (stage 1) shows the expected linear rise in stress with increasing strain. This is followed by a transition point (stage 2) marked by dips and recovery in the stress with strain increased, which is caused by the fibre splitting and stitching breakage, until reaching the failure point. Visual confirmation of fibre splitting, which is

influenced by the weakened weft direction due to thermoplastic breakage, is provided in Figure 5.5 (images e-g).

The fibre orientation images that show the fibre's behaviour with increasing strain and at the dips in the stress for the sample shown in Figure 5.5 (sample-3) are presented in Figure 5.16. The fibre orientation images at the dips show the fibre splitting at the edge of the machined hole (b), which in turn influences the fibre orientations near the splitting along the tension direction. The fibre orientation (c) shows the changes in the orientation of the fibres at the edge of the machined hole (in the vertical direction), as well as fibre splitting at the edge of the sample. Image (d) shows the fibre splitting in different areas in the sample and the deformation in the machined hole before the total failure.

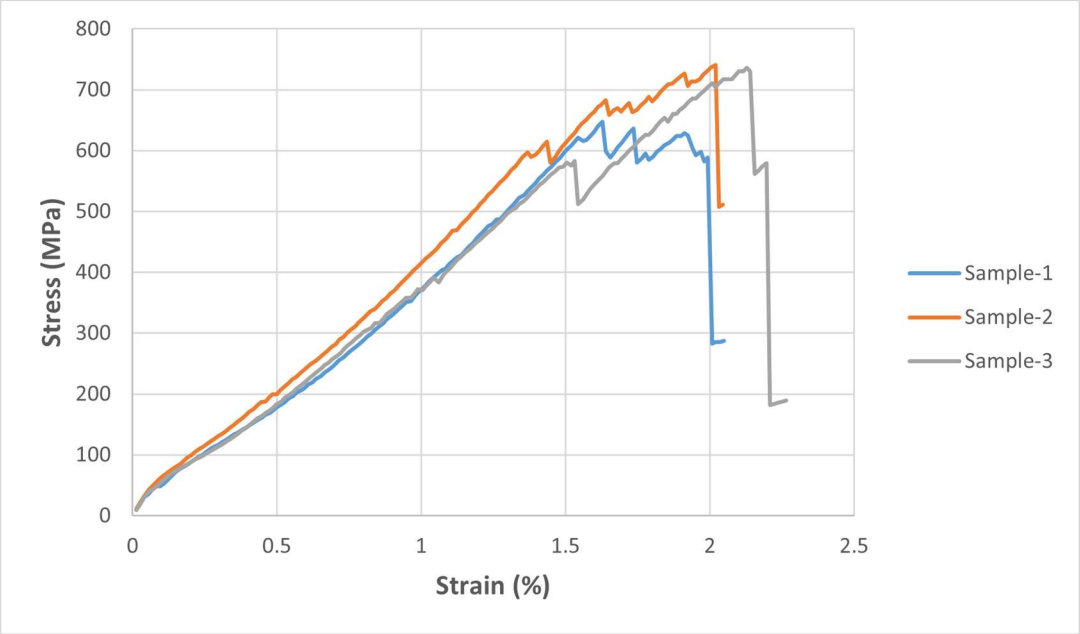


Figure 5.15 - The stress and strain curve for three samples of UD-NCF carbon fibre with a 12 mm hole diameter and consisting of two layers.

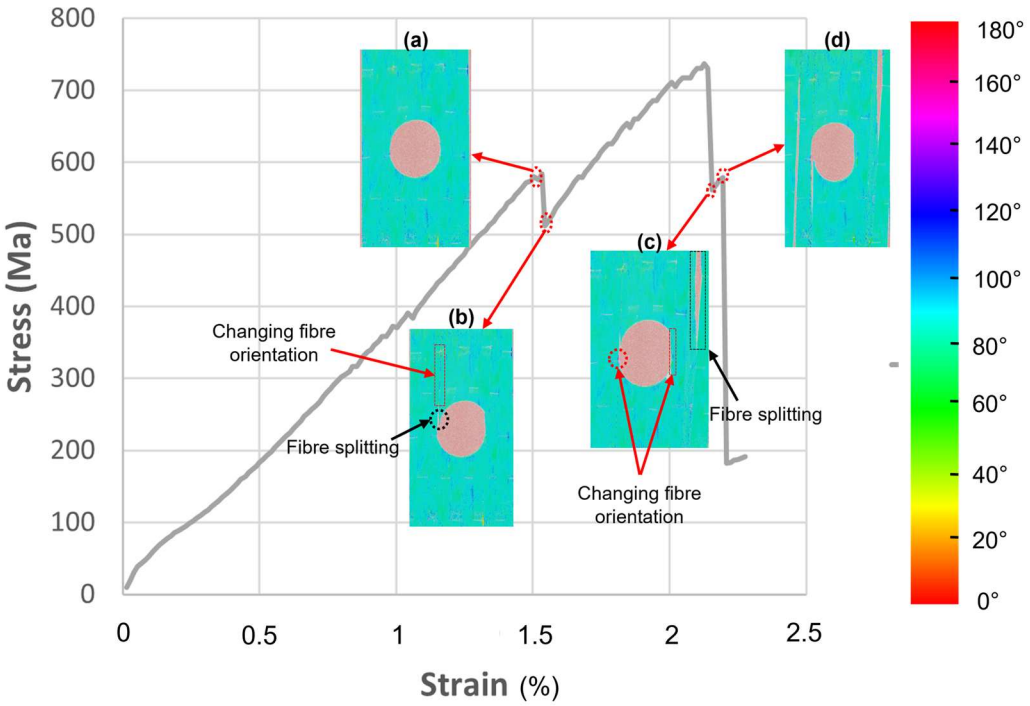


Figure 5.16 - The stress and strain curve for the UD-NCF sample with a 12 mm machined hole (sample-3) and the fibre orientation images representing the dips with increasing the stress are presented.

To conclude the findings obtained from the results of the UD-NCF samples with a 12 mm machined hole, the outcomes strongly indicate that the relative position of the machined hole with respect to the weft material significantly influences the mechanical performance. When the weft yarns are positioned close to the machined hole, as observed in sample (1), local fibre curvature and waviness are introduced near the hole edge, thereby leading to a reduction in the mechanical properties. However, as previously discussed, further investigation is required to validate this hypothesis and to optimise the placement of the machined hole through detailed analysis of the DoLP images.

Following the 12 mm hole sample analysis, the same investigative process were applied to UD-NCF samples with a 10 mm hole diameter (Figure 5.17).

Before tensile testing, the samples were again captured using a polarisation camera for (offline inspection). The captured data, including raw saturation, degree of linear polarisation (DoLP), and the fibre orientation image, are presented in Figure 5.18 (a-c), respectively. The yellow area in the raw saturation image shows the

overexposed area, which is in the background and does not affect the sample's surface.

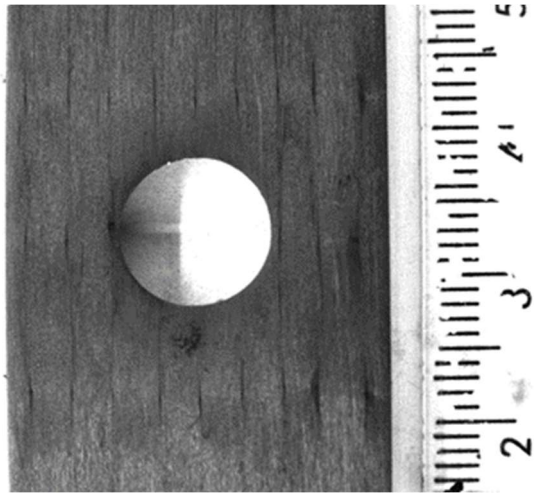


Figure 5.17 - The raw image of the two layers UD-NCF sample with a 10 mm hole diameter captured using the polarisation camera.

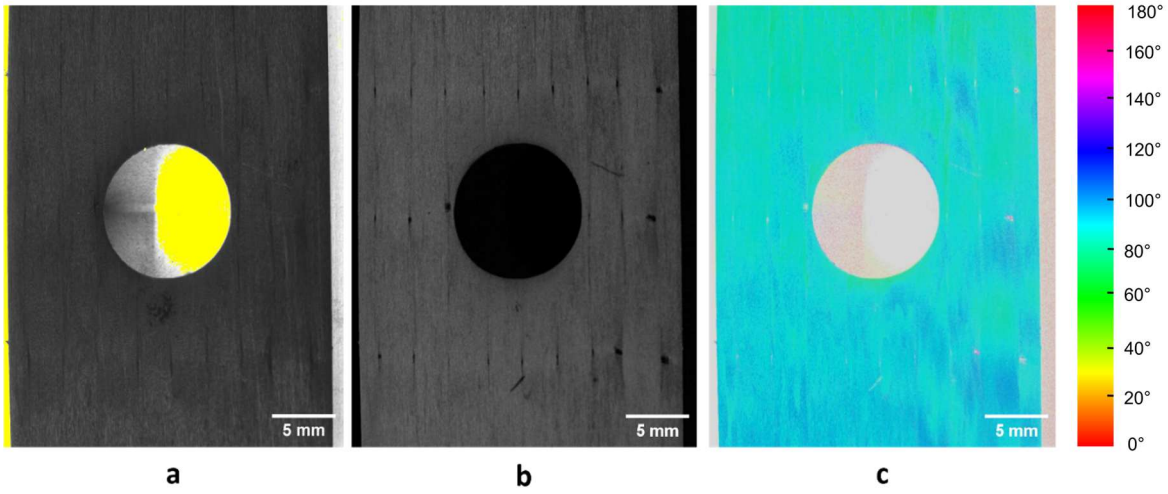


Figure 5.18 - A two layers UD-NCF sample, (sample-2), with 10 mm hole diameter imaged using the polarisation camera, where images (a-c) are the raw saturation, DoLP and fibre orientation images, respectively.

Figure 5.19 shows selected fibre' orientation images captured during tensile testing using the polarisation camera for the two layers UD-NCF sample, (sample-2), with 10 mm machined hole. Image (a) shows the initial state of the sample before testing at 0 % strain. Image (b) shows the sample one second after the test started at strain equals 0.01 %. Image (f) is captured at maximum load force with 1.86 % strain, while image (g) shows the sample after failure.

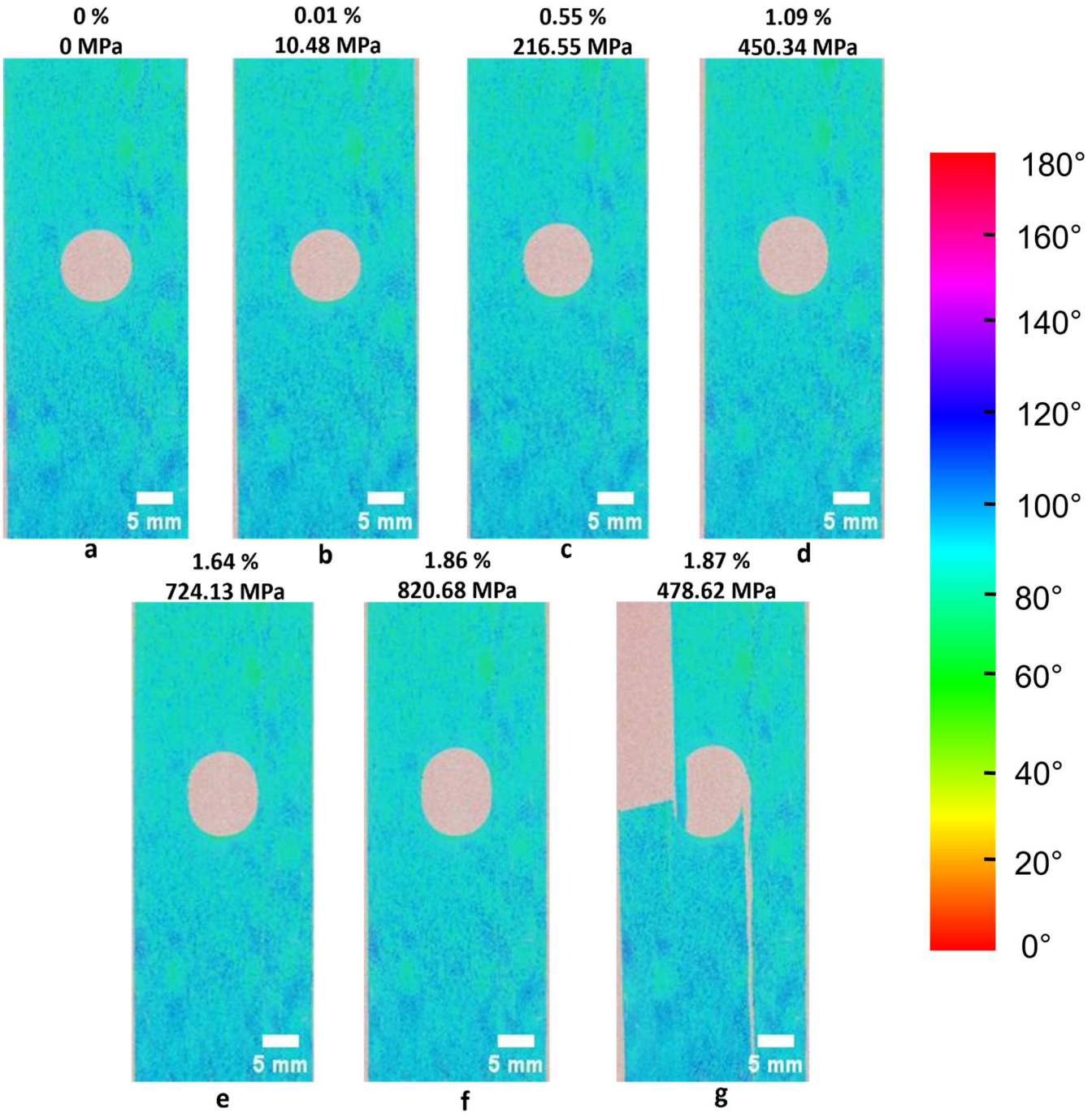


Figure 5.19 - Fibre orientation images of two layers UD-NCF sample, (sample-2), with a 10 mm hole captured during the tensile test using the polarisation camera. The stress and strain corresponding to each image during the test are presented above the figure.

To examine the change behaviour of fibre orientations under increasing strain, Figure 5.20-a presents selected regions of interest within fibre orientation images around the 10 mm machined hole. These regions were captured before the initiation

of the test (at 0 % strain) and at 1.86% strain. Figure 5.20-b illustrates the corresponding histograms of the AoLP data extracted from these fibre orientation images, where AoLP is encoded within the hue channel.

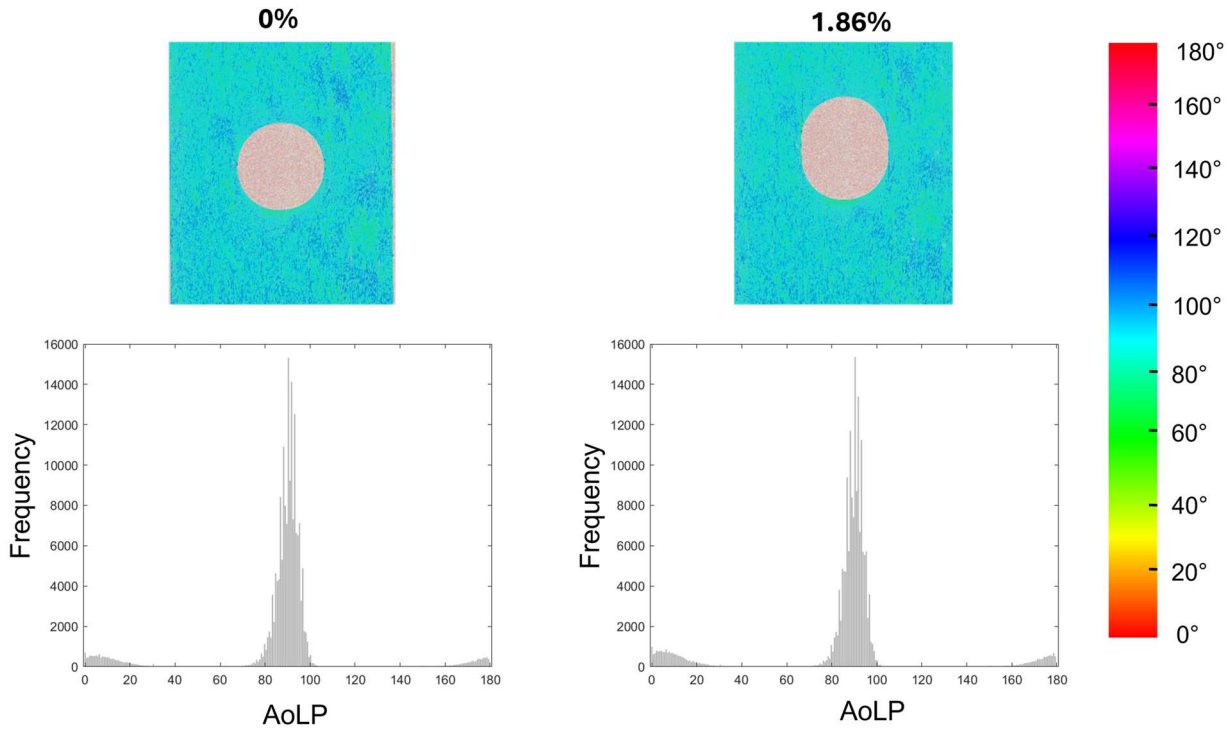


Figure 5.20 - The selected region of interest around the 10 mm machined hole of the UD-NCF sample consists of two layers, where (a) shows the fibres' orientation image at different strains and (b) represents the corresponding histogram of the AoLP data.

Figure 5.21 illustrates the outcomes of fitting a Gaussian curve to the AoLP data, enabling a comparative analysis of the mean AoLP at 0% and 1.86% strain. The mean AoLP at 0% strain was determined to be 90.79° ± 0.71 with a standard deviation of 5.68° ± 1.00. Conversely, when the strain reached 1.86%, the mean AoLP was observed to be 90.29° ± 0.69 with a standard deviation of 5.55° ± 0.98.

To further explore the changing behaviour of fibre orientation behaviour under increasing strain, the fibre orientations within the selected region of interest surrounding the machined hole were separated at 0 % and 1.86 % strain. Figure 5.22 depicts the outcomes of the fibre orientation separation, revealing that a significant proportion of fibres exhibit orientations within the range of 85° to 95°.

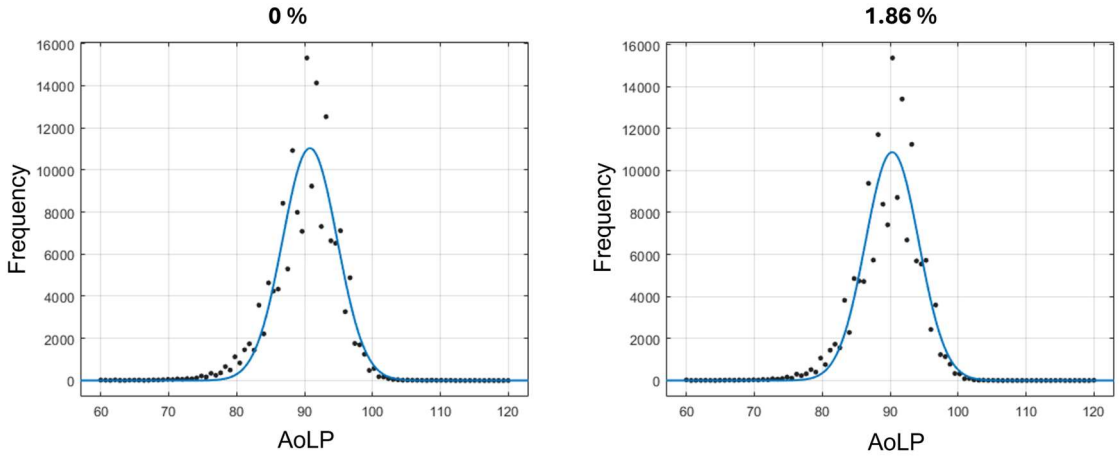


Figure 5.21 - MATLAB fitting of Gaussian curve to the histogram data of two layers UD-NCF sample with 10 mm machined hole at 0 % and 1.86 % strain.

Within the 0 % strain fibre orientation image, fibres exhibiting orientations between 85° and 90° occupied 40.14 % of the total image area, whereas fibres with orientations between 90° and 95° accounted for 40.31 %. Upon increasing strain to 1.86 %, fibres with orientations between 85° and 90° presented 42.10 %, while fibres oriented between 90° and 95° show 36.40 % of the total image's area.

The fibre orientation separation process provides more detail about small changes in the fibre orientations with increasing strain. The figure shows the fibre orientation changes when strain increases (in red circles) from 0 % and reaches 1.86 %. Fibres with orientations between (80° - 85°) and (95° - 100°) changes to have orientations between (85° - 90°) and (90° - 95°).

Table 5.3 summarises the maximum load, tensile strength, failure strain, and tensile modulus for the two layers UD-NCF tested samples containing a 10 mm diameter hole. The results exhibit variability between the three specimens, which could be caused by the hole's positional differences from the weft material between the samples. As observed in the UD-NCF sample with a 12 mm machined hole, the results reveal noticeable variations in the maximum force and ultimate tensile strength (UTS) among the three tested specimens. Sample (3) exhibited the highest UTS, which can be attributed to its comparable hole position relative to the weft material, similar to that of the 12 mm sample, as illustrated in Figure 5.23. Although Sample (2) has the weft material positioned centrally, as in Sample (3) (red box

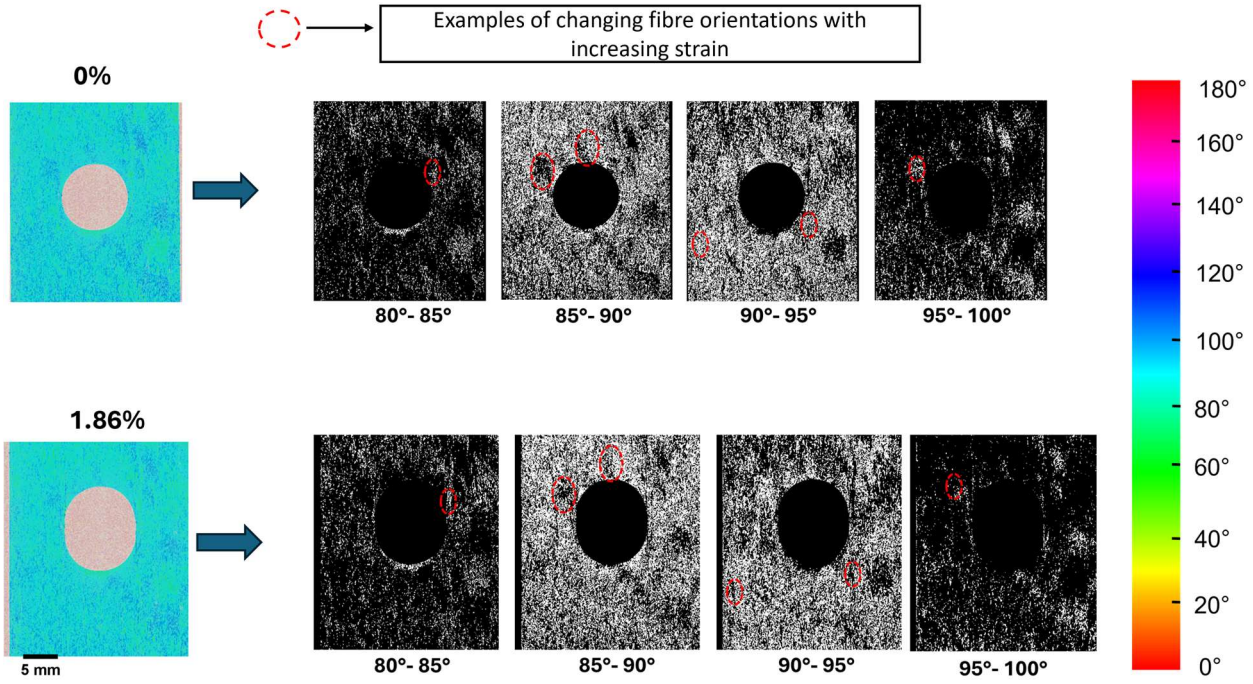


Figure 5.22 - Separating the fibre orientation of the selected region image in the two layers UD-NCF sample, (sample-2), with a 10 mm machined hole at 0 % and 1.86 % strain using a colour threshold.

Table 5.3 - The mechanical properties of three UD-NCF samples consist of two layers and contain a 10 mm hole diameter.

Sample Number	Maximum force (N)	Ultimate tensile strength (MPa)	Strain at break (%)	E-modulus (GPa)
Sample-1	11700	806.89	1.73	46.48
Sample-2	11900	820.68	1.86	44.12
Sample-3	15700	872.22	2.03	42.83
Average	13100	833.26	1.87	44.48
Standard Deviation	2253.88	34.43	0.15	1.84

labelled (b)), the fibres around the left-side machined hole are situated above the weft material. This configuration induces local waviness and curvature in the fibres aligned with the loading direction. As previously discussed, further investigation is required to verify this hypothesis through detailed analysis of the DoLP images, with the aim of optimising the machined-hole position and thereby enhancing the mechanical performance.

Figure 5.23 shows the DoLP images for samples 1, 2, and 3, as an illustrative example. The red rectangles, labelled (a.), show the distance difference between the weft material and the machined hole in the three samples. Sample (1) shows that the weft material is close to the machined hole's edge, which causes curvature from the weaving pattern near the machined hole edge. The red boxes, labelled (b), show the weft material at the left edge of the machined hole, showing that the position of the stitching is different between the three samples. Also, the red box shows that the weft material near the machined hole edge sample (2), unlike samples (1 and 3), is under carbon fibre (because of the weaving pattern).

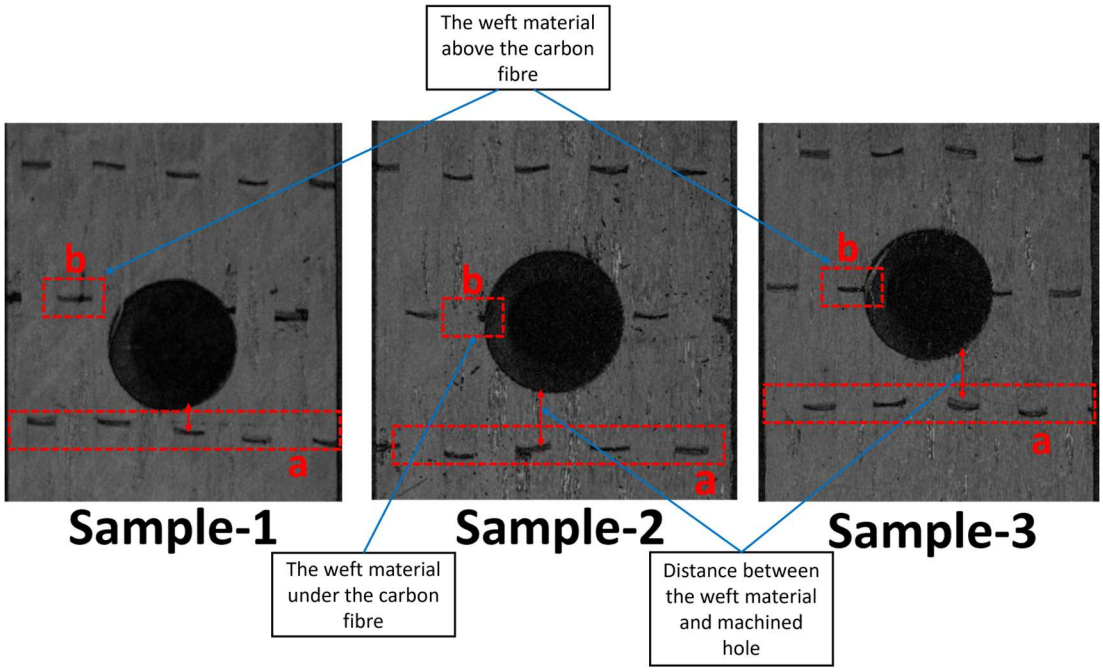


Figure 5.23 - DoLP images for three samples of UD-NCF with a 10 mm hole were captured using the polarisation camera, showing the difference in the warp and weft materials after the machining process.

Table 5.4 represents the mean of the AoLP and the standard deviation for the fibre orientation images during the tensile testing, Figure 5.19, after applying the Gaussian fitting curve. The mean of the AoLP of the UD-NCF sample with a 10 mm machined hole shows the change behaviour in fibre orientation with an increase in the strain. Figure 5.24 represents the fibre orientation behaviour around the reinforced hole with increasing strain. The mean of the AoLP of the fibres at 0 % strain changes from (90.79° ± 0.71) to (90.29° ± 0.69) with increasing strain to 1.86 %.

Table 5.4 - The mean of the AoLP and standard deviation results in the corresponding strain after applying the Gaussian curve fitting to the fibres' orientation images of two layers UD-NCF sample, (sample-2), with a 10 mm machined hole that were captured during tensile testing, (Figure 5.19).

The mean of AoLP (degree)	Standard deviation (the width of the peak)	Strain (%)
90.79 ± 0.71	5.68 ± 1.00	0
90.81 ± 0.71	5.70 ± 1.01	0.01
90.40 ± 0.68	5.52 ± 0.96	0.55
90.70 ± 0.70	5.61 ± 0.98	1.09
90.18 ± 0.71	5.67 ± 1.00	1.64
90.29 ± 0.69	5.55 ± 0.98	1.86
90.96 ± 0.73	5.89 ± 1.03	1.87

The stress-strain curves for the UD-NCF samples with a 10 mm hole diameter are presented in Figure 5.25. The dips and recovery in the stress with an increase in the strain indicates that fibre splitting occurred in the early stage compared with the UD-NCF sample with 12 mm. The fibre orientation images illustrating what happened to the fibre orientations at the dips are shown in Figure 5.26. The fibre orientation image (b) shows the initiation stage of the fibre splitting at the edge of the machined hole. The fibre orientation image (c) shows the change in the fibre

orientation at the edge of the machined hole (in the vertical direction). Although fewer fibres were removed in the 10 mm machined-hole specimen, fibre splitting occurred earlier than in the 12 mm specimen, primarily due to the fracture of the weft material under increasing strain. Crack initiation in the machined-hole specimen typically begins at the edge of the hole, where the local discontinuity in the fibres generates a stress concentration. Variations in fibre geometry and orientation at the hole edge between the 12 mm and 10 mm specimens influenced the overall mechanical performance and fibre-splitting behaviour. The geometry of the remaining fibres after machining directly affected the alignment of fibres in the loading direction, leading to a reduction in the mechanical properties of the tested specimens (as discussed in **Section 2.5**). Thus, the relative position of the machined hole with respect to the weft material played a significant role in determining the structural response. Optimising this positioning could therefore enhance the mechanical performance of the composite specimens.

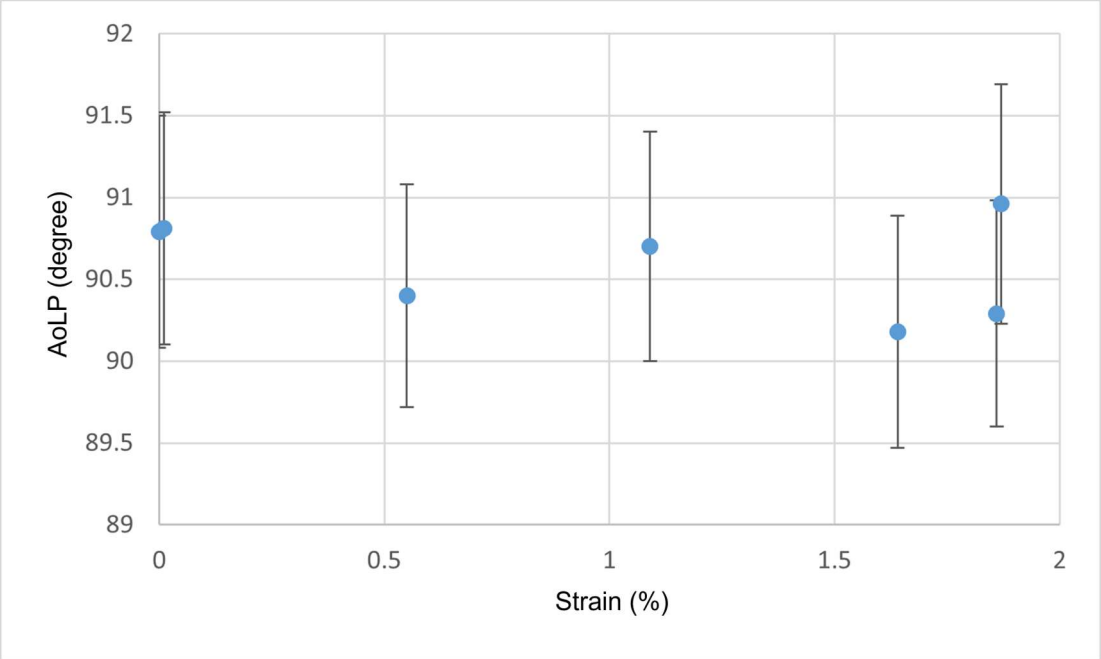


Figure 5.24 - The mean of the AoLP changes behaviour for UD-NCF sample, (sample-2), with a 10 mm machined hole with increasing strain (for the seven selected images in Figure 5.19).

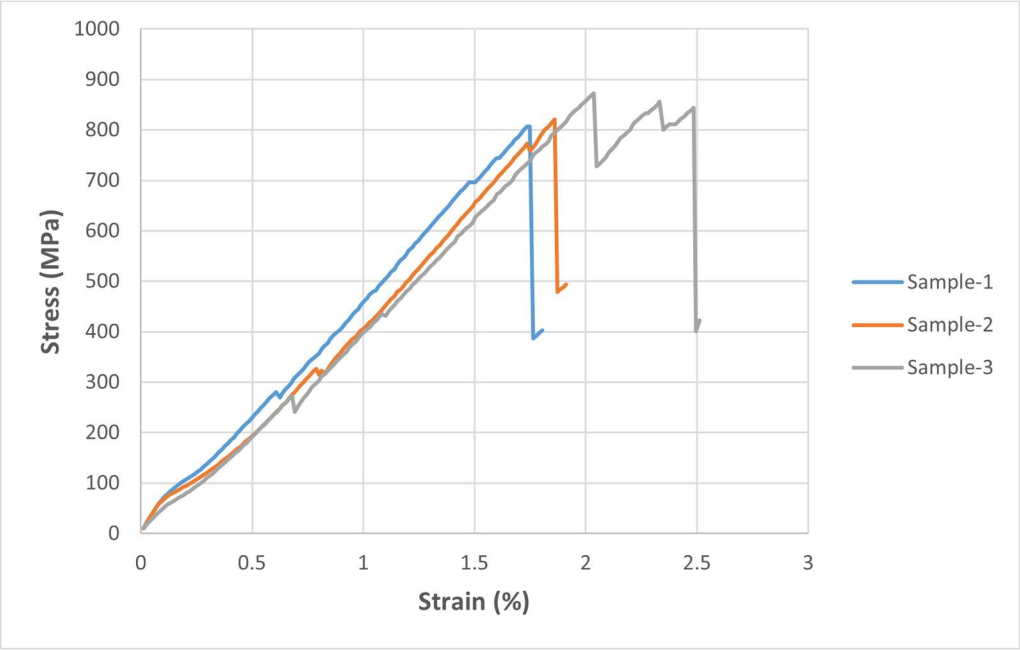


Figure 5.25 - The stress and strain curve for three samples of UD-NCF carbon fibre with a 10 mm machined hole and consisting of two layers.

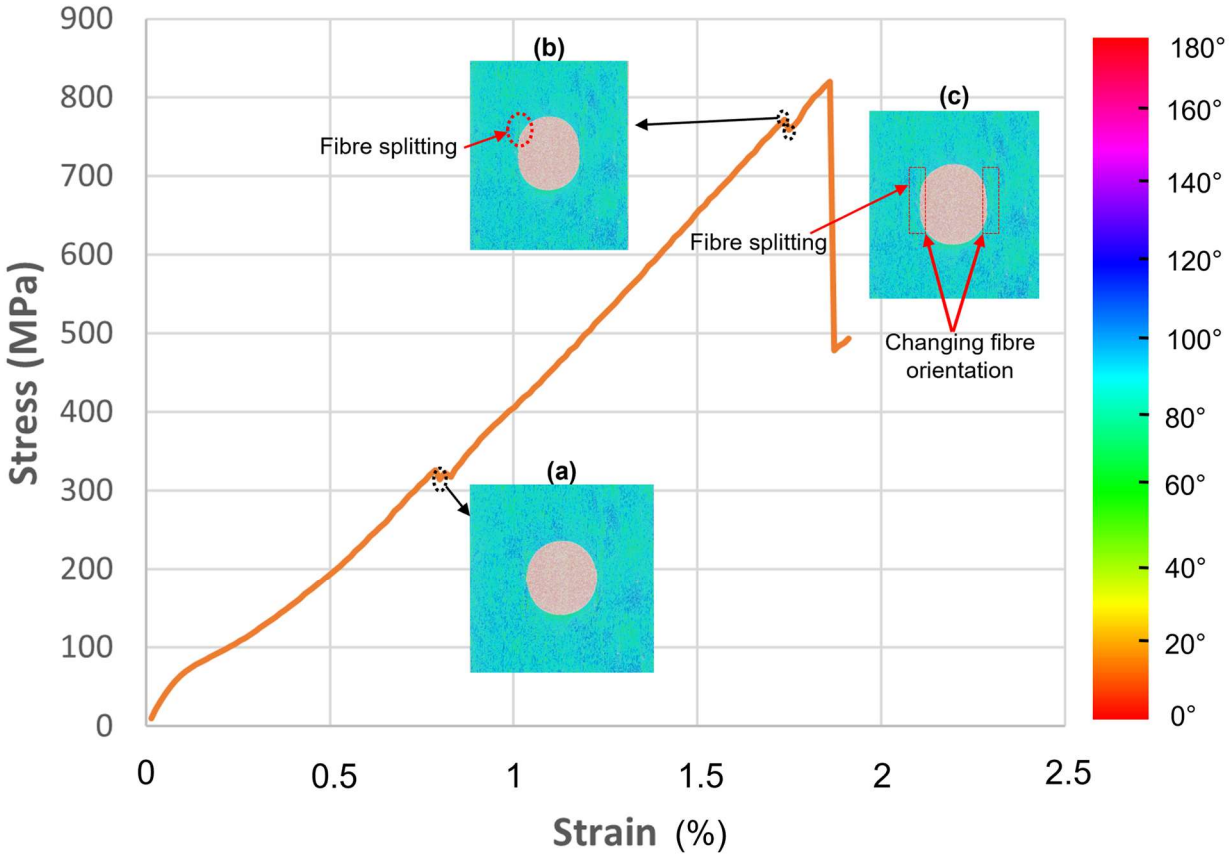


Figure 5.26 - The stress and strain curve for the UD-NCF sample with a 10 mm machined hole (sample-2) and the fibre orientation images representing the dips with increasing the stress are presented.

The final sample set of the UD-NCF samples has an 8 mm hole diameter, (sample-1), as shown in Figure 5.27. These samples will undergo the same investigative process as the 12 mm and 10 mm diameter samples. Before tensile testing, the samples were captured using the polarisation camera and the corresponding raw saturation, degree of linear polarisation (DoLP), and the fibre orientation images are presented in Figure 5.28 (a-c), respectively. The colours in Figure 5.28-c represent the carbon fibre orientations using the hue channel information, which encodes the AoLP.

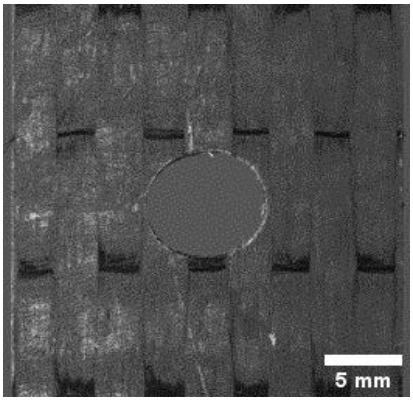


Figure 5.27 - An example of the raw image of a UD-NCF sample with an 8 mm hole diameter and consisting of two layers was imaged using the polarisation camera.

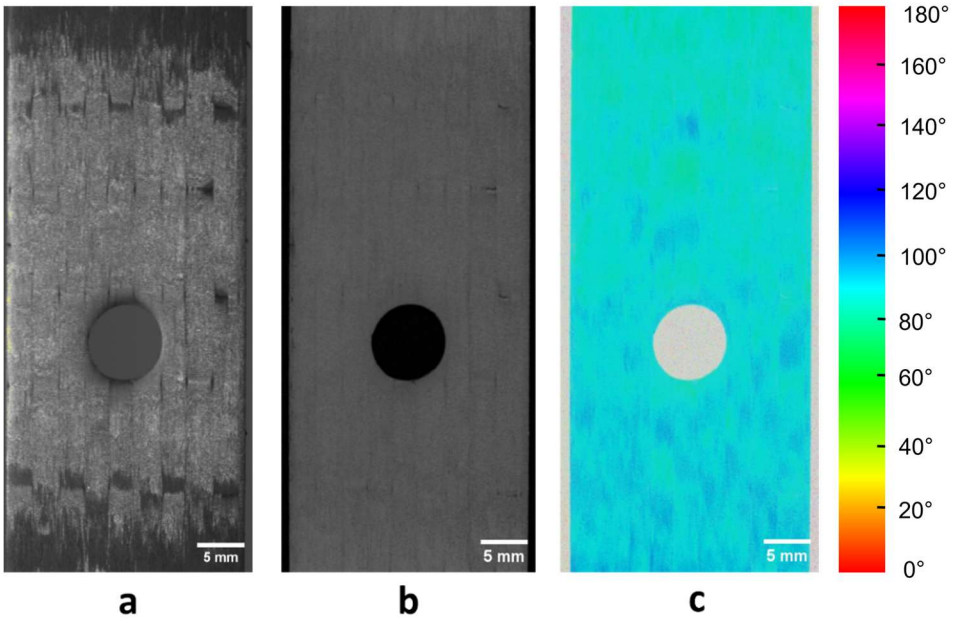


Figure 5.28 - The two layers UD-NCF sample, (sample-1), with an 8 mm hole diameter was captured using the polarisation camera, where images (a-c) are the raw saturation, DoLP and fibre orientation images, respectively.

Figure 5.29 shows a sequence of images of the two layers UD-NCF sample, (sample-1), with an 8 mm hole diameter representing carbon fibre's orientation captured during the tensile test. Image (a) shows the initial state of the sample (0 % strain), while image (b) shows the sample one second after test initiation (at strain equal 0.01 %). Images (c-f) were captured at 40-second intervals throughout the test. Image (g) represents the sample at maximum force load (at strain equal 2.70 %), and image (h) shows the sample five seconds after reaching the maximum force load (strain 2.76 %).

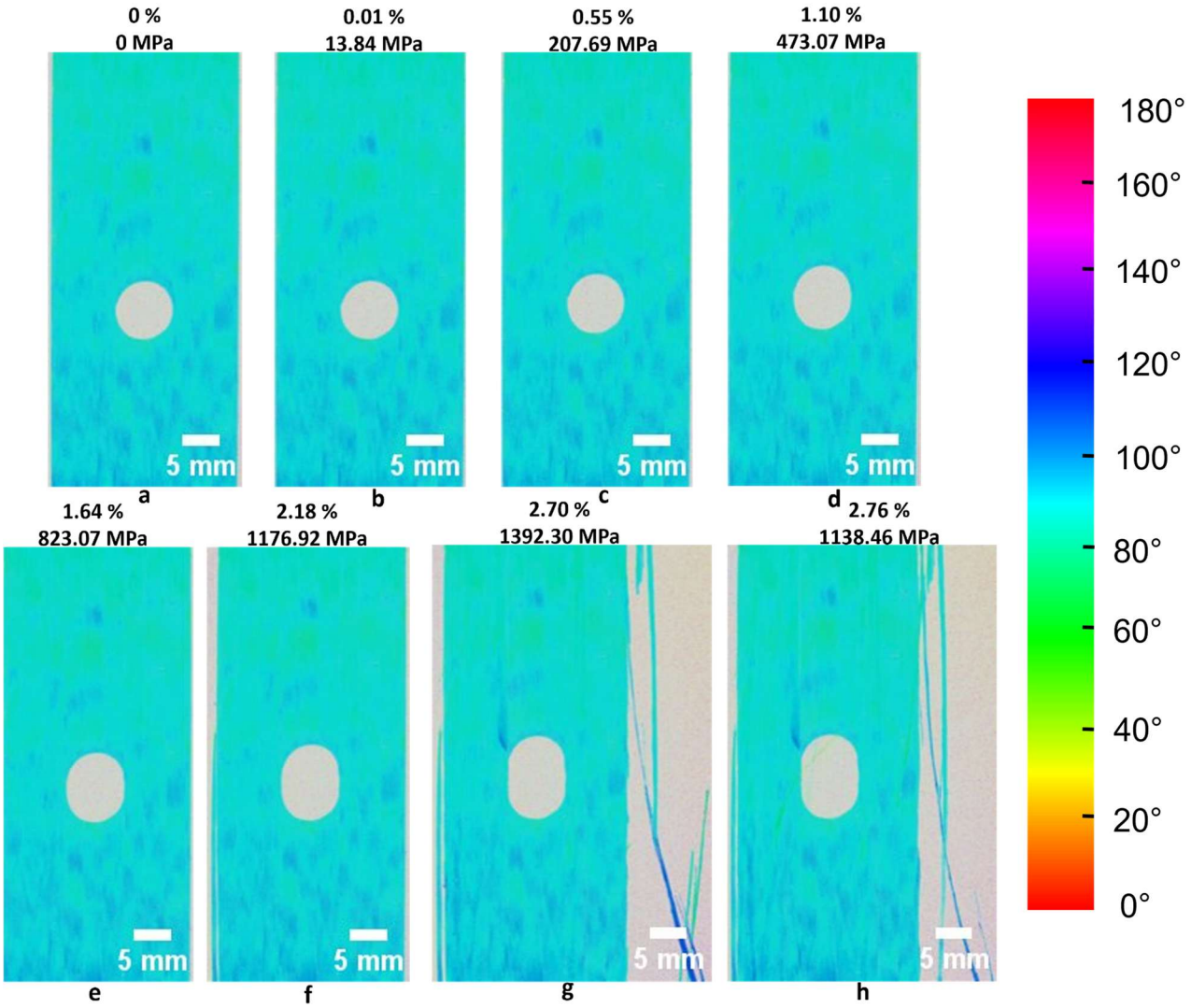


Figure 5.29 - Fibre orientation images of the two layers UD-NCF sample, (sample-1), with an 8 mm hole representing the orientation of the fibres before and during the tensile test. The stress and strain corresponding to each image during the test are presented above the figure.

Figure 5.30-a shows the selected area around the machined hole of the fibre orientation images at different strains to investigate the orientation behaviour with increasing strain, while Figure 5.30-b represents the corresponding histogram of the AoLP data. The histogram shows that the fibre orientations are distributed between 85° and 95°.

Figure 5.31 shows the AoLP data after fitting a Gaussian curve, enabling a comparative analysis of the mean AoLP at 0 % and 2.70 % strain by calculating the mean of the AoLP. The mean AoLP at 0% strain was determined to be 90.21° ± 0.39 with a standard deviation of 2.74° ± 0.55. However, when the strain reached 2.70%, the mean of the AoLP was 90.14° ± 0.41 with a standard deviation of 2.94° ± 0.59.

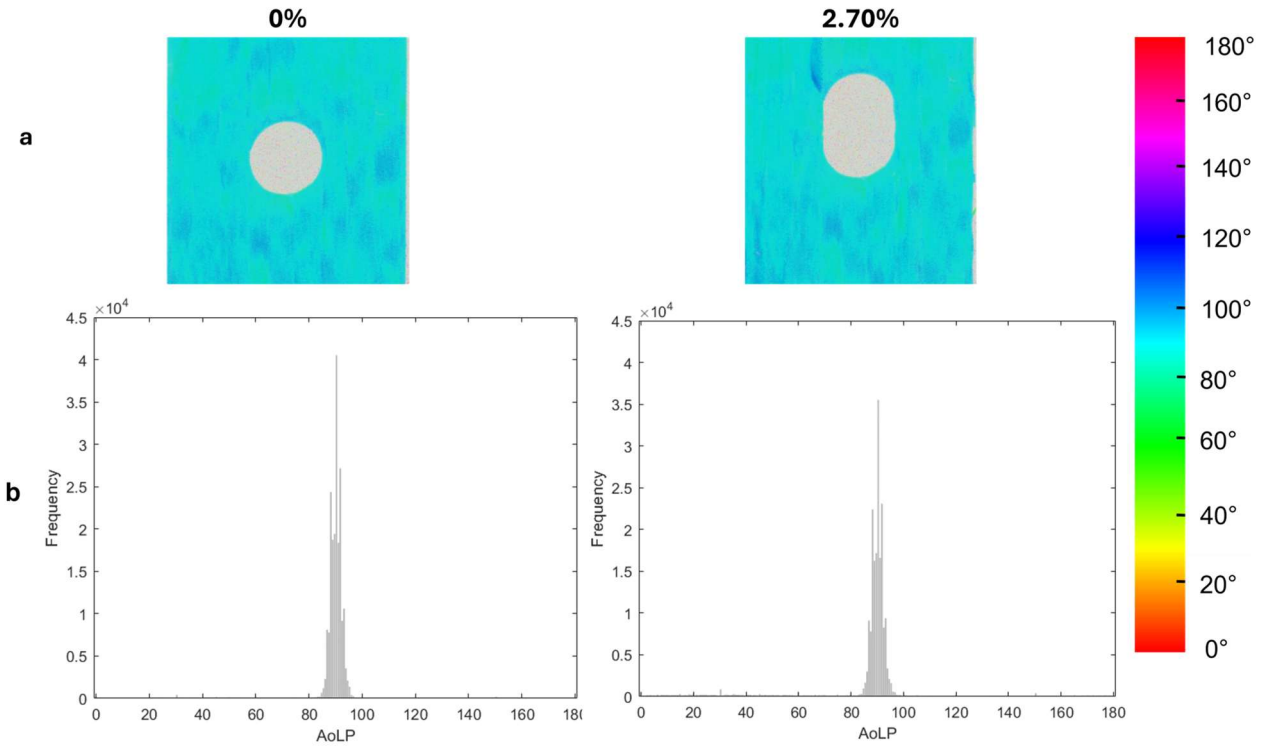


Figure 5.30 - The selected region of interest around the 8 mm machined hole of the UD-NCF sample consists of two layers, where (a) shows the fibres' orientation image at different strains and (b) represents the corresponding histogram of the AoLP data.

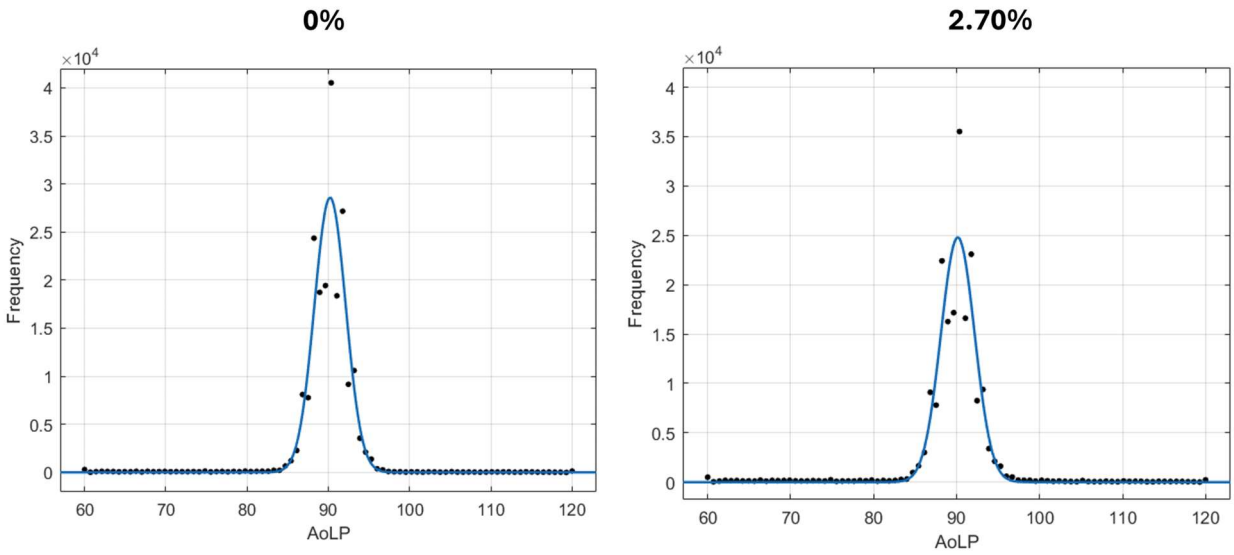


Figure 5.31 - MATLAB fitting of Gaussian to the histogram data of two layers UD-NCF sample with an 8 mm machined hole at 0 % and 2.70 % strain.

To have a better understanding of the changing behaviour of the fibre orientations around the machined hole with increasing strain, the fibre orientations were separated at 0 % and 2.70 % strain using the colour threshold. Figure 5.32 shows the results after separating the fibre orientations at the different strains, showing that a higher percentage of the fibres have orientations between 85° and 90°.
In the fibre orientation image with 0 % strain, fibres exhibiting orientations between 85° and 90° presented 65.11 % of the total image's area, whereas fibres with orientations between 90° and 95° obtained a percentage of 42.79 %. With increasing strain to 2.70 %, fibres with orientations between 85° and 90° presented 60.17 %, while fibres oriented between 90° and 95° show 38.21 % of the total image's area.

The fibre orientation separation process provides greater detail regarding slight variations in fibre orientation with increasing strain. The figure shows (in red circles) the changes in fibre orientation around the machined hole, where with strain increased, fibres with orientations between 85° and 90° at the edge of the machined hole change orientations to 95° and 100°. Also, fibres with orientations between 90° and 95° change to have orientations between 80° and 85° with increasing strain.

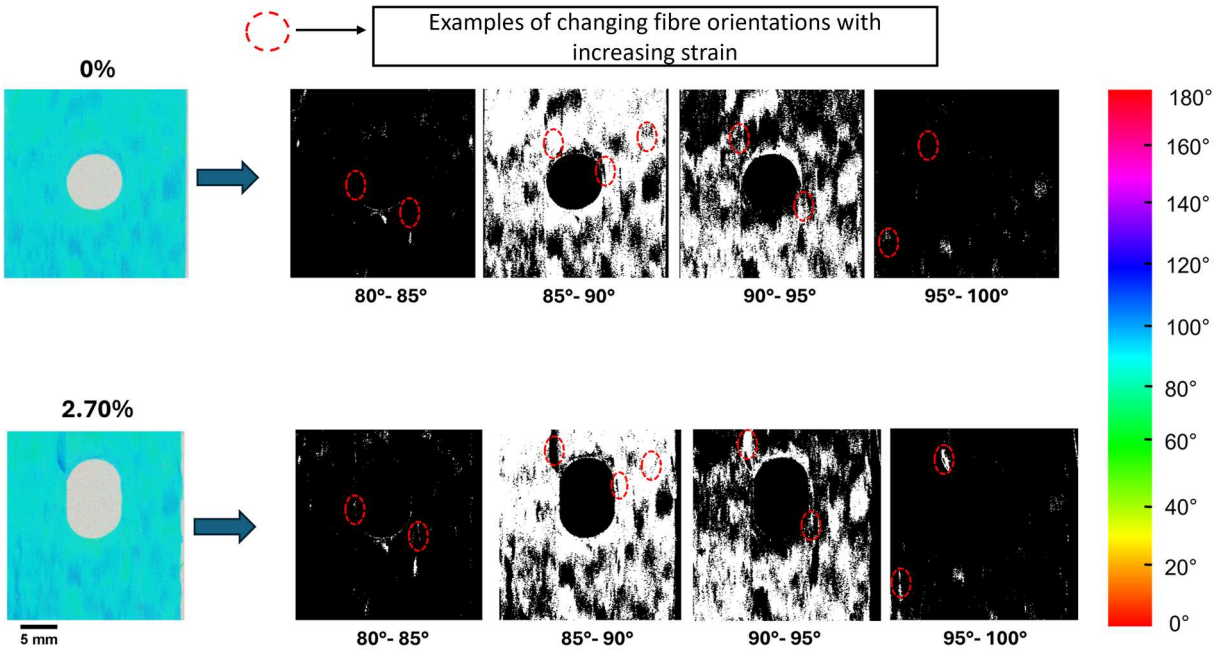


Figure 5.32 - Separating the fibre orientation of the selected region image in the two layers UD-NCF sample, (sample-1), with an 8 mm machined hole at 0 % and 2.70 % strain using a colour threshold.

Table 5.5 summarises the force, tensile strength, failure strain, and tensile modulus for the two layers UD-NCF tested samples containing an 8 mm diameter hole. As the case with the other sample sets, the results show variation between the three samples.

Table 5.5 - The mechanical properties of three UD-NCF samples consist of two layers and contain an 8 mm hole diameter.

Sample Number	Maximum force (N)	Ultimate tensile strength (MPa)	Strain at break (%)	E-modulus (GPa)
Sample-1	18100	1392.30	2.70	51.56
Sample-2	14800	1057.14	2.16	48.93
Sample-3	14200	979.31	2.03	48.09
Average	15700	1142.91	2.29	49.53
Standard Deviation	2100	219.48	0.35	1.80

The mean of the AoLP and the standard deviation for the fibre orientation images during the tensile testing, Figure 5.29, after applying the Gaussian fitting curve, is presented in Table 5.6. The mean of the AoLP of the UD-NCF sample with an 8 mm machined hole shows the change behaviour in the fibre orientation with an increase in the strain. Figure 5.33 visually represents the fibre orientation behaviour around the reinforced hole with increased strain.

The stress-strain curves for the UD-NCF samples with an 8 mm hole diameter are presented in Figure 5.34. The dips and recovery in the stress with increased strain caused by the fibre's splitting during the tensile testing. The curve of the sample (sample-1) presented in Figure 5.29 shows small dips occurring compared with the 12 mm and 10 mm machined hole samples.

Table 5.6 - The mean of the AoLP and standard deviation results in the corresponding strain after applying the Gaussian curve fitting to the fibres' orientation images of two layers UD-NCF sample, (sample-1), with a 8 mm machined hole that were captured during tensile testing, (Figure 5.29).

The mean of AoLP (degree)	Standard deviation (the width of the peak)	Strain (%)
90.21 ± 0.39	2.74 ± 0.55	0
90.21 ± 0.40	2.73 ± 0.55	0.01
90.21 ± 0.41	2.76 ± 0.58	0.55
90.09 ± 0.40	2.74 ± 0.57	1.10
90.18 ± 0.42	2.77 ± 0.59	1.64
90.13 ± 0.41	2.80 ± 0.59	2.18
90.14 ± 0.41	2.87 ± 0.57	2.70
90.03 ± 0.42	2.94 ± 0.59	2.76

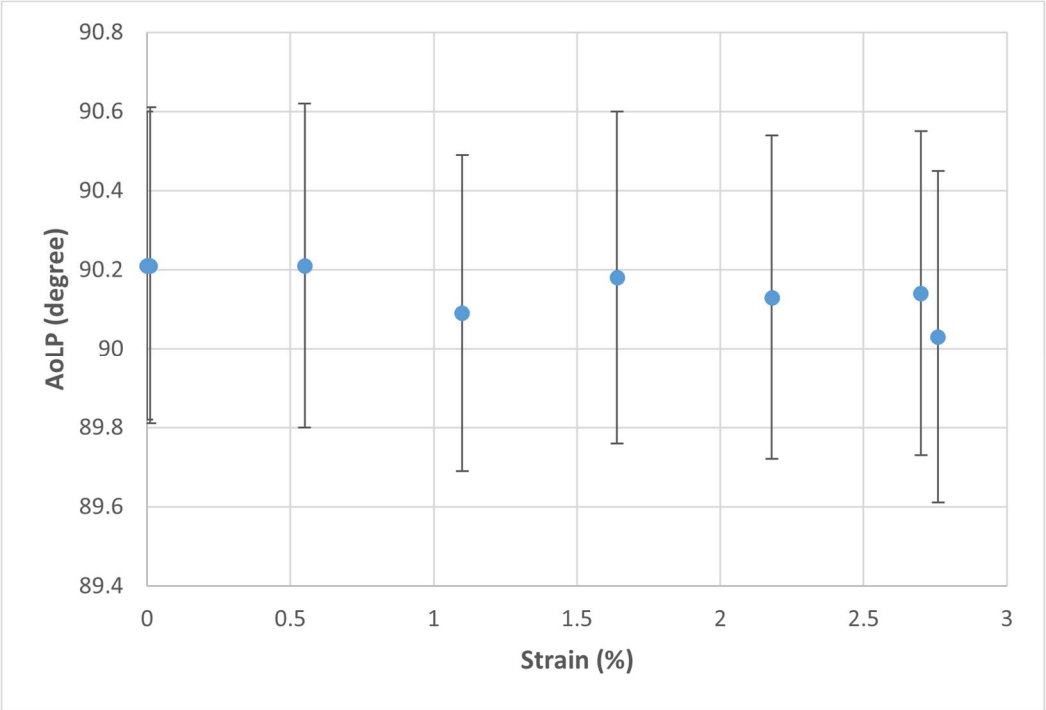


Figure 5.33 - The mean of the AoLP changes behaviour for UD-NCF sample, (sample-1), with an 8 mm machined hole with increasing strain (for the eight selected images in Figure 5.29).

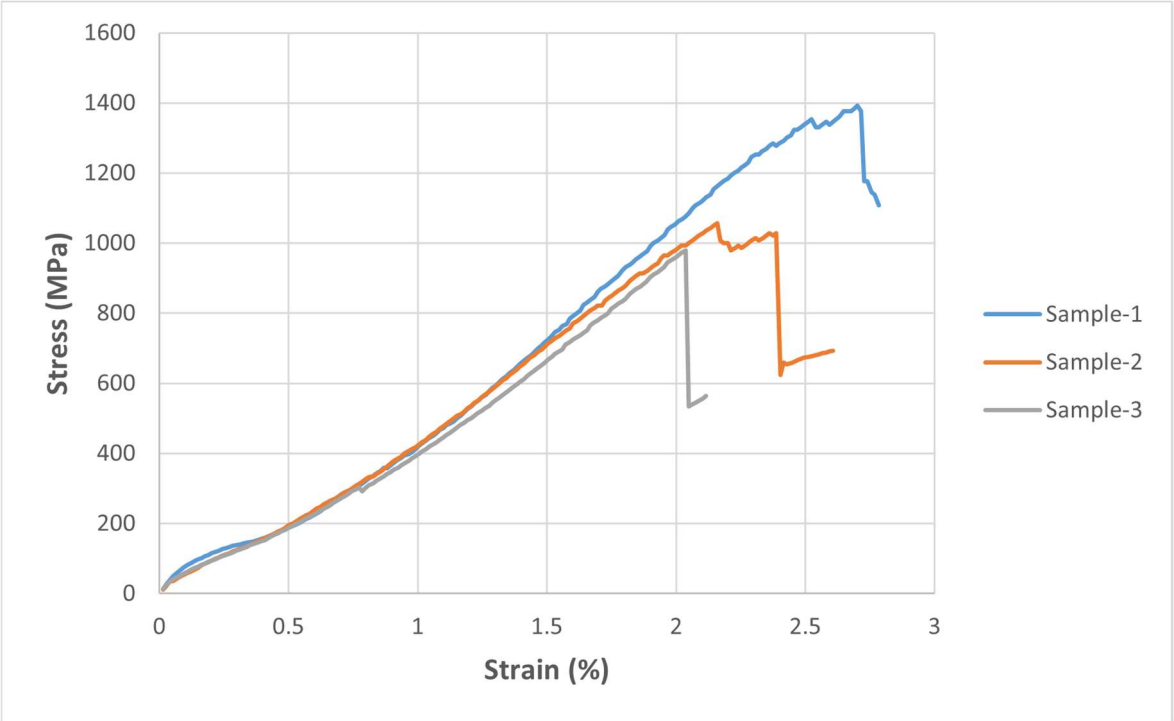


Figure 5.34 - The stress and strain curve for three samples of UD-NCF carbon fibre with an 8 mm machined hole and consisting of two layers.

To summarise the influence of the hole diameter on the elastic modulus of UD-NCF samples, Table 5.7 presents the average, standard deviation, and coefficient of variation for the elastic modulus. As expected, the elastic modulus decreases with increasing hole diameter. The average elastic modulus for samples with an 8 mm hole diameter is 49.53 GPa, while it is only 37.01 GPa for the 12 mm hole diameter samples, which indicates a reduction of 33.14% and 60.62% in the average elastic modulus for the 8 mm and 12 mm hole diameter samples, respectively, compared to the baseline sample. Figure 5.35 shows the average elastic modulus for each hole diameter category. The error bar is the standard deviation for the three samples. The polarisation image analysis indicated that the variations observed between samples with identical hole diameters arose from differences in the hole positioning relative to the weft and warp directions of the textile architecture. Furthermore, the geometry of the remaining fibres along the machined hole edges influenced the evolution of fibre orientation with increasing strain. The hole diameter also affected the mechanical performance of the tested specimens, as larger diameters resulted in the removal of a greater number of fibres during machining.

The insights obtained from this analysis enhance the understanding of fibre orientation behaviour around machined holes and form the basis for the next investigation presented in Chapter 6, which focuses on unidirectional UD-TFP samples with reinforced holes. In that chapter, particular attention will be given to the resin-rich regions that remain around smaller machined holes (8 mm), allowing an assessment of their influence on the mechanical response and local fibre orientation behaviour in UD-TFP reinforced hole specimens.

The polarisation camera captured and presented the change in the behaviour of fibre orientations around the machined hole during tensile testing. Moreover, the polarisation camera detected the initiation of the fibre spitting near the machined hole from the change in the fibre orientation. Furthermore, the DoLP images show the difference between the samples regarding the position of the thermoplastic thread (weft direction) to the edge of the machined hole after machining the hole. The position of the weft material might be a reason for the variation in the results between the samples.

Table 5.7 - The average, standard deviation, and coefficient of variation correspond to the elastic modulus for the baseline and three different hole diameters of UD-NCF samples consisting of two layers.

	Elastic modulus (GPa)		
UD-NCF samples	**Average**	**Standard deviation**	**Coefficient of variation (%)**
Baseline	69.21	9.34	13.49
12mm hole diameter	37.01	2.59	7.00
10mm hole diameter	44.48	1.84	4.15
8mm hole diameter	49.53	1.80	3.65

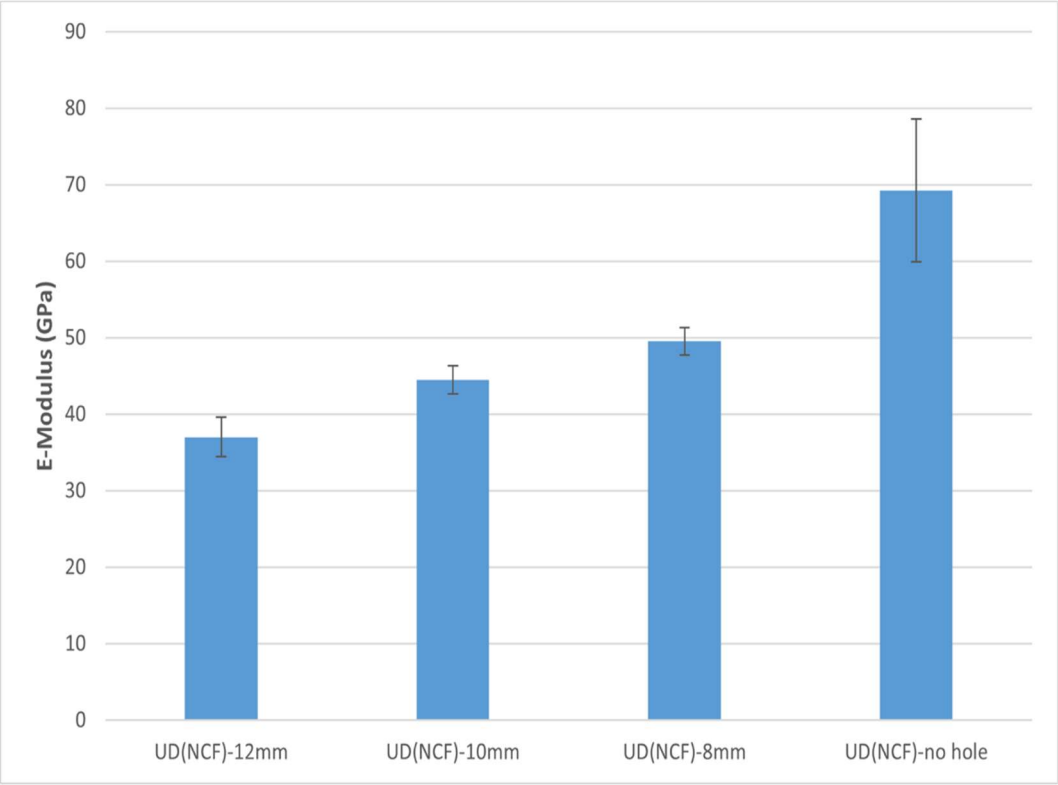


Figure 5.35 - The average modulus (GPa) is shown as a bar chart for UD-NCF samples, baseline (no hole), and different hole diameters (12,10 and 8) mm, with the error bar as the standard deviation for three samples.

5.4 Twill 2x2 carbon fibre

Twill 2x2 carbon fibre samples, consisting of a single layer of fabric, were prepared for tensile testing with three different hole diameters (12 mm, 10 mm, and 8 mm). The first category is the 12 mm hole diameter samples. Before starting tensile testing, the samples were imaged using the polarisation camera (offline inspection).

The captured images, including raw saturation, degree of linear polarisation (DoLP), and fibre orientation, are presented in Figure 5.36 (a-c), respectively. The raw saturation image (a) shows the overexposed regions (in yellow) in the sample's surface caused by the illumination source. The HSV colour map in image (c) provides a comprehensive representation of fibre orientation, where the hue channel encodes the angle of linear polarisation (AoLP), and the saturation channel encodes the DoLP. The value channel will not be used for these images. Fibres oriented at 0°, perpendicular to the applied tension (weft direction), are depicted in red, whereas fibres oriented at 90° (warp direction) are presented in cyan.

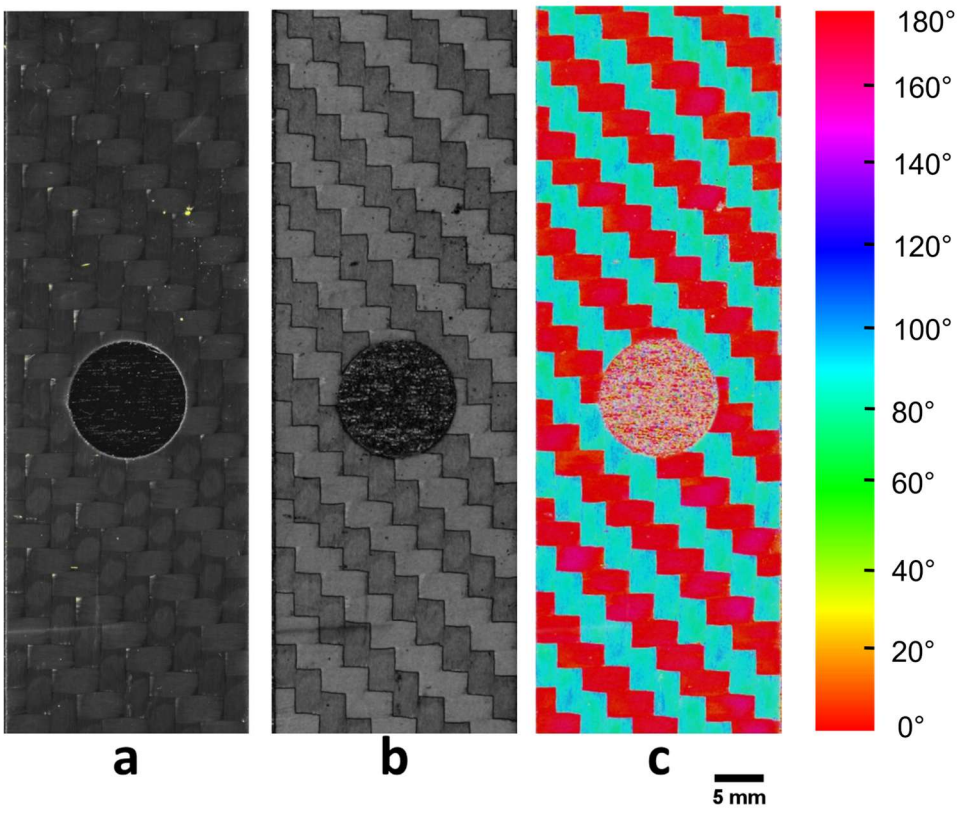


Figure 5.36 - Twill 2x2 sample, (sample-3), consisting of one layer, with a 12 mm hole diameter captured using the polarisation camera, where images (a-c) are the raw saturation, DoLP and the fibre orientation, respectively.

Figure 5.37 presents a region of interest, (sample-3), that was selected to investigate the fibre orientations around the machined hole (offline inspection). Image (c) shows the fibres with 0° (weft direction) in red, while the fibres in the 90° (warp direction) in cyan. However, the weaving pattern creates curvature in the fibres, causing different orientations to appear. For more investigation about the fibre orientation around the machined hole, a histogram of the AoLP data is presented in Figure 5.38.

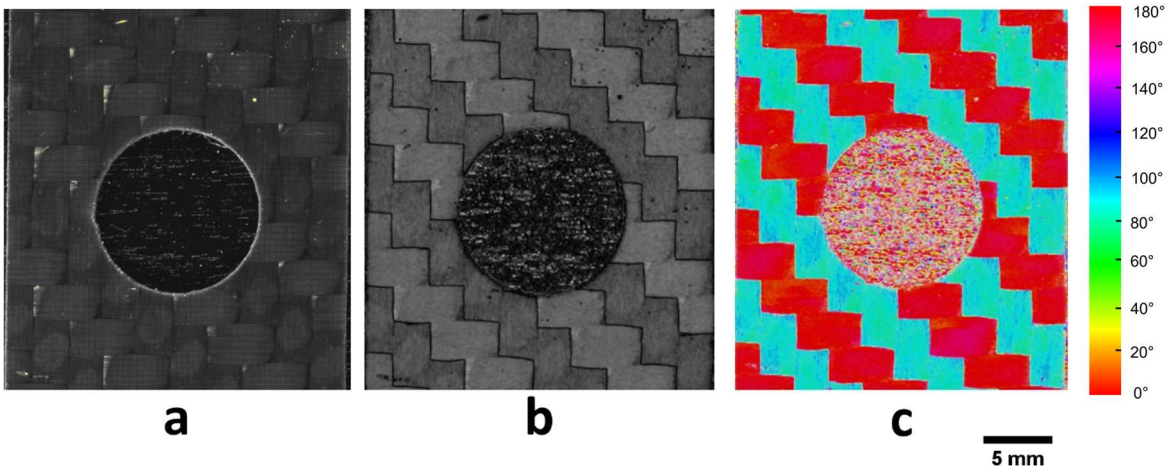


Figure 5.37 - A selected region of interest around the machined hole, presenting the fibre orientation in the image (c).

Figure 5.38-a presents the histogram of the AoLP data for the fibre orientations between 0° and 180°. The histogram after the shifting process (the orientations 160° - 180° shifted to -20° - 0°) is shown in (b). The Gaussian curve fitting for the AoLP data after shifting is presented in (c). The histogram shows that fibres in the warp direction have orientations between 80° - 100°, while fibres in the weft direction have orientations between (-20° - 20°). The mean of the AoLP calculated after fitting the curve was determined to be 1.08° ± 0.41 with a standard deviation of 5.04° ± 0.59 for the first peak. The mean of the AoLP in the second peak was 91.14° ± 0.35.

Figure 5.39 presents a sequence of fibre orientation images captured during the tensile test of the Twill 2x2 sample with a 12 mm machined hole. Image (a) shows the sample before the test started (0 % strain), while image (e) shows the sample at maximum load force (at strain equal to 1.46 %). Image (f) presents the post-failure

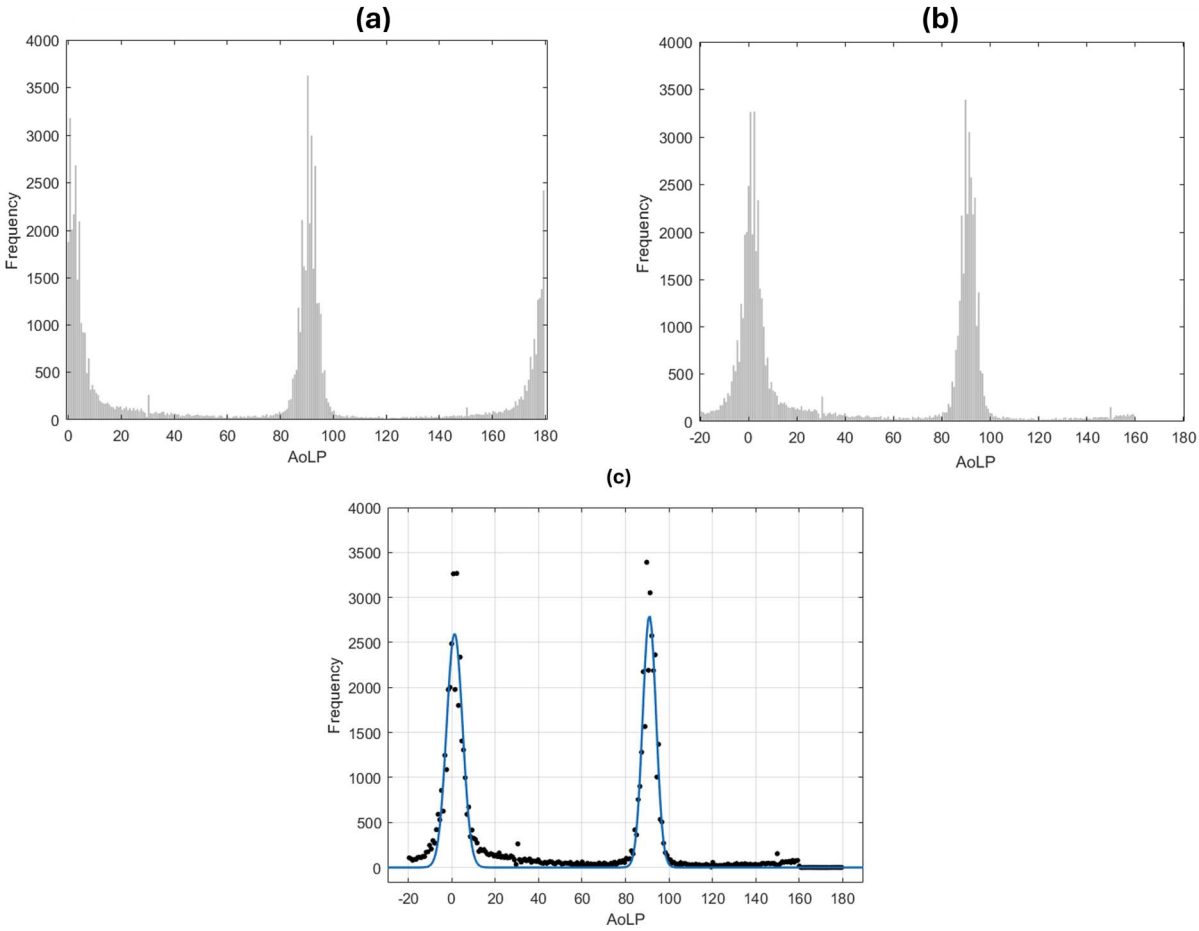


Figure 5.38 - The histogram of the AoLP data (a: before the shifting process and b: after the shifting process) and the MATLAB fitting of Gaussian curve results after the shifting process (c) for the Twill 2x2 sample with one layer at the selected area around the 12 mm machined hole.

state of the sample, where the fracture pattern aligns with expectation (initiating near the central region of the machined hole). The raw saturation images (in Figure 5.39) show the lighting source's effect on the sample surface with increasing strain, even when the autoexposure feature is applied.

Figure 5.40-a shows the selected area around the machined hole of the fibre orientation images in the Twill 2x2 sample at different strains to investigate the orientation behaviour with increasing strain, while Figure 5.40-b represents the corresponding histogram of the AoLP data. The histogram shows that the fibre orientations are distributed between (-20° and 20°) for the first peak, while it is between (80° and 100°) for the second peak.

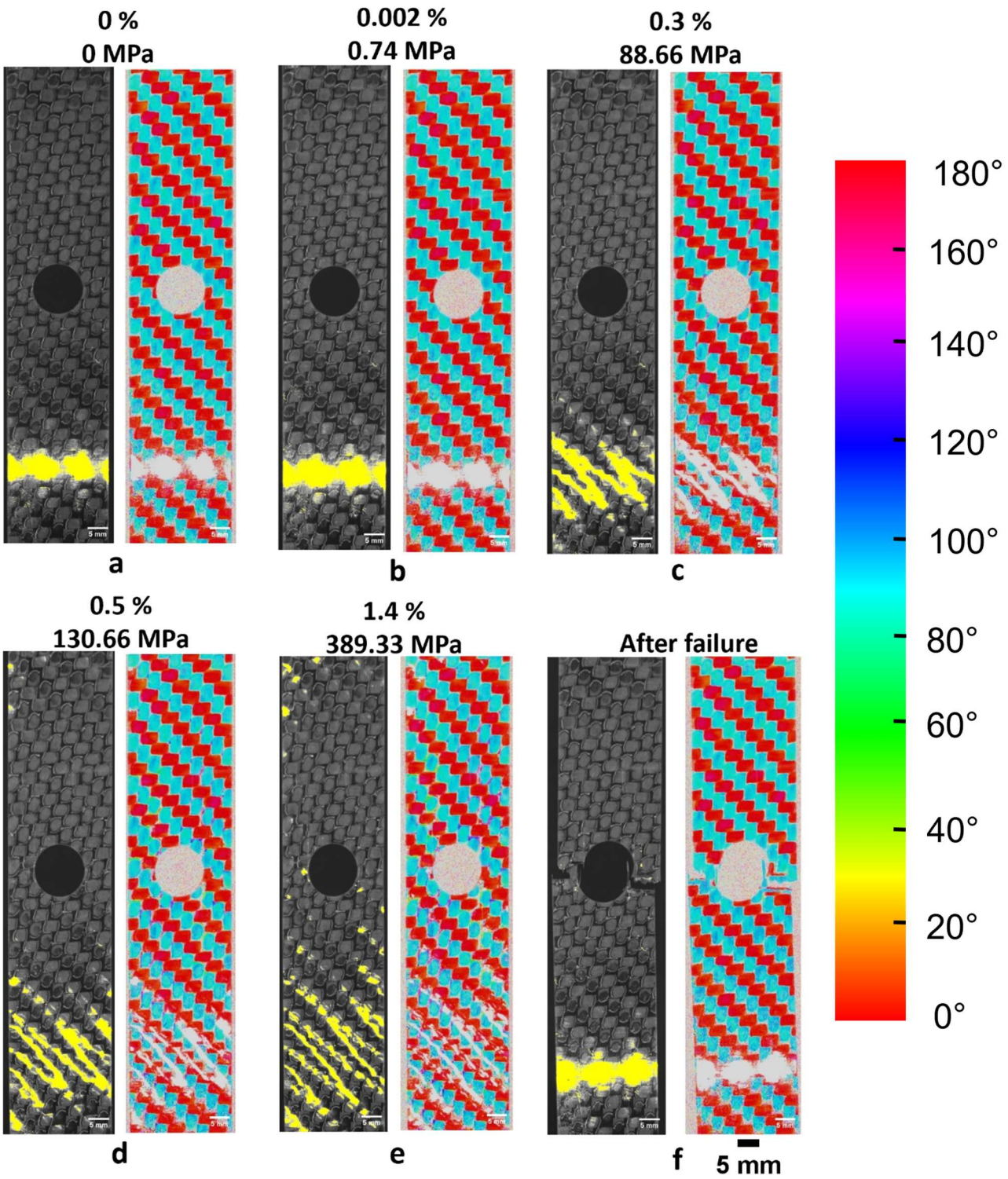


Figure 5.39 - The raw saturation and fibres' orientation images of Twill 2x2 sample, (sample-3), with a 12 mm hole diameter were captured using the polarisation camera before and during the tensile test. The yellow colour in the raw saturation images shows the lighting effect on the sample surface with increasing strain. The stress and strain corresponding to each image during the test are presented above the figure.

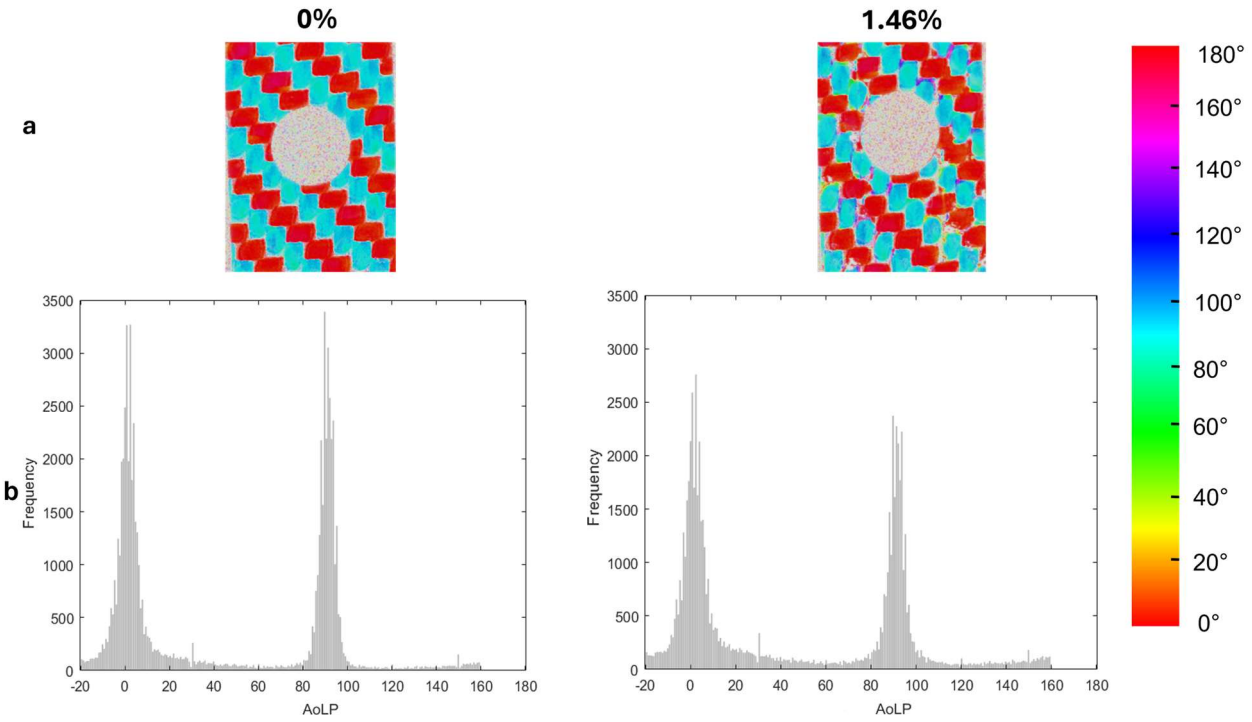


Figure 5.40 - The selected region of interest around the 12 mm machined hole of the Twill 2x2 sample consists of one layer, where (a) shows the fibres' orientation image at different strains and (b) represents the corresponding histogram of the AoLP data.

The Gaussian curve fitting was applied to the AoLP data after the shifting process for the Twill 2x2 sample with a 12 mm machined hole to determine the mean of the AoLP at the different strains, as shown in Figure 5.41. The figure shows two fitting peaks corresponding to the weft and warp fibre's directions. The mean of the AoLP for the first peak of the fibre orientation image at 0 % strain was determined to be 1.08° ± 0.41 with a standard deviation of 5.04° ± 0.59, and the mean of the AoLP for the second peak was 91.14° ± 0.35 with a standard deviation 4.35° ± 0.50.

A further fibre orientation investigation was conducted around the machined hole by separating the orientations of the fibres of the selected region of interest image at different strains using the colour threshold. Figure 5.42 shows the results of separating the fibre orientations at 0 % and 1.46 % strain.

The fibres with orientations between 0° and 20° in the fibre orientation image with 0 % strain present 24.85 % of the image's total area, fibres having orientations between 80° and 100° present 37.06 % of the total area, and fibres with orientations

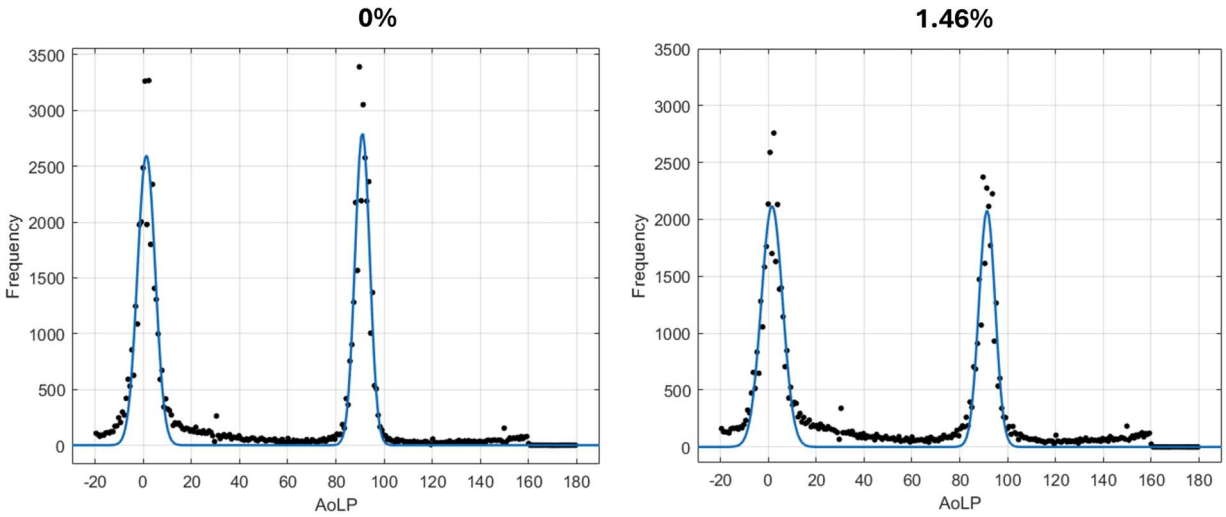


Figure 5.41 - MATLAB fitting of Gaussian curve to the histogram of AoLP data after the shifting process for the Twill 2x2 sample with 12 mm machined hole at 0 % and 1.46 % strain.

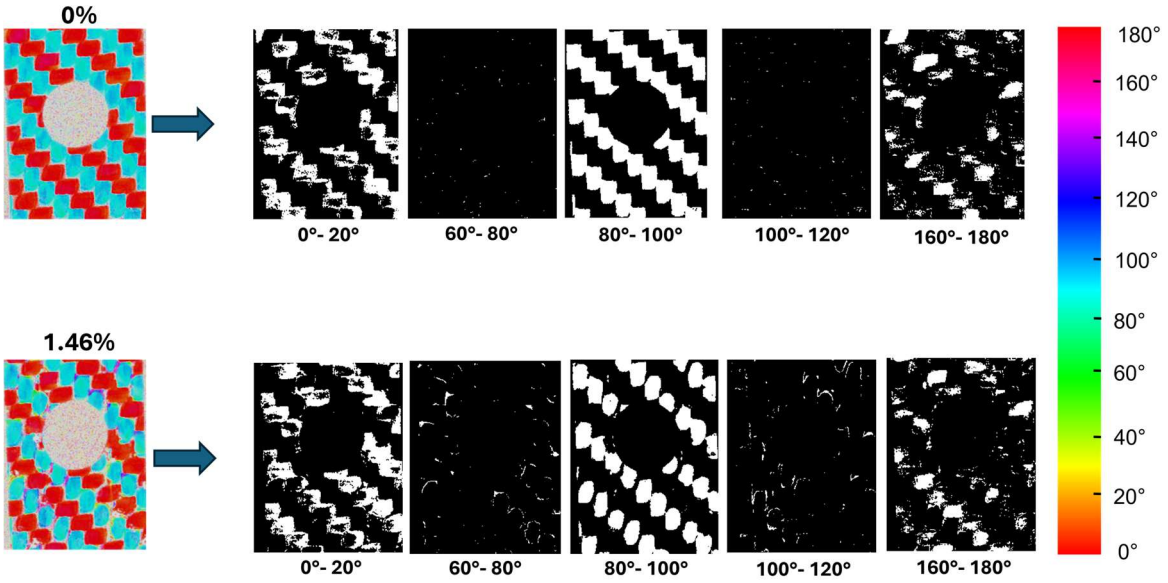


Figure 5.42 - Separating the fibre orientation of the selected region image in the Twill 2x2 sample, (sample-3), with a 12 mm machined hole at 0 % and 1.46 % strain using a colour threshold.

between 160° and 180° present 13.72 %. When strain increased to 1.46 %, the fibres with orientations between 0° and 20° present 24.09 % of the image's total area, fibres with orientations between 80° and 100° show 30.66 % of the total area, and 11.95 % for the fibres with orientations between 160° and 180°.

Figure 5.43 shows a schematic diagram illustrating how the weaving pattern (weft fibres) affects the fibres' orientation when strain increases. The orientation of fibres aligned with the loading direction, particularly those located near the fibre edges, was influenced by the interaction between the weft and load-bearing fibres within the weaving pattern, as the weft alternated above and beneath them. This interlacing action altered the fibre alignment at the fibre edges, thereby affecting the fibre orientation behaviour as strain increased. Furthermore, the geometry of the remaining fibres after hole machining played a crucial role in determining the alignment of fibres in the loading direction, which, in turn, influenced the overall mechanical performance of the composite.

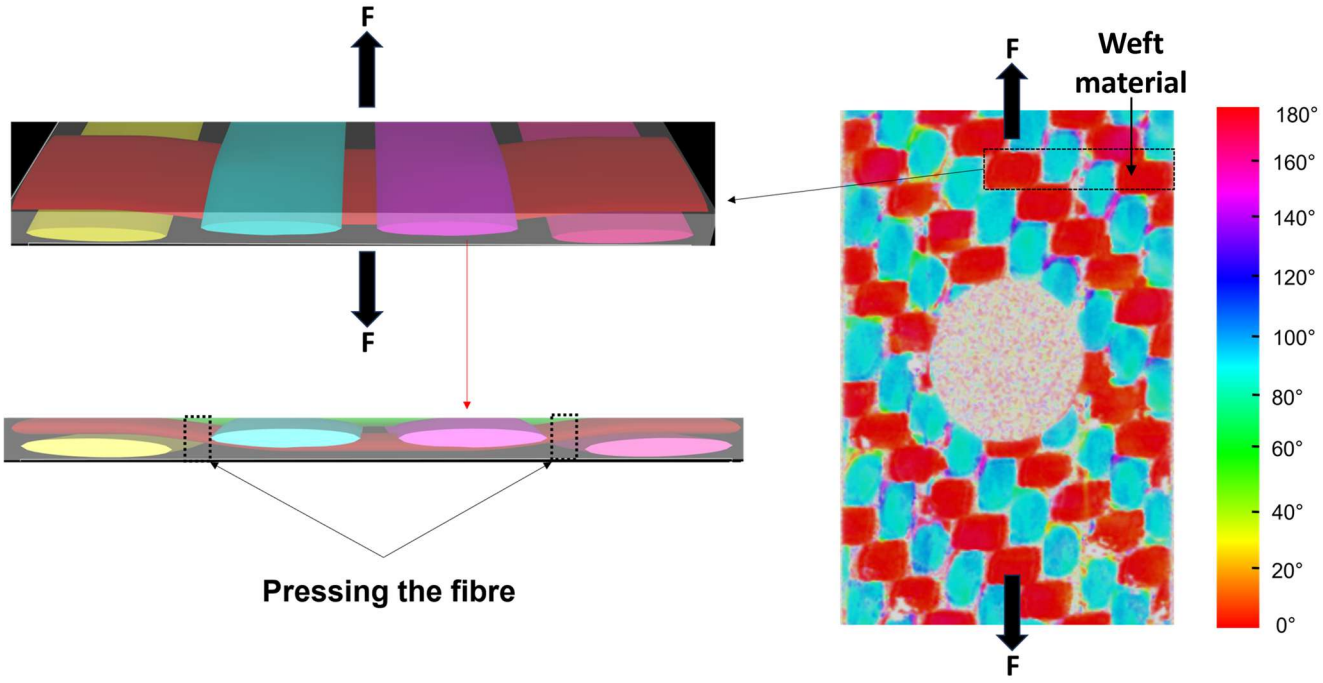


Figure 5.43 - A schematic diagram shows the effect of weft fibres on the fibre orientation when strain increases, (sample-3).

A summary of maximum force, tensile strength, failure strain and tensile modulus for one layer Twill 2x2 tested samples with a 12 mm machined hole is presented in Table 5.8. The results show a variation between the three samples, even though they were prepared from the same panel. The relative amount of weft and warp material removed due to machining the hole differs between the three samples.

Figure 5.44 shows the DoLP and corresponding fibre's orientation image for the three samples of Twill 2x2 with a 12 mm hole prepared from the same panel, illustrating the difference in the cutting of the warp and weft material around the machined hole. The regions close to the hole's horizontal edges, where the stress is concentrated, are labelled with yellow rectangles. By taking the fibre's pattern at the machined hole edge in the left yellow rectangle (as an example) for the three samples, it can be noticed that samples (2 and 3) have some similarity in the fibres' structure after machining the hole. However, after machining the hole, sample (1) lost more fibres in the 90° orientation (in the tension direction) at the top left hole's edge compared with the other samples, creating a point in the fibre near the expected breakage starting region. The fibres' structure after machining the hole, especially near the expected breakage starting region, plays a role in influencing the sample's strength.

The results obtained from the analysis of the Degree of Linear Polarisation (DoLP) and Angle of Linear Polarisation (AoLP) images support the hypothesis that the position of the machined hole relative to the weft and warp materials influences the mechanical performance of the open-hole tensile specimens. However, as previously discussed, further investigation and analysis of DoLP images for specimens with holes located at different positions are required to verify this hypothesis. Once validated, optimisation of the hole position through the analysis of DoLP images captured using the polarisation camera could lead to an enhancement in the mechanical performance of the tested specimens. Furthermore, the analysis could be utilised to predict the weaker specimens based on the orientation of the weft and warp relative to the machined hole. Moreover, these findings contribute to improving the manufacturing process of TFP-reinforced hole specimens through the accurate placement of fibres.

Table 5.8 - The tensile test information for three Twill 2x2 samples, consist of one layer, with a 12 mm machined hole.

Sample Number	Maximum force (N)	Ultimate tensile strength (MPa)	Strain %	E-modulus (GPa)
Sample-1	5520	388.66	1.54	25.10
Sample-2	6400	368	1.39	26.43
Sample-3	5840	389.33	1.46	26.52
Average	5920	381.99	1.46	26.02
Standard Deviation	445.42	12.12	0.07	0.79

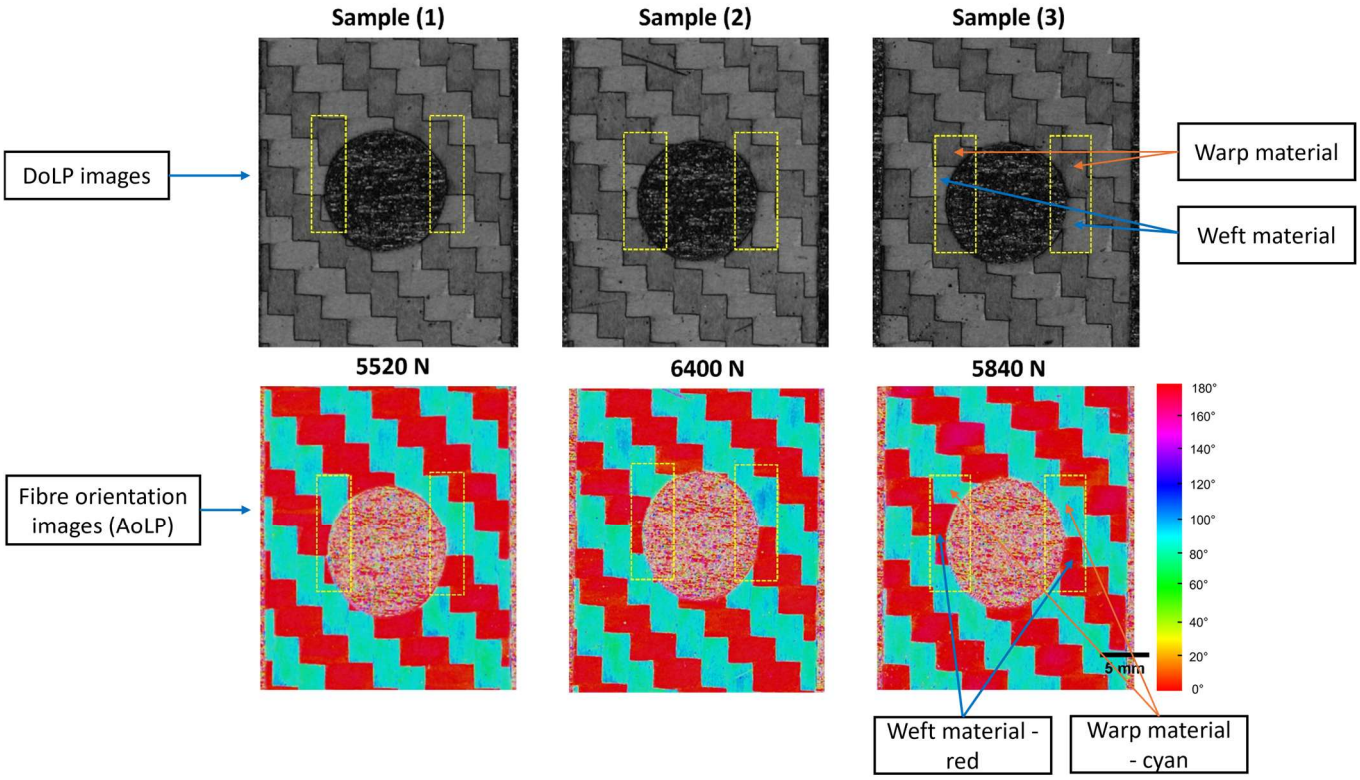


Figure 5.44 - The fibres' orientation and the corresponding DoLP images for three samples of Twill 2x2 with a 12 mm hole were imaged using the polarisation camera, showing the difference in weft and warp material after machining the hole.

Table 5.9 summarizes the mean of the AoLP and its standard deviation for fibre orientations observed during tensile testing (Figure 5.39). In a one-layer Twill 2x2 sample with a 12mm hole, the mean AoLP exhibited changes as the strain increased. Figure 5.45 visually illustrates the fibre orientation behaviour around the reinforced hole. The mean of the AoLP of the fibres in the weft direction (Peak-1) exhibit changes from (1.08° ± 0.41) at 0 % strain to (1.49° ± 0.55) when strain reached 1.46 %, while the AoLP of the fibres in the warp direction (peak-2) changes from (91.14° ± 0.35) at 0 % strain to (91.41° ± 0.49) at 1.46 %.

The stress and strain curves for the three Twill 2x2 carbon fibre samples are shown in Figure 5.46, which shows brittle failure with a linear response up to the failure point in the samples (1 and 3). However, sample (2) shows a linear response until reaching a point where the stress dips and then recovers linearly up to the failure point.

Table 5.9 - The mean of the AoLP and standard deviation result in the corresponding strain after applying the Gaussian curve fitting to the fibres' orientation images of the one-layer Twill 2x2 sample, (sample-3), with a 12 mm machined hole captured during tensile testing (Figure 5.39).

The mean of AoLP (degree) – Peak (1)	Standard deviation (the width of the peak)	Strain (%)	The mean of AoLP (degree) – Peak (2)	Standard deviation (the width of the peak)
1.08 ± 0.41	5.04 ± 0.59	0	91.14 ± 0.35	4.35 ± 0.50
1.26 ± 0.43	5.18 ± 0.61	0.002	91.01 ± 0.36	4.32 ± 0.51
1.28 ± 0.44	5.28 ± 0.62	0.33	91.31 ± 0.38	4.35 ± 0.54
1.41 ± 0.51	5.84 ± 0.72	0.53	91.46 ± 0.44	4.60 ± 0.63
1.49 ± 0.55	6.28 ± 0.78	1.46	91.41 ± 0.49	4.79 ± 0.69
1.86 ± 0.53	5.84 ± 0.75	1.47	91.54 ± 0.41	4.75 ± 0.58

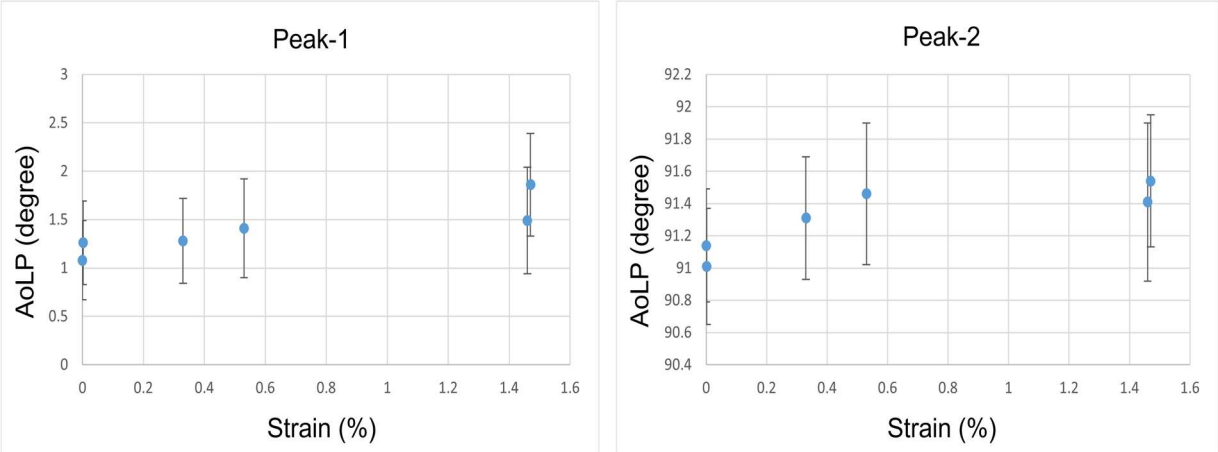


Figure 5.45 - The mean of the AoLP behaviour for a one-layer of Twill 2x2 sample, (sample-3), containing a 12 mm machined hole with increasing strain (for the six selected images in Figure 5.39) for the two peaks.

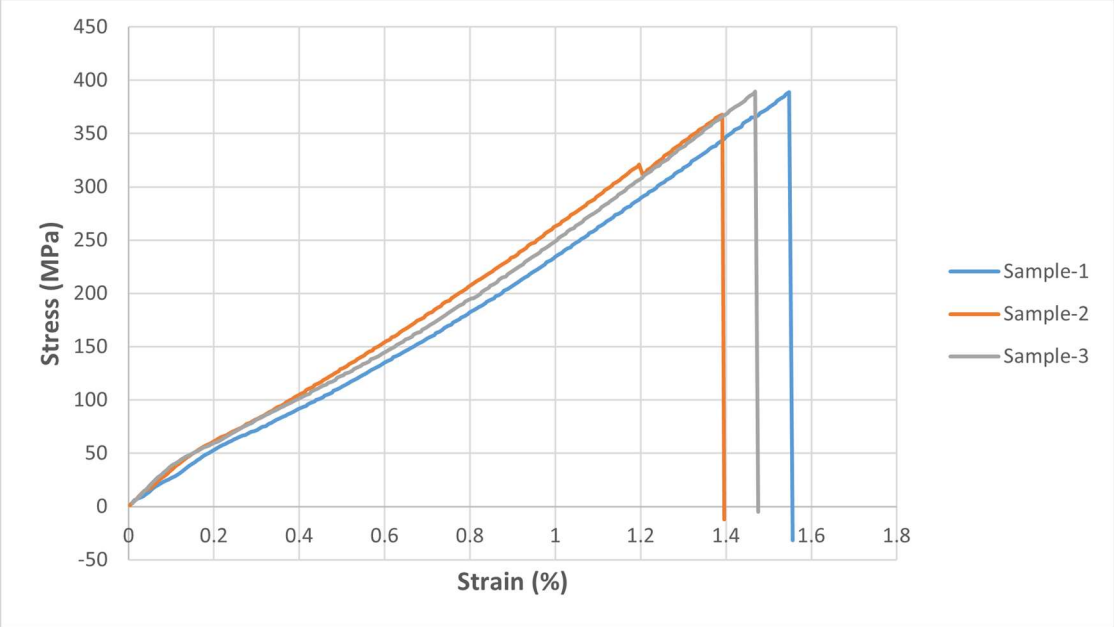


Figure 5.46 - The stress and strain curve for three Twill 2x2 samples, consist of one-layer, with a 12 mm machined hole.

Following the analysis of the 12 mm hole diameter samples, the investigative process was repeated for Twill 2x2 carbon fibre samples with a 10 mm hole diameter (Figure 5.47), (sample-2).

As with the previous samples, pre-test inspection was conducted (offline inspection) using the polarisation camera. The captured images, including raw saturation, degree of polarisation (DoLP), and fibre orientation images, are presented in Figure

5.48 (a-c), respectively. Figure 5.48-c represents the fibres' orientation from the hue (angle of linear polarisation) channel.

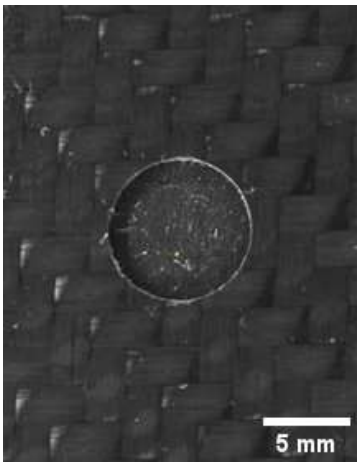


Figure 5.47 - Raw image of one-layer Twill 2x2 sample, (sample-2), with 10 mm machined hole captured using the polarisation camera.

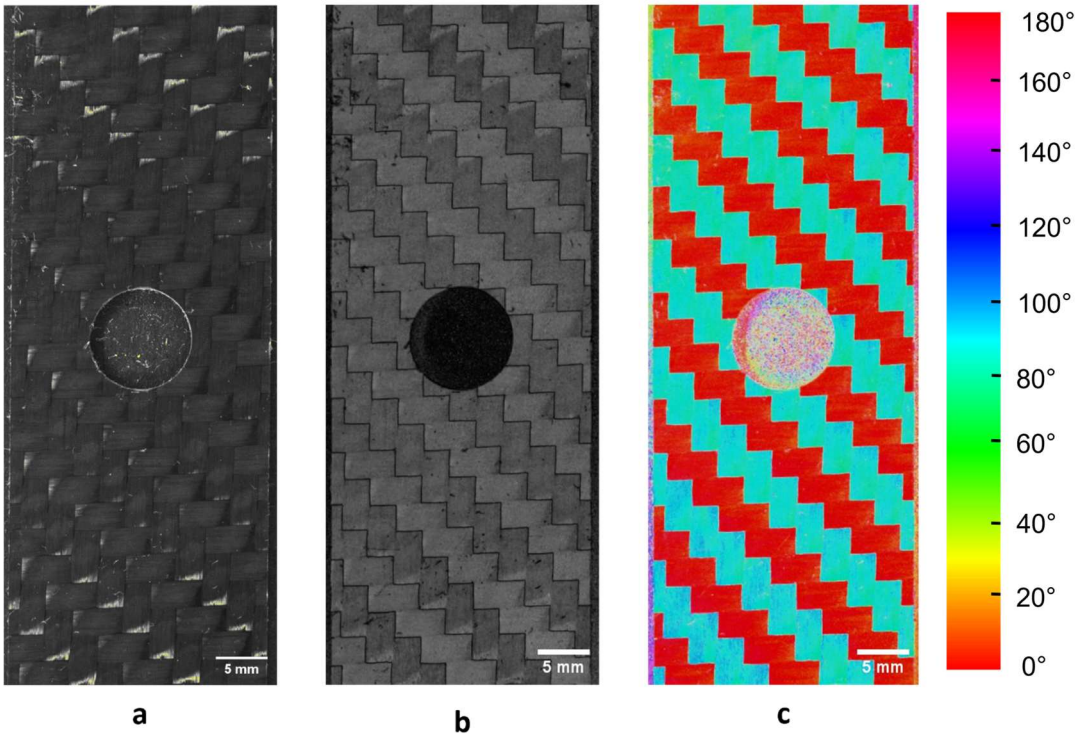


Figure 5.48 - The one-layer Twill 2x2 sample, (sample-2), with a 10 mm machined hole was captured using the polarisation camera. Images (a-c) present the raw saturation, DoLP, and fibre orientation images.

Figure 5.49 shows the sequence of raw saturation and corresponding fibres' orientation images captured during the tensile test of the Twill 2x2 sample, (sample-2), with a 10 mm machined hole consisting of one layer. Image (a) shows the sample

at the initial state before starting the test (0 % strain), while image (e) shows the sample at maximum load force (at strain equal to 0.93 %). The red and black circles in image (e) highlight the initiation of fibre breakage near the machined hole at 0.93% strain, while image (f) shows the sample after failure.

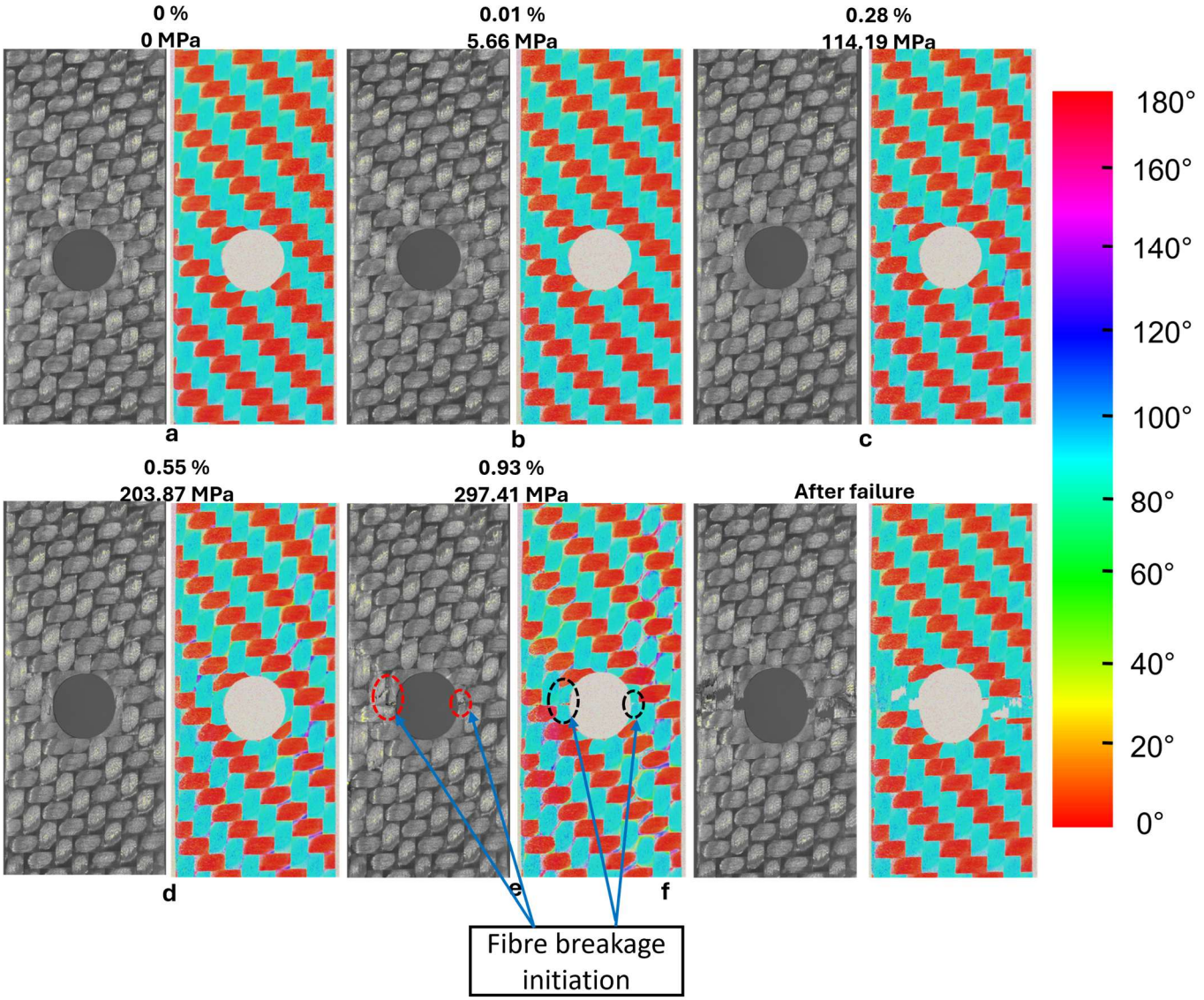


Figure 5.49 - The raw saturation and fibres' orientation images of the one-layer Twill 2x2 sample, (sample-2), with a 10 mm machined hole were captured using the polarisation camera before and during the tensile test. The stress and strain corresponding to each image during the test are presented above the figure.

Figure 5.50-a displays fibre orientation images of the selected area around a machined hole at various strain levels. Figure 5.50-b presents the corresponding histogram of the Angle of Linear Polarisation (AoLP) data. The histogram reveals two distinct peaks in fibre orientation distribution. The first peak (after shifting) shows fibres with orientations between -20° and 20°, while the second peak covers orientations between 80° and 100°.

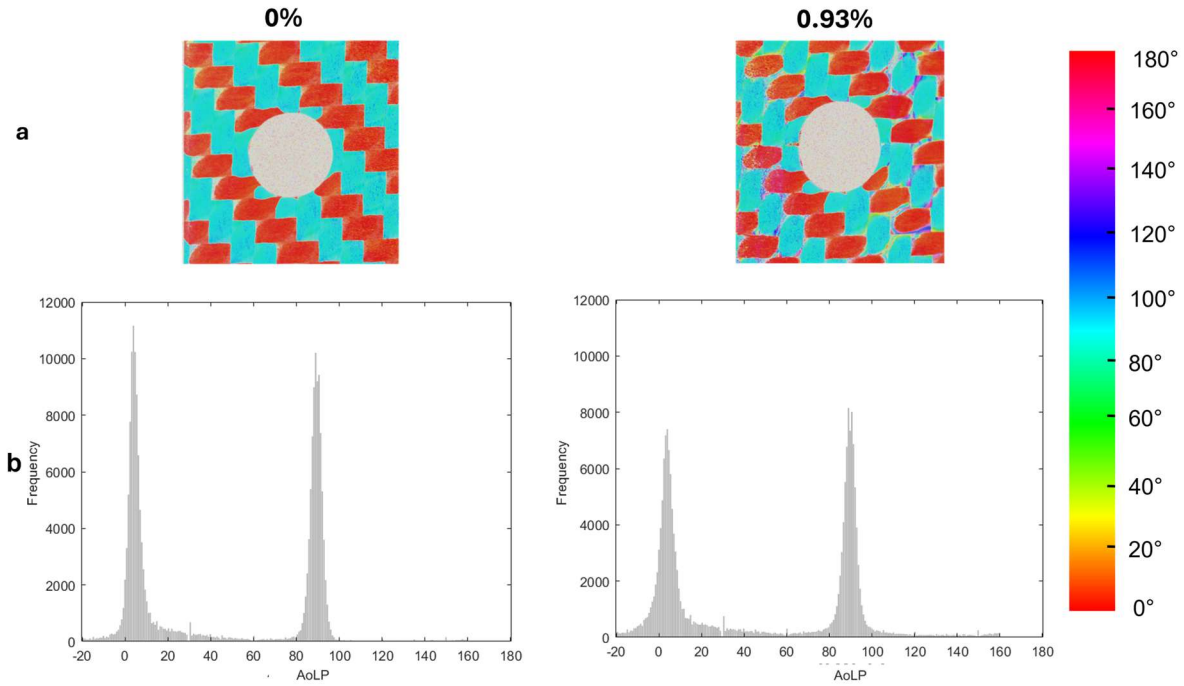


Figure 5.50 - The selected region of interest around the 10 mm machined hole of the Twill 2x2 sample consists of one layer, where (a) shows the fibres' orientation image at different strains and (b) represents the corresponding histogram of the AoLP data.

Gaussian curve fitting was employed on the AoLP data after the shifting process for the Twill 2x2 sample with a 10 mm machined hole to determine the mean of the AoLP at the different strains, as shown in Figure 5.51. The figure shows two fitting peaks corresponding to the weft and warp fibre's directions. The mean of the AoLP for the first peak of the fibre orientation image at 0 % strain was determined to be 4.04° ± 0.14 with a standard deviation of 3.45° ± 0.20, and the mean of the AoLP for the second peak was 89.35° ± 0.15 with a standard deviation 3.54° ± 0.21. When strain increased to 0.93 %, the mean of the AoLP for the first peak was found to be 3.72° ± 0.30 with a standard deviation of 4.84° ± 0.42, and 89.66° ± 0.23 for the second peak with a standard deviation of 4.01° ± 0.32.

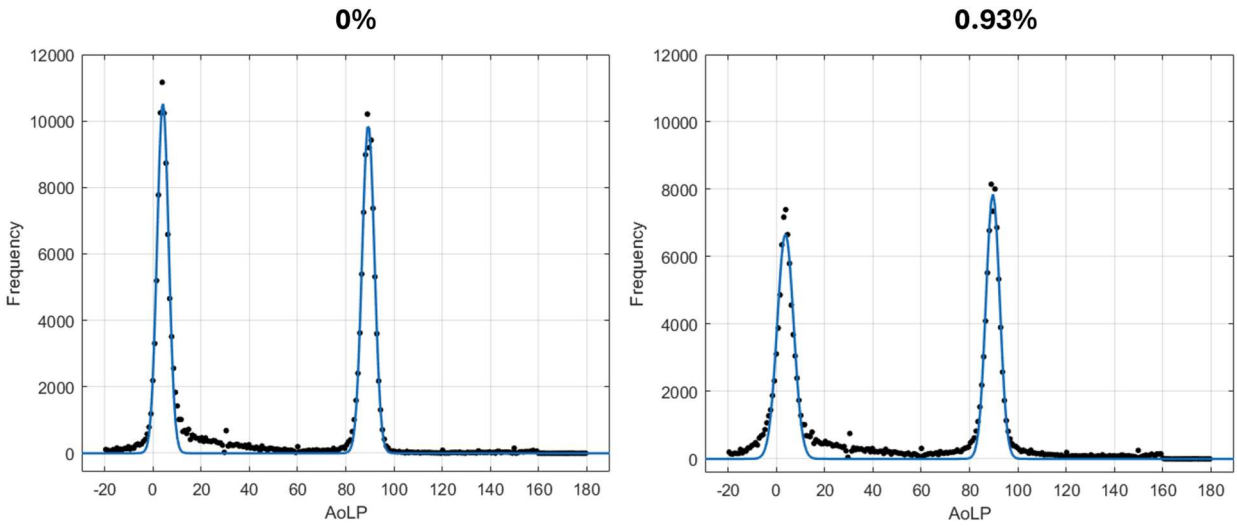


Figure 5.51 - MATLAB fitting of Gaussian curve to the histogram of AoLP data after the shifting process for the Twill 2x2 sample with 10 mm machined hole at 0 % and 0.93 % strain.

Fibre orientation was further investigated around the machined hole. Fibre orientations within the selected region of interest image were separated by applying a colour threshold at different strain levels. Figure 5.52 presents the results of the separation analysis for 0% and 0.93% strain, (sample-2).

In the fibre orientation image at 0 % strain, fibres with orientations between 0° and 20° occupied 40.72 % of the image's total area, those between 80° and 100° occupied 41.03 %, and those between 160° and 180° occupied 1.51 %. When strain increased to 0.93%, the fibres occupied 32.06 %, 37.66 %, and 6.44 % of the total image area for the same orientation range. Furthermore, the fibres with orientations between (60° and 80°) and (100° and 120°) show how the weaving pattern influences fibre orientations, especially at the edges, with increasing strain.

Table 5.10 summarises the maximum force, tensile strength, failure strain, and tensile modulus for one-layer Twill 2x2 samples tested with a 10 mm machined hole. Variations in these properties are observed between the three samples despite their origin from the same manufactured panel. As mentioned for the samples with 12 mm machined holes, the difference in the amount of weft and warp material removed due to machining the hole might be a reason for this variation.

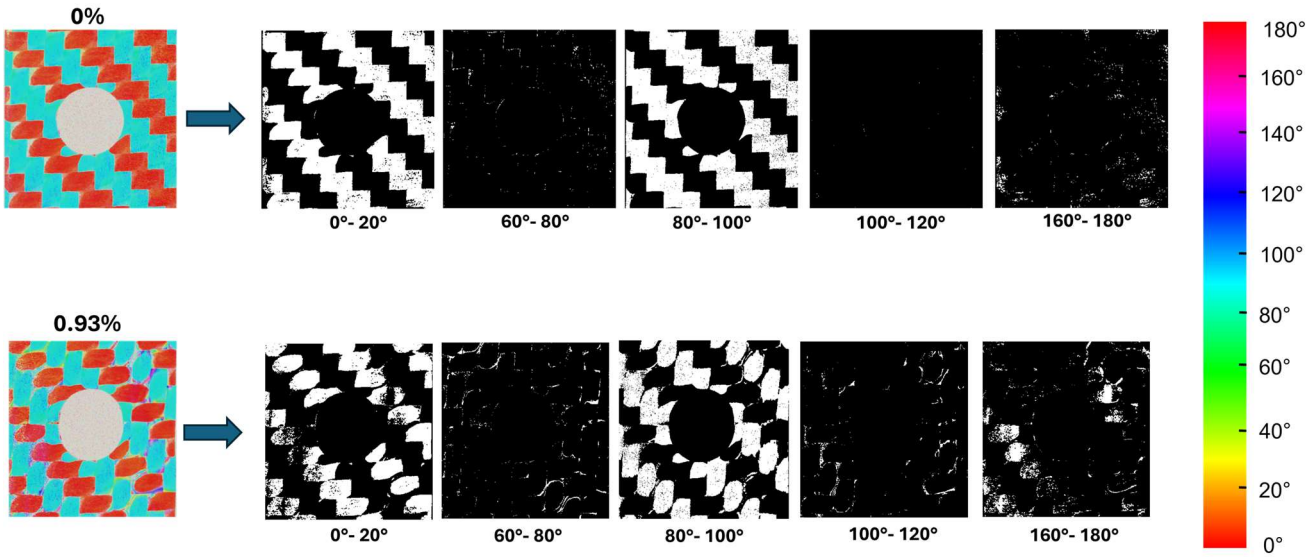


Figure 5.52 - Separating the fibre orientation of the selected region image in the Twill 2x2 sample, (sample-2), with a 10 mm machined hole, consisting of one layer of fabric, at 0 % and 0.93 % strain using a colour threshold.

Table 5.10 - The tensile test information for three Twill 2x2 samples, consist of one layer, with a 10 mm machined hole.

Sample Number	Maximum force (N)	Ultimate tensile strength (MPa)	Strain %	E-modulus (GPa)
Sample-1	7470	498	1.68	29.57
Sample-2	4610	297.41	0.93	31.77
Sample-3	6070	373.53	1.14	32.76
Average	6050	389.65	1.25	31.37
Standard Deviation	1430.10	101.25	0.38	1.63

Figure 5.53 shows the DoLP and fibre orientation images for the three Twill 2x2 tested samples, manufactured from the same panel, with a 10 mm machined hole to present the difference in the fibre orientation of the fibres at the hole's edges (vertical direction).

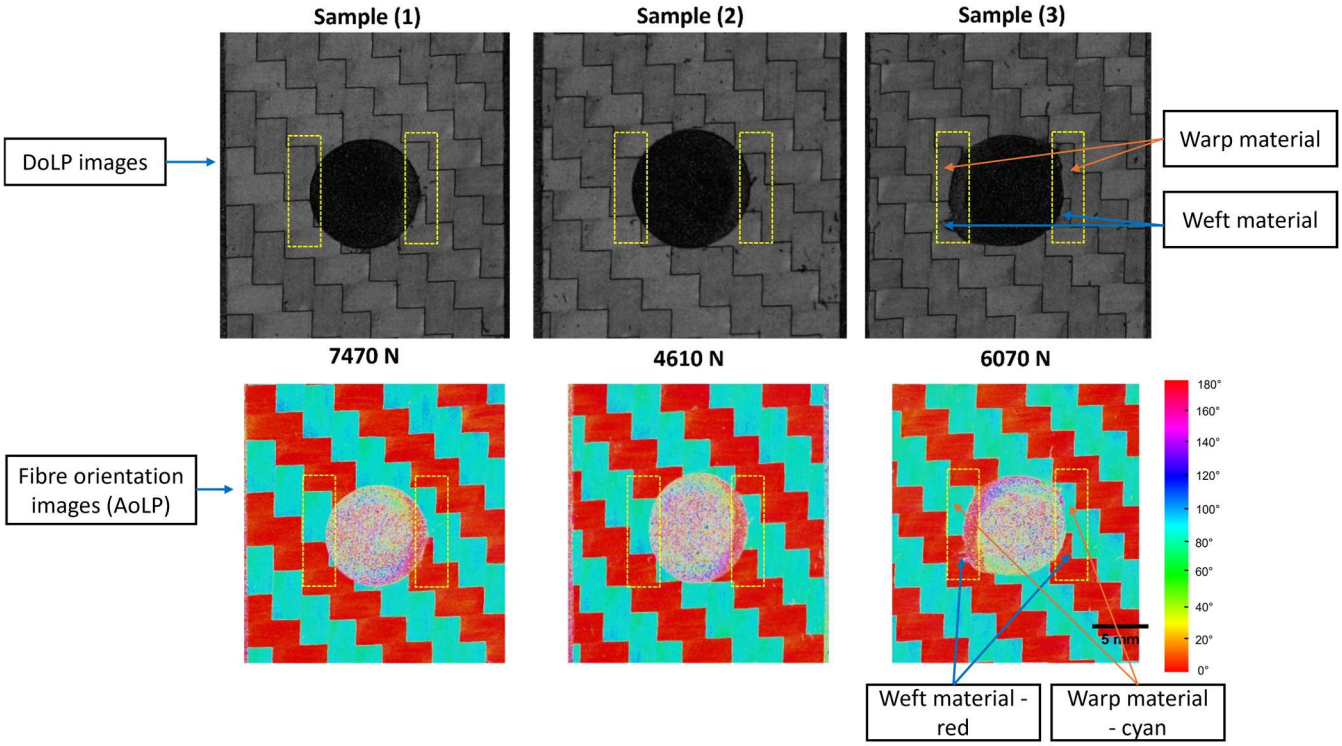


Figure 5.53 - The DoLP and the corresponding fibres' orientation images for three samples of Twill 2x2 with a 10 mm hole were captured using the polarisation camera, showing the difference in the weft and warp material at the edge of the machined hole.

Table 5.11 summarizes the mean of the AoLP and its standard deviation for fibre orientations observed during tensile testing (Figure 5.49). In a one-layer Twill 2x2 sample with a 12 mm hole, the mean of the AoLP exhibited changes as the strain increased. Figure 5.49 shows the change in the fibre orientation behaviour around the reinforced hole. The mean of the AoLP of the fibres in the weft direction (Peak-1) exhibit changes from (4.04° ± 0.14) at 0 % strain to (3.72° ± 0.30) when strain reached 0.93 %, while the AoLP of the fibres in the warp direction (peak-2) changes from (89.35° ± 0.15) at 0 % strain to (89.66° ± 0.23) at 0.93 %.

Table 5.11 - The mean of the AoLP and standard deviation result in the corresponding strain after applying the Gaussian curve fitting to the fibres' orientation images of the one-layer Twill 2x2 sample, (sample-2), with a 10 mm machined hole captured during tensile testing (Figure 5.49).

The mean of AoLP (degree) – Peak (1)	Standard deviation (the width of the peak)	Strain (%)	The mean of AoLP (degree) – Peak (2)	Standard deviation (the width of the peak)
4.04 ± 0.14	3.45 ± 0.20	0	89.35 ± 0.15	3.54 ± 0.21
4.10 ± 0.13	3.38 ± 0.19	0.01	89.35 ± 0.14	3.57 ± 0.21
3.85 ± 0.16	3.44 ± 0.22	0.28	89.48 ± 0.16	3.56 ± 0.23
3.86 ± 0.18	3.82 ± 0.26	0.55	89.55 ± 0.18	3.64 ± 0.25
3.72 ± 0.30	4.84 ± 0.42	0.93	89.66 ± 0.23	4.01 ± 0.32
3.94 ± 0.20	3.58 ± 0.28	0.96	89.38 ± 0.19	3.78 ± 0.27

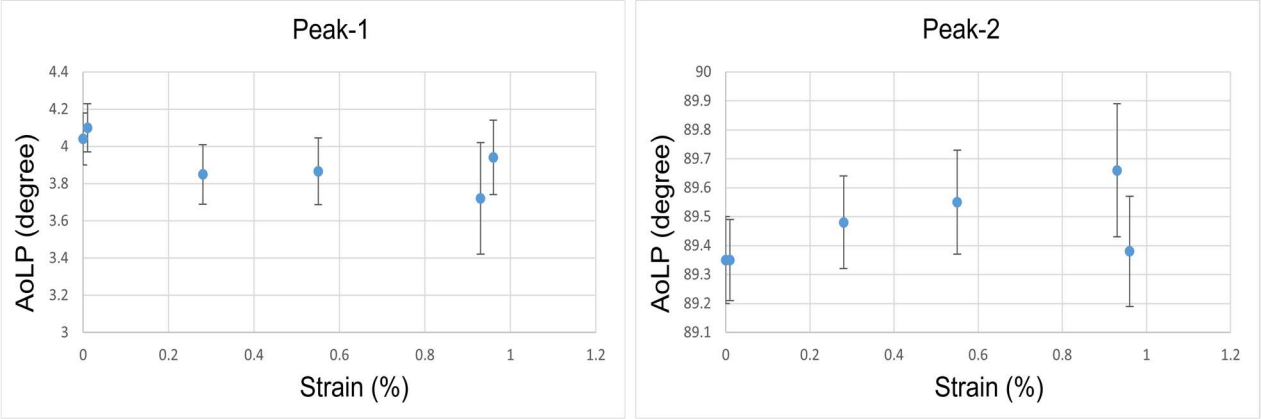


Figure 5.54 - The mean of the AoLP behaviour for a one-layer of Twill 2x2 sample, (sample-2), containing a 10 mm machined hole with increasing strain (for the six selected images in Figure 5.49) for the two peaks.

Figure 5.55 shows the stress and strain curves for the three samples of Twill 2x2 with a 10 mm hole diameter, consisting of one layer. The graph shows that samples (1 and 2) present a linear response to a point where the stress dips and then recovers linearly up to the failure point, while sample (3) shows an expected brittle behaviour up to the failure point.

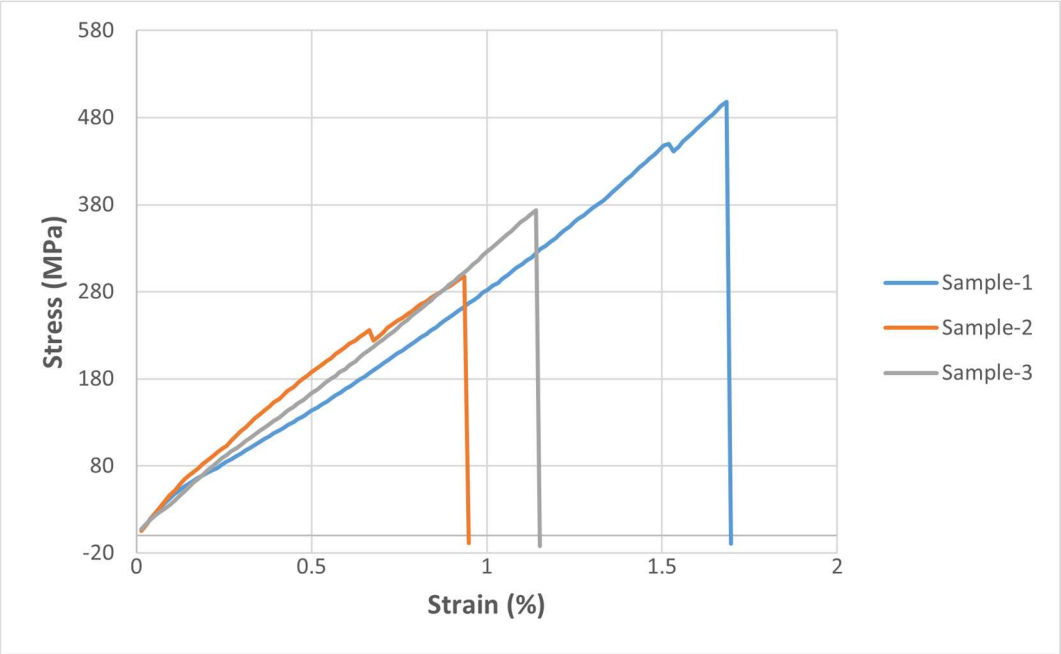


Figure 5.55 - The stress and strain curve for three Twill 2x2 samples, consist of one-layer, with a 10 mm machined hole.

The final category of Twill 2x2 carbon fibre samples is the 8 mm hole diameter, as shown in Figure 5.56, (sample-2). Again, before starting the tensile test, an offline inspection was performed on the sample using a polarisation camera. The raw saturation, degree of linear polarisation (DoLP), and the fibres' orientation images resulting from the offline inspection are presented in Figure 5.57 (a-c), respectively.

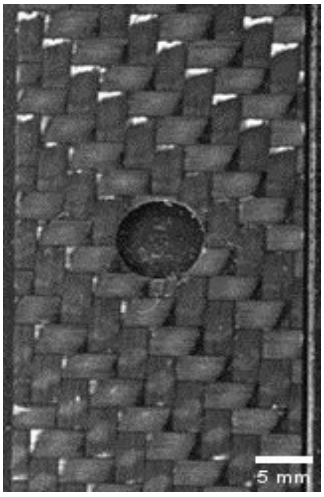


Figure 5.56 - Raw image of one-layer Twill 2x2 sample with 8 mm machined hole captured using the polarisation camera.

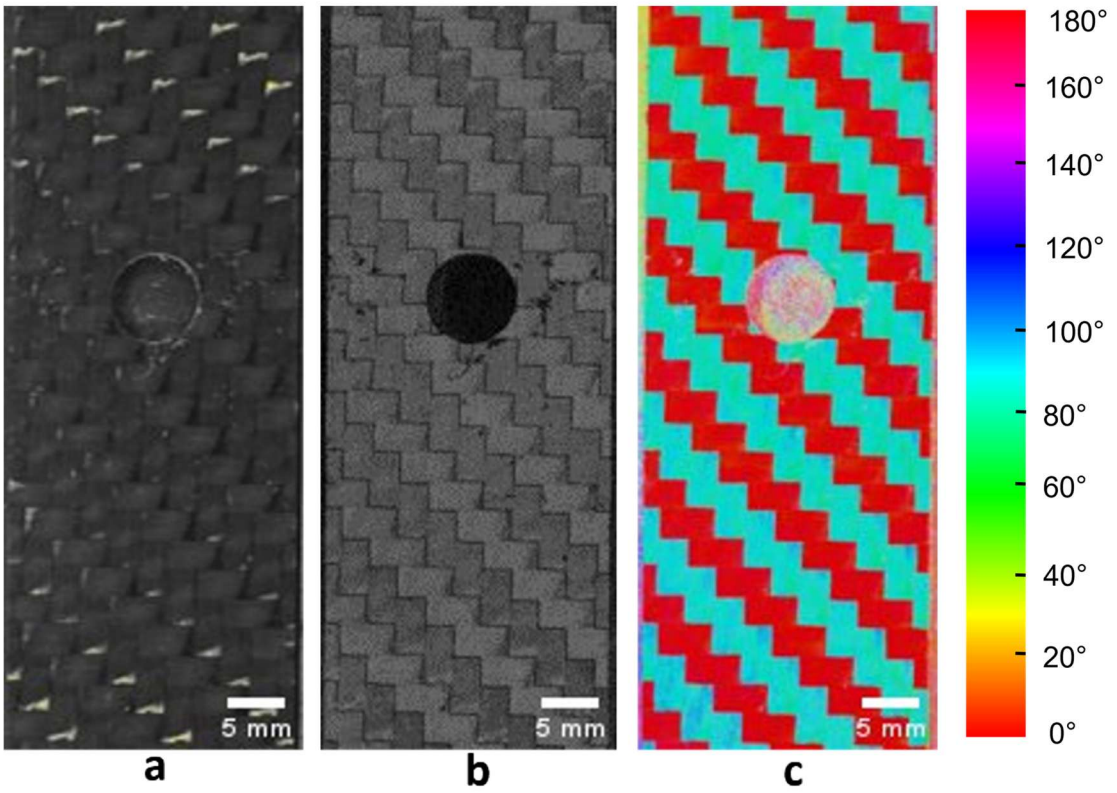


Figure 5.57 - The one-layer Twill 2x2 sample, (sample-2), with an 8 mm machined hole was captured using the polarisation camera. Images (a-c) present the raw saturation, DoLP, and fibre orientation images.

Figure 5.58 shows a sequence of raw saturation and fibre orientation images captured before and during the tensile test, (sample-2). Image (a) shows the initial state of the sample before starting the test (0 % strain), while image (e) shows the sample at maximum load force (at 0.97% strain). The post-failure state of the sample is shown in image (f).

The same comparison process applied to the other categories were repeated, where the region of interest was selected around the machined hole to investigate the fibres' orientation behaviour at 0% and 0.97% strain, images (a and e) in Figure 5.58, respectively.

Figure 5.59-a shows the selected area around the machined hole of the fibre orientation images in the Twill 2x2 sample at 0 % and 0.97 % strain to investigate the change in the fibre orientation behaviour with increasing strain, while Figure

5.59-b represents the corresponding histogram of the AoLP data. The histogram shows the weft fibres orientations distributed between (-20° and 20°) for the first peak, while it is between (80° and 100°) for the fibres in the warp direction (the second peak).

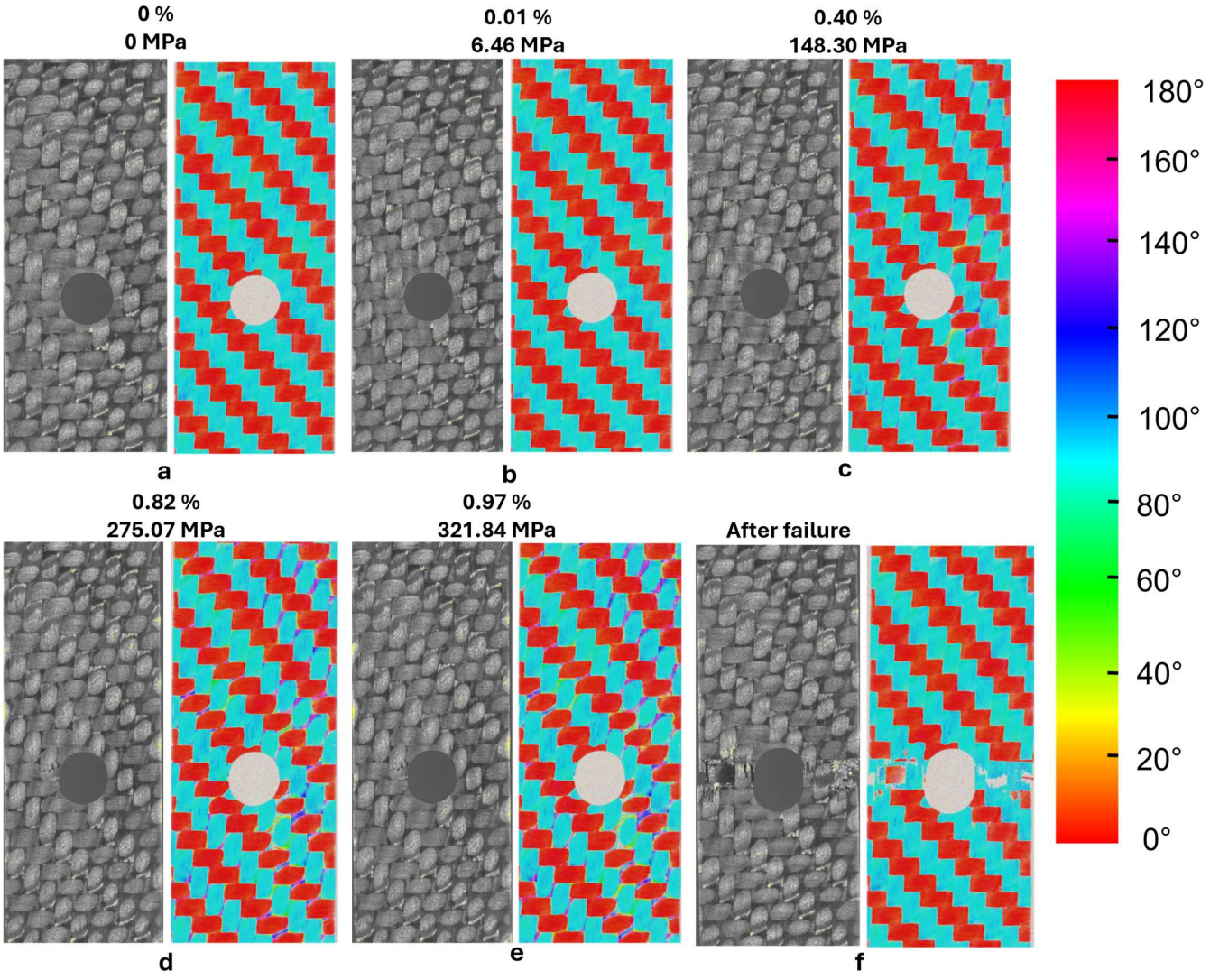


Figure 5.58 - The raw saturation and fibres' orientation images of the one-layer Twill 2x2 sample, (sample-2), with an 8 mm machined hole were captured using the polarisation camera before and during the tensile test. The stress and strain corresponding to each image during the test are presented above the figure.

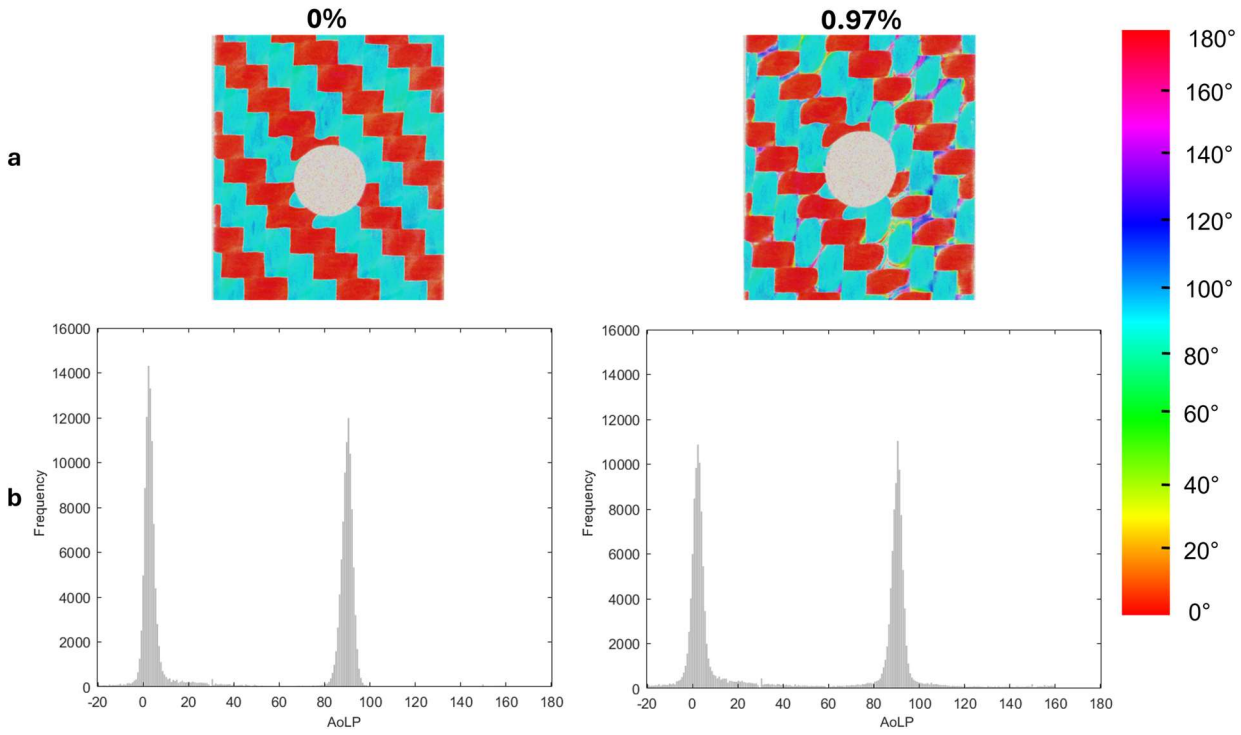


Figure 5.59 - The selected region of interest around the 8 mm machined hole of the Twill 2x2 sample consists of one layer, where (a) shows the fibres' orientation image at different strains and (b) represents the corresponding histogram of the AoLP data.

The mean of the AoLP was calculated for the fibre orientation images at 0 % and 0.97 % strain after applying the Gaussian curve fitting to the AoLP's histogram data, as shown in Figure 5.60. The figure presents two peaks corresponding to the directions of the weft and warp fibres. The mean of the AoLP of the fibres in the weft direction was 2.56° ± 0.06 with a standard deviation of 2.68° ± 0.09 at 0 % strain image, and the mean of the AoLP for the warp direction was 90.10° ± 0.09 with a standard deviation 3.34° ± 0.12. With increasing strain to 0.97 %, the mean of the AoLP was determined to be 2.17° ± 0.12 with a standard deviation of 3.16° ± 0.16 and 90.40° ± 0.13 with a standard deviation of 3.27° ± 0.17 for the weft and warp fibre's direction.

For a better understanding of the effect of the strain on the fibre orientation behaviour around the machined hole, the fibre orientations at different strains were separated using the colour threshold. Figure 5.61 shows the results of separating the fibre orientations at 0 % and 0.97 % strain.

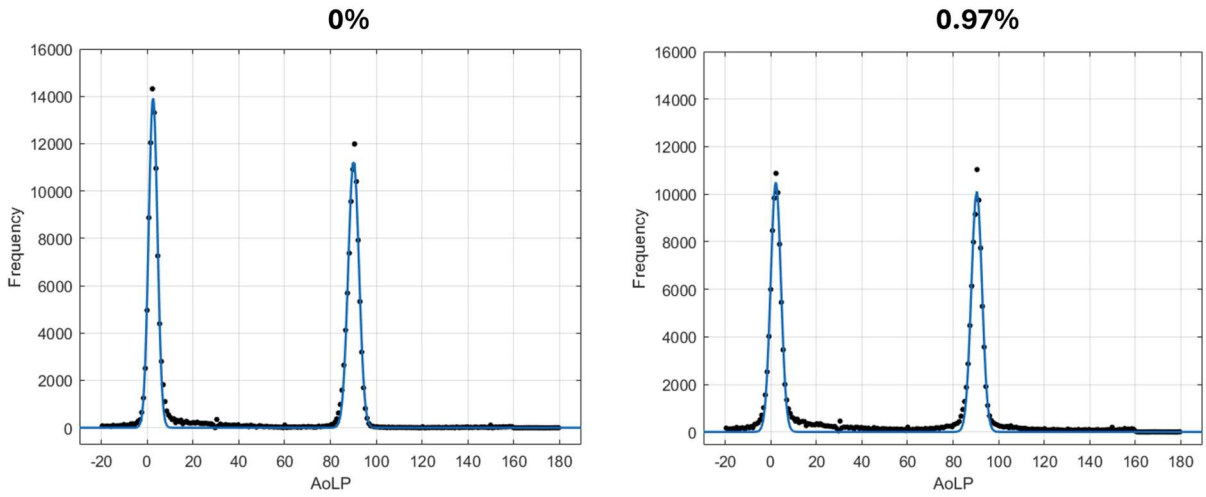


Figure 5.60 - MATLAB fitting of Gaussian curve to the histogram of AoLP data after the shifting process for the Twill 2x2 sample with 8 mm machined hole at 0 % and 0.97 % strain.

The figure shows that fibres with orientations between 0° and 20° in the image at 0 % strain present 41.52 % of the image's total area, fibres having orientations between 80° and 100° present 44.88 % of the total area, and fibres with orientations between 160° and 180° present 3.35 %. When strain increased to 0.97 %, the fibres present 33.98 %, 41.03 %, and 6.99 % of the total image's area for the same fibre orientation range.

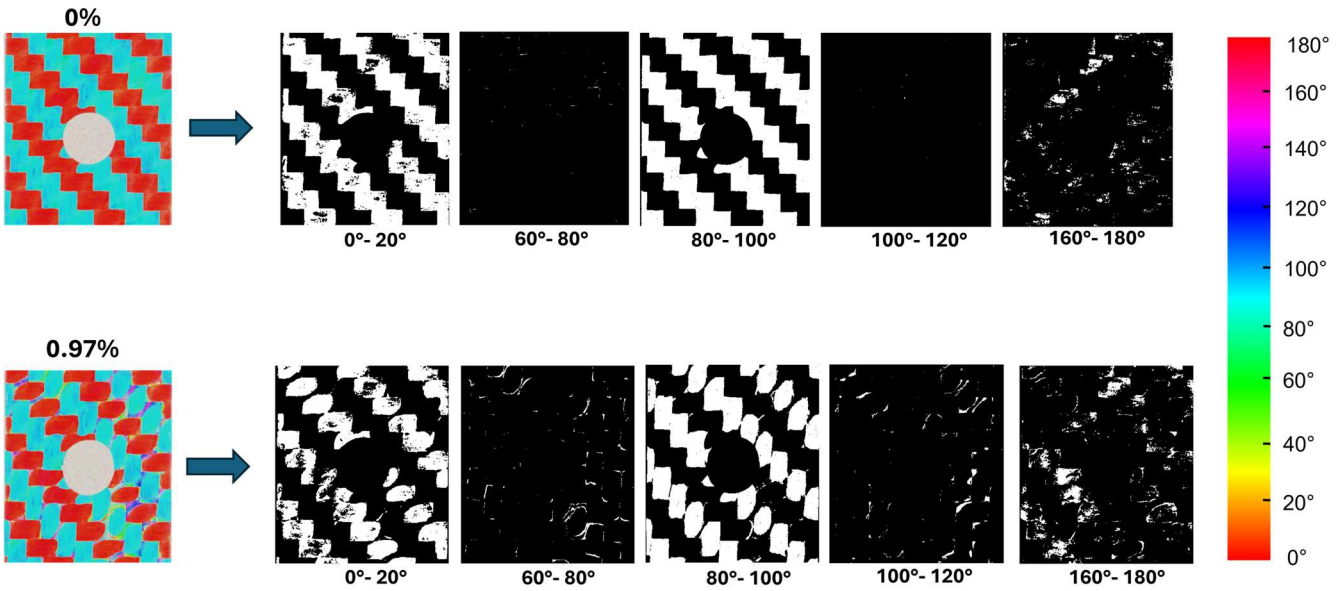


Figure 5.61 - Separating the fibre orientation of the selected region image in the Twill 2x2 sample, (sample-2), with a 12 mm machined hole at 0 % and 1.46 % strain using a colour threshold.

A summary of maximum force, tensile strength, failure strain and tensile modulus for one layer Twill 2x2 tested samples with an 8 mm machined hole is presented in Table 5.12. The variation in the fibre orientations at the machined hole edges is captured using the polarisation camera, where Figure 5.62 shows the DoLP and fibre orientation images for the Twill 2x2 sample with an 8 mm machined hole. The geometry of the fibres following the machining of the hole, particularly at the left edge of sample (1), differs from that observed in samples (2) and (3). In sample (1), a small proportion of fibres aligned in the loading direction were removed during the machining process, while the weft fibres were positioned above the load-bearing fibres owing to the weaving pattern. In contrast, the fibre geometry at the right edge of the machined hole in sample (1) indicates that the fibres aligned in the loading direction were largely unaffected by the machining process, unlike those in sample (2). This suggests that a greater number of fibres in sample (1) contributed to load transfer compared with the other samples. To further prove these observations, additional investigations are required in which holes are machined at different positions within the preform.

Table 5.12 - The tensile test information for three Twill 2x2 samples, consist of one layer, with an 8 mm machined hole.

Sample Number	Maximum force (N)	Ultimate tensile strength (MPa)	Strain (%)	E-modulus (GPa)
Sample-1	7700	473.84	1.39	33.94
Sample-2	5230	321.84	0.97	32.97
Sample-3	4310	265.23	0.092	28.70
Average	5746.66	353.64	1.09	31.87
Standard Deviation	1753.06	107.88	0.25	2.78

This would enable a detailed examination of the remaining fibre geometry in the loading direction around the machined edges through the analysis of Degree of Linear Polarisation (DoLP) and Angle of Linear Polarisation (AoLP) images.

Table 5.13 summarizes the mean of the AoLP and its standard deviation for fibre orientations observed during tensile testing (Figure 5.58), and Figure 5.63 illustrates the change in the fibre orientation behaviour around the reinforced hole with increasing strain. The mean of the AoLP of the fibres in the weft direction (Peak-1) exhibit changes from (2.56° ± 0.06) at 0 % strain to (2.17° ± 0.12) when strain reached 0.97 %, while the AoLP of the fibres in the warp direction (peak-2) changes from (90.10° ± 0.09) at 0 % strain to (90.40° ± 0.13) at 0.97 %.

The stress and strain curves for the three Twill 2x2 carbon fibre samples are shown in Figure 5.64, which shows a linear response up to the failure point. However, sample (3) behaves differently from samples (1 and 2), showing early failure.

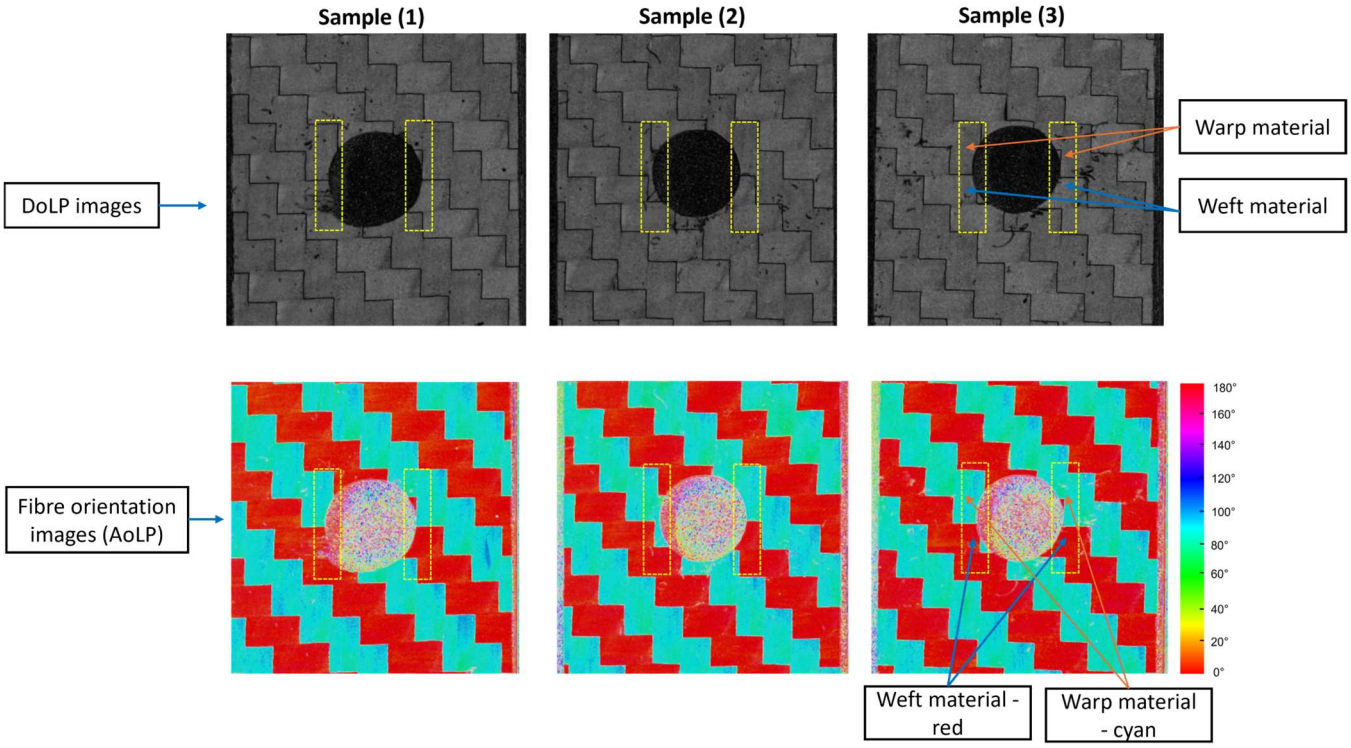


Figure 5.62 - The fibres' orientation and the corresponding DoLP images for three samples of Twill 2x2 with an 8 mm hole were imaged using the polarisation camera, showing the difference in weft and warp material after machining the hole.

Table 5.13 - The mean of the AoLP and standard deviation result in the corresponding strain after applying the Gaussian curve fitting to the fibres' orientation images of the one-layer Twill 2x2 sample, (sample-2), with an 8 mm machined hole captured during tensile testing (Figure 5.58).

The mean of AoLP (degree) – Peak (1)	Standard deviation (the width of the peak)	Strain (%)	The mean of AoLP (degree) – Peak (2)	Standard deviation (the width of the peak)
1.08 ± 0.41	5.04 ± 0.59	0	91.14 ± 0.35	4.35 ± 0.50
1.26 ± 0.43	5.18 ± 0.61	0.002	91.01 ± 0.36	4.32 ± 0.51
1.28 ± 0.44	5.28 ± 0.62	0.33	91.31 ± 0.38	4.35 ± 0.54
1.41 ± 0.51	5.84 ± 0.72	0.53	91.46 ± 0.44	4.60 ± 0.63
1.49 ± 0.55	6.28 ± 0.78	1.46	91.41 ± 0.49	4.79 ± 0.69
1.86 ± 0.53	5.84 ± 0.75	1.47	91.54 ± 0.41	4.75 ± 0.58

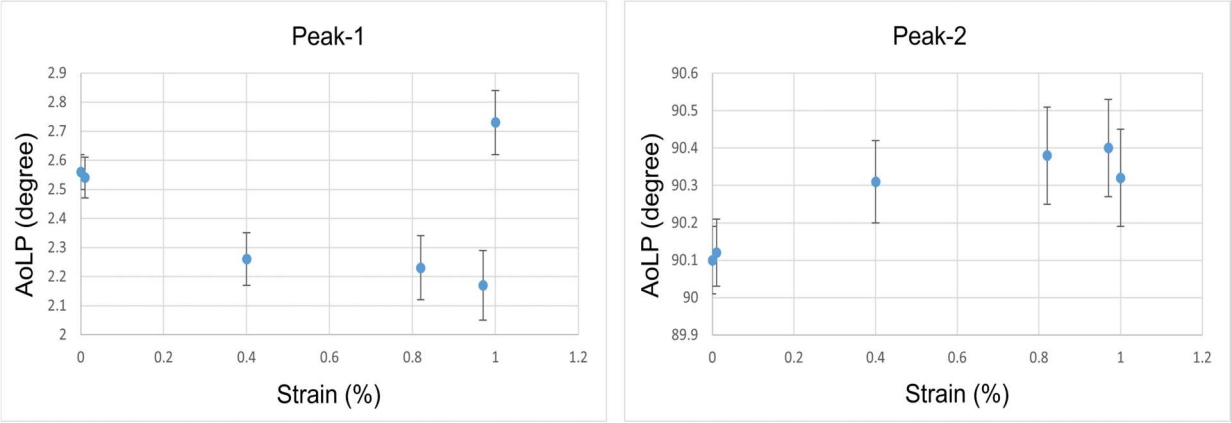


Figure 5.63 - The mean of the AoLP behaviour for a one-layer of Twill 2x2 sample, (sample-2), containing an 8 mm machined hole with increasing strain (for the six selected images in Figure 5.58) for the two peaks.

To summarise the influence of hole diameter on the elastic modulus of Twill 2x2 carbon fibre samples, Table 6.14 presents the average, standard deviation, and coefficient of variation for elastic modulus. As expected, a decreasing trend is observed in the average elastic modulus with increasing hole diameter. Compared to baseline samples, the average elastic modulus for the 12 mm and 8 mm hole diameter samples decreased by 24.75% and 4.59%, respectively. Figure 5.65 shows a visual representation of the average elastic modulus for each hole diameter category. The results indicated that an increase in hole diameter led to a reduction in the average modulus. This reduction is attributed to the removal of a greater

number of fibres from the total width of the specimen. As expected, failure in the open-hole samples initiated at the edges of the machined holes, where stress concentrations developed due to fibre discontinuities introduced during the machining process. The AoLP images captured using the polarisation camera during tensile testing revealed the behaviour of fibre orientation near the machined hole under increasing strain. Furthermore, the analysis of both DoLP and AoLP images suggested that the relative position of the machined hole with respect to the weft and warp fibre directions significantly influenced the mechanical performance of the specimens. This positional dependency is considered a factor contributing to the observed variation in the mechanical properties among the tested samples. The geometry of the remaining fibres adjacent to the machined hole in each sample exhibited different orientation behaviour with increasing strain. Further investigation, incorporating detailed DoLP and AoLP analyses, is required to optimise the positioning of the machined hole to enhance the mechanical performance of the tested samples.

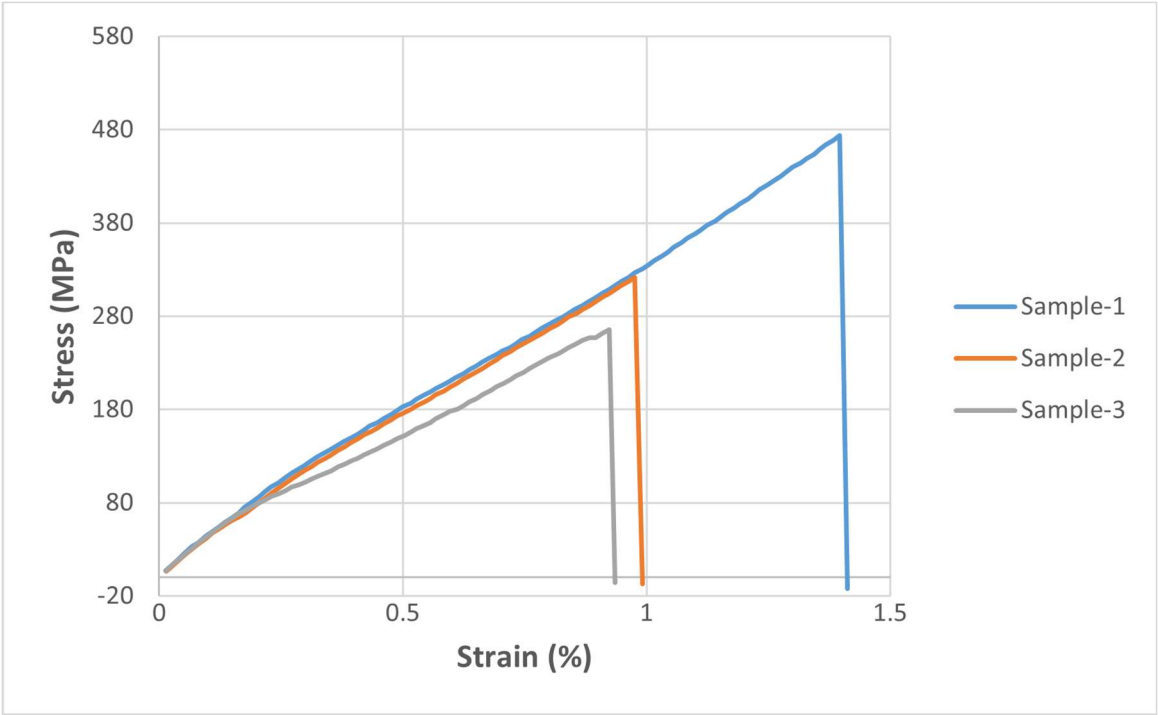


Figure 5.64 - The stress and strain curve for three Twill 2x2 samples, consist of one-layer, with an 8 mm machined hole.

Table 5.14-The average, standard deviation and coefficient of variation corresponding to the elastic modulus for the baseline and three different hole diameters of Twill 2x2 samples.

Elastic modulus (GPa)			
Twill 2x2 samples	**Average**	**Standard deviation**	**Coefficient of variation (%)**
Baseline	33.37	1.95	5.87
12mm hole diameter	26.02	0.79	3.04
10mm hole diameter	31.37	1.63	5.21
8mm hole diameter	31.87	2.78	8.74

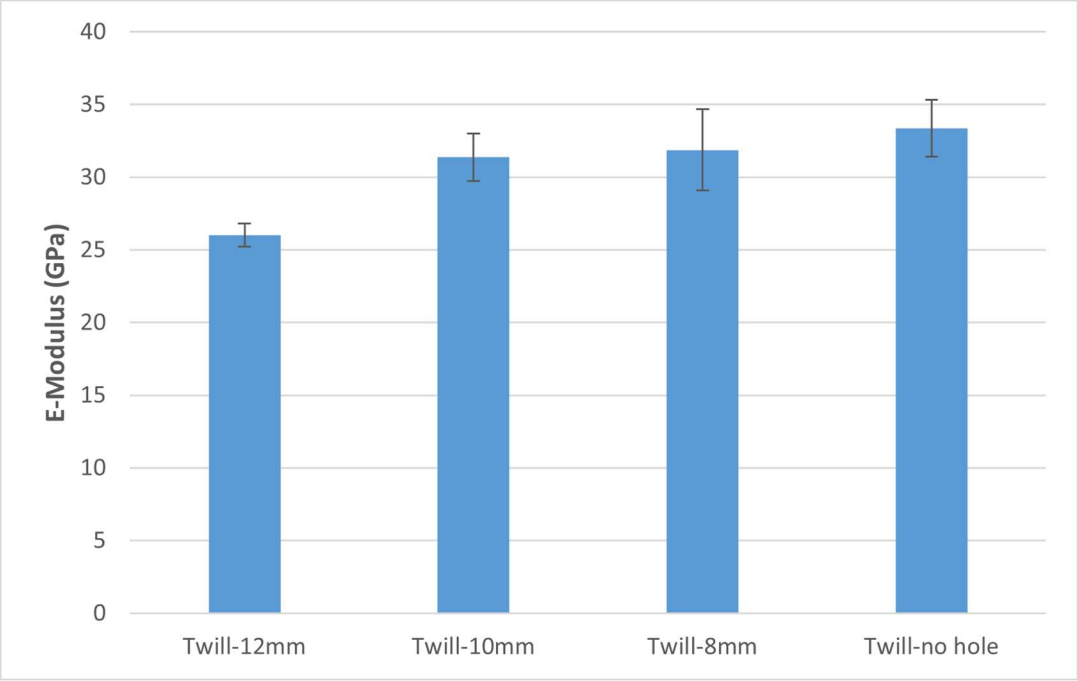


Figure 5.65 - The average modulus (GPa) is shown as a bar chart for Twill 2x2 samples, baseline and with different hole diameters (12,10 and 8) mm, with an error bar as the standard deviation for three samples.

5.5 Conclusion

This chapter investigated the fibres' orientation behaviour around a machined hole applied to UD-NCF and Twill 2x2 samples with three different hole diameters. The polarisation camera was employed to capture the samples before and during the tensile test, investigating and comparing the fibres' orientation behaviour. The hue

channel in the fibre orientation image (HSV colour space) encodes the AoLP data, which matches the fibre's direction. The mean of the AoLP was extracted after applying a Gaussian curve fitting to the histogram of the AoLP data. The mean of the AoLP was compared at different strain levels to investigate the fibre orientation behaviour with increasing strain.

The fibre orientation images captured using the polarisation camera detected the fibre splitting and the change in the fibre orientation of UD-NCF samples. Moreover, the fibre orientation and DoLP images show the possible effect of the difference in the cutting of the warp and weft material around the machined hole. The DoLP images of the UD-NCF samples manufactured from the same panel show a difference between the thermoplastic thread (weft) and the machined hole edge between the samples, which might be one of the reasons for the variations that occurred between the samples' mechanical properties. Also, the DoLP and fibre orientation images of Twill 2x2 samples show the difference in the fibre orientations at the machined hole edges between the three samples.

The effect of the fibre orientation in the machined hole edges on the mechanical properties needs more investigation by positioning the machined hole in the UD-NCF samples (from the same panel) at different calculated distances from the thermoplastic thread (weft material). Also, the machined hole in the Twill 2x2 samples needs to be positioned in different places to investigate the fibre orientation effects of the different shapes resulting after machining the hole (fibres in the tension direction). The DoLP and AoLP images revealed notable distinctions among the UD-NCF samples with machined holes, particularly in relation to the relative position of the hole and the orientation of the weft material. This differentiation arises because the thermoplastic thread in the weft direction was readily distinguishable from the carbon fibres aligned along the loading direction when observed using the polarisation camera. In the DoLP images, the carbon fibres appeared in greyscale, whereas the thermoplastic thread was represented in black. In contrast, for the Twill 2×2 woven samples, both the warp and weft carbon fibres exhibited similar greyscale appearances in the DoLP images. However, the AoLP images effectively captured variations in fibre orientation at the edges of the machined holes, thereby enabling an assessment of the influence of hole position. Furthermore, the geometry

of the remaining fibres around the machined holes in the Twill 2×2 samples was examined to facilitate a comparison between the tested specimens.

The polarisation images and the corresponding analysis of fibre orientation behaviour around the machined hole, presented in this chapter, provide valuable insights that serve as a foundation for understanding the evolution of fibre orientation in the UD-TFP reinforced-hole samples under increasing strain, as examined in the next chapter.

6 POLARISATION ANALYSIS OF FIBRE ORIENTATION OF TAILORED FIBRE PLACEMENT SAMPLES WITH LOCAL REINFORCED HOLE DURING TENSILE TESTING

6.1 Introduction

The open-hole tensile tests were applied to unidirectional tailored fibre placement (UD-TFP) samples with a TFP reinforced hole of 12 mm diameter to investigate the fibre behaviour around the reinforced hole during the test and the polarisation camera's sensitivity to changes in orientation. Three-hole diameters (12 mm, 10 mm, and 8 mm) were machined into the 12mm TFP-reinforced hole using a CNC machine (with the 4mm tool, as explained in the Methodology chapter **section 3.3.1**) to investigate the influence of hole size on tensile response and fibre orientation. These different hole sizes were applied to two groups of samples with varying numbers of layers (two and four layers) to assess the impact of layer count on material behaviour around the reinforced hole. The CNC and 4mm tools were chosen so all the machined holes would experience the same cutting process.

The limitations in the experimental rigs regarding the maximum force load and the effect of the number of layers on the TFP samples, where more layers were applied, required a complicated stitching pattern and led to the choice of the number of layers in this test. As explained in the Methodology chapter, (**section 3.2.4**), consideration of the ply symmetry (mirroring) and non-symmetrical fibre placement in relation to the local reinforcement was the reason for choosing TFP samples with four and two layers to investigate the fibre orientation behaviour during the test using the polarisation camera.

6.2 Sample preparation

UD-TFP-reinforced hole specimens were fabricated using VARTM technique and cured in a programmable oven. Two batches, two and four plies of three specimens were prepared for each machined hole size, each with standardised dimensions of 25 mm width and 250 mm length. For more details about the process of preparing the sample, see the Methodology **section 3.2.1**.

6.3 Variability

The variability in the manufacturing process, Figure 6.1, which may affect the properties of UD-TFP samples are considered as follows:

- Sample width: Some of the TFP preforms have less width than expected (25 mm), which creates a resin-rich area at the edge of the sample.
- Loop-back carbon fibre: the size and position of the curvature from the loop-back path when placing the UD-carbon fibre tow varies.
- Stitch position: the position of the stitches around and in the local reinforced hole varies between the samples.

Figure 6.1 illustrates the manufacturing variability in TFP preforms. In the image (a), some preforms exhibit a width less than the required 25 mm, resulting in resin-rich areas at the sample's edges. This variability can negatively impact the mechanical properties. The carbon fibre covers approximately 23 mm of the sample's width, with the remaining 2 mm consisting of resin and the base material (glass fibre). Image (b) highlights variations in the loop-back paths of UD-TFP reinforced preforms. Inconsistent loop-back paths lead to non-uniform resin-rich areas within the same sample. Image (c) demonstrates differences in loop-back position relative to local reinforced holes, both within and between samples. Samples exhibiting more than 10% (2.5mm) resin-rich area at the edge were excluded from tensile testing.

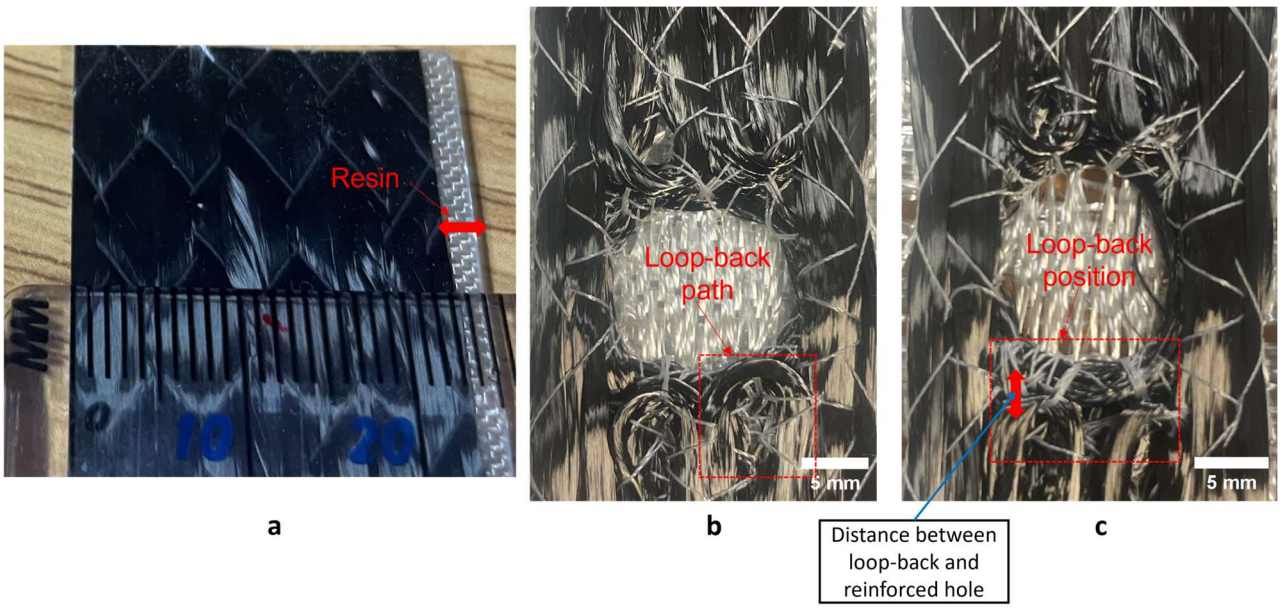


Figure 6.1 - Examples of manufacturing uncertainty of UD-TFP reinforced hole samples with four layers, (a) shows that sample's width less than what expected, (b) shows the loop-back path, and (c) shows the loop-back position regarding the reinforced hole.

Figure 6.2 emphasises the impact of stitch placement on UD-TFP reinforced hole preforms and the curvature of the carbon fibre loop-back path. Image (a) shows a lack of stitches in the loop-back curvature, while image (b) illustrates stitches holding and applying tension to the curvature. Image (c) represents overlapping stitches between the reinforced hole and the loop-back curvature. The position of these stitches significantly influences the carbon fibre orientation between samples.

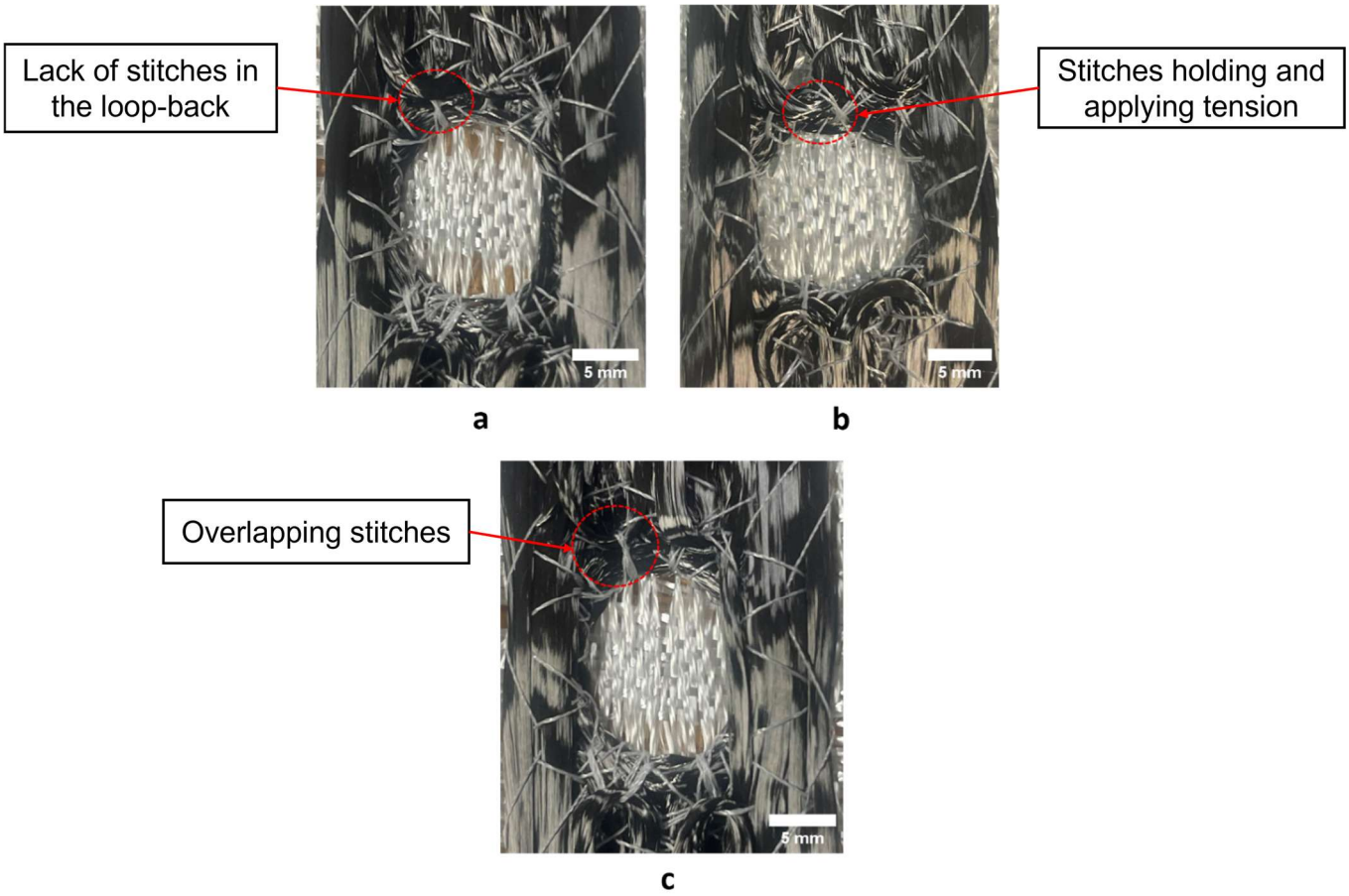


Figure 6.2 - Three UD-TFP reinforced hole preforms showing an example of stitch placement around the local reinforced hole. a) shows a lack of stitches in the loop-back, b) shows stitches applying tension on the fibre, c) shows an overlapping between the stitches.

6.4 VARTM UD-TFP reinforced hole with four layers

To inspect the fibres' orientation behaviour around the reinforced hole during tensile testing, UD-TFP reinforced hole samples with four plies were prepared. The polarisation camera was used to capture the raw saturation and the fibres' orientation image at the same time during the test. The sample set with a 12 mm

diameter machined hole was the first set to be inspected using the polarisation camera during the tensile test, (sample-1).

Figure 6.3 presents images captured using a polarisation camera before tensile testing (offline inspection). Images (a-c) depict the raw saturation image, Degree of Linear Polarisation (DoLP) image, and fibres' orientation image, respectively, (sample-1). The DoLP image (b) identifies carbon fibres (grey), resin-rich areas, glass fibre, and polyester stitches (black). The fibres' orientation image (c) visualises the fibres' orientations based on Angle of Linear Polarisation (AoLP) information stored in the hue channel of the HSV image. The colours observed within the reinforced hole are caused by background reflections, which was neglected later in the image analysis. The carbon fibres within the loop-back path show varying orientations, particularly at the curvature near the local reinforcement. Therefore, the polarisation camera will focus on capturing fibre orientations around the reinforced hole and loop-back path during the tensile test. The sample shows a resin-rich area at its right edge, and the carbon fibres near the resin-rich area are misaligned with regard to the tension direction.

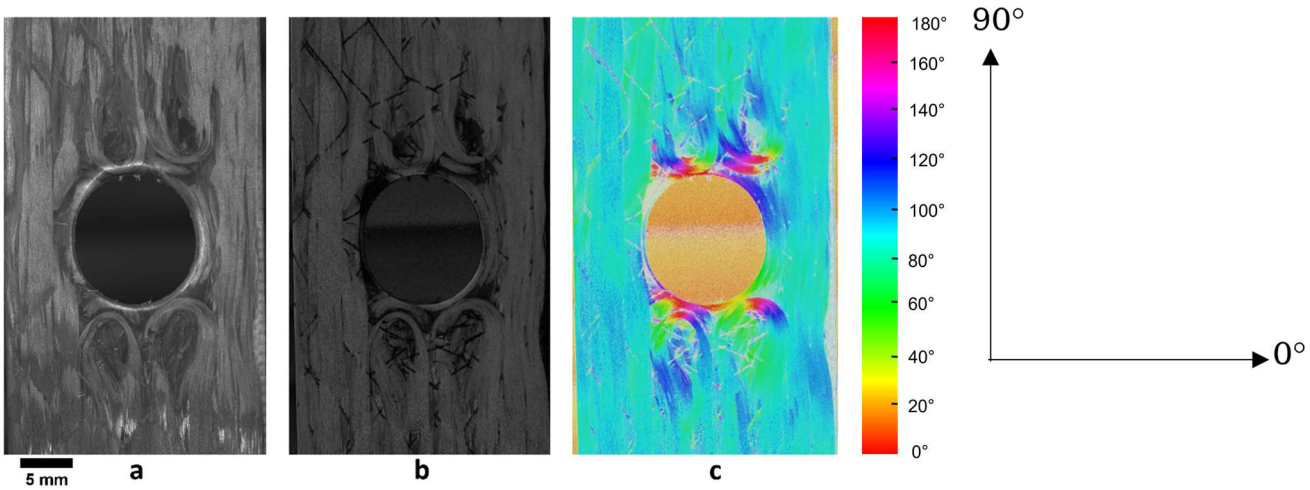


Figure 6.3 - UD-TFP reinforced hole (12 mm local reinforced hole and 12 mm machined hole) sample, (sample-1), with four layers was imaged using the polarisation camera, where (a) the raw saturation image, (b) the DoLP image and (c) the fibres' orientation image.

Following an offline inspection, the sample was mounted on the tensile machine for polarisation camera-based fibre orientation monitoring during the tensile test. Figure 6.4 presents a sequence of fibres' orientation images for the UD-TFP reinforced hole

sample, (sample-1), with a 12 mm machined hole. Image (a) shows the initial fibre orientation at 0 % strain, while image (b) represents the orientation after one second (0.01 % strain).

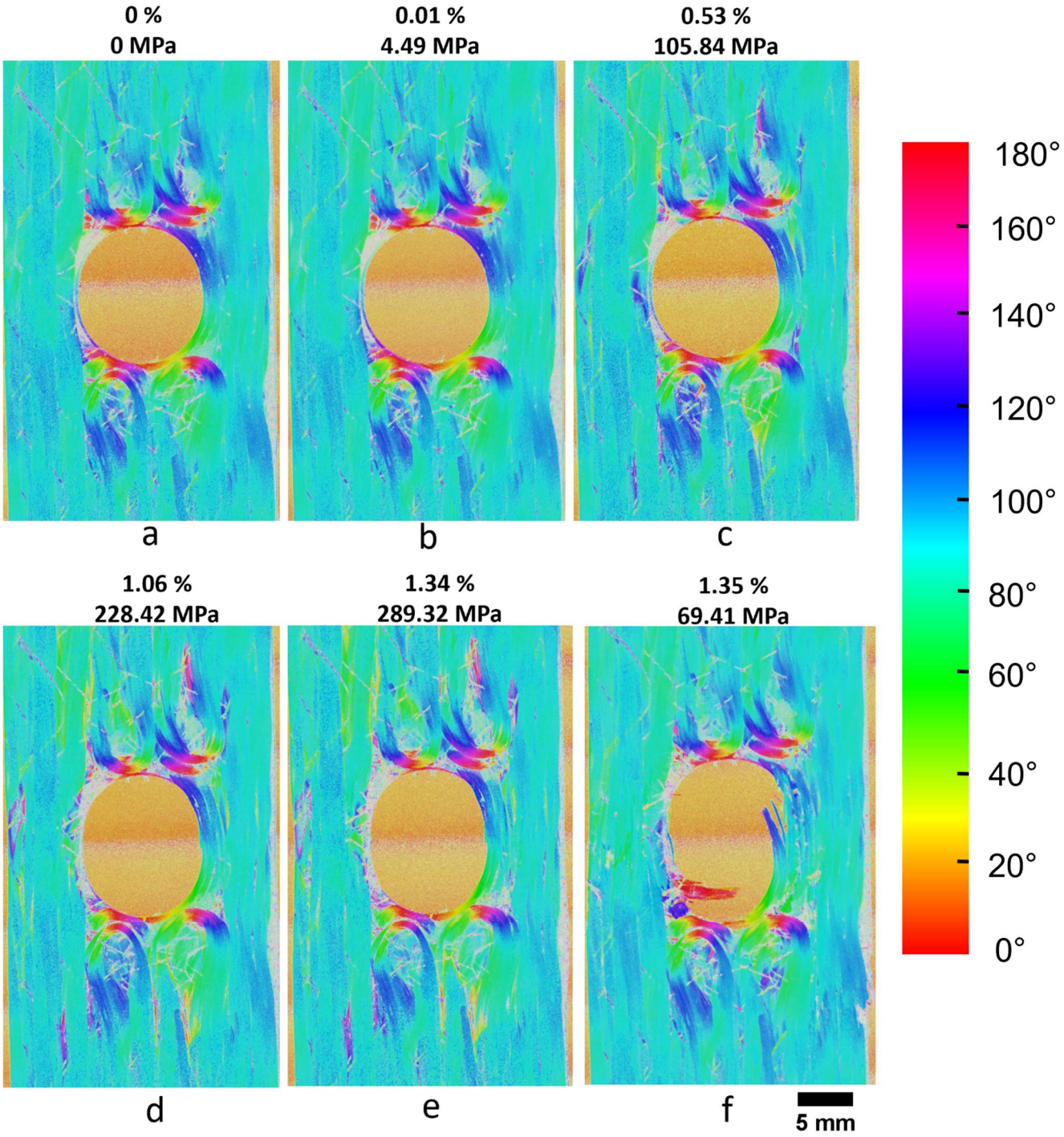


Figure 6.4 - The fibres' orientation images of a four-layer UD-TFP reinforced hole sample, (sample-1) with a 12 mm machined hole were captured during tensile testing using the polarisation camera. The corresponding stress and strain for each image are presented above the figure.

Images (c) and (d) illustrate orientations at 40 seconds (53 % strain) and 80 seconds (1.06 % strain), respectively. Image (e) captures the orientation at maximum force load (1.34 % strain), and image (f) shows the fibres' orientation after two seconds from reaching the maximum force load at 1.35 % strain.

A comparison of fibre orientation images at 0% and 1.34% strain reveals that increased strain impacts the orientations of the carbon fibres around the reinforced hole and the loop-back path. To provide further information about fibre orientation around the reinforced hole, histograms of the AoLP data extracted from the hue channel was presented at 0 % and 1.34 % strain to analyse the fibres' orientation distribution. Figure 6.5 presents the region of interest around the reinforced hole before and at maximum tensile load, along with the corresponding histograms of the

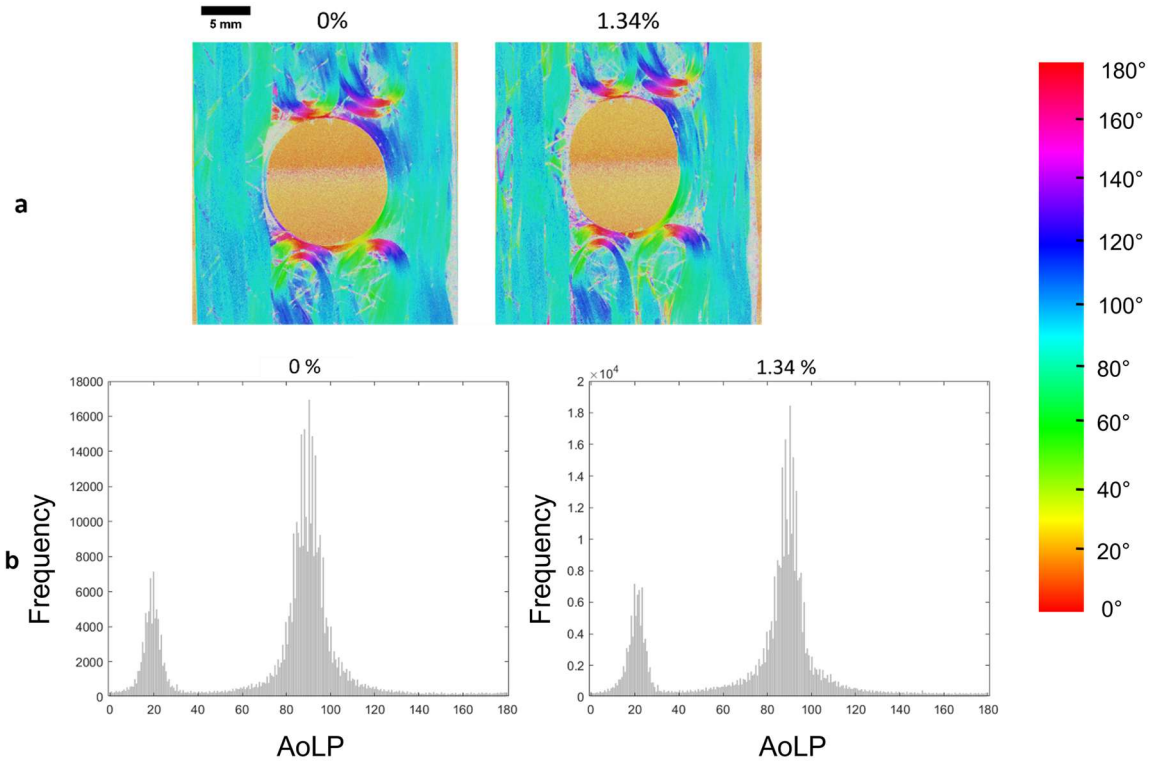


Figure 6.5 - The selected region of interest around the reinforced hole of the UD-TFP sample with a 12 mm machined hole, where (a) shows the fibres' orientation image at different strains and (b) represents the corresponding histogram of the AoLP information (hue channel) in (a).

hue channel, representing the fibres' orientation distribution. The histograms reveal a dominant peak for fibre orientations between 60° and 120°, indicating the primary

fibre orientation. The secondary peak at 20° represents the background reflections through the reinforced hole.

Figure 6.6 illustrated Gaussian curve fitting applied to the histogram data presented in Figure 6.5. A standard MATLAB curve fitting algorithm was employed to fit the Gaussian curve to the histogram peak corresponding to fibre orientations between 60° and 120°, both before the tensile test (0 %) and at maximum force load (1.34 %). The mean and standard deviation of the AoLP distribution were calculated for both states. Before the test, the mean was 89.72° with a standard deviation of 8.99°. At maximum force load, the mean decreased slightly to 89.51° with a standard deviation of 7.77°.

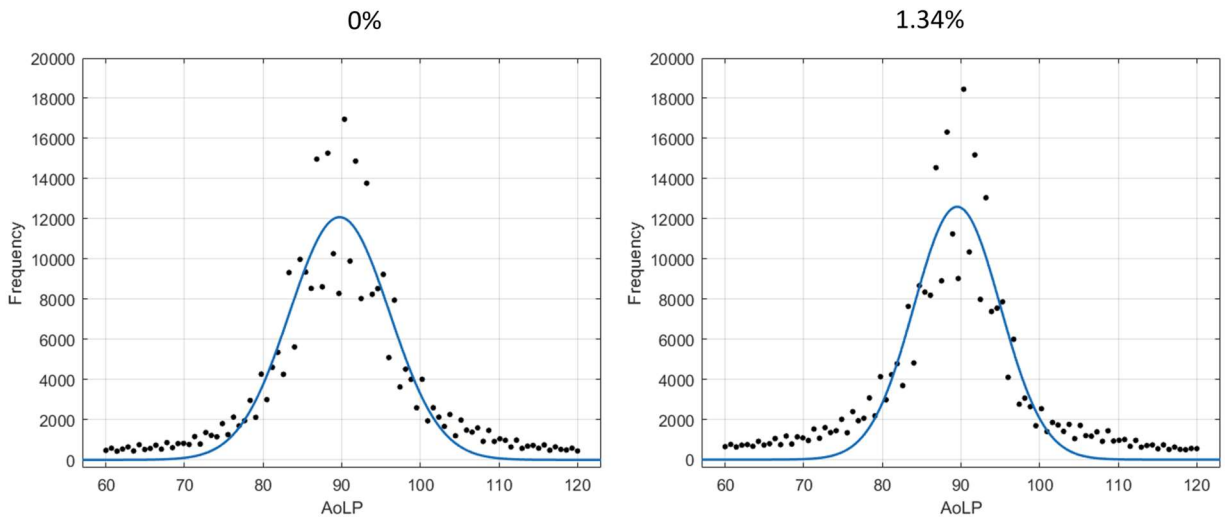


Figure 6.6 - MATLAB fitting of Gaussian curve to the histogram data of four layers UD-TFP reinforced hole sample with 12 mm machined hole before starting the tensile test and at maximum load force.

For deeper insights into fibre orientation behaviour during tensile testing, fibres within a ± 5° range of the mean orientation were isolated in the orientation image using hue channel information. Figure 6.7 highlights fibres with orientations between 84.72° and 94.72° (hue values 120 - 134) in white for 0 % and 1.34 % strain samples (a and b, respectively). Image (c) presents the difference between these two images, revealing how increasing strain affects the fibres' orientation around the reinforced hole in the four layers of the UD-TFP reinforced sample with a 12 mm machined hole.

Table 6.1 summarises the maximum force load, tensile strength, failure strain, and tensile modulus for four layers UD-TFP reinforced hole samples with a 12 mm machined hole. The differences in the results are due to variations in manufacturing factors, such as the resin-rich area at the sample's edge and around the reinforced hole, the loop-back position corresponding to the reinforced hole, the orientations of the carbon fibres in the loop-back, and stitch positioning.

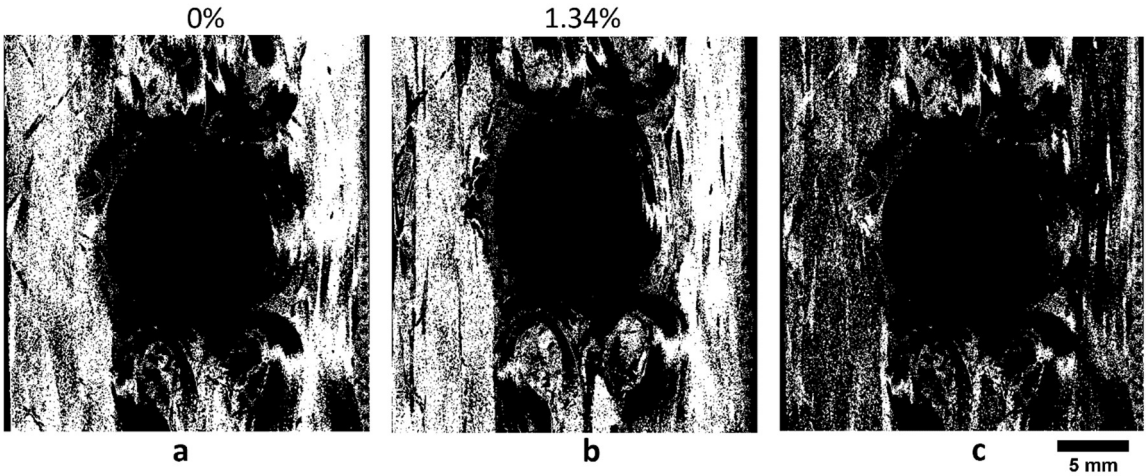


Figure 6.7 - The fibres with orientations between ± 5° from the mean of the AoLP in the Gaussian distribution (89.72°) of a four-layer UD-TFP reinforced hole sample, (sample-1), with a 12 mm machined hole are presented in white. Image (a) represents the fibres with orientations between 84.72° and 94.72° for the fibres' orientation image at 0 % strain, while image (b) at strain equals 1.34 %. Image (c) shows the subtracting results of image (b) from image (a).

Figure 6.8 presents three UD-TFP reinforced hole samples, each with four layers and a 12 mm machined hole into the local reinforcement. The samples were subjected to tensile testing. Images (a) show the raw images of the samples, while images (b) represent the orientation of the fibres within the samples. The images highlight the variations in the manufacturing factors of the three samples, particularly in terms of the factors mentioned in **Section 6.3**.

A selected region around the reinforced hole and the loop-back path was chosen from the fibre orientation images taken during the tensile test (Figure 6.4). The

Table 6.1 - The tensile test information for three UD-TFP reinforced hole samples with four layers and a 12 mm machined hole.

Sample Number	Maximum force (N)	Ultimate tensile strength (MPa)	Strain (%)	E-modulus (GPa)
Sample-1	13887	289.32	1.34	21.48
Sample-2	12947	264.22	1.20	22.01
Sample-3	17164	345.01	1.61	21.38
Average	14666	299.52	1.38	21.62
Standard Deviation	2213	41.34	0.20	0.34

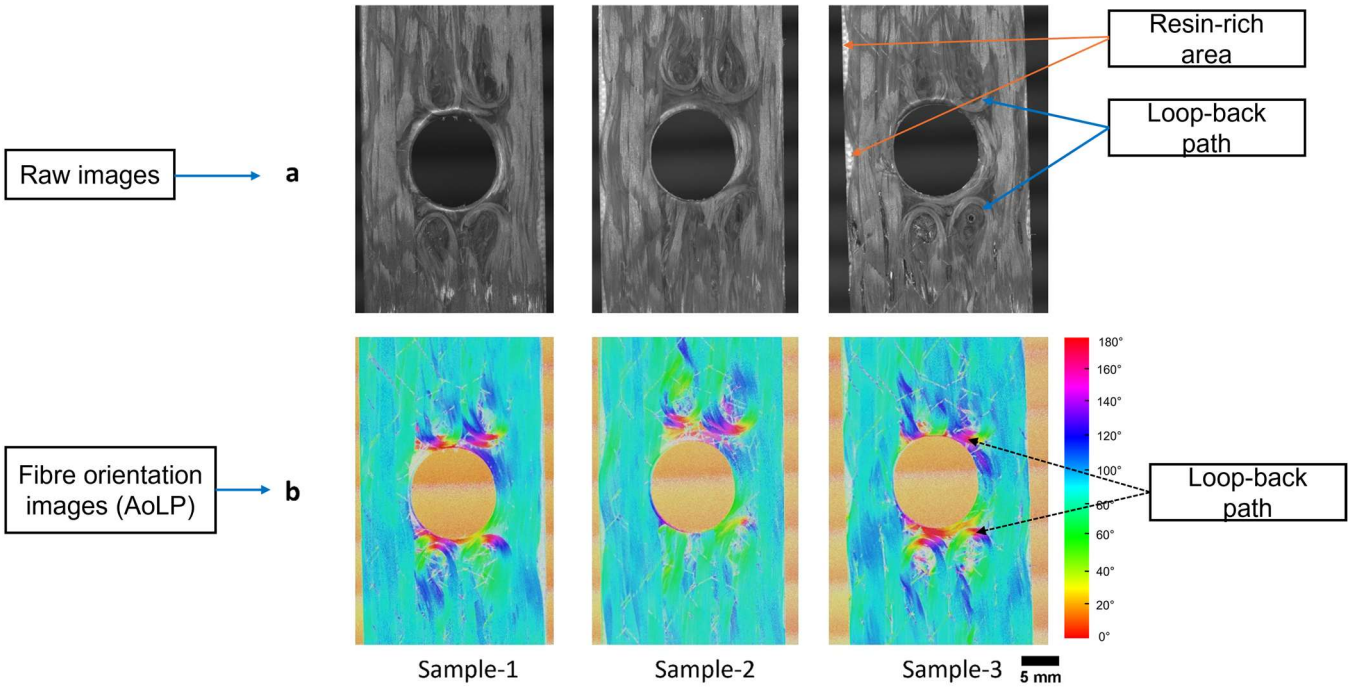


Figure 6.8 - Example of three samples UD-TFP reinforced hole, (before starting the test), with four layers and 12 mm machined hole subjected to tensile test, showing the difference between the samples regarding the loop-back position and fibres orientations, samples' width and the resin at the samples' edge, and stitch position. (a) represents the raw image and (b) the corresponding fibres' orientation image for three samples captured using the polarisation camera.

Gaussian curve was fitted to the histogram of fibre angles between 60° and 120°, as shown in Figure 6.6, to calculate the average of AoLP at different strain levels. Table 6.2 shows the mean AoLP and its standard deviation for each strain level. As seen in Figure 6.9, the average AoLP changes as the strain increases. The largest decrease in AoLP, 0.30°, occurred between 0.53% and 1.06% strain. After this point, the AoLP only increased slightly, by 0.06°, until the sample failed.

Table 6.2 - The mean of the AoLP and standard deviation results to the corresponding strain after applying the Gaussian curve fitting to the fibres' orientation images that were captured during the tensile test (Figure 6.4), (sample-1).

The mean of AoLP (degree)	Standard deviation (the width of the peak)	Strain (%)
89.72 ± 1.10	8.99 ± 1.55	0
89.59 ± 1.08	8.69 ± 1.54	0.01
89.75 ± 1.14	8.51 ± 1.61	0.53
89.45 ± 1.14	8.36 ± 1.61	1.06
89.51 ± 1.04	7.77 ± 1.47	1.34
89.71 ± 1.09	8.68 ± 1.54	1.35

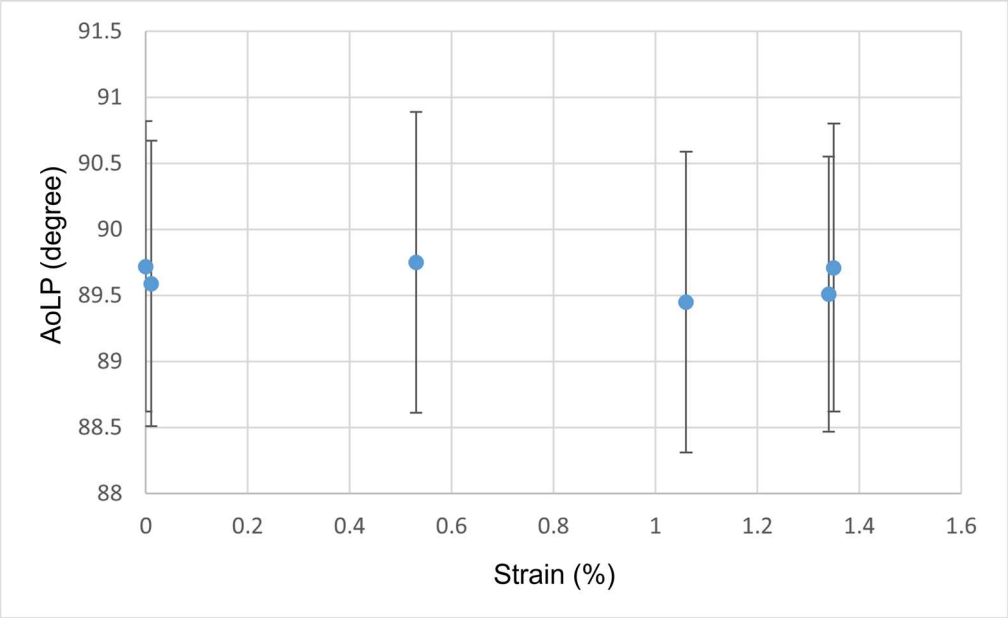


Figure 6.9 - The mean of the AoLP behaviour for sample-1 during the tensile test for the UD-TFP reinforced hole sample with four layers and a 12 mm machined hole.

Figure 6.10 illustrated the mean fibre orientation (AoLP) values for the three tensile test samples in the selected six fibre orientation images during increased strain. The figure demonstrates how the different manufacturing factors influence the fibres' orientation behaviour as the strain increases.

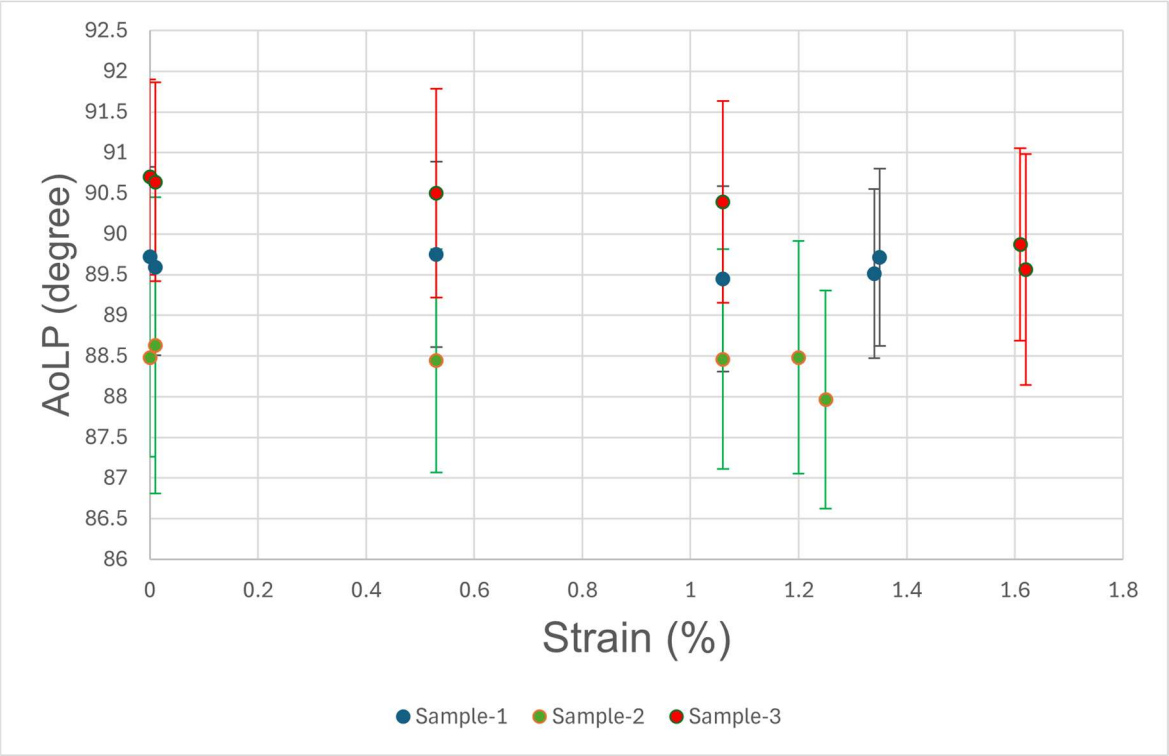


Figure 6.10 - The mean of the AoLP behaviour during the tensile test (of the selected images) for three UD-TFP reinforced hole samples with four layers and a 12 mm machined hole.

To provide more in-depth analysis and comparison of how fibre orientation behaves step by step during tensile testing in the three samples, Figure 6.11 displays the mean of the AoLP values for all the fibre orientation images captured during the tensile test using the polarisation camera (one image taken per second).

Figure 6.12 illustrated the stress and strain curves for three UD-TFP reinforced hole samples, each with four layers and a 12 mm machined hole in the local reinforcement. Sample (1) exhibits a linear response when the stress reaches 38 MPa up to the failure point. Sample (2) shows a linear response when the stress reaches 50 MPa up to 250 MPa, and after that, sample shows a dip and then recovers in the stress to the failure point. Sample (3) shows a brittle failure with a linear response up to the failure point.

The images captured using the polarisation camera during tensile testing revealed distinct failure mechanisms among the samples. In Sample (1), as the applied strain increased, the fibres located on the left side near the reinforced hole began to fracture following the breakage of the adjacent stitches. This progressive damage propagated to neighbouring fibres until the stitches holding the fibres at the left edge of the sample also failed, ultimately leading to complete specimen failure. In contrast, Sample (2) exhibited a different failure pattern. The stitches positioned near the loop-back region on the right side began to fail progressively with increasing strain. This localised stitch failure affected the fibres adjacent to the reinforced hole, initiating further fibre breakage around the hole and resulting in the final failure of the sample. Similarly, in Sample (3), failure was primarily initiated by the breakage of the stitches securing the fibres near the left edge of the specimen. After that, fibre breakage occurred near the reinforced hole on the right side, after which the sample experienced total failure.

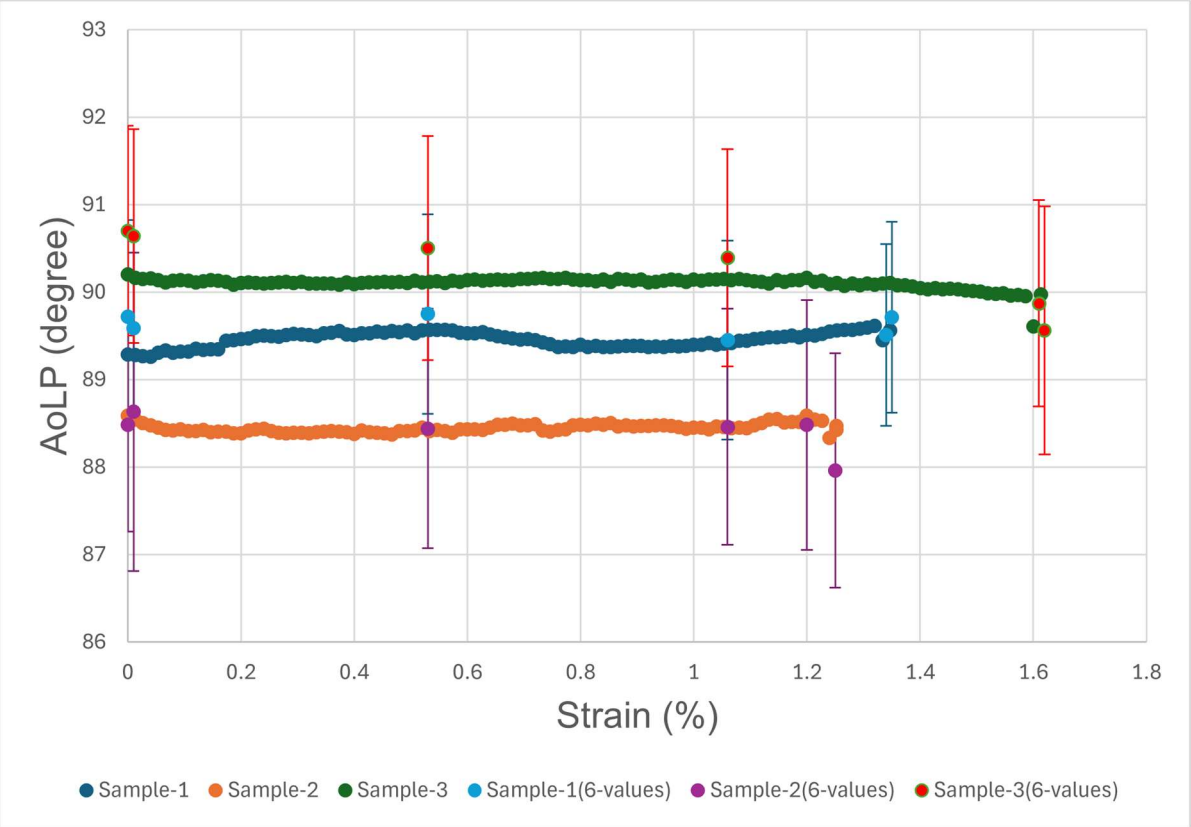


Figure 6.11 - The mean of the AoLP behaviour during tensile testing (of all images captured during tensile testing) for three UD-TFP reinforced hole samples with four layers and a 12 mm machined hole and the selected images (6-values).

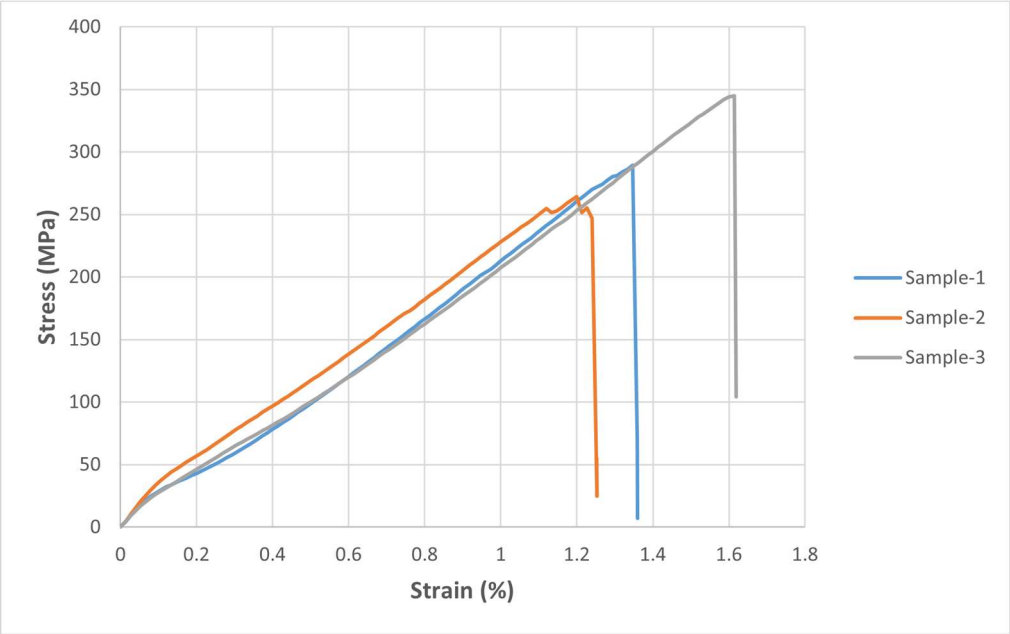


Figure 6.12 - The stress and strain curve for three UD-TFP reinforced hole samples with four layers and a 12 mm machined hole.

The second sample set, modified with a 10 mm hole, (sample-3), machined into the local reinforcement with a 12 mm diameter, underwent the same investigative process. Offline inspection, conducted with a polarisation camera, generated raw saturation, DoLP, and fibres' orientation images, as illustrated in Figure 6.13 a-c.

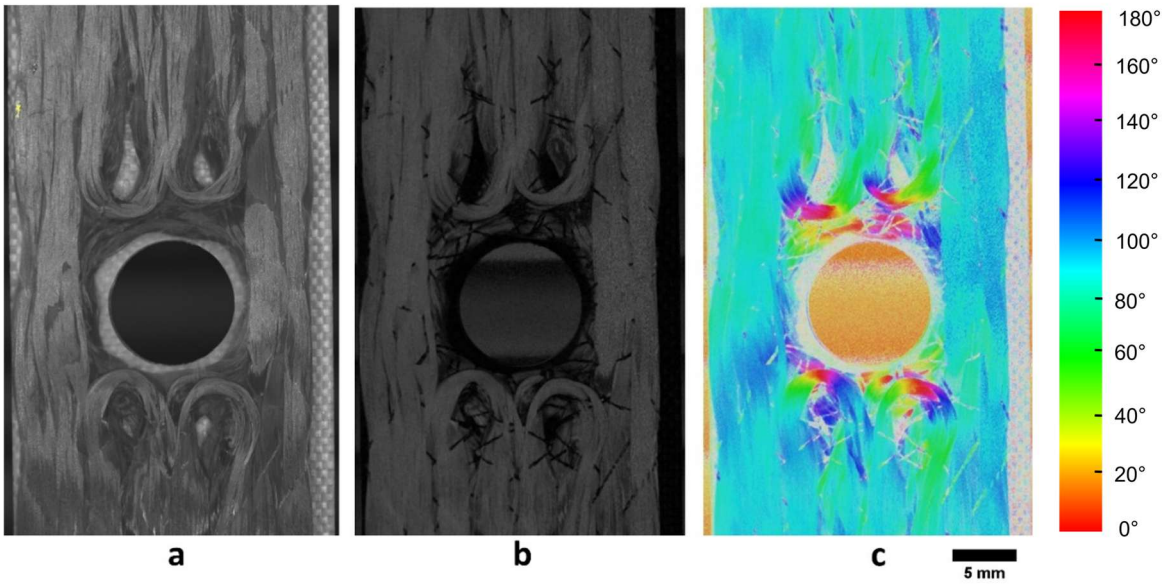


Figure 6.13 - UD-TFP reinforced hole sample, (sample-3), with four layers and a 10 mm machined hole into the 12 mm reinforced hole was imaged using the polarisation camera, where (a) the raw saturation image, (b) the DoLP image and (c) the fibres' orientation image.

Image (a) illustrates the raw saturation image, highlighting overexposed and underexposed regions in yellow and red, respectively. A minor overexposure is observed in the top-left corner. The DoLP presents resin-rich areas surrounding local reinforcements and within the loop-back region, as well as the stitching threads in black. Image (c) represents the fibres' orientation; as previously noted, the AoLP information is encoded in the hue channel of the HSV image.

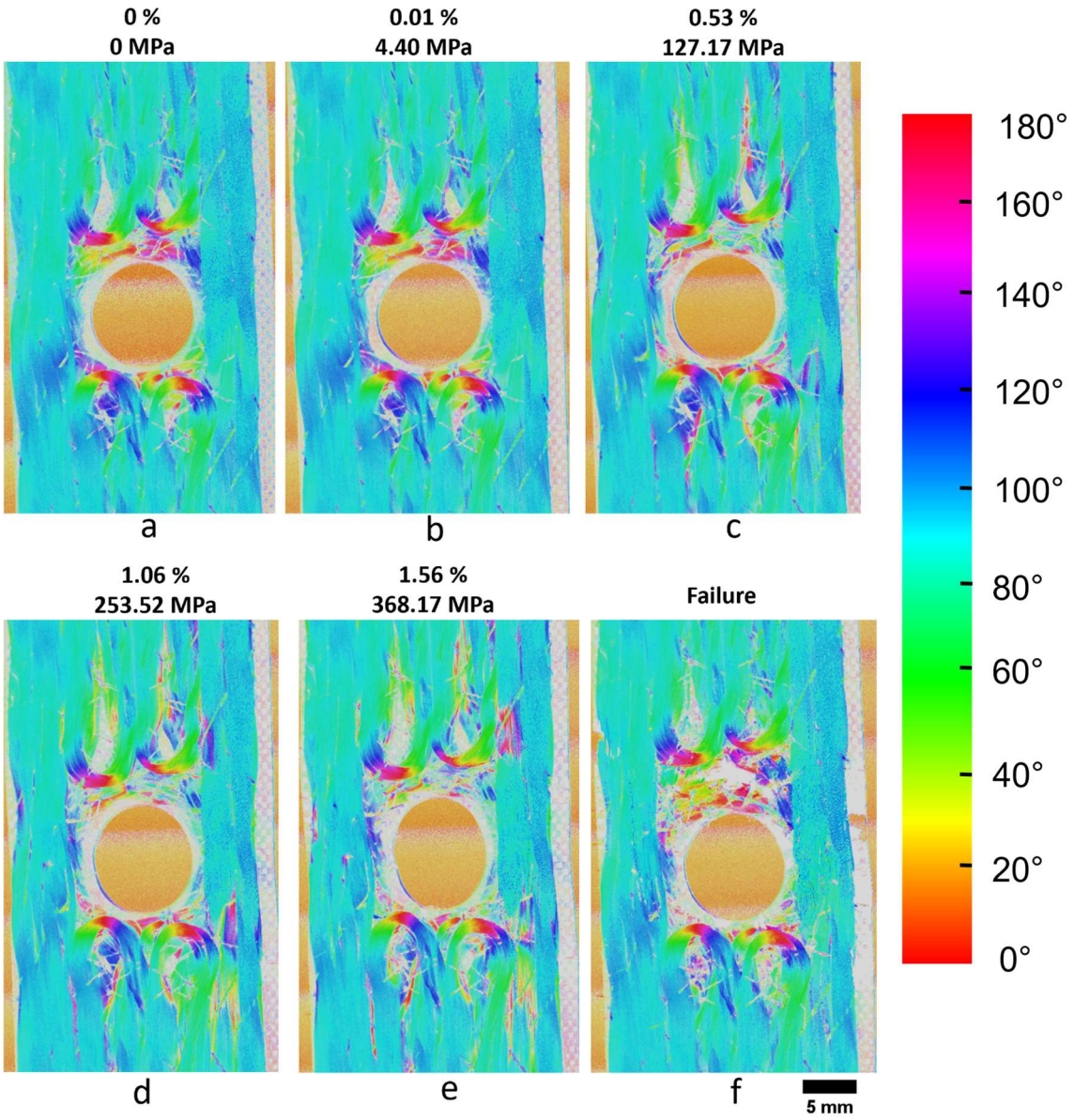


Figure 6.14 - The fibres' orientation images of a four-layer UD-TFP reinforced hole sample, (sample-3), with a 10 mm hole machined into a 12 mm reinforced hole were captured during tensile testing using the polarisation camera. The corresponding stress and strain for each image are presented above the figure.

Figure 6.14 shows the selected fibres' orientation images captured during the tensile test, (sample-3), using the polarisation camera to inspect the fibres' orientation behaviour with increasing strain. Image (a) was captured before starting the test at strains equal to 0 %, while image (e) was captured at maximum force load, which has a strain equal to 1.56 %. The images in Figure 6.14 show the influence of increasing strain on the fibres' orientation at the sample edge, near the reinforced hole, and along the loop-back carbon fibre path.

For a better understanding of the influence of strain on fibres' orientation, a comparative analysis was conducted between the initial fibre orientation image (0 % strain) and the image captured at maximum force load (1.56 % strain). Figure 6.15 presents the fibres' orientation images in the selected region around the local reinforcement at both 0% and 1.56% strain. Additionally, the figure includes a histogram representing the AoLP information derived from the hue channel of the corresponding HSV images. The black dashed circles in Figure 6.15-a highlight that the fibre orientation around the reinforced hole, near the loop-back carbon fibre path, and at the sample's edge was influenced by increasing the strain. Figure 6.15-b presents a histogram of the AoLP values associated with the fibres' orientation images shown in Figure 6.15-a. As previously discussed, the AoLP distribution at 20° represents the reflections from the background through the reinforced hole. Therefore, the peak representing the AoLP distribution between 60° and 120° was subjected to Gaussian curve fitting to calculate the mean of the AoLP under increased strain conditions.

To estimate the mean AoLP within the 60° to 120° range for fibre orientation images at 0 % and 1.56 % strain, a Gaussian curve was fit to the histogram data presented in Figure 6.15 (Figure 6.16). At 0 % strain, the mean AoLP was calculated to be 90.51° with a standard deviation of 10.02°. Upon increasing the strain to 1.56 %, the mean AoLP was calculated to be 90.76° and the standard deviation was 9.03°.

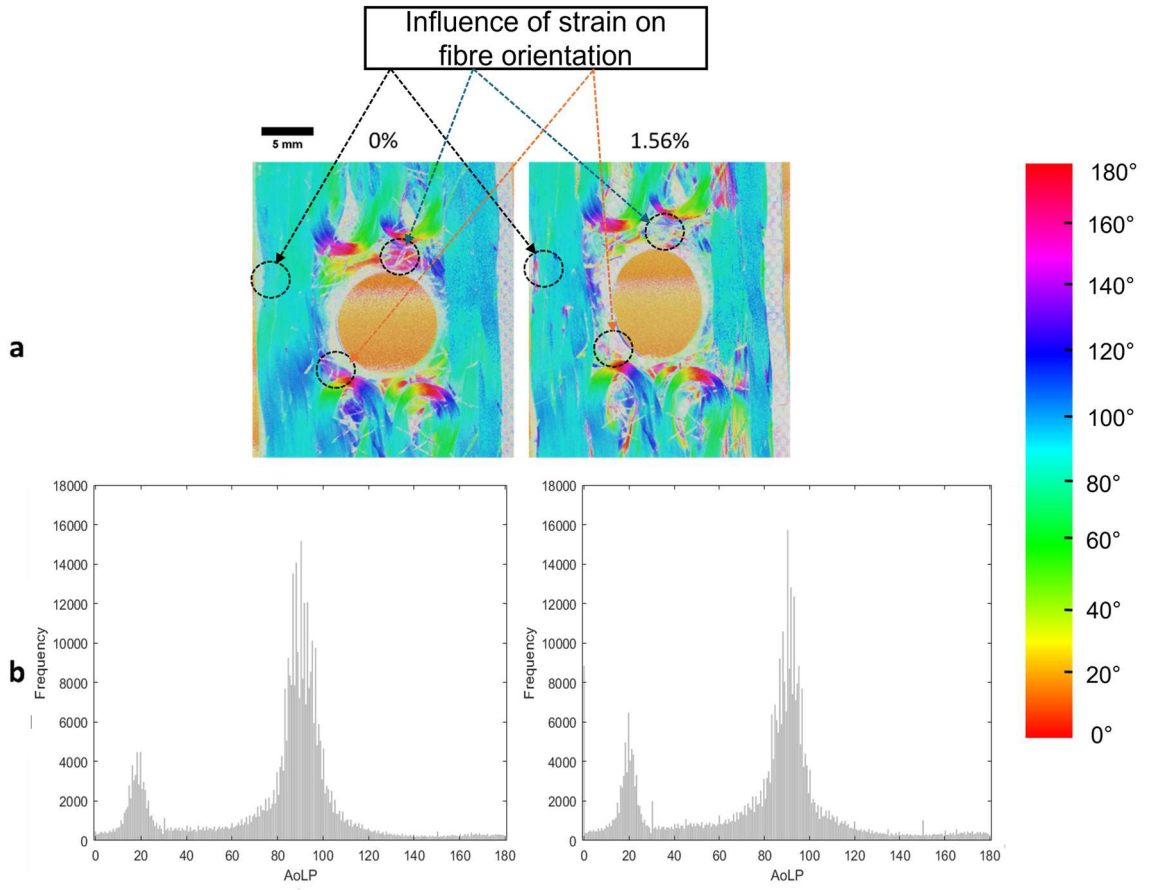


Figure 6.15 - The selected region of interest around the reinforced hole of the four layers of UD-TFP reinforced hole sample with a 10 mm hole machined into the 12 mm reinforced hole. (a) represent the fibres' orientation images at different strains, and (b) shows the corresponding histogram of the AoLP information in (a).

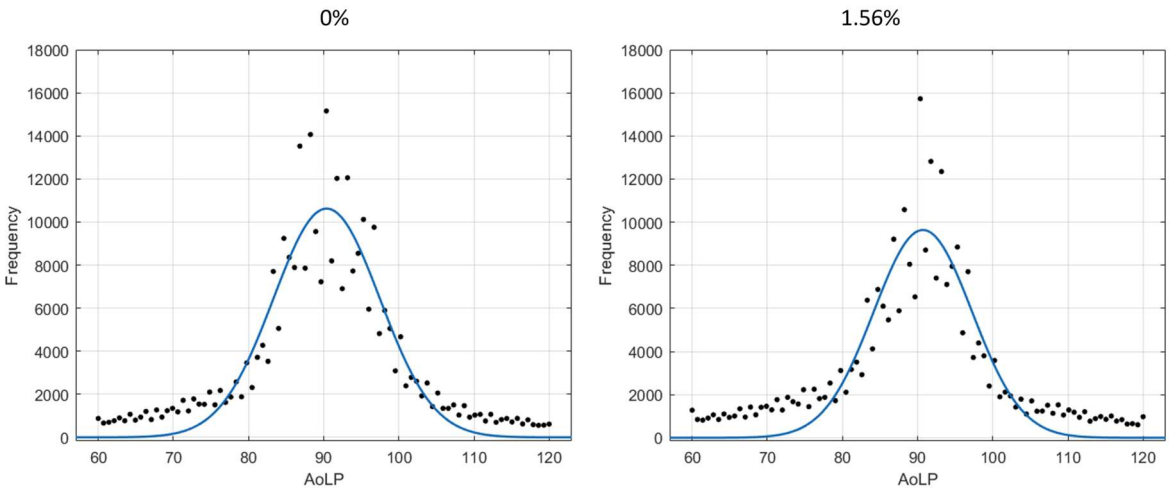


Figure 6.16 - MATLAB fitting of Gaussian curve to the histogram data of four layers UD-TFP reinforced hole sample, with 10 mm hole machined into the 12 mm reinforced hole, before starting the tensile test (0 % strain) and at maximum force load (1.56 % strain).

To present fibres with specific orientations in the fibre orientation image, a mask was employed for the hue channel information to specify the fibres' orientation range. The mask identified fibres whose orientations are within the range of ± 5° from the mean AoLP. Figure 6.17 illustrated the process, highlighting fibres with orientations between 85.51° and 95.51° in white (other fibres in black) at different strain levels. Image (a) showed the selected fibres at 0 % strain, while image (b) showed them at the maximum force load of 1.56 % strain. Subtracting image (b) from image (a) (image c) revealed the influence of increasing strain on fibre orientation, particularly around the reinforced hole and the carbon fibre loop-back path.

Table 6.3 presents a summary of the maximum load, tensile strength, failure strain, and tensile modulus for the four layers of UD-TFP reinforced hole samples with a 10 mm machined hole into a 12 mm local reinforcement. Similar to the UD-TFP samples with a 12 mm machined hole, manufacturing factors variations influenced the observed results. Several factors influenced the failure behaviour of the samples, including the presence of resin-rich regions at the sample edges and around the reinforced holes, the positioning of the loop-back paths relative to these holes, the orientation of the carbon fibres within the loop-back regions, and the location of the stitching. Sample (1) exhibited a large resin-rich area along the sample edge and surrounding the reinforced hole, which significantly affected its mechanical performance. The failure originated from a crack initiated within the resin-rich zone at the sample edge, corresponding to the centre of the machined hole, and also propagated through the resin-rich region located at the left edge of the hole.

Similarly, Sample (2) contained resin-rich regions both at the sample edge and around the reinforced hole. However, in this case, the location of the loop-back path influenced the failure-initiation site. The crack began within the resin-rich area near the loop-back at the sample edge rather than at the machined-hole edges. Sample (3) also exhibited a comparable failure pattern to Sample (2), with the failure initiating in the resin-rich zone at the sample edge close to the loop-back position.

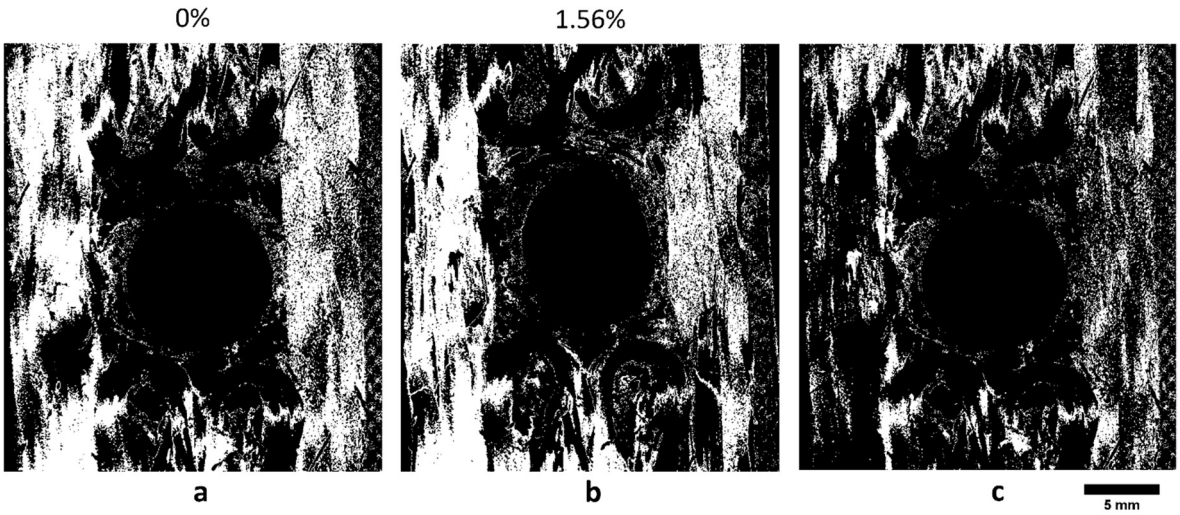


Figure 6.17 - The separation of fibres' orientations of four layers UD-TFP reinforced hole sample, (sample-3), with 10 mm machined hole into 12 mm reinforced hole, using the hue channel information. The fibres with orientations between 85.51° and 95.51° are presented in white, and the other fibres' orientations are in black, where (a) at 0 % strain, (b) at 1.56 % strain, and (c) is the result of subtracting image (b) from (a).

The mean of the AoLP and its standard deviation, derived from Gaussian curve fitting of selected regions within the fibres' orientation images during tensile testing (Figure 6.14), are presented in Table 6.4.

Table 6.3 - Tensile test information for three UD-TFP reinforced hole samples with four layers and a 10 mm machined hole into the 12 mm local reinforcement hole.

Sample Number	Maximum force (N)	Ultimate tensile strength (MPa)	Strain (%)	E-modulus (GPa)
Sample-1	13965	275.19	1.30	21.06
Sample-2	18602	372.04	1.66	22.32
Sample-3	18988	368.71	1.56	23.63
Average	17185	338.65	1.51	22.33
Standard Deviation	2795.06	54.98	0.18	1.29

Table 6.4 - The mean of the AoLP and standard deviation results to the corresponding strain after applying the Gaussian curve fitting to the fibres' orientation images with that were captured during the tensile test (Figure 6.14), (sample-3).

The mean of AoLP (degree)	Standard deviation (the width of the peak)	Strain (%)
90.51 ± 1.26	10.02 ± 1.79	0
90.48 ± 1.23	9.68 ± 1.75	0.01
90.46 ± 1.27	9.41 ± 1.80	0.53
90.52 ± 1.38	9.48 ± 1.95	1.06
90.76 ± 1.33	9.03 ± 1.89	1.56
90.61 ± 1.33	10.27 ± 1.88	1.57

Figure 6.18 illustrated the behaviour of the mean AoLP with increasing strain. An increase of 0.24° in the mean AoLP was observed as the strain progressed from 1.06% to 1.56%, reaching the maximum force load. Subsequently, a decrease of 0.15° in the mean AoLP was recorded upon reaching the ultimate failure point of the sample.

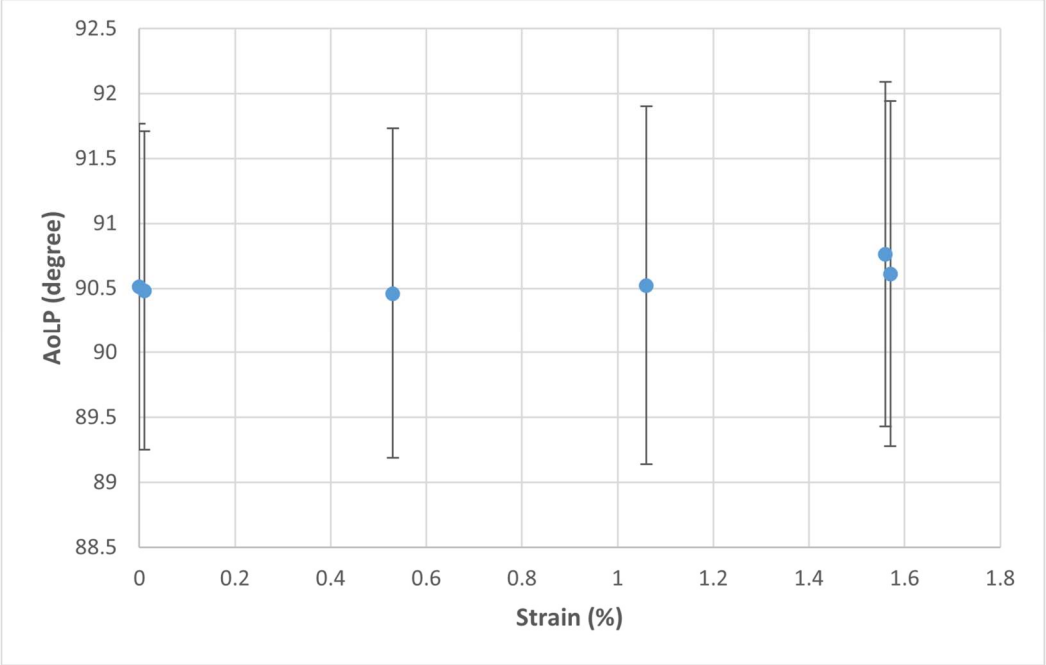


Figure 6.18 - The mean of the AoLP behaviour during the tensile test (selected images) for the UD-TFP reinforced hole sample, (sample-3), with four layers and a 10 mm machined hole.

Figure 6.19 illustrates the stress-strain curves for three UD-TFP reinforced hole samples, each consisting of four layers with a 10 mm machined hole into a 12 mm local reinforcement. Sample (1) exhibits linear behaviour from 39 MPa to 249 MPa, followed by a dip in the stress and subsequent linear recovery to 270 MPa. A minor stress fluctuation precedes final failure. Sample (2) demonstrates a linear response starting from 50 MPa, followed by a nonlinear region with a small stress dip and linear recovery to failure. Sample (3) maintains linear elastic behaviour until failure, initiating at 50 MPa.

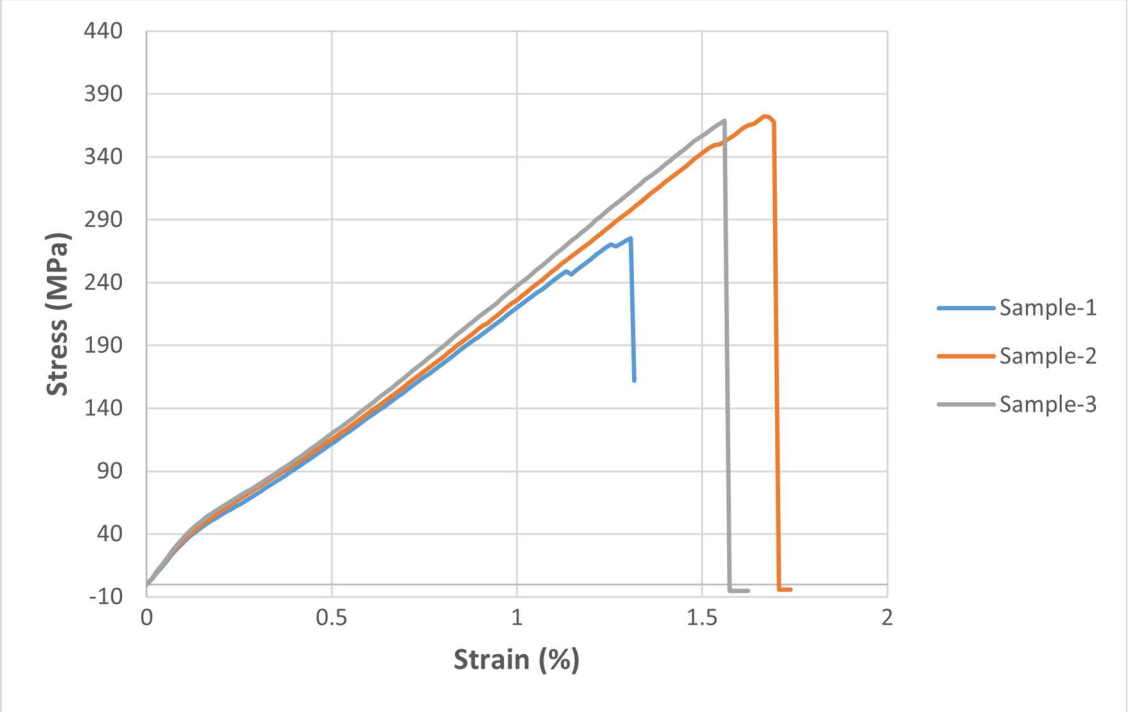


Figure 6.19 - The stress and strain curve for three UD-TFP reinforced hole samples with four layers and a 10 mm hole machined into the 12 mm reinforced hole.

The third set of samples with an 8 mm machined hole into the local reinforcement underwent the same investigative procedures. Both offline and online inspections during tensile testing were conducted using a polarisation camera. Figure 6.20 illustrates the offline inspection of a UD-TFP sample, (sample-1), with four layers and an 8 mm machined hole. The polarisation camera captured the raw saturation, DoLP, and fibres' orientation images (a-c, respectively). The DoLP image (b) highlighted the stitching securing the carbon fibres to the base material and resin-rich regions in black. 8 mm machined hole was positioned at a distance of 12.5 mm

from the sample edge, as detailed in **Section 3.3.1**. The hole's machining process into the 12 mm local reinforcement resulted in a localised resin-rich zone surrounding the local reinforcement. Additionally, resin-rich areas were observed in the loop-back path and at the sample edge, likely due to the fibre placement process. Image (c) illustrated the fibres' orientation extracted from the hue channel information of the HSV image. The hue channel provided the AoLP information, which directly corresponded to the fibre's orientation.

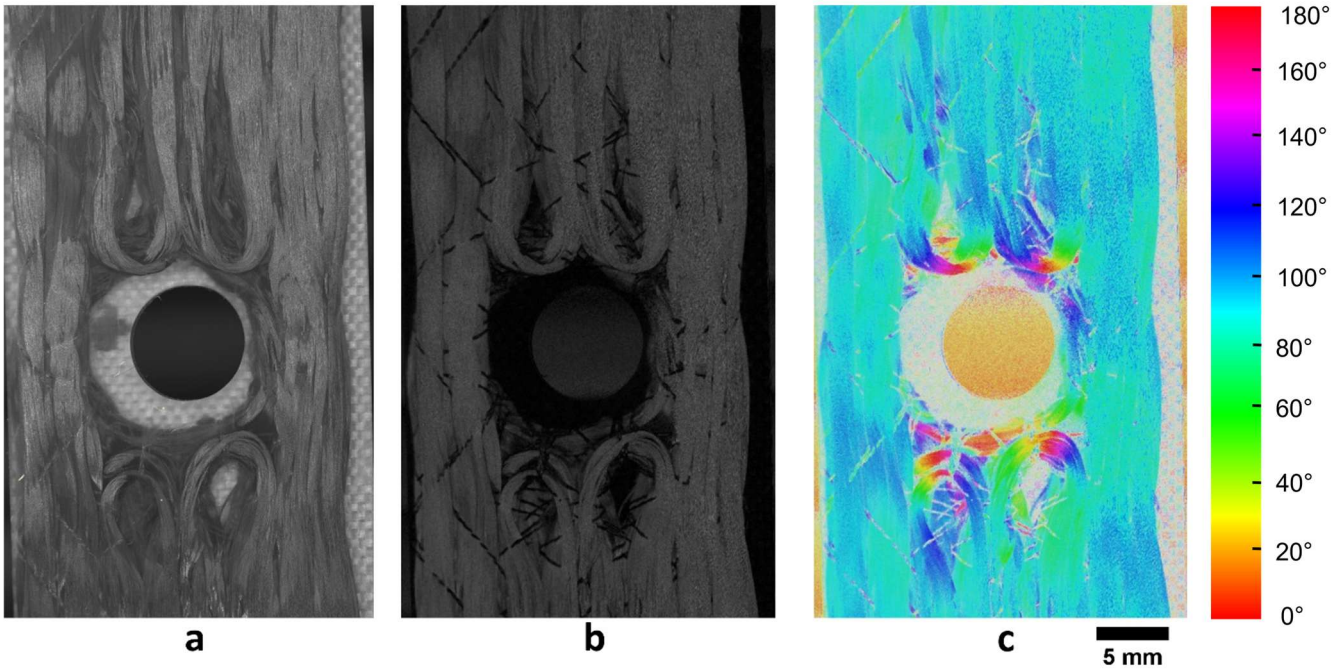


Figure 6.20 - UD-TFP reinforced hole sample, (sample-1), with four layers and an 8 mm machined hole into the 12 mm reinforced hole was imaged using the polarisation camera, where (a) the raw saturation image, (b) the DoLP image and (c) the fibres' orientation image.

Figure 6.21 represents a series of fibres' orientation images captured using the polarisation camera, illustrating the orientation behaviour of carbon fibres during a tensile test, (sample-1). The initial state (0 % strain) is shown in image (a), while image (e) corresponds to the maximum force load (1.60 % strain). The sequence highlights the impact of increasing strain on fibre orientation, particularly at the sample edge, around the reinforced hole, and along the loop-back carbon fibre path.

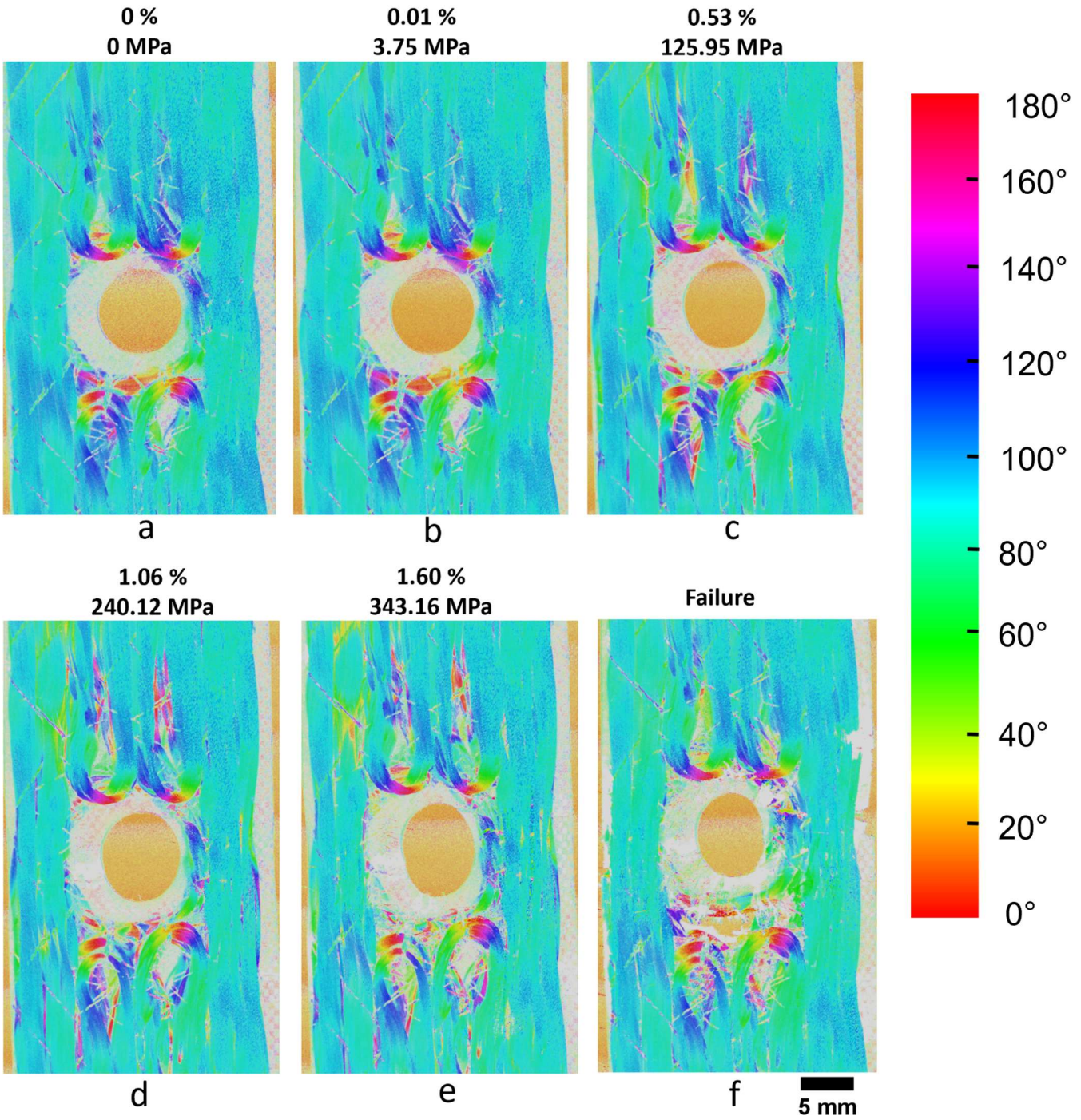


Figure 6.21 - The fibres' orientation images of a four-layer UD-TFP reinforced hole sample, (sample-1), with an 8 mm hole machined into a 12 mm reinforced hole were captured during tensile testing using the polarisation camera. The corresponding stress and strain for each image are presented above the figure.

A comparative analysis was conducted between fibre orientation images captured at 0 % strain (pre-test) and 1.60 % strain (maximum force load) to visualise the influence of strain on fibre orientation around the reinforced hole and loop-back path.

Figure 6.22 illustrated the fibre orientation within the reinforced hole sample at 0 % and 1.60 % strain, and histograms show the distribution of AoLP derived from the hue channel of the corresponding HSV images. To quantify fibre orientation changes with increasing strain, a Gaussian curve was fitted to the dominant peak within the 60° to 120° AoLP range. The mean AoLP value extracted from this curve was used for subsequent analysis.

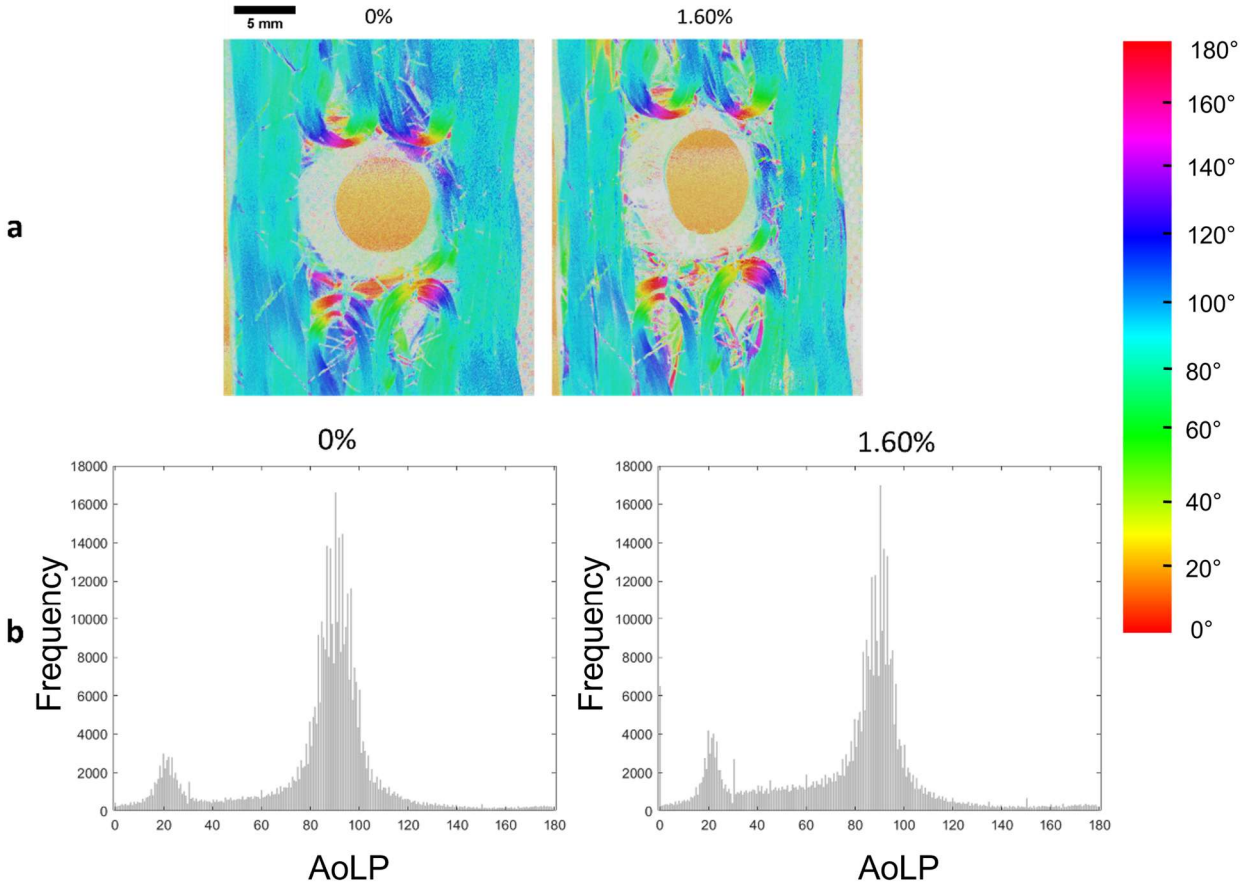


Figure 6.22 - The selected region of interest around the reinforced hole of the four layers of UD-TFP reinforced hole sample with an 8 mm hole machined into the 12 mm reinforced hole. (a) represent the fibres' orientation images at different strains, and (b) shows the corresponding histogram of the AoLP information in (a).

Figure 6.23 displays the Gaussian curve fit applied to the histogram data presented in Figure 6.22-b. This fitting technique was employed to compute the mean of the AoLP value within the 60° to 120° range for fibre orientation images at 0 % and 1.60 % strain. At 0 % strain, the mean AoLP value within the specified range was 90.64° with a standard deviation of 10.74°. Upon increasing the strain to 1.60 %, the mean AoLP value was calculated to be 89.52° with a standard deviation of 9.84°.

Figure 6.24 illustrates the behaviour of fibres' orientation within a ± 5° range of the mean of the AoLP value. Image (a) depicts the fibres' orientation in the selected range at an initial strain of 0 %, while image (b) represents the same range of fibres' orientation at a strain of 1.60%. By subtracting image (b) from image (a), as shown in the image (c), the difference in the fibres' orientation around the reinforced hole and along the loop-back path can be visualised.

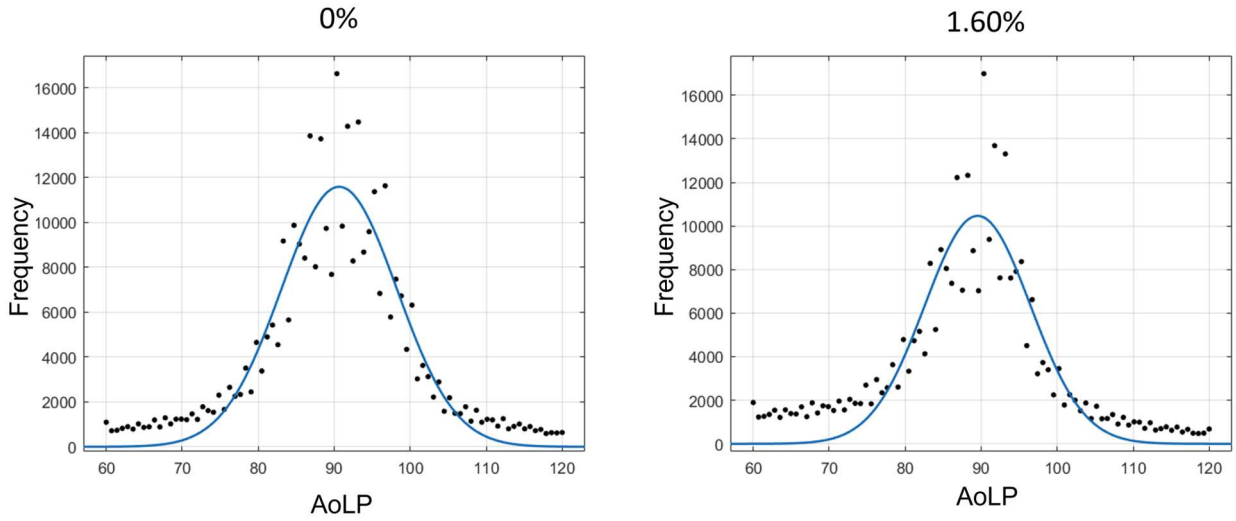


Figure 6.23 - MATLAB fitting of Gaussian curve to the histogram data of four layers UD-TFP reinforced hole sample, with an 8 mm hole machined into the 12 mm reinforced hole, before starting the tensile test (0 % strain) and at maximum force load (1.60 % strain).

Table 6.5 presents the maximum load, tensile strength, strain at failure, and tensile modulus for the four layers of UD-TFP reinforced hole samples with an 8 mm machined hole into a 12 mm local reinforcement. As previously discussed, the variability in the results is caused by the manufacturing-induced differences, such as the hole's position relative to resin-rich regions, sample width and associated edge effects, and the loop-back path placement. Additionally, variations in fibre orientation around the reinforced hole among the samples resulted in differing fracture behaviours of the stitching threads that secured the fibres in the vicinity of the reinforced hole.

Table 6.6 presents the mean and standard deviation of the AoLP derived from Gaussian fits of fibre orientation images (Figure 6.21) within the selected region during the tensile test. Figure 6.25 illustrates that as the strain increased from 1.06

% to 1.60 %, reaching the maximum force load, the mean AoLP decreased by 0.28°. Subsequently, with strain increasing from 1.60 % to 1.62 %, the mean AoLP further decreased by 1.84°.

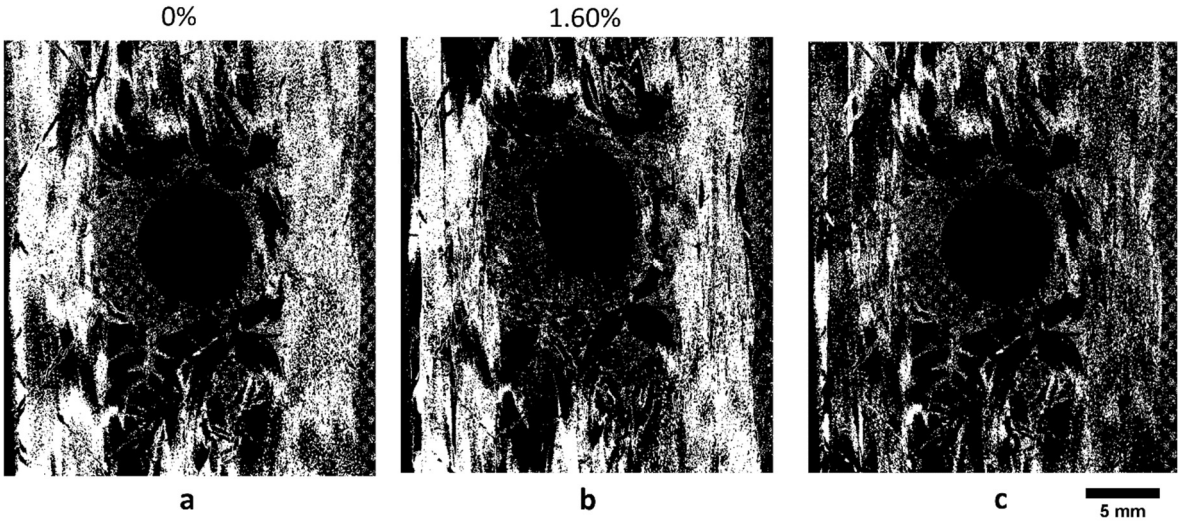


Figure 6.24 - The separation of fibres' orientations of four layers UD-TFP reinforced hole sample, (sample-1), with 8 mm machined hole into 12 mm reinforced hole, using the hue channel information. The fibres with orientations between 85.64° and 95.64° are presented in white, and the other fibres' orientations are in black, where (a) at 0 % strain, (b) at 1.60 % strain, and (c) is the result of subtracting image (b) from (a).

Table 6.5 - Tensile test information for three UD-TFP reinforced hole samples with four layers and an 8 mm machined hole into the 12 mm local reinforcement.

Sample Number	Maximum force (N)	Ultimate tensile strength (MPa)	Strain %	E-modulus (GPa)
Sample-1	18874	343.16	1.60	21.44
Sample-2	20998	392.48	1.92	20.44
Sample-3	13764	260.94	1.25	20.82
Average	17878	332.19	1.59	20.90
Standard Deviation	3717	66.45	0.33	0.50

Table 6.6 - The mean of the AoLP and standard deviation results to the corresponding strain after applying the Gaussian curve fitting to the fibres' orientation images that were captured during the tensile test (Figure 6.21), (sample-1).

The mean of AoLP (degree)	Standard deviation (the width of the peak)	Strain (%)
90.64 ± 1.26	10.74 ± 1.78	0
90.02 ± 1.28	10.57 ± 1.82	0.01
89.52 ± 1.39	10.65 ± 1.97	0.53
89.80 ± 1.37	9.71 ± 1.94	1.06
89.52 ± 1.42	9.84 ± 2.01	1.60
87.68 ± 1.42	11.19 ± 2.01	1.62

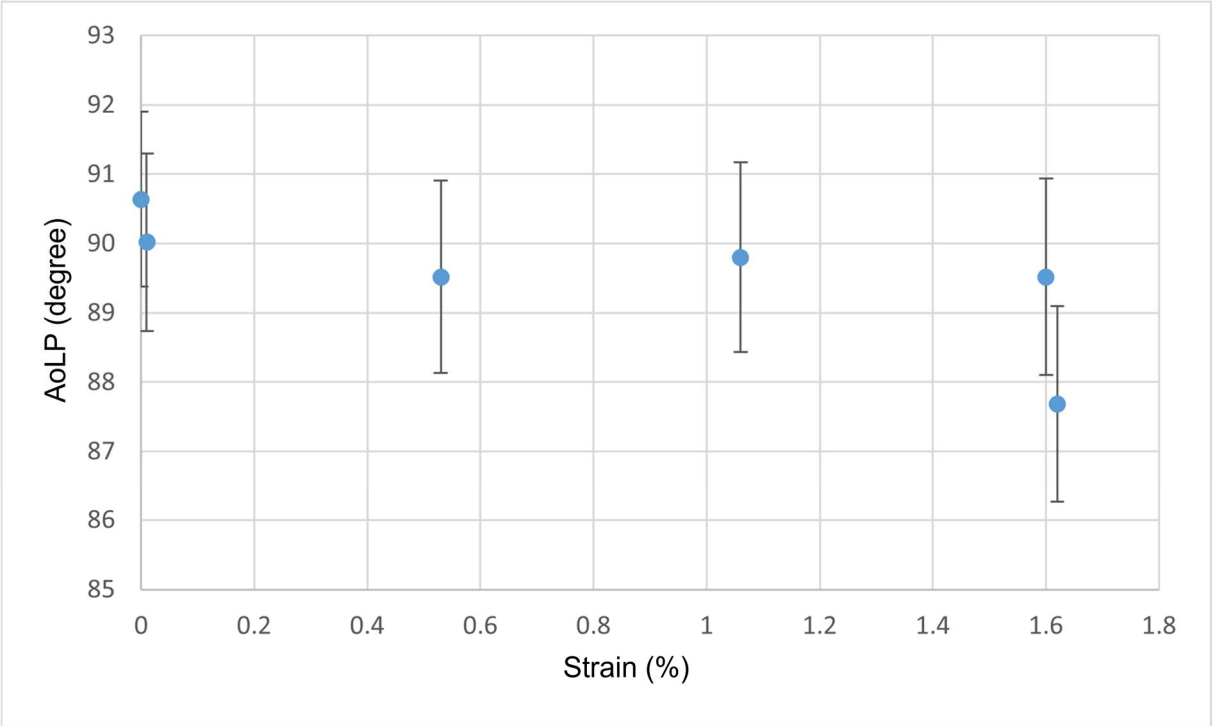


Figure 6.25 - The mean of the AoLP behaviour during the tensile test (selected images) for the UD-TFP reinforced hole sample, (sample-1), with four layers and an 8 mm machined hole.

Figure 6.26 illustrated the stress and strain curves of three UD-TFP reinforced hole samples with four layers and an 8 mm machined hole into the 12 mm local reinforcement. Sample (1) exhibits a linear response after the stress reaches 62 MPa up to 336 MPa. Subsequently, a slight stress reduction to 327 MPa occurs before the curve recovers with a linear trend until the failure point. Sample (2) demonstrates a linear response from stress reaching 61 MPa up to the failure point. Sample (3) exhibits a linear response from 50 MPa to the failure point.

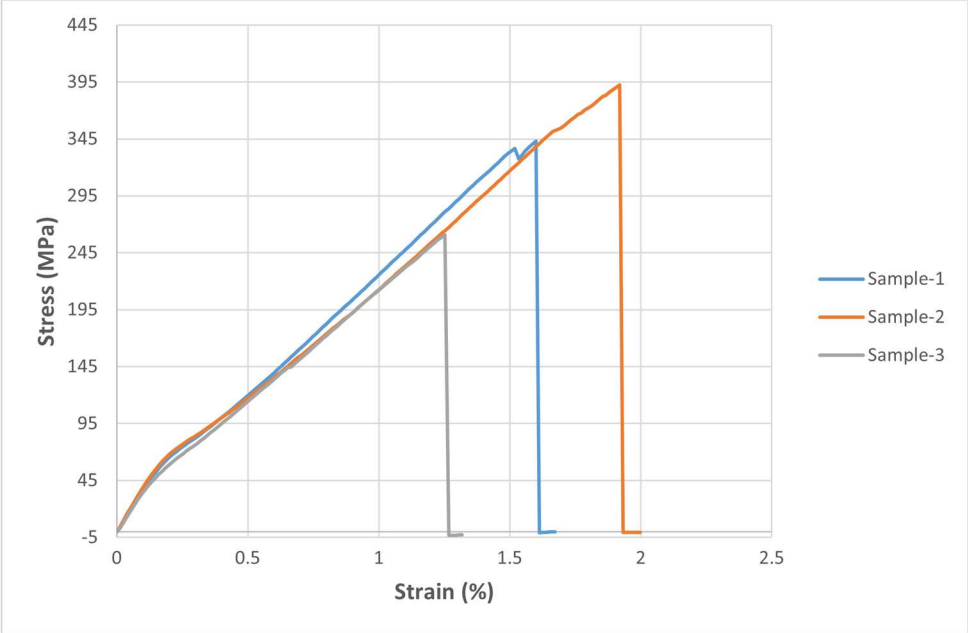


Figure 6.26 - The stress and strain curve for three UD-TFP reinforced hole samples with four layers and an 8 mm hole machined into the 12 mm reinforced hole.

6.4.1 Discussion

The polarisation-camera analysis demonstrated that, in all samples, the fibres remained predominantly aligned along the tensile axis, with mean AoLP values close to 90°. However, slight variations in the evolution of AoLP and its standard deviation with increasing strain indicated local reorientation behaviour influenced by resin distribution, loop-back geometry, and stitch positioning. In the case of the 12 mm machined hole, the mean AoLP decreased marginally from 89.72° ± 8.99° to 89.51° ± 7.77° as the strain increased to 1.34 %, reflecting a minor but measurable realignment of fibres within the reinforced zone. This modest decrease suggests that the larger hole diameter induced some disturbance in the surrounding fibre

paths, particularly near the loop-back curvature and stitching points, where fibre waviness was observed.

For the 10 mm machined hole, the mean AoLP increased slightly from 90.51° ± 10.02° to 90.76° ± 9.03° at 1.56 % strain. This minimal change indicates a realignment of fibres towards the loading direction, confirming that the 10 mm hole caused less disruption to the local reinforcement compared with the 12 mm configuration. The smaller hole enabled more uniform load transmission across the surrounding fibre bundles, thus maintaining the orientation stability of the stitched tows within the loop-back path. In contrast, the 8 mm machined-hole samples exhibited a more pronounced decrease in mean AoLP from 90.64° ± 10.74° to 89.52° ± 9.84°, followed by a further reduction of approximately 1.84° at failure. This result is attributed to the presence of an extensive resin-rich region, which separated the reinforcing fibres from the machined boundary and consequently allowed increased local rotation and slippage of the fibre bundles under load.

The comparison among the three-hole diameters highlights the critical interplay between reinforcement geometry, resin distribution, and fibre orientation stability in determining the tensile performance of UD-TFP reinforced laminates. The results demonstrate that the 10 mm machined-hole configuration provided the most effective balance between reinforcement continuity and structural integrity. The fibres in this configuration exhibited minimal angular deviation under load, and failure occurred in a controlled and progressive manner. The 12 mm machined-hole samples maintained acceptable stiffness but exhibited greater variability due to direct fibre exposure and machining-induced defects. The 8 mm configuration, although reducing the damaged fibre zone during drilling, introduced excessive resin content that reduced the effective stiffness and strength of the laminate.

6.4.2 Conclusion

To summarise the impact of machining holes with different diameters into the 12 mm local reinforcement of a four-layer UD-TFP reinforced hole samples, Table 6.7 provides the average, standard deviation, and coefficient of variation of the elastic modulus. The findings indicate that samples with 8 mm machined holes exhibit a

lower elastic modulus compared to those with 12 mm and 10 mm holes. This reduction is caused by the resin-rich area surrounding the 8 mm hole. While the elastic modulus of 12 mm machined hole samples is influenced by the machining process, the 10 mm hole samples demonstrate the highest elastic modulus. The 10 mm hole creates a minimal resin-rich area between the hole and the local reinforcement, preventing the effects on the reinforcing fibres. In contrast, the 12 mm hole, coinciding with the local reinforcement diameter, sometimes compromises the surrounding fibres during the machining process. Figure 6.27 illustrates the average of the elastic modulus for both the reference specimens and the 12 mm locally reinforced samples with three varying hole diameters, incorporating error bars.

Table 6.7 - The average, standard deviation and coefficient of variation correspond to the elastic modulus for the baseline and three different hole diameters of the UD-TFP reinforced hole with four layers.

	Elastic modulus (GPa)		
UD-TFP with four layers	**Average**	**Standard deviation**	**Coefficient of variation (%)**
Baseline	33.84	0.81	2.41
12mm hole diameter	21.62	0.34	1.57
10mm hole diameter	22.33	1.29	5.77
8mm hole diameter	20.90	0.50	2.42

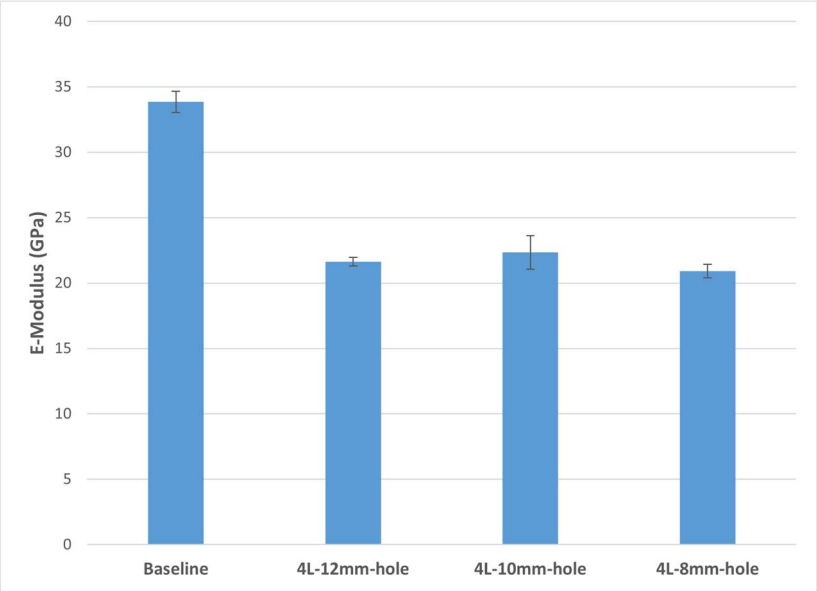


Figure 6.27 - The average of elastic modulus (GPa) is shown as a bar chart for the UD-TFP reinforced hole samples with four layers, baseline and with different machined hole diameters (12,10 and 8) mm, with an error bar as the standard deviation for three samples.

6.5 UD-TFP reinforced hole with two layers

As the UD-TFP reinforced hole samples with four layers, this section presented the UD-TFP reinforced hole samples with two layers to investigate the fibres' orientation behaviour during the tensile test with non-mirror reinforced hole samples. The same fibres' orientation monitoring process as with four layers of samples were repeated with the two layers using the polarisation camera. Since the same sequence of investigation was applied, the offline images and the tensile test images were not presented, but only the resultant analysis. This section focused on the image processing results and the AoLP data.

The first sample set was the 12 mm diameter hole machined into the 12 mm local reinforcement. Figure 6.28-a showed the fibres' orientation images before starting the tensile test at 0 % strain, and the maximum force load occurred at strain of 0.98 % for the selected region of interest around the reinforced hole, (sample-1). Also, Figure 6.28-b showed the histogram representing the AoLP distribution, which was extracted from the hue channel information. Again, the peak representing the information from the reflection of the background through the machined hole was

excluded. Fitting the Gaussian curve was applied to the peak in the AoLP range of 60° and 120°.

Figure 6.29 illustrated the Gaussian curve fit applied to the histogram data depicted in Figure 6.28-b within the AoLP range of 60° to 120°. This analysis was conducted to determine the mean AoLP at 0% and 0.98% strain. The mean AoLP was calculated to be 89.24° with a standard deviation of 9.7° at 0% strain. Upon increasing the strain to 0.98%, the mean AoLP was calculated to be 89.19° with a corresponding standard deviation of 8.71°.

The orientations of the fibres with 0 % and 0.98 % strain were separated to present the fibres in the range of ± 5° from the mean of the AoLP. Figure 6.30 showed the fibres with orientation between 84.24° and 94.24° in white, where (a) represented the fibres with selected AoLP range at 0 % strain, and (b) showed the fibres at 0.98 % strain. Image (c) presented the result of subtracting the image at 0.98 % strain from the image at 0 % strain.

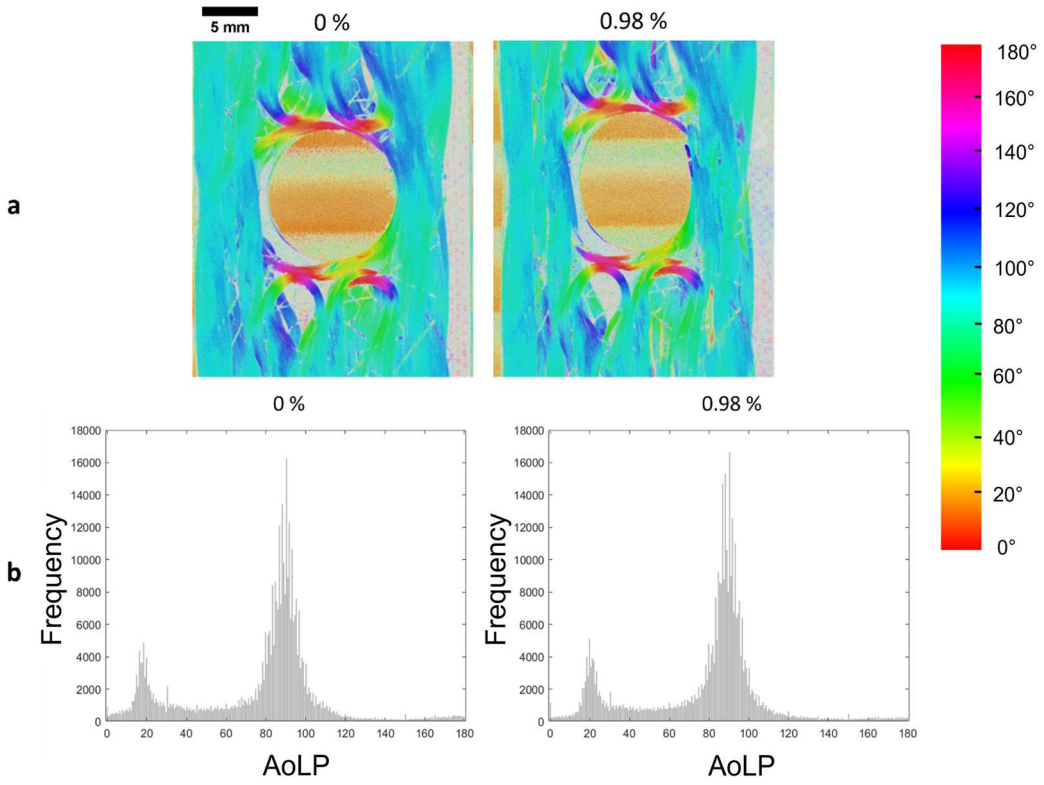


Figure 6.28 - The selected region of interest around the reinforced hole of the two layers of UD-TFP reinforced hole sample, (sample-1), with a 12 mm hole machined into the 12 mm reinforced hole. (a) represent the fibres' orientation images at different strains, and (b) shows the corresponding histogram of the AoLP information in (a).

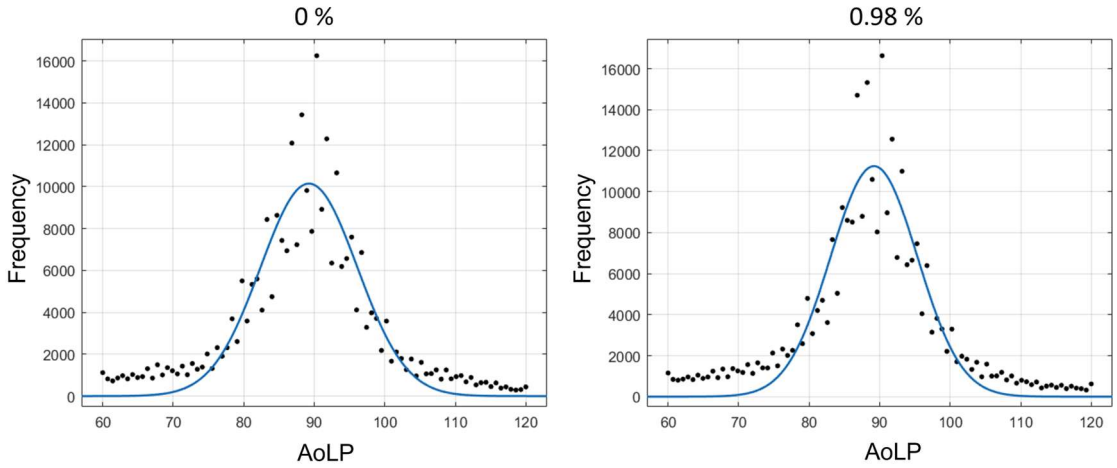


Figure 6.29 - MATLAB fitting of Gaussian curve to the histogram data of two layers UD-TFP reinforced hole sample, with a 12 mm hole machined into the 12 mm reinforced hole, before starting the tensile test (0 % strain) and at maximum force load (0.98 % strain).

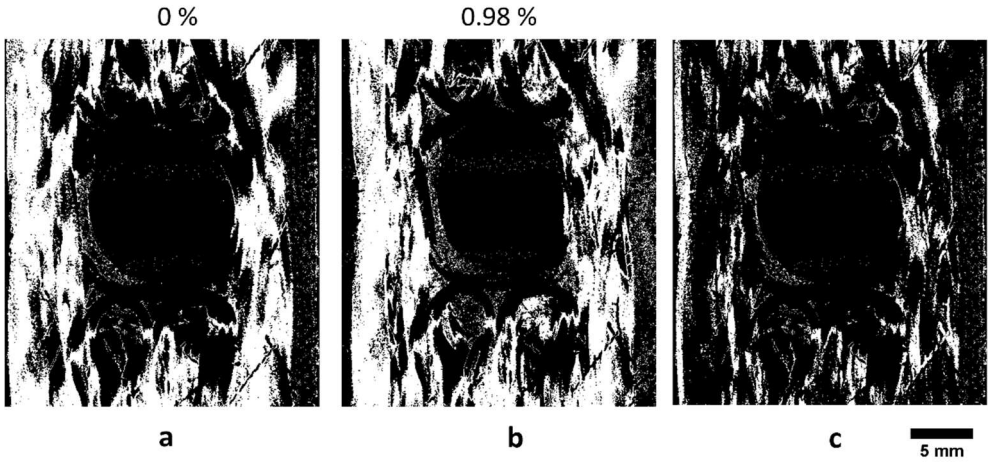


Figure 6.30 - The separation of fibres' orientations of two layers UD-TFP reinforced hole sample, (sample-1), with 12 mm machined hole into 12 mm reinforced hole, using the hue channel information. The fibres with orientations between 84.24° and 94.24° are presented in white, and the other fibres' orientations are in black, where (a) at 0 % strain, (b) at 0.98 % strain, and (c) is the result of subtracting image (b) from (a).

Table 6.8 summarizes the mechanical properties, including maximum load, tensile strength, strain at failure, and tensile modulus, for two layers of UD-TFP reinforced composite with a 12 mm hole machined in the 12 mm local reinforcement. As discussed in this chapter, variations in the position of the machined hole, the extent of resin-rich areas at the sample edges, the loop-back path, and the loop-back position contributed to the observed differences in the results.

Table 6.8 - Tensile test information for three UD-TFP reinforced hole samples with two layers and a 12 mm machined hole into the 12 mm local reinforcement.

Sample Number	Maximum force (N)	Ultimate tensile strength (MPa)	Strain %	E-modulus (GPa)
Sample-1	8391	211.09	0.98	21.38
Sample-2	8625	219.77	0.80	27.47
Sample-3	10097	249.33	1.10	22.52
Average	9038	226.73	0.96	23.79
Standard Deviation	925.13	20.04	0.15	3.23

Table 6.9 presents the mean and standard deviation of the Angle of Linear Polarisation (AoLP) within the 60° to 120° range, determined by fitting a Gaussian curve to the orientation data obtained from tensile test images.

Table 6.9 - The mean and standard deviation results of the AoLP with increasing strain after applying the Gaussian curve fitting to the fibres' orientation images that were captured during the tensile test for the UD-TFP reinforced hole sample, (sample-1), with two layers and a 12 mm machined hole.

The mean of AoLP (degree)	Standard deviation (the width of the peak)	Strain (%)
89.24 ± 1.28	9.70 ± 1.81	0
89.60 ± 1.26	9.64 ± 1.78	0.01
89.48 ± 1.26	8.82 ± 1.78	0.53
89.31 ± 1.17	8.66 ± 1.66	0.86
89.19 ± 1.15	8.71 ± 1.62	0.98
87.90 ± 1.25	9.56 ± 1.77	0.99

The behaviour of fibre orientation with increasing strain for the UD-TFP reinforced hole sample, with two layers and a 12 mm machined hole within the local reinforcement, is shown in Figure 6.31. This figure illustrates the mean AoLP as the strain increases. Upon initiation of the tensile test (at 0.01 % strain), the mean AoLP exhibited an initial increase of 0.36°. Subsequently, as the strain increased, the mean AoLP demonstrated a decreasing trend. Specifically, at 0.98 % strain, the mean AoLP decreased by 0.41° relative to the value at 0.01 % strain. A comparative analysis between the initial state (0 % strain) and the maximum force load (at 0.98 % strain) reveals a decrease of 0.05° in the mean AoLP.

Figure 6.32 presents more information about the fibre orientation behaviour during the tensile testing for the three samples. The figure shows how the fibre orientation behaves differently with increasing strain caused by the variation introduced during the manufacturing process.

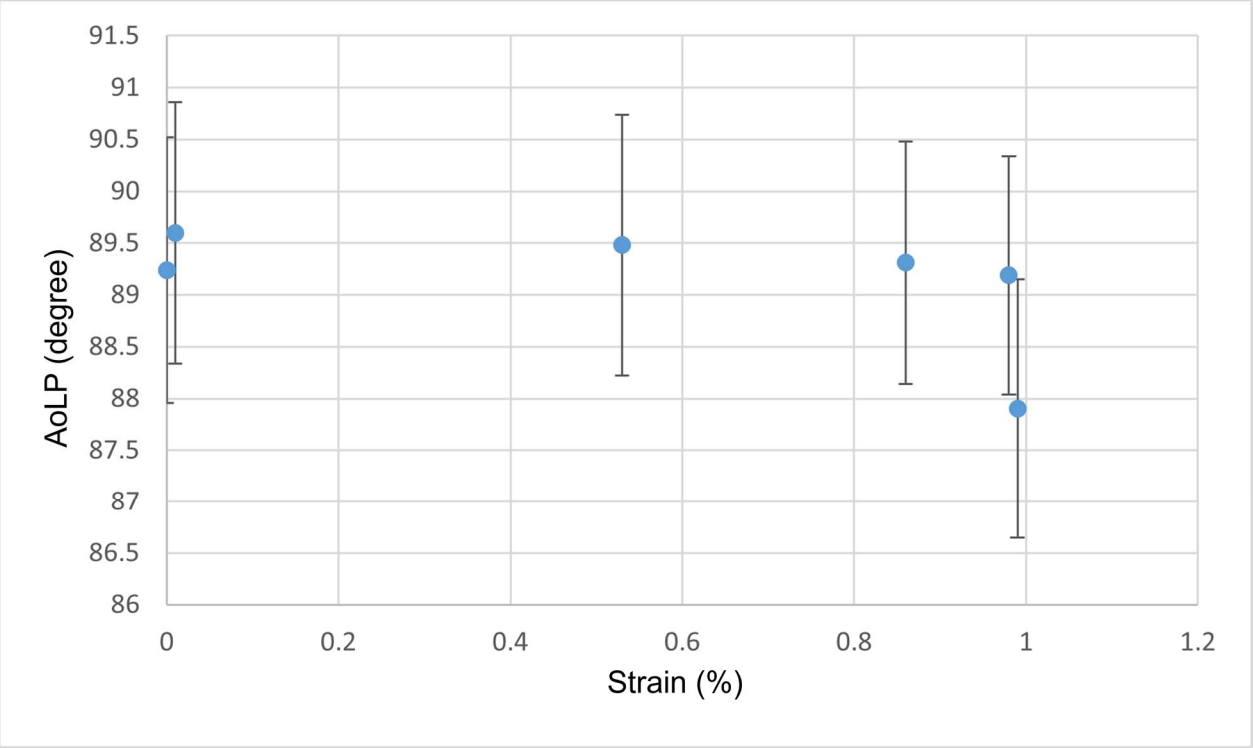


Figure 6.31 - The mean of the AoLP behaviour during the tensile test (selected images) for the UD-TFP reinforced hole sample, (sample-1), with two layers and a 12 mm machined hole.

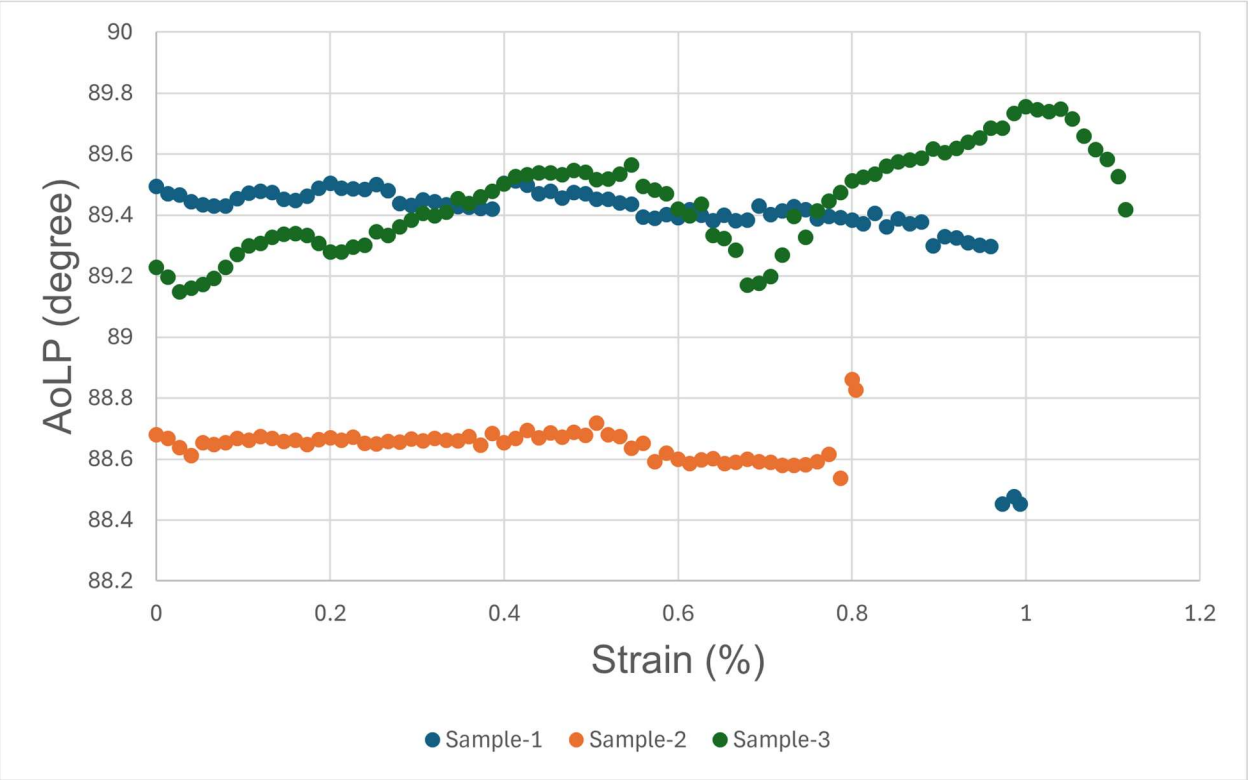


Figure 6.32 - The mean of the AoLP behaviour during tensile testing (of all images captured during tensile testing) for three UD-TFP reinforced hole samples with two layers and a 12 mm machined hole.

Figure 6.33 presents the stress and strain curves for three UD-TFP reinforced hole samples with two layers and a 12 mm machined hole into the local reinforcement. Sample (1) exhibits a linear elastic response after the stress reaches 45 MPa, extending to 202 MPa. Subsequently, a minor stress reduction is observed, followed by a return to linear behaviour until failure. In contrast, samples (2) and (3) demonstrate brittle failure characterised by a linear elastic response up to the point of fracture.

The fibres' orientation inspection and analysis were repeated for the sample set with a 10 mm machined hole into the 12 mm local reinforcement during the tensile testing. The fibres' orientation images with the selected region of interest around the reinforced hole before starting the test and at maximum force load to the equal strain 0 % and 1.12 %, respectively (sample-3), are shown in Figure 6.34-a, while Figure 6.34-b represents the histogram of the AoLP distribution at 0 % and 1.12 % strain. As explained previously, the Gaussian fitting curve was applied to the AoLP distribution between 60° and 120°.

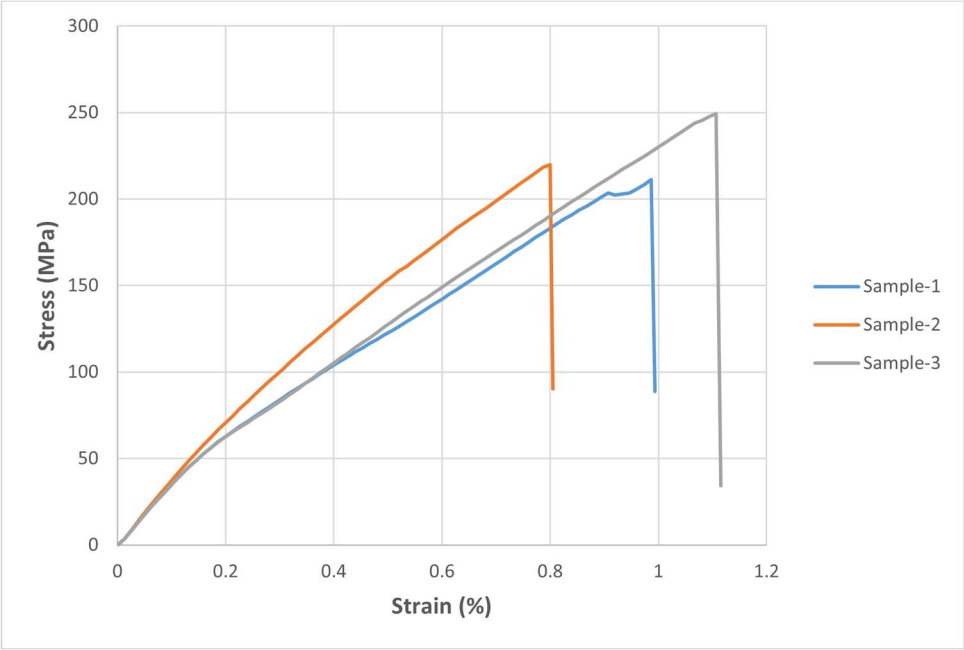


Figure 6.33 - The stress and strain curve for three UD-TFP reinforced hole samples with two layers and a 12 mm hole machined into the 12 mm reinforced hole.

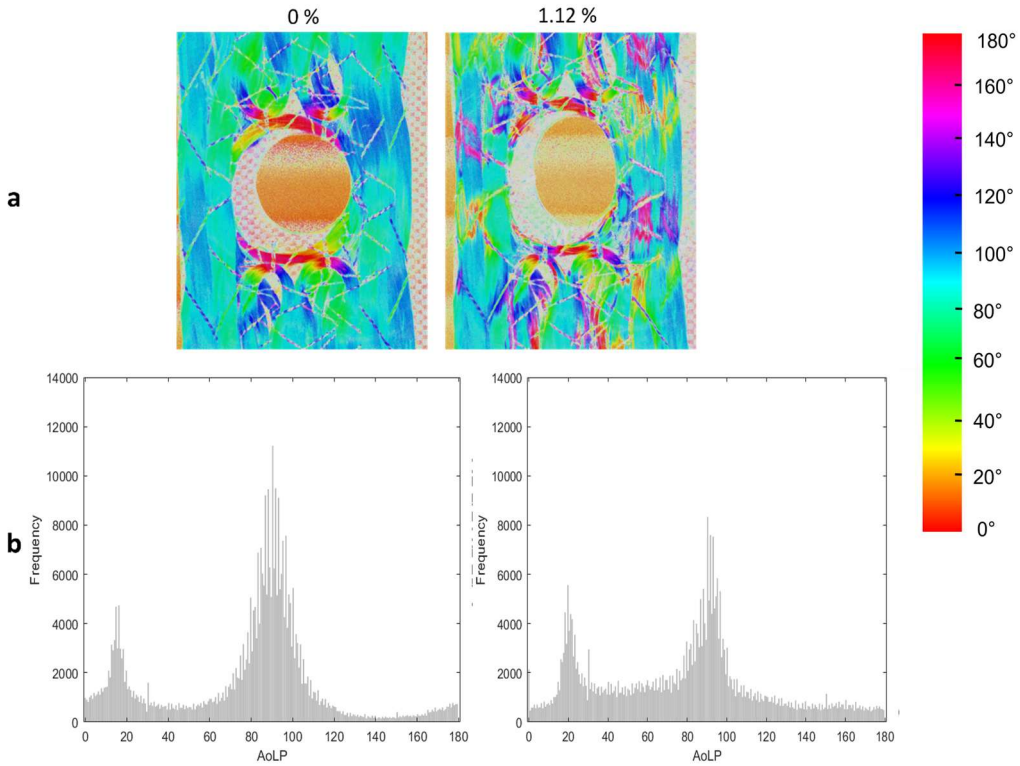


Figure 6.34 - The selected region of interest around the reinforced hole of the two layers of UD-TFP reinforced hole sample, (sample-3), with a 10 mm hole machined into the 12 mm reinforced hole. (a) represent the fibres' orientation images at different strains, and (b) shows the corresponding histogram of the AoLP information in (a).

Figure 6.35 presents the Gaussian curve fitting applied to the AoLP histogram data of a UD-TFP reinforced hole containing a 10 mm hole machined into the 12 mm local reinforcement. The analysis was focused on the AoLP range of 60° to 120° to calculate the mean of the AoLP values at 0 % and 1.12 % strain. The mean of the AoLP at 0 % strain was found to be 90.31°, with a standard deviation of 13.46°. As the strain increased to 1.12 %, the mean AoLP was calculated to be 90.11°, accompanied by a slight increase in standard deviation to 15.56°.

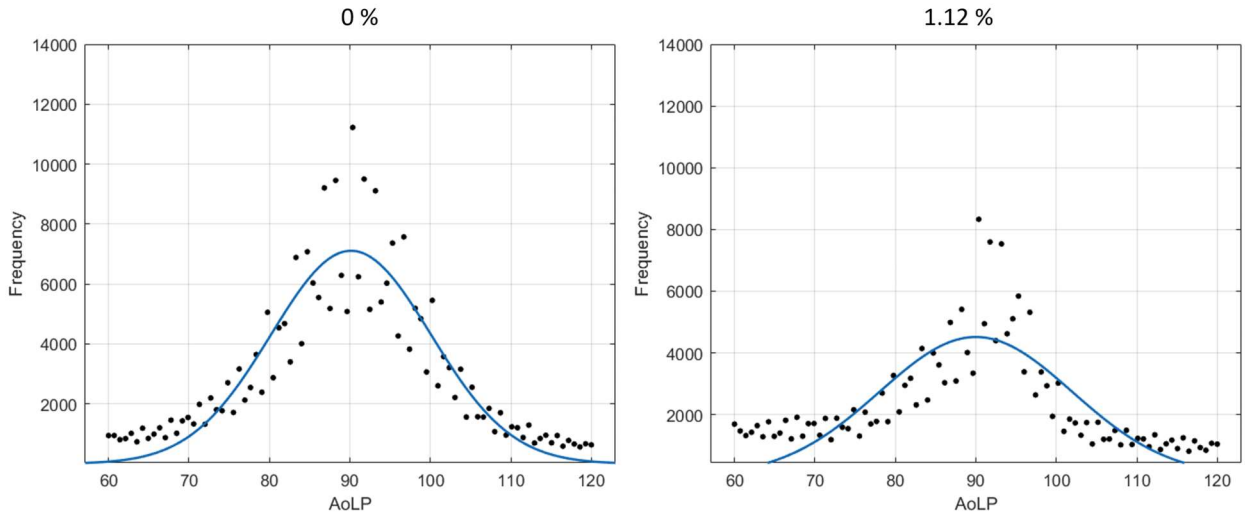


Figure 6.35 - MATLAB fitting of Gaussian curve to the histogram data of two layers UD-TFP reinforced hole sample, with a 10 mm hole machined into the 12 mm reinforced hole, before starting the tensile test (0 % strain) and at maximum force load (1.12 % strain).

To present fibres within a specific orientations range (± 5° from the mean AoLP), to monitor the orientation of the fibres with increasing strain, a mask was applied to the fibre orientation images specifying the hue channel range to represent the corresponding fibres' orientation information. Figure 6.36 presents a visual representation of separating the orientations of the carbon fibres from the fibres' orientation images to represent the fibres with orientations between 85.31° and 95.31° in the 0 % and 1.12 % strain images. Image (a) represents fibres at the 0 % strain in the selected orientations range, image (b) shows fibres at the 1.12 % strain, and image (c) illustrates the difference by subtracting the image with high strain from the image with 0 % strain.

Table 6.10 presents a summary of the mechanical properties of two layers of UD-TFP reinforced hole samples with a 10 mm diameter hole machined into the 12 mm local reinforcement, including maximum load, tensile strength, strain at failure, and tensile modulus.

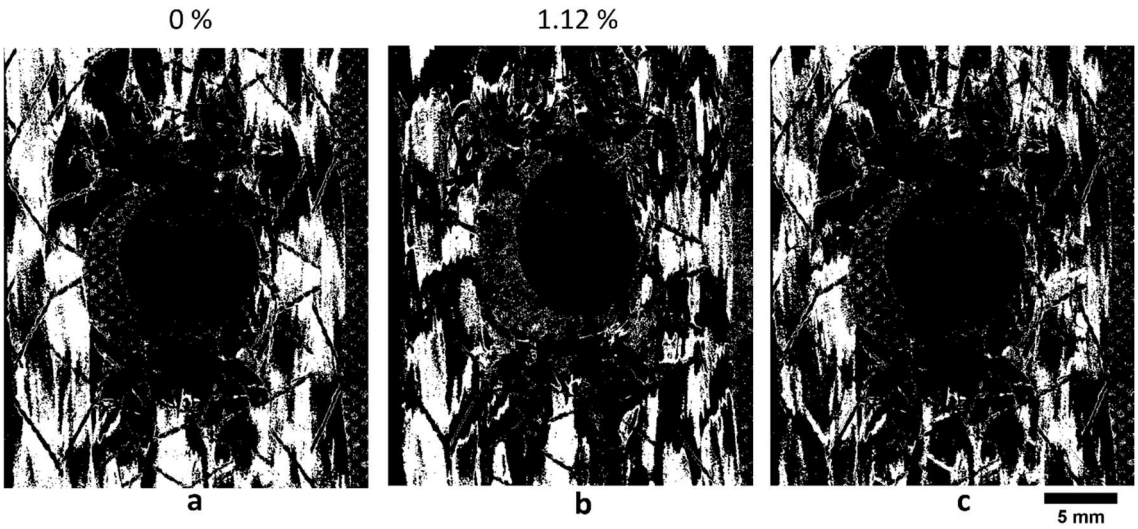


Figure 6.36 - The separation of fibres' orientations of two layers UD-TFP reinforced hole sample, (sample-3), with 10 mm machined hole into 12 mm reinforced hole, using the hue channel information. The fibres with orientations between 85.31° and 95.31° are presented in white, and the other fibres' orientations are in black, where (a) at 0 % strain, (b) at 1.12% strain, and (c) is the result of subtracting image (b) from (a).

Table 6.10 - Tensile test information for three UD-TFP reinforced hole samples with two layers and a 10 mm machined hole into the 12 mm local reinforcement.

Sample Number	Maximum force (N)	Ultimate tensile strength (MPa)	Strain %	E-modulus (GPa)
Sample-1	11912	283.63	1.26	22.38
Sample-2	11781	285.60	1.16	24.62
Sample-3	11554	276.74	1.12	24.70
Average	11749	281.99	1.18	23.90
Standard Deviation	181.47	4.65	0.07	1.31

Table 6.11 provides the mean and standard deviation of the Angle of Linear Polarisation (AoLP) obtained from Gaussian curve fitting within a specific range during tensile testing.

Table 6.11 - The mean and standard deviation results of the AoLP with increasing strain after applying the Gaussian curve fitting to the fibres' orientation images that were captured during the tensile test for the UD-TFP reinforced hole sample, (sample-3), with two layers and a 10 mm machined hole.

The mean of AoLP (degree)	Standard deviation (the width of the peak)	Strain (%)
90.31 ± 1.69	13.46 ± 2.39	0
90.13 ± 1.73	13.71 ± 2.46	0.01
90.62 ± 1.99	12.74 ± 2.82	0.53
90.63 ± 2.52	14.32 ± 3.57	0.85
90.11 ± 2.64	15.56 ± 3.76	1.12
89.95 ± 1.68	12.67 ± 2.38	1.122

Figure 6.37 illustrated the changes in fibre orientation within two layers of the UD-TFP reinforced hole sample with a 10 mm machined hole into a 12 mm local reinforcement as strain increases during tensile testing. After an initial strain of 0.01 %, the mean AoLP decreased by 0.18°. Subsequently, as the strain increased to 0.53 %, the mean AoLP exhibited a 0.49° increase. A slight further increase of 0.01° in the mean AoLP was observed when the strain reached 0.85 %. However, a significant decrease of 0.52° in the mean AoLP occurred as the strain increased to 1.12 %, reaching the maximum force load. Post-failure, with a strain increase of 0.002%, the mean AoLP decreased by 0.16° compared to the previous state and by 0.36° relative to the initial 0 % strain.

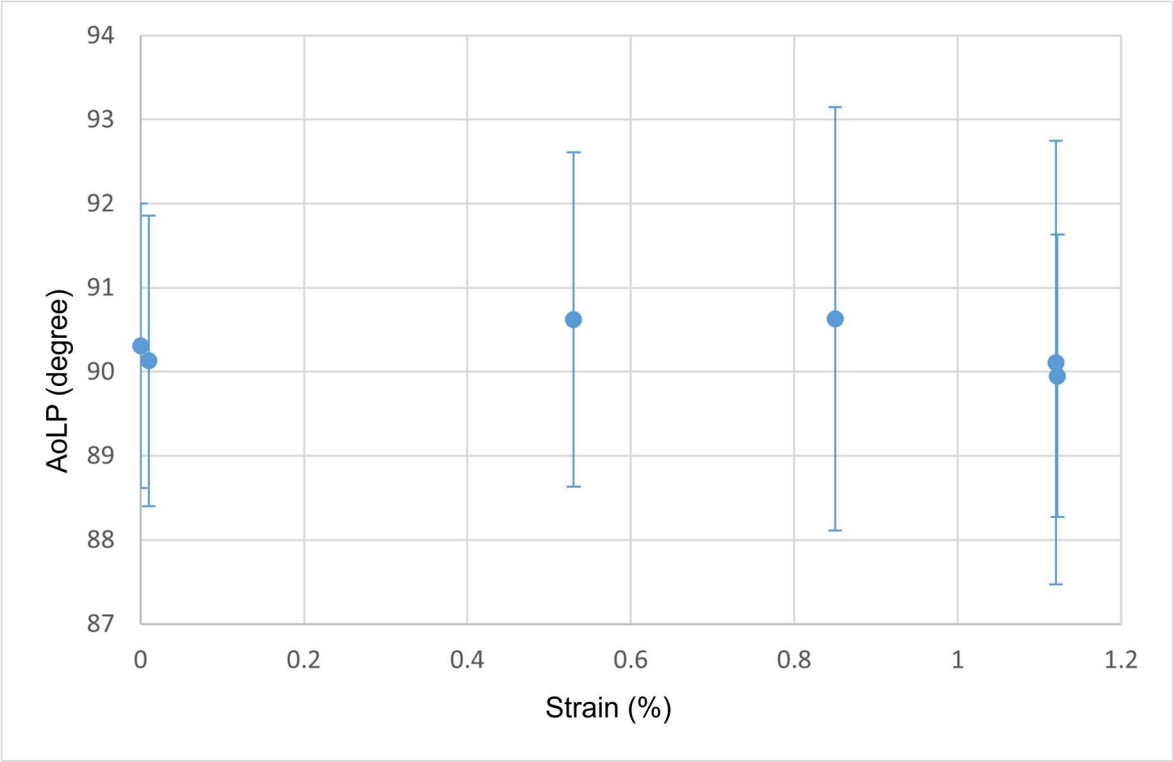


Figure 6.37 - The mean of the AoLP behaviour during the tensile test (selected images) for the UD-TFP reinforced hole sample, (sample-3), with two layers and a 10 mm machined hole.

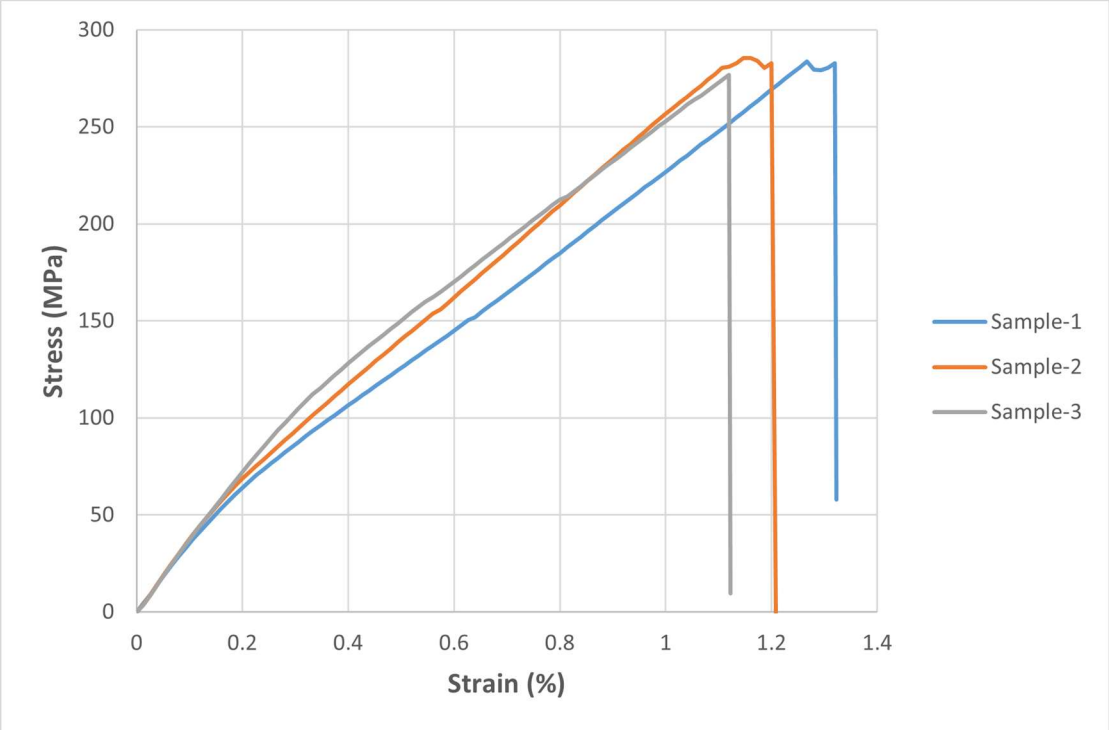


Figure 6.38 - The stress and strain curve for three UD-TFP reinforced hole samples with two layers and a 10 mm hole machined into the 12 mm reinforced hole.

Figure 6.38 presents the stress and strain curves for three UD-TFP reinforced hole samples with two layers and a 10 mm machined hole into the 12 mm reinforced area. Sample 1 exhibits a linear elastic response from 45 MPa to 279 MPa, followed by a slight stress dip and subsequent recovery until failure. Sample 2 also demonstrates a linear elastic region from 48 MPa onwards, but it experiences a stress reduction and partial recovery prior to failure. Sample 3 maintains a linear elastic response from 54 MPa until failure.

The third sample set with an 8 mm hole machined into the 12 mm local reinforcement will undergo the same inspection process and analysis to investigate the fibres' orientation behaviour with strain increased during tensile testing. Figure 6.39-a shows the fibres' orientation images around the reinforced hole before the test (0 % strain) and at the maximum force load (1.16 % strain), (sample-2), while Figure 6.39-b displays the corresponding histogram of the Angle of Linear Polarisation (AoLP) distribution. The mean of the AoLP was determined within the 60° to 120° range during the tensile test.

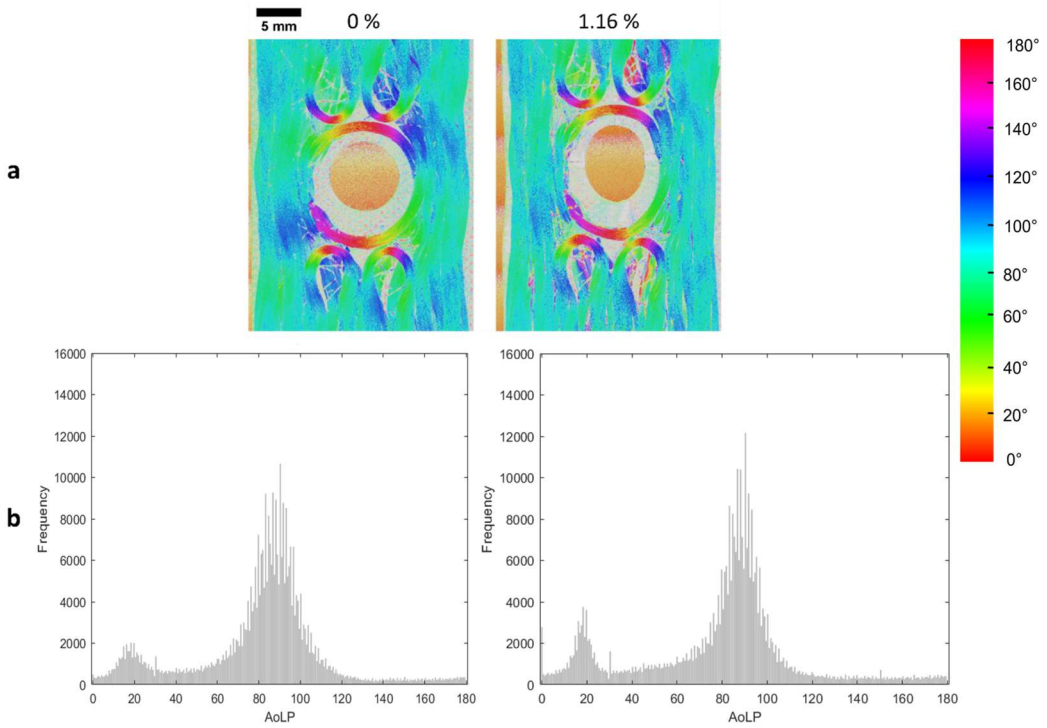


Figure 6.39 - The selected region of interest around the reinforced hole of the two layers of UD-TFP reinforced hole sample, (sample-2), with an 8 mm hole machined into the 12 mm reinforced hole. (a) represent the fibres' orientation images at different strains, and (b) shows the corresponding histogram of the AoLP information in (a).

A Gaussian curve was fitted to the AoLP data within the selected range, as illustrated in Figure 6.40, to track the fibres' orientation behaviour with increasing strain by calculating the mean AoLP. The mean AoLP at 0 % strain was calculated to be 87.77°, with a standard deviation of 15.11°. At 1.16 % strain, the mean AoLP was calculated to be 88.18°, with a corresponding standard deviation of 12.01°.

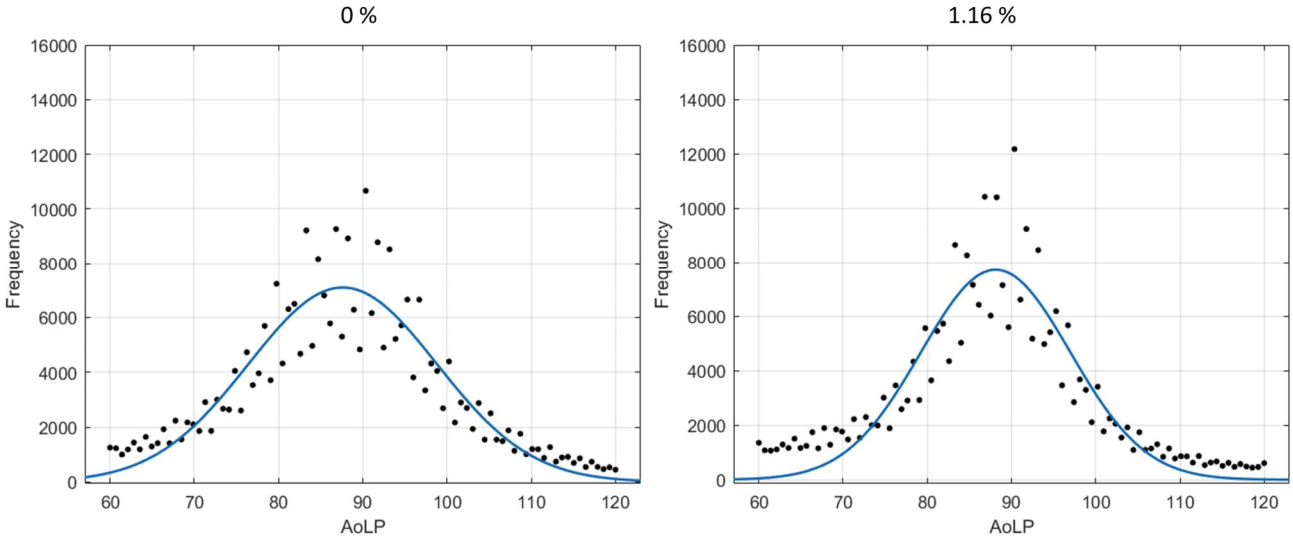


Figure 6.40 - MATLAB fitting of Gaussian curve to the histogram data of two layers UD-TFP reinforced hole sample, with an 8 mm hole machined into the 12 mm reinforced hole, before starting the tensile test (0 % strain) and at maximum force load (1.16 % strain).

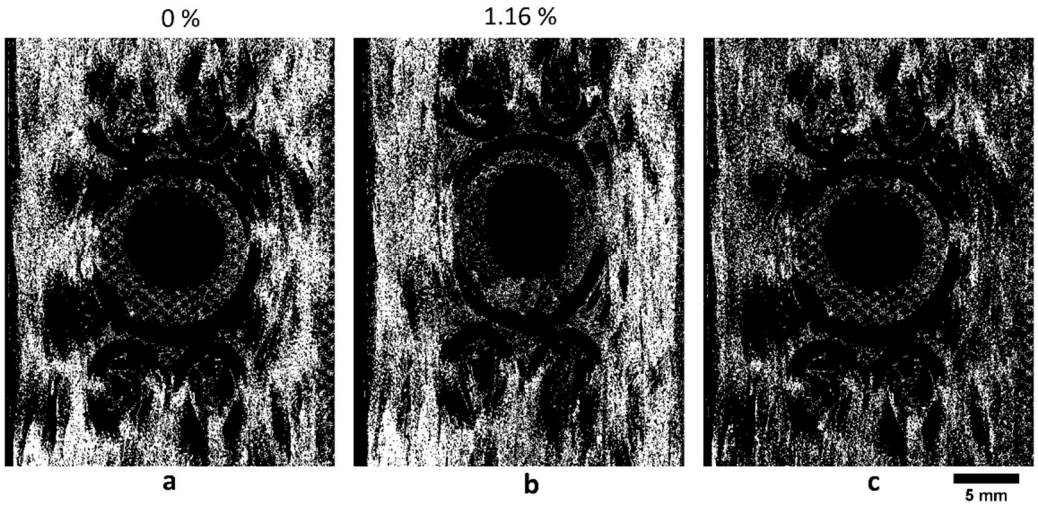


Figure 6.41 - The separation of fibres' orientations of two layers UD-TFP reinforced hole sample, (sample-2), with 8 mm machined hole into 12 mm reinforced hole, using the hue channel information. The fibres with orientations between 82.77° and 92.77° are presented in white, and the other fibres' orientations are in black, where (a) at 0 % strain, (b) at 1.16% strain, and (c) is the result of subtracting image (b) from (a).

The fibres within range ± 5° from the mean of the AoLP of the UD-TFP reinforced hole sample with an 8 mm machined hole was separated using the hue channel information to monitor the fibres' orientation behaviour with strain increased. Figure 6.41 represents the fibres with orientation in the range between 82.77° and 92.77° in the 0 % and 1.16 % strain images, where image (a) shows the fibres in the selected range (in white) at the 0 % strain, image (b) shows the fibres at 1.16 % strain, and image (c) represents the difference between the fibres' orientation between the image at 0 % and 1.16 % strain by subtracting image (b) from image (a).

Table 6.12 presents a summary of the mechanical properties of two layers of the UD-TFP reinforced hole samples with an 8 mm hole machined into a 12 mm local reinforcement, including maximum load, tensile strength, strain at failure, and tensile modulus.

Table 6.12 - Tensile test information for three UD-TFP reinforced hole samples with two layers and an 8 mm machined hole into the 12 mm local reinforcement.

Sample Number	Maximum force (N)	Ultimate tensile strength (MPa)	Strain %	E-modulus (GPa)
Sample-1	14376	344.33	1.44	23.91
Sample-2	8546	205.93	1.16	17.75
Sample-3	14440	343.81	1.60	21.48
Average	12454	298.03	1.40	21.05
Standard Deviation	3384	79.75	0.22	3.10

Furthermore, Table 6.13 provides the mean and standard deviation of the AoLP values within the 60° to 120° range to illustrate the orientational behaviour of the fibres during the tensile test with increasing strain.

Figure 6.42 visually represents the fibres' orientation behaviour by plotting the mean AoLP for each strain level, as determined from the selected fibre orientation images. Upon initiation of the tensile test, the mean AoLP increased by 0.28° at a strain of 0.01 %. As strain increased from 0.01 % to 0.53 %, the mean AoLP exhibited a minimal increase of 0.07°. A similar marginal increase of 0.08° was observed when the strain was further elevated to 0.86 %. However, upon reaching the maximum force load (1.16 % strain), a slight decrease of 0.02° in the mean AoLP was noted. Post-failure (1.26 % strain), a 0.06° increase in the mean AoLP was observed and an increase of 0.47° relative to the initial 0 % strain value.

Table 6.13 - The mean and standard deviation results of the AoLP with increasing strain after applying the Gaussian curve fitting to the fibres' orientation images captured during the tensile test for the UD-TFP reinforced hole sample, (sample-2), with two layers and an 8 mm machined hole.

The mean of AoLP (degree)	Standard deviation (the width of the peak)	Strain (%)
87.77 ± 1.72	15.11 ± 2.45	0
88.05 ± 1.70	14.87 ± 2.42	0.01
88.12 ± 1.61	13.47 ± 2.28	0.53
88.20 ± 1.57	12.45 ± 2.22	0.86
88.18 ± 1.52	12.01 ± 2.15	1.16
88.24 ± 1.77	14.88 ± 2.51	1.26

Figure 6.43 presents the stress and strain curves for three UD-TFP reinforced hole samples with two layers and an 8 mm machined hole into the 12 mm local reinforcement. Sample (1) exhibits a linear elastic response from 44 MPa to 342 MPa, followed by a stress reduction and subsequent recovery until failure. Sample (2) displays a linear elastic region from 34 MPa to 205 MPa, followed by a stress drop to 110 MPa and then a recovery phase to the failure point. Sample (3) demonstrates a linear elastic response from 60 MPa until failure.

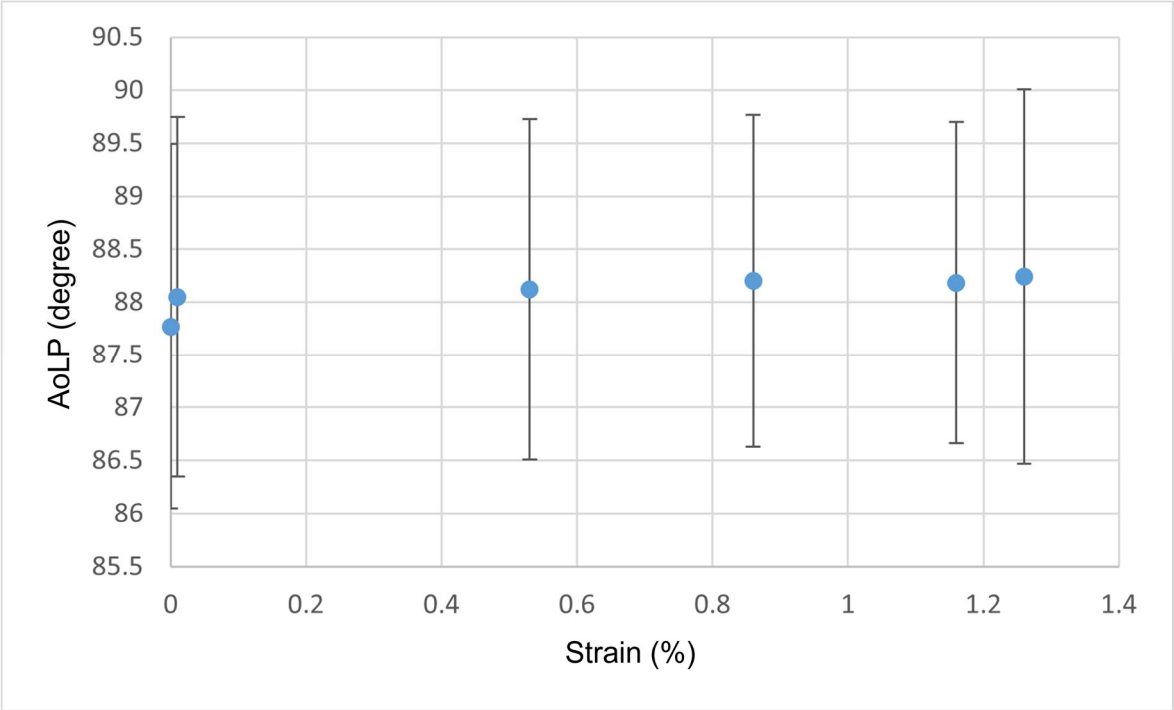


Figure 6.42 - The mean of the AoLP behaviour during the tensile test (selected images) for the UD-TFP reinforced hole sample, (sample-2), with two layers and an 8 mm machined hole.

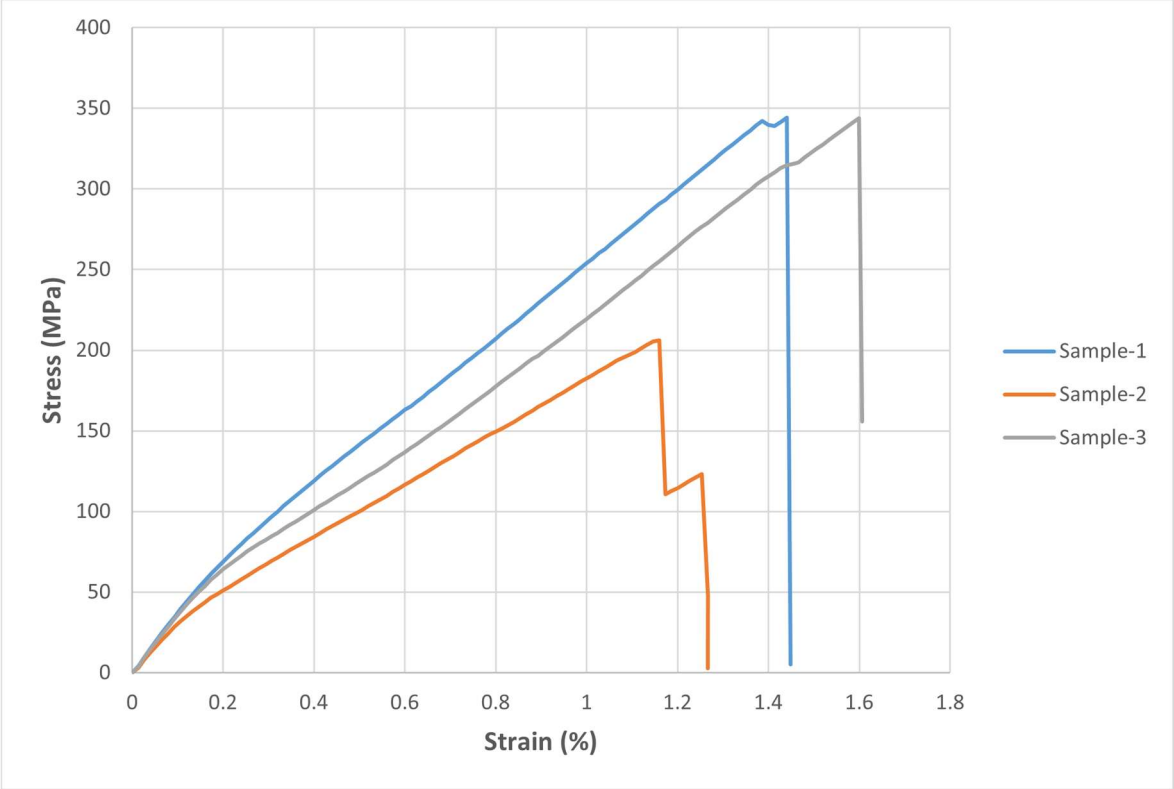


Figure 6.43 - The stress and strain curve for three UD-TFP reinforced hole samples with two layers and an 8 mm hole machined into the 12 mm reinforced hole.

Summarising the effect of the different machined hole's diameters on the local reinforcement with the 12 mm diameter of the two layers of the UD-TFP reinforced hole samples when having samples with non-mirrored local reinforcement. Table 6.14 presents the elastic modulus information, including the samples' modulus average, standard deviation, and coefficient of variation.

Table 6.14 - The average, standard deviation and coefficient of variation correspond to the elastic modulus for the baseline and three different hole diameters of the UD-TFP reinforced hole with two layers.

	Elastic modulus (GPa)		
UD-TFP with two layers	**Average**	**Standard deviation**	**Coefficient of variation (%)**
12mm hole diameter	23.79	3.23	13.59
10mm hole diameter	23.90	1.31	5.50
8mm hole diameter	21.05	3.10	14.73

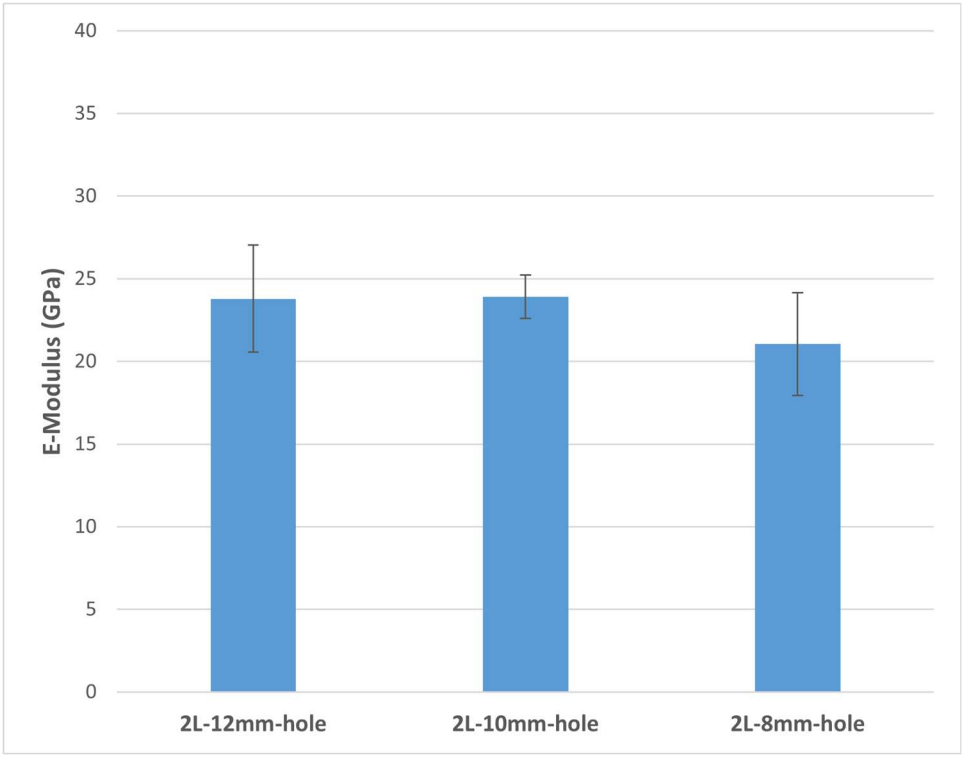


Figure 6.44 - The average of elastic modulus (GPa) is shown as a bar chart for the UD-TFP reinforced hole samples with two layers and different machined hole diameters (12,10 and 8) mm, with an error bar as the standard deviation for three samples.

The results with two layers of UD-TFP reinforced hole samples show the same behaviour as the samples with four layers regarding machining the holes with different diameters. The 8 mm machined hole samples represent the lowest average elastic modulus, and the 10 mm machined hole samples show the highest average modulus compared with the other machined hole diameters.

Figure 6 44 visually represents the average elastic modulus for the samples with three different holes' diameters (12 mm, 10 mm, and 8 mm) machined into the 12 mm local reinforcement, representing the error bar for the three tested samples.

6.6 Discussion

The failure behaviour of the specimens was influenced by several manufacturing factors, including the formation of resin-rich regions along the specimen edges and around the reinforced holes, the relative positioning of the loop-back paths with respect to these holes, the alignment of the carbon fibres within the loop-back zones, and the placement of the stitching points. The images obtained using the polarisation camera revealed that the number of layers in the UD-TFP reinforced-hole specimens significantly affected the fibre orientation behaviour with increasing strain, as well as the overall failure mode.

In the two-layer UD-TFP reinforced hole specimens, the loop-back configuration led to the formation of resin-rich regions, which in turn caused the fibre orientation within the loop-back area to vary progressively with applied strain. This resin-rich region promoted failure near the loop-back zone rather than at the expected stress concentration region around the machined hole. In contrast, in the four-layer UD-TFP specimens, such resin-rich regions were not observed, owing to the increased number of fibre layers and the repeated placement of tows in the same region. Nevertheless, failure did not initiate at the stress-concentration point, instead it originated from the breakage of the stitching threads located near the machined hole and along the specimen edges.

The fibre orientation images (AoLP) effectively captured the evolution of fibre orientation with increasing strain and demonstrated the influence of the stitching threads on the onset and progression of failure. Therefore, the combined analysis

of the AoLP and DoLP images provides valuable insights for improving the manufacturing process of TFP preforms, particularly through in-process monitoring of fibre orientation and the optimisation of stitching-thread positioning during preform fabrication.

6.7 Conclusion

In this chapter, the fibres' orientation behaviour around the reinforced hole for UD-TFP reinforced hole samples with two and four layers was investigated when three different hole diameters (12 mm, 10 mm, and 8 mm) were machined into samples with a TFP hole of 12 mm stitched into the backing woven glass fibre. The polarisation camera was used to capture the samples before and during the tensile test to compare the fibres' orientation. The orientation of the carbon fibre was extracted from the hue channel in the HSV image.

The comparison between the fibres' orientation images, before starting the test and at maximum load force, was performed by examining the histogram of the AoLP values, via fitting of a Gaussian curve. The mean of the Gaussian was then used to create images where the orientation of the fibre was AoLP ± 5° from the mean AoLP. The manufacturing variability inherent in the TFP samples, including the width of the samples, resin-rich area at the edge of the sample, the orientation and position of the loop-back carbon fibre regarding the reinforced hole, and the stitching location, made direct comparisons of the samples difficult. Furthermore, these variations between the samples in the same sample set led to different fibre orientations' behaviour with increasing strain during the tensile testing, as shown as an example in Figure 6.10, which in turn affects the mechanical properties.

The UD-TFP reinforced hole tested samples with two and four layers show that samples with a 10 mm machined hole into the 12 mm local reinforcement, creating a small resin-rich area around the local reinforcement, have higher elastic modulus than samples with a large resin-rich area (8 mm machined hole) and samples with same no resin-rich area around the local reinforcement (12 mm machined hole) affecting the local reinforcement carbon fibres during the machining process. The

samples with large resin-rich areas around the local reinforcement (8 mm machined holes) show the lowest elastic modulus.

7 CONCLUSION AND FUTURE WORK

7.1 Conclusion

This thesis aimed to investigate and track how the fibre orientation within unidirectional tape-placed (UD-TFP) composites, particularly around a locally reinforced hole, affects their mechanical performance during tensile testing by employing the polarisation camera. Additionally, the study explores how the presence of resin-rich zones surrounding the drilled hole influences the carbon fibre loop-back path. The positioning of the stitching threads relative to the drilled hole edges is also examined in relation to its impact on the material's properties.

The carbon fibres polarise light on reflection when illuminated by an unpolarised source. Therefore, the optical inspection technique, the polarisation camera, was utilized in the experimental work because it provides the capability of identifying the fibre orientation on the sample's surface, in dry and composite cases, using the angle of linear polarisation information (AoLP). Two inspection rigs were developed to facilitate both offline and online monitoring of carbon-fibre orientation using a polarisation camera. The offline rig was designed to optimise illumination conditions and calibration, while the online system enabled real-time observation during tensile testing. Experimental trials demonstrated that fibres with differing architectures exhibited distinct reflective behaviours under illumination, which, in some cases, resulted in data loss due to specular reflection. Therefore, achieving uniform lighting, such as through the use of LED strips providing a broad illumination region, was found to be essential for accurately capturing fibre orientations. The polarisation-based inspection method successfully identified fibre orientations in both dry carbon-fibre and composite specimens. Furthermore, continuous monitoring during tensile testing provided valuable insights into the behaviour of fibre orientation with increasing strain, offering a basis for improving the manufacturing process of TFP reinforced-hole samples. In addition, the Degree of Linear Polarisation (DoLP) images obtained from the polarisation camera effectively revealed manufacturing-related defects, including missing fibres, fibre misalignment, and stitching discontinuities within TFP preforms. These findings highlight the capability of the polarisation camera as a non-destructive optical inspection tool suitable for enhancing the manufacturing quality and process control of composite materials.

To investigate the fibre orientation behaviour within unidirectional tailored fibre placement (UD-TFP) samples with reinforced holes, the dry carbon fibre with different architectures (UD, UD-NCF, Twill 2x2, and UD-TFP) was subjected to the tensile test to inspect the fibre orientation behaviour with increased strain using the polarisation camera. Then, as a preliminary step for the main study using epoxy resin, silicon rubber resin was introduced into the samples as an intermediate stage to examine the behaviour of the fibre orientation during tensile testing. Additionally, the behaviour of carbon fibre orientation, both woven (Twill 2x2) and unidirectional non-crimp (UD-NCF) with epoxy resin, were studied around machined holes with different diameters during tensile loading.

The experimental results of dry fibres show that, as expected, the UD and UD-NCF samples do not show a significant change in the fibre orientation during the tensile testing, where the fibre orientation was compared before starting the test (at 0% strain) and with increased strain. However, the Twill 2x2 weave demonstrated a clear alteration in fibre orientation as the strain increased, highlighting the influence of the twill weaving pattern on fibre orientation. The weaving pattern, where tows interlace by passing over and under two adjacent tows, caused waviness in the weft fibres (those running perpendicular to the loading direction). As the strain increased, the waviness straightened progressively, influencing the fibre orientation. Furthermore, the fibre orientation within reinforced hole TFP preforms, comprising two and four layers, was observed around the reinforced hole and at the fibre loop-back paths curvature as the strain increased. Fibre orientations moved to have orientations between 85° and 95° (along the tension direction) with strain increased.

Experimental data from samples impregnated with silicone rubber resin, Chapter 4, revealed the fibre orientation behaviour of the Twill 2x2 sample with increased strain. However, in the reinforced hole TFP samples, some fibres appeared black in the Degree of Linear Polarisation (DoLP) image. This indicates a lack of reflected light from these fibres, resulting in a loss of information. The high viscosity of the silicone rubber resin diminished the specular reflection from some areas in the sample surface, further leading to loss of information in these areas.

The results of samples with machined holes (UD-NCF and Twill 2x2), Chapter 5, revealed that the fibre orientation around the holes changed as the strain increased. Both material types exhibited a dependence of mechanical properties on the hole diameter, with smaller holes demonstrating higher modulus. Moreover, images of the Degree of Linear Polarisation (DoLP) and Angle of Linear Polarisation (AoLP) highlighted distinct characteristics between samples within the same set. These differences were observed in the positioning of the weft material relative to the hole edge and the shape of the remaining fibres at the hole edges. The research findings suggest that minor variations in the position of the weft material within US-NCF material relevant to the machined hole edge influence the composite strength.

The analysis of reinforced-hole UD-TFP specimens, Chapter 6, revealed how fibre orientation behaviour and movement change with increasing strain. Moreover, the study demonstrated the influence of the machined hole diameter relative to the reinforced hole diameter on the mechanical properties. Specimens with an 8 mm machined hole exhibited lower elastic modulus due to the formation of a resin-rich zone around the reinforced hole. However, samples with a 10 mm machined hole demonstrated higher average elastic modulus compared to those with 12 mm and 8 mm holes. The 12 mm hole diameter, resembling the reinforced hole diameter, exhibited some fibre disruption at the reinforced hole edges, likely resulting from the machining process, which influenced the mechanical properties. Furthermore, variations in the manufacturing process, including final sample width, stitching placement, and loop-back position and size, could have significantly affected the mechanical properties. Ideally, more samples with improved control over the manufacturing variation would allow more definitive conclusions to be drawn.

Experimental results show that variations in manufacturing processes between samples within the same batch can lead to differences in their mechanical performance. Consequently, greater care must be exercised when handling TFP preforms (during production or transportation) compared to other materials, which makes it easier (in some cases) to use conventional preforms rather than TFP.

7.2 Future work

The experimental findings presented in this thesis, particularly those concerning unidirectional non-crimp fabric (UD-NCF) with a drilled hole, suggested that the mechanical properties are influenced by the distance and location of the weft thread relative to the hole edge. To further explore this hypothesis, the position of the machined hole and the distance between the weft thread and the machined hole edge could be systematically varied. The outcomes of such an investigation would enable the optimisation of the distance between the hole edge and the weft thread to obtain better mechanical properties.

Additionally, it would be essential to investigate TFP samples that contain reinforced holes manufactured in different approaches (for example, without the loop-back fibre placement path) to gain a comprehensive understanding of the fibre orientation behaviour around the reinforced hole during tensile testing, which would help improve the manufacturing process.

To enhance the analysis of fibre orientation (AoLP information) around machined or reinforced holes, the surrounding fibre region could be subdivided into four quadrants (at the edges of the hole) for a more detailed assessment of fibre orientation in each area. Furthermore, the fibre orientation's monitoring during tensile testing could be improved by modifying the inspection methodology and employing two polarisation cameras to build a 3D view, which can be represented by a 3D array of grayscale points. Additionally, using two cameras can improve the results of the AoLP around the machined hole.

Since the separation of the fibre orientation process was able to provide more information about small changes in the fibre orientation at different strains, the potential of enhancing the image analysis methodology coupled with machine learning may offer a means of detecting alterations in fibre orientation as the strain increases for each image captured during tensile testing.

8 REFERENCE

[1] F. C. Campbell, *Structural Composite Materials*. 2010.
[2] S. K. Mazumdar, *COMPOSITES Manufacturing*. 2001.
[3] D. Hull, “An Introduction to composite Materials, 2nd ed. Cambridge,” 1996.
[4] P. Mattheij, K. Gliesche, and D. Feltin, “Tailored Fiber Placement-Mechanical Properties and Applications.” pp. 774–786, 1998.
[5] H. M. El-Dessouky, M. N. Saleh, M. Gautam, G. Han, R. J. Scaife, and P. Potluri, “Tailored fibre placement of commingled carbon-thermoplastic fibres for notch-insensitive composites,” *Compos. Struct.*, vol. 214, no. February, pp. 348–358, 2019, doi: 10.1016/j.compstruct.2019.02.043.
[6] V. I. Khaliulin, P. A. Khilov, and D. M. Toroptsova, “Prospects of applying the tailored fiber placement (TFP) technology for manufacture of composite aircraft parts,” *Russ. Aeronaut.*, vol. 58, no. 4, pp. 495–500, 2015, doi: 10.3103/S1068799815040236.
[7] H. Rahmani, S. H. M. Najafi, and A. Ashori, “Mechanical performance of epoxy/carbon fiber laminated composites,” *J. Reinf. Plast. Compos.*, vol. 33, no. 8, pp. 733–740, 2014, doi: 10.1177/0731684413518255.
[8] A. Parmiggiani, M. Prato, and M. Pizzorni, “Effect of the fiber orientation on the tensile and flexural behavior of continuous carbon fiber composites made via fused filament fabrication,” *Int. J. Adv. Manuf. Technol.*, vol. 114, no. 7–8, pp. 2085–2101, 2021, doi: 10.1007/s00170-021-06997-5.
[9] R. H. Knibbs and J. B. Morris, “The effects of fibre orientation on the physical properties of composites,” *Composites*, vol. 5, no. 5, pp. 209–218, 1974, doi: 10.1016/0010-4361(74)90141-4.
[10] M. Schöberl, K. Kasnakli, and A. Nowak, “Measuring Strand Orientation in Carbon Fiber Reinforced Plastics (CFRP) with Polarization,” in *World Conference on Non-Destructive Testing*, 2016, pp. 1–8.
[11] M. Damghani, J. Saddler, E. Sammon, G. A. Atkinson, J. Matthews, and A. Murphy, “An experimental investigation of the impact response and Post-impact shear buckling behaviour of hybrid composite laminates,” *Compos. Struct.*, vol. 305, no. July 2022, p. 116506, 2023, doi: 10.1016/j.compstruct.2022.116506.
[12] G. A. Atkinson, S. O. Nash, and L. N. Smith, “Precision fibre angle inspection for carbon fibre composite structures using polarisation vision,” *Electron.*, vol. 10, no. 22, 2021, doi: 10.3390/electronics10222765.
[13] L. Chiominto, G. D’Emilia, and E. Natale, “Using Light Polarization to Identify Fiber Orientation in Carbon Fiber Components: Metrological Analysis,” *Sensors*, vol. 24, no. 17, 2024, doi: 10.3390/s24175685.
[14] S. K. Mazumdar, *COMPOSITES Manufacturing*. 2001.
[15] D. Hull, *An Introduction to Composite Materials, 2nd ed*. Cambridge, 1996.
[16] L. Nijssen, *Composite Materials an introduction*. 2015.
[17] K. K. Chawla, *Composite Materials: Sience and Engineering*. 2012.
[18] R. A. P. M. Wambua, “A Review of Preforms for the Composites Industry,” *Ind. Text.*, vol. 40, no. 4, pp. 310–333, 2011, doi: 10.1177/1528083709092014.
[19] S. B. Sharma, P. Potluri, J. Atkinson, and I. Porat, “Mapping of tubular woven composite preforms on to doubly-curved surfaces,” *Comput. Des.*, vol. 33, pp. 1035–1048, 2001.

[20] K. Kim, J. I. Curiskis, L. Ye, and S. Fu, “Mode-I interlaminar fracture behaviour of weft-knitted fabric reinforced composites,” *Compos. Part A Appl. Sci. Manuf.*, vol. 36, no. 2005, pp. 954–964, 2005, doi: 10.1016/j.compositesa.2004.12.004.
[21] A. W. Van Vuure, J. A. Ivens, and I. Verpoest, “Mechanical properties of composite panels based on woven sandwich-fabric preforms,” *Compos. Part A Appl. Sci. Manuf.*, vol. 31, no. 7, pp. 671–680, 2000, doi: 10.1016/S1359-835X(00)00017-8.
[22] J. A. Soden and B. J. Hill, “Conventional weaving of shaped preforms for engineering composites,” *Compos. Part A Appl. Sci. Manuf.*, vol. 29, no. 7, pp. 757–762, 1998, doi: 10.1016/S1359-835X(98)00053-0.
[23] H. El-dessouky and R. Scaife, “DESIGN , WEAVING AND MANUFACTURE OF A LARGE 3D COMPOSITE STRUCTURES FOR AUTOMOTIVE,” *3D Fabr. Their Appl.*, no. June 2019, 2016.
[24] C. Ayranci and J. Carey, “2D braided composites : A review for stiffness critical applications,” vol. 85, pp. 43–58, 2008, doi: 10.1016/j.compstruct.2007.10.004.
[25] Z. Wu, H. Ding, Z. Ying, Y. Yuan, and X. Hu, “Influence of braided fabric on the fracture modes of a composite tube under quasi-static compression,” *J. Reinf. Plast. Compos.*, vol. 36, no. 10, pp. 766–779, 2017, doi: 10.1177/0731684417690927.
[26] G. W. Melenka and J. P. Carey, “Development of a generalized analytical model for tubular braided-architecture composites,” *J. Compos. Mater.*, 2017, doi: 10.1177/0021998317695421.
[27] K. H. Leong, S. Ramakrishna, Z. M. Huang, and G. A. Bibo, “The potential of knitting for engineering composites - a review,” *Compos. Part A Appl. Sci. Manuf.*, vol. 31, no. 3, pp. 197–220, 2000, doi: 10.1016/S1359-835X(99)00067-6.
[28] H. Hasani, S. Hassanzadeh, M. J. Abghary, and E. Omrani, “Biaxial weft-knitted fabrics as composite reinforcements: A review,” *J. Ind. Text.*, vol. 46, no. 7, pp. 1439–1473, 2017, doi: 10.1177/1528083715624256.
[29] Ö. Demircan, S. Ashibe, T. Kosui, and A. Nakai, “Effect of various knitting techniques on mechanical properties of biaxial weft-knitted thermoplastic composites,” *J. Thermoplast. Compos. Mater.*, vol. 28, no. 6, pp. 896–910, 2015, doi: 10.1177/0892705713519121.
[30] M. Saeedifar, M. Nasr, H. M. El-dessouky, and D. Freitas, “Damage assessment of NCF , 2D and 3D woven composites under compression after multiple-impact using acoustic emission,” *Compos. Part A Appl. Sci. Manuf.*, vol. 132, no. February, 2020, doi: 10.1016/j.compositesa.2020.105833.
[31] O. İnal and A. Ataş, “Mechanical Properties of NCF Composites and Mechanical Joints in Composite Laminates: A Review,” *16th Int. Mater. Symp. IMSP’2016*, no. October 2016, pp. 1072–1080, 2016.
[32] K. Vallons, G. Adolphs, P. Lucas, S. V. Lomov, and I. Verpoest, “Quasi-UD glass fibre NCF composites for wind energy applications: A review of requirements and existing fatigue data for blade materials,” *Mech. Ind.*, vol. 14, no. 3, pp. 175–189, 2013, doi: 10.1051/meca/2013045.
[33] F. Stig, “An Introduction to the Mechanics of {3D}-Woven Fibre Reinforced Composites,” 2009.
[34] L. Greve and A. K. Pickett, “Delamination testing and modelling for composite crash simulation,” *Compos. Sci. Technol.*, vol. 66, no. 6, pp. 816–826, 2006,

doi: 10.1016/j.compscitech.2004.12.042.
[35] P. Mattheij, K. Gliesche, and D. Feltin, “3D reinforced stitched carbon / epoxy laminates made by tailored fibre placement,” vol. 31, pp. 571–581, 2000.
[36] K. Dransfield, C. Baillie, Y. Mai, K. Dransfield, C. Baillie, and Y. Mai, “IMPROVING THE D E L A M I N A T I O N RESISTANCE OF CFRP BY STITCHING A REVIEW,” vol. 50, no. 1994, pp. 305–317, 1994.
[37] P. P. H.M. El-Dessouky, M.N. Saleh, M. Gautam, G. Han, R.J. Scaife, “Tailored fibre placement of commingled carbon-thermoplastic fibres for notch- insensitive composites,” 2019.
[38] K. Gliesche, T. Hu, and H. Orawetz, “Application of the tailored fibre placement (TFP) process for a local reinforcement on an ‘“ open-hole ”’ tension plate from carbon / epoxy laminates,” *Compos. Sci. Technol.*, vol. 63, pp. 81–88, 2003.
[39] L. Bittrich *et al.*, “Optimizing Variable-Axial Fiber-Reinforced Composite Laminates: The Direct Fiber Path Optimization Concept Lars,” vol. 2019, 2019.
[40] G. Marsh, “Prepregs - raw material for high-performance composites,” no. October, pp. 24–28, 2002.
[41] P. Šimáček and S. G.Advani, “Desirable Features in Mold Filling Simulations for Liquid Composite Molding Processes,” *Polym. Compos.*, vol. 25, no. 4, pp. 355–367, 2004, doi: 10.1002/pc.20029.
[42] N. Sahbaz Karaduman, Y. Karaduman, H. Ozdemir, and G. Ozdemir, “Textile Reinforced Structural Composites for Advanced Applications,” *Text. Adv. Appl.*, 2017.
[43] R. . Smith, Z. Quereshi, R. . Scaife, and H. . El-Dessouky, “On the limitations of processing CFRP material using automated fibre placement technology,” *J. Reinf. Plast. Compos.*, 2016.
[44] E. Oromiehie, B. G. Prusty, P. Compston, and G. Rajan, “Automated fibre placement based composite structures: Review on the defects, impacts and inspections techniques,” *Compos. Struct.*, vol. 224, no. May, 2019, doi: 10.1016/j.compstruct.2019.110987.
[45] S. Sun, Z. Han, H. Fu, H. Jin, J. S. Dhupia, and Y. Wang, “Defect characteristics and online detection techniques during manufacturing of FRPs using automated fiber placement: A review,” *Polymers (Basel).*, vol. 12, no. 6, p. 1337, 2020, doi: 10.3390/POLYM12061337.
[46] Z. Han, S. Sun, H. Fu, and Y. Fu, “Multi-scale low-entropy method for optimizing the processing parameters during automated fiber placement,” *Materials (Basel).*, vol. 10, no. 9, pp. 1–18, 2017, doi: 10.3390/ma10091024.
[47] C. Wanigasekara, E. Oromiehie, A. Swain, B. G. Prusty, and S. Kiong Nguang, “Machine Learning Based Predictive Model for AFP-Based Unidirectional Composite Laminates,” *IEEE Trans. Ind. INFORMATICS*, vol. 16, no. 4, pp. 2315–2324, 2020.
[48] K. M. Kaleemulla and B. Siddeswarappa, “Influence of fiber orientation on the in-plane mechanical properties of laminated hybrid polymer composites,” *J. Reinf. Plast. Compos.*, vol. 29, no. 12, pp. 1900–1914, 2010, doi: 10.1177/0731684409340806.
[49] Y. S. Mohamed and A. Abdelbary, “Theoretical and experimental study on the influence of fiber orientation on the tensile properties of unidirectional carbon fiber/epoxy composite,” *Alexandria Eng. J.*, vol. 67, pp. 693–705, 2023, doi: 10.1016/j.aej.2022.12.058.

[50] K. Uhlig *et al.*, “Meso-scaled finite element analysis of fiber reinforced plastics made by Tailored Fiber Placement,” *Compos. Struct.*, vol. 143, pp. 53–62, 2016, doi: 10.1016/j.compstruct.2016.01.049.
[51] A. Leif, F. Donald, and R. Byron, *Experimental Characterization of Advanced Composite Materials*. 2014.
[52] Q. Guo, Y. Zhang, D. Li, Q. Lv, X. Sun, and M. Ma, “Experimental and numerical investigation of open-hole tensile properties and damage mechanisms of 3D woven composites under weft-loading,” *Thin-Walled Struct.*, vol. 161, no. January, p. 107455, 2021, doi: 10.1016/j.tws.2021.107455.
[53] A. J. Mendoza, J. E. Goodsell, A. J. Ritchey, R. B. Pipes, and M. Koslowski, “A parametric study of fiber volume fraction distribution on the failure initiation location in open hole off-axis tensile specimen,” *Compos. Sci. Technol.*, vol. 71, no. 16, pp. 1819–1825, 2011, doi: 10.1016/j.compscitech.2011.08.008.
[54] M. Medetbekova, H. F. Christensen, F. Amour, S. Salimzadeh, and H. M. Nick, “High pressure jet drilling effect in chalk and alteration of local geomechanics properties surrounding the radial hole,” *Int. J. Mech. Sci.*, vol. 191, no. March 2020, p. 105954, 2021, doi: 10.1016/j.ijmecsci.2020.105954.
[55] H. Wu, G. Zhao, and W. Liang, “Investigation of cracking behavior and mechanism of sandstone specimens with a hole under compression,” vol. 163, no. August, 2019, doi: 10.1016/j.ijmecsci.2019.105084.
[56] Y. Sun, W. Hu, F. Shen, Q. Meng, and Y. Xu, “Numerical simulations of the fatigue damage evolution at a fastener hole treated by cold expansion or with interference fi t pin,” *Int. J. Mech. Sci.*, vol. 107, pp. 188–200, 2016, doi: 10.1016/j.ijmecsci.2016.01.015.
[57] D. S. Sharma, “Stress distribution around polygonal holes,” *Int. J. Mech. Sci.*, vol. 65, no. 1, pp. 115–124, 2012, doi: 10.1016/j.ijmecsci.2012.09.009.
[58] D. Zhang, X. Zheng, and T. Wu, “Damage characteristics of open-hole laminated composites subjected to longitudinal loads,” *Compos. Struct.*, vol. 230, no. September, p. 111474, 2019, doi: 10.1016/j.compstruct.2019.111474.
[59] D5766/D5766M-11, “Standard Test Method for Open-Hole Tensile Strength of Polymer Matrix Composite,” vol. 11, no. Reapproved, pp. 1–7, 2018, doi: 10.1520/D5766.
[60] E. Strungar, D. Lobanov, and V. Wildemann, “Evaluation of the Sensitivity of Various Reinforcement Patterns for Structural Carbon Fibers to Open Holes during Tensile Tests,” 2021.
[61] J. Liu, L. Wang, Y. He, Y. Zhang, X. Yuan, and W. Li, “Experimental study of notched tensile strength of large open-hole carbon fiber reinforced polymer laminates at low temperature,” *Compos. Commun.*, vol. 39, no. December 2022, p. 101546, 2023, doi: 10.1016/j.coco.2023.101546.
[62] N. Shaari and A. Jumahat, “Hole Size Effects on the Open Hole Tensile Properties of Woven Kevlar-Glass SCIENCE & TECHNOLOGY Hole Size Effects on the Open Hole Tensile Properties of Woven Kevlar-Glass Fibre Hybrid Composite Laminates,” no. March, 2017.
[63] Z. Su, C. Xie, and Y. Tang, “Stress distribution analysis and optimization for composite laminate containing hole of different shapes,” *Aerosp. Sci. Technol.*, vol. 76, pp. 466–470, 2018, doi: 10.1016/j.ast.2018.01.046.
[64] R. Mohammadi, M. A. Najafabadi, M. Saeedifar, J. Yousefi, and G. Minak, “Correlation of acoustic emission with finite element predicted damages in

open-hole tensile laminated composites," *Compos. Part B Eng.*, vol. 108, pp. 427–435, 2017, doi: 10.1016/j.compositesb.2016.09.101.
[65] R. K. Gupta, A. Mahato, and A. Bhattacharya, *Notch Shape Influence on Damage Evolution of Al/CFRP Laminates Under Tensile Loading: Experimental and Numerical Analysis*, vol. 29, no. 5. Springer Netherlands, 2022.
[66] A. A. Khodunov, V. V Bogachev, and A. S. Borodulin, "Advances in tailored fiber placement technology," *J. Phys. Conf. Ser.*, vol. 1990, no. 1, p. 012041, Aug. 2021, doi: 10.1088/1742-6596/1990/1/012041.
[67] K. Uhlig *et al.*, "Strength of CFRP open hole laminates made from NCF , TFP and braided preforms under cyclic tensile loading Strength of CFRP open hole laminates made from NCF , TFP and braided preforms under cyclic tensile loading," vol. 8011, 2013, doi: 10.1179/174328910X12647080902772.
[68] S. A. Jr, L. Bittrich, and A. Spickenheuer, "Improving the open-hole tension characteristics with variable-axial composite laminates : Optimization , progressive damage modeling and experimental observations," vol. 185, no. August 2019, 2020, doi: 10.1016/j.compscitech.2019.107889.
[69] M. A. Orlov, I. A. Polikarpova, and V. I. Solodilov, "Research of physical and mechanical properties of reinforced carbon fiber plastics based on tfp-preforms," *IOP Conf. Ser. Mater. Sci. Eng.*, vol. 934, no. 1, 2019, doi: 10.1088/1757-899X/934/1/012066.
[70] L. Bittrich *et al.*, "On the Resin Transfer Molding (RTM) Infiltration of Fiber-Reinforced Composites Made by Tailored Fiber Placement," *Polymers (Basel).*, vol. 14, no. 22, pp. 1–13, 2022, doi: 10.3390/polym14224873.
[71] P. Mattheij, K. Gliesche, and D. Feltin, "Tailored Fiber Placement-Mechanical Properties and Applications.pdf." 1998.
[72] H. M. El-dessouky, "Tailored fi bre placement of commingled carbon-thermoplastic fi bres for notch-insensitive composites," *Compos. Struct.*, vol. 214, no. February, pp. 348–358, 2019, doi: 10.1016/j.compstruct.2019.02.043.
[73] B. C. Kim, K. Hazra, P. Weaver, and K. Potter, "Limitations of fibre placement techniques for variable angle tow composites and their process-induced defects," *ICCM Int. Conf. Compos. Mater.*, no. August, 2011.
[74] P. Schiebe, J. K. Backhaus, and A. S. Herrmann, "Investigation of the deformation of carbon fibre rovings in curved paths," *ICCM Int. Conf. Compos. Mater.*, 2009.
[75] S. K. Dwivedi, M. Vishwakarma, and P. A. Soni, "Advances and Researches on Non Destructive Testing: A Review," *Mater. Today Proc.*, vol. 5, no. 2, pp. 3690–3698, 2018, doi: 10.1016/j.matpr.2017.11.620.
[76] M. Jolly *et al.*, "Review of Non-destructive Testing (NDT) Techniques and their Applicability to Thick Walled Composites," *Sci. Direct*, vol. 38, pp. 129–136, 2015, doi: 10.1016/j.procir.2015.07.043.
[77] M. Asif, M. A. Khan, S. Z. Khan, R. S. Choudhry, and K. A. Khan, "Identification of an effective nondestructive technique for bond defect determination in laminate composites—A technical review," *J. Compos. Mater.*, vol. 52, no. 26, pp. 3589–3599, 2018, doi: 10.1177/0021998318766595.
[78] P. Duchene, S. Chaki, A. Ayadi, and P. Krawczak, "A review of non-destructive techniques used for mechanical damage assessment in polymer composites," *J. Mater. Sci.*, vol. 53, no. 11, pp. 7915–7938, 2018, doi:

10.1007/s10853-018-2045-6.
[79] P. Vaara and J. Leinonen, *Technology Survey on NDT of Carbon-fiber Composites*. 2012.
[80] S.Gholizadeh, “A review of non-destructive testing methods of composite materials,” *ScienceDirect*, vol. 1, no. 00, pp. 50–57, 2016, [Online]. Available: www.sciencedirect.com%5Cnwww.elsevier.com/locate/procedia.
[81] S. Kumar and D. Mahto, “Recent Trends In Industrial And Other Engineering Applications Of Non Destructive Testing: A Review,” *Int. J. Sci. Eng. Res.*, vol. 4, no. 9, pp. 183–195, 2013.
[82] R. D. Adams and P. Cawley, “Defect types and non-destructive testing techniques for composites and bonded joints,” *Constr. Build. Mater.*, vol. 3, no. 4, pp. 170–183, 1988, doi: 10.1016/0950-0618(89)90011-1.
[83] M. Bowkett and K. Thanapalan, “Comparative analysis of failure detection methods of composites materials’ systems,” *Syst. Sci. Control Eng.*, vol. 5, no. 1, pp. 168–177, 2017, doi: 10.1080/21642583.2017.1311240.
[84] N. Mccormick and J. Lord, “Digital Image Correlation,” *Mater. Today*, vol. 13, no. 12, pp. 52–54, 2014, doi: 10.1016/S1369-7021(10)70235-2.
[85] B. Pan, “Digital image correlation for surface deformation measurement : historical developments , recent advances and future goals,” *Meas. Sci. Technol.*, 2018.
[86] F. Hild and S. Roux, “Digital image correlation: From displacement measurement to identification of elastic properties - A review,” *Strain*, vol. 42, no. 2, pp. 69–80, 2006, doi: 10.1111/j.1475-1305.2006.00258.x.
[87] T. C. Chu, W. F. Ranson, and M. A. Sutton, “Applications of digital-image-correlation techniques to experimental mechanics,” *Exp. Mech.*, vol. 25, no. 3, pp. 232–244, 1985, doi: 10.1007/BF02325092.
[88] B. Pan, K. Qian, H. Xie, and A. Asundi, “Two-dimensional digital image correlation for in-plane displacement and strain measurement: A review,” *Meas. Sci. Technol.*, vol. 20, no. 6, 2009, doi: 10.1088/0957-0233/20/6/062001.
[89] M. L. Aparna, G. Chaitanya, K. Srinivas, and J. Appa, “Fatigue Testing of Continuous GFRP Composites Using Digital Image Correlation (DIC) Technique a Review,” vol. 2, pp. 3125–3131, 2015, doi: 10.1016/j.matpr.2015.07.275.
[90] H. Zhang *et al.*, “Failure analysis of 3D printed woven composite plates with holes under tensile and shear loading,” *Compos. Part B Eng.*, vol. 186, 2020, doi: 10.1016/j.compositesb.2020.107835.
[91] M. Elyoussef, W. Abuzaid, and M. Alkhader, “Experimental assessment of temperature effect on open-hole notch sensitivity in woven carbon fiber composites,” *Arch. Appl. Mech.*, vol. 91, no. 4, pp. 1273–1290, 2021, doi: 10.1007/s00419-020-01822-z.
[92] S. Venkatachalam, S. M. Khaja Mohiddin, and H. Murthy, “Determination of damage evolution in CFRP subjected to cyclic loading using DIC,” *Fatigue Fract. Eng. Mater. Struct.*, vol. 41, no. 6, pp. 1412–1425, 2018, doi: 10.1111/ffe.12786.
[93] Y. Y. Hung, “Shearography: A New Optical Method For Strain Measurement And Nondestructive Testing,” *Opt. Eng.*, vol. 21, no. 3, 1982, doi: 10.1117/12.7972920.
[94] Y. Y. Hung, W. D. Luo, L. Lin, and H. M. Shang, “Shearography for rapid nondestructive evaluation of bonded composite structures,” *Opt. Lasers Eng.*,

vol. 24, pp. 161–182, 1996, doi: 10.4271/1999-01-0947.
[95] Y. Y. Hung *et al.*, “Review and comparison of shearography and active thermography for nondestructive evaluation,” *Mater. Sci. Eng. R Reports*, vol. 64, no. 5–6, pp. 73–112, 2009, doi: 10.1016/j.mser.2008.11.001.
[96] D. Francis, R. P. Tatam, and R. M. Groves, “Shearography technology and applications: A review,” *Meas. Sci. Technol.*, vol. 21, no. 10, 2010, doi: 10.1088/0957-0233/21/10/102001.
[97] R. M. Groves, E. Chehura, W. Li, S. E. Staines, S. W. James, and R. P. Tatam, “Surface strain measurement: A comparison of speckle shearing interferometry and optical fibre Bragg gratings with resistance foil strain gauges,” *Meas. Sci. Technol.*, vol. 18, no. 5, pp. 1175–1184, 2007, doi: 10.1088/0957-0233/18/5/003.
[98] Y. Y. Hung, “Shearography for Non-destructive Evaluation of Composite Structures,” in *Optics and Lasers in Engineering*, 1996, vol. 24, pp. 161–182, doi: 10.4271/1999-01-0947.
[99] Y. Y. Hung, “Digital Shearography versus TV-holography for Non-destructive Evaluation,” *Opt. Lasers Eng.*, vol. 26, no. 4-5 SPEC. ISS., pp. 421–436, 1997, doi: 10.1016/0143-8166(95)00141-7.
[100] Y. Y. Hung, “A SPECKLE-SHEARING INTERFEROMETER A TOOL FOR MEASURING DERIVATIVES OF SURFACE DISPLACEMENTS,” *Opt. Commun.*, vol. 11, no. 2, pp. 1–23, 1974.
[101] M. Burkov, P. Lyubutin, A. Byakov, and S. Panin, “Detecting barely visible impact damages of honeycomb and laminate CFRP using digital shearography,” *AIP Conf. Proc.*, vol. 1909, no. December, 2017, doi: 10.1063/1.5013703.
[102] G. De Angelis, E. Dati, M. Bernabei, and F. Leccese, “Development on aerospace composite structures investigation using thermography and shearography in comparison to traditional NDT methods,” *2nd IEEE Int. Work. Metrol. Aerospace, Metroaerosp. 2015 - Proc.*, vol. 1, pp. 49–55, 2015, doi: 10.1109/MetroAeroSpace.2015.7180625.
[103] M. Georges, C. Srajbr, P. Menner, J. Koch, and A. Dillenz, “Thermography and Shearography Inspection of Composite Hybrid Sandwich Structure Made of CFRP and GFRP Core and Titanium Skins,” no. Figure 1, p. 484, 2018, doi: 10.3390/icem18-05384.
[104] N. Xu, X. Xie, X. Chen, and L. Yang, “Shearography for specular object inspection,” *Opt. Lasers Eng.*, vol. 61, pp. 14–18, 2014, doi: 10.1016/j.optlaseng.2014.04.015.
[105] X. Xie, C. P. Lee, J. Li, B. Zhang, and L. Yang, “Polarized digital shearography for simultaneous dual shearing directions measurements,” *Rev. Sci. Instrum.*, vol. 87, no. 8, 2016, doi: 10.1063/1.4961473.
[106] P. Blain *et al.*, “Artificial defects in CFRP composite structure for thermography and shearography nondestructive inspection,” *Fifth Int. Conf. Opt. Photonics Eng.*, vol. 10449, no. June 2017, p. 104493H, 2017, doi: 10.1117/12.2271701.
[107] Y. Ye, K. Ma, H. Zhou, D. Arola, and D. Zhang, “An automated shearography system for cylindrical surface inspection,” *Meas. J. Int. Meas. Confed.*, vol. 135, pp. 400–405, 2019, doi: 10.1016/j.measurement.2018.11.085.
[108] F. A. Jenkins and H. E. White, *FUNDAMENTALS Of OPTICS, fourth edition*. 1957.
[109] A. Frommknecht and I. Effenberger, “3D Milling Edge Inspection of Cfrp Parts

By Optical Methods," *Int. Symp. Struct. Heal. Monit. Nondestruct. Test.*, no. October, pp. 1–8, 2018.
[110] D. Girolamo, H. Y. Chang, and F. G. Yuan, "Impact damage visualization in a honeycomb composite panel through laser inspection using zero-lag cross-correlation imaging condition," *Ultrasonics*, vol. 87, pp. 152–165, 2018, doi: 10.1016/j.ultras.2018.02.014.
[111] A. Bondyra, P. Pastuszak D., M. Chwał, and A. Stawiarski, "Analysis of composite structure deformations based on 3D laser scanner measurements," *Compos. Theory Pract.*, vol. 1, pp. 38–42, 2014.
[112] F. Shadmehri *et al.*, "Laser-vision inspection system for Automated Fiber Placement (AFP) process," *ICCM Int. Conf. Compos. Mater.*, vol. 2015-July, no. July, pp. 19–24, 2015.
[113] Hexagon, "Pioneering composite inspection technology," no. January, 2020, [Online]. Available: http://www.amrc.co.uk/about/background.
[114] Hexagon Manufacturing Intelligence, "COMPOSITE INSPECTION SOLUTIONS," no. 514, pp. 1–2, 2020.
[115] J. Dong, A. Locquet, N. F. Declercq, and D. S. Citrin, "Polarization-resolved terahertz imaging of intra- A nd inter-laminar damages in hybrid fiber-reinforced composite laminate subject to low-velocity impact," *Compos. Part B Eng.*, vol. 92, pp. 167–174, 2016, doi: 10.1016/j.compositesb.2016.02.016.
[116] D. Abbott and X. C. Zhang, "Scanning the issue: T-ray imaging, sensing, and retection," *Proc. IEEE*, vol. 95, no. 8, pp. 1509–1513, 2007, doi: 10.1109/JPROC.2007.900894.
[117] W. L. Chan, J. Deibel, and D. M. Mittleman, "Imaging with terahertz radiation," *Reports Prog. Phys.*, vol. 70, no. 8, pp. 1325–1379, 2007, doi: 10.1088/0034-4885/70/8/R02.
[118] I. Amenabar, F. Lopez, and A. Mendikute, "In Introductory Review to THz Non-Destructive Testing of Composite Mater," *J. Infrared, Millimeter, Terahertz Waves*, pp. 152–169, 2013, doi: 10.1007/s10762-012-9949-z.
[119] J. Zhang, W. Li, H. Cui, C. Shi, X. Han, and Y. Ma, "Nondestructive Evaluation of Carbon Fiber Reinforced Polymer Composites Using Reflective Terahertz Imaging," *Sensors*, 2016, doi: 10.3390/s16060875.
[120] V. P. Wallace, E. MacPherson, J. A. Zeitler, and C. Reid, "Three-dimensional imaging of optically opaque materials using nonionizing terahertz radiation," *J. Opt. Soc. Am. A*, vol. 25, no. 12, p. 3120, 2008, doi: 10.1364/josaa.25.003120.
[121] N. Karpowicz, H. Zhong, J. Xu, K. Lin, J. Hwang, and X. Zhang, "Comparison between pulsed terahertz time-domain imaging and continuous wave terahertz imaging," *Semicond. Sci. Technol.*, 2005, doi: 10.1088/0268-1242/20/7/021.
[122] F. Ospald, J. Guillet, and R. M. Edo, "Aeronautics composite material inspection with a terahertz time- domain spectroscopy system," *Opt. Eng.*, 2013.
[123] S. Zhong, "Progress in terahertz nondestructive testing: A review," *Front. Mech. Eng.*, vol. 14, no. 3, pp. 273–281, 2019, doi: 10.1007/s11465-018-0495-9.
[124] C. Ciccarelli *et al.*, "Terahertz Time-Domain Spectroscopy," *Sci. VIDEO Protoc.*, 2019.
[125] C. Stoik, M. Bohn, and J. Blackshire, "Nondestructive evaluation of aircraft composites using reflective terahertz time domain spectroscopy," *NDT E Int.*,

vol. 43, no. 2, pp. 106–115, 2010, doi: 10.1016/j.ndteint.2009.09.005.
[126] F. Rutz, M. Koch, S. Khare, M. Moneke, H. Richter, and U. Ewert, “Terahertz quality control of polymeric products,” *Int. J. Infrared Millimeter Waves*, vol. 27, no. 4, pp. 547–556, 2006, doi: 10.1007/s10762-006-9106-7.
[127] N. Palka and D. Miedzinska, “Detailed non-destructive evaluation of UHMWPE composites in the terahertz range,” *Opt. Quantum Electron.*, vol. 46, no. 4, pp. 515–525, 2014, doi: 10.1007/s11082-013-9836-4.
[128] N. (DE) Juergen Ernst, Erlangen (DE); Stephan Junger, Bubenreuth (DE); Wladimir Tschekalinskij, “MEASUREMENT OF A FIBER DIRECTION OFA CARBON FIBER MATERIAL AND FABRICATION OF AN OBJECT IN CARBON FIBER COMPOSITE TECHNIQUE,” *United States Pat.*, vol. 2, no. 12, 2016.
[129] Fraunhofer IIS, “POLKA – polarization camera uncover the invisible,” pp. 1–2, 2019.
[130] LUCID Vision Labs, “Carbon Fiber Inspection with the Phoenix Polarization Camera,” 2019. https://thinklucid.com/carbon-fiber-inspection-with-the-phoenix-polarization-camera/ (accessed Jun. 10, 2020).
[131] Novus Light. Technologies Today, “CX Polarization Cameras Detect Defects in Glass, CFRP, Reflective Surfaces,” 2020. https://www.novuslight.com/cx-polarization-cameras-detect-defects-in-glass-cfrp-reflective-surfaces_N8530.html (accessed Jun. 14, 2020).
[132] OEM Automatic Ltd, “Sony - Polarized Camaera XCG-CP510.” https://www.oem.co.uk/products/machine-vision-,-a-,-code-reading/machine-vision-cameras/area-scan-_-486689/gig-e-cameras-_-636035/sony---polarized-camaera-_-640519 (accessed Jun. 24, 2020).
[133] J. Ernst, “PolKa – A Polarization Camera for NDT of Carbon Fiber Reinforced Plastics and More …,” *4th Int. Symp. NDT Aerosp. 2012 - Th.2.A.4*, p. 2012, 2012.
[134] G. A. Atkinson, S. O. H. Nash, and L. N. Smith, “Precision Fibre Angle Inspection for Carbon Fibre Composite Structures Using Polarisation Vision,” 2021.
[135] J. Dong *et al.*, “Visualization of subsurface damage in woven carbon fiber-reinforced composites using polarization-sensitive terahertz imaging,” *NDT E Int.*, vol. 99, no. March, pp. 72–79, 2018, doi: 10.1016/j.ndteint.2018.07.001.
[136] S. Kharkovsky, A. C. Ryley, V. Stephen, and R. Zoughi, “Dual-polarized microwave near-field reflectometer for non-invasive inspection of carbon fiber reinforced polymer (CFRP) strengthened structures,” in *IEEE Instrumentation and Measurement Technology Conference Proceedings*, 2006, vol. 57, no. 1, pp. 168–175, doi: 10.1109/TIM.2007.909497.
[137] Huntsnan, “Araldite ® LY 1564* / Aradur ® 2954 *, (https://files.ekmcdn.com/mouldlife/resources/other/araldite-ly-1564-aradur-2954-eur-e-1-.pdf),” 2011.
[138] Easycomposites, “Addition cure silicone rubber (AS40), (https://media.easycomposites.co.uk/datasheets/EC-TDS-AS40-Addition-Cure-Silicone-Rubber.pdf),” 2020.
[139] S. C.-A. C. Materials, “VTC401 Epoxy Component Prepreg, Product Data,” no. February, pp. 4–7, 2022.
[140] F. Meriaudeau, M. Ferraton, C. Stolz, O. Morel, and L. Bigué, “Polarization imaging for industrial inspection,” *Image Process. Mach. Vis. Appl.*, vol. 6813, no. May 2014, p. 681308, 2008, doi: 10.1117/12.767915.

[141] J. S. Tyo, D. L. Goldstein, D. B. Chenault, and J. A. Shaw, “Review of passive imaging polarimetry for remote sensing applications,” *Appl. Opt.*, vol. 45, no. 22, pp. 5453–5469, 2006, doi: 10.1364/AO.45.005453.
[142] TORALF SCHARF, *Polarized light in liquid crystals and polymers*. 2006.
[143] “Polarization-based Industrial Cameras: Basics and Applications.”
[144] L. Chiominto, G. D’Emilia, and E. Natale, “Using light polarization to identify fiber orientation in carbon fiber components: metrological analysis.” Aug. 05, 2024, doi: 10.20944/preprints202408.0310.v1.
[145] MATLAB, “Fit curves and surfaces to data using regression, interpolation, and smoothing,” pp. 1–7, 2025.
[146] Y. Chen, Q. Yu, and C. B. Xu, “A convenient method for quantifying collagen fibers in atherosclerotic lesions by imagej software,” *Int. J. Clin. Exp. Med.*, vol. 10, no. 10, pp. 14904–14910, 2017.
[147] J. Schindelin, C. T. Rueden, M. C. Hiner, and K. W. Eliceiri, “The ImageJ ecosystem: An open platform for biomedical image analysis,” *Mol. Reprod. Dev.*, vol. 82, no. 7–8, pp. 518–529, 2015, doi: 10.1002/mrd.22489.
[148] M. D. Abràmoff, P. J. Magalhães, and S. J. Ram, “Image processing with imageJ,” *Biophotonics Int.*, vol. 11, no. 7, pp. 36–41, 2004, doi: 10.1201/9781420005615.ax4.
[149] T. J. Collins, “ImageJ for Microscopy,” *Biotechniques*, vol. 43, no. sup1, 2007, doi: 10.2144/000112517.
[150] H. Anton, B. Florin, V. Andrei-Daniel, V. Daniel, T. Daniela-Ioana, and A. Cătălin, “Mechanical Characteristics Evaluation of a Single Ply and Multi-Ply Carbon Fiber-Reinforced Plastic Subjected to Tensile and Bending Loads,” *Polymers (Basel).*, vol. 14, no. 15, 2022, doi: 10.3390/polym14153213.
[151] R. Kumar, L. P. Mikkelsen, H. Lilholt, and B. Madsen, “Data Analysis,” 2021.
[152] F. Mesquita *et al.*, “Tensile failure strain and microstructure of unidirectional carbon fibre non-crimp fabric composites,” *Compos. Part B Eng.*, vol. 243, pp. 1–17, 2022, doi: 10.1016/j.compositesb.2022.110123.
[153] T. Tagawa and T. Miyata, “Size effect on tensile strength of carbon fibers,” *Mater. Sci. Eng. A*, vol. 238, no. 2, pp. 336–342, 1997, doi: 10.1016/S0921-5093(97)00454-1.
[154] M. A. Lepore, L. Ferrante, L. Sanguigno, and A. R. Maligno, “A non-crimp fabric mechanical characterization for the production of aerospace components,” *Mater. Des. Process. Commun.*, vol. 3, no. 5, 2021, doi: 10.1002/mdp2.222.
[155] W. Najjar, X. Legrand, D. Soulat, and P. Dal Santo, “Experimental analysis and numerical modelling of dry carbon woven reinforcement preforming,” *J. Reinf. Plast. Compos.*, vol. 38, no. 21–22, pp. 974–994, 2019, doi: 10.1177/0731684419859071.